รายงานวิจัยฉบับสมบูรณ์

การเตรียมสารประกอบไฮบริดอนินทรีย์และสารประกอบโลหะออกไซด์กลุ่มเพอรอฟสไกต์ด้วยเทคนิคโซลโวเทอร์มอล

โดย รองศาสตราจารย์ ดร. อภินภัส รุจิวัตร์

พฤษภาคม ๒๕๕๔

สัญญาเลขที่ 5180012

รายงานวิจัยฉบับสมบูรณ์

โครงการ การเตรียมสารประกอบไฮบริดอนินทรีย์และสารประกอบโลหะออกไซด์กลุ่มเพอรอฟสไกต์ด้วยเทคนิคโซลโวเทอร์มอล

โดย รองศาสตราจารย์ ดร. อภินภัส รุจิวัตร์

ภาควิชาเคมี คณะวิทยาศาสตร์ มหาวิทยาลัยเชียงใหม่

สนับสนุนโดยสำนักงานกองทุนสนับสนุนการวิจัย

(ความเห็นในรายงานนี้เป็นของผู้วิจัย สกว. ไม่จำเป็นต้องเห็นด้วยเสมอไป)

PREAMBLE & ACKNOWLEDGEMENTS

This report is a summarization of the research project funded by the Thailand Research Fund under grant number *RSA5180012*, which is the continuation of the prior, *RMU4880031*. Due to the diversifying nature of the project, the report starts with the basic technical note which is the main stream of the work, followed by scientific contents which are divided according to the published articles, and the brief articles reporting on crystallographic data for some of our newly synthesized structure published in *Acta Crystallographica E*.

Here in, I also would like to express my sincere and deepest gratitude to the TRF who has cherished and fostered basic scientific research in Thailand since day one. Without the TRF, the passion in my research would not be real, but reel. Special thanks also go to the members of the Inorganic Materials Research Units who dedicated their hard work in the project, Prof. Natarajan and Dr. Prior who are our good friends and helping us to move toward our better as always.

(Assoc. Prof. Apinpus Rujiwatra)
May 9th, 2011

บทคัดย่อ

เทคนิคการสังเคราะห์สารแบบโซลโวเทอร์มอล (รวมถึงเทคนิคไฮโดรเทอร์มอล) เป็นเทคนิคทางเคมีที่ได้รับความสนใจจากนักวิทยาศาสตร์และนักเทคโนโลยีเป็นอย่างมาก เนื่องด้วยข้อดีหลายประการของเทคนิคนี้ที่ได้เปรียบเทคนิคการสังเคราะห์อื่นๆ เช่น การไม่เป็นพิษต่อสิ่งแวดล้อม ความคุ้มค่าด้านพลังงานที่ใช้ รวมทั้งความเป็นไปได้ในการใช้เทคนิคนี้ในการเตรียมสารที่ไม่เสถียรทางเทอร์โมไดนามิกส์ ซึ่งไม่สามารถเตรียมได้ด้วยเทคนิคอื่นๆ และการขยายขนาดการเตรียมไปสู่ระดับอุตสาหกรรม ในโครงการวิจัยนี้ได้ประยุกต์ใช้เทคนิคโซลโวเทอร์มอลเพื่อการสังเคราะห์สารสองกลุ่มด้วยกัน ได้แก่ กลุ่มโครงข่ายผสมอนินทรีย์–อินทรีย์ (hybrid inorganic–organic materials) และ กลุ่มวัสดุโครงข่ายโลหะออกไซด์ที่มีโครงสร้างแบบเพอรอฟสไกต์ (perovskite metal oxide framework) แนวคิดในการออกแบบโครงสร้างผลึกทั้งในระดับโมเลกุล และระดับไมโครได้ถูกนำมาใช้ร่วมกับเทคนิคการสังเคราะห์สารแบบโซลโวเทอร์มอลอย่างจริงจัง โดยมีทั้งแนวทางการใช้กระบวนการควบคุมโครงข่ายของโครงสร้างผลึกผ่านการเลือกโมเลกุลสารอินทรีย์ในระบบการสังเคราะห์ และแนวทางการปรับพารามิเตอร์ของกระบวนการสังเคราะห์อย่างละเอียด

ในส่วนของสารกลุ่มโครงข่ายผสมอนินทรีย์–อินทรีย์นั้น ในโครงการนี้ได้มีการออกแบบและเตรียมสารประกอบโครงสร้างใหม่ได้ทั้งหมด 11 โครงสร้าง: $[V_{10}O_{27}(OH)]_2(C_6N_2H_{14})(C_6N_2H_{13})(C_6N_2H_{12}).2H_2O$ (**I**), $Co^{II}(\mu\text{–}C_2N_2H_8)_2[V_4^{IV}V_2^{V}O_{14}]$ (**II**), $[C_{10}H_{10}N_2][La(SO_4)_2]_32H_2O$ (**III**), $[C_{10}H_{10}N_2][La(SO_4)_2(H_2O)_2]_2$ (**IVa**), $[C_{10}H_{10}N_2][Pr(SO_4)_2(H_2O)_2]_2$ (**IVb**), $[C_{10}H_{10}N_2][Nd_2(SO_4)_4(H_2O)_2]_2$ (**Va**), $[C_{10}H_{10}N_2][Sm_2(SO_4)_4(H_2O)_2]_2$ (**Vb**), and $[C_{10}H_{10}N_2][Eu_2(SO_4)_4(H_2O)_2]_2$ (**Vc**), $[Co(H_2O)_4(4,4'\text{–bipy})](4,4'\text{–bipyH}_2)](SO_4).2H_2O$ (**VI**), $[Co_2(4,4'\text{–bipy})_2(SO_4)_2(H_2O)_6].4(H_2O)$ (**VII**), $[Co_2(4,4'\text{–bipy})_2(SO_4)_2(H_2O)_6].4(H_2O)$ (**VII**), $[Co(C_{10}H_{21}N_2)C_{l3}]$ (**IX**), $[Co(OH_2)_6]_{0.35}[Co_2(SO_4)(OH)_3]$ (**X**), $[Co^{II}(C_2H_8N_2)_3]SO_4$ (**XI**) โดยที่โครงสร้างบางโครงสร้างในกลุ่มนี้ได้แสดงสมบัติทางแสงที่น่าสนใจด้วย จากการวิเคราะห์โครงสร้างอย่างละเอียดพบว่าพันธะไฮโดรเจนทั้งแบบทั่วไปและแบบที่มีพลังงานพันธะต่ำมากๆ มีส่วนสำคัญเป็นอย่างมาก นอกเหนือไปจากพันธะโคออร์ดิเนตโควาเลนต์ ในการกำหนดโครงข่ายของสารประกอบที่เตรียมได้ ซึ่งเป็นแนวทางสำคัญในการกำหนดโครงข่ายในรายละเอียดที่แตกต่างกันของสารอินทรีย์ที่ใช้ศึกษา อันได้แก่กลุ่มสารประกอบไดเอมีน ถึงแม้ว่าอันตรกิริยาระหว่างหมู่ไดเอมีนกับโลหะที่ใช้ศึกษาจะไม่ปรากฏรูปแบบที่ชัดเจนเช่นในกรณีของสารประกอบไดคาร์บอกซิเลท บทบาทการเป็นสารกำหนดโครงสร้างของสารประกอบเอมีนนั้นมีความชัดเจน และซับซ้อน นอกจากนี้แล้วยังได้มีความพยายามในการใช้ซัลเฟต ซึ่งมีรูปร่างเป็นแบบทรงเหลี่ยมสี่หน้าในการเป็นหน่วยโครงข่ายทุติยภูมิของโครงข่าย ซึ่งพบว่าโดยมากแล้วซัลเฟตจะเกาะอยู่กับโครงข่ายในลักษณะโมโนเดนเทตมากกว่าที่จะทำหน้าที่เป็นสะพานเชื่อมโครงข่ายอย่างแท้จริง

ในส่วนของกลุ่มวัสดุโครงข่ายโลหะออกไซด์ที่มีโครงสร้างแบบเพอรอฟสไกต์นั้น ในที่นี้ได้มีการศึกษาโครงข่ายของไททาเนต เซอร์โคเนต และไนโอเบต โดยได้มีการปรับแปรตัวแปรของสภาวะโซลโวเทอร์มอลโดยเฉพาะอย่างยิ่ง ชนิดของของเหลวตัวกลาง และแหล่งของการให้พลังงานกระตุ้นปฏิกิริยา ที่มีบทบาทอย่างมากในการกำหนดอัตลักษณ์ของอนุภาคนาโนที่ต้องการสังเคราะห์

ABSTRACT

Due to numerous superiority to the other synthetic processes, the environmentally benign "*solvothermal technique*" has been applied to the design and synthesis of two different types of technologically important materials, namely the *hybrid inorganic-organic materials* and the *perovskite metal oxide frameworks*. The concept of "*structural design*" in association with the "*organic templation*" strategies as well as the fine-tuning of processing parameters have been exercised in the syntheses at both molecular and microscopic scales.

Regarding the hybrid inorganic-organic materials, *eleven new complexes* have been designed, synthesized and fully characterized by crystallographic and spectroscopic techniques: $[V_{10}O_{27}(OH)]_2(C_6N_2H_{14})(C_6N_2H_{13})(C_6N_2H_{12}).2H_2O$ (**I**), $Co^{II}(\mu\text{-}C_2N_2H_8)_2[V_4^{IV}V_2^{V}O_{14}]$ (**II**), $[C_{10}H_{10}N_2][La(SO_4)_2]_32H_2O$ (**III**), $[C_{10}H_{10}N_2][La(SO_4)_2(H_2O)_2]_2$ (**IVa**), $[C_{10}H_{10}N_2][Pr(SO_4)_2(H_2O)_2]_2$ (**IVb**), $[C_{10}H_{10}N_2][Nd_2(SO_4)_4(H_2O)_2]_2$ (**Va**), $[C_{10}H_{10}N_2][Sm_2(SO_4)_4(H_2O)_2]_2$ (**Vb**), and $[C_{10}H_{10}N_2][Eu_2(SO_4)_4(H_2O)_2]_2$ (**Vc**), $[Co(H_2O)_4(4,4'\text{-bipy})](4,4'\text{-bipyH}_2)](SO_4).2H_2O$ (**VI**), $[Co_2(4,4'\text{-bipy})_2(SO_4)_2(H_2O)_6].4(H_2O)$ (**VII**), $[Co_2(4,4'\text{-bipy})_2(SO_4)_2(H_2O)_6].4(H_2O)$ (**VII**), $[Co(C_{10}H_{21}N_2)C_{l3}]$ (**IX**), $[Co(OH_2)_6]_{0.35}[Co_2(SO_4)(OH)_3]$ (**X**), $[Co^{II}(C_2H_8N_2)_3]SO_4$ (**XI**). Some of these newly synthesized compounds exhibit intriguing optical properties. The structures are fully analyzed, revealing important role of both conventional and very weak hydrogen bonding interactions in addition to the coordinate covalent bonding in regulate the final network structures of the hybrid inorganic-organic materials. The template function of the organic molecules, particularly of diamine functional group, is vividly demonstrated, although no rigid pattern for the employed synthons can be established. This is the distinguish difference between the organic molecules possessing N- and O-donor atoms. The attempt to introduce the tetrahedral sulphate anion as the secondary inorganic building block into the structures is successful with the lanthanide frameworks, where most of the cooperated sulphates are present as pendants.

The manipulation of solvothermal processing parameters has been experimented with the preparation of nano-particles of three perovskite metal oxide frameworks, including *lead titanate*, *lead zirconate* and *potassium niobate*. The introduction of microwave irradiation as an alternative heating source has also attempted. The results suggested close correlation between different processing parameters on the characteristics of the yielded particles. The fine-tune of these parameters, especially type of liquid media, heating source, reaction temperature and time, can help accelerate the processing time as well as improve the characteristics of the obtained nano-powders.

EXECUTIVE SUMMARY

PROJECT TITLE

Solvothermal Preparation of Inorganic-Organic Hybrid and Perovskite Metal Oxide Compounds (Grant RSA5180012)

AREA OF STUDY/KEYWORDS

Solid state chemistry,
Chemistry of Materials,
Preparative Chemistry,
Crystallography

PROJECT DURATION

May 01, 2008 – April 30, 2011

PROJECT RATIONAL & SIGNIFICANCE

Driven by the global concerns on the critics of economic, energy, and environmental issues, a great demand for green and sustainable technologies has been erupted during the last few decades. Science serving as an important platform has also been inquired for responsibility. Innovation and development of an alternative technologies and therefore materials is one way among the many that science can offer.

Regarding an innovation of futuristic materials, chemistry has made an increasing important contribution over the last thirty years, so much so that the terms *solid state chemistry* and/or *chemistry of materials* have come into being. Fundamental research in this branch of chemistry primarily needs to achieve three goals: (*a*) development of preparative techniques to prepare new compounds or to improve their properties, (*b*) discovery of new phases with desired properties from crystal chemical criteria, and (*c*) full characterization of new phases from chemical and structural point of view. Along this line, *preparative chemistry* is bedrock, among which the so-called *hydrothermal* technique, which is later on broadened to *solvothermal*, has garnered great interests from scientists and technologists of different disciplines. Although the 'hydrothermal' term is the foremost with geological origin, the solvothermal analogue provides broader and more accurate meaning and is therefore preferable by chemists. In contrast to other conventional techniques, it offers several advantages, *e.g.* environment benignity, cost effectiveness, facility, and ability to prepare novel phases. The unique nature of the technique can also provide controllability over the uniformity of nucleation, growth and aging process. This can take the technique altogether in a direction towards a sustained human development. The solvothermal technique has also proved to be very successful for a preparation of the forthcoming technologically important compounds; *inorganic-organic hybrid materials (IOHs).* Paramount numbers of IOHs with novel structures and functions, as well as the known materials in all sorts of forms in *nano*-scale where size-dependent properties may reveal, have been achieved *via* this route. The structures in both molecular and microscopic levels can allegedly be regulated by the addition of particular organic templates to the solvothermal reactions. These templating agents may either associate as part of the final structures or function as only the matrix to control the

morphologies of the desired compounds. The as-described usage of organic templates is considered as the basic of *crystal engineering*, which has thus far proved to be the loftiest capable strategies for the design of structures and therefore functions regarding the *bottom-up* approach, albeit the fact that the fundamentals need, yet, to be established for further effective employment.

Despise of the advancement in global research and development, the current status of the research in *solid state chemistry* and/or *chemistry of materials* in Thailand is still very much in its youth. A deficiency in corresponding expertise and knowledge is apparent. With the goal of being knowledge based society and technologically independent country, it is compulsory for Thailand to establish the scientific platform in various disciplines including also those relating to *solid state chemistry* and/or *chemistry of materials* despise the lacking in many ways. This has a close correlation with a promotion in graduate studies and research of the country into the global stage. This research project should certainly fortify the national research caliber in this field to a certain extent.

Here, the usage of organic templates has been adopted for the solvothermal preparation of two different classes of the compounds, including (*a*) *transition metal-organodiamine based IOHs*, of which the diversities in both structures and properties capture the frontier research worldwide, and (*b*) *perovskite-based oxide frameworks*, which have already found tremendous usage in electronic industries.

RESEARCH OBJECTIVES

[1] To exercise the concept of *crystal engineering* and *templating approach* for the preparation of *transition metal-organodiamine* based *IOHs* with new structures using *solvothermal* technique.
[2] To adapt the solvothermal crystallization knowledge in coupling with templating approach for the preparation of *nano-particles* of *perovskite-based oxide frameworks*.
[3] To establish new knowledge and create research works of international standard.
[4] To fortify the fundamental study and research activities in solid state chemistry and crystallography in the country.
[5] To found the cooperation with both national and international research groups sharing the common research interests.

RESEARCH SCOPE & METHODOLOGY

Transition metal-organodiamine based IOHs

[1] Design and solvothermally synthesize single crystals of transition metal-organodiamine based IOHs using organodiamines of different molecularshape, flexibility and aromaticity.
[2] Characterize single crystal structures by single crystal X-ray diffraction, FT-IR and Raman spectroscopy, CHNS/O analysis and energy dispersive elemental micro-analysis.
[3] Study thermal properties by thermogravimetric and scanning caloricmetric analysis, optical properties by UV-vis and photoluminescence spectroscopy.
[4] Establish relation between molecular structures of organodiamines, type and coordination chemistry of transition metals and the yielded framework structures, and therefore template functions of the organodiamines in the studied system.

Perovskite-based oxide frameworks

[1] Study the influences of different solvothermal variables, *e.g.* type and concentration of mineralizer, solvothermal temperature and time and type and concentration of organic

additives, on the formation of perovskite-based oxide frameworks, *i.e.* lead titanates, lead zirconates and potassium niobates.

[2] Characterize phase formation by powder X-ray diffraction, electron diffraction, transmission electron microscopy and FT-IR and Raman spectroscopy, particle size and morphology and elemental composition by scanning electron microscopy and energy dispersive elemental micro-analysis.

[3] Study particle size and aggregation by laser diffraction analysis.

[4] Study electrical and optical properties of selected samples.

[5] Establish knowledge on the relation between different solvothermal parameters and yielded powders/particles.

RESEARCH OUTPUTS

Research Award

[1] CST Distinguished Young Chemist Award 2010 (Inorganic Chemistry), The Chemical Society of Thailand under the Patronage of Her Royal Highness Princess Chulabhorn Mahidol

International Publications (See Appendix)

[1] R. Wongmaneerung, **A. Rujiwatra**, R. Yimnirun, S. Ananta, Fabrication and dielectric properties of lead titanate nanocomposites, *J. Alloy Comp*. **475**(1-2), 2009, 473-478.

[2] Banlawee Yotnoi, Saranpong Yimgran, Timothy J. Prior, **Apinpus Rujiwatra**, Microwave assisted crystal growth of a new organic - decavanadate assembly: $[V_{10}O_{27}(OH)].2(C_6N_2H_{14}).(C_6N_2H_{13}).(C_6N_2H_{12}).2H_2O$, *J. Inorg. Organomet. Polym. Mater*. **18**(3), 2009, 306-313.

[3] Bunlawee Yotnoi, Jumras Limtrakul, Timothy Prior, **Apinpus Rujiwatra**, Bis(μ-1,2–diaminoethane)cobalt(II) hexavanadate, *J. Chem. Crystallogr.* **39**, 2009, 525-529.

[4] Sanchai Luachan, Bunlawee Yotnoi, Timothy Prior, **Apinpus Rujiwatra**, Trichloro-(N-butyl-1,4-diazabicyclo(2.2.2)octonium) cobalt(II), *Acta Crystallographica* E**65**(3), 2009, m321-m322.

[5] Bunlawee Yotnoi, Sanchai Luachan, Timothy Prior, **Apinpus Rujiwatra**, Intercalated brucite-type layered cobalt(II) hydroxysulfate, *Acta Crystallographica* E**65**(7), 2009, i52.

[6] Chaiyos Chankaew, **Apinpus Rujiwatra**, Hydrothermal Synthesis of Lead Titanate Fine Powders at Water Boiling Temperature, *Chiang Mai Journal of Science* **36**(3), 2010, 92-98.

[7] Bunlawee Yotnoi, Athittaya Seeharaj, Yothin Chimupala, **Apinpus Rujiwatra**, Tris(ethylenediamine cobalt(II)sulfate, *Acta Crystallographica* E**66**, 2010, m628.

[8] Saowalak Tapala, **Apinpus Rujiwatra**, Microwave-assisted hydrothermal synthesis of lead zirconate fine powders , *Maejo Intenational Journal of Science and Technology* **5**(01), 2011, 24-31.

[9] Timothy J. Prior, Bunlawee Yotnoi, **Apinpus Rujiwatra**, Microwave synthesis and crystal structures of two cobalt-4,4′-bipyridine-sulfate frameworks constructed from 1-D coordination polymers linked by hydrogen bonding, *Polyhedron* **30**, 2011, 259-268.

[10] Bunlawee Yotnoi, **Apinpus Rujiwatra**, M. L. P. Reddy, Debajit Sarma, Srinivasan Natarajan, Lanthanide sulfate frameworks: Synthesis, structure and properties, *Crystal Growth and Design* **11**(4), 2011, 1347-1356.

[11] Yothin Chimupala, Wasinee Phonsri, Timothy J. Prior, **Apinpus Rujiwatra**, Crystal growth and characterisation of a unique trinuclear V^{IV}/V^{V} complex, *Maejo Intenational Journal of Science and Technology* **5**(01), 2011, 83-95.

[12] Kittichai Jinachai, Athipong Ngamjarurojana, **Apinpus Rujiwatra**, Solvothermal Synthesis, Sintering Behavior and Dielectric Properties of Potassim Niobate Fine Powders, *Chiang Mai Journal of Science* **38**(2), 2011, 252-262.

Invited Presentations for International Conferences

[1] *Crystal growth and structures of hybrid frameworks based on cobalt/vanadium and organodiamines*, The 2nd Asian Conference on Coordination Chemistry (2nd ACCC), Jinling Riverside Conference Hotel, Nanjing, China, November 1-4, 2009.

[2] *Rapid crystal growth of two metal-organic frameworks constructed by linking of 1-D coordination polymers by hydrogen bonding*, The 10th Conference of the Asian Crystallographic Association (AsCa2010), BEXCO, Busan, Korea, October 31 – November 3, 2010.

[3] *Influences of Hydrogen Bonding Interactions in the Fabrication of Metal-Organic Coordination Compounds*, First Chiang Mai – Kyoto Symposium on Materials Science and Technology, Chiang Mai University, Thailand December 2-4, 2010.

Selected Schools/Workshops

[1] Special tutorial Course on *Reticular Chemistry* by Prof. Michael O'Keeffe, Kasetsart University, Bangkok, Thailand, January 18-22, 2010.

[2] Workshop for *ab initio Powder Structure Determination for Chemists and Materials Scientists*, Third Powder Crystallography Tutorial Course, POSCO, Pohang, Korea, October 27-29, 2010.

Research Students

There are two Ph.D. and five M.S. students enrolled in this research project. While the Ph.D. students are currently of their 4th and 3rd years under the financial support of the Royal Golden Jubilee project, all of the M.S. students who started in 2008 graduated in either 2009 or 2010. These students were either partially or fully supported financially by this project to attend various workshops and international conferences.

Research Collaboration

The collaboration with *Prof. Srinivasan Natarajan* (Indian Institute of Science, Bangalore, India) and *Dr.Timothy J. Prior* (Hull University, UK) has been fortified. The Ph.D. student, namely Ms. Bunlawee Yotnoi (under the support of the RGJ), spent 6 months with Prof. Natarajan and resulted in the publication in *Crystal Growth and Design*, and currently is conducting research under the co-supervision of Dr. Prior in UK.

In addition, the project also led to the establishment of collaboration with *Asst. Prof. Winita Boonyodom* (Department of Chemistry, Chiang Mai University) and *Asst. Prof. Mookda Pattarawarapan* (Department of Chemistry, Chiang Mai University regarding the assessment of selected compounds as potential catalysts and the design and synthesis of new organic ligands, respectively. The extension of the collective knowledge and expertise in the field to *functional design* and *practical applications* may well be expected.

BUDGET

1.2 million Baht

หมวดงบประมาณ	งบประมาณโครงการ (หมื่นบาท)				
	งวดที่ 1	งวดที่ 2	งวดที่ 3	งวดที่ 4	รวม
หมวดค่าตอบแทน (ค่าตอบแทนหัวหน้าโครงการ)	18.0	18.0	9.0	9.0	54.0
หมวดค่าวัสดุ (สารเคมี วัสดุวิทยาศาสตร์ วัสดุสำนักงาน)	6.0	7.0	6.0	0.0	19.0
หมวดค่าใช้สอยและอื่นๆ (ค่าส่งไปรษณีย์ ค่าวิเคราะห์ตัวอย่าง ค่าเดินทางภายในประเทศ ค่าถ่ายเอกสาร ค่าใบอนุญาตการใช้ฐานข้อมูล Cambridge Crystal Structure Database)	7.0	8.0	8.0	0.0	23.0
หมวดค่าเดินทางต่างประเทศ	0.0	0.0	8.0	0.0	8.0
หมวดค่าครุภัณฑ์ 1. High power microwave model 2. Infrared thermometer gun	9.0	7.0	0.0	0.0	16.0
รวม	40.0	40.0	31.0	9.0	120.0

CONTENTS

CHAPTER I

BASIC TECHNICAL NOTES

SOLVOTHERMAL (HYDROTHERMAL) SYNTHESIS

Broad definition of *hydrothermal synthesis* is *the use of aqueous solvent in the presence of mineralizers to perform any heterogeneous reaction under high pressure and temperature conditions*. This is generally performed in a close system, with the principal objective in dissolving and re-crystallizing materials that are relatively insoluble under ordinary conditions. The lower limits of temperature and pressure at which hydrothermal conditions are generated vary controversially. Byrappa and Yoshimura, for example, proposed as low temperatures and pressures as those just above room temperature and 1 atmosphere [1, 2]. Rabenau, on the other hand, defined only the temperatures to be well above 100 ^{o}C, with the pressure to be autogenously generated inside a closed reaction container [3]. Based on the definition proposed by Rabenau, s*olvothermal synthesis* can be considered as the extension of the hydrothermal predecessor, referring to *any chemical reaction in the presence of non-aqueous solvent, or solvent in supercritical or near supercritical conditions.* Because of a better extensive meaning, chemists generally prefer the term solvothermal. Fig. 1 shows distinguish position the process grips a central station, linking different important technologies, when the pressure-temperature map showing relative grids of various preparative techniques is depicted in Fig. 2, from which an environmental benignity of the technique is comprehensive.

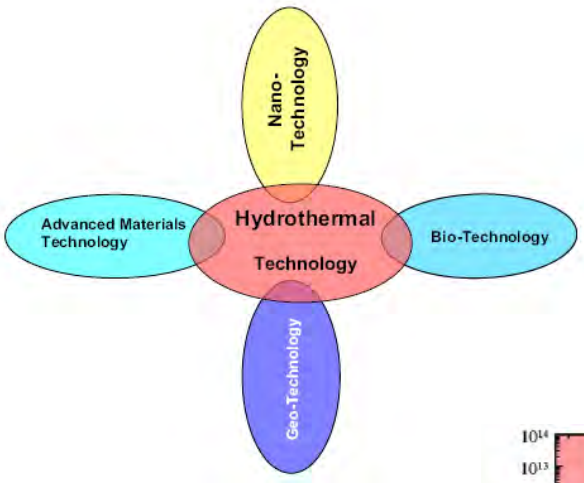

Fig. 1 *The hydrothermal process as a central node, linking different important technologies of the future [2].*

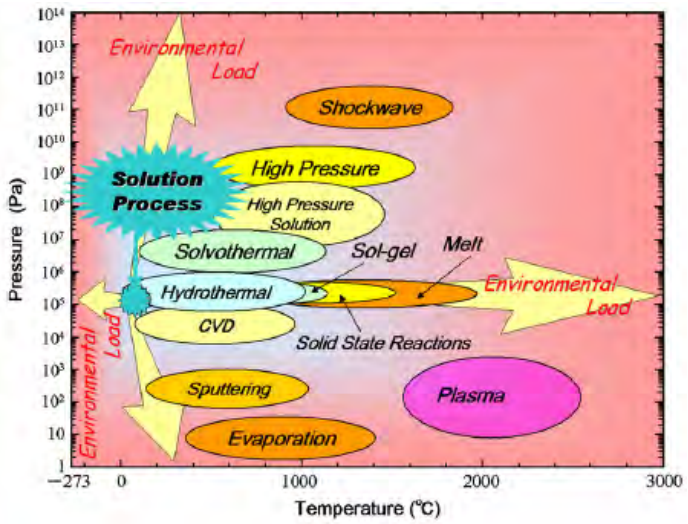

Fig. 2 *Pressure-Temperature diagram of various preparative techniques regarding to also a relative environmental load [2].*

The use of water as a solvent has been most widely investigated, and the most practical data are those describing the pressure developed as a function of percentage fill of the container and the temperature employed (Fig. 3 and Fig. 4). Other solvent systems, except that of ammonia, have been less studied, and the vast majority of solvothermal syntheses performed today utilise subcritical (low solution vapour pressure) conditions. Some critical data for typical non-aqueous solvents are listed in Table 1. Numbers of excellent reviews and also a dedicated handbook on the hydrothermal process are available nowadays [1], which is contrary to the solvothermal process where it is extremely difficult to find ones [4-6]. Further investigation on physics and chemistry of the non-aqueous systems is apparently an ongoing matter.

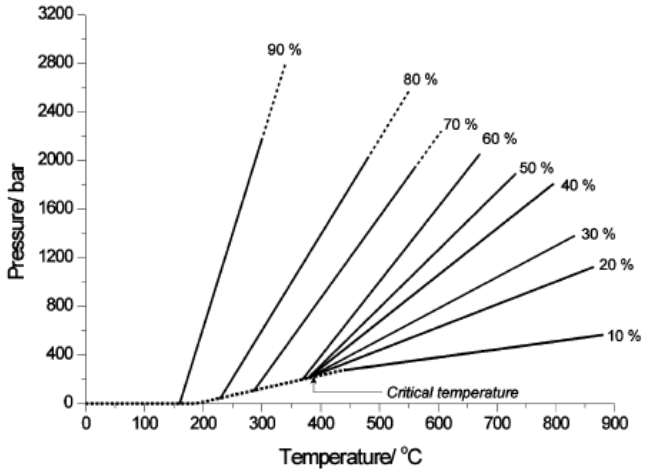

Fig. 3 *Pressure-Temperature diagram for water under hydrothermal conditions, as a function of percentage filling [2].*

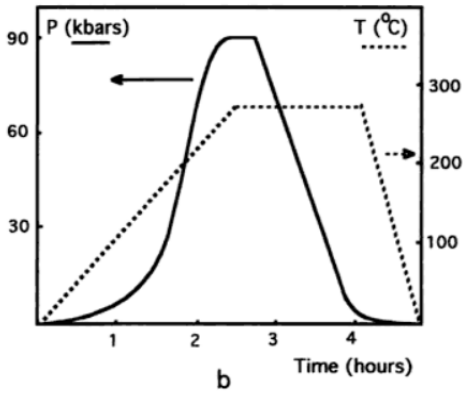

Fig. 4 *Simplified diagram showing hydrothermal process conditions in a typical run [4].*

Table 1 *Some physical constants of typical non-aqueous solvents [2].*

Solvent	Boiling temperature/°C	Critical temperature/°C	Critical pressure/bar
NH_3	-33.5	132.3	111
HCl	110	51.4	832.
CO_2	-78.5	31.3	73
SO_2	-10	157.8	78.7
H_2S	-60	100.4	90.1
CS_2	46.3	279	79
C_2H_5OH	78.3	243	63.8
CH_3NH_2	-6.4	156.9	40.7
CH_3OH	65.0	240	81
HCOOH	100.7	308	-

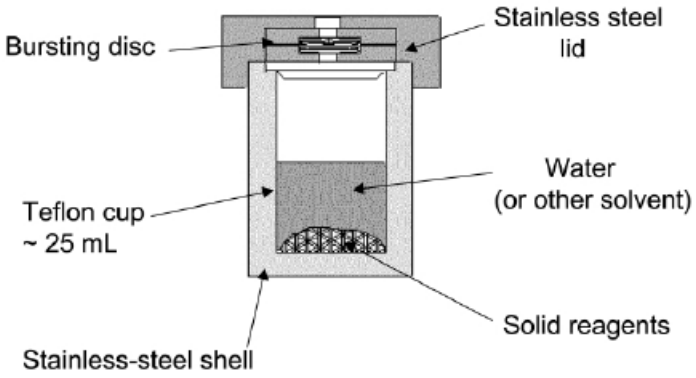

Fig. 5 *Schematic diagram showing parts of a general purpose Teflon-lined stainless steel autoclave [4].*

Subcritical solvothermal synthesis is commonly performed using Teflon-lined, stainless steel autoclaves (Fig. 5). The use of an autoclave is necessitated by the pressures developed in the reactions, and the inert liner is used to protect the stainless steel outer shell from the corrosive reagents typically used in synthesis. Such autoclaves can be used at up to 270 °C, and depending on the engineering specification of the steel walls, pressures of *ca.* 150 bar can be withheld [4].

HYBRID INORGANIC – ORGANIC MATERIALS

Terms *hybrid inorganic-organic materials*, *inorganic-organic hybrid materials* and *hybrid organic-inorganic materials* are interchangeably and equivalently used by researchers of different disciplines depending on field interest. According to IUPAC, these terms signify *the materials composing an intimate mixture of inorganic, organic components or both types of components* [7]. Renowned chemists in the fields suggested also the other terms. For example, C.N.R. Rao and A.K. Cheetham suggested also an additional, yet similar, term *hybrid inorganic–organic frameworks*, denoting *crystalline systems in which both inorganic and organic structural elements co-exist within a single phase* [8-12]. Despise of different terms of different degree of restrictions, the main idea in a development of the hybrid materials was to take advantage of the best properties of each component that forms a hybrid, trying to decrease or eliminate their drawbacks getting in an ideal way a synergic effect; that results in the development of new materials with new properties. The main characteristics of hybrid materials bind to the physical and chemical activity of their components, resulting in the expectation in the novelty of mechanical, optical and electrical properties. Luminescence, ionic conductivity and selectivity, as well as chemical or biochemical activity, give a way to the materials that can be applied for: sensors, selective membranes provided potential applications for all sorts of electrochemical devices, from actuators to batteries or electrochemical supercapacitors, supported catalysts or photoelectrochemical energy conversion cells, *etc* [8-12].

The hybrid inorganic-organic materials can be classified into two classes according to nature of the inorganic-organic interfacial interactions; class I, where organic and inorganic components are embedded and only weak interactions give the cohesion to the whole structure, and class II, where two components are linked together through strong chemical bonds [13]. Regarding morphological combination of the two components, the materials can be grouped into five classes [13]:

- class I; *inorganic matrix systems*, where organic materials were embedded in an inorganic polymer.
- class II; *organic matrix systems*, where inorganic materials are embedded in an organic polymer. Some of the oldest and well-known organic-inorganic hybrids of this category are used in the paint industry by dispersion of the inorganic pigments into organic binders.

- class III; *interpenetrated networks systems*, where inorganic and organic polymeric networks are independently formed without mutual chemical bonds.
- class IV; truly hybrids systems, where inorganic and organic polymeric systems with mutual chemical bonds are formed.
- Class V, *inorganic core/shell matrix systems*, where, the potential and ability of the core/shell nanoparticles to obtain structures with combinations of the properties that neither individual material possesses is in consideration.

Among the five classes of the hybrid materials, the truly hybrid systems (class IV) have been extensively explored. These materials are typically polymeric in nature, and known by various names, particularly *coordination polymers* (CPs) and *metal-organic frameworks* (MOFs), the former of which is more preferred by inorganic chemists whereas the latter by solid state scientists. Due to an exceptional interest in this group of hybrid materials during the last few decades, terms CPs and MOFs are somewhat used to denote any kind of the hybrid materials. Even between the terms CPs and MOFs, there have been attempts to distinguish differences between the two. Coordination polymers are *compounds that consist of metals or metal clusters linked to multifunctional organic ligands in at least one dimension to form an infinite array through extended covalent or coordinate interactions* [9]. They are also characterized by highly crystalline solid state structure, which cannot be processed like organic counterparts. When structures are *three dimensional extended and porous*, they are often referred to as MOFs [9]. The pioneer of MOFs, O. Yaghi, made nonetheless a positive comment on the term CP: “the term CP is undoubtedly the most nebulous, as it simply signifies the extended connection of metal and ligand monomers through coordination bonds with no regard towards the final structure or morphology” [14]. Fig. 6 and Fig. 7 depict schematic representations of the definition of CPs with different dimensionality and the difference between CPs and other extended metal-ligand structures.

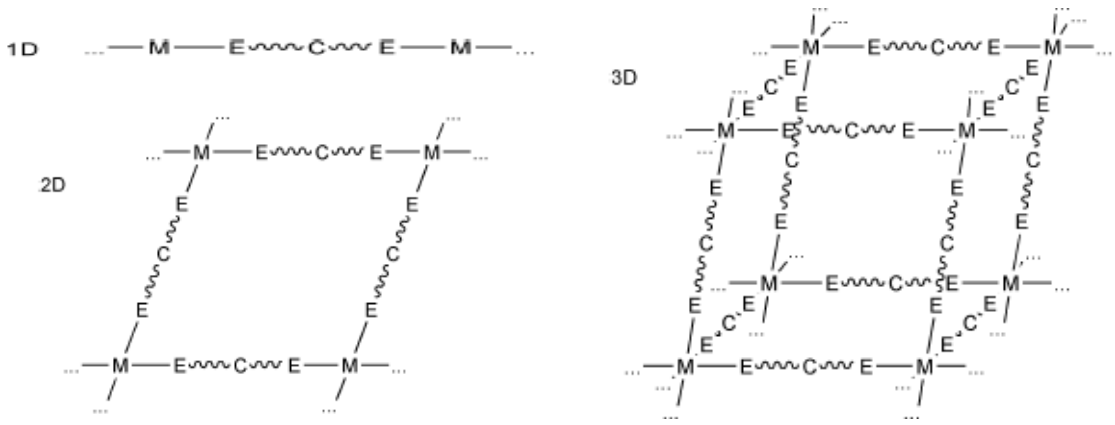

Fig. 6 *Schematic representation of the definition of one-, two- and three-dimensional CPs, where M and E signify metal and donor atoms, respectively [11].*

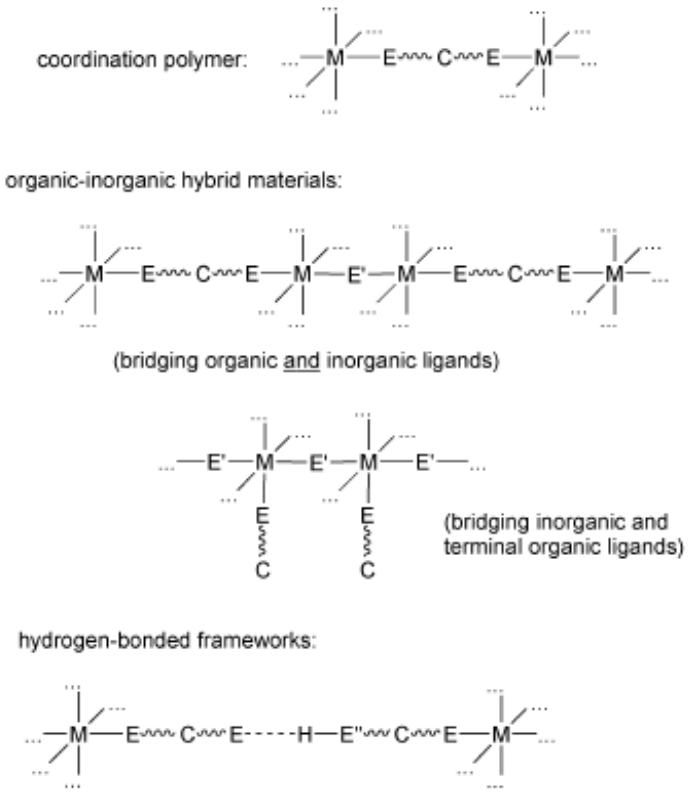

Fig. 7 *Schematic diagram showing characteristic differences between CPs and other extended frameworks [11].*

The field of CPs since the last few decades has expanded exponentially. Legitimately, a major portion of works were of structural investigation in terms of *crystal engineering*, *structure design* or control of *architecture*. Until recently the exploration and the establishment on structural design principal have been regarded as approaching its maturity, and the kick off of the *functional design*.

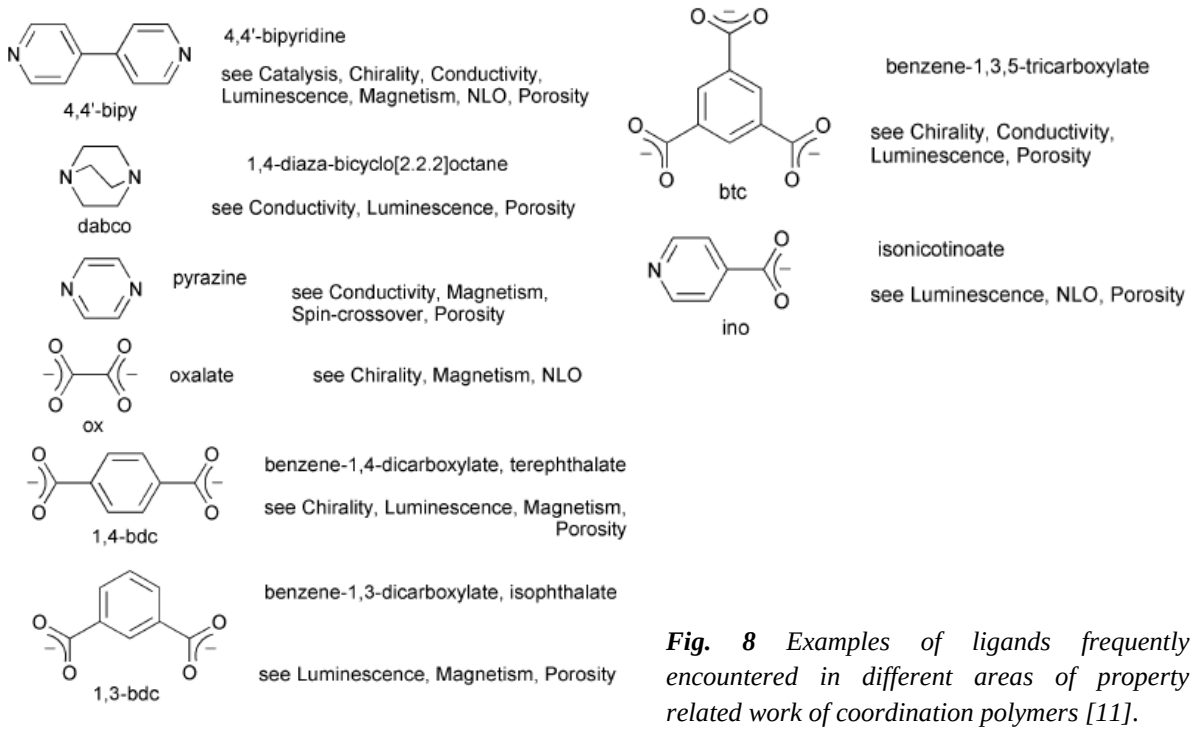

Fig. 8 *Examples of ligands frequently encountered in different areas of property related work of coordination polymers [11].*

The organic molecules used in the construction of CPs are usually multi-dentate ligands with two or more donor atoms, and are called di-, tri-, tetratopic depending on the number of donor atoms. Of special importance are rigid bridging ligands since they allow for a certain control in the assembly process. The flexible ligands have nonetheless been drawing greater attention from structural solid state chemists recently due to the beauty and diversity of the frameworks as well as multy-functionality they may provide. The concurrent introduction of different ligands for better competitive function is also the other direction the crystal engineers are moving forward to. The diversity of organic components is, of course, the basis for the variety in structural topologies. By carefully selecting the organic ligand one also aims to tune the physical properties and, thus, realize various applications, such as catalysis, electrical conductivity, luminescence, magnetism, non-linear optics or zeolitic behaviour. Fig. 8 shows some of popular organic molecules employed in the design of CPs, all of which posses either O- or N- donor atoms (Fig. 9).

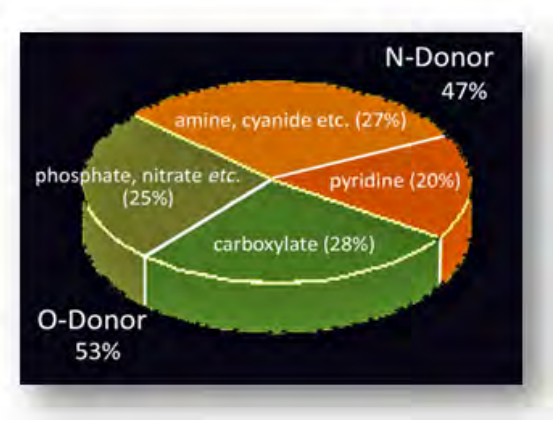

Fig. 9 *Pie chart illustrating the relative percentiles of different structure-directing organic agents reported until 2006 in CCSD [15].*

There stated a “golden-rule” in crystal engineering; the crystal architecture can be determined by the strength and directionality of covalent and non-covalent intermolecular interactions. A crystal structure can in principle be regarded as a manifestation of self-assembly and self-organization, whereby the solid-state architecture determines function which is therefore a driving force behind the desire to rationally design.

PEROVSKITE METAL OXIDE FRAMEWORKS

Most of industrially important ferroelectric/piezoelectric ceramics are of perovskite family, such as $BaTiO_3$, $PbTiO_3$, $Pb(Zr,Ti)O_3$, $(Pb,La)(Zr,Ti)O_3$, $KNbO_3$ and $(K,Na)NbO_3$. The general formula is often referred to as ABO_3, where O is oxygen, A a cation of larger ionic radius, and B a cation of smaller ionic radius [16]. For example, the perovskite structure of lead titanate ($PbTiO_3$ or PT) in a space group *P4mm* or *P4/mmm* is composed of titanium atoms located at the corners and lead atom located at the center of the unit cell cube as shown in Fig. 10. The oxygen atoms are placed at the centers of the twelve cube edges [17-19]. The first alternative is a cubic cell that has the titanium atom at the center, the lead atoms are on the cell corners and the oxygen atoms are on the cell faces [17-19]. The perovskite structure can be presented also as linked framework made up of BO_6 octahedra with the A cations occupying the 12-fold coordination site. Two different cationic sites, namely A-site and B-sites, are commonly useful in describing the structures. One of the most distinguished characteristics of the perovskite structures is that they can tolerate a very wide range of multiple cation substitutions on both the A- and B-sites. The anions and cations can be interchanged with ions of different valences, as long as charge neutrality is maintained. According to the general formula ABO_3, three different combinations of A and B are possible, as shown in Fig. 11 [17-19]:

- type I: $A^{I}B^{V}O_3$ with $KNbO_3$ and $NaNbO_3$ as typical examples,
- type II: $A^{II}B^{IV}O_3$ which is the most studied group among the three including $PbTiO_3$ and $BaTiO_3$,
- type III: $A^{III}B^{III}O_3$ such as $BiFeO_3$ and $BiScO_3$.

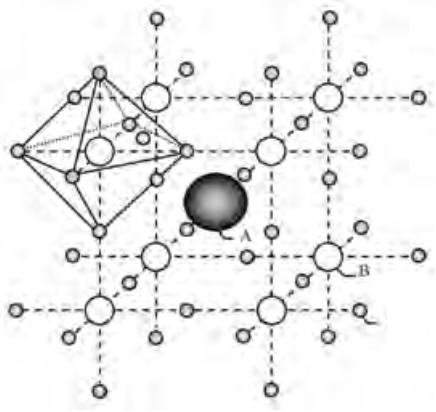

Fig. 10 *Representation of the perovskite crystal structure [17].*

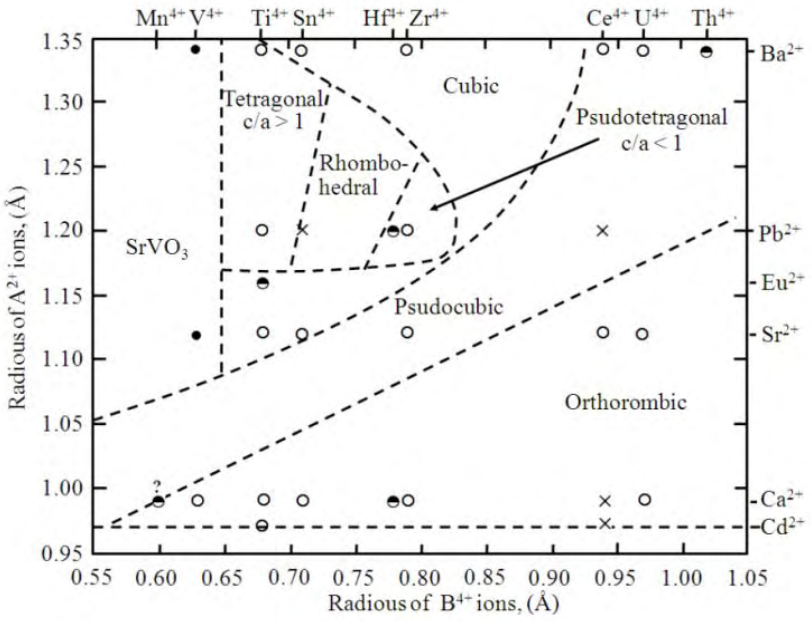

Fig. 11 *Classification of the perovskite $A^{II}B^{IV}O_3$-type compounds according to the constituent ionic radii [20].*

Table 2 *Interrelationship of electric properties and crystallographic point groups [21].*

Crystal Structure	Point Groups	Centro- Symmetry	Non- Centrosymmetry	
			Piezoelectric	Pyroelectric
Triclinic	*1,$\bar{1}$*	*$\bar{1}$*	*1*	*1*
Monoclinic	*2, m, 2/m*	*2/m*	*2, m*	*2, m*
Orthorhombic	*222, mm2, mmm*	*mmm*	*222, mm2*	*mm2*
Tetragonal	*4,$\bar{4}$, 4/m, 422, 4mm, $\bar{4}$2m, (4/m)mmm*	*4/m, (4/m)mmm*	*4, $\bar{4}$, 422, 4mm, $\bar{4}$2m,*	*4, 4mm*
Trigonal	*3, $\bar{3}$, 32, 3m, $\bar{3}$m*	*$\bar{3}$, $\bar{3}$m*	*3, 32, 3m*	*3, 3m*
Hexagonal	*6, $\bar{6}$, 6/m, 622, 6mm, $\bar{6}$2m, (6/m)mmm*	*6/m, (6/m)mmm*	*6, $\bar{6}$, 622, 6mm, $\bar{6}$2m,*	*6, 6mm*
Cubic	*23, m3, $\bar{4}$32, 43m, m3m*	*m3, m3m*	*23, $\bar{4}$32*	*None*

Close correlation between structures and properties of materials are long known. This includes also piezoelectricity and pyroelectricity, which are crucially determined by symmetries of the structures, as summarized in Table 2. The structure of PT, for example, possessing the *4mm* point group, the material is therefore non-centrosymmetric and can exhibit both of piezoelectric and pyroelectric properties.

Lead titanate (PT), for instance, is ferroelectric at room temperature and has a Curie point of 490°C at which the phase transition from the cubic paraelectric (above Curie point) to the tetragonal ferroelectric phase (below Curie point) occurs [18]. At room temperature, the structure of PT showed a tetragonal distortion from the cubic perovskite lattice with the axes ratio *c/a* ~1.063. This is markedly larger than that of barium titanate, where *c/a* ~1.01 [22]. It is very appropriate for high frequency and high temperature applications in electronics and microelectronics, due to its desirable dielectric constant (ε_r ~200), pyroelectric, and piezoelectric (k_t/k_p>10) properties [22]. Moreover, lead titanate can make a series of solid solutions with the other perovskites, lead zirconate ($PbZrO_3$ or PZ), *e.g.* $Pb(Zr,Ti)O_3$, $PbZrO_3$-$Pb(Mg_{1/3}Nb_{2/3})O_3$ and $PbZrO_3$-$PbTiO_3$-$Pb(Fe_{1/5}Nb_{1/5}Sb_{3/5})O_3$, finding important roles in electroceramic industries *e.g.* piezoelectric sensors, transducers, actuators, pyroelectric detectors, resonators and electro-optic devices [16].

Among a series of titanate based solid solutions, lead zirconate titanate ($Pb(Zr_{1-x},Ti_x)O_3$ or PZT) in particular finds tremendous use as piezoelectric sensors, transducers, actuators, resonators and electro-optic devices. There reported that the PZT ceramics with chemical compositions near a morphotropic phase boundary (MPB) (Fig. 12), which is the boundary between the high temperature rhombohedral and tetragonal phases and found at x ~ 0.48, have anomalous dielectric constant and piezoelectric electromechanical coupling factor (Fig. 13) due to a sudden change in the structure caused by either a mechanical or electrical field [19].

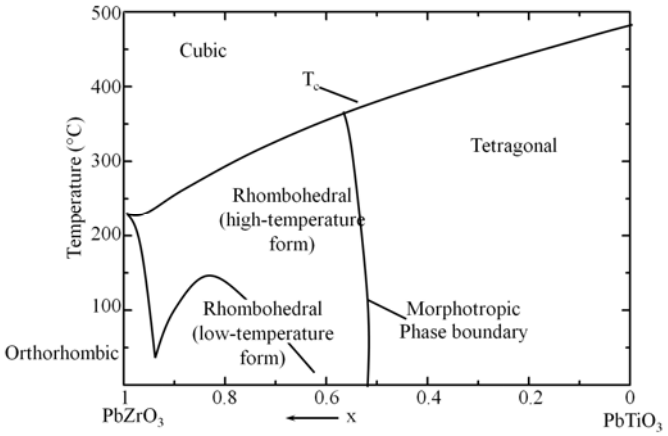

Fig. 12 *Phase diagram for $Pb(Zr_{1-x},Ti_x)O_3$ system [19].*

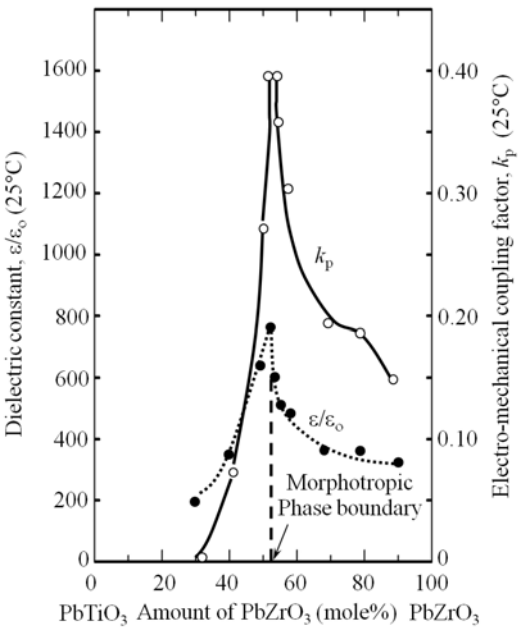

Fig. 13 *Dielectric and piezoelectric properties of PZT ceramics as a dependence of chemical composition [16].*

Two primary goals in powder synthesis are (a) to achieve polycrystalline powders which yield a product satisfying specified standard performance after consolidation, and (b) to produce powders that can be consolidated at as low temperatures as feasible. The ideal powder characteristics proposed by Somiya and Roy [23] are listed in Table 3. Such qualities will be key factors allowing the development of fine-grained microstructures with enhanced mechanical and electrical properties. Most importantly, fine particulates are critical for the continuing miniaturization of wherefrom fabricated devices [24]. The current trend in powder synthesis is nonetheless towards the preparation of powders having particle sizes in sub-micrometer and nanometer range with as small degree of agglomeration or aggregation as possible. Five common methods available for the synthesis of fine polycrystalline powders are solid state reaction, thermal decomposition, precipitation or hydrolysis and hydrothermal reactions [23]. These techniques possess characteristic pros and cons. Some comparisons between the popular preparative techniques are concluded in Table 4.

Table 3 *List of ideal powder characteristics [23].*

1.	Submicron size	8.	Free flowing
2.	Soft or no agglomeration	9.	Less defect, dense particle
3.	Narrow particle size distribution	10.	Less stress
4.	Sphere morphology	11.	Reactivity, sinterability
5.	Chemical composition controllable	12.	Crystallinity
6.	Microstructure controllable	13.	Reproducibility
7.	Uniformity	14.	Process controllable

Table 4 *Comparisons between the hydrothermal technique and the other preparative techniques [1].*

Comparative details	Solid state reaction	Sol-gel	Coprecipitation	Hydrothermal
Cost	Low-moderate	High	Moderate	Moderate
Compositional control	Poor	Excellent	Good	Good-Excellent
Morphology control	Poor	Moderate	Moderate	Good
Powder reactivity	Poor	Good	Good	Good
Purity (%)	< 99.5	< 99.9	> 99.9	> 99.9
Calcination step	Yes	Yes	Yes	No
Milling step	Yes	Yes	Yes	No

Hydrothermally derived powders however exhibit various preferential merits as listed below [1, 25];

- powders are formed directly from solution,
- powders are mostly anhydrous and crystalline,
- powders are highly reactive in sintering,
- powders show good homogeneity and sinterabiltity,
- powders show no or weak agglomeration,
- powders have narrow size distribution,
- various chemical composition and stoichiometry can be prepared,
- powders can be synthesized at low temperatures and/or metastable phases can be synthesized,

- powders compose of particles whose sizes can be controlled and generally less than 1 micron, and
- powders compose of particles whose shape can be controlled.

In addition, the hydrothermal technique can be hybridized with other processes such as ultrasonication and microwave irradiation in order to enhance the chemical reactions [25].

REFERENCES

1. K. Byrappa, M. Yoshimura, Handbook of Hydrothermal Technology: A Technology for Crystal Growth and Materials Processing, Noyes Publication, New Jersey (2001).
2. K. Byrappa, T. Adschiri, *Prog. Cryst. Growth Charac. Mater.* **53** (2007) 117-166.
3. A. Rabenau, *Angew. Chem., Inter. Ed. Eng*. **24**(12) (1985)1026-1040.
4. R.I. Walton, *Chem. Soc. Rev*. **31** (2002) 230-238.
5. S. Feng, G. Li, Modern Inorganic Synthetic Chemistry, Elsevier (2011) 63-95.
6. Y. Zhao, L. Kunhao, L. Jing, *Z. Naturforsch.* **65**b (2010) 976-998.
7. J. Alemán, A.V. Chadwick, J. He, M. Hess, K. Horie, R.G. Jones, P. Kratochvíl, I. Meisel, I. Mita, G. Moad, S. Penczek, R.F.T. Stept, *Pure Appl. Chem*. **79**(10) (2007) 1801-1829.
8. C.N.R. Rao, A.K. Cheetham, A. Thrirumurugan, *J. Phys.: Condens. Matter*. **20**(8) (2008) 083202.
9. K. Biradha, A. Ramanan, J.J. Vittal, *Cryst. Growth Des.* **9**(7) (2009) 2969-2970.
10. S. Natarajan, *Proc. Indian Acad. Sci.* (*Chem. Sci*.) **112**(3) (2000) 249-272.
11. C. Janiak, *Dalton Trans.* (2003) 2781-2804.
12. S.R. Batten, S.M. Neville, D.R. Turner, Coordination Polymers: Design, Analysis and Application, Royal Society of Chemistry Publishing, Cambridge, UK (2009).
13. M.S. Sadjadi, N. farhadyar, K. Zare, Advances in Nanocomposites - Synthesis, Characterization and Industrial Applications, InTech, Winchester, UK (2011).
14. J.L.C. Rowsell, O.M. Yaghi, *Microporous Mesoporous Mater.* **73** (2004) 3-14.
15. K. Biradha, M. Sarkar, L. Rajput, *Chem. Commun.* (2006) 4169-4179.
16. Y. Xu, Ferroelectric Materials and Their Applications, North-Holland, New York (1991).
17. S. Kasap, P. Capper, Hand book of Electronic and Photonic Materials, Springer Science-Business Media, Inc., New York (2006).
18. B. Jaffe, W.R. Cook, H. Jaffe, Piezoelectric Ceramics, Academic Press, London (1971).
19. A.J. Moulson, J.M. Herbert, Electroceramics: Materials, Properties, Applications, 2nd ed.,Wiley, New York (2003).
20. R.S. Roth, *J. Res. Natl. Bur. Stand.* **58** (1957) 75-88.
21. A. Safari, R.K. Panda, V.F. Janas. Ferroelectric Ceramics: Processing, Properties & Applications [Online].Available:http://www.rci.rutgers.edu/ ~ecerg/projects/ferroelectric.html [2009, October 27].
22. K. Uchino, Piezoelectrics and Ultrasonic Applications, Kluwer, Deventer (1998).
23. S. Somiya, R. Roy, *Bull. Mater. Sci*. **23** (2000) 453-460.
24. M.M. Lencka, R.E. Riman, *J. Am. Ceram. Soc.* **76** (1993) 2649-2659.
25. R.E. Riman, W.L. Suchanek, M.M. Lencka, *Annales de Chimie Science des Matriaux* **27** (2002) 15-36.

CHAPTER II

MICROWAVE ASSISTED CRYSTAL GROWTH OF A NEW ORGANIC-DECAVANADATE ASSEMBLY: $[V_{10}O_{27}(OH)]_2(C_6N_2H_{14})(C_6N_2H_{13})(C_6N_2H_{12}).2H_2O$

Banlawee Yotnoi, Saranpong Yimgran, Timothy J. Prior, **Apinpus Rujiwatra**,
Journal of Inorganic and Organometallic Polymers and Materials **18**(3) (2009) 306-313.

INTRODUCTION

Polyoxometallates (POMs) are one of the best known classes of complex anions and these continue to attract interest from both scientists and technologists. This is due to the diversity and richness in their chemistry and physics, which have led to a rapid expansion in the number of potential applications [1-3]. Among the well studied POMs, polyoxovanadates (POVs) compose a unique class, displaying a distinct potential for biology, materials science and medicinal applications [4-7]. The usage of these POVs, and decavanadates in particular, as structural building units in the synthesis of high dimensional hydrogen bond-assisted supramolecular assemblies composed of both inorganic and organic components such as $[H_2V_{10}O_{28}](C_{20}N_8H_{32})(H_2O)_4$, $[(C_2H_5)_3NH]_4[H_2V_{10}O_{28}]$, $(C_4N_2S_2H_{14})_2[H_2V_{10}O_{28}]$ and $[C_{211}H_2]_2[H_3O]_2[V_{10}O_{28}].7H_2O$ where C211 is a cryptand, is however still scattered [8-12]. The supramolecular arrangement of these compounds depends strongly on the abundance and locations of protonation sites on the decavanadates, and the nature of the organic molecules. These factors can impart immense influence via the synergistic interplay of Coulombic, van der Waals and hydrogen bonding interactions. While the structure of the decavanadate is well documented [8], the choice of organic molecules and synthetic conditions can be varied and these are therefore of utmost importance in directing the supramolecular organization. All previous reports of organic-decavanadate assemblies describe direct crystallization from solution under either ambient or hydro/solvothermal conditions. These reactions commonly require days or weeks to afford single crystals suitable for complete structural characterization. Recently microwave synthesis has been utilized in the synthesis of inorganic and inorganic–organic hybrid materials as well as ceramics, following the demonstration of tremendous advantages of this technique in organic synthesis [13-16]. The application of the technique in the growth of single crystals of inorganic-organic hybrid compounds is however novel. The fast kinetics of microwave reactions may shorten the reaction times, although this can induce disorder in the structure and hence hinder the growth of single crystals which generally requires very high degree of internal order.

Here we introduce the usage of microwave technique for a rapid single crystal growth of a new three dimensional hydrogen-bond assisted supramolecular assembly, based on the decavanadatemonomer and 1,4-diazabicyclo[2.2.2]octane. Structural characterization based on single crystal X-ray diffraction data and synergistic interactions analysis is reported.

EXPERIMENTAL

Microwave-Assisted Crystal Growth and Spectroscopic Characterization

Crystals of $[V_{10}O_{27}(OH)]_2(C_6N_2H_{14})(C_6N_2H_{13})(C_6N_2H_{12}).2H_2O$ (**I**) were readily grown from aqueous reactions between V_2O_5 and 1,4-diazabicyclo[2.2.2]octane (DABCO). In a typical experiment, a

mixture of 0.4044 g of V_2O_5 (Fluka 98.0%) and 0.2492 g of DABCO (Fluka 95.0%) was prepared in 9.00 mL deionized water, giving a molar ratio of 1:1:225. The mixture was stirred vigorously for 30 min at ambient temperature and pressure, before being transferred into an 18 mL Teflon reactor. The reactor was then placed in a 95(±5)^{o}C water bath, covered with a polypropylene cover and located in a domestic microwave oven (Whirlpool XT-25ES/S, 900 W, 2.45 GHz). Although the microwave power can be adjusted to a full range of 100%, reactions were conducted under autogenous pressure using a constant power of 70% (630 W) for varying duration between 1 and 3 h. After the microwave power was switched off, the reaction was cooled down to room temperature in a conventional oven using a cooling rate of 0.5^{o}C/min. Due to the static model of the reactor, the temperature inside the reactor was not measured, and it should be referred to solely by the employed microwave power. The solid products were separated from the supernatant solution by filtration, washed with deionized water and dried in air. Yields of the synthesized solid products were typically *ca*. 60% based on the V_2O_5. Size and habit of the crystals were examined using a field-emission scanning electron microscope (FESEM: JEOL JSM-6335F). In order to study the influence of DABCO on the formation of **I**, the V_2O_5:DABCO molar ratio was varied from 1:0.5 to 1:1.5. The pH of each mixture was measured before and after each reaction using a pH meter (Metrohm Siam Model 744). No attempt to adjust the pH of reaction mixtures prior to synthesis was carried out.

The crystals of **I** were separated under optical microscope from the solid product of the reaction using an equimolar V_2O_5:DABCO ratio and 2 h of microwave heating, and ground for further experiments. Elemental analysis was performed using a Perkin Elmer Series II 2400 CHN/S analyzer. Infrared spectra were collected on a Bruker Tensor 27 FT - IR instrument (4000-400 cm^{-1}, resolution 0.5 cm^{-1}) using a KBr (BDH 98.5%) pellet. The UV spectrum of **I** was collected on a Perkin Elmer UV LAMDA 25 spectrophotometer. The X-ray powder diffraction (XRD) pattern was collected using a Bruker D8 Advance diffractometer, operating with a Ni filtered Cu *K*α radiation (λ = 1.540558 Å, 48 kV and 30 mA).

X-Ray Crystal Structure Determination

A number of batches of products were examined and apparently crystalline material was present in all of them. Crystals of two morphologies were identified from the reaction using a V_2O_5:DABCO ratio of 1:1; namely hexagonal plates and rhombic bars. A large number of crystals were of examined. The plates were frequently found to be twinned with diffraction images showing the presence of multiple crystallites. Full data sets were collected from two such crystals and afforded moderate quality solutions on account of unresolved twinning. The rhombic bars were not subject to the same accidental twinning and diffraction images did not suggest the presence of multiple crystallites. Data were collected from an orange bar of size 0.1x0.05x0.05 mm^3 at 150(2) *K* using a Stöe IPDS2 image plate diffractometer operating with Mo *K*α radiation using a single ω-scan. Crystals were cooled using an Oxford Instruments nitrogen gas cryostream. The faces of the crystal were indexed and an analytical absorption correction applied to the data. Systematic absences in the data suggested one of two orthorhombic space groups, either *Pna2$_1$* (no. 33, non-centrosymmetric) or *Pnam* (no. 62, centrosymmetric). It was not possible to solve the structure in *Pnam* but routine automatic Direct Methods implemented within SHELXS-93 [17] located all non-hydrogen atoms in the structure in *Pna2$_1$*. Following completion of the structure by using SHELXL-97 [18], there was no evidence for additional symmetry found by PLATON [19]. The crystal examined was found to be racemically twinned with two roughly equal components, but there was no evidence that the true symmetry of the structure was centrosymmetric. Data were weak but the final refinement converged with excellent functionality of the DABCO were placed so as to generate chemically sensible

hydrogen bonds where necessary. The balancing of charge suggested the decavanadate unit bears a single proton. The protonation site was determined from Bond Valence Sum (BVS) calculations [20, 21].

RESULTS & DISCUSSION

Microwave-Assisted Crystal Growth and Spectroscopic Characterization

In the synthesis and crystal growth of **I**, microwave heating has been proved to afford crystals suitable for single crystal diffraction experiments, although twinning seems to be common. Non-merohedral twinning may be an inherent drawback. This may be due to the fast mass transport near surface and/or at structural interface associated with the growth of the crystals, which is known to induce disorder to the growth [16]. Variation of the V_2O_5:DABCO molar ratio from 1:0.5 to 1:1.5, which results in slightly different pH - 6.44, 6.52 and 6.58 for 1:0.5, 1:1 and 1:1.5, respectively, - evidently led to different phase formation using the same microwave heating time of 3 h. Figure 14 shows the XRD patterns of the solid products synthesized using different V_2O_5:DABCO molar ratio (Fig. 14d-f) in comparison to the simulated pattern of 1 (Fig. 14a). It can be clearly seen that the usage of equimolar V_2O_5:DABCO ratio (Fig. 14d) provides the nearly phase-pure product of **I**.

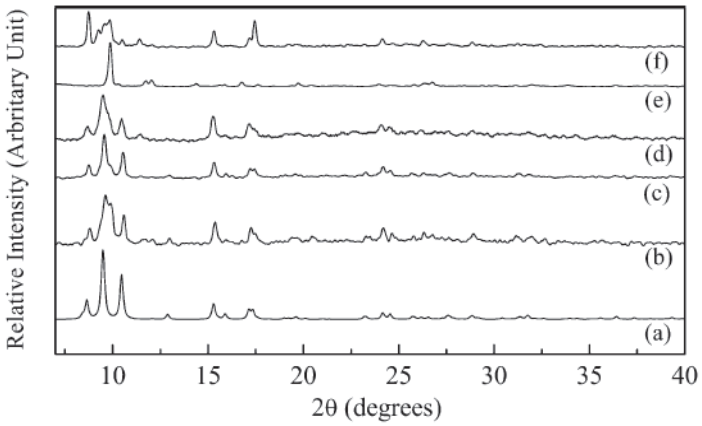

Fig. 14 *The powder XRD patterns of the products obtained from the reactions using 1:1 V_2O_5:DABCO but different reaction time - (b) 1 h, (c) 2 h and (d) 3 h - and a constant 3 h of microwave heating but different V_2O_5:DABCO molar ratio - (d) 1:1, (e) 1:0.5 and (f) 1:1.5 - in comparison to (a) the simulated pattern of **I**.*

The SEM micrographs of the crystals obtained from this reaction show two crystal habits - hexagonal plates and rhombic bars (Fig. 15a, b), the single crystal experiments, however, reveal the common crystal structure. The deviation of the V_2O_5:DABCO ratio from the equimolar stoichiometry results in the formation of the totally different phases (Fig. 14e, f) of possibly layer structures. These phases could not be identified due to the insufficient number of the diffraction peaks. The SEM micrographs of the crystals obtained from the reaction using 1:0.5 and 1:1.5 of V_2O_5:DABCO accordingly reveal different crystal habit of truncated octahedra of relatively smaller sizes as illustrated in Fig. 15c.

Based on the XRD result (Fig. 14b-c), a reduction of microwave heating time to 2 h gave similar result of a nearly phase-pure **I**. This indicates the formation of **I** to commence as a dominant phase since the first 2 h of microwave heating. SEM photographs (Fig. 16) reveal the crystals obtained from the reaction employing 2 h of microwave heating to be larger and better quality than those from the 3 h duration synthesis. A reduction of the microwave reaction time to 1 h however resulted in a mixed product of **I** and the other unidentified phase.

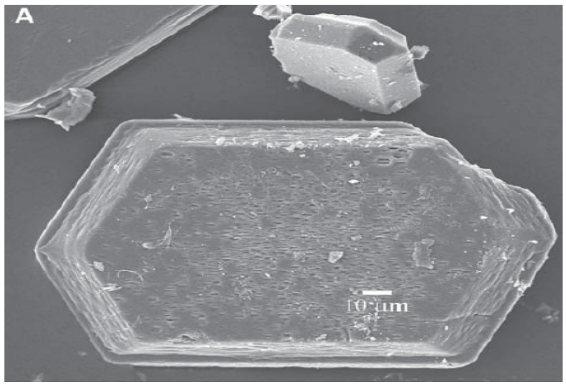

Fig. 15 *SEM micrographs showing different crystals habits in the products obtained from the reactions using different V_2O_5:DABCO molar ratios – (a) and (b) 1:1, and (c) 1:1.5.*

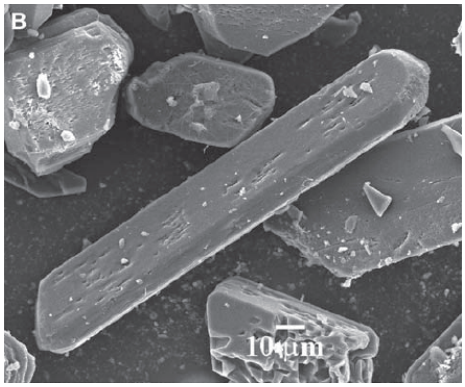

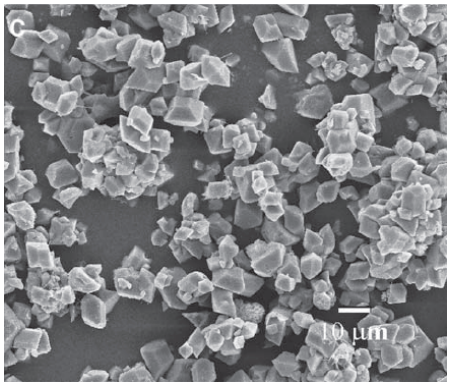

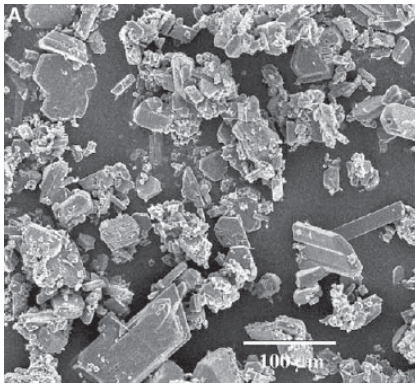

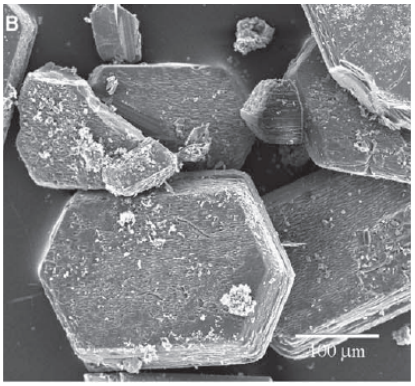

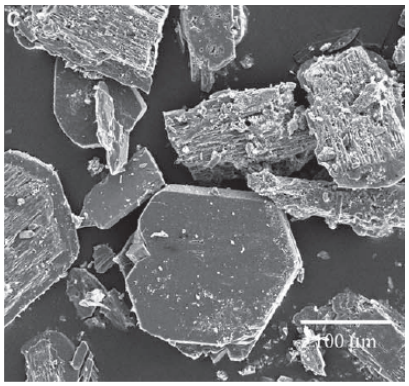

Fig. 16 *SEM micrographs showing different crystals habits and size in the products obtained from the reactions using an equimolar V_2O_5:DABCO molar ratio but different microwave heating time - (a) 1 h, (b) 2 h and (c) 3 h.*

Sizes of the obtained crystals were also smaller than the other cases and the morphology was irregular. The single crystal experiments were then conducted on the crystals chosen from the reaction using equimolar stoichiometry of V_2O_5:DABCO and 2 h of microwave heating. A reduction in the synthesis time required for the growth of single crystals of appropriate quality for full structure determination from days or weeks to only a few hours demonstrates the possible advantage

of microwave synthesis. The current study indicates the induced kinetic enhancement in the growth of single crystals of new compounds in an inorganic-organic hybrid system. The phase purity, crystal quality and crystal size depend, however, on both the reagent stoichiometry and microwave heating time.

The UV spectrum of **I** exhibited an intense and broad peak at 204-227 nm, which can be ascribed to the O→V charge transfer band, and in accordance with the existence of the decavanadate monomer. The elemental analysis shows an acceptable agreement between the experimental and the calculated figures: element, %calc. (%found): C, 19.89(20.19(5)); N, 7.73 (6.97(7)). The FT-IR spectrum also affirms the presence of the functionalities in **I** (frequency assignment, cm^{-1}): ν(N–H), 3436 s; ν(C–H), 3015 m; δ_{as}(N–H), 1616 m; δ(C–H), 1466 m; δ_s(N–H), 1338 m; ν(C–N), 1056 m; ν_s(V–O_T), 956vs; ν_{as}(V–O_T), 835vs; ν_s(V–O_b–V), 750 s; ν_{as}(V–Ob–V), 619 s.

Table 5 *Crystallographic data for structural solution and refinement of* ***I***

CCDC no.	688180
Formula	$[V_{10}O_{27}(OH)] \cdot 2(C_6N_2H_{14}) \cdot (C_6N_2H_{13}) \cdot (C_6N_2H_{12}) \cdot 2H_2O$
Formula weight	1448.18
Crystal size/mm^3	0.1 × 0.05 × 0.05
Crystal system	Orthorhombic
Space group	*Pna2₁*
a/Å	20.972(4)
b/Å	10.3380(14)
c/Å	20.432(3)
V_{cell}/$Å^3$	4429.83(12)
Z	4
ρ_{calc}/gcm^{-3}	2.171
T/K	150(2)
Radiation (λ/Å)	Mo (0.71073)
μ/mm^{-1}	2.117
θ_{min}, θ_{max}	1.94, 26
Total data	8693
Unique data	3451
Parameters no.	665
Restraints no.	272
Goodness of fit	0.643
$R(F^2)$, R_w (all data)	0.1395, 0.0878
$R(F^2)$, $R_w(I > 2\sigma(I))$	0.0431, 0.0674

Crystal Structure Determination of ***I***

The structure of **I** determined by single crystal diffraction has the empirical formula, $[V_{10}O_{27}(OH)]_2(C_6N_2H_{14})(C_6N_2H_{13})(C_6N_2H_{12}).2H_2O$, and is built up from the following building units: a monoprotonated decavanadate cation $[V_{10}O_{27}(OH)]^{5-}$, two water molecules, and three different types of the organic moieties, including two diprotonated H_2DABCO^{2+}, a monoprotonated $HDABCO^+$ and a neutral DABCO molecule. Crystal data for **I** are summarized in Table 5. The decavanadate anion comprises ten crystallographically distinct vanadium atoms. These all adopt a distorted coordination octahedral geometry (Fig. 17), which are connected via edge-sharing. Four distinct types of oxygen coordination are present; these can be classified as the bridging μ_6-O (O8, O19), μ_3-O (O11, O12, O18, O25), μ_2-O (O2, O4, O5, O6, O7, O9, O10, O13, O14, O16, O17, O22, O27, O28) and the terminal oxygen O_T (O1, O3, O15, O20, O21, O23, O24, O26) [8]. The bond lengths and angles found in the decavanadate anion are in good accordance with those found in previously reported decavanadate structures [10–12]. The BVS calculations based on the refined bond lengths listed in Table 6 suggest the pentavalence of vanadium, V^V, and the under-bonded character of O17 (BVS = 1.35) is indicative of the protonation site. Table 7 summarizes the calculated BVS results. The location of a single proton determined by BVS calculations corresponds well with the slight acidity of the reaction mixture promoting the protonation and a known tendency of the decavanadate-to-oxygen atom basicity where μ_2-O and μ_3-O are the most probable atoms to be protonated [8].

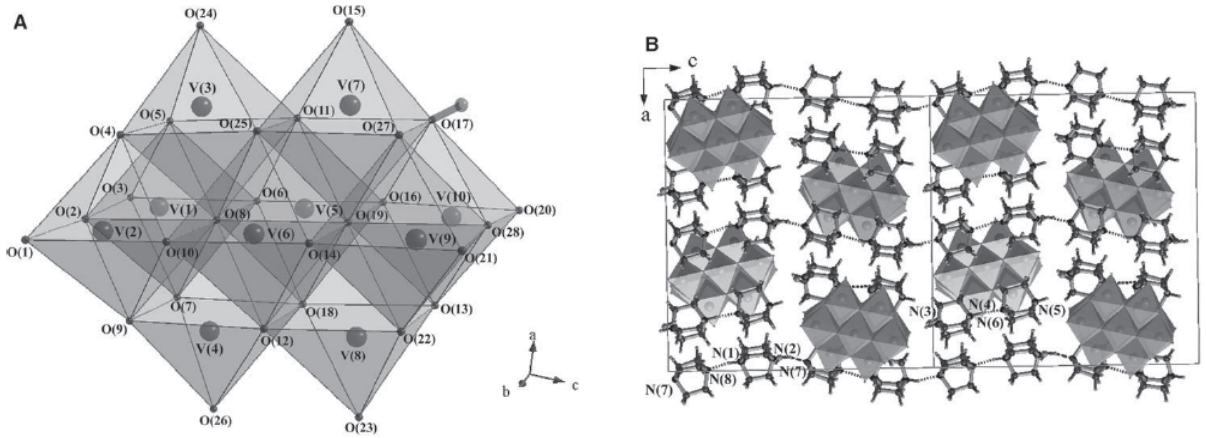

Fig. 17 *(a) Polyhedral representation of the decavanadate complex anion and (b) the spatial arrangement of the decavanadate and the DABCO molecules/ions viewed along the b-axis.*

Table 6 *Selected bond lengths (Å) with their standard deviations in brackets for* ***I***.

O1–V2	1.589(10)	O15–V7	1.582(9)	C3–C4	1.561(15)
O2–V1	1.829(10)	O16–V5	1.704(9)	C4–N1	1.469(16)
O2–V2	1.838(10)	O16–V10	1.986(9)	C5–N1	1.488(16)
O3–V1	1.605(9)	O21–V9	1.595(8)	C5–C6	1.512(15)
O4–V3	1.828(9)	O22–V8	1.812(9)	C6–N2	1.477(15)
O4–V2	1.880(9)	O22–V9	1.819(9)	C31–N3	1.509(17)
O5–V3	1.802(9)	O23–V8	1.586(9)	C31–C32	1.547(14)
O5–V1	1.846(8)	O24–V3	1.575(9)	C32–N4	1.483(15)
O6–V5	1.670(8)	O25–V7	1.931(9)	C33–N4	1.488(16)
O6–V1	2.082(8)	O25–V6	1.926(10)	C33–C34	1.548(14)
O7–V4	1.805(9)	O25–V3	2.029(9)	C34–N3	1.467(15)
O7–V1	1.902(9)	O26–V4	1.576(9)	C35–N3	1.469(16)
O8–V5	2.086(10)	O27–V7	1.851(9)	C35–C36	1.540(15)
O8–V6	2.093(10)	O27–V9	1.933(9)	C36–N4	1.469(16)
O8–V3	2.237(9)	O28–V9	1.844(9)	C55—N6	1.472(15)
O8–V4	2.251(9)	O28–V10	1.854(9)	C55–C56	1.527(15)
O8—V1	2.351(9)	O17–V7	1.916(9)	C51–N5	1.473(15)
O8–V2	2.344(9)	O17–V10	1.984(9)	C51–C52	1.544(15)
O9–V4	1.812(8)	O18–V5	1.930(1)	C52–N6	1.478(16)
O9–V2	1.840(9)	O18–V8	1.960(9)	C53–N6	1.487(16)
O10–V6	1.688(9)	O18–V4	2.017(8)	C53–C54	1.544(15)
O10–V2	2.038(9)	O19–V6	2.115(11)	C54–N5	1.501(17)
O11–V5	1.915(9)	O19–V5	2.135(10)	C56–N5	1.510(16)
O11–V7	1.988(8)	O19–V7	2.263(10)	C71–N7	1.482(15)
O11–V3	2.015(8)	O19–V8	2.241(10)	C71–C72	1.540(16)
O12–V6	1.929(9)	O19–V9	2.281(10)	C72–N8	1.484(16)
O12–V8	1.940(9)	O19–V10	2.307(10)	C73–N8	1.447(18)
O12–V4	2.023(9)	O20–V10	1.601(10)	C73–C74	1.577(17)
O13–V10	1.783(10)	C1–N1	1.495(17)	C74–N7	1.457(16)
O13–V8	1.885(9)	C1–C2	1.532(15)	C75–C76	1.549(15)
O14–V6	1.696(8)	C2–N2	1.495(15)	C75–N7	1.493(16)
O14–V9	2.034(9)	C3–N2	1.445(15)	C76–N8	1.483(16)

Table 7 *Calculated BVS for vanadium and oxygen atoms involving decavanadate anion.*

Atom	BVS	Atom	BVS
V1	4.99	V6	5.02
V2	5.17	V7	5.03
V3	5.21	V8	5.23
V4	5.23	V9	5.12
V5	5.06	V10	5.13
μ2-O2	1.84	μ6-O8	1.99
μ2-O4	1.75	μ6-O19	1.96
μ2-O5	1.89	μ3-O11	1.91
μ2-O6	1.90	μ3-O12	1.95
μ2-O7	1.76	μ3-O18	1.92
μ2-O9	1.88	μ3-O25	1.97
μ2-O10	1.89	$O1_T$	1.78
μ2-O13	1.86	$O3_T$	1.71
μ2-O14	1.87	$O15_T$	1.82
μ2-O16	1.92	$O20_T$	1.73
μ2-O17	1.35	$O21_T$	1.75
μ2-O22	1.93	$O23_T$	1.78
μ2-O27	1.58	$O24_T$	1.85
μ2-O28	1.77	$O26_T$	1.85

The existence of the protonation is also supported by the formation of the hydrogen bonding network in **I**, which is discussed later in detail. The monoprotonated decavanadate, $[V^{V}_{10}O_{27}(OH)]^{5-}$ is accordingly composed of two $[V(\mu_2\text{-}O)_2(\mu_3\text{-}O)_2(\mu_6\text{-}O)_2]$ (V5, V6), four $[VO_T(\mu_2\text{-}O)_2(\mu_3\text{-}O)_2(\mu_6\text{-}O)]$ (V3, V4, V7, V8) and four $[VO_T(\mu_2\text{-}O)_4(\mu_6\text{-}O)]$ (V1, V2, V9, V10). The existence of only the fully oxidized V^V suggests that under the conditions employed DABCO is stable. This is intriguing because the reactions between V_2O_5 and organodiamines, including DABCO, under solvothermal conditions generally result in a partial reduction of V^V–V^{IV} and, therefore, a degree of mixed valence states in the final structures. Each decavanadate anion is surrounded by organic moieties and water molecules and shows no direct contact with the same species (Fig. 17b). It can therefore be flagged as a monomer according to the classification of the decavanadate network structures proposed by J.L. Ferreira da Silva [8]. This agrees well with the assumption that approximately spherical organic molecules, DABCO in this case, promote the monomer function of the decavanadate in the formation of organic-inorganic supramolecular assemblies [8, 10]. Regarding the organic building units in **I**, there are two distinct pairs of H_2DABCO^{2+}-$HDABCO^{+}$ and H_2DABCO^{2+}-DABCO units in the asymmetric unit (Fig. 17b). Th significantly short intermolecular N···N distances - N1···N8 2.65(2) Å, N2···N7 2.67(2) Å and N4···N6 2.64(2) Å - are an indication of the presence of hydrogen atoms and hence hydrogen bonds between each pair of these DABCO molecules [22]. Each H_2DABCO^{2+}-$HDABCO^{+}$ hydrogen-bonded pair forms an isolated unit, whereas the H_2DABCO^{2+}-DABCO pairs are arranged in a fashion that leads to an infinite H-DABCO-H···DABCO···H-DABCO-H···DABCO··· hydrogen-bonded sinusoidal chain, each of which is aligned along the *c*-axis. According to the hydrogen bonding analysis results conducted using PLATON, there are both conventional and weak hydrogen bonds established between these building units as summarized in Table 8 and illustrated in Fig. 18. The large number of the otherwise weak hydrogen bonds is not common and should be noted. These weak interactions help enforce the spatial arrangement of the organic building units in the network and, therefore, impart a distinct

influence on the supramolecular organization in addition to the stronger hydrogen—bonding and electrostatic interactions. The single proton attached to the decavanadate forms a classical hydrogen bond with the water oxygen atom, which acts as the hydrogen-bond acceptor (O17•••O2w 2.926(13) Å, ∠O17-H•••O2w 177(11) °). The formation of this hydrogen bond supports the choice of protonation site suggested by BVS calculations. The impact of the electrostatic interactions undoubtedly results in the dense network of **I**, which is characteristic of an ionic structure. Therefore, the electrostatic and hydrogen bonding interactions are synergistically responsible for the observed dense supramolecular assemblies in **I**.

D	A	H···A	D···A	∠D–H·A
N1	N8	1.76	2.682(12)	170
O1w	O20	2.24(8)	2.963(14)	152(8)
N2	N7#2	1.84	2.729(13)	160
O1w	O7#7	2.09(9)	2.855(12)	147(9)
O1w	O9#7	2.53(9)	3.263(12)	142(8)
N3	O28#5	1.76	2.657(12)	161
O2w	O4	2.14(5)	2.910(13)	146(8)
N4	N6	1.72	2.649(12)	176
O2w	O27#8	2.21(9)	2.960(14)	139(7)
N5	O1w	2.19	2.938(13)	137
N5	O2#7	2.13	2.818(12)	129
O17	O2w#1	2.11(9)	2.926(13)	177(11)
C1	O27#3	2.50	3.328(16)	140
C1	O23#4	2.42	3.102(17)	125
C2	O23#4	2.46	3.108(15)	123
C2	O21#3	2.36	3.223(15)	145
C3	O21#3	2.38	3.219(16)	142
C3	O20	2.49	3.268(16)	135
C4	O17	2.44	3.207(17)	134
C4	O14#3	2.41	3.358(17)	159
C5	O23#4	2.59	3.199(15)	119
C5	O15	2.57	3.544(15)	169
C6	O23#4	2.42	3.121(15)	127
C31	O1#3	2.50	3.174(16)	125
C31	O3	2.49	3.222(17)	131
C32	O6	2.43	3.363(15)	157
C32	O9#3	2.49	3.274(15)	136
C33	O24#6	2.50	3.156(17)	123
C33	O7	2.44	3.296(16)	144
C34	O3	2.38	3.222(15)	143
C34	O24#6	2.43	3.079(15)	123
C35	O24#6	2.30	3.056(16)	132
C35	O20#5	2.56	3.278(15)	129
C36	O26#3	2.56	3.516(15)	163
C55	O23#3	2.56	3.299(16)	131
C51	O16	2.57	3.277(16)	128
C51	O20	2.49	3.422(16)	156
C51	O22#3	2.47	3.287(16)	139
C52	O12#3	2.45	3.412(16)	163
C52	O16	2.47	3.199(17)	130
C53	O16	2.53	3.352(17)	140
C53	O15#6	2.56	3.414(17)	144
C54	O2w#7	2.57	3.521(18)	160
C56	O22#3	2.51	3.380(15)	146
C56	O23#3	2.54	3.261(15)	129
C71	O5	2.55	3.435(16)	148
C72	O24	2.59	3.366(16)	135
C73	O10#3	2.51	3.239(18)	130

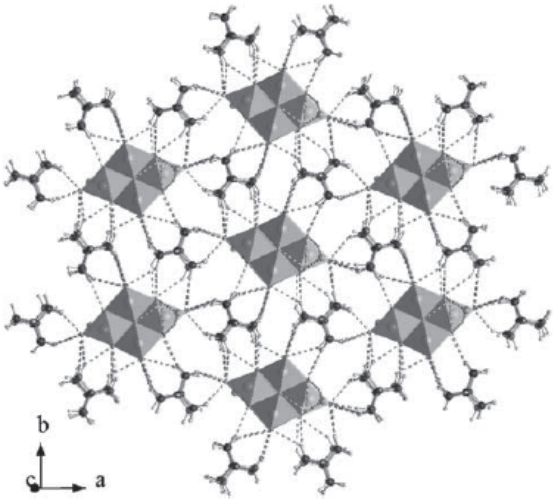

Fig. 18 *The abundance of the hydrogen bonding interactions (dotted lines) between the supramolecular assemblies building units, viewed along the c-axis.*

Table 8 *Hydrogen bonding distances (Å) and angles (°) in* ***I****.*

D	A	H···A	D···A	∠D–H·A
C73	O11	2.47	3.443(17)	168
C74	O5	2.52	3.317(16)	138
C74	O1#3	2.43	3.374(16)	158
C74	O10#3	2.59	3.307(16)	129
C75	O4#3	2.55	3.436(16)	149
C76	O26#4	2.55	3.411(15)	146

Symmetry codes: *#1* −x, 2−y, 1/2 + z ; *#2* −x, 1−y, 1/2 + z; *#3* x, −1 + y, z; *#4* −1/2 + x, 3/2-y, z; *#5* 1/2−x, −1/2 + y, −1/2 + z; *#6* 1/2 + x, 3/2−y, z; *#7* 1/2−x, −1/2 + y, 1/2 + z; *#8* −x, 2−y, −1/2 + z

CONCLUSIONS

Microwave heating has been successfully applied to the synthesis and growth of single crystals in a very short reaction time of a new three-dimensional hydrogen bond assisted organic–inorganic supramolecular assembly based on decavanadate and DABCO. Single crystals suitable for complete structural characterization can be produced although twinning seems to be an inherent problem due to the fast mass transport induced by microwave heating. The nature of the crystalline product in the V_2O_5-DABCO-water system depends on the initial V2O5:DABCO ratio and microwave heating time; to generate single crystals of **I**, an equimolar mixture of reactants and a few hours of microwave heating is required. The single crystal experiment reveals the importance of both the abundant hydrogen bonds and the stronger electrostatic interactions in regulating the architecture of the assembly. The hydrogen bonding on the other hand is governed by the number and spatial orientation of protonation on the structural building units.

REFERENCES

1. D.E. Katsoulis, *Chem. Rev.* **98** (1998) 359.
2. N. Mizuno, M. Misono, *Chem. Rev.* **98** (1998) 199.
3. M. Aureliano, *J. Inorg. Bio.* **80** (2000) 141.
4. M. Aureliano, R.M.C. Gandara, *J. Inorg. Bio.* **99** (2005) 979.
5. L.J. Csanyi, K. Jakya, G. Dombi, F. Evanics, G. Dezso, Z. Kota, *J. Mol. Catal. A: Chem.* **195** (2003) 101.
6. S.S. Soares, H. Martins, R.O. Duarte, J.J.G. Moura, J. Coucelo, C. Gutierrez-Merino, M. Aureliano, *J. Inorg. Bio.* **101** (2007) 80.
7. D.C. Crans, B. Baruah, N.E. Levinger, *Biomed. Pharmacother.* **60** (2006) 174.
8. J.L. Ferreira da Silva, M.F. Minas da Piedade, M.T. Duarte, *Inorg. Chim. Acta* **356** (2003) 222.
9. H. Kumagai, M. Arishima, S. Kitagawa, K. Ymada, S. Kawata, S. Kaizaki, *Inorg. Chem.* **41** (2002) 1989.
10. I. Correia, F. Avecilla, S. Marcao, J.C. Pessoa, *Inorg. Chim. Acta.* **357** (2004) 4476.
11. K. Pavani, S. Upreti, A. Ramanan, *J. Chem. Sci.* **118** (2006) 159.
12. D. Wang, W. Zhang, K. Gruning, D. Rehder, *J. Mol. Struct.* **656** (2003) 79.
13. C.O. Kappe, *Angew. Chem. Int. Ed.* **43** (2004) 6284.
14. S. Shi, J.-Y. Hwang, *J. Mineral Mater. Charac. Eng.* **2** (2003) 101.
15. D.E. Clark, W.H. Sutton, Annu. Rev. Mater. Sci. 26, 299 (1996)
16. J.H. Boosk, R.F. Cooper, S.A. Freeman, *Mat. Res. Innovat*. **1** (1997) 77.
17. G.M. Sheldrick, SHELEXS-93: A Program for Sloving Crystal Structure, University of Goettingen, Germany, 1993.
18. G.M. Sheldrick, SHELEXL-97: a program for crystal structurerefinement, Release 97–2, University of Goettingen, Germany, 1997.
19. A.L. Spek, A preliminary Introduction to the PLATON Program, Utrecht, Netherlands, 1997.
20. V.S. Urusov, I.P. Orlov, *Cryst. Rep.* **44** (1999) 686.
21. I.D. Brown, The Chemical Bond in Inorganic Chemistry: The Bond Valence Model, Oxford University Press, Oxford, 2002.
22. T. Akutagawa, S. Takeda, T. Hasegawa, T. Nakamura, *J. Am. Chem. Soc.* **126** (2004) 291.

CHAPTER III

PREPARATION AND CHARACTERIZATION OF Bis(μ-1,2-DIAMINOETHANE)COBALT(II) HEXAVANADATE: A LAYERED POLYOXOVANADATE PILLARED BY A COBALT COORDINATION COMPLEX

Bunlawee Yotnoi, Jumras Limtrakul, Timothy Prior, **Apinpus Rujiwatra**,
Journal of Chemical Crystallography **39** (2009) 525–529.

INTRODUCTION

Polyoxovanadate frameworks (POVs) have been capturing broad interest from materials chemists primarily because of their technological potential, *e.g.*, as oxidative catalysts and secondary cathode materials for advanced lithium batteries [1, 2]. The inherent ability of vanadiumatom to adopt various coordination geometries and oxidation states while being a good electron-acceptor and electron relay-station is also a driving force for the research in the field [3, 4]. Current interest regarding the preparation of POVs focuses on the introduction of a secondary metal, particularly a transition metal to the coordinate covalent POV frameworks. Cobalt is unique in its coordination chemistry, redox activity and potential magnetic functionality, and therefore has been one of the most studied secondary metals. Although there are earlier reports on the successful introduction of cobalt into POV frameworks (Co-POV) *e.g.* $[Co(2,2'\text{-bpy})_2]_2[As_8VO_{42}(H_2O)].H_2O$ [5], $[Co(en)_2(H_2O)]\{[Co(en)_2]_2As_8V_{14}O_{42}(SO_4)\}.3H_2O$ [6], $[Co(Hdpa)_2V_4O_{12}]$ [7], $Co_2(4,4'\text{-bipy})_2(V_4O_{12})$ [8] and $\{[H_2(en)]Co(ox)(V_4O_{12})\}_n$ [9], none of these are the Co-POV structures in which the cobalt present as a pillaring unit. Examples of POV frameworks where the secondary metal present acts as a pillar motif between POV sheets are rare, and limited to $(C_2N_2H_8)_2Zn[V_6O_{14}]$, $(C_2N_2H_8)_2Cu[V_6O_{14}]$, $[Ni(C_2N_2H_8)_2]_{0.5}[V_3O_7]$ and $[Ni(en\text{-}Me)_2]_{0.5}[H_2enMe]_{0.5}[V_6O_{14}]$ [10, 11]. Here, we report the preparation and crystal structure of $Co^{II}(\mu\text{-}C_2N_2H_8)_2[V_4^{IV}V_2^{V}O_{14}]$, which is the first example of a layered POV pillared by cobalt.

EXPERIMENTAL

Crystals of $Co^{II}(\mu\text{-}C_2N_2H_8)_2[V_4^{IV}V_2^{V}O_{14}]$ (**II**) were readily prepared from a reaction between $Co(NO_3)_2.6H_2O$ (98% Aldrich, 0.1006 g), V_2O_5 (99% Fluka, 0.2519 g) and ethylenediamine (99% Fluka, 0.0719 g) in deionized water (2.80 mL) using a 17 mL Teflon container. The reaction was conducted under autogenous pressure at 473 *K* for 60 h before being cooled down to room temperature using a rather rapid rate of 30 *K* h^{-1}. Black crystals of **II** were then separated from the supernatant solution by filtration, washed with deionized water and dried in air. The elemental composition in **II** was determined using the energy dispersive X-ray spectroscopic (EDS) microanalyzer present on the scanning electron microscope (FESEM, JEOL JSM-6335F) and a Perkin Elmer Series II 2400 CHN/S analyzer. Infrared spectra of also the ground crystals were collected on a Bruker Tensor 27 FT-IR instrument (4,000-400 cm^{-1}, resolution 0.5 cm^{-1}) using a KBr (BDH 98.5%) pellet. The X-ray powder diffraction (XRD) pattern was collected using a Bruker D8 Advance diffractometer, operating with a Ni filtered Cu Ka radiation (λ = 1.5405 Å, 48 kV and 30 mA).

In order to determine the crystal structure of **II**, a full set of intensity data was collected on a single crystal of size 0.20x0.04x0.04 mm^3 at 150(2) *K* using a Stoe IPDS2 image plate diffractometer

operating with Mo *K*α radiation, employing a single ω-scan. The crystal was cooled using an Oxford Instruments nitrogen gas cryostream. The collected data were analytically corrected for absorption using the Tompa method [12]. The structure was then solved by direct methods implemented within SHELXS-97 [13] and full-matrix least squares refinement carried out within SHELXL-97 [14] *via* the WinGX [15] program interface. All non-hydrogen atoms were located from direct and difference Fourier maps and refined anisotropically. The hydrogen atoms in the ethylenediamine were apparent from final difference Fourier maps, and were then placed and refined using a riding model with the following bond lengths: C-H 0.99(3) Å; N-H 0.92(3) Å. Details of the data collection and structure refinements are summarized in Table 8.

Table 8 *Crystallographic data for structural solution and refinement of* ***II***

CCDC no.	704646
Formula	$Co(C_2N_2H_8)_2[V_4^{IV}\ V_2^{V}O_{14}]$
Formula weight	708.78
Crystal size/mm	0.20 × 0.04 × 0.04
Crystal system	Monoclinic
Space group	$P2_1/n$
a (Å)	9.143(3)
b (Å)	6.5034(11)
c (Å)	15.874(4)
β (°)	101.90(2)
V_{cell} (Å^3)	923.6(4)
Z	2
ρ_{calc} (g cm^{-3})	2.549
T (K)	150(2)
Radiation (*λ*/Å)	Mo K_α(0.71069)
μ (mm^{-1})	3.854
θ_{min}, θ_{max}	2.85, 26.00
Unique data	1,799
Observed data	1,071
Parameters no.	134
Restrains no.	4
Goodness of fit	0.840
R, Rw (all data)	0.0853, 0.0730
R, Rw ($I > 2\sigma(I)$)	0.0399, 0.0652

RESULTS & DISCUSSION

The crystal structure of $Co^{II}(\mu\text{-}C_2N_2H_8)_2[V_4^{IV}V_2^{V}O_{14}]$ (**II**) was successfully solved and refined in the monoclinic space group $P2_1/n$ with the final refined cell parameters *a* = 9.143(3) Å, *b* = 6.5034(11) Å, *c* = 15.874(4) Å, β = 101.90(2) ° and V = 923.6(4) Å^3. The ORTEP plot of the extended asymmetric unit showing the coordination environments of the structural building motifs and atomic numbering scheme is shown in Fig. 19. The atomic coordinates and equivalent isotropic displacement parameters are listed in Table 9. There are three crystallographically distinct sites of vanadium. The bond valence calculations based on a single point energy model [16], and refined bond distances listed in Table 10 suggest the presence of both pentavalent vanadium (V1) and tetravalent vanadium (V2, V3). Although the starting vanadium source is V_2O_5, the mild reducing power of the organic component results in the mixed V^{IV}/V^{V} structure. The tetravalent V2 and V3 are characterized by square pyramidal geometry, $\{V^{IV}O_5\}_{sq}$, of 4+1 type, each of which shows four long equatorial bonds - V2-O2, V2-O3, V2-O6, V3-O2, V3-O3, V3-O5 and V3-O6 in range

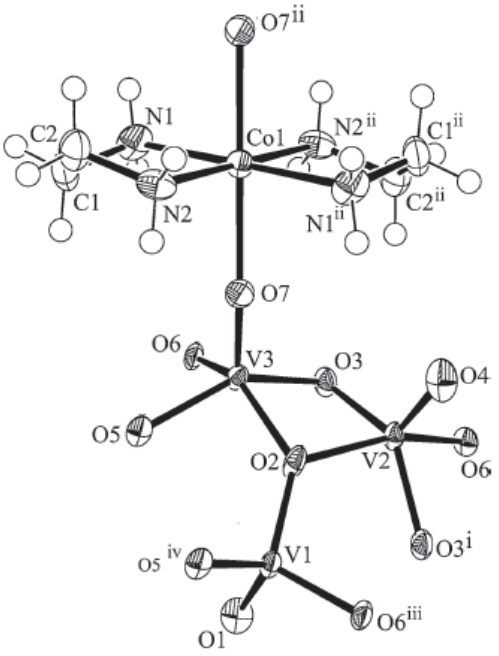

1.894(4)-2.017(4) Å with an average of 1.958(4) Å and one short vanadyl bond - V2=O4 (1.609(5) Å) and V3=O7 (1.616(5) Å). The pentavalent V1 on the other hand shows a 3+1 tetrahedral coordination, $\{V^{V}O_4\}_{tet}$, of which the bond lengths of the bridging V1-O2 (1.821(4) Å), V1-O5 (1.695(4) Å) and V1-O6 (1.792(4) Å) bonds are longer than the terminal V1-O1 (1.599(5) Å) bond. The distortion of the $\{V^{V}O_4\}_{tet}$ from the regular tetrahedron is apparent.

Fig. 19 *An ORTEP view of the extended asymmetric unit of* ***II*** *drawn at 80% probability level with hydrogen atoms omitted for clarity. [Symmetry codes: (i) -x, -y+2, -z; (ii) x, y+1, z; (iii) –x+1/2, y+ 1/2, -z+ 1/2; (iv) -x+1, -y+ 1, -z]*

Table 9 *Atomic coordinates and equivalent isotropic displacement parameters of non-hydrogen atoms.*

	x	*y*	*z*	*Ueq*
V_1	0.04285(11)	1.21858(15)	0.09298(6)	0.0112(2)
V_2	0.32600(11)	1.00000(15)	0.23310(6)	0.0120(2)
V_3	0.19319(11)	0.71902(15)	0.10076(6)	0.0116(2)
O_1	–0.1016(5)	1.1633(6)	0.1306(3)	0.0195(10)
O_2	0.1848(5)	1.0192(6)	0.1188(2)	0.0147(9)
O_3	0.2778(4)	0.7166(6)	0.2232(3)	0.0149(9)
O_4	0.4825(5)	1.0572(6)	0.2077(3)	0.0236(11)
O_5	0.0077(5)	0.7489(5)	0.0151(2)	0.0144(9)
O_6	0.1161(4)	0.4589(6)	0.1384(2)	0.0133(9)
O_7	0.3237(5)	0.6607(6)	0.0501(3)	0.0184(10)
Co_1	0.50000	0.50000	0.00000	0.0140(3)
N_1	0.3691(6)	0.2363(8)	–0.0417(3)	0.0228(13)
N_2	0.3993(6)	0.6049(8)	–0.1210(4)	0.0189(12)
C_1	0.2589(7)	0.2940(11)	–0.1201(4)	0.0239(16)
C_2	0.3322(8)	0.4276(10)	–0.1741(4)	0.0242(17)

V_1–O_1	1.599(5)	V_3–O_5	1.953(4)
V_1–O_5^{I}	1.695(4)	V_3–O_6	1.972(4)
V_1–O_6^{II}	1.792(4)	V_3–O_2	1.976(4)
V_1–O_2	1.821(4)	Co_1–O_7	2.202(5)
V_2–O_4	1.609(5)	Co_1–N_2^{IV}	2.067(5)
V_2–O_3	1.894(4)	Co_1–N_2	2.067(5)
V_2–O_3^{III}	1.908(4)	Co_1–N_1	2.118(5)
V_2–O_2	2.002(4)	Co_1–N_1^{IV}	2.118(5)
V_2–O_6^{III}	2.017(4)	N_1–C_1	1.479(8)
V_3–O_7	1.616(5)	N_2–C_2	1.484(8)
V_3–O_3	1.938(4)	C_1–C_2	1.475(10)

Symmetry codes: (i) $-x, -y + 2, -z$; (ii) $x, y + 1, z$; (iii) $-x + 1/2, y + 1/2, -z + 1/2$; (iv) $-x + 1, -y + 1, -z$

Table 10 *Selected bond distances for II (Å).*

The interatomic distances involving with the triply bridging oxygen, *i.e.* μ3-O2 and μ3-O6, are significantly longer than that of the doubly bridging oxygen, *i.e*. μ2-O5. The correlation between the refined bond distances and their corresponding polyhedral configurations agree well with the previously reported POV layer frameworks of the same composition and registry, *e.g.* $[V_6O_{14}](C_4H_{14}N_2)$, $[V_6O_{14}](C_5H_{16}N_2)$, $(C_2N_2H_8)_2Zn[V_6O_{14}]$ and $(C_2N_2H_8)_2Cu[V_6O_{14}]$ [10, 17]. Two adjacent {VIVO5}sq units share edges in a *trans* conformation to form a larger binuclear $\{V_2^{IV}O_8\}$ unit, which is then fused through *cis* edge sharing to the neighbouring binuclear units to generate the {UuDd} or {Z} chain with a zigzag configuration as shown in Fig. 20. Each chain is connected to the adjacent chains by the $\{V^{V}O_4\}_{tet}$, each of which share two basal corners with one chain and the other basal corner with the other chain. This results in a mixed valence $[V_4^{IV}O_{10}V_2^{V}O_4]^{2-}$ anionic layer of ({UuDd}:T.) β type in SP+T class and Z-T subclass [18]. These anionic POV layers extend parallel to the [101], and are linked further by the octahedral $\{Co^{II}O_2(C_2N_2H_8)_2\}$ pillars *via* the two *trans* apical O7 atoms of the $\{V^{IV}O_5\}_{sq}$ from two adjacent layers to generate a three-dimensional pillared Co-POV structure (Fig. 21), which is isostructural with the zinc, copper and nickel analogues, $(C_2N_2H_8)_2Zn[V_6O_{14}]$, $(C_2N_2H_8)_2Cu[V_6O_{14}]$ and $[Ni(C_3N_2H_{11})_2]_{0.5}[C_3N_2H_{13}]_{0.5}[V_6O_{14}]$ [10, 11]. This implies the template function of the ethylenediamine and therefore the feasibility in crystal engineering of other analogous pillared structures.

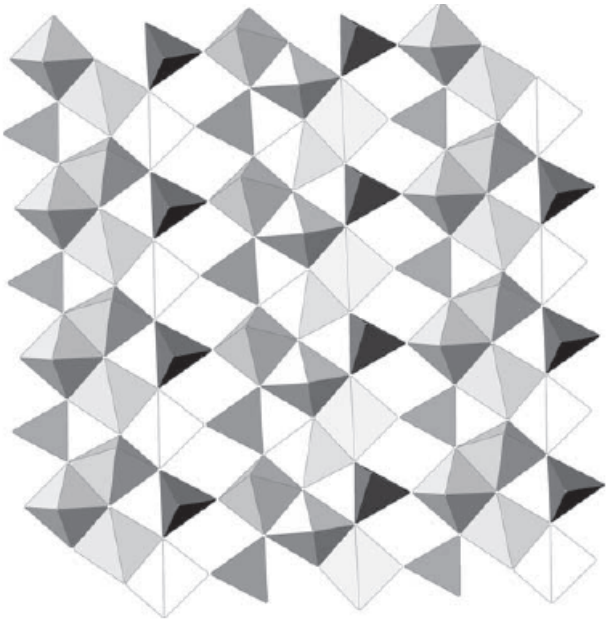

Fig. 20 *A polyhedral view of the ({UuDd}:T.) b-POV layer in* ***II****.*

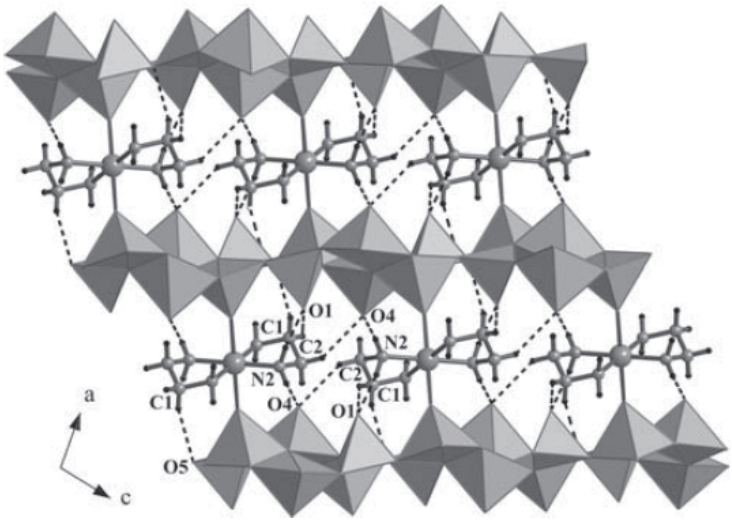

Fig. 21 *View of the three-dimensional structure of* ***II*** *with hydrogen bonds shown in dotted lines.*

The pseudo-octahedral coordination of the cobalt is completed by four nitrogen atoms from two *trans* ethylenediamine ligands, locating about the inversion centre at the cobalt atom. The bond valence calculations suggested the divalent state of the cobalt and therefore a dipositively charged $\{Co^{II}O_2(C_2N_2H_8)_2\}$ pillar, which consequently balances the negatively charged POV layer. **II** is similar in some respects to the framework $[\{Co(pyz)\}(V_2O_5)_2]$, pyz=pyrazine [19], which has been reported recently. In **II** the layers are linked by discrete $Co(en)_2^{2+}$ units, but in $[\{Co(pyz)\}(V_2O_5)_2]$ layers are linked by a series of 1-D chains of formulation Co(pyz)2. However, a different POV layer of type 2({UUDD}) is present within $[\{Co(pyz)\}(V_2O_5)_2]$.

The analysis of hydrogen bonding interactions as listed in Table 11 suggests spatial arrangement of the ethylenediamine to be partially imparted by the hydrogen bonds established between both the polar nitrogen atoms and the methylene carbon atoms of the organic molecule, and the vanadyl oxygen atoms of the POV layer, *i.e.* N-H•••O and C-H•••O. Although the established C-H•••O hydrogen bonds are very weak [20], they play a part in synergistic with the octahedral coordination geometry of the Co^{II} ion, in regulating the spatial arrangement of the ethylenediamine in relative to the POV layer. It is apparent from Fig. 21 that the ethylenediamines acting as a bidentate ligand are arranged roughly in a plane parallel to the POV layers, which is also the case for the analogous $(C_2N_2H_8)_2Zn[V_6O_{14}]$ and $(C_2N_2H_8)_2Cu[V_6O_{14}]$ structures [17].

Table 11 *Hydrogen bonding geometries in* ***II***.

D–H···A	D–H	H···A	D···A	D–H···A
N_2–H_2C···O_1^{I}	0.92	2.21	3.088(7)	159
N_2–H_2D···O_4^{V}	0.92	2.12	2.916(7)	144
C_1–H_1A···O_1^{VI}	0.99	2.47	3.293(8)	140
C_1–H_1B···O_5^{VI}	0.99	2.51	3.237(9)	130
C_2–H_2A···O_4^{VII}	0.99	2.54	3.359(8)	140

Symmetry codes: (i) $-x, -y+2, -z$; (v) $-x+1, -y+2, -z$; (vi) $-x, -y+1, -z$; (vii) $x-1/2, -y+3/2, z-1/2$

Elemental analysis of ground crystal using an energy dispersive X-ray spectroscopic (EDS) microanalyzer confirms the crystallographically observed ratio of 1:6 for Co:V. CHNS analysis data of bulk samples fit rather poorly to the crystallographically observed formulation. [found - C 46.61%, N 39.97%, H 13.42%; calculated - C 50.04%, N 39.45%, H 10.50%]. The data suggest impurities are present, possibly with coordinated water. However, the X-ray powder diffraction data show that the pillared phase is the dominant crystalline component present in the bulk. The FT-IR spectrum collected on the ground crystals reveals the existence of the major functional groups of the ethylenediamine and the ligated atoms to the cobalt; 3452vs, 3015vs (ν(N–H; NH_2)); 1630s (δ(N–H)); 1463m (δ(C–H; CH_2)); 1055m (ν(C–N)); 973s (ν(V–O_T)); 740s (ν(V–O_B)); 673m (ν(Co–N)); 465m (ν(Co–O)). The broadening effect is also observed in the spectrum which is consistent with the presence of the hydrogen bonds.

CONCLUSIONS

In conclusion, a new pillared POV layer structure of the Co-POV system has been prepared and fully characterized. This expands a series of the pillared POV layer structures to include Zn-POV, Cu-POV, Ni-POV and Co-POV, which in turn suggest the template function of the ethylenediamine

and therefore the feasibility in extending this structural series to other secondary metals with possibly better potential functions. Work to prepare a pure sample of **II** is underway with a view to examining the magnetic behavior of the pillared framework.

REFERENCES

1. P.J. Hagrman, R.C. Finn, J. Zubieta, *Solid State Sci.* **3** (2001) 745.
2. R.N. Davi, J. Zubieta, *Inorg. Chim. Acta* **343** (2003) 313.
3. G.H. Li, Z. Shi, Y.H. Xu, S.H. Feng, *Inorg. Chem*. **42** (2003) 1170.
4. E. Coronado, C.L. Gomez-Garcya, *Chem. Soc*. **121** (1999) 11459.
5. C.M. Wang, Q.X. Zeng, J. Zhang, G.Y. Yang, *J. Clust. Sci.* **16** (2005) 65.
6. G. Zhou, Y. Xu, C. Guo, X. Zheng, *Inorg. Chem. Commun.* **10** (2007) 849.
7. R.L. LaDuca, R.S. Rarig, J. Zubieta, *Inorg. Chem.* **40** (2001) 607.
8. L.M. Zheng, X. Wang, Y. Wang, A.J. Jacobson, *J. Mater. Chem.* **11** (2001) 1100.
9. C.L. Pan, J.Q. Xu, K.X. Wang, X.B. Cui, L. Ye, Z.L. Lu, D.Q. Chu, T.G. Wang, *Inorg. Chem. Commun*. **6** (2003) 370.
10. Y. Zhang, J.R.D. DeBord, C.J. O'Connor, R.C. Haushalter, A. Clearfield, J. Zubieta, *Angew. Chem. Int. Ed. Engl.* **35** (1996) 989.
11. Z. Shi, L. Zhang, G. Zhu, G. Yang, J. Hua, H. Ding, S. Feng, *Chem. Mater.* **11** (1999) 3565.
12. J. de Meulener, H. Tompa, *Acta Crystallogr*. **19** (1965) 1014.
13. G.M. Sheldrick, SHELEXS-97: A Program for Sloving Crystal Structure, University of Goettingen, Germany, 1997.
14. G.M. Sheldrick, SHELEXL-97: a program for crystal structurerefinement, Release 97–2, University of Goettingen, Germany, 1997.
15. L.J. Farrugia, *J. Appl. Crystallogr*. **32** (1999) 837.
16. V.S. Urusov, I.P. Orlov, *Crystallogr. Rep.* **44** (1999) 686.
17. T. Settheeworrarit, T.J. Prior, S. Meansiri, J. Limtrakul, A. Rujiwatra, *J. Inorg. Organomet. Polym*. **18** (2008) 253.
18. P.Y. Zavalij, M.S. Whittingham, *Acta Crystallogr.* B**55** (1999) 627.
19. M.I. Khan, E. Yohannes, V.O. Golub, C.J. O'Connor, R.J. Doedens, *Chem. Mater*. **19** (2007) 1890.
20. G. Desiraju, *J. Mol. Struct.* **656** (2003) 5.

CHAPTER IV

LANTHANIDE SULFATE FRAMEWORKS: SYNTHESIS, STRUCTURE, AND OPTICAL PROPERTIES

Bunlawee Yotnoi, **Apinpus Rujiwatra**, M. L. P. Reddy, Debajit Sarma, Srinivasan Natarajan

Crystal Growth & Design **11** (2011) 1347–1356.

INTRODUCTION

Traditional open-framework compounds are based on tetrahedral anions such as silicates and phosphates [1]. Persistent research over the years has established that other tetrahedral anions such as the arsenates [2], sulphates [3], selenates [4], and borates [5] can, in fact, become part of the extended structures. The wide structural and compositional diversity exhibited by this class of compounds is a testimony for the flexible nature of the structures. Of the many open-framework compounds that have been synthesized and characterized, those of the sulphates are an important family. The synthesis, structure, and properties of a number of transition metal sulphates have been reported in recent years [6]. Many transition metal sulphates have one- or two-dimensional structures, and it has been observed that the formation of three-dimensionally extended sulphate networks is difficult [7]. It is likely that the sulphate, $[SO_4]^{2-}$, is much less reactive compared to the phosphate, $[PO_4^{3-}]$, and the arsenate, $[AsO_4^{3-}]$, anions. It has been shown that the elements that prefer a higher coordination environment could be employed for the synthesis of the sulphate networks with three-dimensional structures. One such family of elements is the lanthanides [8].

Lanthanide-based compounds are being studied for their varied structural, physical, and chemical properties. It is known that the lanthanide-based compounds exhibit interesting luminescence behaviour [9]. Lanthanides exhibit intense photoluminescence behaviour and find applications as fluorescent probes in biochemistry and other emission-related properties [10]. It has been known that the lanthanide ions exhibit narrow *f-f* transitions, which could be exploited for light emitting device applications. Unfortunately, the *f-f* transitions are spin and parity forbidden, and exploiting such sharp transitions requires the use of sensitizers. Recently, aromatic carboxylates have been employed as a sensitizer for observing the metal-cantered emission of the rare earth ions [11]. Among the rare earth ions, Eu^{3+}, Tb^{3+}, and Nd^{3+} ions are important for use as optical centres. Eu^{3+} and Tb^{3+} ions are useful in the visible region (λ = *ca.* 400-800 nm), whereas Nd^{3+} ions are useful in the near infrared (IR) region (λ = 800-1700 nm). It has been shown that the Nd^{3+} ions also exhibit up-conversion behaviour of converting the IR radiation to the visible region through a two-photon absorption process [12].

In spite of the considerable progress achieved toward the understanding of the photophysical behaviour of the lanthanides, the subtle relationship that exists between the photophysical properties and the structure suggests the need for further studies. It occurred to us that the lack of higher dimensional structures in sulphates and the need for larger coordination numbers for the lanthanide ions can be gainfully employed in preparing new three dimensionally extended lanthanide sulphate compounds. It has been shown that the use of 4,4′-bipyridine (4,4′-bipy) enhances the dimensionality of the structures by acting as a rigid linker between the metal centres [13]. In addition, the use of 4,4′-bipy might assist in the luminescence behaviour of the lanthanides through initial absorption and energy transfer. We used a combination of these during the preparation of a new family of lanthanide sulphate compounds. Our efforts were successful and we have isolated three new lanthanide sulphate compounds. The compounds $[C_{10}H_{10}N_2][La(SO_4)_2]_3 2H_2O$ (**III**),

$[C_{10}H_{10}N_2][La(SO_4)_2(H_2O)_2]_2$ (**IVa**), $[C_{10}H_{10}N_2][Pr(SO_4)_2(H_2O)_2]_2$ (**IVb**), $[C_{10}H_{10}N_2][Nd_2(SO_4)_4(H_2O)_2]_2$ (**Va**), $[C_{10}H_{10}N_2][Sm_2(SO_4)_4(H_2O)_2]_2$ (**Vb**), and $[C_{10}H_{10}N_2][Eu_2(SO_4)_4(H_2O)_2]_2$ (**Vc**) all have a two-dimensional layer structure formed by the connectivity between the rare earth ions and the sulfate units. The 4,4′-bipy ligand occupies the interlamellar spaces. In this paper, we present the synthesis, structure, and photophysical properties of all the compounds.

EXPERIMENTAL

Synthesis and Initial Characterization

The compounds were prepared by employing the hydrothermal method. In a typical synthesis, for **III**, La_2O_3 (0.2283 g, 0.70 mmol) was added to 10 mL of deionized water. To this, 4,4′-bipy (0.3283 g, 2.10 mmol) and concentrated sulfuric acid (0.3 mL) were added under continuous stirring. The mixture was homogenized for 30 min at room temperature. The final mixture was transferred, sealed in a 23 mL PTFE lined autoclave, and heated at 200 ^oC for 24 h under autogenous pressure. The final product contained large quantities of colorless rod-shaped single crystals, which were filtered under a vacuum, washed with deionized water, and dried at ambient conditions (yield *ca.* 68% based on La). The other compounds were obtained employing similar conditions (Table 12). In the case of Pr (**IVb**), Nd (**Va**), Sm (**Vb**), and Eu (**Vc**), the final product contains large quantities of light green (Pr), light purple (Nd), light purple (Sm), and colorless (Eu) rod-type single crystals. In the case of compound **IVa**, the product was found to be a polycrystalline white powder. The product was later characterized by powder X-ray diffraction (PXRD) studies by comparing with the PXRD pattern of the related Pr compound (**IVb**). The PXRD pattern of **IVa** matched well with the simulated XRD pattern generated from the single crystal structure of Pr (**IVa**) compound. The microcrystalline phase **IVa** was indexed and the unit cell parameters were obtained from the PXRD patterns by the Le Bail method [14]. The Eu doped (4 mol % and 8 mol %) and Tb doped (4 mol % and 8 mol %) in place of La in **III** and Eu doped (4 mol % and 8 mol %) and Tb doped (4 and 8 mol) in place of La in **IVa** were prepared using the same experimental procedure as that employed for **III** and **IVa**. Initial characterizations were carried out by elemental analysis, PXRD, thermogravimetric analysis (TGA), and IR studies. PXRD patterns were recorded in the 2θ range 5-50^o using Cu K_α radiation (Philips X′pert).

Table 12 *Synthesis Conditions Employed for the Compounds.*

synthesis condition				composition
mole ratio	temp (°C)	time (h)	yield (%)	product
0.70 La_2O_3 + 2.10 4,4′-bipyridine + 0.3 mL of H_2SO_4 (conc) + 556 H_2O	200	24	68	$[C_{10}H_{10}N_2][La(SO_4)_2]\cdot 2H_2O$, (I)
0.70 La_2O_3 + 2.10 4,4′-bipyridine +0.5 mL of H_2SO_4 (conc) + 556 H_2O	125	24	65	$[C_{10}H_{10}N_2][La(SO_4)_2(H_2O)_2]_2$, (IIa)
0.23 Pr_6O_{11} + 2.10 4,4′-bipyridine +0.5 mL of H_2SO_4 (conc) + 556 H_2O	125	24	63	$[C_{10}H_{10}N_2][Pr(SO_4)_2(H_2O)_2]_2$, (IIb)
0.23 Nd_2O_3 + 2.10 4,4′-bipyridine +0.5 mL of H_2SO_4 (conc) + 556 H_2O	125	24	72	$[C_{10}H_{10}N_2][Nd_2(SO_4)_4(H_2O)_2]_2$, (IIIa)
0.23 Sm_2O_3 + 2.10 4,4′-bipyridine +0.5 mL of H_2SO_4 (conc) + 556 H_2O	125	24	68	$[C_{10}H_{10}N_2][Sm_2(SO_4)_4(H_2O)_2]_2$, (IIIb)
0.23 Eu_2O_3 + 2.10 4,4′-bipyridine +0.5 mL of H_2SO_4 (conc) + 556 H_2O	125	24	70	$[C_{10}H_{10}N_2][Eu_2(SO_4)_4(H_2O)_2]_2$, (IIIc)

The IR spectra for the compounds were recorded as KBr pellets (Perkin-Elmer, SPECTRUM 1000). The IR spectroscopic studies exhibit typical peaks corresponding to the hydroxyl group, the amino groups, *etc*. The main IR bands are (KBr): $\nu(H_2O)$ = 3230-3450 cm^{-1}, ν(N-H) = 3070-3110 cm^{-1}, ν(C-H) = 2670-2780 cm^{-1}, ν(C-H) = 1300-1500 cm^{-1}, $\nu_1(SO_4)$ = 950-1000 cm^{-1}, $\nu_3(SO_4)$ = 1100-1150 cm^{-1}, $\delta(SO_4)$ = 500-700 cm^{-1}. The IR spectrum can be useful for investigating the sulphate species.

In general, the free sulfate ions exhibit two bands at 1105 and 615 cm^{-1}, which are assigned to the $\nu_3(F2)$ stretching [$\nu_d(SO)$] and $\nu_4(F2)$ stretching [$\delta_d(OSO)$] modes, respectively. The coordination of the free sulphate group to the metal centres would lower the overall symmetry of the sulphate group and lead to the splitting of the ν_3 and ν_4 modes. The IR spectrum of the present compounds exhibits characteristic IR bands for the sulphate ions, SO_4^{-2}, with the IR-active region for the SO_4 tetrahedron located between 500 and 1150 cm^{-1}. In addition, we observed that the sulphate site symmetry is also lowered due to the many bridging coordination modes of the sulphate ions. The observed shoulders in the IR bands, thus, in the region 1025-1185 cm^{-1} may be attributed to the ν_3 modes and the shoulders in the region 554-670 cm^{-1} can be assigned to the ν_4 modes.

Table 13 *Crystal data and structure refinement parameters for the reported compounds.*

empirical formula	$C_5H_7NLaS_2O_9$	$C_5H_9NPrS_2O_{10}$	$C_{10}H_{14}N_2Nd_2S_4O_{18}$	$C_{10}H_{14}N_2Sm_2S_4O_{18}$	$C_{10}H_{14}N_2Eu_2S_4O_{18}$
formula weight	426.13	448.16	866.95	875.14	878.36
crystal system	triclinic	triclinic	triclinic	triclinic	triclinic
space group	$P\bar{1}$	$P\bar{1}$	$P\bar{1}$	$P\bar{1}$	$P\bar{1}$
a/Å	5.6238(2)	5.0354(1)	8.0119(5)	7.9585(2)	7.9370(6)
b/Å	7.3489(3)	7.0079(1)	9.4075(6)	9.3752(3)	9.3612(7)
c/Å	12.9709(5)	16.6321(3)	14.9538(9)	14.9270(4)	14.9214(10)
α/°	90.821(2)	88.50	79.439(1)	79.327(2)	79.348(1)
β/°	96.912(2)	87.94	83.749(1)	83.927(2)	83.996(1)
γ/°	100.159(2)	75.47	73.988(1)	73.830(2)	73.777(1)
vol/$Å^3$	523.48(3)	567.67(2)	1062.99(11)	1049.44(5)	1044.52(13)
Z	2	2	2	2	2
T/K	293(2)	293(2)	293(2)	293(2)	293(2)
ρ_{calc} (g cm^{-3})	2.703	2.622	2.696	2.769	2.793
μ (mm^{-1})	4.522	4.711	5.320	6.036	6.448
θ range (deg)	1.58−26.00	2.45−26.00	2.28−26.00	2.48−26.00	1.39−26.00
λ (Mo Kα) (Å)	0.71073	0.71073	0.71073	0.71073	0.71073
R_{int}	0.0262	0.0244	0.0252	0.0568	0.0416
reflection collected	7955	8568	11057	25572	10666
unique reflections	2007	2217	4159	4119	4082
no. of parameters	163	188	325	325	325
R indices [$I > 2\sigma(I)$]	$R_1 = 0.0161$, $wR_2 = 0.0438$	$R_1 = 0.0160$, $wR_2 = 0.0428$	$R_1 = 0.0215$, $wR_2 = 0.0538$	$R_1 = 0.0420$, $wR_2 = 0.1141$	$R_1 = 0.0534$, $wR_2 = 0.1400$
R indices (all data)	$R_1 = 0.0163$, $wR_2 = 0.0439$	$R_1 = 0.0166$, $wR_2 = 0.0431$	$R_1 = 0.0249$, $wR_2 = 0.0551$	$R_1 = 0.0438$, $wR_2 = 0.1154$	$R_1 = 0.0542$, $wR_2 = 0.1412$

[a] $M = Nd^{3+}$ (**IIIa**), Sm^{3+} (**IIIb**), and Eu^{3+} (**IIIc**). $R_1 = \Sigma||F_o| - |F_c||/\Sigma|F_o|$; $wR_2 = \{\Sigma[w(F_o^2 - F_c^2)]/\Sigma[w(F_o^2)^2]\}^{1/2}$. $w = 1/[\rho^2(F_o)^2 + (aP)^2 + bP]$. $P = [\max(F_o, O) + 2(F_c)^2]/3$, where $a = 0.0188$ and $b = 0.7083$ for **I**, where $a = 0.0190$ and $b = 0.7399$ for **IIb**, where $a = 0.0257$ and $b = 1.0297$ for **IIIa**, where $a = 0.0879$ and $b = 4.0864$ for **IIIb**, where $a = 0.1103$ and $b = 2.2382$ for **IIIc**.

Single Crystal Structure Determination

A suitable single crystal of each compound was carefully selected under a polarizing microscope and glued to a thin glass fibre. The single crystal data were collected on a Bruker AXS smart Apex CCD diffractometer at 293(2) *K*. The X-ray generator was operated at 50 kV and 35mA using Mo *K*α (λ = 0.71073 Å) radiation. Data were collected with ω scan width of 0.3°. A total of 606 frames were collected in three different settings of φ (0, 90, 180°) keeping the sample-to-detector distance fixed at 6.03 cm and the detector position (2θ) fixed at -25°. The data were reduced using SAINTPLUS [15] and an empirical absorption correction was applied using the SADABS program [16]. The structure was solved and refined using SHELXL97 [17] present in the WinGx suite of programs (Version 1.63.04a) [18]. All the hydrogen positions were initially located in the difference Fourier maps, and for the final refinement, the hydrogen atoms were placed in geometrically ideal positions and refined in the riding mode. Final refinement included atomic positions for all the atoms, anisotropic thermal parameters for all the non-hydrogen atoms, and isotropic thermal parameters for all the hydrogen atoms. Full-matrix least-squares refinement against $|F^2|$ was carried out using the

WinGx package of programs [18]. Details of the structure solution and final refinements for the compounds are given in Table 13.

RESULTS & DISCUSSION

*Structure of $[C_{10}H_{10}N_2][La(SO_4)_2]_3.2H_2O$ (**III**):* The asymmetric unit of **III** consists of 18 non-hydrogen atoms. It has one crystallographically independent La^{3+} ion, two sulphate groups, half a molecule of protonated 4,4′-bipy molecule, and a lattice 4,4′-bipy unit is related to the other half through the C-C bond, which lies on the centre of symmetry. The La^{3+} ions are surrounded by nine sulfate oxygens forming a LaO_9 polyhedra, with a distorted tricapped trigonal prismatic coordination environment. The oxygen atoms O3, O5, and O6 were found to be three coordinated, binding two La atoms and one S atom. The La-O bond distances are in the range of 2.474(2)-2.624(2) Å (*av.* 2.563 Å). The O-La-O bond angles are in the range 53.59(6)- 160.11(6)°. The selected bond distances are given in Table 14.

Table 14 *Selected Observed Bond Distances in the Lanthanide Sulphate Compounds.*

bond	distance (Å)	bond	distances (Å)	bond	distances (Å)
		III			
La(1)−O(1)#1	2.473(2)	La(1)−O(4)	2.555(1)	La(1)−O(6)#5	2.610(2)
La(1)−O(2)#2	2.474(2)	La(1)−O(5)#4	2.575(2)	La(1)−O(3)	2.613(2)
La(1)−O(3)#3	2.555(2)	La(1)−O(5)	2.589(2)	La(1)−O(6)	2.623(2)
		IVb			
Pr(1)−O(1)#1	2.402(2)	Pr(1)−O(4)#3	2.480(2)	Pr(1)−O(7)	2.602(2)
Pr(1)−O(2)#2	2.434(2)	Pr(1)−O(5)	2.504(2)	Pr(1)−O(8)	2.615(2)
Pr(1)−O(3)	2.469(2)	Pr(1)−O(6)	2.527(2)	Pr(1)−O(7)#3	2.820(2)
		IVa			
Nd(1)−O(1)	2.378(3)	Nd(1)−O(4)	2.471(2)	Nd(1)−O(7)	2.526(2)
Nd(1)−O(2)	2.429(3)	Nd(1)−O(5)#2	2.482(2)	Nd(1)−O(4)#3	2.603(2)
Nd(1)−O(3)#1	2.460(3)	Nd(1)−O(6)	2.490(3)	Nd(1)−O(8)	2.731(2)
Nd(2)−O(9)#2	2.340(2)	Nd(2)−O(12)	2.473(3)	Nd(2)−O(8)	2.517(2)
Nd(2)−O(10)	2.423(3)	Nd(2)−O(13)#4	2.489(2)	Nd(2)−O(15)	2.548(3)
Nd(2)−O(11)	2.470(3)	Nd(2)−O(14)#5	2.509(2)		

[a] Symmetry transformations used to generate equivalent atoms: For I: #1 $x+1, y, z$. #2 $x-1, y, z$. #3 $-x+1, -y+1, -z+2$. #4 $-x, -y+1, -z+2$. #5 $-x, -y, -z+2$. For II: #1 $-x+1, -y, -z$ #2 $x, y+1, z$ #3 $x+1, y, z$. For IIIa: #1 $x, y+1, z$. #2 $-x+1, -y, -z+1$ #3 $-x+1, -y+1, -z+1$. #4 $x, y-1, z$ #5 $-x, -y, -z+1$.

The structure of **III** consists of linkages between LaO_9 tricapped trigonal prisms and SO_4 tetrahedral units. The LaO_9 units are connected through three coordinated oxygen atoms (O3, O5, and O6) forming an infinite two-dimensional La-O-La network (Fig. 22a). The two sulphate tetrahedral units, $S1O_4$ and $S2O_4$, are connected to the La-O-La two-dimensional layers in such a way that they connects with four and three La atoms respectively, and each possess one terminal S=O bond (S1-O7 and S2-S8) (Fig. 22b). The layers are arranged in a *ABABAB⋯* fashion and are stabilized by the N-H⋯O interaction between the protonated 4,4′-bipy cation and the framework oxygen (N1-H1 ⋯O7, N-O = 2.72 Å, angle = 143°) (Fig. 22c).

*Structure of $[C_{10}H_{10}N_2][Pr(SO_4)_2(H_2O)_2]_2$ (**IVb**)*: The asymmetric unit of **IVb** consists of 19 non-hydrogen atoms. It has one crystallographically independent Pr^{3+} atoms, two sulphate units, half a molecule of protonated 4,4′-bipy molecule, and two coordinated water molecules. The Pr^{3+} ions are coordinated by seven sulphate oxygen and two aqua oxygen forming a PrO_9 polyhedra with a

distorted tricapped trigonal prism arrangement. The half 4,4′-bipy molecule is related to the other half *via* the C-C bond, which lies on the centre of symmetry. The Pr-O bond distances are in the range of 2.402(2)-2.820(2) Å (*av.* 2.539 Å). The O-Pr-O bond angles are in the range 54.65(6)-149.31(6)°. The selected bond distances are given in Table 14.

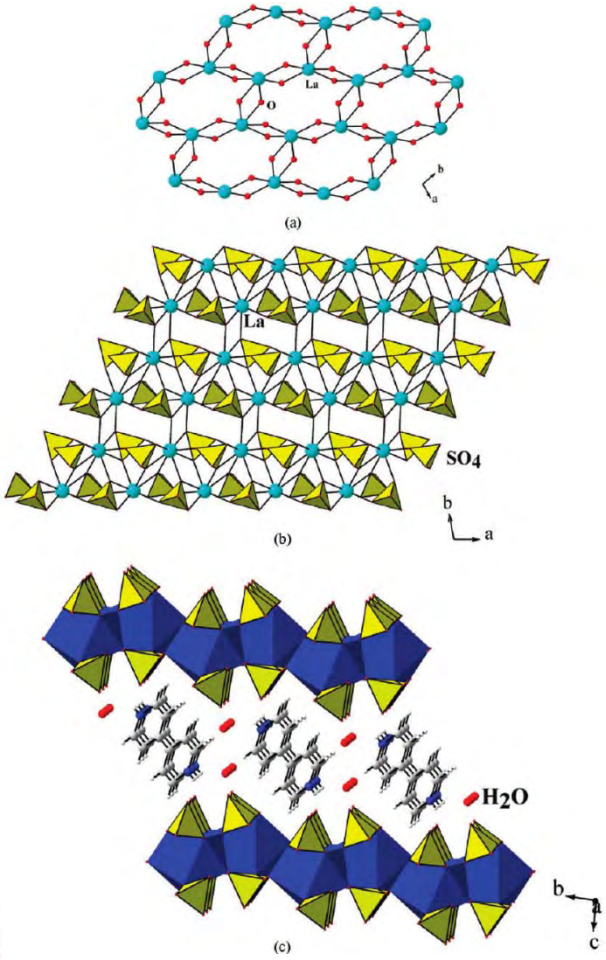

Fig. 22 *(a) View of the two-dimensional infinite La-O-La layer in* $[C_{10}H_{10}N_2][La(SO_4)_2]_3.2H_2O$, ***III****. Only the lanthanide ion connectivity is shown. (b) View of the two-dimensional lanthanide sulphate layer in the ab plane. (c) The arrangement of layers in the bc plane. Note that the 4,4′-bipy molecules occupy interlamellar spaces along with the water molecules.*

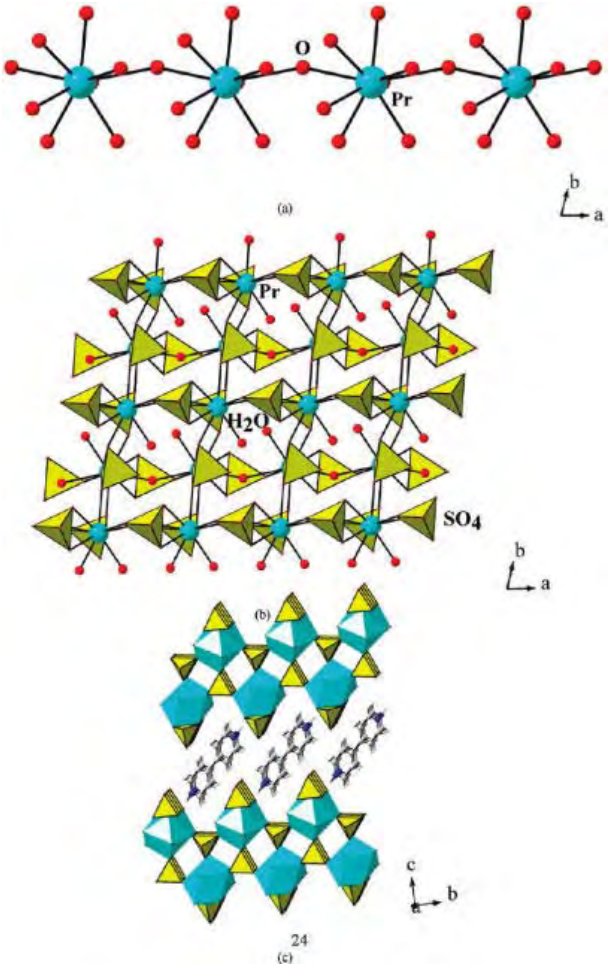

Fig. 23 *(a) The one-dimensional infinite Pr-O-Pr chains observed in* $[C_{10}H_{10}N_2][Pr(SO_4)_2(H_2O)_2]_2$, ***IVb****. (b) View of the two-dimensional praseodymium sulfate layer in the ab plane. Note that the bound water molecules project out of the plane of the layers. (c) Arrangement of the layers in the bc plane*

The structure of **IVb** consists of a linkage between PrO_9 and SO_4 units forming a two-dimensional structure. The Pr atoms are connected through a μ_2 oxygen atom forming one-dimensional Pr-O-Pr infinite chains (Fig. 23a). The sulphate tetrahedra $S1O_4$ connects the Pr-O-Pr chains forming the two-dimensional structure, which is anionic. The other sulphate tetrahedral $S2O_4$ connects only to the Pr centres and is not employed in extending the dimensionality of the structure. This arrangement appears to satisfy the coordination requirement of the central Pr atoms only (Fig. 23b). Another view to understand the structure is to consider the connectivity between PrO_9 and $S1O_4$ polyhedral units, which forms a one-dimensional edge-shared ladder-like structure. The ladder units are connected with the Pr-O-Pr linkages giving rise to the two-dimensional layers. The layers are arranged in a *ABABAB*••• fashion and the interlamellar space is occupied by the protonated 4,4′-bipy cataions (Fig. 23c). Only one hydrogen bond interaction is observed (N(1)-H(1)-O(8); N-O = 2.77 Å, angle = 155°) between the bipyridinium cation and the framework oxygen, which is not very strong [19].

*Structure of $[C_{10}H_{10}N_2][M_2(SO_4)_4(H_2O)_2]_2$, M = Nd^{3+} (**Va**), Sm^{3+} (**Vb**), and Eu^{3+} (**Vc**):* The asymmetric unit of $[C_{10}H_{10}N_2][M_2(SO_4)_4(H_2O)_2]_2$, M = Nd^{3+} (**Va**), Sm^{3+} (**Vb**), and Eu^{3+} (**Vc**) consists of 36 non-hydrogen atoms. It has two crystallographically independent M^{3+} ion, four sulphate groups, one protonated 4,4′-bipy molecule, and two coordinated water molecules. The $M1^{3+}$ ions are surrounded by eight sulphate oxygen and one aqua oxygen to form a $M1O_9$ polyhedra, which has a distorted tricapped trigonal prismatic coordination environment. In the case of $M2^{3+}$ ions, seven sulfate oxygen and one aqua oxygen surround the central metal atom forming a $M2O_8$ polyhedra, with a distorted square antiprism coordination geometry. The oxygen atoms, O4 and O8, are three coordinated connecting two metal centres and a sulphate unit. The M-O bond distances are in the range for Nd: 2.340(2)-2.731(2) Å (*av.* 2.490 Å); for Sm: 2.306(4)-2.734(4) Å (*av.* 2.462 Å) and for Eu: 2.292(4)-2.733(4) Å (*av.* 2.450 Å). The O-M-O bond angles are in the range for Nd: 53.76(7)-151.02(9)°; for Sm: 54.14(12)-150.76(14)° and for Eu: 54.04(13)-151.09(15)°. The selected bond distances are given in Table 14.

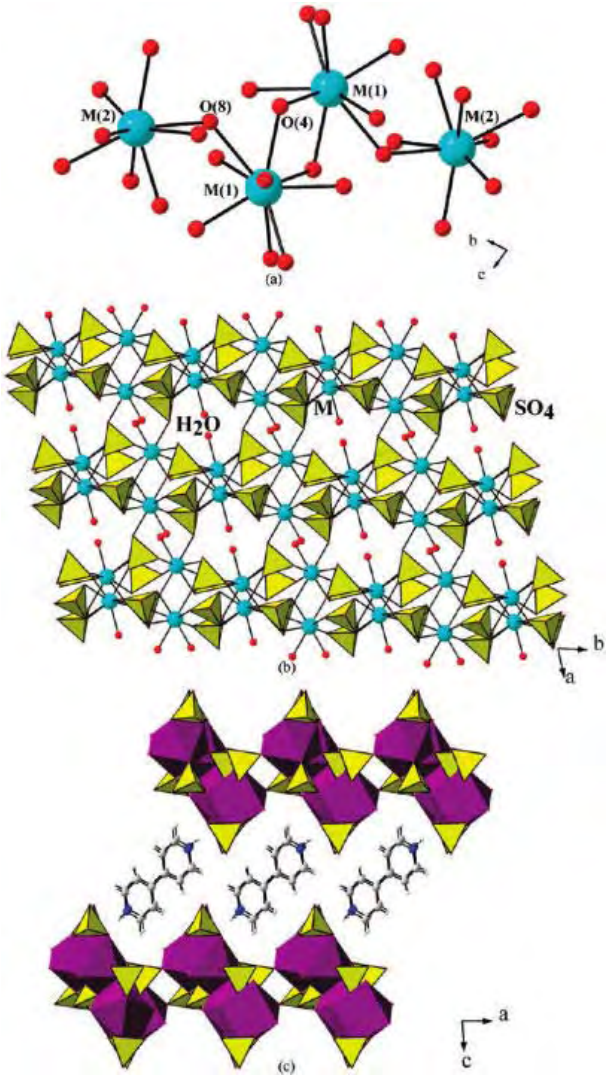

Fig. 24 *(a) View of the tetrameric unit found in $[C_{10}H_{10}N_2][Nd_2(SO_4)_4(H_2O)_2]_2$, **Va**. (b) The two-dimensional layer in the ab plane. (c) The arrangement of the layers in **Va** .*

In the structure of **Va**, the MO_9 and MO_8 polyhedral units are linked with the sulphate tetrahedra giving rise to a two-dimensional anionic layer structure. The $M1O_9$ units are linked through the three-connected oxygen atom, O8, with $M2O_8$ units forming a four-membered cluster (Fig. 24a). The sulphate tetrahedral units bridge the four-membered clusters giving rise to the two-dimensional layer arrangement with an overall anionic layer of the formula, $[M_2(SO_4)_4(H_2O)_2]^-$ (Fig. 24b). The charge is balanced by the presence of the protonated 4,4′-bipy cations, which occupies the interlamellar spaces. N-H•••O hydrogen bond interactions (N1-H1•••O1; N-O = 2.757 Å, angle = 170°, N2-H2•••O6; N-O = 2.830 Å, angle = 171°) have been observed, which appears to be strong [18].

Structural comparison: The three structures (**III**, **IVb**, and **Va**) identified in the present study have some common features: (*i*) The lanthanide ions have predominantly a tricapped trigonal prismatic coordination, (ESI, X); (*ii*) the lanthanide ions are connected through the three-coordinated oxygen atoms forming two-dimensional La-O-La layers in **IIIa**, a one-dimensional chain in **IVb** and a four-member cluster in **Va**. In addition, the sulphate connectivity in these structures also exhibit subtle differences. The sulphate groups participate in bonding between two lanthanide centres in **III**, while half the sulphate units in **IVa** and **Va** appear to satisfy the coordination requirement of the lanthanide centres only. The larger coordination (8 and 9) requirement of the lanthanide ions could be responsible for this, which also resulted in having coordinated aqua ligands in the structures of **IVa** and **Va**. Exclusive use of ligands for coordination requirements is not new, and examples of such roles for the participating ligands have been observed earlier in framework compounds [20]. The presence of 4,4′-bipy as a cation in the structure is also important and noteworthy. In many framework compounds, the 4,4′-bipy generally binds with the metal centers extending dimensionality [21] but here it performs the role of a template molecule.

When the lanthanide connectivity alone is considered in these structures, we observed a honeycomb arrangement in the case of **III** and **Va**, whereas a square-grid results for **IVb** (Fig. 25). The formations of such networks in lanthanide containing compounds are rare.

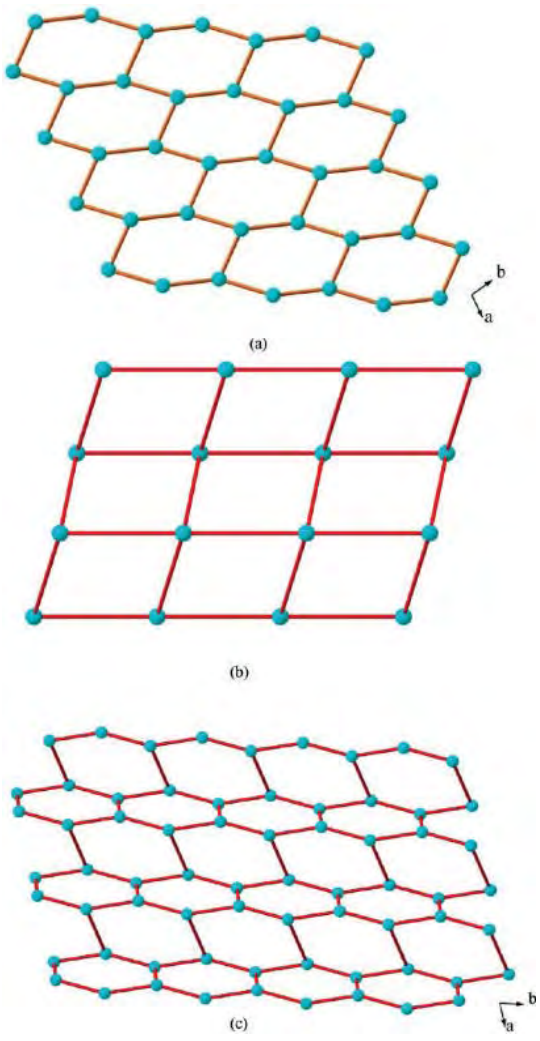

Fig. 25 *The lanthanide ion connectivity in the present structures: (a) the honeycomb layer in **III**; (b) the square-grid layer in **IVb**; (c) the honeycomb layer in **Va**.*

Thermogravimetric Studies: TGA (Fig. 26)on all the compounds has been carried out in flowing air (flow rate = 20 mL min^{-1}) in the temperature range 30-850 ^{o}C (heating rate = 5 ^{o}C min^{-1}). All the compounds exhibit comparable thermal behaviour. For compound **III**, two step weight loss was observed. The first weight loss of 3.7% observed in the range 150-250 ^{o}C corresponds to the loss of water molecules (4.2%). The second sharper weight loss of 44.9% in the range 480-520 ^{o}C corresponds to the loss of the 4,4′-bipy and some sulphate (calc. 46.5%). In the case of **IVa** and **IVb** we observed a near identical behaviour in terms of the weight losses though the total weight loss was different. The first weight loss of 7.8% in the range 140-190 ^{o}C corresponds to the loss of water molecules (calc. 8% for **IVa** and **IVb**). The second weight loss 31.2% for **IVa** and 44.2% for **IVb** in the range 410-500 ^{o}C corresponds to the loss of the 4,4′-bipy and sulphate (calc. 44.4% for **IVa**: 45.6% for **IVb**). In the case of compounds **III** and **IVa**, the calcined product was found to be crystalline and corresponds to the compound $La_2O_2SO_4$ (JCPDS: 85-1535). In the case of **IVb**, the final calcined product was found to be $Pr_2O_2SO_4$ (JCPDS: 29-1073). The TGA behaviour of compounds **Va**, **Vb** and **Vc** are also similar, exhibiting a two-step weight loss. For **Va**, the first weight loss of 3.7% in the range 180-250 ^{o}C, corresponds to the loss of the coordinated water molecules (calc. 4.4%). The second weight loss of 25.3% in the range 470-500 ^{o}C is followed by another loss. The total weight loss of 55% corresponds to the loss of the 4,4′-bipy along with some sulphate. The calcined product was found to be crystalline and corresponds to the phase $Nd_2O_2SO_4$ (JCPDS: 48-1829). Similarly for **Vb** and **Vc**, we observed the formation of $Sm_2O_2SO_4$ (JCPDS: 41-0681) and $Eu_2O_2SO_4$ (JCPDS: 48-1211) phases after the TGA studies.

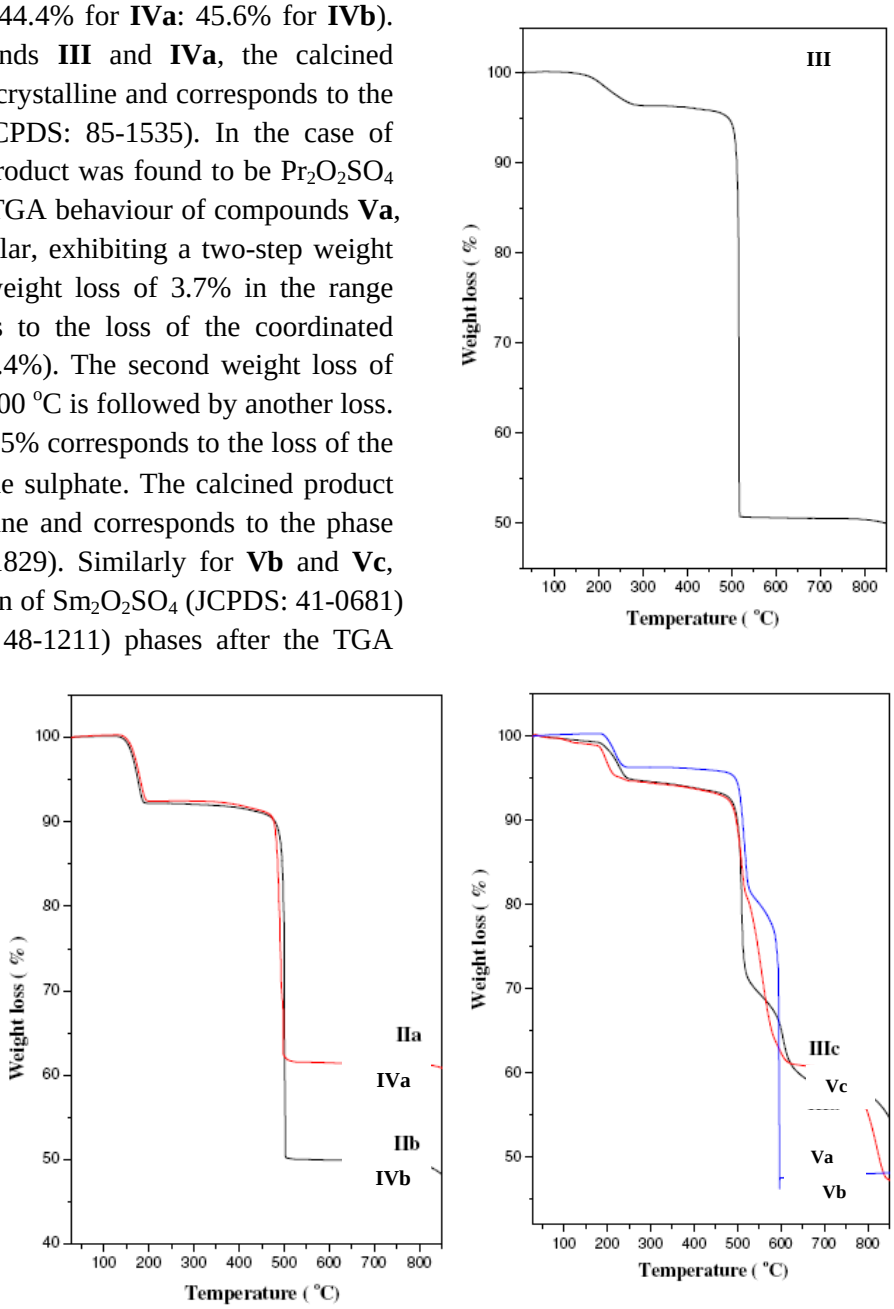

Fig. 25 *TGA of the reported compounds.*

<u>*Luminescence studies*</u>: All the compounds exhibited one strong absorption band cantered around 450 nm, which corresponds to the ligand to metal charge transfer (LMCT) band, when excited using a wavelength of λ = 310 nm. To probe and to appreciate the LMCT effect further, we have prepared two sets of compounds by doping a small concentration of Eu^{3+} and Tb^{3+} (4% and 8%) in place of La^{3+} (compounds **III** and **IVa**). The results of the photoluminescence studies were shown in Fig. 26 and 27. The doped samples exhibited sharp characteristics peaks, in addition to the LMCT peak at 450 nm. We also observed a pink colour for Eu^{3+} doped samples and a green colour for the Tb^{3+} doped samples when observed under the UV illumination. When excited using a wavelength of λ = 310 nm, we observed the characteristic $^5D_0 \rightarrow {}^7F_J$ (J = 1, 2) emission lines for Eu^{3+} and $^5D_4 \rightarrow {}^7F_J$ (J = 3, 4, 5, 6) emission lines for Tb^{3+}, respectively (Fig. 26 and 27). It may be noted the intensity of the characteristic lanthanide emission due to Eu^{3+} and Tb^{3+} is not strong, suggesting that the energy transfer process in the present compounds are quite poor. This situation is in contrast to the behaviour observed in many of the lanthanide benzene carboxylate frameworks, where intense lanthanide emissions have been observed [22]. Even though the intensity of the emission in the present compounds is not strong, we sought to investigate the lifetime of the excited states in the doped compounds.

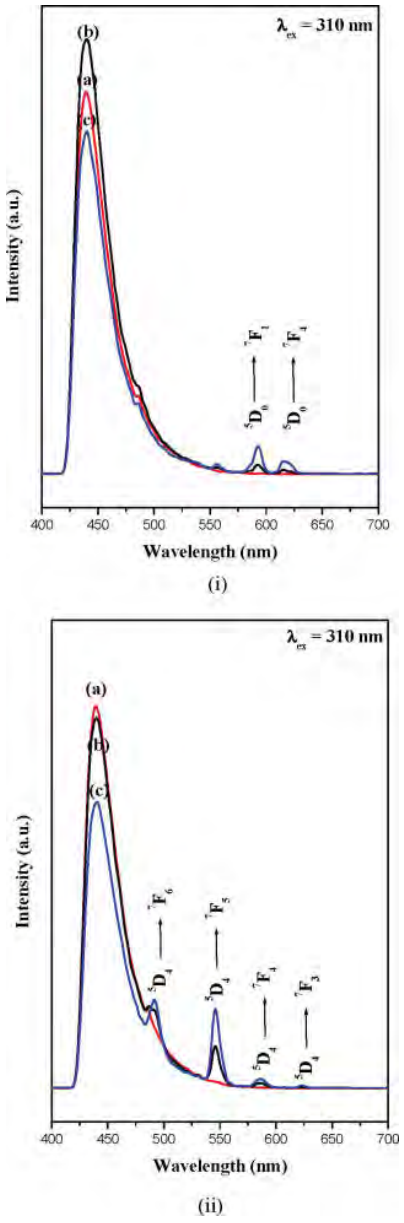

Fig. 26 *Room temperature photoluminescence spectra of **III** and the corresponding Eu^{3+} and Tb^{3+} doped samples. (i) (a) **III**, (b) 4 mol % and (c) 8 mol % Eu^{3+} doped samples. (ii) (a) **III**, (b) 4 mol % and (c) 8 mol % Tb^{3+} doped samples.*

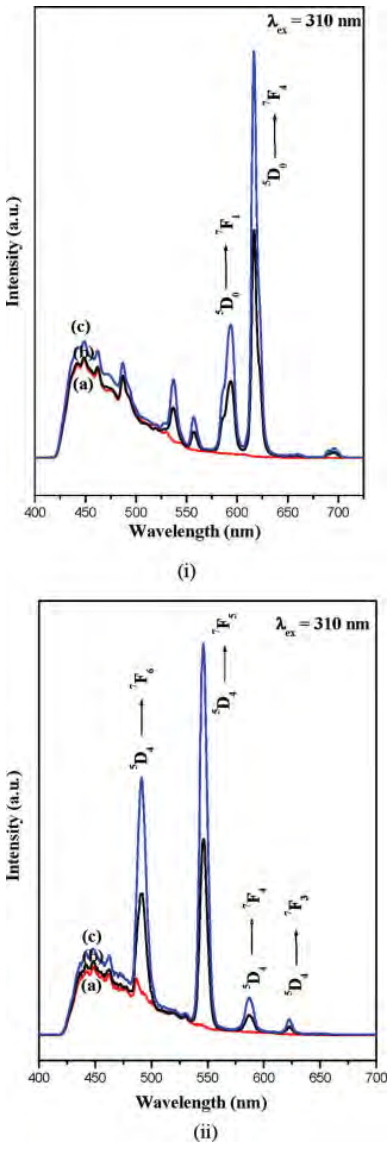

Fig. 27 *Room temperature photoluminisence spectra of **IVa** and the corresponding Eb^{3+} and Tb^{3+} doped samples.(i) (a) **IVa**, (b) 4 mol % and (c) 8 mol % Eu^{3+} doped samples. (ii) (a) Compound **IVa**, (b) 4 mol % and (c) 8 mol % Tb^{3+} doped samples.*

Lifetime studies: The luminescence lifetimes of the excited states of the 4 mol % doped samples of I and IIa were investigated. The $^5D_0 \rightarrow {}^7F_1$ band for the Eu^{3+} samples **III** (4% Eu) and **IVa** (4% Eu) and the $^5D_4 \rightarrow {}^7F_6$ emission band for the Tb^{3+} samples **III** (4% Tb) and **IVa** (4% Tb) were monitored for the lifetime studies employing 310 nm excitation at room temperature. The experimental luminescent decay curve was fitted to a single exponential decay function as

$$I = I_0 \exp(-t/\tau)$$

where I and I_0 stands for the luminescent intensities at time $t = t$ and $t = 0$ and τ is defined as the luminescent lifetime. The fit of the curve for a single exponential decay suggests a lifetime value of 0.38 ms for **III** (4% Eu) (Fig. 28). The lifetime values for the other samples are given in Table 15.

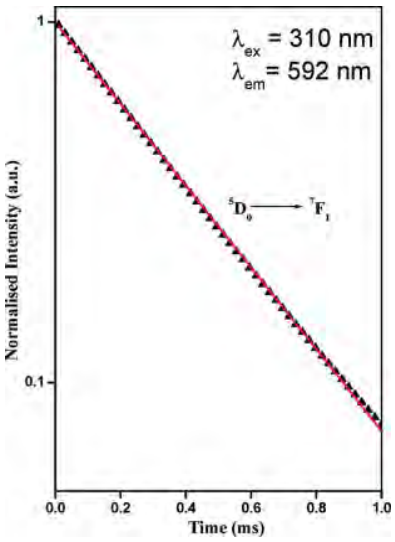

Fig. 28 *Room temperature luminescence decay of the $^5D_0 \rightarrow {}^7F_1$ emission band for the 4 mol % Eu3þ doped compound **III**.*

Table 15 *Lifetime values for **III** (4% Eu), **IVa** (4% Eu), **III** (4% Tb), and **IVa** (4% Tb).*

S. no.	compound	lifetime (in ms)
		$^5D_0 \rightarrow {}^7F_1$
1.	I (4 mol % Eu)	0.3833
2.	IIa (4 mol % Eu)	0.2726
		$^5D_4 \rightarrow {}^7F_6$
4.	I (4 mol % Tb)	1.1801
5.	IIa (4 mol % Tb)	1.3420

The values of the lifetime observed in the present compounds are comparable to the values generally known for the pure Eu^{3+} and Tb^{3+} compounds reported in the literature [23].

Up-conversion Studies: There has been some recent interest in the study of a possible two-photon up-conversion processe in compounds containing Nd^{3+} ions [24]. The up-conversion in these compounds are actually anti-Stokes emissions. Among the present compounds, $[C_{10}H_{10}N_2][Nd_2(SO_4)_4(H_2O)_2]_2$, **Va**, could exhibit this up-conversion emission. The room temperature UV-vis spectrum of **Va** indicated that the absorption increases rapidly with decreasing wavelength due to the intra-ligand absorption (Fig. 29). From the UV studies, the absorption bands of the Nd^{3+} ions appear to exhibit primary ground state Stark splitting of the Eigen states due to the possible crystal field effects [25].

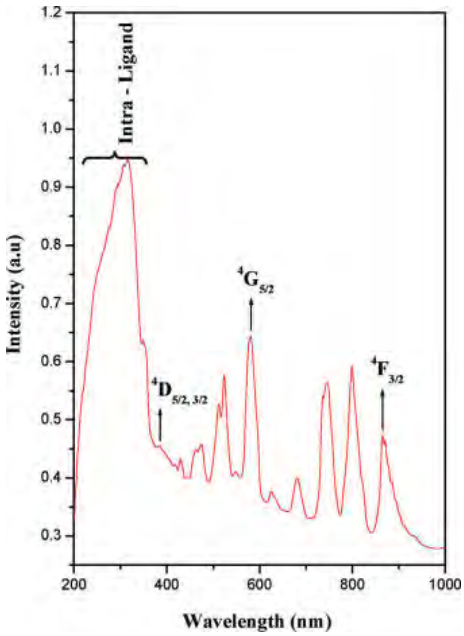

Fig. 29 *Room temperature UV-vis spectra of compound* $[C_{10}H_{10}N_2][Nd_2(SO_4)_4(H_2O)_2]_2$, ***Va.***

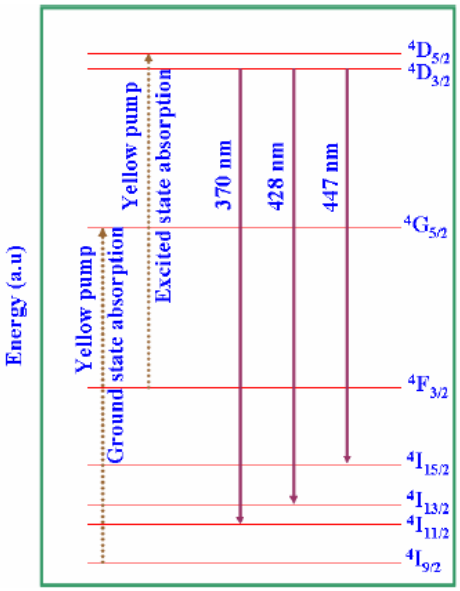

Fig. 30 *schematic energy level diagram for* Nd^{3+} *in* ***Va.***

A schematic of the energy transfer process in the up-conversion using Nd^{3+} ions suggests the possible pathway for the two-photon up-conversion processes (Fig. 30). The Nd^{3+} compound (**Va**) has an intense absorption at *ca.* 582 nm, which corresponds to the $^4I_{9/2} \rightarrow {}^4G_{5/2}$ transition. This is a hypersensitive band and also satisfies the selection rules of $\Delta J = \pm 2$, $\Delta L = \pm 2$, and $\Delta S = 0$. The luminescence of **Va** at short wavelength results from the $^4D_{3/2}$ levels. In order to observe the possible two-photon absorption in **Va**, one needs to excite the photon to either the $^4D_{3/2}$ or $^4D_{5/2}$ levels. The direct excitation to this level may be limited due to the intra-ligand absorption by the short wavelength radiation. In addition, the excitation wavelength ($\lambda = 582$ nm) is far from the wavelength that may be required for the intra-ligand absorption. Thus, during our studies, the first excited $^4G_{5/2}$, level can relax non-radiatively to the $^4F_{3/2}$ level where some population can occur. This photon may further undergo excited state absorption (ESA), while the others relax to lower energy levels. The excitation wavelength (*ca.* 582 nm) was used to populate the $^4F_{3/2}$ levels and efficient re-excitation from the $^4F_{3/2}$ to the $^4D_{5/2}$ levels. It is likely that the excited $^4D_{5/2}$ levels from the ESA also relax non-radiatively to the $^4D_{3/2}$ levels from which the up-converted luminescence may be observed. The up-

converted luminescence spectra for this yellow pumping (582 nm excitation) from $^4D_{3/2}$ levels are shown in Fig. 31.

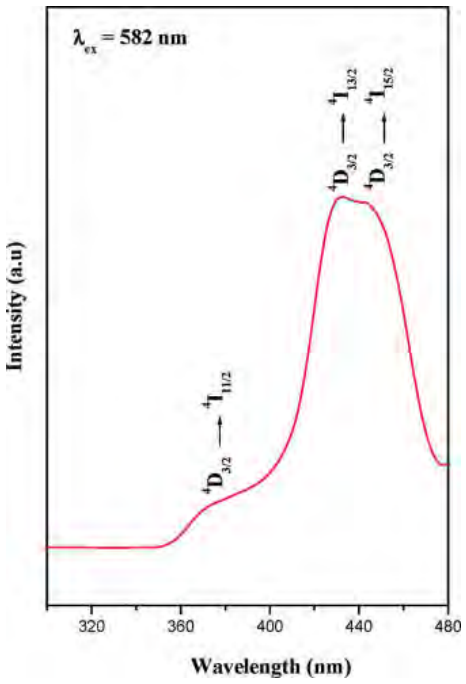

Fig. 31 *Room temperature up-conversion spectra of* ***Va****, using 582 nm radiation.*

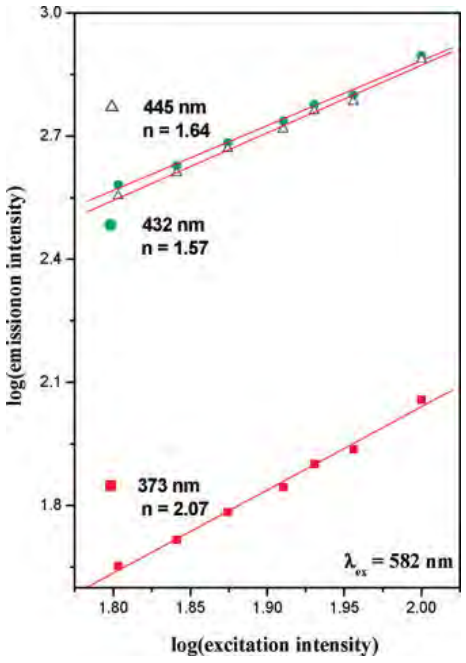

Fig. 33 *The log-log plot of the excitation intensity dependence of the luminescence intensity for λ = 373, 432, and 445 nm.*

To study the dependence of the excitation intensity on the Up-converted luminescence intensity, we have also performed a simple power dependence study. Here a series of sterile glass plates are placed sequentially in the pathway between the excitation source and the sample. The decrease in excitation intensity per glass plate was pre-calibrated using the UV-vis spectrometer in the transmission mode and also normalized with respect to the transmission obtained in the absence of any glass slides. The decrease in the luminescence intensity for six successive glass plates is shown in Fig. 32. We have plotted the log-log plot of the luminescence intensity versus the excitation intensity, and a fit could provide a clue to the number of photons involved in the up-conversion process (Fig. 33).

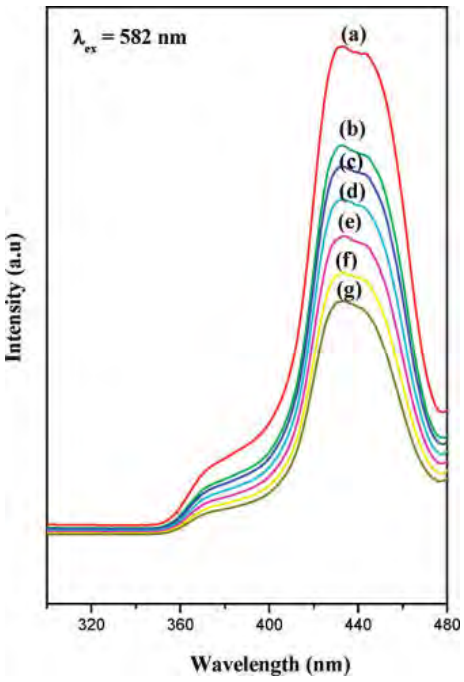

Fig. 32 *The observed emission dependence on the excitation intensity of* ***Va****. (a) 100%, (b) 90.32% (c) 85.19%, (d) 81.34%, (e) 74.86%, (f) 69.38% and (g) 63.56%.*

The plot for the three emission peaks at 373, 432, and 445 nm was found to be linear with a slope of 2.07, 1.57, and 1.64, respectively. These values suggest that the excitation may be due to two photons that are employed successfully. The ideal value for the two photon absorption should be closer to 2, and the decreased value may be due to the loss of some of the excitation energy at the one-photon absorption level, which could result from the $^4F_{3/2} \rightarrow {}^4I_{11/2}$, $^4F_{3/2} \rightarrow {}^4I_{9/2}$ level in the near-IR region.

CONCLUSIONS

The synthesis, structure, and characterization of a family of layered lanthanide sulphate phases have been accomplished. The formation of related compounds by subtle variations of the synthesis conditions suggests the importance of the reaction parameters in the formation of framework compounds. The observation of 4,4′-bipyridine molecules being protonated and occupying the interlamellar spaces is important and not common. The formation of two-dimensional La-O-La network in **III** is noteworthy as such networks are not commonly observed. The observation of two-photon up-conversion behaviour in the Nd containing compound (**Va**) and metal cantered emission in Eu^{3+} (red) and Tb^{3+} (green) doped samples of lanthanum (**III** and **IV**) indicates the possibility of using these compounds as optical probes. Further study is required to evaluate the structure-property relationship in these compounds.

REFERENCES

1. (a) S. Natarajan, S. Mandal, *Angew. Chem., Int. Ed*. **47** (2008) 4798. (b) R. Murugavel, A. Choudhury, M.G. Walawalkar, R. Pothiraja, C.N.R. Rao, *Chem. Rev.* **109** (2009) 4283. (c) A.K. Cheetham, G. Ferey, T. Loiseau, *Angew. Chem., Int. Ed.* **38** (1999) 3268. (d) S.T. Wilson, B.M. Lok, C.A. Messina, T.R. Cannan, E.M. Flanigen, *J. Am. Chem. Soc.* **104** (1982) 1146. (e) W.M. Meier, D.H. Oslen, C. Baerlocher, Atlas of Zeolite Structure Types; Elsevier: London, 1996. (f) L. Chen, X. Bu, *Inorg. Chem.* **45** (2006) 4654. (g) C.N.R. Rao, S. Natarajan, A. Choudhury, S. Neeraj, A.A. Ayi, *Acc. Chem. Res.* **34** (2001) 80. (h) R. Murugavel, M.G. Walawalkar, M. Dan, H.W. Roesky, C.N.R. Rao, *Acc. Chem. Res.* **37** (2004) 763.
2. (a) V.K. Rao, S. Chakrabarti, S. Natarajan, *Inorg. Chem.* **46** (2007) 10781. (b) V.K. Rao, M.A. Green, S.K. Pati, S. Natarajan, *J. Phys. Chem. B* **111** (2007) 12700. (c) S. Chakrabarti, S. Natarajan, *Angew. Chem., Int. Ed.* **41** (2002) 1224. (d) S. Chakrabarti, S.K. Pati, M.A. Green, S. Natarajan, *Eur. J. Inorg. Chem.* (2003) 4395. (e) S. Ekambaram, S.C. Sevov, *Inorg. Chem*. **39** (2000) 2405. (f) X. Bu, T.E. Gier, G. Ferey, *Chem. Commun.* (1997) 2271.
3. (a) J. Lin, D.-W. Dong-Wei Guo, Y.-Q. Tian, *Cryst. Growth Des.* **8** (2008) 4571. (b) C.N.R. Rao, J.N. Behera, M. Dan, *Chem. Soc. Rev.* **35** (2006) 375. (c) G. Paul, A. Choudhury, C.N.R. Rao, *Chem. Mater.* **15** (2003) 1174.
4. S.V. Krivovichev, V. Kahlenberg, I.G. Tananaev, B.F. Myasoedov, *Z. Anorg. Allg. Chem*. **631** (2005) 2358.
5. (a) A.K. Paul, S. Natarajan, *Cryst. Growth Des.* **10** (2010) 765. (b) A.K. Paul, K. Sachidananda, S. Natarajan, *Cryst. Growth Des.* **10** (2010) 456.
6. (a) Y. Fu, Z. Xu, J. Ren, H. Wu, R. Yuan, *Inorg. Chem.* **45** (2006) 8452. (b) J.N. Behera, C.N.R. Rao, *Chem. Asian J.* **1** (2006) 742. (c) J.N. Behera, K.V. Gopalkrishnan, C.N.R. Rao, *Inorg. Chem.* **43** (2004) 2636. (d) G. Paul, A. Choudhury, E.V. Sampathkumaran, C.N.R. Rao, *Angew. Chem. Int. Ed.* **41** (2002) 4297.

7. (a) A. Rujiwatra, C.J. Kepert, M.J. Rosseinsky, *Chem. Commun.* (1999) 2307. (b) A. Rujiwatra, C.J. Kepert, J.B. Claridge, M.J. Rosseinsky, H. Kumagai, M. Kurmoo, *J. Am. Chem. Soc.* **123** (2001) 10584. (c) J.N. Behera, C.N.R. Rao, *Can. J. Chem.* **83** (2005) 668.
8. (a) H. Akkari, P. Benard-Rocherulle, H. Merazig, T. Roisnel, J. Rocherulle, *Solid State Sci.* **8** (2006) 704. (b) S. Ding, Y. Xu, L. Nie, W. Feng, *J. Cluster Sci.* **17** (2006) 627. (c) R. Bataille, D. Louer, *J. Mater. Chem*. **12** (2002) 3487.
9. (a) K. Binnemans, *Chem. Rev.* **109** (2009) 4283. (b) L. Yan, Q. Yue, Q.-X. Jia, G. Lemercier, E.-Q. Gao, *Crys. Growth Des.* **9** (2009) 2984. (c) S.J.A. Pope, B.J. Coe, S. Faulkner, E.V. Bichenkova, X. Yu, K. Douglas, *J. Am. Chem. Soc*. **126** (2004) 9490. (d) B. Zhao, X.Y. Chen, P. Cheng, D.Z. Liao, S.P. Yan, Z.H. Jiang, *J. Am. Chem. Soc.* **126** (2004) 15394. (e) C.M. Rudzinski, A.M. Young, D.G. Nocera, *J. Am. Chem. Soc.* **124** (2002) 1723. (f) T. Justel, H. Nikol, C. Ronda, *Angew. Chem., Int. Ed.* **37** (1998) 3084.(g) G. Blasse, B.C. Grabmaier, Luminescent Materials; Springer: Berlin, 1994. (h) J.C.G. Bunzli, G.R. Choppin, Lanthanide Probes in Life, Chemical and Earth Science, Theory and Practice; Elsevier: Amsterdam, 1989.
10. (a) D. Sendor, M. Hilder, T. Juestel, P.C. Junk, U.H. Kynast, *New J. Chem.* **27** (2003) 1070. (b) D.T. de Lill, A. de Bettencourt-Dias, C.L. Cahill, *Inorg. Chem*. **46** (2007) 3960. (c) G.A. Crosby, *Mol. Cryst.* **1** (1966) 37. (d) J. Eisinger, A.A. Lamola, *Biochem. Biophys. Acta* **240** (1971) 299. (e) N. Filipescu, G.W. Mushrush, *J. Phys. Chem.* **72** (1968) 3516. (f) A. Heller, E. Wasserman, *J. Chem. Phys.* **42** (1956) 949.
11. (a) D. Sarma, M. Prabu, S. Biju, M.L.P. Reddy, S. Natarajan, *Eur. J. Inorg. Chem.* (2010) 3813. (b) P. Mahata, S. Natarajan, *Inorg. Chem*. **46** (2007) 1250.
12. (a) V. Kiritsis, A. Michaelides, S. Skoulika, S. Golhen, L. Ouahab, *Inorg. Chem.* **37** (1998) 3407. (b) T.M. Reineke, M. Eddaoudi, D. Moler, M. O'Keeffe, O.M. Yaghi, *J. Am. Chem. Soc.* **122** (2000) 4843. (c) L. Pan, K.M. Adams, H.E. Hernandez, X.T. Wang, C. Zheng, Y. Hattori, K. Kaneko, *J. Am. Chem. Soc.* **125** (2003) 3062. (d) B. Zhao, P. Cheng, X.Y. Chen, C. Cheng, W. Shi, D.Z. Liao, S.P. Yan, Z.H. Jiang, *J. Am. Chem. Soc*. **126** (2004) 3012. (e) D.L. Long, R.J. Hill, A.L. Blake, N.R. Champness, P. Hubberstey, D.M. Proserpio, C. Wilson, M. Schroder, *Angew. Chem., Int. Ed*. **43** (2004) 1851. (f) M.B. Zhang, J. Zhang, S.T. Zheng, G.Y. Yang, *Angew. Chem., Int. Ed.* **44** (2005) 1385. (g) B. Chen, L. Wang, F. Zapata, G. Qian, B. Lobkovsky, *J. Am. Chem. Soc*. **130** (2008) 6718. (h) F.N. Shi, L. Cunha-Silva, R.A. Sa Ferreira, L. Mafra, T. Trindade, L.D. Carlos, F.A. Almeida Paz, J. Rocha, *J. Am. Chem. Soc.* **130** (2008) 150.
13. (a) Y. Jiang, J. Huang, B. Kasumaj, G. Jeschke, M. Hunger, T. Mallat, A. Baiker, *J. Am. Chem. Soc.* **131** (2009) 2058. (b) Y. Li, L. Xie, Y. Liu, R. Yang, X.Li, *Inorg. Chem.* **47** (2008) 10372. (c) A. Pichon, C.M. Fierro, M. Nieuwenhuyzen, S.L. James, *Cryst. Eng. Comm.* **9** (2007) 449. (d) T.K. Maji, M. Ohba, S. Kitagawa, *Inorg. Chem.* **44** (2005) 9225. (e) K. Biradha, M. Fujita, *Chem. Commun*. (2001) 15. (f) S. Noro, S. Kitagawa, M. Kondo, K. Seki, *Angew. Chem., Int. Ed*. **39** (2000) 2082. (g) M. Kondo., T. Yoshitomi., K. Seki., H. Matsuzaka., S. Kitagawa., *Angew. Chem., Int. Ed.* **36** (1997) 1725.
14. A. Le Bail, H. Duroy, J.L. Fourquet, *Mater. Res. Bull.* **23** (1988) 447.
15. SMART (V 5.628), SAINT (V 6.45a), XPREP, SHELXTL; Bruker AXS Inc.: Madison, Wisconsin, USA, 2004.
16. G.M. Sheldrick, Siemens Area Correction Absorption Correction Program; University of G€ottingen: Gottingen, Germany, 1994.
17. G.M. Sheldrick, G. M. SHELXL-97 Program for Crystal Structure Solution and Refinement; University of G€ottingen: Gottingen, Germany, 1997.
18. J.L. Farrugia, WinGx suite for small-molecule single crystal crystallography. *J. Appl. Crystallogr*. **32** (1999) 837.

19. (a) G.R. Desiraju, *Angew. Chem., Int. Ed. Engl*. **34** (1995) 2311. (b) G.R. Desiraju, Perspective in Supramolecular Chemistry: The Crystal as a Supramolecular Entity; Wiley: Chichester, 1996, 2.
20. (a) P. Ramaswamy, N.N. Hegde, R. Prabhu, V.M. Vidya, A. Datta, S. Natarajan, *Inorg. Chem.* **48** (2009) 11697. (b) S. Mandal, S. Natarajan, *Chem. Eur. J.* **13** (2007) 968.
21. (a) A.K. Paul, G. Madras, S. Natarajan, *Dalton Trans*. **39** (2010) 2263. (b) A.K. Paul, G. Madras, S. Natarajan, *Cryst. Eng. Comm*. **11** (2009) 55. (c) A.K. Paul, G. Madras, S. Natarajan, *Phys. Chem. Chem. Phys.* **11** (2009) 11285.
22. (a) P. Mahata, K.V. Ramya, S. Natarajan, *Chem. Eur. J.* **14** (2008) 5839. (b) P. Mahata, K.V. Ramya, S. Natarajan, *Dalton Trans*. **36** (2007) 4017.
23. Z.H. Zhang, T. Okamura, Y. Hasuchika, H. Kawaguchi, L.Y. Kong, W.Y. Sun, N. Ueyam, *Inorg. Chem.* **44** (2005) 6219.
24. F. Auzel, *Chem. Rev.* 104 (2004) 139.
25. J.J. Ju, T.Y. Kwon, H.K. Kim, J.H. Kim, S.C. Kim, M. Cha, S.I. Yun, *Mater. Lett*. **29** (1996) 13.

CHAPTER V

MICROWAVE SYNTHESIS AND CRYSTAL STRUCTURES OF TWO COBALT-4,4′-BIPYRIDINE-SULFATE FRAMEWORKS CONSTRUCTED FROM 1-D COORDINATION POLYMERS LINKED BY HYDROGEN BONDING

Timothy J. Prior, Bunlawee Yotnoi , **Apinpus Rujiwatra**

Polyhedron **30** (2011) 259–268.

INTRODUCTION

Historically, the best known of the framework solids were the naturally-occurring aluminosilicate zeolites which have extended structures based on tetrehedra [1]. The synthesis of artificial zeolites led to a huge interest in the synthesis of other phases based on tetrahedra such as the aluminophosphates and gallophosphates [2]. The basic technique for directing the formation of these phases is to utilise suitable sources of metal and non-metal with a so-called structure directing agent (a template), typically a quaternary amine. The size, shape, and charge of this template are all important in determining the nature of the framework obtained [3,4]. In some examples the hydrogen-bonding propensity of the template was also shown to be important [5].

There has been considerable interest in simulating and expanding upon the structures displayed by the aluminosilicate zeolites and other oxide frameworks through the construction of metal-interactions and other parameters, such as metal co-ordination, ligand geometry and co-ordination preference, have produced chemistry in MOFs which is not known for classical framework solids [8]. In particular, structural design in MOFs is now well established [9,10]. This chemistry has generated a huge range of novel structures with potentially useful properties, for example, porosity [11], chirality [12], selective sorption [13], gas storage [14–16], catalysis [17], non-linear optical properties [18], and guest-responsive magnetism [19]. Some examples exist where MOFs have been templated by a specific guest species [20–22]. For example, naphthalene has been shown to have a profound influence on the structures of frameworks constructed from Ni^{2+} with 1,3,5-benzenetricarboxylate and 4,4′-bipyridine [23].

In the construction of MOFs, assembly of the structural building units is by strong co-ordinative covalent bonds. In many MOF examples, weaker interactions such as classical (*e.g.* O-H···O) [24] and non-classical [25] (*e.g.* C-H···O) hydrogen bonding interactions are present as secondary structural components [26]. Examples are also emerging where there are genuinely two distinct structural units including a coordination polymer and a hydrogen bonded architecture [26–29].

One of the most widely studied linear bidentate ligands is 4,4′- bipyridine (4,4′-bipy) which is found in a very great number of MOFs, with examples extending from 1-D to 2-D and 3-D architectures [30]. The inflexibility of the ligand along its long axis and the predictable coordination chemistry make the ligand a very attractive framework-former, both on its own and with auxiliary ligands. For example, a hybrid framework, $[Co_2(4,4'\text{-bipy})_3(SO_4)_2(H_2O)_2](4,4'\text{-bipy})(CH_3OH)$, in which both 4,4′-bipy and sulphate act as framework-forming ligands has been reported [31]. This compound displays remarkable, reversible, behaviour upon dehydration; unbound encapsulated 4,4′-bipy becomes involved in the formation of a new framework when coordinated water is removed. Sulphate is found as a framework former in many examples with linear dipyridines. It has diverse

coordination chemistry to transition metal ions, sometimes displaying more than one coordination mode in a single framework [32]. Sulphate is also a very suitable anion for the construction of hydrogen bonded networks because it readily forms strong hydrogen bonds [33].

In our study, we sought to combine the ability of 4,4′-bipy to form coordination polymers with the strong (classical) hydrogen bonding properties of the sulphate anion to produce solids which featured both coordination polymer and hydrogen-bonding motifs in the extended structures. Our previous experience of this system suggested it would be important that the pH of the solution and the amount of water present were carefully controlled [34] to achieve this aim, so that other previously observed phases were not formed [31,35-37].

Hydrothermal synthesis is one widely exploited route for crystal growth of MOFs and this typically takes days or weeks to generate crystals of an appropriate size for diffraction experiments. Despite the great success of microwave heating in organic synthesis [38], the application of this technique to inorganic materials is poorly developed. Recently, microwave-assisted hydrothermal chemistry has been utilised in the crystal growth of MOFs [39,40]. The microwave heating helps to shorten the reaction time to minutes [41]. Here, microwave-assisted hydrothermal synthesis was employed in growing crystals of two new extended metal–organic frameworks. The two extended solids have both coordination polymer and hydrogen-bonding structural features. Intriguingly though, one of these solids is assembled around a twice-protonated 4,4′-bipy molecule which appears to act as a template. The other has a much more extensive 3-D hydrogen bonding arrangement.

EXPERIMENTAL

Microwave-assisted hydrothermal crystal growth

Each reaction was conducted using a tightly closed Teflon container under an autogenous pressure generated at 630W for 5 min using a domestic microwave oven (Whirlpool XT – 25ES/S, 900 W, 2.45 GHz). The pH of each mixture was measured using universal pH strips (Merck, 1.09535.0001), and in each case there was no change in the pH of the mixture after the reaction. Crystalline products were separated from supernatant, washed with deionized water and dried in air. In each case the solid products had a uniform appearance under magnification and the chemical analysis described later on show these are single phase products. The yield of each reaction was of the order of 30%.

- *Reaction A*: Pale pink needles were grown from the mixture of 0.1395 g cobalt(II) nitrate hexahydrate ($Co(NO_3)_2.6H_2O$, 98% Aldrich), 0.4475 g 4,4′-bipyridine ($C_{10}H_8N_2$, 99% Fluka) and sulphuric acid (H_2SO_4, 98% Merck) in 9.50 g of deionized water. (Co:bipy:sulfate:water molar ratio = 1:6:1:1128) The initial pH of the solution was 6.
- *Reaction B*: Pale orange sagittate crystals of $[Co(H_2O)_4(4,4'\text{-bipy})](4,4'\text{-bipyH}_2)](SO_4).2H_2O$ (**VI**) were grown from the mixture of 0.1400 g cobalt(II) nitrate hexahydrate, 0.4502 g 4,4′-bipyridine and 0.0923 g sulphuric acid in 9.50 g of deionized water. (Co:bipy:sulfate:water molar ratio = 1:6:2:1100) The initial pH of the solution was 4.
- *Reaction C*: Pink acicular crystals of $[Co_2(4,4'\text{-bipy})_2(SO_4)_2(H_2O)_6].4(H_2O)$ (**VII**) were grown from the mixture of 0.3299 g cobalt(II) sulphate heptahydrate ($Co(SO_4)_2.7H_2O$, 99% Fluka) and 0.1833 g 4,4′-bipyridine in 9.50 g of deionized water. (Co:bipy:sulfate: water molar ratio = 1:1:2:454) The pH of the mixture was 6. No further attempt was performed to vary the pH of the mixture.

X-ray diffraction structure determination

Routine data collection and structure solution procedures were adopted. Data were collected in series of x-scans using a Stoe IPDS2 diffractometer. Full matrix least squares refinement against F^2 was employed for structure refinement. Crystals of each phase displayed a tendency to form aggregates. This may prove to be a general feature of microwave hydrothermal synthesis [42]. The crystal of **VII** examined was found to be subject to non-merohedral twinning which was dealt with using the program ROTAX [43]. Use of this and omission of a few partially overlapped reflections yielded a vast improvement in the quality of the final structure. Final residual electron density maxima and minima were improved thus: initially 4.11 and -0.943 e $Å^3$; after treatment these were 0.564 and -0.564 e $Å^3$ (*sic*).

For each structure the final data were of good quality and hydrogen atoms were located from difference Fourier maps. Hydrogen atoms attached to 4,4′-bipyridine were refined using a riding model. Those of water were located in difference Fourier maps and refined with sensible restraints. A small portion of disorder within the crystal structure of **VII** was modelled using standard techniques.

*Spectroscopic studies of **VI** and **VII**.*

The Fourier-transform IR spectra of the ground crystals of **VI** and **VII** were recorded using a Bruker Tensor 27 FT-IR instrument (4000-400 cm^{-1}, resolution 0.5 cm^{-1}) using KBr (BDH 98.5%) disks. Raman spectra were collected using a HORIBA JOBIN YVON T64000 spectrophotometer, employing the 514.5 nm line of an Ar laser excitation source with 0.5 mW at the sample for a total integration time of 120 s. The UV-Vis spectra of **VI** and **VII** were collected on both the aqueous solution and the suspension in hexane at room temperature from 200 nm to 800 nm using UV-1800 spectrophotometer (Shimudzu, Japan).

RESULTS & DISCUSSION

Microwave synthesis

Although the microwave-assisted hydrothermal process is not new, examples of the application of the process in growing single crystals of MOFs are limited. Here the process was successfully applied for the rapid synthesis of single crystals of two new phases in the cobalt-4,4′-bipy-sulfate-water system. In each case the reaction duration was only 5 min, in contrast to traditional hydrothermal chemistry reactions lasting days. The reaction products are schematically summarised in Fig. 34 below. During the synthesis it was found that the nature of the product obtained was very sensitive to the initial pH; no crystalline products were obtained where the initial pH of the mixture was lower than 4. If the reaction is too acidic, the 4,4′-bipy present should all be protonated and thus not available for coordination. *Reaction A* (pH 6) yielded crystals of the phase $CoSO_4(H_2O)_3$(4,4′-bipy).$2H_2O$ which has been reported before [35]. *Reaction B* (pH 4) rapidly yielded pale orange sagittate crystals that were shown by X-ray diffraction to be an unknown phase, hereafter labelled **VI**. A third synthesis (*Reaction C*) with subtly different initial conditions yielded compound **VII**.

*Bipyridinium-templated phase, **VI***

This compound crystallises in the centrosymmetric space group $P2_1/n$ (number 14) with a single Co^{2+} ion within the asymmetric unit located on a *4e* Wyckoff position. Crystal data and basic refinement information is contained within Table 16. The chemical formula for **VI** is best expressed

as $[Co(H_2O)4(4,4'\text{-bipy})](4,4'\text{-bipyH}_2)](SO_4)_2.2H_2O$ and in this formulation the diprotonated 4,4′-bipy may be regarded as an occluded cation which is enclosed within an anionic framework composed of 1-D coordination polymer extended into 3-D by hydrogen bonding of sulfate and water. The asymmetric unit is depicted in Fig. 35. Full crystal structure data are included within the Supplementary Information. The composition of a bulk sample of **VI** was determined by chemical analysis and this demonstrated a good fit between the calculated and observed compositions. Percentage C/H/N composition was as follows; Anal. Calc.: C, 35.78; H, 4.51; N, 8.35. Found: C, 35.63; H, 4.45; N, 8.31%.

Reaction A – initial pH = 6	**$CoSO_4(H_2O)_3(4,4'\text{-bipy}).2H_2O$** [35]
Co:bipy:sulfate:water molar ratio = 1:6:1:1128	
Reaction B – initial pH = 4	**$[Co(H_2O)_4(4,4'\text{-bipy})].(4,4'\text{-bipyH}_2).2(SO_4).2H_2O$**
Co:bipy:sulfate:water molar ratio = 1:6:2:1100	(compound **1**)
Reaction C – initial pH = 6	**$[Co_2(4,4'\text{-bipy})_2(SO_4)_2(H_2O)_6].4(H_2O)$**
Co:bipy:sulfate:water molar ratio = 1:1:2:454	(compound **2**)

Fig. 34 *Reaction products.*

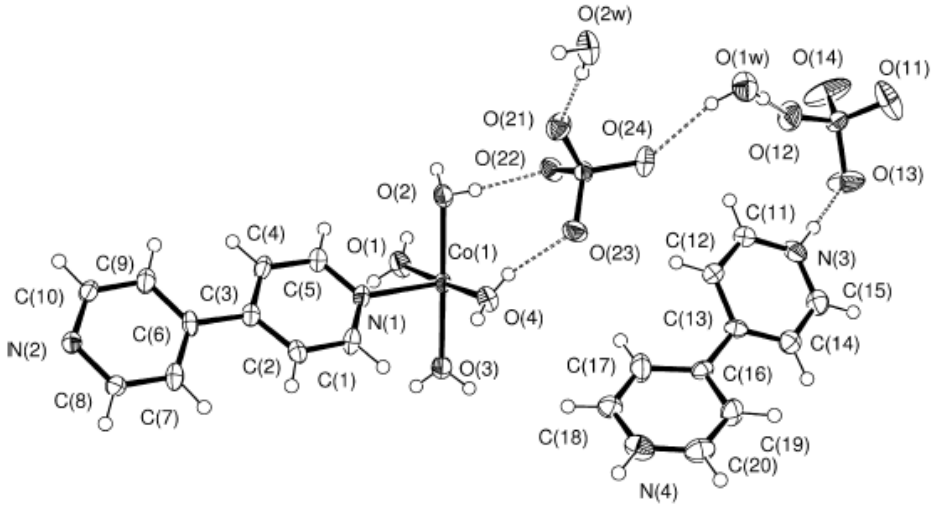

Fig. 35 *ORTEP representation of the asymmetric unit of* ***VI****. Atoms are drawn as 50% thermal ellipsoids. Only non-hydrogen atoms are labelled for clarity. Selected bonds lengths (in Å): Co1-O1 2.075(7); Co1-O2 2.109(6); Co1-O3 2.062(7); Co1-O4 2.112(6); Co1-N2i 2.154(6); Co1-N1 2.155(6); S1-O11 1.426(9); S1-O12 1.438(7); S1-O14 1.460(8); S1-O13 1.490(7); S2-O21 1.465(7); S2-O22 1.491(6); S2-O23 1.477(6); S2-O24 1.453(6). Symmetry equivalent atom generated by the operator (i) x-1/2, -y+1/2, z-1/2.*

Each Co^{2+} adopts pseudo-octahedral coordination and is surrounded by four water molecules in a square plane and furthermore by two *trans* 4,4′-bipy molecules, the first of which binds through N1, while the second binds through N2 and is generated from the first by the symmetry operator *x-1/2, -y+1/2, z-1/2*. The Co^{2+} and 4,4′-bipy therefore form a one-dimensional chain which runs parallel to the crystallographic [*1 0 1*] direction. There is a little twisting of the 4,4′-bipy about the central C-C bond; the angle between the mean planes of the two six-membered rings is 10.36(10)°. This chain is illustrated in Fig. 36. The 1-D linear chain is an important motif in metal-bipyridine frameworks; there are a large number of MOFs based on this arrangement [30]. The arrangement of metal and

4,4′-bipy in 1 is typical of this type of chain. Co-N distances are in good agreement with those of similar frameworks [44]. The angle subtended by the bipyridine molecules at the Co^{2+} is 178.9(3)°.

Table 16 *Summary of crystal refinement data for* ***VI*** *and* ***VII***.

Identification code	**1**	**2**
Structural formula	$[Co(H_2O)_4(4,4'\text{-bipy})](4,4'\text{-bipyH}_2)\cdot 2(SO_4)\cdot 2H_2O$	$[Co(H_2O)_3(SO_4)(4,4'\text{-bipy})_2]_2\ Co(H_2O)_4Co(H_2O)_2(SO_4)_2\cdot 8H_2O$
Empirical formula	$C_{20}H_{30}CoN_4O_{14}S_2$	$C_{20}H_{36}Co_2N_4O_{18}S_2$
Formula weight	673.54	802.52
Temperature (K)	150(2)	150(2)
Wavelength (Å)	0.71073	0.71073
Crystal system	monoclinic	monoclinic
Space group	$P2_1/n$	$P2_1/c$
Unit cell dimensions		
a (Å)	9.4120(18)	7.4347(5)
b (Å)	13.0143(13)	40.573(4)
c (Å)	22.155(3)	11.4833(8)
α (°)	90	90
β (°)	97.943(13)	117.405(5)
γ (°)	90	90
Volume (Å^3)	2687.8(7)	3075.2(4)
Z	4	4
D_{calc} (mg/m^3)	1.664	1.733
Absorption coefficient (mm^{-1})	0.872	1.301
F(0 0 0)	1396	1656
Crystal size (mm^3)	0.35 × 0.14 × 0.12	0.4 × 0.1 × 0.1
θ Range for data collection (°)	3.09–26.14	2.01–27.13
Index ranges		
	$-11 \leqslant h \leqslant 11$ $0 \leqslant k \leqslant 16$ $0 \leqslant l \leqslant 27$	$0 \leqslant h \leqslant 9$ $-51 \leqslant k \leqslant 51$ $-14 \leqslant l \leqslant 13$
Reflections collected	5150	6320
Independent reflections	5150 [R_{int} = 0.068]	6320 [R_{int} = 0.048]
Completeness to θ = 26.00°	95.8%	94.0%
Absorption correction	analytical	analytical
Maximum and minimum transmission	0.8324 and 0.6966	0.9624 and 0.8381
Refinement method	full-matrix least-squares on F^2	full-matrix least-squares on F^2
Data/restraints/parameters	5150/22/408	6320/235/474
Goodness-of-fit on F^2	1.087	1.091
Largest difference in peak and hole (e Å^{-3}) (sic)	0.729 and −0.594	0.564 and −0.564
Final R indices [$I > 2\sigma(I)$]	R_1 = 0.0683, $wR(F^2)$ = 0.2381	R_1 = 0.0559, $wR(F^2)$ = 0.1514
R indices (all data)	R_1 = 0.1105, $wR(F^2)$ = 0.2469	R_1 = 0.0832, $wR(F^2)$ = 0.1566

Where $R_1 = \frac{\sum||F_o|-|F_c||}{\sum|F_o|}$, $wR(F^2) = \sqrt{\frac{\sum w(F_o^2-F_c^2)^2}{\sum wF_o^4}}$ and F_o and F_c are the observed and calculated structure factors for each reflection and w is the weight for each reflection.

There are two unbound sulphate anions in the asymmetric unit and these are located such that four sulphates are arranged around the Co^{2+} ion forming hydrogen bonds to the four water molecules bound in a square plane with O···O hydrogen bond distances indicative of relatively strong hydrogen bonds (Table 17). The hydrogen bonds formed to each sulphate have the effect of linking together the 1-D coordination polymer chains; each sulfate is involved in bridging between the $Co(H_2O)_4$ square planes to form infinite 2-D hydrogen-bonded sheets in the *xy* plane. Each of the 1-D cobalt-bipyridine polymer chains cuts this plane at any angle of 61.37°. Fig. 37 illustrates the interaction between the cobalt centres and each sulphate. Two sulphate molecules (central atom S1) form an embrace with multiple hydrogen bonds while for the second sulphate (central atom S2) a centrosymmetric $R^2_4(8)$ embrace is observed and this is augmented by other hydrogen bonds.

Fig. 36 *Illustration of the 1-D coordination polymer chain within* ***VI*** *that has composition [Co(4,4′-bipyridine)$(H_2O)_4$]$^{2+}$.*

Table 17 *Details of the classical hydrogen bonds and C-H···O interactions in* ***VI****. A hydrogen bond donor is signified as D-H, where D is the donor atom. The hydrogen bond acceptor atom is labelled A.*

Hydrogen bond donor (D–H)	D–H bond length (Å)	H···A distance (Å)	D–H···A angle (°)	D···A distance (Å)	Acceptor atom (A) [symmetry operator]
O1–H1A	0.83(4)	1.82(8)	173(7)	2.645(12)	O14 [x + 1/2, −y + 1/2, z + 1/2]
O1–H1B	0.86(4)	1.89(5)	165(8)	2.735(10)	O2W [−x, −y + 1, −z + 1]
O2–H2A	0.82(4)	1.88(7)	168(8)	2.674(9)	O22
O2–H2B	0.85(4)	1.93(6)	169(10)	2.773(10)	O21 [−x, −y + 1, −z + 1]
O3–H3A	0.80(4)	1.97(8)	157(8)	2.729(10)	O13 [x + 1/2, −y + 1/2, z + 1/2]
O3–H3B	0.84(4)	2.08(8)	173(11)	2.919(12)	O11 [−x + 1/2, y − 1/2, −z + 1/2]
O3–H3B	0.84(4)	2.47(8)	126(8)	3.048(10)	O13 [−x + 1/2, y − 1/2, −z + 1/2]
O4–H4A	0.76(4)	2.05(8)	155(8)	2.755(9)	O23
O4–H4B	0.82(4)	2.02(8)	160(8)	2.807(9)	O23 [−x + 1, −y + 1, −z + 1]
O1W–H1X	0.85(4)	2.01(9)	166(10)	2.845(9)	O24
O1W–H1Y	0.80(4)	2.00(8)	165(8)	2.782(10)	O12
O2W–H2X	0.86(5)	1.89(5)	173(11)	2.746(10)	O21
O2W–H2Y	0.81(5)	2.19(9)	151(10)	2.933(12)	O11 [x + 1/2, −y + 3/2, z + 1/2]
O2W–H2Y	0.81(5)	2.49(8)	150(8)	3.222(13)	O14 [x + 1/2, −y + 3/2, z + 1/2]
N3–H3C	0.88	1.712	177	2.592(11)	O13
N4–H4C	0.88	1.791	162	2.641(10)	O22 [x + 1, y, z]
C7–H7	0.95	2.57	163	3.487(11)	O1W [1 + x, y, z]
C11–H11	0.95	2.54	124	3.167(12)	O12 [1/2 − x, 1/2 + y, 1/2 − z]
C12–H12	0.95	2.46	125	3.110(11)	O24 [1/2 − x, 1/2 + y, 1/2 − z]
C14–H14	0.95	2.52	143	3.329(13)	O14 [3/2 − x, 1/2 + y, 1/2 − z]
C15–H15	0.95	2.33	147	3.168(11)	O2W
C18–H18	0.95	2.49	153	3.367(11)	O21 [1/2 + x, 1/2 − y, 1/2 + z]
C19–H19	0.95	2.42	137	3.181(12)	O12 [3/2 − x, 1/2 + y, 1/2 − z]
C20–H20	0.95	2.44	134	3.176(12)	O24 [3/2 − x, 1/2 + y, 1/2 − z]

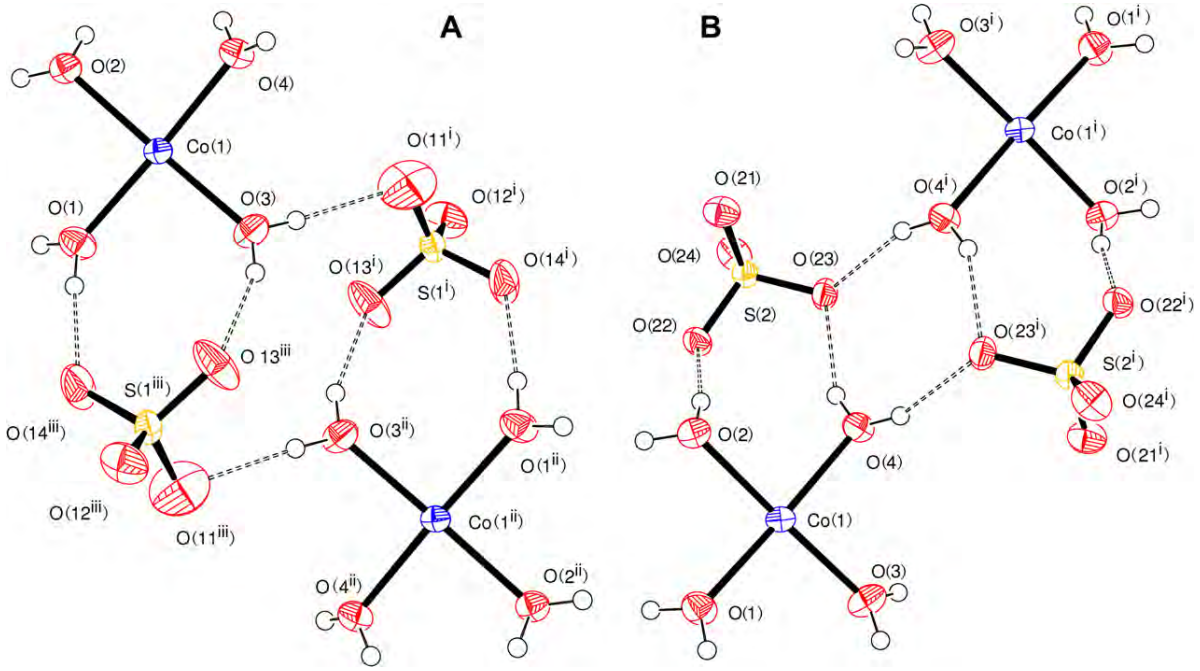

Fig. 37 *(A) Hydrogen bonding of sulphate (S1) linking two $Co(H_2O)_4$ units. Symmetry equivalent atoms are generated by the symmetry operations: (i) 0.5-x, y-0.5, 0.5- z; (ii) 1- x, -y, 1-z; (iii) 0.5+x, 0.5-y, 0.5+z. (B) Augmented $R^2_4(8)$ embrace between two $Co(H_2O)_4$ units mediated by sulphate (S2). Symmetry equivalent atoms are generated by the symmetry operation: (i) 1- x, 1- y, 1- z.*

Located between these sulphate anions are two further symmetry independent water molecules. These two unbound water molecules act as hydrogen bond donors to the sulphate anions. Short OH···O interactions form infinite sulphate-water-sulphate chains which run parallel to the [*1 0 1*] direction. These chains runs parallel to the cobalt-bipyridine 1-D chain and reinforce the bonding in this direction. Finally, contained between the chains is located twice protonated 4,4′-bipy ($C_{10}H_{10}N_2^{2+}$). This cation forms a remarkable set of contacts to the framework and to sulphate, which are detailed in Table 17. Each protonated pyridine function forms one hydrogen bond (through N3 and N4) to sulphate and there are supplementary C-H···O interactions which hold the dication in place; for example there are six C-H···O contacts where the C···O distance is in the range 3.1-3.2 Å.

These are in good agreement with other species containing this cation and somewhat shorter than many of those for uncharged 4,4′-bipy bound to a metal [44]. Alone, this is a relatively weak interaction, but the cumulative effect of six such interactions becomes important. The protonation of the 4,4′-bipy must play a role in strengthening these interactions through an additional coulombic interaction not present for uncharged species. Interestingly the two rings of the diprotonated 4,4′-bipy are not coplanar with the angle between the mean planes of the two six-membered rings being 29.9(2)^{o}. This rotation facilitates the formation of these non-classical hydrogen bonds by rotating the 4,4′-bipy towards the sulphate ions. The relatively short C-H•••O distances promoted by protonation of the 4,4′-bipy, suggest this dication has a key role in templating 1. The protonated 4,4′-bipy is crucial in filling space within the other network, but the close interaction with surrounding species suggests this acts as a template around which the framework assembles. Fig. 38 shows the location of the $(4,4'\text{-bipyH}_2)^{2+}$ cation within the framework and the interactions between cation and framework. The role of the 4,4′-bipy may be considered directly analogous to its role in templating the gallium oxyfluorophosphate DIPYR-GaPO [45]. The interaction between framework and twice protonated 4,4′-bipy in the two phases is very similar when the hydrogen bonds between cation and framework are considered. The $(4,4'\text{-bipyH}_2)^{2+}$ cation has been observed in similar phases before [20,21] but to our knowledge detailed description of the interaction of this cation with a framework has not appeared.

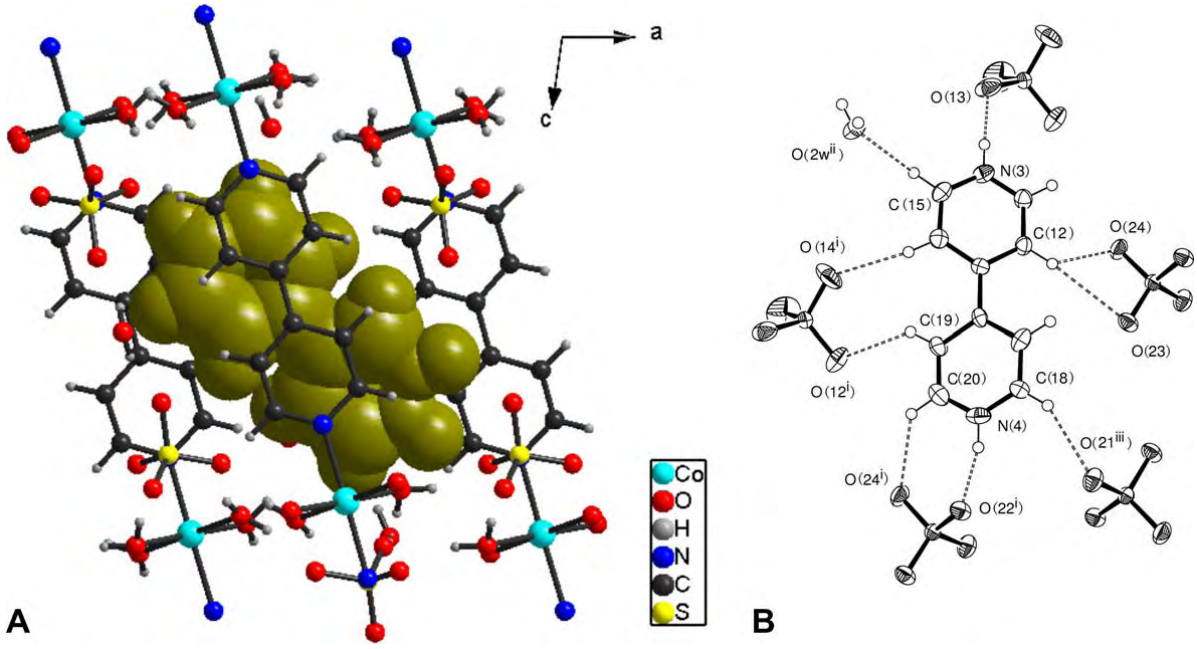

Fig. 38 *(A) Space filling representation of the bipyridinium cation $(C_{10}N_2H_{10})^{2+}$ occluded within the coordination polymer and hydrogen bonding framework. (B) ORTEP representation of the bipyridinium cation and the interactions it makes to the surrounding species. Short contacts which are indicative of favourable interactions are shown as dashed lines. Symmetry equivalent atoms are generated by the symmetry operations: (i) 1+x, y, z; (ii) 0.5-x, y- 0.5, 0.5- z; (iii) 1- x, 1- y, 1-z.*

The 1-D coordination polymer chain with composition $M(H_2O)_4(4,4'\text{-bipy})$ is known in other examples [46,47], but this is the first example of any 1-D cobalt-bipyridine chain that is template by $(4,4'\text{-bipyH}_2)^{2+}$. A similar compound containing manganese has recently been reported [48] but the description of the interaction of template and framework is rather scant. One similar example composed of chains of 4,4′-bipy with Co^{2+} that contains a guest molecule is $[Co(H_2O)_4(4,4'\text{-}$

bipy)](SO$_4$).3H$_2$O (PABA) (where PABA = para-aminobenzoic acid) [49]. This phase is less dense than 1 and has a greater cobalt to sulphate ratio but has similar structural features. However, the guest is uncharged and forms fewer short contacts with the framework than 1 suggesting a less important role in templating the framework. A similar example containing (4,4′-bipyH$_2$)$^{2+}$ but with a framework composed Co^{2+} coordinated by both 4,4′-bipy and 1,2,4,5-benzene-tetracarboxylate has been reported [50].

As **VI** is heated under nitrogen, it decomposes in well-defined steps. First the coordinated and uncoordinated water is lost in the range 70–155 ^{o}C to form a species with approximate composition Co(4,4′-bipy)(4,4′-bipyH$_2$)(SO$_4$)$_2$. This loses the template above 155 ^{o}C to form Co(4,4′-bipy)(SO$_4$H)$_2$ at 270 ^{o}C. This is stable until 320 ^{o}C above which it decomposes to CoSO$_4$. The sulphate is stable up to 700 ^{o}C when it decomposes to Co$_3$O$_4$.

Sulphate-decorated coordination polymer, ***VII***

A second reaction with similar initial conditions to those used to generate **VI** but employing a different source of sulphate (Reaction C), and therefore the most basic reaction attempted, was found to yield pink needles of a compound with an unknown structure, hereafter **VII**. Compound **VII** crystallises in the centric space group *P2$_1$/c* with three independent Co^{2+} ions within the asymmetric unit, located on *4e*, *2a*, and *2c* Wyckoff positions. The chemical formula may be written in a short form as [Co$_2$(4,4′-bipy)$_2$(SO$_4$)$_2$(H$_2$O)$_6$].4(H$_2$O) although this formulation does not elucidate the structure very effectively. It is more enlightening to write the composition of **VII** as [Co(H$_2$O)$_3$(SO$_4$)(4,4′-bipy)$_2$]$_2$Co(H$_2$O)$_4$Co(H$_2$O)$_2$(SO$_4$)$_2$.8H$_2$O where the coordination about each cobalt is more clearly defined. An ORTEP representation of the asymmetric unit is shown in Fig. 39 and basic crystal structure and refinement data are contained within Table 16. The composition of a bulk sample of **VII** was determined by chemical analysis and this demonstrated a satisfactory fit between the calculated and observed compositions. Percentage C/H/N composition was as follows; Anal. Calc.: C, 30.67; H, 4.47; N, 7.01. Found: C, 29.91; H, 4.49; N, 6.98%.

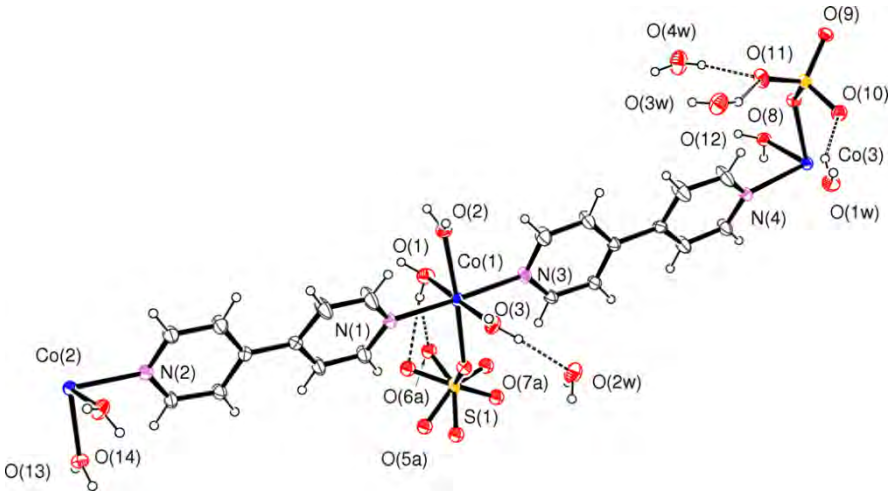

Fig. 39 *ORTEP representation of the asymmetric unit of* ***VII****. Atoms are drawn as 50% thermal ellipsoids. Carbon and hydrogen atoms have not been labelled to aid clarity. Similarly only the major orientation of the disordered sulphate is labelled. Selected bonds lengths (in Å): Co1-O1 2.030(6); Co1-O2 2.160(5); Co1-O3 2.032(6); Co1-N1 2.168(5); Co1-N3 2.180(5); Co1-O4 2.197(4); Co2-O13 2.127(5); Co2-O14 1.997(5); Co2-N2 2.168(5); Co3-O8 2.168(4); Co3-O12 2.068(5); Co3-N4 2.189(5); S1-O4 1.492(5); S1-O5A 1.488(5); S1-O6A 1.493(6); S1-O7A 1.475(5); S2-O8 1.491(5); S2-O9 1.479(5); S2-O10 1.484(5); S2-O11 1.462(5).*

The structure has many features in common with **VI** but there are important differences. Compound **VII** is a rather more dense phase than 1 and contains one-dimensional coordination polymer chains based on linear coordination of Co^{2+} by trans 4,4′-bipy which is further decorated with coordinated water and sulphate. Importantly in **VII**, there is no uncoordinated sulphate, but further uncoordinated water is found within the structure. Hydrogen bonding between the ligands (sulphate and water) and uncoordinated water forms a three dimensional honeycomb net which is in addition to the 1-D polymer.

Each Co^{2+} adopts pseudo-octahedral geometry, linking *trans* 4,4′-bipy molecules to form a 1-D chain. The chain contains two symmetry independent 4,4′-bipy molecules which display very similar geometry. The planes of the six-membered rings of each of the two 4,4′-bipy molecules are twisted a little way from being parallel. The angles between the mean planes of the two sets of rings are 8.5(3)^o and 9.3(3)^o. The coordination environment about each of the three Co^{2+} ions is different and varies in the amount of bound sulphate. Coordination about Co1 is completed by three water molecules and one sulphate. The sulphate is disordered by rotation about the S1-O4 bond. The two orientations which are approximately 39.3^o apart are occupied in the ratio 82.1:17.9(5). Co2 resides on an inversion centre and coordination is completed by four bound water molecules. Similarly Co3 is located on an inversion centre, but is coordinated by two sulphate groups and two molecules of water in an 'all *trans*' arrangement. For Co2 and Co3 the N-Co-N angle is 180^o, but for Co1, this angle is 174.0(2)^o, possibly as a result of the greater steric demand of the sulphate group than the water molecule trans to it. The deviation from linearity that occurs at Co1 produces a sinusoidal form to the chain as shown in Fig. 40. This gentle curvature at Co1 is rather unusual in chains of this type. Examination of the Cambridge Structural Database [44] reveals a strong preference for a strictly linear coordination in transition metal compounds in which a metal cations links two 4,4′-bipy ligands in a trans arrangement. (See Supplementary Information) These infinite chains run parallel to the [*2 1 2*] direction and the sinusoidal variation has a wavelength of four 4,4′-bipy links which corresponds to a translation of (x+2, y+1, z+2); a distance of 45.611(4) Å. Adjacent chains are related by a translation of (x+1, y, z+1). A second set of identical chains related to the first by the symmetry operator -x, 1/2+y, ½-z run parallel to the [*-2 1 -2*] direction and are inter-digitated with the first. The set of infinite chains are illustrated in Fig. 41.

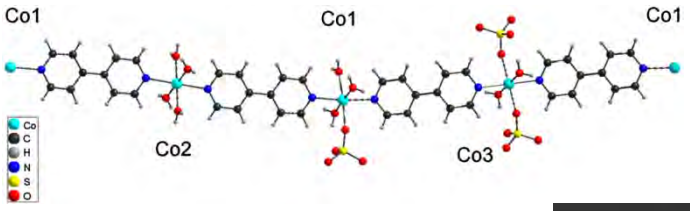

Fig. 40 *Part of the infinite coordination polymer chain in* ***VII****. The section drawn represents one period of the sinusoidal chain.*

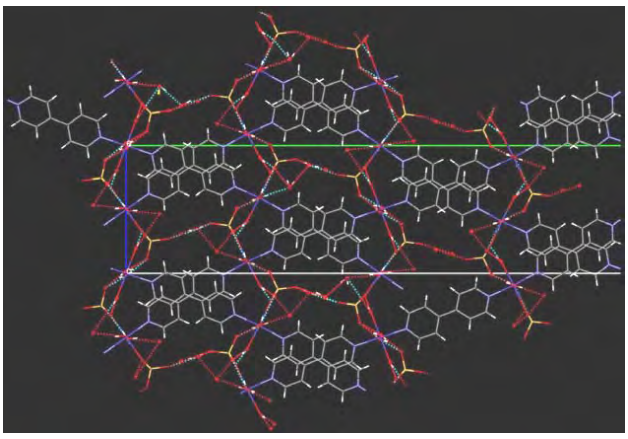

Fig. 41 *The structure of* ***VII*** *viewed down [1 0 0] showing the inter-digitated Co^{2+}-4,4′-bipy chains. The six-membered rings of the 3-D hydrogen bonding network are also shown.*

The sulphate is not observed bridging between cations in contrast to other 4,4′-bipy frameworks [32]. It is monodentate and decorates the chain rather than being involved in framework formation. By careful choice of metal-sulphate ratio we sought to limit the coordination of sulphate and to promote the formation of hydrogen bonds involving sulphate. The water and sulphate ligands attached to each Co^{2+} ion have considerable hydrogen bonding capability. This is augmented by the presence of four molecules of uncoordinated water in the asymmetric unit. Compound **VII** contains a three dimensional O-H•••O hydrogen bond network in addition to the coordination polymers. If the structure is viewed along the [*1 0 0*] direction, a network which contains rings of six sulphate anions is visible (Fig. 41). The coordinated sulphate, and bound and unbound water assemble into network reminiscent of honeycomb with channels along a. Each six-ring has a sulphate at each vertex; one side is composed of two sulphates bound to Co^{2+}; another side is formed from sulphates bridged by a $Co(H_2O)_4$ square plane; two more are formed from two uncoordinated water molecules bridging between two sulphates to form an $R^2_4(8)$ embrace; a further two sides exist with two sulphates bridged by two bound water and one unbound water molecule to give an asymmetric motif with the graph set notation $R^3_5(10)$. The hydrogen bonding within **VII** is very complicated and there are further interactions which sustain the formation of this honeycomb arrangement. Full details of the O-H•••O hydrogen bonds in **VII** are given in Table 18. There are a small number of C-H•••O interactions present in the structure of **VII**. The majority of these are short contacts between the 4,4′-bipy hydrogen atoms and sulphate or water bound to the same infinite chain. However, it is noteworthy that H2 and H7 form contacts to the uncoordinated water, O2W. Although these contacts are rather long, they are close to linear, which has been identified as signifying a hydrogen bond rather than van der Waals contact [51]. Notably, H19 forms a contact to one of the sulphate anions attached to a neighbouring parallel chain, enhancing the interaction between adjacent chains. Details of selected C-H•••O interactions are given in Table 18.

Table 18 *Details of the classical hydrogen bonds and selected C-H•••O interactions in* ***VII****. A hydrogen bond donor is signified as D–H, where D is the donor atom. The hydrogen bond acceptor atom is labelled A.*

Hydrogen bond donor (D–H)	D–H bond length (Å)	H···A distance (Å)	D–H···A angle (°)	D···A distance (Å)	Acceptor atom (A) [symmetry operator]
O1–H1B	0.83(6)	1.87(4)	157(8)	2.65(8)	O6A
O1–H1B	0.83(6)	2.16(6)	149(10)	2.90(2)	O6B
O1–H1A	0. 83(6)	1.79(4)	166(10)	2.602(8)	O5A [*x*, −*y* + 1/2, *z* + 1/2]
O1–H1A	0. 83(6)	2.19(4)	165(9)	3.00(2)	O5B [*x*, −*y* + 1/2, *z* + 1/2]
O2–H2A	0. 83(6)	2.03(4)	164(9)	2.845(8)	O6A [*x* + 1, −*y* + 1/2, *z* + 1/2]
O2–H2A	0. 83(6)	2.20(6)	138(8)	2.87(2)	O6B [*x* + 1, −*y* + 1/2, *z* + 1/2]
O2–H2B	0. 83(6)	2.13(3)	169(8)	2.949(7)	O4 [*x*, −*y* + 1/2, *z* + 1/2]
O3–H3B	0.82(6)	1.88(3)	176(10)	2.701(8)	O5A [*x* + 1, −*y* + 1/2, *z* + 1/2]
O3–H3B	0.82(6)	2.14(8)	131(9)	2.75(2)	O6B [*x* + 1, −*y* + 1/2, *z* + 1/2]
O3–H3A	0.82(6)	1.92(4)	162(8)	2.715(7)	O2W
O12–H12A	0.83(6)	1.90(4)	168(9)	2.713(7)	O1W [*x* − 1, *y*, *z*]
O12–H12B	0.82(6)	1.94(4)	161(10)	2.731(7)	O10 [−*x* + 2, −*y* + 1, −*z* + 2]
O13–H13B	0.84(6)	2.01(4)	164(10)	2.827(7)	O10 [*x* − 2, −*y* + 1/2, *z* − 3/2]
O13–H13A	0.83(6)	2.09(3)	171(10)	2.916(7)	O8 [*x* − 1, −*y* + 1/2, *z* − 3/2]
O14–H14B	0.83(6)	1.86(4)	162(10)	2.656(7)	O9 [−*x* + 2, *y* − 1/2, −*z* + 3/2]
O14–H14A	0.83(6)	1.86(4)	163(10)	2.665(7)	O9 [*x* − 1, −*y* + 1/2, *z* − 3/2]
O1W–H1D	0.83(6)	2.05(5)	152(9)	2.800(8)	O10
O1W–H1C	0.82(6)	1.94(4)	166(9)	2.744(9)	O4W [*x* + 1, *y*, *z*]
O2W–H2D	0.84(6)	1.96(4)	159(9)	2.757(9)	O6A [*x* + 1, *y*, *z*]
O2W–H2D	0.84(6)	2.45(7)	146(9)	3.18(2)	O7B [*x* + 1, *y*, *z*]
O2W–H2C	0.84(6)	1.94(5)	160(10)	2.740(8)	O3W [*x* − 1, *y*, *z* − 1]
O3W–H3C	0.83(6)	2.04(5)	155(9)	2.808(9)	O11
O3W–H3D	0.83(6)	1.98(3)	172(11)	2.808(9)	O7A [*x* + 1, *y*, *z* + 1]
O4W–H4C	0.84(6)	2.02(3)	171(11)	2.851(9)	O11
O4W–H4D	0.83(6)	2.01(8)	136(9)	2.666(16)	O7B [*x* + 1, *y*, *z* + 1]
O4W–H4D	0.83(6)	2.20(8)	137(10)	2.860(9)	O7A [*x* + 1, *y*, *z* + 1]
C2–H2	0.95	2.48	170	3.420(9)	O2W [*x* − 1, 1/2 − *y*, *z* − 1/2]
C7–H7	0.95	2.68	173	3.625(9)	O2W [*x* − 1, 1/2 − *y*, *z* − 1/2]
C9–H9	0.95	2.49	148	3.333(9)	O1W [*x* − 1, 1/2 − *y*, *z* − 1/2]
C19–H19	0.95	2.41	147	3.254(8)	O9 [*x* − 1, *y*, *z* − 1]

As **VII** is heated in flowing nitrogen, it decomposes in well-defined steps. Similarly to **VI**, when **VII** is heated it loses all of the coordinated and uncoordinated water first in the range 60-160 ^{o}C to

produce a phase with approximate composition Co(bipy)(OH)(SO_4) which is stable until 285 ^oC. Above this temperature it decomposes slowly until at 420 ^oC a phase with composition Co(OH)(SO_4) is formed. This is stable until 570 ^oC at which point $CoSO_4$ forms rapidly and is stable until 680 ^oC. Above this point cobalt oxide is obtained. Phase **VI** contains much more sulphate than **VII** and this appears to have a profound influence on the nature of the intermediate phases upon thermal decomposition. In phase **VII**, it appears that some water is retained as hydroxide (perhaps bridging) to satisfy the coordination requirement of the cobalt. The control of synthesis for frameworks of this type is clearly dependent upon a number of factors. The reactions presented here are examples of different regions of a complex composition space. For example, in reactions A and B, a small change in the initial pH of the mixture coupled with variation of the cobalt to sulphate ratio leads to different products. It is notable that variation of cobalt to 4,4′-bipy ratio leads to different products (Reactions B and C). Experiments are currently underway to alter the initial pH of the mixture while preserving the cobalt to sulphate ratio, along with an investigation of the effect of metal source on the nature of the products.

*Vibrational spectra of **VI** and **VII***

The differences in coordination modes of sulphate and 4,4′-bipy with the additional influence of hydrogen bonding interactions and local structural disorder in structures **VI** and **VII** are clearly manifested in the IR and Raman spectra of the ground crystals of **VI** and **VII**. Four normal modes of vibration including the stretching $\nu_1(A_1)$ and $\nu_3(T_2)$, and the bending $\nu_2(E)$ and $\nu_4(T_2)$ are expected for uncoordinated sulphate anions with a regular tetrahedral geometry of Td point symmetry. While all of these vibrations are expected to be Raman-active, only the stretching $\nu_3(T_2)$ and the bending $\nu4(T_2)$ are IR-active. Upon coordination, the symmetry of the coordinated sulphate will be lowered; C_{3v} and C_{2v} for monodentate and bidentate sulphate ligands, respectively. A reduction in point symmetry should result in the appearance of $\nu_1(A_1)$ and $\nu_2(E)$, and the splitting of $\nu_3(T_2)$ and $\nu_4(T_2)$ in the IR. The presence of one, three and four ν(S–O) bands can therefore be expected in the IR for the uncoordinated, monodentate and bidentate sulphate. However, in the spectrum of uncoordinated sulphate the appearance of a weak $\nu_1(A_1)$ band and a broadening of the $\nu_3(T_2)$ band is commonly reported, due to the other non-bonding interactions of the sulphate with the neighbouring species in the crystal structures [52,53].

Fig. 42 shows portions of the IR spectra of **VI** and **VII**. Despite a different coordination mode of the sulfate anions, the IR spectra of the two compounds are rather similar at the first glance, notably the presence of the very intense ν_3 and ν_4 and the very weak ν_1 and ν_2, with the broadening of ν_3 band. The broadening of these m3 bands is similar in each case and clearly visible. The clear splitting of the ν_4 band in **VII** compared with that of **VI** is notable. The observed features in the IR spectra indicate the lowering of point symmetry of both the uncoordinated sulphate in **VI** and the monodentate sulphate in **VII**, which is consistent with the crystallographic information. In the structure of **VII**, although the two distinct sulphate ligands adopt the same coordination mode, crystallographic disorder and the dissimilarity of the hydrogen bonding interactions (Tables 17 and 18) differentiate the two sulphate ligands, which accounts for the apparent features in the IR spectrum. Regarding the uncoordinated sulfate anions in structure **VI**, a distortion of the sulfate local environment is due to O-H···O hydrogen bonding (Fig. 37) reducing the symmetry from the expected Td. The influence of hydrogen bonding interactions in lowering local symmetry is demonstrated by the observed spectra.

The vibrational bands of the sulphate anions are not clearly visible in the Raman spectra, which are dominated by bands due to the 4,4′-bipy species. The di-protonation of the 4,4′-bipy (4,4-bipyH_2^{2+}) and range of local environments for 4,4′-bipy introduce a huge degree of splitting in the characteristic vibrational bands in the IR. However, the presence of characteristic bands for the $\nu(NH^+)$ and the $\delta(NH^+)$ of the protonated species is obvious in the IR spectra of **VI**. The splitting of the breathing modes in the Raman can also be used to distinguish the protonated 4,4′-bipyH_2^{2+} in **VI** from the neutral 4,4′-bipy molecule in **VII**.

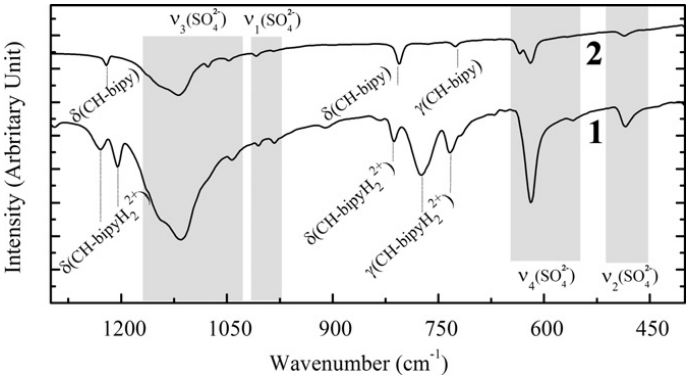

Fig. 42 *Portions of the FT-IR spectra of* ***VI*** *and* ***VII*** *in the range 400-1300 cm^{-1}. Selected band assignments are overlaid to illustrate the difference between the spectra.*

UV–Vis spectra of ***VI*** *and* ***VII***

The electronic spectra of **VI** and **VII** in hexane are noticeably similar, both dominated by a broad band centred around 42,500 cm^{-1} with a shoulder centred on 37,200 cm^{-1}, which are characteristic of the phenyl ring of 4,4′-bipy and can be assigned as the ligand π-π* transitions. In addition to these intense bands, there are also weak absorptions at frequencies lower than 30, 000 cm^{-1}, particularly in the case of **VI**. A weak broad band centred on 16,000 cm^{-1} is consistent with two overlapped transitions, $^4T_{1g}(P) \leftarrow {}^4T_{1g}(F)$ and $^4A_{2g}(F) \leftarrow {}^4T_{1g}(F)$ of the high spin Co^{II} in a distorted octahedral field demonstrated by the crystal structure.

CONCLUSIONS

Microwave-assisted hydrothermal synthesis is an extremely promising technique for the growth of MOFs. It cuts typical reaction times from a few days to a few minutes. In this study and others though, we have noticed the tendency for the products to grow as aggregates of crystals which can complicate structure determination. However, it is emerging as a very useful synthetic protocol in this field. In a previous study, changes to the cobalt source and reaction conditions were found to influence the nature of the products in a similar system [54]. The frameworks described here suggest that even in the seemingly simple system cobalt-4,4′-bipy-sulphate-water, there is considerable scope for the synthesis of new frameworks by small changes in the initial conditions. We are currently exploring this system with a view to mapping how the nature of the product varies with initial composition. Furthermore, alteration of the amount of water present will prove another variable to control the nature and likely density of framework obtained. Fortified by the success of our approach, we are also investigating similar syntheses using other positively charged species such as quaternary amines that may act as templates for cavities of this sort of 3-D network composed of 1-D coordination polymer and 2-D hydrogen-bonded sheets in attempts to mimic **VI**.

REFERENCES

1. A. Dyer, Introduction to Zeolite Molecular Sieves, John Wiley & Sons, 1988.
2. A.K. Cheetham, G. Ferey, T. Loiseau, *Angew. Chem., Int. Ed. Engl.* **38** (1999) 3268.
3. C.R.A. Catlow, D.S. Coombes, J.C.G. Pereira, *Chem. Mater.* **10** (1998) 3249.
4. M.E. Davis, R.F. Lobo, *Chem. Mater.* **4** (1992) 756.
5. S. Natarajan, M.P. Attfield, A.K. Cheetham, *J. Solid State Chem.* **132** (1997) 229.
6. C.N.R. Rao, S. Natarajan, R. Vaidhyanathan, *Angew. Chem., Int. Ed.* **43** (2004) 1466.
7. S. Natarajan, P. Mahata, *Chem. Soc. Rev.* **38** (2009) 2304.
8. O.M. Yaghi, M. O'Keeffe, N.W. Ockwig, H.K. Chae, M. Eddaoudi, J. Kim, *Nature* **423** (2003) 705.
9. H.K. Chae, J. Kim, O.D. Friedrichs, M. O'Keefe, O.M. Yaghi, *Angew. Chem., Int. Ed. ngl*. **42** (2003) 3907.
10. H. Li, M. Eddaoudi, M. O'Keeffe, O.M. Yaghi, *Nature* **402** (1999) 276.
11. G. Ferey, *Mol. Networks* **132** (2009) 87.
12. R.E. Morris, X.H. Bu, *Nat. Chem.* **2** (2010) 353.
13. R.J. Kuppler, D.J. Timmons, Q.R. Fang, J.R. Li, T.A. Makal, M.D. Young, D.Q. Yuan, D. Zhao, W.J. Zhuang, H.C. Zhou, *Coord. Chem. Rev.* **253** (2009) 3042.
14. R.Q. Zou, A.I. Abdel-Fattah, H.W. Xu, Y.S. Zhao, D.D. Hickmott, *Cryst. Eng. Commun.* **12** (2010) 1337.
15. H.J. Park, M.P. Suh, *Chem. Commun*. **46** (2010) 610.
16. L.J. Murray, M. Dinca, J.R. Long, *Chem. Soc. Rev.* **38** (2009) 1294.
17. D. Farrusseng, S. Aguado, C. Pinel, Angew. *Chem., Int. Ed. Engl.* **48** (2009) 7502.
18. J.D. Lin, X.F. Long, P. Lin, S.W. Du, *Cryst. Growth Des.* **10** (2010) 146.
19. K.S. Murray, C.J. Kepert, Cooperativity in Spin Crossover Systems: Memory, Magnetism and Microporosity, Springer-Verlag, 2004.
20. M.L. Tong, X.M. Chen, *Cryst. Eng. Commun*. **2** (2000) 1.
21. M.L. Tong, B.H. Ye, J.W. Cai, X.M. Chen, S.W. Ng, *Inorg. Chem.* **37** (1998) 2645.
22. D.T. De Lill, N.S. Gunning, C.L. Cahill, *Inorg. Chem*. **44** (2005) 258.
23. E.Y. Choi, Y.U. Kwon, *Inorg. Chem*. **44** (2005) 538.
24. T. Steiner, *Angew. Chem., Int. Ed. Engl.* **41** (2002) 48.
25. T. Steiner, *Chem. Commun*. (1997) 727.
26. M.D. Stephenson, T.J. Prior, M.J. Hardie, *Cryst. Growth Des.* **8** (2008) 643.
27. T.J. Prior, M.J. Rosseinsky, *Chem. Commun.* (2001) 1222.
28. A.D. Burrows, D.M.P. Mingos, A.J.P. White, D.J. Williams, *Chem. Commun*. (1996) 97.
29. S.R. Breeze, S.N. Wang, *Inorg. Chem.* **32** (1993) 5981.
30. K. Biradha, M. Sarkar, L. Rajput, *Chem. Commun.* (2006) 4169.
31. D. Bradshaw, J.E. Warren, M.J. Rosseinsky, *Science* **315** (2007) 977.
32. S.D. Huang, R.G. Xiong, P.H. Sotero, *J. Solid State Chem.* **138** (1998) 361.
33. G.A. Jeffrey, An Introduction to Hydrogen Bonding, OUP, 1997.
34. L.S. Long, *Cryst. Eng. Commun.* **12** (2010) 1354.
35. S. Luachan, C. Pakawatchai, A. Rujiwatra, *J. Inorg. Organomet. Polym. Mater.* **17** (2007) 561.
36. X.H. Li, Q. Miao, H.P. Xiao, M.L. Hu, *Acta Crystallogr., Sect. E* **60** (2004) m1784.
37. W.J. Lu, Y.M. Zhu, K.L. Zhong, *Acta Crystallogr., Sect. C* **62** (2006) m448.
38. C.O. Kappe, *Angew. Chem., Int. Ed. Engl.* **43** (2004) 6250.
39. H. Phetmung, S. Wongsawat, C. Pakawatchai, D.J. Harding, *Inorg. Chim. Acta* **362** (2009) 2435.

40. P. Amo-Ochoa, G. Givaja, P.J.S. Miguel, O. Castillo, F. Zamora, *Inorg. Chem. Commun.* **10** (2007) 921.
41. Z. Ni, R.I. Masel, *J. Am. Chem. Soc*. **128** (2006) 12394.
42. B. Yotnoi, S. Yimklan, T.J. Prior, A. Rujiwatra, *J. Inorg. Organomet. Polym. Mater.* **19** (2009) 306.
43. R.I. Cooper, R.O. Gould, S. Parsons, D.J. Watkin, *J. Appl. Cryst.* **35** (2002) 168.
44. F.H. Allen, *Acta Crystallogr., Sect. B* **58** (2002) 380; (see <www.ccdc.cam.ac.uk>.)
45. S.J. Weigel, R.E. Morris, G.D. Stucky, A.K. Cheetham, *J. Mater. Chem.* **8** (1998) 1607.
46. L.P. Zhang, L.G. Zhu, *Acta Crystallogr., Sect. E* **61** (2005) m1264.
47. Z.-X. Lian, J. Cai, C.-H. Chen, *Polyhedron* **26** (2007) 2647.
48. S.R. Fan, L.G. Zhu, *Acta Crystallogr., Sect. E* **61** (2005) m1689.
49. H. Chen, (Jiegou Huaxue) *Chin. J. Struct. Chem.* **24** (2005) 236.
50. C. Ruiz-Pérez, P. Lorenzo-Luis, M. Hernández-Molina, M.M. Laz, F.S. Delgado, P. Gili, M. Julve, *Eur. J. Inorg. Chem*. (2004) 3873.
51. T. Steiner, G.R. Desiraju, *Chem. Commun.* (1998) 891.
52. C. Papatriantafyllopoulou, E. Manessi-Zoupa, A. Escuer, S.P. Perlepes, *Inorg. Chim. Acta* **362** (2009) 634.
53. V.P. Mahadevan Pillai, V.U. Nayar, V.B. Jordanovska, *J. Solid State Chem.* **133** (1997) 407.
54. J. Lu, C. Yu, T. Nui, T. Paliwala, G. Crisci, F. Somosa, A.J. Jacobsen, *Inorg. Chem.* **37** (1998) 4637.

CHAPTER VI

CRYSTAL GROWTH AND CHARACTERISATION OF A UNIQUE TRINUCLEAR V^{IV}/V^{V} COMPLEX

Yothin Chimupala, Wasinee Phonsri, Timothy J. Prior and **Apinpus Rujiwatra**
Maejo International Journal of Science and Technology **2011**, 5(01), 83-95.

INTRODUCTION

Prompted by a variety of valences and coordination chemistry that can be adopted by vanadium and a wide range of potential applications of its complexes [1-3], the interest in vanadium complexes has been unceasing, particularly in those of high nuclearity and mixed valence state. The bi-nuclear complexes containing a mono-μ-oxo $[V_2O_3]^{2+}$ core are thus far the largest class in which the mixed valence state of vanadium is common. Examples of polynuclear V^{IV}/V^{V} complexes with mono-μ-oxo vanadium cores are still limited: the tetra-nuclear $[V_40_6(C_2H_5O)_6(C_{12}H_8N_2)_2]$, penta-nuclear $\{[V_2O_4(C_{12}H_8N_2)_2(PO_4)]_2VO(OH)\}_{3/4}\{[V_2O_4(C_{12}H_8N_2)_2(HPO_4)]_2\}_{1/4}.4.5H_2O$ and nona-nuclear $K_7[V_9O_{16}(bdta)_4].27H_2O$ (bdta = butanediaminetetraacetate) are known [4-6]. To the best of our knowledge, the first example of the tri-nuclear vanadium complex of this kind with a chemical formula of $[VO_2(\textit{phen})(SO_4)(H_2O)]_2(VO(\textit{phen})(H_2O)].4H_2O$ (*phen* = phenanthroline ligand) was reported by Huang *et al.* in 2008 [7]. Its hydrothermal synthesis and the novel characteristic of its structure in exhibiting a practically linear $[V_3O_5]^{4+}$ core were reported with a brief description on the EPR and UV-vis study of the complex.

As a continuation of our interest in the synthesis of new polyoxovanadates using organodiamines of different molecular flexibility and aromaticity, we embark on the synthesis and growing of single crystals of compound $[V_2{}^{V}V^{IV}O_5(C_{12}H_8N_2)_3(SO_4)_2(H_2O)_3].6H2O$ **(VIII)**. Although reported earlier [7], the synthesis and crystal growth of **1** by a different route carried out in this study and a detailed description of its crystal structure should be worth reporting. Different ways of determining the mixed valence state of vanadium are presented. The UV-vis spectroscopic study, cyclic voltammetric analysis and thermorgravimetric-differential scanning calorimetric analysis of **VIII** were also performed.

EXPERIMENTAL

Chemicals

All chemicals were used as-received: 1,10-phenanthroline ($C_{12}H_8N_2$; Fluka, 99%), ethyl alcohol (Merck, 99.9%), ammonium metavanadate (Ajax, 99.5%), sodium hydroxide (Merck, 99%), sulphuric acid (Merck, 95-97%), potassium permanganate (BDS, 99%), sodium sulphite (Ajax, 98%) and potassium bromide (BDH 98.5%).

Crystal Growth and Characterisation

An ethanolic solution of organic ligand (solution A) was prepared by dissolving 0.495 g of 1,10-phenanthroline (*phen*) in 15.0 mL of ethyl alcohol. An aqueous solution of VO^{2+} (solution B) was prepared by dissolving 2.00 g of ammonium metavanadate in 50.0 mL of warm 1.00 mol dm^{-3} sodium hydroxide solution, followed by addition of 80.0 mL of 1.00 mol dm^{-3} sulphuric acid. A portion of solution B (1.50 mL) was gently loaded into a glass test tube of 5 mm in diameter and 10

cm in length, followed by 1.50 mL of solution A. Dark green crystals of **VIII** appeared at the boundary between solutions A and B after leaving for 5 days at atmospheric condition.

The elemental composition of the crystals was semi-quantified using an energy-dispersive X-ray micro-analyser equipped with a field-emission scanning electron microscope (JEOL JSM-6335F), whereupon a consistent V:S:O:C:N atomic ratio of 2.8:1.0:3.2:6.7:1.5 (exp.) compared to 2.4:1.0:5.5:6.7:1.3 (calc.) was obtained. A Fourier transform infrared (FTIR) spectrum of the ground crystals as a KBr pellet was collected on a Bruker Tensor 27 FT-IR instrument (4000-400 cm^{-1}, resolution 0.5 cm^{-1}): 3450 cm^{-1}, ν(O-H); 3065 cm^{-1}, ν(aromatic C-H); 1626, 1583, 1519 and 1427 cm^{-1}, ν(aromatic C=C); 1187, 1125 and 1032 cm^{-1}, ν(SO_4); 970 and 937 cm^{-1}, ν(V=O); 870, 848, 778, 736 and 723 cm^{-1}, δ_{oop}(aromatic C-H); 647 and 593 cm^{-1}, δ(V-O-V).

The purity of **VIII** was assured by X-ray powder diffraction pattern collected on a Bruker D8 Advance diffractometer (Ni filter, Cu *K*α, λ=1.540558 Å, 48 kV, 30 mA). In order to determine the amount of V^{IV} and total $V^{IV,V}$ the aqueous solutions of **VIII** and its reduced form were titrated against standardised potassium permanganate solution. The solution of the reduced form of **VIII** was obtained by a reaction with sulphur dioxide generated from sodium sulphite. Cyclic voltammetry (CV) was also conducted using a BAS CV-50W voltammetric analyser (Bioanalytical System, Inc., USA) with Pt (MF-2013, 1.6 mm in diameter), Ag/AgCl (MF-2063) and Pt wire (MW-1032) as working, reference and auxiliary electrodes respectively.

Themogravimetric-differential scanning calorimetric (TG-DSC) analysis was performed using ETZSCH STA 409 PC/PG thermal analyser (Netzsch-Gerätebau GmbH, Germany) (20-1200 ^oC, rate 10 $^oC\ min^{-1}$, N_2 gas) to evaluate the thermal stability of **VIII**. A UV-vis spectrum of an aqueous solution of **VIII** from 200 nm to 800 nm was measured with a Perkin Elmer UV LAMDA 25 spectrophotometer. The loss of crystal colour after complete dissolution was noted.

Crystal Structure Determination

Data of 8699 independent reflections were collected in a range of $2.5 \leq \theta/^o \leq 26.1$ on a 0.45x0.25x0.15 mm^3 greenish lozenge crystal of **1** using a Stoe IPDS2 diffractometer (Stoe & Cie GmbH, Germany) and Stoe *X*-Area software [8]. A face indexed absorption correction was applied within the Stoe *X*-RED software using Tompa method [9-10]. The data were then reduced and refined resulting in 5365 reflections with $I > 2\sigma(I)$ and internal R of 0.070. The structure was determined by direct method and refined by full-matrix least-square methods using SHELXS97 and SHELXL97 programs via the WinGx program interface [11-13]. The structure was solved and refined in $P2_1/c$, a = 20.5448(11) Å, b = 11.7647(9) Å, c = 18.1871(9) Å, β = 92.64(0)^o, V = 4391.22(93) $Å^3$, Z = 4, R = 0.0941 and Rw = 0.1345. The data were of reasonable quality. However, it was not possible to locate hydrogen atoms of the included water molecules. Some disorder in the positions of the water molecules was also detected. Details on data collection and structural deduction and refinement are summarised in Table 18. A rather large deviation of the goodness of fit from unity due to local disorder in the structure of **VIII** may be noted.

The structure of **VIII** was first reported by Huang *et al.* in 2008 [7]. The synthesis by hydrothermal route and the uniqueness of the complex as the first mixed-valence polynuclear vanadium with linear mono-μ-oxo $[V_3O_5]^{4+}$ core were briefly reported. The study of the EPR and electronic spectrum was included. Crystallographic data of the formerly reported structure were compared with the presently reported structure as shown in Table 18, which suggests an approximate equivalence.

Table 18 *Crystal data and structure refinement for* ***VIII.***

	VIII	Data abstracted from Huang et al. [7]
Formula	$[V_2^{V}V^{IV}O_5(phen)_3(SO_4)_2(H_2O)_3]\cdot 6H_2O$	$[VO_2(phen)(SO_4)(H_2O)]_2[VO(phen)(H_2O)]\cdot 4H_2O$
Formula weight	1117	1091.66
Crystal description	Dark green	*N/A*
Crystal system	Monoclinic	Monoclinic
Space group	$P2_{1/c}$	$P2_{1/c}$
a/ Å	20.5448(11)	20.747(4)
b/ Å	11.7647(9)	11.828(2)
c/ Å	18.1871(9)	18.316(4)
β / °	92.639(4)	93.07(3)
Unit cell volume/ Å^3	4391.2(5)	4488.2(16)
Z	4	4
ρ_{calc}/ g.cm^{-3}	1.691	1.616
T/K	150(4)	293(2)
Radiation (λ/Å)	Mo K_α(0.71073)	Mo K_α(0.71073)
Total data collected	24523	37068
R_{int}	0.070	0.0384
Data ($I>2\sigma(I)$)	8699	10059
Goodness of fit (*S*)	0.797	1.049
R, R_w (all data)	0.0941, 0.1345	*N/A*
R, R_w($I>2\sigma(I)$)	0.055, 0.135	0.0558, 0.1488

RESULTS & DISCUSSION

Crystal Structure of ***VIII***

Compound **VIII,** $[V_2^{V}V^{IV}O_5(C_{12}H_8N_2)_3(SO_4)_2(H_2O)_3].6H_2O$, crystallises in monoclinic space group $P2_1/c$ with cell parameters a = 20.5448(11) Å, b = 11.7647(9) Å, c = 18.1871(9) Å, β = 92.64(0)°, V = 4391.22(93) Å^3 and Z = 4, which are similar to those of the previously reported structure [7]. Figure 34 shows an asymmetric unit of **VIII**, depicting three distinct vanadium atoms linked by two μ_2-O11 and μ_2-O12 to form an approximately linear trinulcear vanadium oxide backbone with bond angles being close to linearity: V1-O11-V2 = 163.1° and V(2)-O(12)-V(3) = 159.2°. Selected bond lengths and bond angles in **VIII** are listed in Table 19 and Table 20 respectively. The terminal V1 and V3 share the common distorted octahedral geometry, coordinated to two N atoms of the chelating *phen* and four O atoms from a monodentate sulphate, a terminal aqua ligand, the vanadyl bond and the oxo-bridge. Similar distorted octahedral geometry is adopted by the mediating V2, coordinated to two N atoms of the chelating *phen*, two *trans* μ_2-O atoms of oxo-bridges, and the vanadyl and sulphate O atoms. The chemical formula of $[V_3O_5(phen)_3(SO_4)_2(H_2O)_3]$ can thus be derived. A common question for polynuclear vanadium complexes is, however, the valence states of the vanadium atoms.

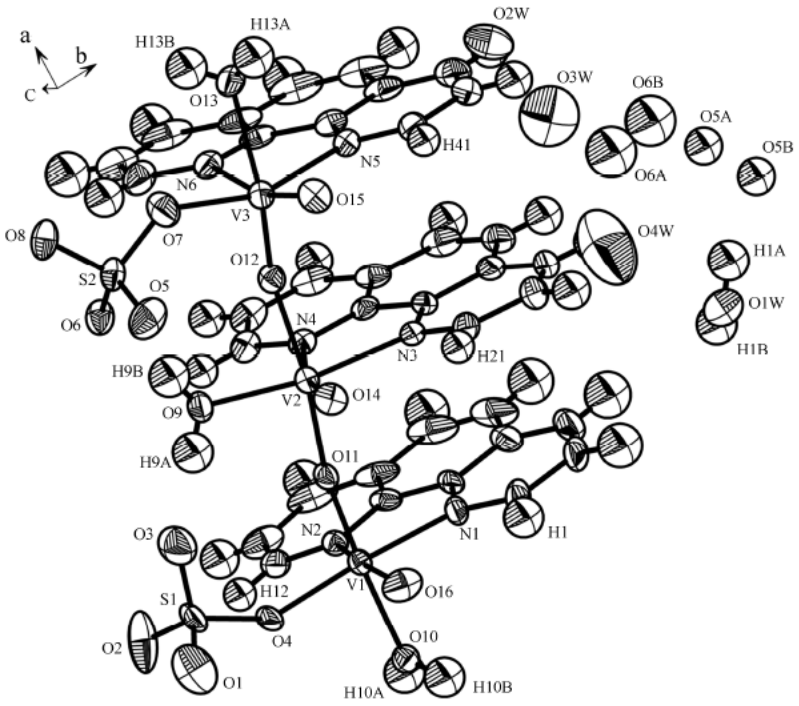

Fig. 34 Asymmetric unit of **VIII** with atomic numbering scheme and drawn with 50% thermal elliptical possibility.

Table 19 Selected bond distances (Å) in **VIII** with standard deviations in brackets.

V1—O16	1.600(3)	V3—O12	1.677(3)
V1—O11	1.675(3)	V3—O7	1.930(3)
V1—O4	1.917(3)	V3—O13	2.123(4)
V1—N1	2.132(4)	V3—N5	2.136(4)
V1—O10	2.149(4)	V3—N6	2.296(4)
V1—N2	2.249(3)	S2—O5	1.430(4)
V2—O14	1.592(3)	S2—O8	1.455(3)
V2—O12	1.932(3)	S2—O6	1.468(3)
V2—O11	1.947(3)	S2—O7	1.521(4)
V2—O9	1.998(3)	S1—O2	1.421(4)
V2—N3	2.124(4)	S1—O1	1.457(4)
V2—N4	2.307(3)	S1—O3	1.462(5)
V3—O15	1.596(3)	S1—O4	1.510(3)

The bond valence sum (BVS) calculation was attempted using the refined bond lengths listed in Table 19 with the following assumed parameters: $R_0(V^{V,IV}\text{-}O^{-II})$ = 1.735, $R_0(V^{V}\text{-}O^{-II})$ = 1.803, $R_0(V^{IV}\text{-}O^{II})$ = 1.780, $R_0(V^{V,IV}\text{-}N^{-III})$ = 1.875, and b = 0.370 [14]. The BVS of 4.81, 4.15 and 4.85 were obtained for V1, V2 and V3 respectively, indicating the presence of the expected V^{IV} and V^{V} with twice the amount of the latter. The result of manganometric titration confirms the calculation: 0.915 mol of V^{IV} per formula unit. The CV analysis confirms this by the presence of an irreducible reduction peak of V^{V} to V^{IV} at +0.242 V *vs* Ag/AgCl with a maximum current of 4.48 A. Based on the BVS calculation, manganometric titration and the CV experiment, a mixed $2V^{V}$:V^{IV} valence state for vanadium and the precise formula of $[V_2{}^{V}V^{IV}O_5(C_{12}H_8N_2)_3(SO_4)_2(H_2O)_3]$ can thus be deduced. This leads to the conclusion on charge neutrality for the cluster, which confirms the presence of only water molecules as the extra-cluster species and justifies the assignment of the extra-cluster O atoms

as water during the crystal structure deduction and refinements. The chemical formula with six extra-cluster water molecules, *viz.* $[V_2^{V}V^{IV}O_5(C_{12}H_8N_2)_3(SO_4)_2(H_2O)_3].6H_2O$, is then established.

Table 20 *Selected bond angles (°) in* ***VIII*** *with standard deviations in brackets.*

O16—V1—O11	104.73(16)	O12-V2-N3	87.57(13)	N5-V3-N6	73.96(13)
O16—V1—O4	104.79(18)	O11-V2-N3	96.01(13)	O5-S2-O8	113.5(2)
O11—V1—O4	99.86(14)	O9-V2-N3	159.64(14)	O5-S2-O6	111.2(2)
O16—V1—N1	92.14(18)	O14-V2-N4	166.12(15)	O8-S2-O6	110.40(19)
O11—V1—N1	88.54(15)	O12-V2-N4	80.55(12)	O5-S2-O7	109.1(2)
O4 —V1—N1	158.32(14)	O11-V2-N4	82.81(12)	O8-S2-O7	103.9(2)
O16—V1—O10	87.57(16)	O9-V2-N4	86.43(14)	O6-S2-O7	108.3(2)
O11—V1—O10	165.39(13)	N3-V2-N4	73.57(13)	O2-S1-O1	109.3(3)
O4 —V1—O10	84.22(13)	O15-V3-O12	104.37(16)	O2-S1-O3	116.4(3)
N1 —V1—O10	83.05(14)	O15-V3-O7	104.52(17)	O1-S1-O3	105.5(3)
O16—V1—N2	161.26(17)	O12-V3-O7	97.97(15)	O2-S1-O4	106.8(2)
O11—V1—N2	88.14(14)	O15-V3-O13	93.89(15)	O1-S1-O4	107.2(2)
O4 —V1—N2	85.91(13)	O12-V3-O13	161.30(13)	O3-S1-O4	111.2(2)
N1 —V1—N2	74.35(14)	O7-V3-O13	81.01(15)	S1-O4-V1	140.7(2)
O10-V1-N2	78.10(13)	O15-V3-N5	89.66(15)	S2-O7-V3	137.3(2)
O14-V2-O12	99.86(15)	O12-V3-N5	95.24(14)	V1-O11-V2	163.10(18)
O14-V2-O11	98.38(15)	O7-V3-N5	157.48(16)	V3-O12-V2	159.23(18)
O12-V2-O11	161.23(12)	O13-V3-N5	80.64(14)		
O14-V2-O9	107.45(16)	O15-V3-N6	162.33(16)		
O12-V2-O9	85.36(14)	O12-V3-N6	84.12(14)		
O11-V2-O9	85.00(13)	O7-V3-N6	89.31(16)		
O14-V2-N3	92.56(15)	O13-V3-N6	77.20(13)		

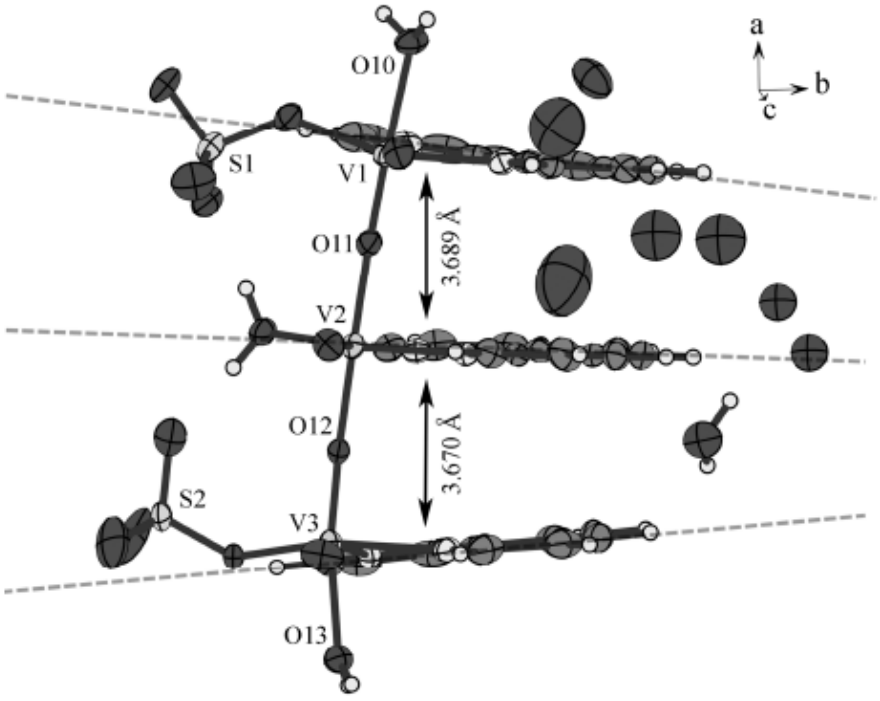

Fig. 35 *Illustration showing the relative spatial arrangement of phen and the corresponding intermolecular planar distances.*

The phenanthroline (*phen*) ligands are located on the same side of the vanadium oxide backbone with the distances of 3.689 Å and 3.670 Å between the centroids of two adjacent molecular planes as shown in Fig. 35. These distances are in a range possible for the π-π interactions to occur [15-17], which can be regarded as an important parameter regulating the spatial arrangement of these chelating ligands. It is apparent that these *phen* ligands are not exactly parallel to each other but slightly converge towards the free end of the molecule. Figure 36 depicts the centroids of the central benzene rings of the *phen* ligands, showing the panning angles of 9.48° and 21.80° for the superjacent and subjacent ligands from the middle one. The relative arrangement of these organic ligands indicates that other interactions are present that subjugate the weak π-π interactions, which favour the superimposed position of the ligands.

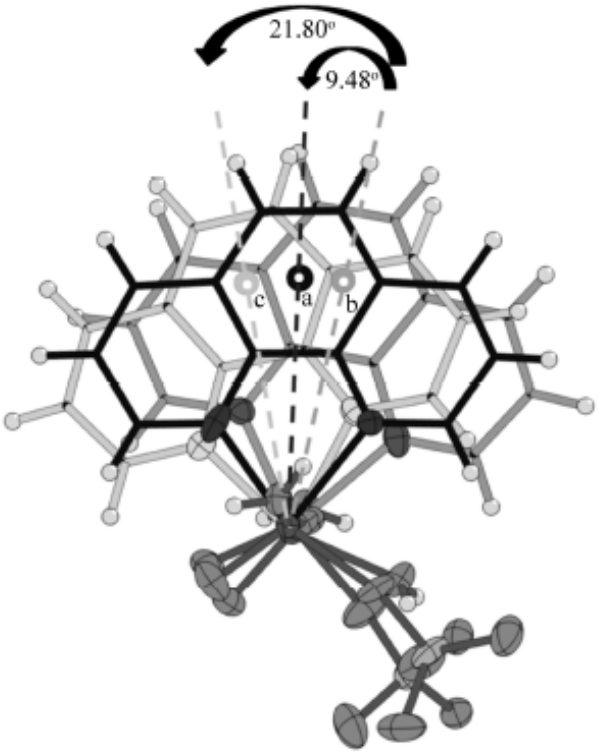

Fig. 36 *Illustration showing relative locations of the centroids (a, b and c) of the central benzene rings of the superjacent, middle and subjacent phen ligands respectively, with relative panning angles of a and c from b.*

The interaction between π electrons commonly encountered in the stacking of aromatic molecules should impart an influence on their aromaticity. Here, the harmonic oscillator model of aromaticity (HOMA) index was used to evaluate the presence of this interaction [18-20]. According to a survey of structures consisting of *phen* in the molecules both in coordination and non-coordination modes found in the Cambridge structural databases [21], it is evident that the values of HOMA indices are distributed in different ranges depending on both the coordination and the π-π interaction. For non-coordinated *phen*, the average indices of three fused benzene rings are distributed in a range of 0.25-0.50 for those without π-π interactions and 0.66-0.83 for those with the interactions. On the other hand, the presence of π-π interactions seems to be common with coordination with average indices distributed in a higher range of 0.70-0.94, suggesting the preference of these aromatic ligands to arrange themselves in such a way as to maximise the interactions. In the structure of **VIII**, the HOMA indices were calculated at similar values of ca. 0.80 for each *phen* ligand. This is in very good agreement with the surveyed HOMA indices for those complexes with π-π interacting *phen* ligands, hence the suggested presence of such weak interaction in **VIII**.

The analysis for hydrogen bonding according to the definition proposed by Jeffrey [22] was performed on the crystal structure and revealed a large number of hydrogen bonding interactions as depicted in Fig. 37 and listed in Table 21. The weak C-H···O hydrogen bonds formed between *phen*

and the neighbouring O atoms of both ligated and free water molecules as well as the nearby sulphate group may account for the subjugation of the π-π interactions and the consequent orientation of these organic ligands. The strong hydrogen bonds of O-H···O type between the ligated water of the mediated V2 and the nearby sulphates also provide explanation for the orientation of the pending SO_3 motifs of V1 and V3 that incline towards each other with the bending angles of 140.71° and 137.32° for V1-O3-S1 and V3-O7-S2 respectively.

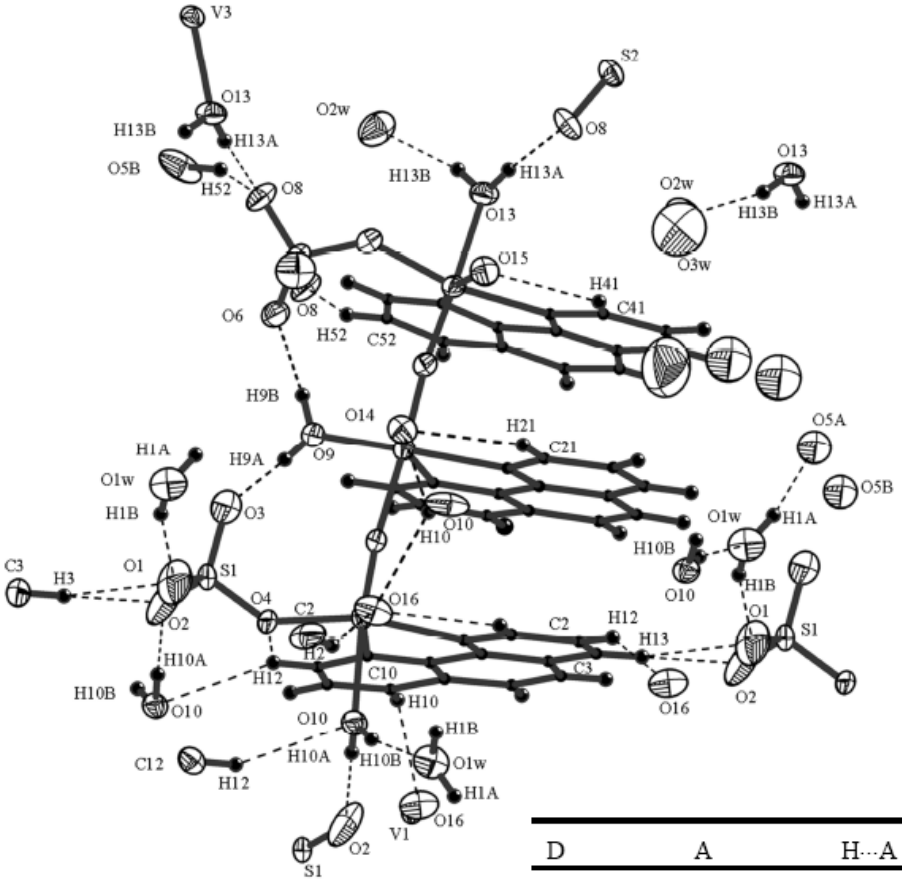

Fig. 37 *Hydrogen bonding interactions (dotted lines) of different types as listed in Table 21.*

Table 21 *Summary of hydrogen bonding geometry for* ***VIII*** *(Standard deviations are in brackets).*

D	A	H···A (Å)	D···A (Å)	∠ D-H···A (°)
$O1_W$	$O5_A$	2.17(5)	2.981(7)	158(5)
$O1_W$	O1	1.99(4)	2.807(5)	161(6)
O9	O3	1.72(4)	2.560(5)	175(7)
O9	O6	1.76(4)	2.604(5)	176(5)
O10	O2	1.91(4)	2.750(5)	179(7)
O10	$O1_W$	1.87(5)	2.690(5)	164(5)
O13	O8	1.82(5)	2.656(5)	174(5)
O13	$O2_W$	1.93(5)	2.728(5)	163(4)
C1	O16	2.57	2.994(7)	108
C2	O16	2.46	3.308(7)	149
C3	O1	2.50	3.270(7)	138
C3	O2	2.35	3.272(8)	163
C10	O14	2.56	3.243(7)	129
C10	O16	2.49	3.212(7)	133
C12	O4	2.56	3.058(5)	113
C12	O10	2.57	3.365(6)	142
C21	O14	2.49	2.957(6)	110
C41	O15	2.43	2.894(6)	110
C52	O8	2.45	3.246(7)	142

Compared to the complex, $[VO_2(phen)(SO_4)(H_2O)]_2(VO(phen)(H_2O)].4H_2O$, reported by Huang *et al*. [7], structure **VIII** contains two more molecules of water of crystallisation and therefore a larger number of hydrogen bonding interactions. This may stem from the difference in crystal growth technique and condition. Crystals of **VIII** were grown at ambient temperature and pressure, whereas those of the former were obtained hydrothermally. The larger number of water outside the coordination sphere, however, does not significantly affect the solid state registry of the compound.

UV-Vis Spectroscopic Study

The UV-vis spectrum measured on the aqueous solution of **VIII** at a concentration of $5x10^{-4}$ mol dm^{-3} (Fig. 38) exhibits absorption only in the UV region. The absorption bands characteristic of *phen* are clearly present with the maxima at 230 nm (3,205 $dm^3mol^{-1}cm^{-1}$) and 264 nm (2,150 $dm^3mol^{-1}cm^{-1}$), both of which are attributable to the intra-ligand π-π* transitions. The most intense band at 206 nm (10,584 $dm^3mol^{-1}cm^{-1}$) can be assigned to the LMCT process of the terminal oxygen while a broad band appearing as shoulder at 270 nm is the characteristic band associated to the LMCT of the bridging oxygen [23-25]. The absorption coefficients (α) can be calculated from the maximum (λmax) of each band, and the plot between $(\alpha h\nu)^2$ and $h\nu$ can be made (inset of Fig. 38) if only the direct electronic transition is assumed [26]. The band gap energy for each transition can be obtained by extrapolation of the positive tangent line for each $h\nu$ to α=0, 4.3017, 5.2317 and 5.8182 eV for the transitions with λmax at 264, 230 and 206 nm respectively. It is intriguing that there was no absorption in the visible light region (325-800 nm) for the solution of **VIII**, which was also colourless. This might be due to the loss of long-range order of the solid state structure when it was made into solution. It has been reported, however, that a broad absorption band which should be evidence for the inter-valence charge transfer between V^{IV} and V^{V} was observed in this region for the spectrum collected on a solid sample [7].

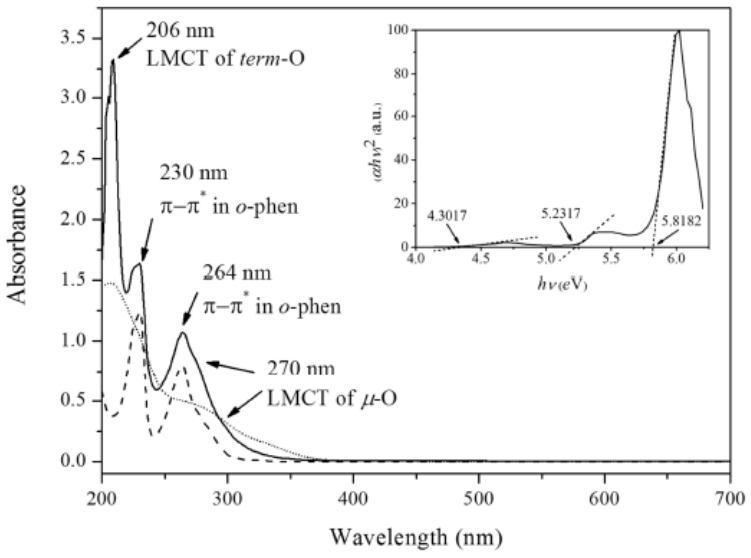

Fig. 38 *The UV-Vis spectrum of aqueous solution of* ***VIII*** *($5x10^{-4}$ $moldm^{-3}$, solid line) compared with those of the ligand (dash line) and vanadium precursor (dotted line). The plot between $(\alpha h\nu)^2$ and hν is provided in the inset.*

Thermogravimetric and differential scanning calorimetric analysis

On heating **VIII** under the flow of N_2 gas, four stages of endothermic weight loss were observed (Fig. 39). The first weight loss of 9.86% occurring between 80-150 ^oC agrees well with the weight of six non-coordinating water molecules (9.58%), while the second loss of 5.14% observed at 150-340 ^oC is approximately equivalent to the weight of three coordinating water molecules (4.79%). The corresponding endothermic features found in the DSC curve reflect the influence of the hydrogen bonding interactions involved with these water molecules. The next two subsequent weight losses found from 340 ^oC to 700 ^oC totalled 45.00%, which corresponds well with the release of three

coordinated *phen* ligands. It should be noted that the argument is made based only on the agreement of weight percentages; further experiments on identification of the liberated species have to be performed if a definite conclusion is to be obtained.

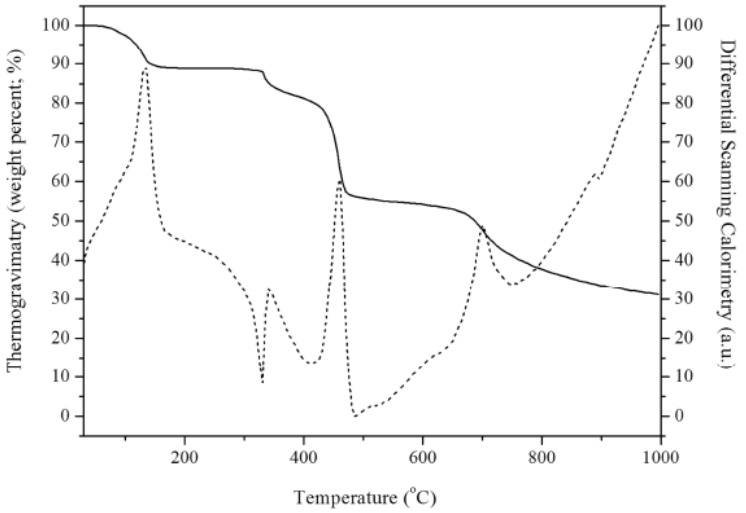

Fig. 39 *Thermogravimetric (solid line) and differential scanning calorimetric (dash line) graphs collected on* ***VIII.***

CONCLUSIONS

A rare example of mixed-valence trinuclear cluster, $[V_2^{V}V^{IV}O_5(C_{12}H_8N_2)_3(SO_4)_2(H_2O)_3].6H_2O$, has been synthesised at ambient atmosphere. Its crystal structure has been determined and refined with excellent agreement with the previously reported structure which had fewer water of crystallisation. Detailed analysis of the structure indicates the presence of both π-π interactions and a large number of intra- and inter-cluster hydrogen bonds, which impart influence on spatial orientation of the cluster building motifs. According to the bond valence sum calculations, the manganometric titration and cyclic voltammetry, the mixed valence of V^{IV} and V^{V} in the ratio of 1:2 can be deduced. The presence of six molecules of water of crystallisation is consistent with the results of the thermogravimetric/differential scanning calorimetric analysis, which suggest sequential loss of water of crystallisation, ligated water and the phenanthroline ligands.

REFERENCES

1. M. R. Maurya and A. Kumar, *J. Mol. Catal. A: Chem.* **250** (2006) 190-198.
2. C. Hiort, J. Goodisman and J. C. Dabrowiak, *Biochem.* **35** (1996) 12354-12362.
3. J. H. Hwang, R. K. Larson and M. M. Abu-Omar, *Inorg. Chem.* **42** (2003) 7967-7977.
4. L. Mafra, F .A. Almeida Paz, F. Shi, C. Fernandez, T. Trindade, J. Klinowski and J. Roch, *Inorg. Chem. Commun.* **9** (2006) 34-38.
5. H. Kumagai, M. Endo, S. Kawata and S. Kitagawa, *Acta Crystallogr. C***52** (1996) 1943-1945.
6. J. P. Launay, Y. Jeannin and M. Daoudi, *Inorg. Chem.* **24** (1985) 1052-1059.
7. X. H. Huang, C. C. Huang, X. H. Qin, L. S. Zhai and D. S. Liu, *Inorg. Chem. Commun.* **11** (2008) 1236-1238.
8. Stoe & Cie X-AREA (Version 1.18), Stoe & Cie , Darmstadt, Germany (2002).
9. 9. Stoe & Cie X-RED (Version 1.04), Stoe & Cie, Darmstadt, Germany (2002).
10. J. D. Meulener and H. Tompa, **19** (1965) 1014-1018.
11. G.M. Sheldrick, "SHELXS-97: Program for solving crystal structure", University of Gottingen, Germany (1997).

12. G.M. Sheldrick, “SHELXL-97: Program for crystal structure refinement”, University of Gottingen, Germany (1997).
13. L.J. Farrugia, “*WinGX* Suite for small-molecule single-crystal crystallography”, *J. Appl. Crystallogr.* **32** (1999) 837-838.
14. V. S. Urusov and I.P. Orlov, *Crystallogr. Rep.* **44** (1999) 686-709.
15. F.J. Carver, C.A. Hunter and E. M. Seward, *Chem. Commun.* (1998) 775-776.
16. S.B. Ferguson, E.M. Sanford, E.M. Seward and F. Diederich, *Am. Chem. Soc.* **113** (1991) 5410-5419.
17. C.A. Hunter and J.K.M. Sanders, *J. Am. Chem. Soc.* **112** (1990) 5525-5534.
18. T.M. Krygowski, M.K. Cyranski, Z. Czarnocki, G. Hafelinger and A.R. Katritzky, *Tetrahedron* **56** (2000) 1783-1796.
19. T.M. Krygowski, *J. Chem. Inf.: Comput. Sci.* **33** (1993) 70-78.
20. T.M. Krygowski and M.K Cyranski, *Phys. Chem. Chem. Phys.* **6** (2004) 249-255.
21. F. H. Allen and W.D.S. Motherwell, *Acta Cryst.* B**58** (2002) 380-388.
22. G.A. Jeffrey, “An introduction to hydrogen bonding”, Oxford University Press, New York, **1997**.
23. L. Chen, F. Jiang, Z. Lin, Y. Zhou, C. Yue and M. Hong, *J. Am. Chem. Soc.* **127** (2005) 8588-8589.
24. Y.C. Liu, Z.F. Chen, S.M. Shi, H.S. Luo, D.C. Zhong, H.L. Zou and H. Liang, *Inorg. Chem. Commun.* **10** (2007) 1269-1272.
25. Y. Gong, C. Hu and H. Li, *J. Mol. Struct.* **749** (2005) 31-35.
26. J.I. Pankove, “Optical processes in semiconductors”, Prentice-Hall, Englewood Cliffs (1971) 34-42.

CHAPTER VII

INORGANIC-ORGANIC HYBRID STRUCTURE REPORTS

IX) 1-Butyl-1,4-diazabicyclo[2.2.2]octon-1-ium-κN^4)trichloridocobalt(II)

Sanchai Luachan, Bunlawee Yotnoi, Timothy J. Prior and **Apinpus Rujiwatra**

*Acta Cryst. E***65** (2009) m321–m322.

Crystal data

$[Co(C_{10}H_{21}N_2)Cl_3]$	$F_{000} = 692$
$M_r = 334.57$	$D_x = 1.490$ Mg m^{-3}
Monoclinic, $P2_1$	Synchrotron radiation $\lambda = 0.69430$ Å
Hall symbol: P 2yb	Cell parameters from 12848 reflections
$a = 8.379$ (2) Å	$\theta = 1.4$–$30.7°$
$b = 12.1090$ (13) Å	$\mu = 1.67$ mm^{-1}
$c = 14.711$ (4) Å	$T = 120$ K
$\beta = 91.683$ (4)°	Needle, blue
$V = 1492.0$ (6) Å^3	0.12 × 0.02 × 0.02 mm
$Z = 4$	

Data collection

Bruker D8 with APEXII detector diffractometer	8831 independent reflections
Radiation source: Daresbury SRS, UK	7018 reflections with $I > 2\sigma(I)$
Monochromator: silicon 111	$R_{int} = 0.054$
$T = 120$ K	$\theta_{max} = 30.7°$
ω scans	$\theta_{min} = 1.4°$
Absorption correction: multi-scan (TWINABS; Bruker, 2004)	$h = -12 \rightarrow 12$
$T_{min} = 0.597$, $T_{max} = 0.746$	$k = -17 \rightarrow 17$
12848 measured reflections	$l = -20 \rightarrow 20$

Refinement

Refinement on F^2	Hydrogen site location: inferred from neighbouring sites
Least-squares matrix: full	H-atom parameters constrained
$R[F^2 > 2\sigma(F^2)] = 0.045$	$w = 1/[\sigma^2(F_o^2) + (0.0352P)^2 + 0.2945P]$ where $P = (F_o^2 + 2F_c^2)/3$
$wR(F^2) = 0.098$	$(\Delta/\sigma)_{max} = 0.001$
$S = 1.04$	$\Delta\rho_{max} = 0.65$ e Å^{-3}
8831 reflections	$\Delta\rho_{min} = -0.43$ e Å^{-3}
292 parameters	Extinction correction: none
1 restraint	Absolute structure: Flack (1983), 3980 Friedel pairs
Primary atom site location: structure-invariant direct methods	Flack parameter: 0.064 (17)
Secondary atom site location: difference Fourier map	

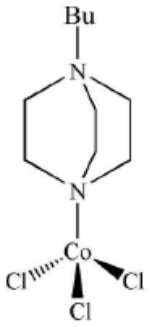

The title compound, $[Co(C_{10}H_{21}N_2)Cl_3]$, was obtained as the by-product of the attempted synthesis of a cobalt sulphate framework using 1,4-diazabicyclo[2.2.2]octane as an organic template. The symmetric unit comprises two distinct molecules, and in each, the cobalt(II) ions are tetrahedrally coordinated by three chloride anions and one 1-butyldiazabicyclo[2.2.2]octan-1-ium cation. The organic ligands are generated *in situ*, and exhibit two forms differentiated by the eclipsed and staggered conformations of the butyl groups. These molecules interact by way of C-H···Cl hydrogen bonds, forming a three-dimensional hydrogen-bonding array.

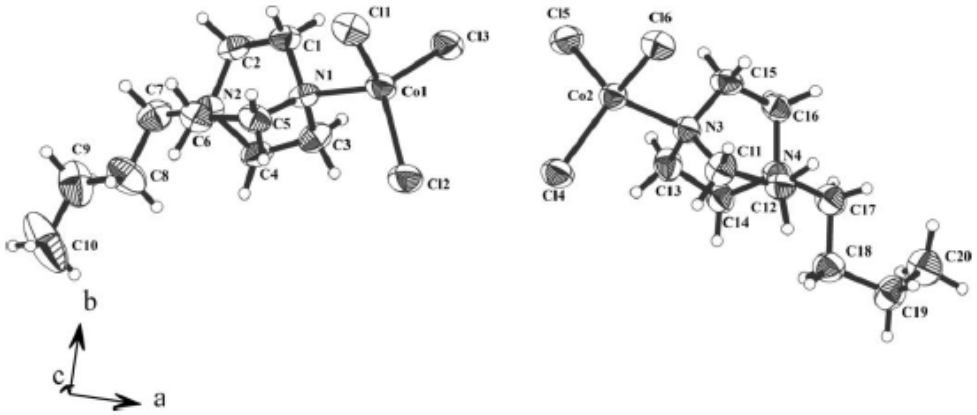

Fig. 40 *View of the title compound with atomic numbering scheme. Displacement ellipsoids for non-hydrogen atoms are drawn at 70% probability level.*

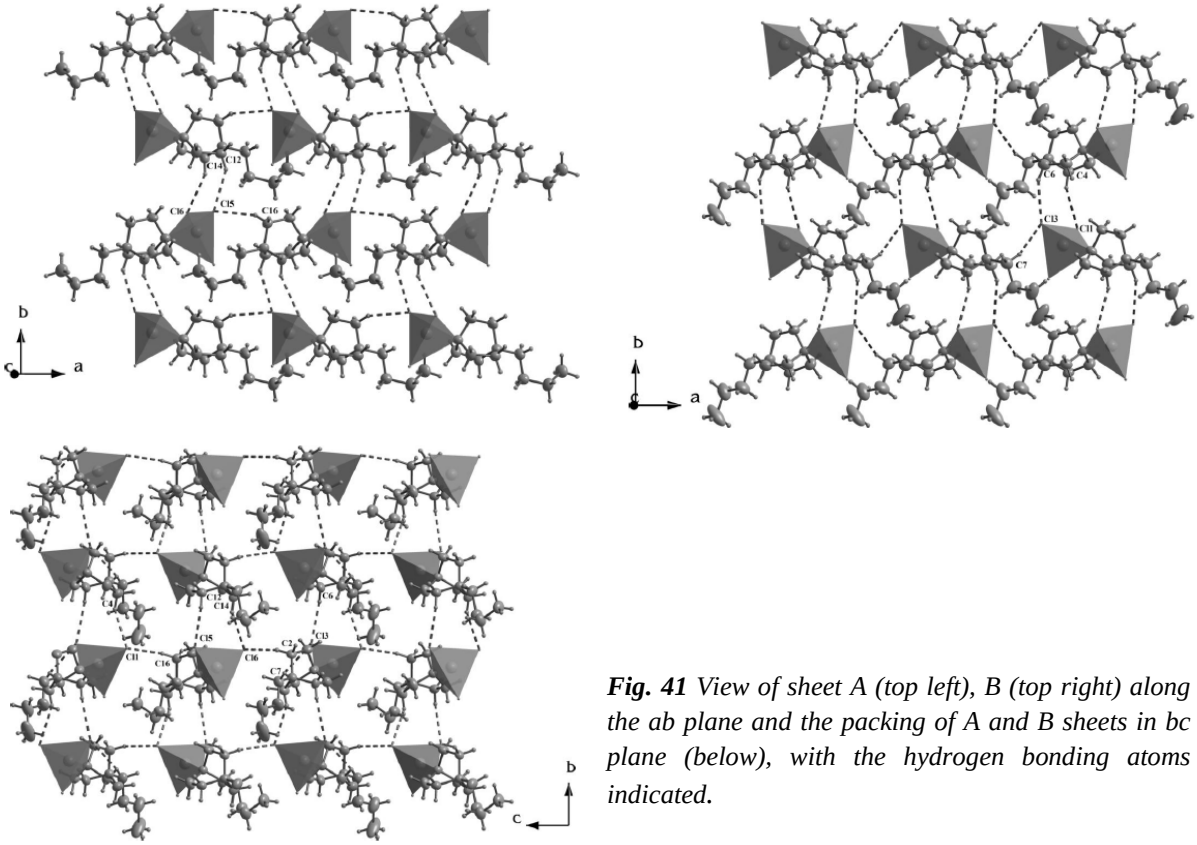

Fig. 41 *View of sheet A (top left), B (top right) along the ab plane and the packing of A and B sheets in bc plane (below), with the hydrogen bonding atoms indicated.*

Examples of closely related structures are N-methyl-1,4-diazabicyclo(2.2.2) octonium trichloro-aqua-nickel(II) (Ross & Stucky, 1969) and N,N′-dimethyl-1,4-diazaniabicyclo[2.2.2]-octane tetrachlorocobaltate ($C_8H_{18}N_2$)[$CoCl_4$] (Qu & Sun, 2005). The organic cations in both structures do not coordinate to the cobalt ion but, in each case, the C-H•••Cl hydrogen bonding interactions are similar to those in the title compound. For hydrogen bonding in related structures, see: Bremner & Harrison (2003).

REFERENCES

Brandenburg, K. & Putz, H. (2005). DIAMOND. Crystal Impact GbR, Bonn, Germany.
Bremner, C. A. & Harrison, W. T. A. (2003). *Acta Cryst. E***59**, m425-m426.
Bruker (2004). TWINABS. Bruker AXS Inc., Madison, Wisconsin, USA.
Bruker (2007). APEX2. Bruker AXS Inc., Madison, Wisconsin, USA.
Flack, H. D. (1983). *Acta Cryst. A***39**, 876-881.
Qu, Y. & Sun, X.-M. (2005). *Acta Cryst. E***61**, m2121-m2123.
Ross, F. K. & Stucky, G. D. (1969). *Inorg. Chem*. **8**, 2734-2740.
Sheldrick, G. M. (2008). *Acta Cryst. A***64**, 112-122.
Spek, A. L. (2009). *Acta Cryst. D***65**, 148-155.

X) poly[0.35-[hexaaquacobalt(II)] [tri-μ-hydroxido-μ-sulfato-dicobalt(II)]]

Bunlawee Yotnoi, Sanchai Luachan, Timothy J. Prior and **Apinpus Rujiwatra**

*Acta Cryst. E***65** (2009) i152.

Crystal data

$[Co(H_2O)_6]_{0.35}[Co_2(OH)_3(SO_4)]$
$M_r = 323.41$
Trigonal, $P\bar{3}m1$
Hall symbol: -P 3 2"
$a = 6.3627\ (19)$ Å
$b = 6.3627\ (19)$ Å
$c = 12.180\ (4)$ Å
$\alpha = 90°$
$\beta = 90°$
$\gamma = 120°$
$V = 427.0\ (2)$ Å^3
$Z = 2$
$F_{000} = 318.9$
$D_x = 2.515$ Mg m^{-3}
Mo $K\alpha$ radiation, $\lambda = 0.71073$ Å
Cell parameters from 1764 reflections
$\theta = 1.7–29.3°$
$\mu = 4.80$ mm^{-1}
$T = 150$ K
Plate, pale pink
0.21 × 0.13 × 0.03 mm

Data collection

Stoe IPDS2 diffractometer
Radiation source: fine-focus sealed tube
Monochromator: graphite
Detector resolution: 6.67 pixels mm^{-1}
$T = 150$ K
ω scans
Absorption correction: multi-scan (X-RED; Stoe & Cie, 2008)
$T_{min} = 0.415$, $T_{max} = 0.862$
1663 measured reflections
497 independent reflections
325 reflections with $I > 2\sigma(I)$
$R_{int} = 0.097$
$\theta_{max} = 29.3°$
$\theta_{min} = 1.7°$
$h = -7\rightarrow8$
$k = -7\rightarrow8$
$l = -14\rightarrow16$

Refinement

Refinement on F^2
Least-squares matrix: full
$R[F^2 > 2\sigma(F^2)] = 0.048$
$wR(F^2) = 0.132$
$S = 0.90$
497 reflections
40 parameters
3 restraints
Primary atom site location: structure-invariant direct methods
Secondary atom site location: difference Fourier map
Hydrogen site location: difference Fourier map
Only H-atom coordinates refined
$w = 1/[\sigma^2(F_o^2) + (0.0839P)^2]$ where $P = (F_o^2 + 2F_c^2)/3$
$(\Delta/\sigma)_{max} < 0.001$
$\Delta\rho_{max} = 1.04$ e Å^{-3}
$\Delta\rho_{min} = -1.05$ e Å^{-3}
Extinction correction: none

In an attempt to synthesize new cobalt(II) sulphate framework structures using 1,4-diazabicyclo[2.2.2]octane as a template, crystals of the title compound were obtained as a mixture with $[Co(H_2O)_6]SO_4$ crystals. The crystal structure can be described as being constructed from discrete Brucite-type $[Co_4(OH)_6(SO_4)_2]$ layers, each of which is built up from edge-shared $[Co(OH)_6]$ and $[Co(OH)_4(OSO_3)_2]$ octahedra, with partial intercalation by $[Co(H_2O)_6]^{2+}$ ions. The absence of *ca.* 30% of the $[Co(H_2O)_6]^{2+}$ cations indicates partial oxidation of cobalt(II) to cobalt(III) within the layer.

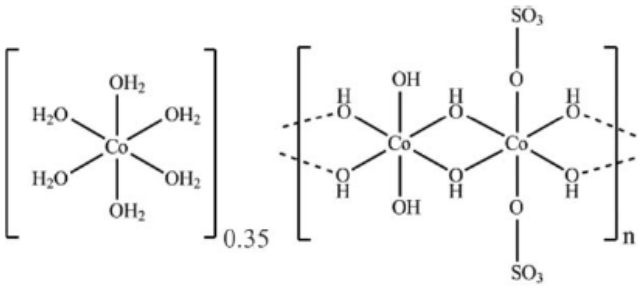

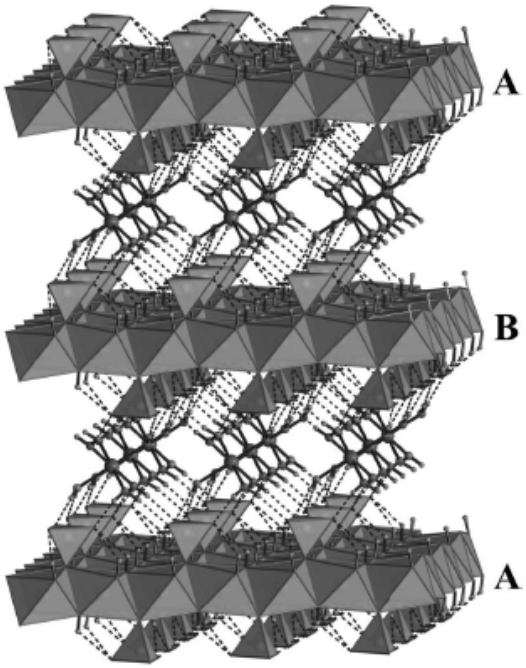

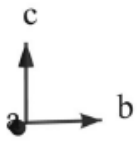

Fig. 42 *View of the crystal structure of the title compound along the a axis showing the Brucite-type $[Co_4(SO_4)_2(OH)_6]$ layers which are intercalatated by the hydrogen bonded (dash lines) $[Co(H_2O)_6]^{2+}$ ions.*

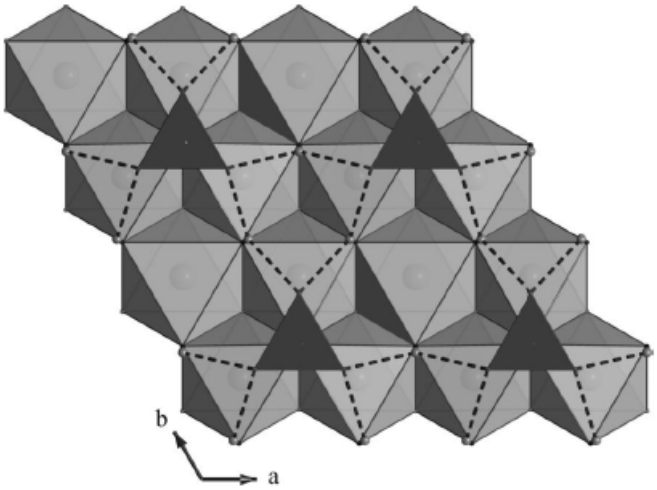

Fig. 43 *Polyhedral representation of the cobalt hydroxysulate layer, built up of the edge-shared $[Co(OH)_6]$ and $[Co(OH)_4(OSO_3)_2]$ octahedra.*

The crystal structure of the title compound is closely related to that of $Co_5(OH)_6(SO_4)_2(H_2O)_4$ (Ben Salah *et al*., 2004, 2006), which is composed of Brucite-type cobalt hydroxide layers. The fundamental difference lies in the way that adjacent layers are linked; being pillared by •••O_3SO-$Co(H_2O)_4$-OSO_3••• groups in $Co_5(OH)_6(SO_4)_2(H_2O)_4$ but partially intercalated by $[Co(H_2O)_6]^{2+}$ ions in the title compound. For the crystal structures of layered materials of this type, see: Poudret *et al.* (2008). For a description of the Cambridge Structural Database, see: Allen (2002).

REFERENCES

Allen, F. H. (2002). *Acta Cryst. B***58**, 380–388.

Ben Salah, M., Vilminot, S., Andre, G., Richard-Plouet, M., Mhiri, T., Takagi, S. & Kurmoo, M. (2006). *J. Am. Chem. Soc.* **128**, 7972-7981.

Ben Salah, M., Vilminot, S., Richard-Plouet, M., Andre, G., Mhiri, T. & Kurmoo, M. (2004). *Chem. Commun.* pp. 2548-2549.

Brandenburg, K. & Putz, H. (1999). DIAMOND. Crystal Impact GbR, Bonn, Germany.

Poudret, L., Prior, T. J., McIntyre, L. J. & Fogg, A. M. (2008). *Chem. Mater.* **20**, 7447-7453.

Sheldrick, G. M. (2008). *Acta Cryst. A***64**, 112-122.

Spek, A. L. (2009). *Acta Cryst. D***65**, 148-155.

Stoe & Cie (2008). X-AREA and X-RED. Stoe & Cie, Darmstadt, Germany.

XI) Tris(ethylenediamine)cobalt(II) sulphate

Bunlawee Yotnoi, Athittaya Seeharaj, Yothin Chimupala and **Apinpus Rujiwatra**

*Acta Cryst. E***66** (2010) m628.

Crystal data

$[Co(C_2H_8N_2)_3]SO_4$	$D_x = 1.658$ Mg m^{-3}
$M_r = 335.30$	Mo $K\alpha$ radiation, $\lambda = 0.71073$ Å
Trigonal, $P\bar{3}1c$	Cell parameters from 589 reflections
Hall symbol: -P 3 2c	$\theta = 2.6$–$31.0°$
$a = 8.9920$ (2) Å	$\mu = 1.45$ mm^{-1}
$c = 9.5927$ (3) Å	$T = 298$ K
$V = 671.71$ (3) Å^3	Block, orange
$Z = 2$	0.48 × 0.22 × 0.20 mm
$F(000) = 354$	

Data collection

Bruker SMART CCD area-detector diffractometer	688 independent reflections
Radiation source: fine-focus sealed tube	589 reflections with $I > 2\sigma(I)$
graphite	$R_{int} = 0.027$
? scan	$\theta_{max} = 31.0°$, $\theta_{min} = 2.6°$
Absorption correction: multi-scan (SADABS; Sheldrick, 1996)	$h = -8 \rightarrow 10$
$T_{min} = 0.543$, $T_{max} = 0.760$	$k = -11 \rightarrow 11$
3638 measured reflections	$l = -11 \rightarrow 13$

Refinement

Refinement on F^2	Primary atom site location: structure-invariant direct methods
Least-squares matrix: full	Secondary atom site location: difference Fourier map
$R[F^2 > 2\sigma(F^2)] = 0.028$	Hydrogen site location: inferred from neighbouring sites
$wR(F^2) = 0.069$	H-atom parameters constrained
$S = 1.06$	$w = 1/[\sigma^2(F_o^2) + (0.0354P)^2 + 0.1217P]$ where $P = (F_o^2 + 2F_c^2)/3$
688 reflections	$(\Delta/\sigma)_{max} < 0.001$
47 parameters	$\Delta\rho_{max} = 0.25$ e Å^{-3}
16 restraints	$\Delta\rho_{min} = -0.29$ e Å^{-3}

The structure of the title compound, $[Co^{II}(C_2H_8N_2)_3]SO_4$, which is the cobalt example of $[M(C_2H_8N_2)_3]SO_4$, is reported. The Co and S atoms are located at the *2d* and *2c* Wyckoff sites (point symmetry 32), respectively. The Co atom is coordinated by six N atoms of three chelating ethylenediamine molecules generated from half of the ethylenediamine molecule in the asymmetric unit. The O atoms of the sulphate anion are disordered mostly over two crystallographic sites. The third disorder site of O (site symmetry 3) has a site occupancy approaching zero. The H atoms of the ethylenediamine molecules interact with the sulfate anions via intermolecular N-H···O hydrogen-bonding interactions.

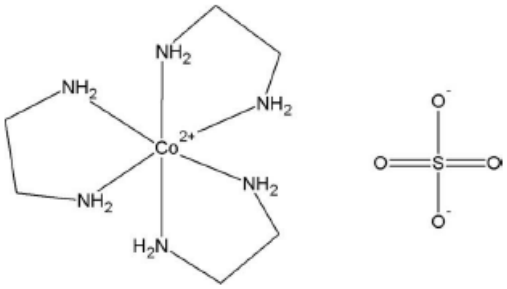

For isostructural $[M(C_2H_8N_2)_3]SO_4$ complexes, see: Haque *et al.* (1970); Cullen & Lingafelter (1970); Daniels *et al.* (1995); Lu (2009) for the nickel, copper, vanadium and manganese analogues, respectively.

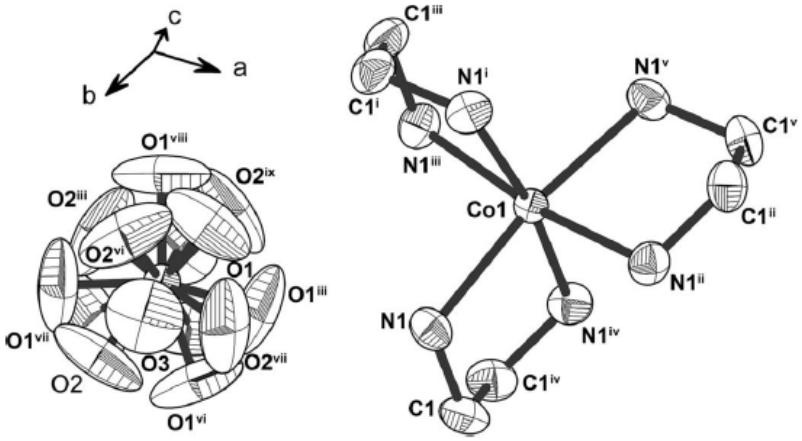

Fig. 44 *View of the title complex showing atom numbering scheme. Displacement ellipsoids for non-hydrogen atoms are draw at 50% probability level.* (i) -y+1, x-y, z; (ii) -x+y+1, -x+1, z; (iii) -y+1, -x+1, -z+1/2; (iv) -x+y+1, y, -z+1/2; (v) x, x-y, -z+1/2; (vi) -y+1, x-y+1, z, (vii) -x+y, -x+1, z; (viii) -x+y, y, -z+1/2; (ix) x, x-y+1, -z+1/2]. Hydrogen

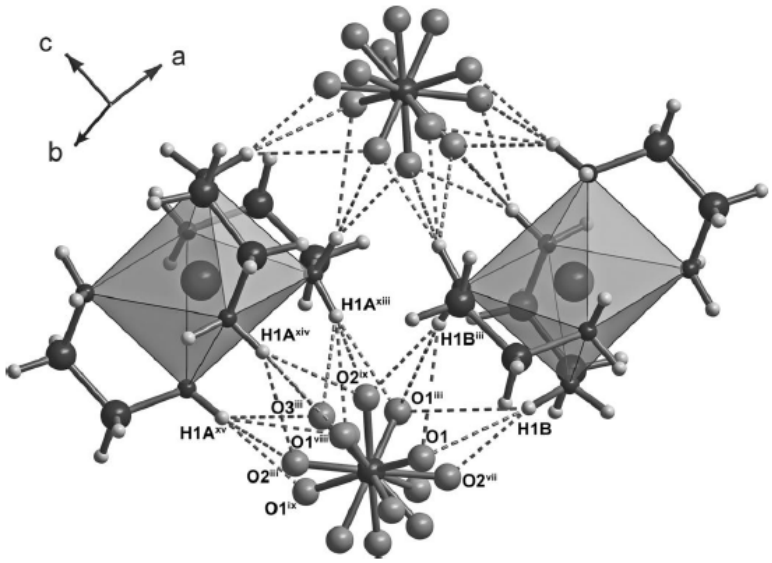

Fig. 45 *View of hydrogen bonding interactions (dotted lines) between the disordered sulphate and the amino H-atoms of the* $[Co^{II}(C_2H_8N_2)_3]^{2+}$.

(ii) -x+y+1, -x+1, z; (iii) -y+1, -x+1, -z+1/2; (viii) -x+y, y, -z+1/2; (ix) x, x-y+1, -z+1/2; (xiii) y, x, z+1/2; (xiv) -y+x, -y+1, -z+1/2; (xv) -x+1, -x+y+1, z+1/2].

The title complex, $[Co^{II}(C_2H_8N_2)_3]SO_4$ (Fig. 1), is isostructural to the earlier reported $[Ni^{II}(C_2H_8N_2)_3]SO_4$ (Haque *et al.*,, 1970), $[V^{II}(C_2H_8N_2)_3]SO_4$ (Daniels *et al.*, 1995), $[Mn^{II}(C_2H_8N_2)_3]SO_4$ (Lu, 2009) and $[Cu^{II}(C_2H_8N_2)_3]SO_4$ (Cullen & Lingafelter, 1970) complexes, constituting the $[M^{II}(C_2H_2N_2)_3]SO_4$ series. The $[M^{II}(C_2H_2N_2)_3]SO_4$ structures crystallize in the same trigonal space group of $P\bar{3}1c$ with quite similar cell parameters. Likewise, the metal and sulfur atoms are positioned in the same crystallographic sites; M^{II} on the 2*d* and S on the 2*c* Wyckoff sites (each with point symmetry 32). The disorder about the six-fold rotation axis found in the sulfate anion is intriguingly common in each structure, although the number of unique O atoms varies from two to four. In the structure of $[Co^{II}(C_2H_8N_2)_3]SO_4$, the O atoms were refined as being disordered over three crystallographic sites, although the site occupancy of O3 located on the 4*f* Wyckoff site approaches zero. The bond length associated with this O3 atom (S1—O3; 1.382 (16) Å) is notably shorter than the other S—O bonds (1.431 (5)–1.445 (5) Å). The disordered sulfate anions are linked to the $[Co^{II}(C_2H_8N_2)_3]^{2+}$ cations by hydrogen bonding interactions of N—H···O type to form a hydrogen-bonding supramolecular network. The hydrogen bonding geometries are consistent with those of the previously reported $[M^{II}(C_2H_2N_2)_3]SO_4$ complexes.

REFERENCES

Brandenburg, K. (2006). DIAMOND. Crystal Impact GbR, Bonn, Germany.
Bruker (2003). SMART and SAINT. Bruker AXS Inc., Madison, Wisconsin, USA.
Cullen, D. L. & Lingafelter, E. C. (1970). *Inorg. Chem.* **9**, 1858-1864.
Daniels, L. M., Murillo, C. A. & Rodriguez, K. G. (1995). *Inorg. Chim. Acta*, **229**, 27-32.
Farrugia, L. J. (1999). *J. Appl. Cryst.* **32**, 837–838.
Haque, M.-U., Caughlan, C. N. & Emerson, K. (1970). *Inorg. Chem.* **9**, 2421-2424.
Lu, J. (2009). *Acta Cryst. E***65**, m1187.
Sheldrick, G. M. (1996). SADABS. University of Gottingen, Germany.
Sheldrick, G. M. (2008). *Acta Cryst. A***64**, 112–122.
Westrip, S. P. (2010). *J. Appl. Cryst. 43*. Submitted.

CHAPTER VIII

FABRICATION AND DIELECTRIC PROPERTIES OF LEAD TITANATE NANOCOMPOSITE

R.Wongmaneerung, **A. Rujiwatra**, R. Yimnirun, S. Ananta
Journal of Alloys and Compounds **475** (2009) 473–478.

INTRODUCTION

Pure and dense lead titanate ($PbTiO_3$ or PT) ceramic, which is of interest as a component in commercial electroceramic materials, is regarded to be one of the most difficult lead-based perovskite ferroelectric ceramics to produce [1-3]. The most important properties of PT ceramics are high Curie temperature (*ca.* 490 ^oC), large mechanical-quality factor and pyroelectric coefficient [4, 5]. Moreover, PT when combined with other oxides can form a series of ferroelectric materials that exhibit many of the most desirable dielectric, piezoelectric and pyroelectric properties for use in electronic and electro-optic devices at high frequency and high temperature, such as infrared sensors, actuators and hydrophones [1-3]. However, PT ceramic is mechanically weak due to large distortion of the tetragonal phase at room temperature which is characterized by the ratio between the lattice parameters (*c*/*a*, hereafter called tetragonality, *ca.* 1.06 [6, 7]). Apart from general problems of PbO volatilization and associated high porosity, the stress induced by cooling through the phase transition can create cracking in bulk ceramics. To overcome these problems, several techniques have been introduced, such as utilizing nanopowders, using additives, employing spark-plasma sintering and carrying out appropriated milling and sintering conditions [8-13]. All these techniques are aimed at reducing the lattice tetragonality of bulk ceramics, even though they inevitably affect the phase formation, structure and electrical properties of materials in different ways. Amongst all the issues reported so far, most attention has been concentrated on the use of additives and chemically derived powder processing, whereas investigations on modified particle packing or composite techniques have not been widely carried out [14, 15].

Recently, ceramic-nanocomposites in which nanosized phases were dispersed within the matrix grains and/or at the grain boundaries have emerged as a novel approach of improving materials properties [16]. The mechanical properties of ceramics are known to be improved significantly by dispersing ceramic-nanoparticles into the ceramic-matrix grains or grain boundaries. However, degree of improvement in their properties is dependent on the type of composite systeminvolved [16]. Few studies have reported on ferroelectric matrix/metal nanodispersoid [17] and ferroelectric matrix/non-ferroelectric nanodispersoid [18] composite systems, and it is not yet clear how these dispersoids affect the properties of nanocomposites. Moreover, the problem of property trade-off, *i.e.*, a deterioration of electrical properties still remains unsolved. In other words, the improvement of mechanical property can only be realized only by sacrificing electrical properties. So far, a little has been reported on the fabrication of ferroelectric matrix/ferroelectric nanodispersoid composite systems [19]. However, no work on the perovskite PT ceramic-nanocomposites has been reported yet.

Therefore, in this work, ferroelectric matrix/ferroelectric nanodispersoid PT composite has been developed to resolve these problems. With this new scheme, instead of using only micron-sized PT powders as reported in our previous works [13, 20], two different types of PT nanodispersoid (nanoparticles and nanofibers) were adopted as starting materials. The influence of both PT

nanodispersoids on densification, microstructure and dielectric properties of the composites will be discussed and compared with the conventional method.

EXPERIMENTAL

The starting PT materials for the fabrication of self-reinforced PT matrix/PT nanodispersoid composites were micron-sized PT powders, nanopowders, and nanofibers (Fig. 46), which were synthesized via ball-milling, vibro-milling, and hydrothermal techniques, respectively. The characteristics of each starting PT materials and their processing details are described in our previous works [21-23]. The powder mixtures (matrix:dispersoid ratio of 1:1) were formed into pellets by adding 3 wt.% polyvinyl alcohol (PVA) binder, prior to pressing in a pseudo-uniaxial die press at 100MPa. It should be noted here that preliminary study of other matrix:dispersoid ratios, *e.g*. 0.7:0.3 and 0.6:0.4 was carried out and the complete solid-solution microstructure type commonly observed in the conventional PT processingwas observed in all cases, indicating the solubility effect of the perovskite PT/PT (although their morphologies are different) limiting the possibility of composite formation. Each pellet was placed in an alumina crucible together with an atmosphere powder of identical chemical composition [20]. Such a composite cannot be fabricated by hot-pressing in the reduced atmosphere because the Pb-based perovskite is easily decomposed in the atmosphere. In this work, the composites were prepared by using simple pressure-less sinteringmethod. Sinteringwas carried out at various temperatures (1000-1225 ^{o}C), for 1 h with heating/cooling rates of 1 ◦C/min [13, 20] applied. These firing conditions were advocated from our previous work on PT ceramics with experimental details presented in Refs. [13, 20].

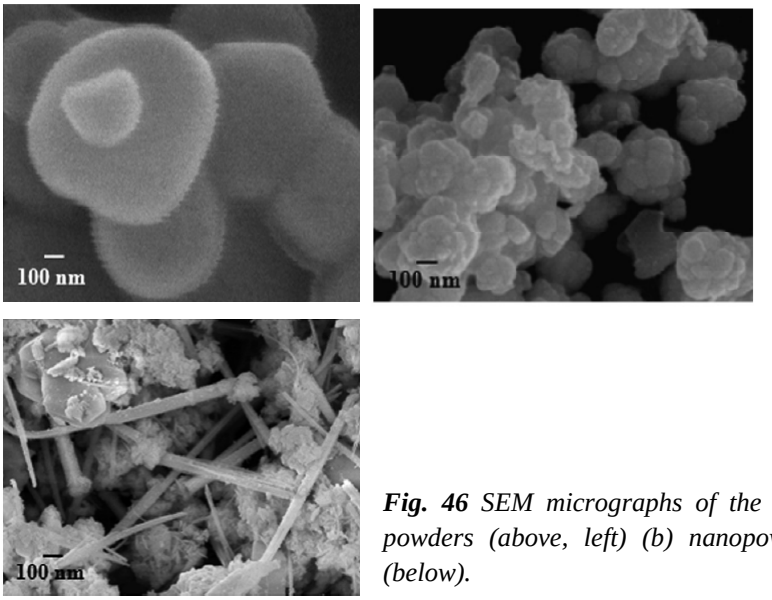

Fig. 46 *SEM micrographs of the starting PT dispersoids: micron-sized powders (above, left) (b) nanopowders (above, right), and nanofibers (below).*

Densities of the sintered products were determined by using the Archimedes principle. X-ray diffraction (XRD; Siemens-D500 diffractometer) was carried out at room temperature using Cu K_ radiation to identify the phase formed. The lattice parameters and tetragonality factor (*c*/*a*) of the sintered ceramics were calculated from the XRD patterns [24]. The microstructural development was characterized using a scanning electron microscopy (SEM; JEOL JSM-840A), equipped with an energy dispersive X-ray (EDX) analyzer. Mean grain sizes of the sintered ceramics were subsequently estimated by employing the linear intercept method [25]. In order to evaluate the dielectric properties, densified ceramicswere polished to form flat and parallel faces. The samples

were coated with silver-paste electrodes which were fired on both sides of the samples at 700 ^{o}C for 1 h. The dielectric properties were measured using a HIOKI 3532-50 LCR meter, on cooling through the transition range (550-25 ^{o}C) with a rate of 5 ^{o}C min^{-1} at high frequencies ranging from 1 to 5 MHz. Values of the dielectric constant were corrected for porosity by using the relationship ε_r = ε_r(measured) x theoretical density/sintered density [26].

RESULTS & DISCUSSION

X-ray diffraction patterns of the PT composites reinforced with various PT dispersoids and sintered at various temperatures are displayed in Fig. 47, indicating the formation of single phase perovskite in all cases. The strongest reflections in the majority of all XRD traces indicate the formation of the PT perovskite phase of lead titanate which could be matched with JCPDS file no. 6-452, in agreement with other works [10-13]. To a first approximation, this phase has a tetragonal perovskite-type structure in space group *P*4/*mmm* with cell parameters *a* = 389.93 pm and *c* = 415.32 pm [27]. All the peaks were assigned to PT, and no reaction phase between different PT starting materials was detected. Moreover, there is no significant difference between the PT nanocomposites reinforced with either PT nanopowders or nanofibers, after sintered at temperatures ranging from 1150 to 1200 ^{o}C. This observation could be attributed mainly to the high purity of the employed starting materials together with the optimized firing conditions. The samples sintered with temperature below 1150 ^{o}C were broken into pieces after sintering process, whilst the samples sintered at 1225 ^{o}C exhibited severe melted areas. Thus, no further characterization can be performed on these samples.

It should be noted that a single phase of perovskite is found in all PT composites similar with the two-stage sintering samples [20], in contrast to the observations for the conventional case [13] (Table 22). No evidence of pyrochlore phase of $PbTi_3O_7$ composition reported earlier by other workers [21, 28] was found, nor was any evidence of other second phases [29] being present. This could be due to the lower firing temperature of the nanocomposite samples as compared to the conventional PT ceramics, leading to a smaller degree of lead losses and consequently avoiding the pyrochlore formation, in consistent with other works [30, 31], whilst a sufficient arrangement of grain-packing required for ceramic densification still be reached. However, many other factors come into play, *e.g.* homogeneity of materials, reactivity of starting powders, and processing variables. These XRD results clearly show that, in general, the different processing methods used for preparing PT ceramics gave rise to a different phase formation in the sintered materials. The absence of minor phase in composite samples was related to the more reactive process used.

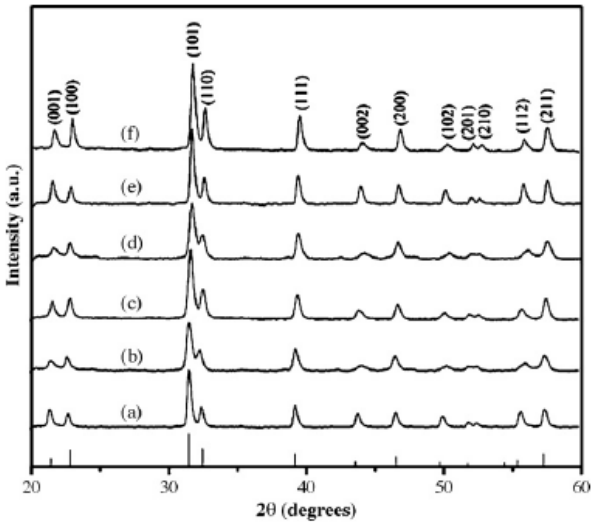

Fig. 47 *XRD patterns of PT composites reinforced with PT nanopowders after sintered at (a) 1150 ^{o}C, (b) 1175 ^{o}C and (c) 1200 ^{o}C, and reinforced with PT nanofibers after sintered at (d) 1150 ^{o}C, (e) 1175 ^{o}C and (f) 1200 ^{o}C, for 2 h.*

Table 22 *Sintering behaviour of PT ceramics derived from different fabrication techniques.*

Processing [Ref.]	Sintering temperature (°C)	Perovskite phase[a] (%)	Relative density[b] (%)	Tetragonality factor (*c*/*a*)	Grain size[c] (μm)	Average grain size (μm)
Normal sintering [13]	1225	89.20	93.00	1.063	41.0–83.0	62.0
Two-stage sintering [20]	900/1200	100.00	97.02	1.061	1.0–2.2	1.6
Composite reinforced with nanopowders	1150	100.00	96.33	1.059	0.2–0.6	0.40
	1175	100.00	97.02	1.053	0.3–1.0	0.65
	1200	100.00	97.85	1.061	0.6–2.0	1.30
Composite reinforced with nanofibers	1150	100.00	95.68	1.053	0.3–1.3	0.80
	1175	100.00	96.76	1.058	0.4–1.3	0.85
	1200	100.00	97.45	1.061	0.5–2.8	1.65

[a] The estimated precision of the perovskite phase is ±0.1%.
[b] The estimated precision of the density is ±0.1%.
[c] The estimated precision of the grain size is ±10%.

Table 22 also shows tetragonality factor (*c*/*a*), relative density and average grain size of each nanocomposite sample, comparing with the conventional and the two-stage sintered samples, respectively. Generally, it is evident that as the sintering temperature increases, the density of almost all the samples increases. However, it can be seen that the sintering behavior of PT ceramics derived fromdifferent processing techniques were dissimilar. Two-stage sintering PT ceramics reached amaximum density of *ca.* 97% at 900/1200 ^{o}C [20]. Whilst conventional PT samples exhibit reduced densification, and a temperature of 1225 ^{o}Cwas required to reach a densification level of *ca.* 94% [13]. On the other hand, both types of PT nanocomposites sintered at 1200 ◦C exhibit the highest relative density of about 98% with a smallest average grain size of less than 1.0 μm. By comparison with conventional PT ceramics, lower values of tetragonality (*c*/*a*) are found in all nanocomposite cases, equivalent to those observed in the two-stage sintering case, indicating lower internal stress in these nanocomposites. More interestingly, all nanocomposite samples do not suffer from severe stresses as a result of the high *c*/*a* ratio so they have not broken into pieces after experienced the sintering process or once subjected to a cycle of high temperature measurement of dielectric properties, as reported previously for the conventional and two-stage sintering PT cases [13, 20].

Microstructural features (free and fracture surfaces) of both PT nanocomposites sintered at different temperatures for 2 h are shown in Figs. 48 and 49. It was found that average grain sizes increase with the sintering temperature (Fig. 48). The PT nanodispersoids were found to locate both within the matrix and at the grain boundaries (see enlarged insertion in Fig. 48(d)). The microstructure of the composites is that of the nanocomposites classified as “nanomicro” and “nanofiber” types [16]. Representative fracture surfaces for both types of PT nanocomposites are given in Fig. 39. It is seen that a uniform grain shape of typical perovskite ceramics [9, 30, 31] is observed, with sizes in the range of 0.2-2.8 μm. It should be noted that the average grain size of both PT nanocomposites is <1.7 μm, which is less than the critical value of 3 μm [11, 32, 33] and gives rise to a volumetric percentage enough to buffer the anisotropic stress caused by the phase transition [32]. Here, it is believed that PT nanodispersoids with random orientations result in lower internal stress in composite samples because they compensate the anisotropy of thermal expansion coefficients.

By comparison with conventional PT ceramics [13], almost clean microstructures with highly uniform, denser angular grain-packing and more homogeneous are generally observed in both types of self-reinforced PT nanocomposites. These microstructures are typical of a solid-state sintering mechanism. In the present study (Figs. 48 and 49), the microstructural features of both types of PT nanocomposites with various sintering temperatures ranging from 1150 to 1200 ^{o}C are not significantly different. However, it should be noted that higher angularly grains were evidenced for higher sintering temperature. The observation that the sintering temperature effect may also play an important role in obtaining a high angularity grains of perovskite ceramics is also consistent with other similar systems [30, 31].

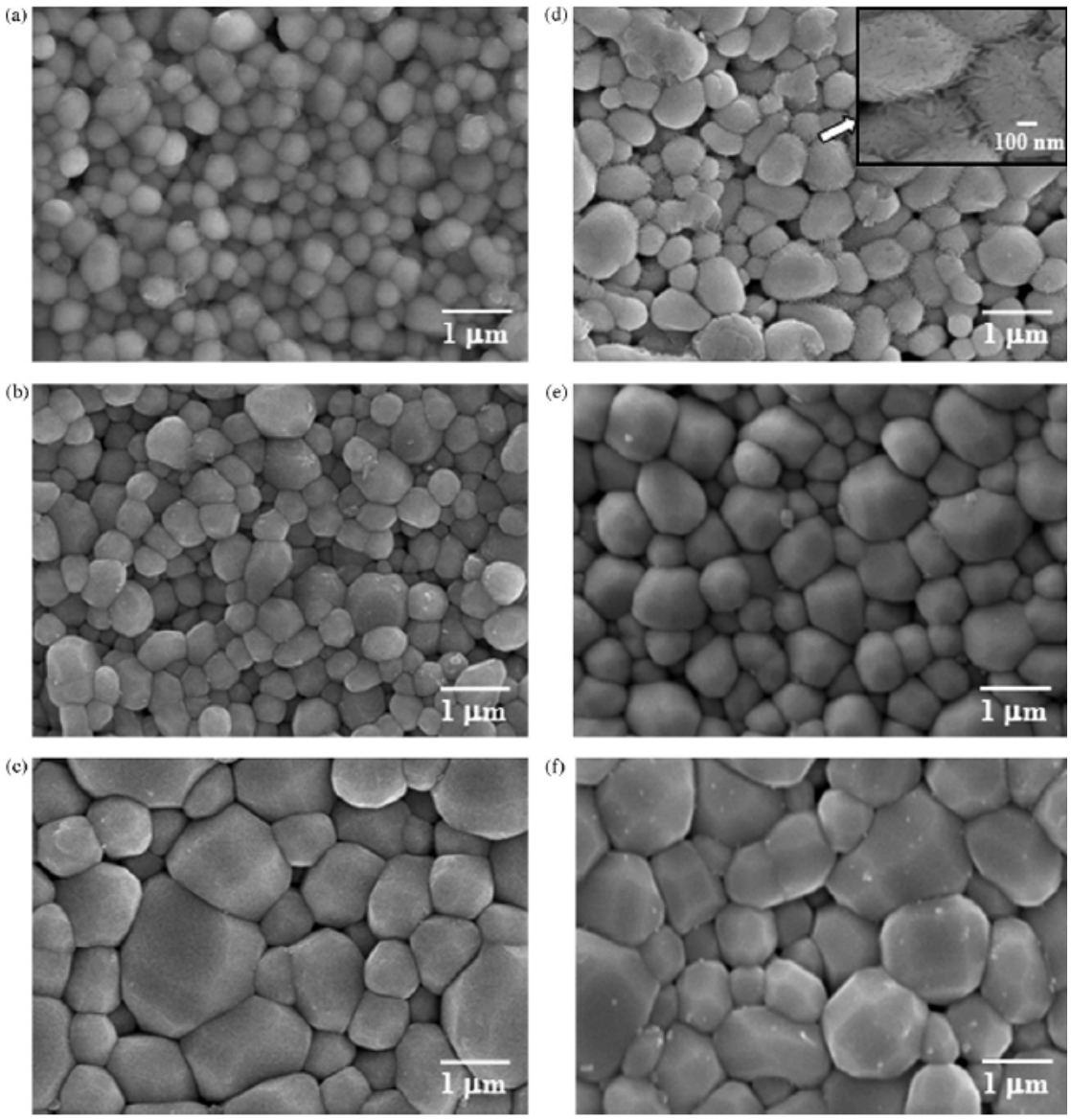

Fig. 48 *Free surface of PT composites reinforced with PT nanopowders after sintered at (a) 1150 °C, (b) 1175 °C and (c) 1200 °C, and reinforcedwith PT nanofibers after sintered at (d) 1150 °C, (e) 1175 °C and (f) 1200 °C, for 2 h.*

Moreover, abnormal grain growth probably due to the inhibition of grain growth mechanism during doubly sintering process [20, 34] was also found in some samples, as shown in Figs. 48(c and d) and 49(f). It is also of interest to point out that evidence of intergranular fracture has been found for the existence of microcracks (arrowed) along the grain boundaries of the composite samples self-reinforced with PT nanoparticles (Fig. 49(a-c)). The different microstructure evolution of PT nanocomposites confirms the importance of the processingmethod including the morphological characteristics of the dispersed phase, consistent with other works [32, 35]. Whilst the grain size of both nanocomposites is approximately the same, the density and microstructure of PT samples sintered at higher temperatures indicated that the composite method of PT matrix reinforced with PT nanofibers was preferable for obtaining dense PT ceramics. Interestingly, all the nanocomposite samples sintered at 1150-1200 °C remained unbroken. It may be assumed that the nanocomposites consisting of very fine dispersoids suffer less deformation, caused by the high value of *c*/*a* ratio, than the ceramics with significantly large grains (Table 22). Consequently, the experimental work carried out here suggests that the optimum conditions for forming the highly dense PT samples in this work

are both types of PT/PT nanocomposites sintered at 1200 °C, 2 h dwell time, and 1 ◦C/min heating/cooling rates.

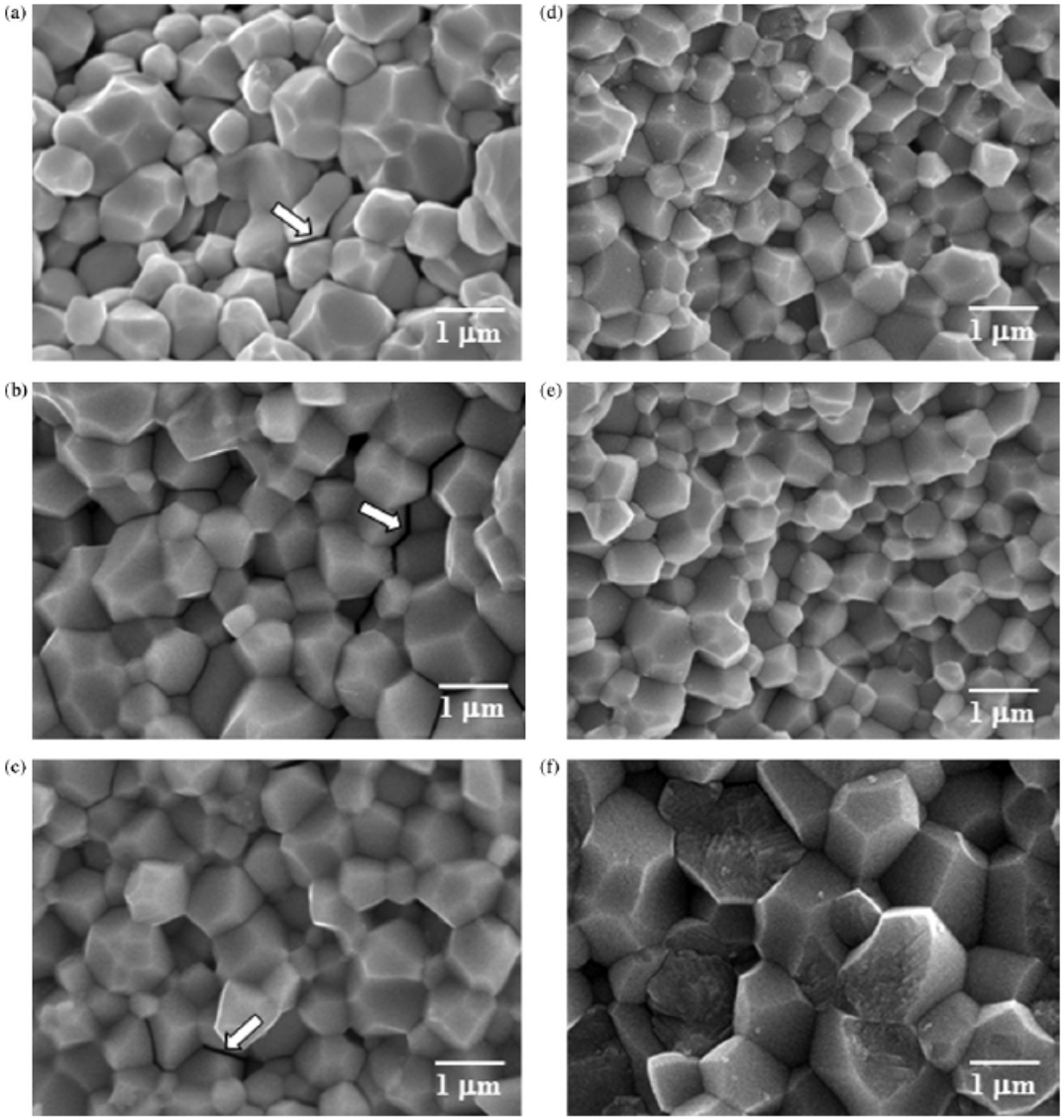

Fig. 49 *Fracture surface of PT composites reinforced with PT nanopowders after sintered at (a) 1150 °C, (b) 1175 °C and (c) 1200 °C, and reinforced with PT nanofibers after sintered at (d) 1150 °C, (e) 1175 °C and (f) 1200 °C, for 2 h.*

Table 23 *Dielectric properties of PT ceramics derived from different fabrication techniques*

Processing [Ref.]	Frequency (MHz)	T_C (°C)	$\varepsilon_{25°}$	$\varepsilon_{r,max}$	tan δ_{max}
Normal sintering [13]	1	482	243	7680	1.07
Two-stage sintering [20]	1	484	209	8198	0.95
Composite reinforced with nanopowders	1	486	244	8523	1.09
	3	486	245	7517	0.91
	5	487	247	7144	0.76
Composite reinforced with nanofibers	1	488	248	9104	0.81
	3	489	246	7110	0.57
	5	489	242	6801	0.45

The dielectric properties of PT samples fabricated with different techniques are also compared in Table 23. In general, they all behave as typical normal ferroelectric materials [3]. The Curie temperatures are about the same for all samples measured whilst the variation of dielectric constant and dielectric loss of both types of PT nanocomposites seems to be somewhat related to the sintering temperatures. This observation indicates that densification and the presence of the second phases accompanied with porosities are the key factors responsible for the dielectric response of the products. Moreover, this study demonstrated that the dielectric properties of PT ceramics are also influenced by microstructural features and arrangement especially the microcracks and final density rather than by only grain size itself.

The different microstructure and the different amount of secondary phases present in the sintered PT ceramics strongly influence the dielectric properties of these materials, leading to relatively superior dielectric behaviour in PT/PT nanocomposites. The secondary phases in conventional PT sample are interconnected at grain boundaries and, as suggested by Wang and Schulze [31], exert more influence on the dielectric properties than when they are isolated. The influence of densification and microcracks on dielectric properties of these PT composites can be clearly observed in Fig. 50, where the dielectric constant and dissipation factor as a function of temperature are shown, respectively. The maximum dielectric constant values at 1MHz in both PT nanocomposites were 2-5% higher than in two-stage sintering and conventional PT samples (Table 23). As mentioned earlier, the reason for this is the high amount of secondary phase present in conventional PT ceramics and the presence of a PbO-rich secondary phase, with low dielectric constant, which could form a continuous layer between grains, decreasing the dielectric constant of the two-stage sintering samples [13,36].

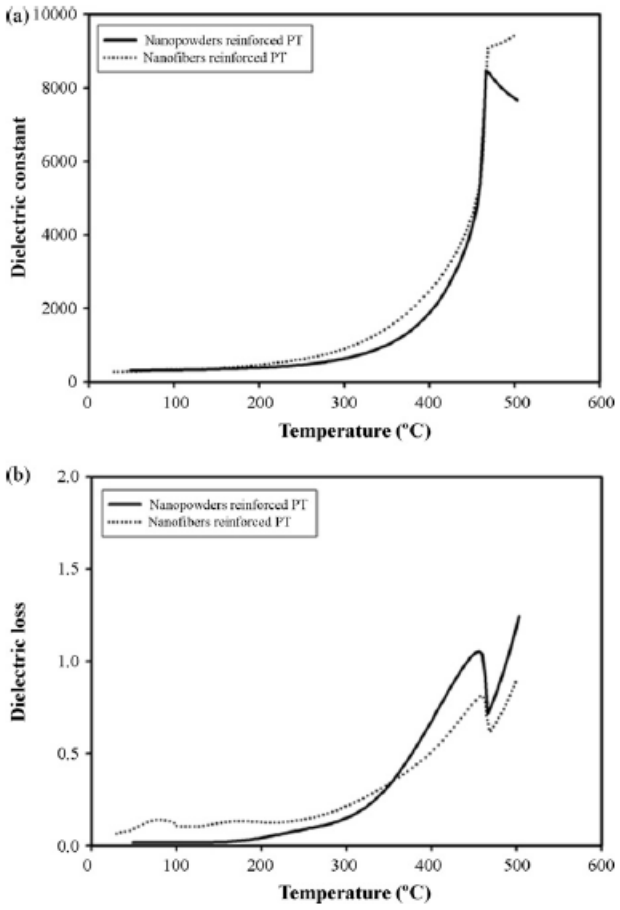

Fig. 50 *Variation with temperature of (a) dielectric constant (εr) and (b) dielectric loss (tan ι) at 1MHz for PT composites reinforced with PT nanopowders compared with those reinforced with PT nanofibers.*

The results obtained in this work suggest that, in general, these PT/PT nanocomposites exhibit complex microstructures which are inherently heterogeneous. The heterogeneity is a result of variation in grain size and orientation; variation in chemical homogeneity; and the presence and distribution of additional minor phase, pores and (micro) cracks. These factors, which are strongly influenced by the sintering conditions, have an important effect on the dielectric properties of the materials and their reproducibility. However, these results suggest that better densification can be introduced into piezoceramics by

fabricating ceramic-nanocomposites reinforced with piezoelectric nanodispersoids. Two aspects of this study are significant: (i) reductions in the maximum required sintering temperature (or the required prolong firing time) are possible as compared to the conventional (or the two-stage sintering) method and (ii) a framework has been established for developing self-reinforced piezoceramic-nanocomposite technique for better densification with retainable electrical properties of other piezoelectric materials, particularly those containing low melting point constituents. For better understanding and verifying the attractiveness of the nanocomposite technique further, a systematic study on the effect of another piezoelectric nanodispersoids such as $BaTiO_3$ or PZT on the phase formation, densification, microstructure and electrical properties of the piezoelectric-based ceramic-nanocomposites is required.

CONCLUSIONS

The potentiality of a ceramic-nanocomposite technique as a low-cost and simple ceramic fabrication to obtain highly dense and pure PT/PT composites was demonstrated. It has been found that both densification and dielectric properties of the composites fabricated in this work were significantly enhanced, as compared to the two-stage sintering and the conventional PT ceramics, which is likely due to the fine-grain and reduced tetragonality as well as anisotropies of stress and domain motion in the composites.

REFERENCES

1. B. Jaffe, W.R. Cook, H. Jaffe, Piezoelectric Ceramics, Academic Press, New York (1971).
2. G.H. Haertling, *J. Am. Ceram. Soc*. **82** (1999) 797-818.
3. A.J. Moulson, J.M. Herbert, Electroceramics, 2nd ed., Wiley, Chichester (2003).
4. T. Takahashi, *Am. Ceram. Soc. Bull*. **69** (1990) 691-695.
5. L.E. Cross, *Mater. Chem. Phys*. **43** (1996) 108-115.
6. G. Shirane, S. Hoshino, *J. Phys. Soc. Jpn*. **6** (1951) 265–270.
7. G. Shirane, R. Pepinsky, B.C. Frazer, *Acta Crystallogr*. **9** (1956) 131-140.
8. H. Takeuchi, S. Jyomura, E. Yamamoto, Y. Ito, *J. Acoust. Soc. Am.* **72** (1982) 1114-1120.
9. L.B. Kong,W. Zhu, O.K. Tan, *J. Mater. Sci. Lett*. **19** (2000) 1963-1966.
10. T. Suwannasiri, A. Safari, *J. Am. Ceram. Soc*. **76** (1993) 3155-3158.
11. T. Takeuchi, M. Tabuchi, I. Kondoh, N. Tamari, H. Kageyama, *J. Am. Ceram. Soc.* **83** (2000) 541-544.
12. J.S. Forrester, J.S. Zobec, D. Phelan, E.H. Kisi, *J. Solid State Chem.* **177** (2004) 3553-3559.
13. A. Udomporn, K. Pengpat, S. Ananta, *J. Eur. Ceram. Soc*. **24** (2004) 185-188.
14. F. Ye, L. Liu, J. Zhang, M. Iwasa, C.L. Su, *Compos. Sci. Technol.* **65** (2005) 2233-2239.
15. R. Gadow, F. Kern, A. Killinger, *Mater. Sci. Eng. B* **148** (2008) 58-64.
16. T. Ohji, Y.K. Jeong, Y.H. Choa, K. Niihara, *J. Am. Ceram. Soc.* **81** (1998) 1453-1460.
17. H.T. Chung, D.S. Cheong, C.S. Kim, *Mater. Lett.* **59** (2005) 920-924.
18. S. Jiansirisomboon, A.Watcharapasorn, *Curr. Appl. Phys*. **8** (2008) 48-52.
19. H. Beltran, N. Maso, E. Cordoncillo, A.R. West, *J. Electroceram*. **18** (2007) 277-282.
20. R.Wongmaneerung, R. Yimnirun, S. Ananta, *Appl. Phys. A* **86** (2007) 249-255.
21. A. Udomporn, S. Ananta, *Mater. Lett*. **58** (2004) 1154-1159.
22. R.Wongmaneerung, R. Yimnirun, S. Ananta, *Mater. Lett*. **60** (2006) 2666-2671.
23. A. Rujiwatra, N. Thammajak, T. Sarakonsri, R. Wongmaneerung, S. Ananta, J. *Crystal Growth* **289** (2006) 224-230.

24. H. Klug, L. Alexander,X-ray Diffraction Procedures for Polycrystalline and Amorphous Materials, 2nd ed., Wiley, New York (1974).
25. R.L. Fullman, Trans. AIME 197 (1953) 447-452.
26. S.L. Swartz, T.R. Shrout, W.A. Schulze, L.E. Cross, *J. Am. Ceram. Soc.* **67** (1984) 311-315.
27. JCPDS-ICDD Card no. 6-452, International Centre for Diffraction Data, Newtown Square, PA (2000).
28. J. Tartaj, C. Moure, L. Lascano, P. Durıın, *Mater. Res. Bull.* **36** (2001) 2301-2310.
29. M.L. Calzada, M. Alguero, L. Pardo, *J. Sol-Gel Sci. Technol.* **13** (1998) 837.
30. S. Ananta, N.W. Thomas, *J. Eur. Ceram. Soc.* **19** (1999) 1873-1881.
31. H.C.Wang,W.A. Schulze, *J. Am. Ceram. Soc.* **73** (1990) 825-832.
32. Y. Matsuo, H. Sasaki, J. Am. Ceram. Soc. 49 (1966) 229-230.
33. S.R. Dhage, Y.B. Khollam, H.S. Potdar, S.B. Deshpande, B.D. Sarwade, D.K. Date, *Mater. Lett.* **56** (2002) 564-570.
34. S. Ananta, N.W. Thomas, *J. Eur. Ceram. Soc.* **19** (1999) 2917-2930.
35. S. Chattopadhyay, P. Ayyub, V.R. Palkar, M. Multani, *Phys. Rev. B* **52** (1995) 13177-13179.
36. M. Villegas, A.C. Caballero, M. Kosec, C. Moure, P. Duran, J.F. Fernandez, *J. Mater. Res.* **14** (1999) 891-897.

CHAPTER VIII

HYDROTHERMAL SYNTHESIS OF LEAD TITANATE FINE POWDERS AT WATER BOILING TEMPERATURE

Chaiyos Chankaew, **A. Rujiwatra**

Chiang Mai Journal of Science **37**(1) (2010) 92-98.

INTRODUCTION

Among several wet-chemical routes available for the synthesis of advanced materials, hydrothermal technique has been proved to be very promising due to its uniqueness in being facile, cost effective, environmentally benign and applicable for the tailored synthesis of various phases in different forms [1]. Along this line, the hydrothermal technique has been applied for the synthesis of lead titanate ($PbTiO_3$ or PT) [2,3] which is one of the most important ferroelectric materials. The high spontaneous polarization and piezoelectric coefficients, but low aging rate of dielectric constant as well as a remarkable anisotropy make the PT-based compounds suitable for a wide range of high temperature and frequency applications, *e.g*. infrared sensors, electro-optic devices and ultrasonic transducers [4-6]. Compared to the other techniques *e.g.* sol-gel [7], chemical precipitation [8] and emulsion [9], the hydrothermal technique is somewhat superior in providing controllability on phase formation, chemical stoichiometry, particle size and morphology by simply fine tuning the processing parameters [3]. The recent stage of development for this technique involves the usage of other heating sources, e.g. a sand bath, an ultrasonic wave and a microwave, instead of the conventional oven [10-11]. The application of an ultrasonic wave on the reaction mixture in precedence to the hydrothermal reaction in particular has added advantages to the technique by both reducing the reaction temperature providing the phase pure PT nanoparticles, and promoting better size homogeneity [10]. The observed phenomena were rationalized by the formation of hot spots and local acoustic microjets from a sudden collapse of cavitational bubbles induced by the ultrasonic wave.

In the present work, a further investigation on the developed technique which has led to a dramatic reduction in the reaction temperature affording the phase-pure PT to an extraordinary low temperature of 100 ^{o}C is reported. The influences of the ultrasonication and hydrothermal processing conditions on phase formation, particle size and habits of the PT powders are discussed.

EXPERIMENTAL

Due to the recent report on the apparent possibility in the synthesis of phase-pure PT fine powders at the water boiling temperature, there were therefore the attempts to conduct the reactions at 100 ^{o}C following the previously reported experimental procedure [10]. Mixtures of lead (II) nitrate ($Pb(NO_3)_2$, Univar 99.0%) and titanium (IV) oxide (TiO_2, Riedelde Haen 99.5-100%) in anatase form were prepared in aqueous media. The amount of Pb^{II} and Ti^{IV} was controlled to be equimolar, and the final concentrations for each precursor were fixed at 1.32 mol dm^{-3}. The pellets of potassium hydroxide (KOH, Merck 85%) as mineralizer were gradually added to each reaction mixture to adjust the pH of the mixture to be 14, reported as the minimal pH required yielding well crystallized powder [2]. Such a high alkalinity is allegedly necessary for the dissolution of the oxide precursors under hydrothermal conditions. The mixtures were transferred into Teflon liners, which were then sealed and ultrasonicated at 70(±5) ^{o}C for varied durations ranging from 1 h to 6 h, using a laboratory ultrasonic bath (Bandelin Electronic RK255H, 160/320W, 35kHz). The liners were fitted

in stainless steel cases for further hydrothermal reactions conducted under autogenous pressure at 100 ^{o}C for 1.5-144 h. The particles were then recovere by filtration, washed with deionized water, and dried in air.

Powder X-ray diffractometer (PXRD, Siemen D500/D501, Cu *K*α, Ni filter, λ=1.54 Å) was used to characterize the crystalline phases, and field emission scanning electron microscope (FESEM, JEOL JSM-6335F) equipped with an energy dispersive X-ray (EDX) analyzer was employed for the investigation of particle morphology, size and elemental composition. In order to study the aggregation of the synthesized PT particles, size distributions of the bulk samples were analyzed by laser diffraction technique (Malvern Instruments Limited, Mastersizer S).

RESULTS & DISCUSSION

According to the PXRD results as shown in Fig. 51 to Fig. 52, the preceding ultrasonication was an important factor in reducing the hydrothermal reaction temperature affording the phase-pure PT powders although the bargaining between the ultrasonication duration and the hydrothermal reaction time was mandatory. It was evident that the tetragonal phase-pure PT powders could be synthesized from the hydrothermal reactions conducted at 100 ^{o}C for reasonable reaction times, *i.e.* 24 and 48 h in this study (Figs. 51 and 52), when the reaction mixtures were ultrasonicated for at least 1.5 h. The achievement of the phase-pure PT at this extraordinary low temperature has thus far never been reported. The application of an ultrasonic wave for an hour nonetheless seemed to be feasibly in affording the phase pure PT, according to the PXRD pattern of the powder obtained from the 48 h reaction as shown in Fig. 52(a) where the desired PT was present as the major phase. Further experiments revealed that the purity of the obtained powders in this case was however rather ambiguous even when the hydrothermal reaction was prolonged for over 120 h, as shown in Fig. 53.

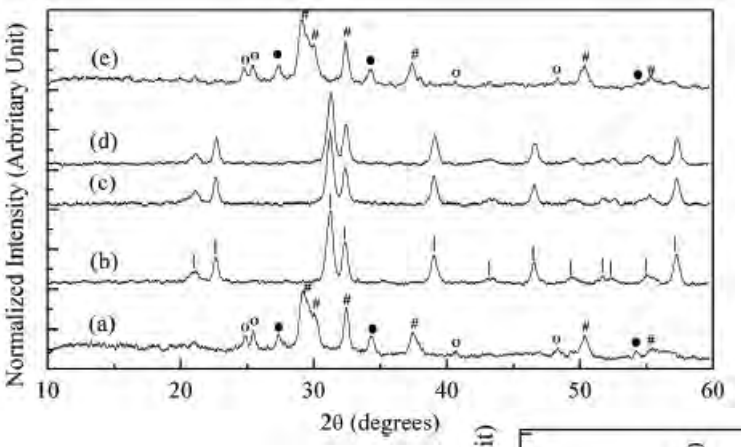

Fig. 51 *PXRD patterns of the particles obtained from the hydrothermal reactions conducted at 100 ^{o}C for 24 h with prior ultrasonication for (a) 1 h (b) 1.5 h (c) 3 h (d) 4.5 h and (e) 6 h;|= tetragonal PT, # = non-stoichiometric PT, # = TiO_2 rultile/anatase and o = Ti_xO_y.*

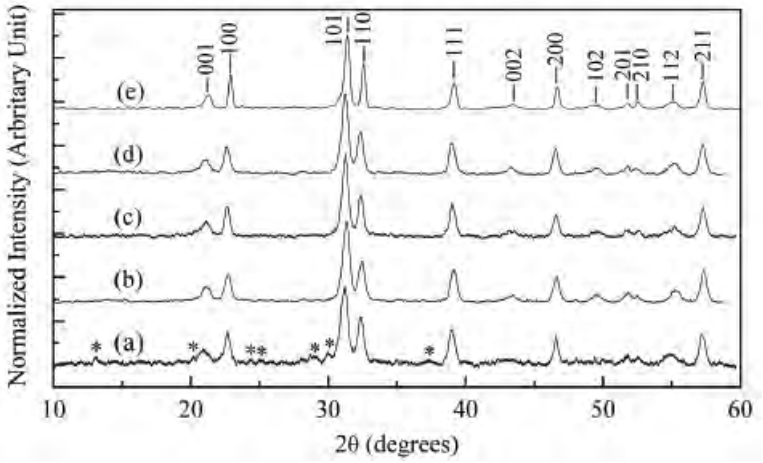

Fig. 52 *PXRD patterns of the particles obtained from the hydrothermal reactions conducted at 100 ^{o}C for 48 h with prior ultrasonication for (a) 1 h (b) 1.5 h (c) 3 h (d) 4.5 h and (e) 6 h, where the asterisks indicate unidentified peaks.*

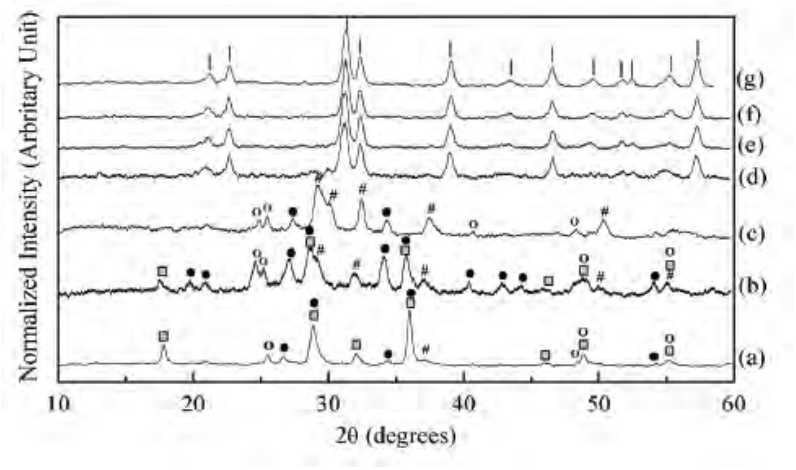

Fig. 53 *PXRD patterns of the particles obtained from the hydrothermal reactions conducted at 100oC for (a) 6 h (b) 12 h (c) 24 h (d) 48 h (e) 72 h (f) 120 h and (g) 124 h with the prior ultrasonication for an hour;|= tetragonal PT, # = non-stoichiometric PT, ● = TiO_2 rultile/anatase, o = Ti_xO_y and ■= PbO.*

This indicated the significance of the ultrasonication in rendering the success of the hydrothermal synthesis of the phase-pure PT at the water boiling temperature. The ultrasonication of 6 h nonetheless led to the formation of other oxide phases instead of the desired PT when the hydrothermal reaction was conducted for 24 h (Fig. 51). This was not the case when the reaction was prolonged for 48 h (Fig. 52), suggesting the influences of the reaction time to overpower that of the ultrasonication. Two observations can be made on the basis of the PXRD results. In the view of the ultrasonication time, it was apparent that the lengthy ultrasonication could reduce the hydrothermal reaction time affording the phase-pure PT powders. This suggests the promotion of the reaction activities by the ultrasonic wave, which may be due to (1) the reduced particle sizes of the starting precursors and/or oxide intermediates caused by the local acoustic microjets, and (2) the better probability for nucleation induced by the formation of the confined hot spots. The important role of the ultrasonication in lessening the thermodynamic barrier and therefore increasing the reactivity of the hydrothermal reaction has therefore been underlined. In the aspect of the hydrothermal reaction time, a distinctly slow reaction rate can be presumed at 100 ^{o}C. For the same ultrasonication duration of 1 and 3 h, the tetragonal phase-pure PT could be yielded hydrothermally in only 6 an 3.5 h at 130 ^{o}C [10], but 72 and 24 h at 100 ^{o}C. The hydrothermal reaction rate should therefore be governed mainly by the hydrothermal reaction temperature, which was well agreed with that reported previously [10].

The obtained PT powders could be well refined in tetragonal *P4/mmm* (JCPDS 6-0425) with a = 3.8940(41)-3.9000(43), and c = 4.185(11)-4.218(55). The variation in ultrasonication time showed no distinct influences on the refined cell parameters and therefore the corresponding c/a ratios 1.073(3)-1.083(2). These values were in good agreement with the values commonly yielded for the hydrothermally derived PT particles [2, 3, 10], but larger than those of the solid state reactions [12]. Regarding the interpretation of the PXRD results, although the presence of other phases beside the desired PT (JCPDS 6-0425) in some cases was plain, the index of these phases to certain JCPDS could be ambiguous. These phases were therefore shown as groups of feasible phases in Fig. 51 and Fig. 53; #, ●, o and ■ were therefore employed to represent lead titanates of other stoichiometry than $PbTiO_3$, a mixture of rultile and anatase TiO_2, various oxides of titanium, and different PbO phases, respectively.

The SEM images as typically illustrated in Fig. 54(a) showed the PT particles to be tetragonal in shape, which was well reflecting the crystallographic internal order, regardless of the synthetic conditions. Sizes of these particles were accordingly measured in two directions along the short and

long axes from the SEM images, and summarized in Table 24. Being independent of also the synthetic conditions, sizes of these particles were distributed regularly from few hundred nanometers to just over one micron, with most of the population distributed in the submicrometer region. The average sizes were *ca.* 500-600 nm alike. According to the SEM images, the PT particles were mostly present as hard aggregates, with the growth of small particles on the surfaces of the larger ones as exemplified in the inset of Fig. 54(a). This observation could lead to the assumption of the layer-by-layer crystal growth model where the nucleation and growth of the new crystals occur on the surfaces of the mature ones [13]. In spite of the variation in synthetic conditions, sizes of the PT aggregates disseminated in a similar trinodal fashion as typically illustrated in Fig. 54(b), centring at *ca.* 0.20, 2.0 and 20 μm. The mean aggregate sizes were rather similar, falling into a narrow range of *ca.* 5-8 μm. There was no apparent correlation between the aggregate sizes and the ultrasonication time (Table 24). The prolongation of the hydrothermal reaction time nonetheless led to the enlargement of both the length of the particles and mean aggregate sizes. This should be due to the growth of the particle with the extended hydrothermal reaction time.

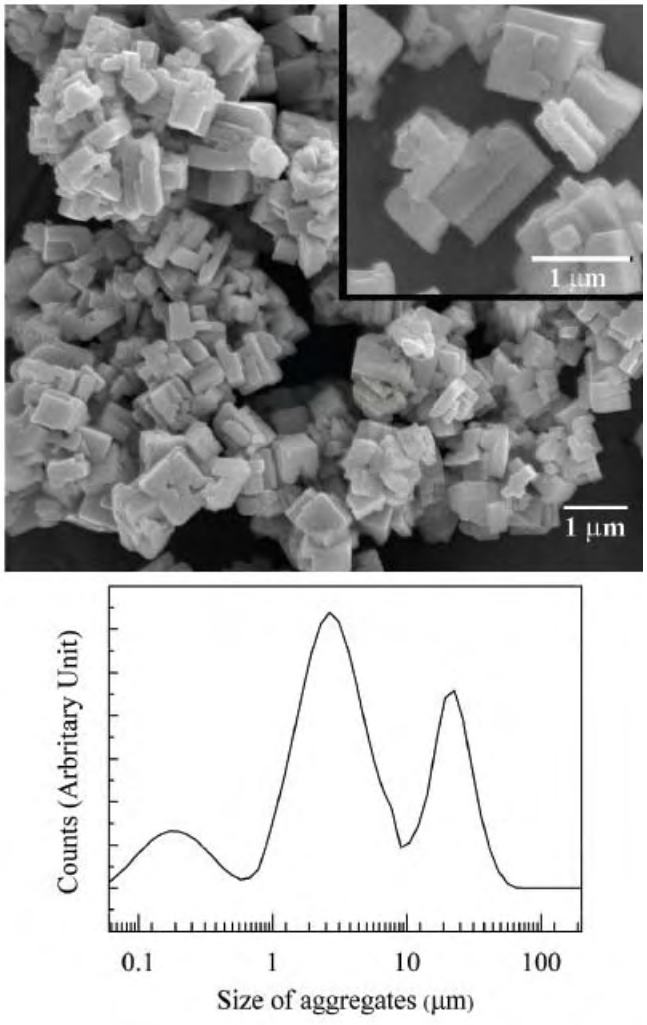

Fig. 54 *(a) Typical SEM image the PT aggregates obtained from the reaction conducted at 100 ^{o}C for 48 h with 4.5 h ultrasonication with the magnified image to illustrate the layer-by-layer growth of the particle in the inset, and (b) the corresponding tri-nodal aggregate size distribution.*

Table 24 *Sizes of PT particles measured from the SEM images, and of the aggregates obtained from laser diffraction experiments.*

Hydrothermal reaction time (h)	Ultrasonication time (h)	Particle sizes (μm)			Aggregate sizes (μm)	
		Short axis	Long axis	Average	D50	Mean
24	1.5	0.19-0.98	0.21-1.30	0.57	2.60(6)	6.14(1)
	3.0	0.16-1.00	0.35-1.62	0.65	1.99(4)	5.18(2)
	4.5	0.23-1.41	0.28-1.26	0.55	3.37(4)	7.59(3)
48	1.5	0.12-0.92	0.28-1.27	0.53	3.37(1)	9.23(7)
	3.0	0.15-1.28	0.17-1.69	0.48	2.72(6)	6.90(7)
	4.5	0.12-0.73	0.22-1.30	0.47	3.01(1)	7.65(2)
72	1	0.19-1.20	0.23-1.30	0.57	1.69(2)	6.05(6)
120		0.13-1.11	0.28-1.32	0.60	2.20(7)	6.54(2)
144		0.18-1.35	0.26-1.59	0.63	2.14(2)	6.73(6)

CONCLUSIONS

In summary, the ultrasonication of the reaction mixture has been proved to be able to reduce the thermodynamic barrier in the synthesis of fine PT powders under hydrothermal conditions, and the sonocatalyzed hydrothermal concept was underlined. The tetragonal phase-pure PT could be achieved at an exceptionally low temperature of 100 ^{o}C for the first time, irrespective to the slow kinetic at this temperature. The synthesized PT particles were tetragonal in shape and mostly submicrometers in sizes. These PT particles were in general comparable to those obtained at high reaction temperature either with or without the ultrasonication process. They were present mostly as hard aggregates of few micrometers. Under the studied conditions, the growth of the PT particles was manifestly occurred *via* the layer-by-layer mechanism.

REFERENCES

1. K. Byrappa and M. Yoshimura, *Handbook of Hydrothermal Technology: A Technology for Crystal Growth and Materials Processing*, Noyes Publication, New Jersey (2001).

2. A. Rujiwatra, J. Jongphiphan and S. Ananta, *Mater. Lett.* **59** (2005) 1871-1875.
3. A. Rujiwatra, N. Thammajak, T. Sarakonsri, R. Wongmaneerung and S. Ananta, *J. Cryst. Growth* **289** (2006) 224-230.
4. A.J. Moulson and J.M. Herbert, *Electroceramics: Materials, Properties Applications*, 2nd Edn., Wiley, New York (2003).
5. Y. Xu, *Ferroelectric Materials and Their Applications*, North-Holland, New York (1991).
6. F. Jona and G. Shirane, *Ferroelectric Crystals*, Dover Publications, New York (1993).
7. A. Udomporn, K. Pengpat K. and S. Ananta, *J. Eur. Ceram. Soc.* **24** (2004) 185-188.
8. J. Tartaj, J.F. Fernandez and F.M.E. Villafuerte-Castrejon, *Mater. Res. Bull.* **36** (2001) 479-486.
9. J. Fang, J. Wang, L.M. Gan and S.C. Ng, *Mater. Lett*. **52** (2002) 304-312.
10. A. Rujiwatra, C. Wongtaewan, W. Pinyo and S. Ananta, *Mater. Lett*. **61** (2007) 4522-4524.
11. S. Tapala, N. Thammajak, P. Laorattanakul and A. Rujiwatra, *Mater. Lett*. **62** (2008) 3685-3687.
12. R. Wongmaneerung, R. Yimnirun and S. Ananta, *Mater. Lett*. **60** (2006) 1447-1452.
13. X. Chen, H. Fan and L. Liu, *J. Cryst. Growth* **284** (2005) 434-439.

CHAPTER X

MICROWAVE-ASSISTED HYDROTHERMAL SYNTHESIS OF LEAD ZIRCONATE FINE POWDERS

Saowalak Tapala, **Apinpus Rujiwatra**

Maejo International Journal of Science and Technology **5**(01) (2011) 24-31.

INTRODUCTION

Lead zirconate ($PbZrO_3$ or PZ) is an important precursor in the preparation of a number of technologically important solid solutions, particularly those of the $PbZr_{1-x}Ti_xO_3$ series [1-2]. Recently , new studies have revealed novel applications of PZ as a phase-transformation-induced electromechanical actuator and a pyroelectric sensor [3-4]. The findings resulted in the reviving of interest in the synthesis of nano-sized PZ powders. Along this line, various synthetic techniques are available, *e.g.* hydrothermal, vibro-milling, sol-gel and precipitation, each of which exhibits characteristic drawbacks. The formation of aggregates, for instance, is an inherent problem for the hydrothermal technique [5-8]. The synthesis of fine PZ powders composing of mono-dispersed particles of uniform shape and size by this technique is therefore a challenge. According to our previous study, the fine powders of orthorhombic PZ could be synthesised as a single phase under hydrothermal conditions at a temperature of at least 180 ^oC for 24 h [8]. The space group of the resulting PZ was the unusual *Pbma* with refined cell parameters *a*=5.88(6) Å and *c*=4.27(3) Å. The formation of aggregates was the major drawback. Nonetheless, the highly dispersed and well-defined cubic particles could be afforded when the reaction temperature and time were increased to 200 ^oC and 72 h respectively [8]. The attempt to use organic additives, *e.g.* polyvinyl alcohol, polyvinylpyrrolidone and cetyltrimethylammonium bromide, which are commonly employed in the synthesis of other oxide powders [9-11], may be an answer to this problem, although they need to be removed in the post-synthesis step.

Herein, the application of the microwave heating in the synthesis of PZ fine powders under hydrothermal conditions is reported. The primary objective of the synthesis is to promote the monodispersion of particles of the synthesised PZ powders without the assistance of organic additives. The influences of various synthetic parameters on the obtained powders and the advantages and shortcomings of the microwave heating are described and discussed.

EXPERIMENTAL

Equimolar mixtures of zirconyl nitrate hexahydrate [$ZrO(NO_3)_2.6H_2O$, 27% Zr (gravimetric), Fluka, 0.0115 mole] and one of the following lead precursors, *i.e.* lead(II) nitrate (99.0%, Univar), lead(II) acetate (99.5%, Ajax Chemicals), lead(II) fluoride (99.0%, Univar), lead(II) chloride (99.0%, Riedel de Haën) and lead(II) iodide (99.0%, Aldrich), were prepared in 10.0 cm3 of deionised water. Pellets of potassium hydroxide (85%, Merck) was gradually added to each mixture with stirring to a concentration ranging from 6 to 14 mole dm^{-3}. Each mixture was then transferred to an 18 cm^3 Teflon reactor, which was sealed and placed in a 95(±5)ºC water bath placed in a domestic microwave oven (Whirlpool XT-25ES/S, 900W, 2.45 GHz). The reaction was performed under autogenous pressure developed by the microwave heating (720W and 810W) for 3-5 h. The resulting powder was recovered by filtration and washed with deionised water until the pH of the filtrate was approximately 7, followed a final washing with dilute acetic acid.

The synthesised powders were characterised for crystalline phases by powder X-ray diffraction (XRD) (using D8 Advance, Bruker, Cu *K*α, Ni filter, λ=1.540598 Å, 40 kV, 30 mA). A field-emission scanning electron microscope equipped with energy-dispersive X-ray spectrometer (JSM-6335F, JEOL) was used in the examination of particle shape and size and elemental composition. In order to evaluate the aggregation, size distributions of the bulk powder samples were measured by light scattering technique (using Zetasizer Nano S, Malvern Instruments, 4 mW He-Ne laser operated at 633 nm, particle size range 0.3nm-10μm).

RESULTS & DISCUSSION

Although different lead precursors were used in the study, every reaction apparently provided the same off-white powders mixed with some red-block crystals, which were identified as lead oxide by XRD study. Although the contamination of lead oxide in the prepared powders seemed to be inevitable, they could be simply removed by washing with dilute acetic acid solution [12]. After the acid washing, it was found that only $Pb(NO_3)_2$ gave the well crystallised PZ while poorly crystallised powders were obtained from the other lead precursors as depicted in Fig. 55. This could be attributed to the low solubility of these lead precursors in aqueous solution compared to the readily dissolved $Pb(NO_3)_2$ 13]. The hardly dissolved lead precursors might bring about an insufficient nutrient in the solution and consequently the nucleation and crystal growth could not occur properly.

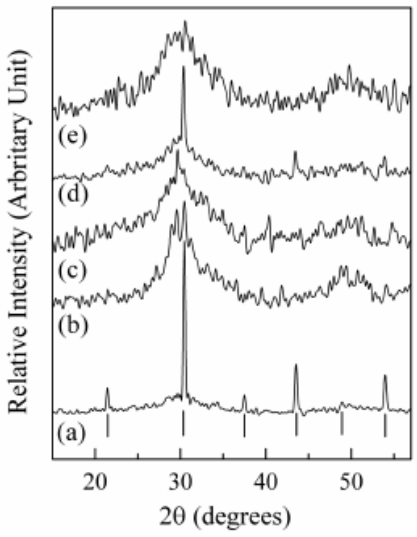

Fig. 55 *XRD patterns of the powders obtained from reactions between $ZrO(NO_3)_2.H_2O$ and different lead precursors in 14 mole dm^{-3} KOH solution for 3 h: (a) $Pb(NO_3)_2$, (b) $Pb(CH_3COO)_2$, (c) PbF_2, (d) $PbCl_2$ and (e) PbI_2. The vertical bars indicate diffraction characteristics of PZ (ICSD 077-0856).*

For the $Pb(NO_3)_2$ case, according to the XRD patterns of the acid-treated powders as shown in Fig. 56, a very high KOH concentration of 14 mole dm^{-3} was required for the success of the synthesis. Lower concentrations resulted in poorly crystallised powders. However, a development in intensity of the *(200)* diffraction peak with increasing KOH concentration was apparent, suggesting the evolvement of the desired PZ. Another observation was a substantial reduction of the effective reaction time from days to hours when compared with the conventional hydrothermal synthesis [8].

According to former studies on similar issues, the observed phenomena could be explained as follows. Under commonly used hydrothermal conditions, the formation of nanocrystalline ZrO_2 as the hydrolysis product of aqueous $ZrO(NO_3)_2$ [14] could also be accelerated by microwave heating. This caused the breaking of large water clusters in the hydration sphere and the formation of the smaller ones [15]. Such mechanism increased the mobility of the dissolved lead species as well as the number of reaction sites on the occurring ZrO_2 surfaces for the hydrated lead ion-water clusters to react. A rapid synthesis should therefore be expected. According to the same studies, the hydrolysis of the aqueous $ZrO(NO_3)_2$ also resulted in the generation of nitric acid, which could neutralise the hydroxide species in solution [14]. In addition, there was evidence for the reduced electrolytic reaction of the KOH solution by the microwave radiation [16]. These phenomena were

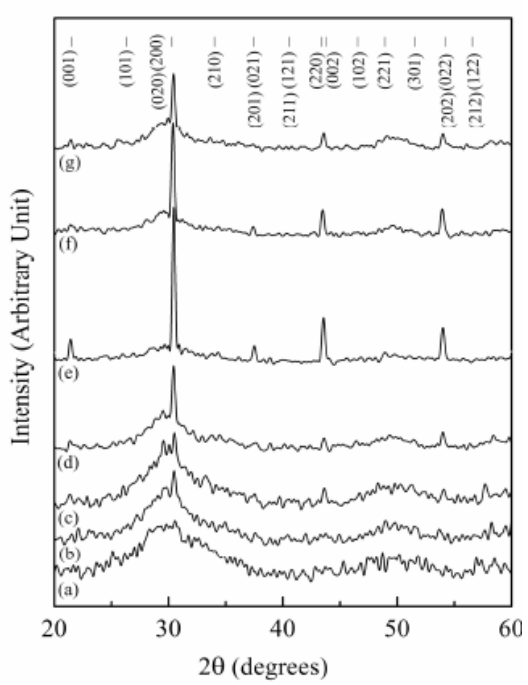

probably responsible for the increase in the high KOH concentration required in this study. This assumption was supported by the experiment in which a higher microwave power of 810 W was used. Rather than the desired PZ, mixtures of different oxides of lead and zirconium were obtained, which are the expected products of the hydrolysis reactions of the metal salts.

Fig. 56 *XRD patterns of the powders obtained from the reaction between $ZrO(NO_3)_2.H_2O$ and $Pb(NO_3)_2$ at 720 W for 3 h in different concentrations of KOH solution: (a) 6 (b) 8 (c) 10 (d) 12 and (e) 14 mole dm^{-3}, compared to those obtained in 14 mole dm^{-3} KOH solution with different reaction times: (f) 4 hours and (g) 5 h. The reference pattern is shown with vertical bars (ICSD 077-0856).*

Based on the XRD patterns of the acid-treated powders, the synthesised PZ could be readily indexed as the orthorhombic *Pbma* phase with refined cell parameters *a*=5.87(1) Å, *b*=5.88(2) Å and *c*=4.15(2) Å (ICSD 077-0856). These results were well consistent with the conventional hydrothermal case, although the refined *c* parameter was shorter than the conventional heating case, *c*=4.27(3) Å [8], but closer to the standard, *c*=4.134 Å (ICSD 077-0856).

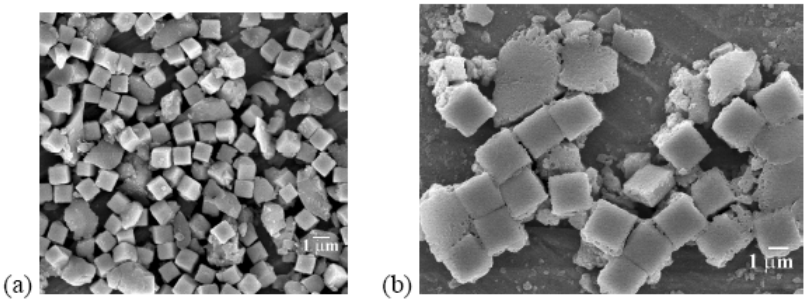

Fig. 57 *Typical FESEM photographs of PZ particles with corresponding XRD patterns shown in Figs. 56(e) and 56(g) for crystals (a) and (b) respectively.*

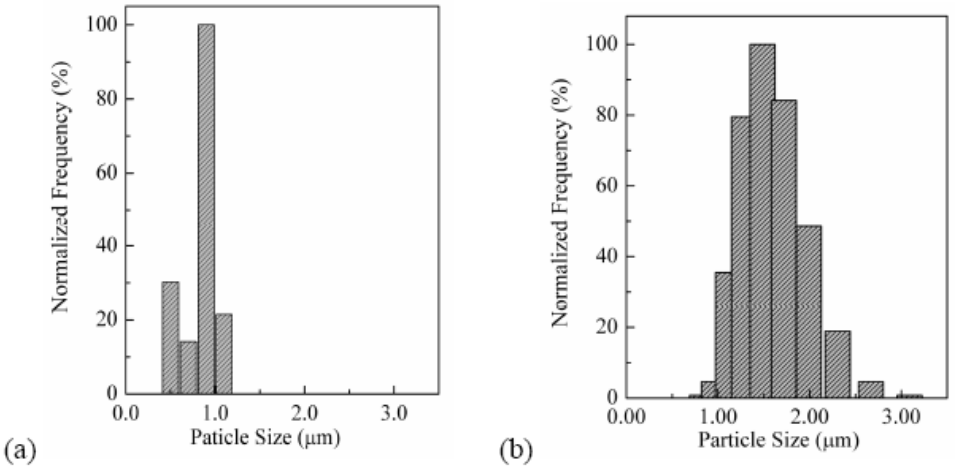

Fig. 58 Particle size distribution of the cubic PZ particles measured from (a) FESEM images and (b) light scattering experiment (measured on the same powder sample).

The field-emmision scanning electron microscopic (FESEM) images, as typically illustrated in Fig. 57(a), showed that the powders largely consisted of discrete cubic particles although some particles with irregular shape were also present. The energy-dispersive X-ray spectroscopic measurements on the surface of several cubic particles indicated stoichiometric Pb:Zr, whereas the irregular-shape particles were found to be Zr-rich. This could account for the noisy background observed for the XRD patterns [Fig. 56(e)]. The sizes of the cubic particles measured from the FESEM images were distributed in a significantly narrow range of 0.4-1.2 μm with approximately 60% of the population having a size of about 1 μm [Fig. 58(a)]. Light scattering experiment on the bulk powder samples showed slightly larger particle sizes distributed mostly between 1-2 μm [Fig. 58(b)]. The difference in particle sizes obtained from the two techniques should be due to a potentially biased analysis of the data. The non-spherical morphology of the particles normally introduces statistical errors to the laser light scattering data while a tendency of the particles to rest with preferred orientation on stub can induce bias in the data representation of the FESEM [17].

Thus, in comparison to the PZ powders derived from a conventional hydrothermal reaction where the particles were reportedly distributed in a 5-15 μm range with an average diameter of 7.5 μm [8], the pronouncedly narrower size distribution and the substantially smaller PZ particles have been achieved, although the negative effect on phase purity of the synthesised PZ and the contamination of some irregular Zr-rich particles were observed. A large number of nucleation induced by the localised microwave heating and the mechanism as described above, coupled with a poor crystal growth due to instantaneous and rapid ramping of such heating, could be the reasons for the approximate uniformity in the particle size [18-19]. Considering the PZ powders obtained from other chemical routes such as precipitation [20] and microemulsion [21], the apparent uniformity in particle shape and size may not be new. Both of these techniques can also give PZ powders composing of mono-dispersed spherical particles typically 20 nm in diameter. However, calcination is required by both techniques, resulting in an unavoidable high temperature treatment and disadvantages incurred therein. As for the modified solid-state preparation of PZ powders, the problems with aggregation and particles with irregular shapes cannot be surmounted even though the vibro-milling is applied for over 25 h [22].

The extension of the microwave heating time from 3 h to 5 h resulted in a reduction in intensity of the most intense *(200)* diffraction peak of the orthorhombic PZ and the appearing of a broad lump at the base of this peak as shown in Fig. 56 (e-g). The FESEM images [Fig. 57(b)] showed that the particles remained in the same cubic shape, although the bubbled surfaces and the necking between the adjacent particles could be observed. This indicated the boiling on the surfaces of these cubic PZ particles, which could be the result of a heat accumulation. The enlargement of the particles, which is a reflection of the particle growth process, and the disappearing of irregular particles with extended reaction time were also apparent.

CONCLUSIONS

In order to promote the mono-dispersion and the uniformity in shape and size of the hydrothermally derived PZ particles without the assistance of organic additives, microwave heating was attempted. The occurrence of lead oxide seemed to be inevitable and washing with dilute acetic acid was necessary. Among different variables studied, the type of lead precursor and the KOH concentration were most critical in the success of the synthesis. It was shown that the critical KOH concentration and the optimal microwave heating time were 14 mole dm^{-3} and 3 h respectively. The highly

dispersed cubic lead zirconate particles of approximately 1 μm in size could be synthesised in only 3 h at 720 W of microwave heating. In comparison to conventional hydrothermal synthesis, the merits of the microwave method were clearly reflected by a shortening in hydrothermal reaction time, a reduction in particle size, an improved particle mono-dispersion, and a uniform particle size. However, the negative effects on the purity of synthesised powders, viz. the contamination of irregular particles, and the requirement for a very high concentration of potassium hydroxide mineraliser should be noted.

REFERENCES

1. T. Asada and Y. Koyama, *Phys. Rev. B* **75** (2007) 214111-214121.
2. C.Z. Rosen, B.V. Hiremath and R.E. Newnham, "Key Papers in Physics; Piezoelectricity", American Institute of Physics, New York, (1992**)** 159-181.
3. K. Yamakawa, S. Trolier-McKinstry and J. P. Dougherty, *Appl. Phys. Lett.* **67** (1995) 2014-2016.
4. P. Ayyub, S. Chattopadhyay, K. Sheshadri and R. Lahiri, "The nature of ferroelectric order in finite systems", *Nano Mater.*, **1999**, *12*, 713-718.
5. Khamman, W. Chaisan, R. Yimnirun and S. Ananta, *Mater. Lett.* **61** (2007) 2822-2826.
6. E.D. Ion, B. Malic and M. Kosec, *J. Eur. Ceram. Soc.* **27** (2007) 4349-4352.
7. E.E. Oren, E. Taspinar and A.C. Tas, *J. Am. Ceram. Soc.* **80** (1997) 2714-2716.
8. A. Rujiwatra, S. Tapala, S. Luachan, O. Khamman and S. Ananta, *Mater. Lett.* **60** (2006) 2893-2895.
9. G. Xu, G. Zhao, Z. Ren, G. Shen and G. Han, *Mater. Lett.* **60** (2006) 685-688.
10. Z. Lu, J. Liu, Y. Tang and W. Li, *Inorg. Chem. Commun.* **7** (2004) 731-733.
11. W.L. Sin, K.H. Wong and P. Li, *Acta Physica. Polonica. A* **111** (2007) 165-171.
12. S. Tapala, N. Thammajak, P. Laorattanakul and A. Rujiwatra, *Mater. Lett.* **62** (2008) 3685-3687.
13. J. G. Speight, "Lange's Handbook of Chemistry", 16th Edn., McGraw-Hill, New York (2005).
14. Y.V. Kolen'ko, V.D. Maximov, A.A. Burukhin, V.A. Muhanov and B.R. Churagulov, *Mater. Sci. Eng. C* **23** (2003) 1033-1038.
15. R. Walczak and J. A. Dziuban, *Sens. Actuators A* **116** (2004**)** 161-170.
16. D. R. Stanisavljev, T. D. Grozdić, M. P. Marĉeta Kaninski, A. R. Djordjević and D. Lj. Stojić, *Electrochem. Commun.* **9** (2007) 901-904.
17. A. Jillavenkatesa, S.J. Dapkunas and L.-S.H. Lum, "Particle Size Characterization; Practice Guide", U.S. Government Printing Office, Washington, D.C., (2001).
18. D.E. Clark and W.H. Sutton, *Annu. Rev. Mater. Sci.* **26** (1996) 299-331.
19. P. Lidström, J. Tierney, B. Wathey and J. Westman, *Tetrahedron* **51** (2001) 9225-9283.
20. T. Ko and D. -K. Hwang, *Mater. Lett.* **57** (2003) 2472-2479.
21. J. Fang, J. Wang, S.-C. Ng, L.-M. Gan, C.H. Quek and C.-H. Chew, *Mater. Lett.* **36** (1998) 179-185.
22. Khamman, W. Chaisan, R. Yimnirun and S. Ananta, *Mater. Lett.* **61** (2007) 2822-2826.

CHAPTER XI

SOLVOTHERMAL SYNTHESIS, SINTERING BEHAVIOR AND DIELECTRIC PROPERTIES OF POTASSIUM NIOBATE FINE POWDERS

Kittichai Jinachai, Athipong Ngamjarurojana, **Apinpus Rujiwatra**
Chiang Mai Journal of Science **38**(2) (2011) 252-262.

INTRODUCTION

The emergence of the "*green attitude*" has resulted in the attempts to develop the green alternatives for various technologically important materials and processes including lead, despise of its important role technologically. Along this line, potassium niobate ($KNbO_3$, KN) has appeared as one of potential candidates for the lead-free piezoelectric materials. This is due to its excellent inherent properties and potential applications, for example, as an optical wave guide and devices for frequency doubling, holographic storage and surface acoustic wave [1-5]. The material is conventionally prepared by solid state reactions, which demand high temperatures and multiple cycles of heating-and- grinding to assure the completeness of the reactions [6]. Besides being the energy consumable process, the other drawbacks of the solid-state processes such as the formation of undesired impurities and aggregations are inherent [7]. During the last decade, the hydrothermal technique has been proved to be efficient for the preparation of KN in various forms, including fine powder, one dimensional structure and thin film [8-11]. Despise of the promising future of the material and the technique, the practical application and commercialization of KN yet faces a major problem with sintering. At effective sintering temperature and duration, the rapid vaporization of potassium oxide (K_2O) and the large difference in properties of the cation involved result in the chemical control and densification problems [1]. The additions of other aiding compounds, such as magnesium oxide (MgO) and lead oxide (PbO), were reported to relieve the problems [12, 13].

Here, the adaptation of hydrothermal process by the use of mixed water-ethyl alcohol as reaction medium for the preparation of KN fine powders is described. The application of the ultrasonic wave on the reaction mixtures in prior to the synthesis is discussed. The sintering behaviour and the preliminary investigation of the dielectric properties of the sintered ceramics are reported.

EXPERIMENTAL

The mixtures of niobium oxide (Nb_2O_5, Sigma-Aldrich 99.99%, 0.0056 mol) and potassium hydroxide (KOH, Merck 85%, 0.0028 mol) were first prepared in mixed water-ethyl alcohol liquid medium (0.278 mol of water, 0.086 mol of ethyl alcohol; C_2H_5OH, Merck 99.9%). The employed amount of KOH functioning as both reagent and mineralizer in the synthesis is the amount reported as the critical limit providing the successful synthesis [14]. Each mixture was then stirred and transferred into Teflon liners up to *ca.* 80% filling volume capacity. The mixtures were subsequently subjected to an autogenous pressure developed at 200 ^oC for 1-24 h. In order to study the effect of ultrasonication, some samples are ultrasonicated at 40(±5) ^oC for 1 h using a laboratory ultrasonic bath (Bandelin Electronic RK255H, 160/320W, 35kHz) before the reactions. The synthesized powders were finally recovered by filtration and washed with water until the pH of the filtrate was *ca.* 7 to assure the complete removal of the alkali.

Powder X-ray diffraction (XRD; Bruker D8 Advance diffractometer, Ni-filtered, Cu *K*a, λ=1.54098 Å, 40 kV, 30 mA) was used in characterizing the synthesized crystalline phases. Lattice parameters of these phases were refined from the collected XRD patterns. Selected area electron diffraction (SAED) equipped by a transmission electron microscope (TEM; JEOL JEM-2010) was also used in characterizing growth direction of the elongated particles, whereas a field emission scanning electron microscope (SEM; JEOL JSM-6335F) was used in examining morphologies and sizes of the composing particles.

The synthesized powders composing of a single orthorhombic KN according to the XRD results were chosen for the sintering experiments. The powders were ground and pressed uniaxially at 100 bars and room temperatures to make the pellets of 10.15 mm in diameter and 2.45-2.75 mm in thickness. The obtained pellets were then sintered at 1,025 ^{o}C for 1 hour (Carbolite, 2416CG) using a heating-cooling rate of 3 ^{o}C min^{-1}. After the sintering, densities of the sintered ceramics were evaluated using Archimedes technique [15]. Phase and microstructure of the sintered pellets were investigated by XRD and FESEM, respectively.

The dielectric properties of the sintered ceramics were studied as functions of both temperature and frequency using an automated dielectric measurement system and a silver electrode (Dupont, QS 171), which was prepared by printing on the lapped surfaces followed by firing at 600 ^{o}C for 1 h. The computer-controlled dielectric measurement system consists of a precision LCR meter (Thonghui, TH2819A) and a temperature chamber. The temperature dependent measurements were performed using a Keithley Model 2,000-digit multimeter which was equipped by a temperature chamber, when the capacitance and the dielectric loss tangent were determined over the temperature range of 50-500 ^{o}C with the frequency ranging from 0.1 to 100 kHz.

RESULTS & DISCUSSION

Figures 59 and 60 shows the XRD patterns of the powders obtained from the reactions conducted at 200 ^{o}C for varied reaction times, with and without prior ultrasonication for an hour, respectively. The application of the ultrasonication as described did not show any significant difference in the XRD patterns of the synthesized powders. When the reactions were conducted for an hour, the presence of the other diffraction peaks which were not of the desired KN was plain. The identification of these phases could not be precisely done due to a deficiency in number and intensity of these peaks. It can be nonetheless ascertained that the formation of KN, which could be indexed as the orthorhombic phase with space group *Cm2m* (JCPDS 32-822), already occurred as the major phase. According to the XRD results, the pure phase of KN could be obtained after 3 h, irrespective to the application of the prior ultrasonication on the reaction mixtures. The obtained KN powders could be readily indexed and refined in orthorhombic *Cm2m* (JCPDS 32-822), giving a = 5.689(8)-5.695(8), b = 5.721(11)-5.737(10) and c = 3.982(11)-3.984(12)). There was not therefore any apparent effect of the ultrasonication on the formation and phase of the synthesized KN powders, within a limit of the XRD technique.

The SEM images show the synthesized KN powders to compose mostly of lumber particles with a few fractions of pseudo-cubic particles, independent also on the preparative conditions. Figure 61 shows the representative images of the particles obtained from the reactions with and without the prior ultrasonication, illustrating well-defined shape from the reactions with the prior ultrasonication. Sizes of these KN particles measured directly from the SEM were distributed in a range of approximately 0.1-1 mm and 0.15-2.5 μm, for the short and long axes, respectively. In contrast, the

particles with a serious melting and poor-defined particle boundary were obtained from the reactions conducted without the prior application of the ultrasonic wave.

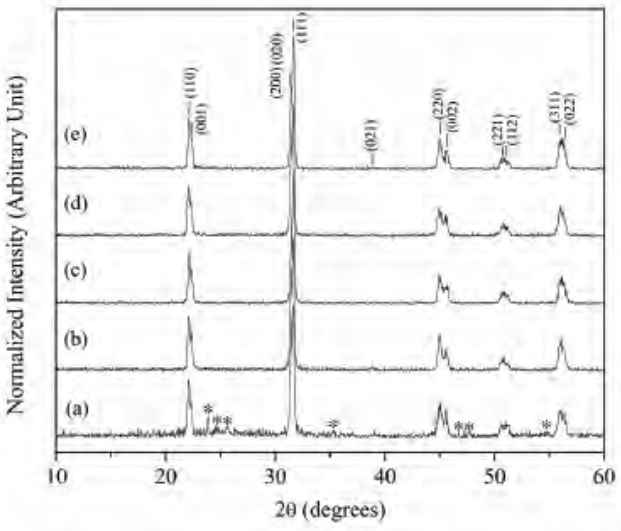

Fig. 59 *The XRD patterns of the powders obtained from the reactions conducted at 200 °C for (a) 1 h, (b) 3 h, (c) 6 h, (d) 12 h and (e) 24 h on the ultrasonicated mixtures; * indicates unidentified diffraction.*

Fig. 60 *The XRD patterns of the powders obtained from the reactions conducted at 200 °C for (a) 1 h, (b) 3 h, (c) 6 h, (d) 12 h and (e) 24 h on the mixtures without the prior ultrasonication; * indicates unidentified diffraction.*

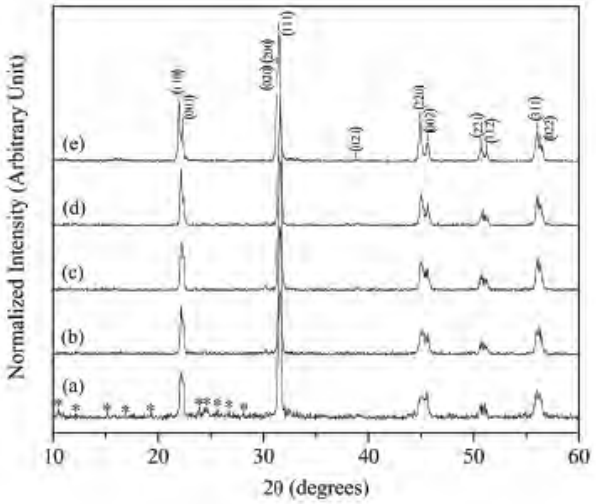

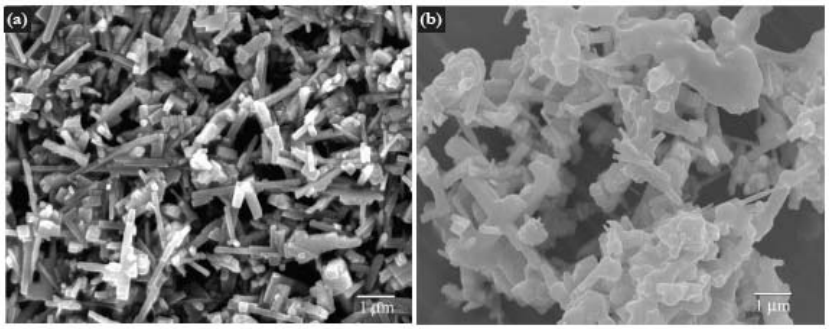

Fig. 61 *The SEM images exemplifying the lumber particles of potassium niobate derived from the reactions on (a) the ultrasonicated reaction mixture and (b) the mixture without prior ultrasonication, conducted under the same synthesis conditions.*

This may be rationalized by the ability of the ultrasonic wave in inducing the nucleation and in creation of the highly reactive and clean surface on the created nuclei which should promote the clean crystal growth in the afterward reactions [16]. The pressure generated under the solvothermal conditions generally causes the nucleation to occur as simultaneously as the crystal growth, which commonly results in hard aggregates [17].

In comparison to the former reports on the synthesis of KN fine powders using the hydrothermal reactions at the same temperature and KOH concentration of 200 °C and 8 mol dm^{-3}, several

differences could be pointed out, although phase of the obtained KN is the same, which is the orthorhombic phase [14]. First, shape of the hydrothermally derived KN particles was largely pseudo-cubic, when the lumber particles could be obtained in this study. Second, sizes of the pseudo-cubic particles were also distributed in a larger size region of 1-4 mm, compared to the sub-micrometer sizes reported here. The use of mixed water-ethyl alcohol as a liquid medium apparently provided smaller sized and more elongated particles. Regarding the effective reaction, the employment of ethyl alcohol and the application of ultrasonic wave on the reaction mixtures did not result in any significant change.

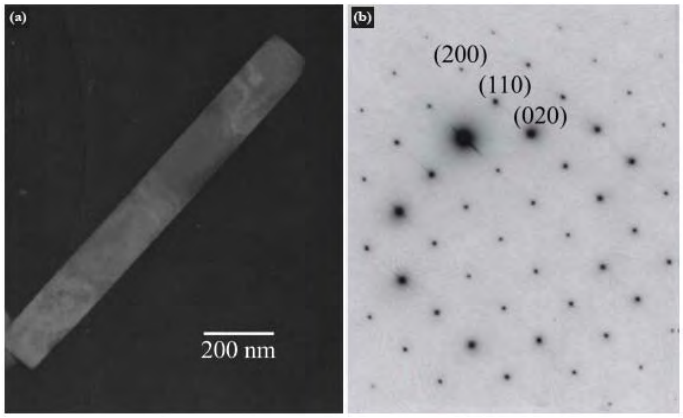

Fig. 62 *(a) The TEM image of the typical lumber potassium niobate particle with (b) the corresponding indexed SAED pattern based on the orthorhombic Cm2m (JCPDS 32-822).*

The structure of the lumber particles was also evaluated through selected area electron diffraction (SAED) in the transmission electron microscope. Figure 62 shows the TEM images of the typical particle and the corresponding SAED pattern, which could be well indexed in the assigned orthorhombic *Cm2m* phase. The growth direction apparently lied along the crystallographic [*110*] direction. The KN powders characterized by the XRD to be of the single orthorhombic phase were chosen for the sintering experiments, including those obtained from the reactions conducted for 3-24 h, both with and without the prior ultrasonication. After the sintering, the diameters and thickness of the sintered bodies were substantially reduced; 8.35-8.60 mm and 2.10-2.30 mm for the sintered pellets compared to 10.15 mm and 2.45-2.75 mm for the green bodies. The contraction in diameter of *ca.* 18% was slightly better than the contraction in thickness, *ca.* 14-16%. This corresponded to the volume shrinkage of *ca.* 36-42%. The densities of the sintered ceramics were measured, giving the results of *ca.* 95-98% in relative to the crystallographic density, 4.62 g cm^{-3}. No correlation between the obtained values and the variation in synthesis reaction time could be observed, although the powders obtained from the reactions with the prior ultrasonication showed slightly better volume shrinkage and densification. The shrinkage and relative densities of *ca*. 40-42% and 96-98%, respectively, could be calculated for the ultrasonication cases, when the shrinkage of 36-39% with the corresponding relative densities of *ca.* 95% were obtained for the other cases. This could be due to the better defined particle shape and less melting between the particles in the former case as revealed by the SEM images.

The SEM images taken on the sintered KN pellets gave supportive evidence, as exemplified in Fig. 63. The grain sizes of the sintered ceramic were measured and a slight growth of the sintered grain was revealed; 0.15-3.95 μm and 0.25-4.45 μm for the short and long axes. These results agree well with the calculated volume shrinkages and the calculated relative densities. It is apparent that the growth process occurred better along the short axis than the long axis, and resulted in an evolution of a pseudo-cubic grain from the pressurized lumber particles. It is also evident that the melting between grains was serious for the pellets which were prepared from the powders derived from prolonged solvothermal reaction, particularly those with the prior ultrasonication treatment. Regarding the hygroscopic problem commonly encountered with the sintering of KN [18], it was not

the case in this study if the washing of the remaining alkali was performed carefully. The sensitivity to the atmospheric water may therefore attribute to the remaining of KOH which is hygroscopic.

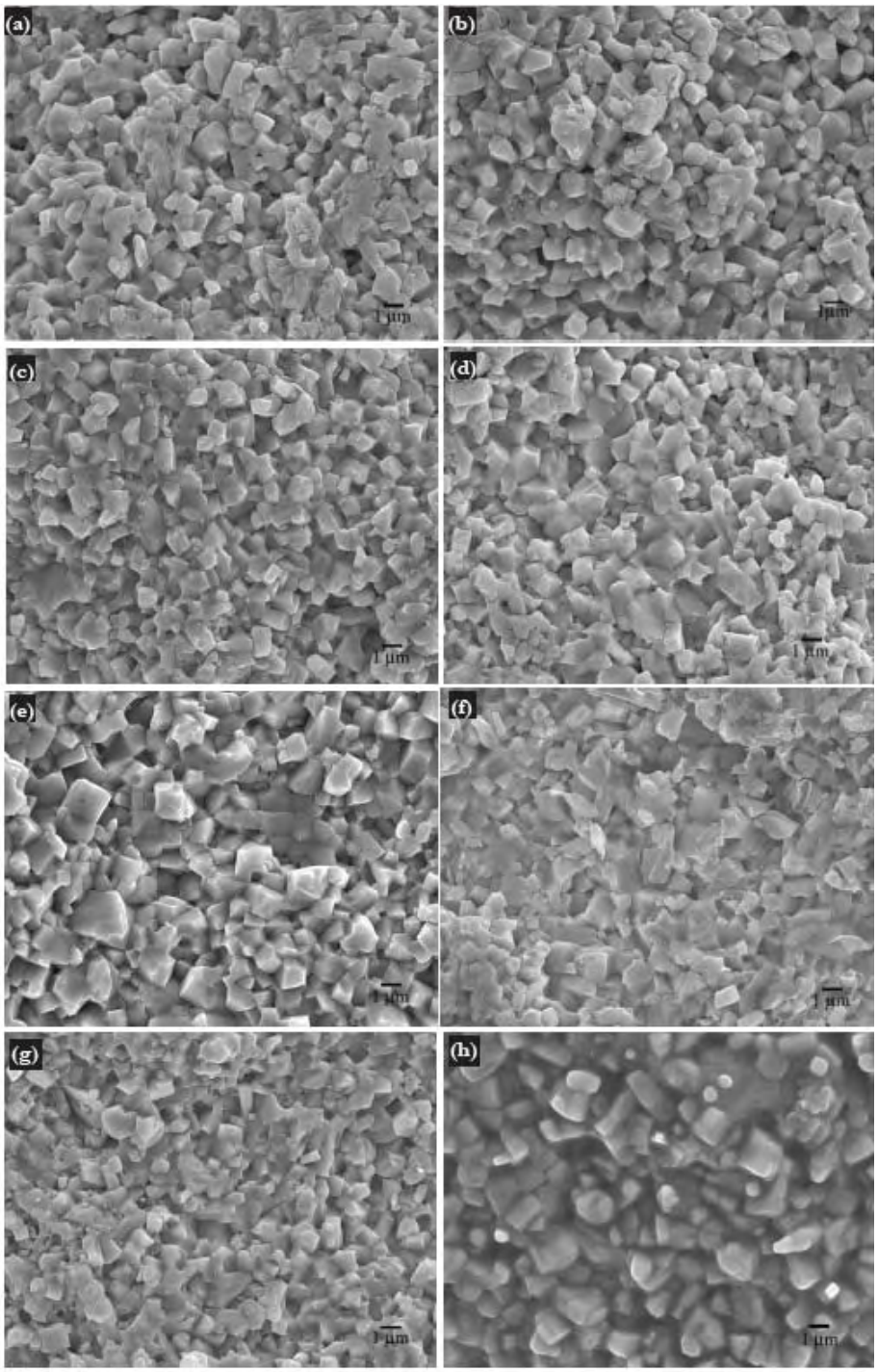

Fig. 63 *The SEM images of the sintered KN ceramics prepared from the powders obtained from the reactions conducted at 200 ^{o}C for (a) 3 h, (b) 6 h, (c) 12 h and (d) 24 h on the mixtures without the prior ultrasonication, compared with those of the sonicated mixtures; (e) 3 h, (f) 6 h, (g) 12 h and (h) 24 h.*

The XRD was used to follow the change in phase, if any, after the sintering and the results are shown in Figs. 64(a) and 65(a). The remaining of the orthorhombic KN was significant, although the formation of the niobium-rich phase, KNb_3O_8, suggesting the loss of K_2O during the sintering were

evident. A develop of a big lump at low 2θ region was additionally plain, implying the corruption of the long range order in the structure although the distinction between the three most intense peaks, including (*020*), (*200*) and (*111*), were clearer after the sintering. The exception was apparent for the sintered pellets which were prepared from the powders obtained from 24 h reaction with the prior ultrasonication, where there was no signature of the KNb_3O_8 phase in the XRD pattern. This again reflects the merit of the application of the prior ultrasonication.

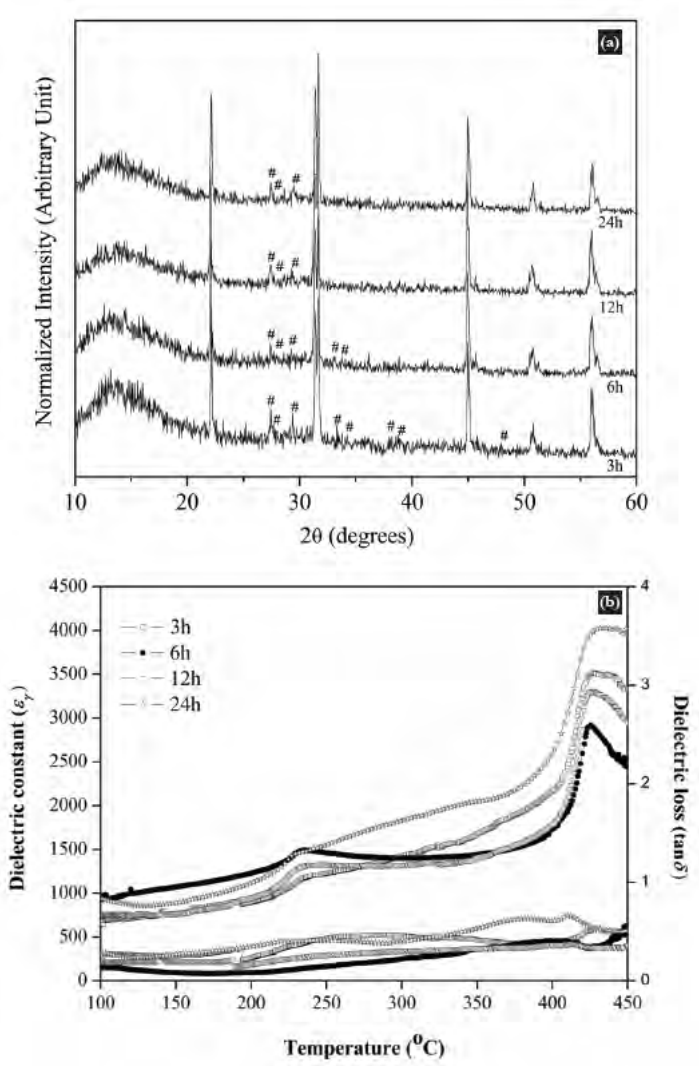

Fig. 64 *(a) The XRD patterns (# = KNb_3O_8) and (b) temperature dependence of dielectric properties measured on the KN ceramics prepared from the powders obtained from the reactions conducted at 200 °C for (a) 3 h, (b) 6 h, (c) 12 h and (d) 24 h on the mixtures without the prior ultrasonication.*

Figure 64(b) and Figure 65(b) show the temperature dependence of dielectric constants (εr) and dielectric loss tangents (tan δ) at 100 kHz for the sintered KN ceramics, revealing a difference in the measured values depending on the purity of KN according to the XRD patterns shown in the corresponding Fig. 64(a) and Fig. 65(a), respectively. Phase transition from the ideal cubic phase to the tetragonal phase was found around 425 °C, while the tetragonal to the orthorhombic occurred around 225 °C. The results are well consistent with the formerly reported values for the KN ceramics [18-21]. In the case of the ceramic composing of KN as nearly a single phase which was the one derived from the powders prepared from 3 h - 24 h reaction with the prior ultrasonication, the dielectric constants has increased with also a sharp peak transition, especially for the KN ceramics of high densities and good crystallinity. The KN ceramics which were fabricated from the powders prepared from the same conditions but without the prior ultrasonication, showed a broad peak transition, which should probably be due to the presence of the liquid phase in microstructure. This results were consistent with the XRD and SEM results that showed the formation of the second

phase KNb_3O_8 and the liquid phase in the microstructure due to the evaporation of K_2O. In general, it was evident that the ceramics prepared from the powders which were derived from the reactions with the prior ultrasonication showed higher dielectric constants and lower dielectric loss than those without the prior ultrasonication. This may attribute to the increase in oxygen vacancies which on the other hand contribute to the increase in conductivity [22].

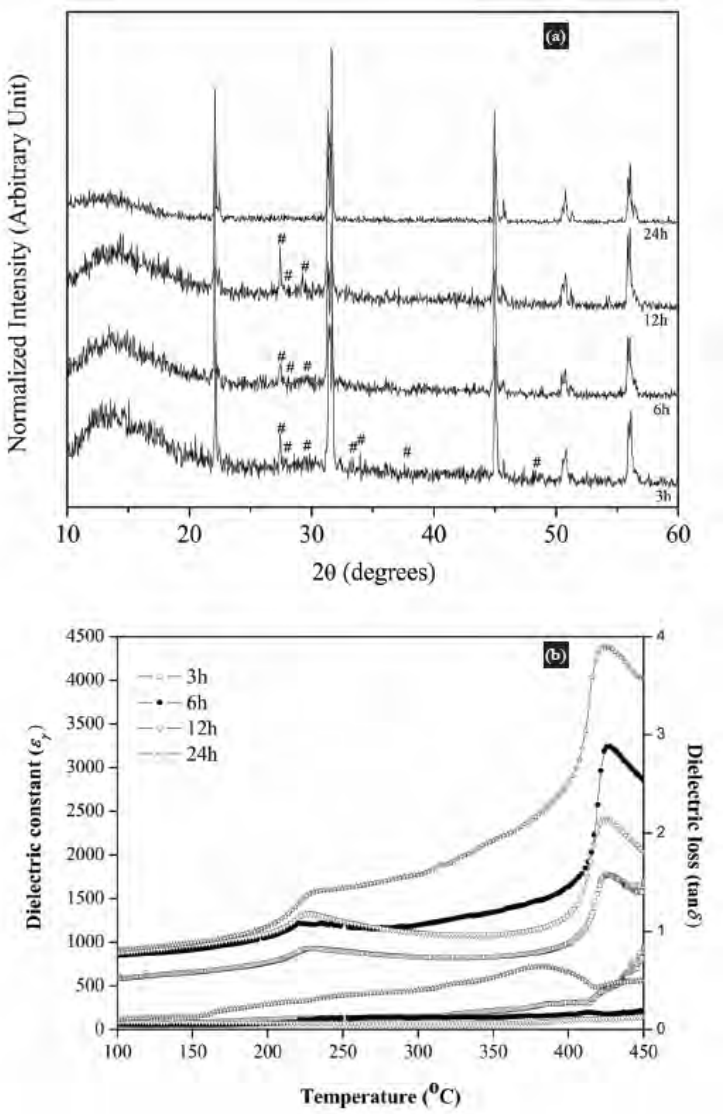

Fig. 65 *(a) The XRD patterns (# = KNb_3O_8) and (b) temperature dependence of dielectric properties of the KN ceramics prepared from the powders obtained from the reactions conducted at 200 ^oC for (a) 3 h, (b) 6 h, (c) 12 h and (d) 24 h on the mixtures with the prior ultrasonication.*

CONCLUSIONS

In summary, the sonocatalyzed ethanothermal process has been attempted with the synthesis of potassium niobate fine powders, and proved to be able to provide the orthorhombic phase-pure KN powders under mild condition and rapid reaction times of at least 3 h. The use of mixed water-ethyl alcohol liquid medium apparently favoured the formation of elongated lumber KN particles of sub-micrometer sizes, when the application of the prior ultrasonication on the reaction mixtures led to significant differences in sintering behavior, loss of K_2O and the tolerance of the orthorhombic KN to the sintering, as well as the corresponding dielectric properties. Dense KN ceramics of over 95% relative densities could be fabricated by conventional sintering without the hygroscopic problem. The significance of the prior ultrasonication on the reaction mixtures during the synthesis in enhancing both physical and electrical properties of the sintered ceramics was clearly illustrated.

REFERENCES

1. K. Kakimoto, I, Masuda, And H. Ohsato, *J. Euro. Ceram. Soc.* **25** (2005) 2719-2722.
2. K. Tanak, K.I. Kakimoto and H. Ohsato, *J. Euro. Ceram. Soc.* **27** (2007) 3591-3595.
3. I. Pribosic, D. Makovec and M. Drofenik, *J. Euro. Ceram. Soc.* **25** (2005) 2713-2717.
4. R. Yang, S.Y. Shen, C.B. Wang, W. Shen and L.M. Zhang, *Thin Solid Films* **516** (2008) 8559-8563.
5. H. Muthurajan, H.H Kumar, V. Samuel, U.N. Gupta and V. Ravi, *Ceram. Int.* **34** (2008) 671-673.
6. T. Su, H. Jiang, H. Gong, Y. Zhai, *J. Mater. Sci.* **45** (2010) 3778-3783.
7. U. Fluckiger, H. Arend, H.R. Oswald, *Am. Ceram. Soc. Bull.* **56** (1977) 575-577.
8. N. Kumada, T. Kyoda, Y. Yonesaki, T. Takei and N. Kinomura, *Mater. Res. Bull.* **42** (2007) 1856-1862.
9. J.W. Liu, G. Chen, Z.H. Li. and Z.G. Zhang, *Int. J. Hydrogen Energy* **32** (2007) 2269-2272.
10. W.L. Suchanek, *Chem. Mater.* **16** (2004) 1083-1090.
11. K. Kajiyoshi, K.Yanagisawa, Q. Feng and M. Yoshimura, *J. Mater. Sci.* **41** (2006) 1535-1540.
12. M. Kosec, D. Kolar, *Mater. Res. Bull.* **10** (1975) 335-340.
13. I. Pribo, D. Makovec, M. Drofenik, *J.Mater. Res.* **17** (2002) 2989-2992.
14. Lu C.H., Lo S.Y., Lin H.C., *Mater. Lett.*, 1998; **34**: 172-176.
15. R. Morrel, Handbook of properties of technical & engineering ceramics, *HMSO Publications*, London (1989).
16. K.S. Suslick, *Science* **247** (1990) 1439-1445.
17. R.E. Riman, W.L. Suchanek and M.M. Lencka, *Ann. Chim. Sci. Mat.* **27** (2002) 15-21.
18. K. Matsumoto, Y. Hiruma, H. Nagata and T. Takenaka, *Ferroelectrics* **358** (2007) 169-174.
19. M. Ishikawa, N. Takiguchi, H. Hosaka and T. Morita, *Jpn. J. Appl. Phys.* **47** (2008) 3824-3828.
20. C.K.Tan, G.K.L. Goh and W.L. Cheah, *Thin Solid Films* **515** (2007) 6577-6581.
21. M. Ishikawa, Y. Kadota, N. Takiguchi, H. Hosaka and T. Morita, *Jpn. J. Appl. Phys.* **47** (2008) 7673-7677.
22. G. Singh, V.S. Tiwari and P.K. Gupta, *J. Appl. Phys.* **107** (2010) 064103.

APPENDIX

REPRINTS OF THE PUBLISHED ARTICLES

J Inorg Organomet Polym (2009) 19:306–313
DOI 10.1007/s10904-009-9271-y

A1

Microwave Assisted Crystal Growth of a New Organic—Decavanadate Assembly: $[V_{10}O_{27}(OH)] \cdot 2(C_6N_2H_{14}) \cdot (C_6N_2H_{13}) \cdot (C_6N_2H_{12}) \cdot 2H_2O$

Bunlawee Yotnoi · Saranphong Yimklan · Timothy J. Prior · Apinpus Rujiwatra

Received: 13 October 2008 / Accepted: 1 April 2009 / Published online: 14 April 2009

Abstract Microwave synthesis was used to grow single crystals of a new organic–inorganic supramolecular assembly, $[V_{10}O_{27}(OH)] \cdot 2(C_6N_2H_{14}) \cdot (C_6N_2H_{13}) \cdot (C_6N_2H_{12}) \cdot 2H_2O$, in a very short time compared to the conventional solution technique. In order to generate crystals suitable for single crystal experiments, an equimolar mixture of reactants and a few hours of microwave heating are required. Although non-merohedral twinning is an inherent problem, the crystal structure can be solved and refined in the orthorhombic space group $Pna2_1$ with $a = 20.972(4)$ Å, $b = 10.3380(14)$ Å, $c = 20.432(3)$ Å, $Z = 4$, with an excellent result, $R(F^2) = 0.0431$. The assembly is hydrogen bond-assisted and built up of the monoprotonated decavanadate and 1,4-diazabicyclo [2.2.2]octane of various degrees of protonation. The number and location of protons on both the inorganic and organic motifs govern the formation of the extensive hydrogen bonding network, which in turn regulates the assembly architecture.

Keywords Single crystal growth · Microwave synthesis · Decavanadate · Supramolecular assembly · Hydrogen bond

1 Introduction

Polyoxometallates (POMs) are one of the best known classes of complex anions and these continue to attract interest from both scientists and technologists. This is due to the diversity and richness in their chemistry and physics, which have led to a rapid expansion in the number of potential applications [1–3]. Among the well studied POMs, polyoxovanadates (POVs) compose a unique class, displaying a distinct potential for biology, materials science and medicinal applications [4–7]. The usage of these POVs, and decavanadates in particular, as structural building units in the synthesis of high dimensional hydrogen bond-assisted supramolecular assemblies composed of both inorganic and organic components such as $[H_2V_{10}O_{28}](C_{20}N_8H_{32})(H_2O)_4$, $[(C_2H_5)_3NH]_4[H_2V_{10}O_{28}]$, $(C_4N_2S_2H_{14})_2[H_2V_{10}O_{28}]$ and $[\boldsymbol{C211}H_2]_2[H_3O]_2[V_{10}O_{28}] \cdot 7H_2O$ where ***C211*** is a cryptand, is however still scattered [8–12]. The supramolecular arrangement of these compounds depends strongly on the abundance and locations of protonation sites on the decavanadates, and the nature of the organic molecules. These factors can impart immense influence *via* the synergistic interplay of Coulombic, van der Waals and hydrogen bonding interactions. While the structure of the decavanadate is well documented [8], the choice of organic molecules and synthetic conditions can be varied and these are therefore of utmost importance in directing the supramolecular organization.

All previous reports of organic—decavanadate assemblies describe direct crystallization from solution under either ambient or hydro/solvothermal conditions. These reactions commonly require days or weeks to afford single crystals suitable for complete structural characterization. Recently microwave synthesis has been utilized in the synthesis of inorganic and inorganic–organic hybrid materials as well as ceramics, following the demonstration of tremendous advantages of this technique in organic synthesis [13–16]. The application of the technique in the growth of single crystals of inorganic–organic hybrid compounds is

B. Yotnoi · S. Yimklan · A. Rujiwatra (✉)
Department of Chemistry, Faculty of Science, Chiang Mai University, Chiang Mai 50200, Thailand
e-mail: apinpus@chiangmai.ac.th

T. J. Prior
Department of Chemistry, University of Hull, HU6 7RX Kingston upon Hull, UK

however novel. The fast kinetics of microwave reactions may shorten the reaction times, although this can induce disorder in the structure and hence hinder the growth of single crystals which generally requires very high degree of internal order.

Here we introduce the usage of microwave technique for a rapid single crystal growth of a new three dimensional hydrogen-bond assisted supramolecular assembly, based on the decavanadate monomer and 1,4-diazabicyclo[2.2.2]octane. Structural characterization based on single crystal X-ray diffraction data and synergistic interactions analysis is reported.

2 Experimental

2.1 Microwave—Assisted Crystal Growth and Spectroscopic Characterization

Crystals of $[V_{10}O_{27}(OH)] \cdot 2(C_6N_2H_{14}) \cdot (C_6N_2H_{13}) \cdot (C_6N_2H_{12}) \cdot 2H_2O$ (**1**) were readily grown from aqueous reactions between V_2O_5 and 1,4-diazabicyclo[2.2.2]octane (DABCO). In a typical experiment, a mixture of 0.4044 g of V_2O_5 (Fluka 98.0%) and 0.2492 g of DABCO (Fluka 95.0%) was prepared in 9.00 mL deionized water, giving a molar ratio of 1:1:225. The mixture was stirred vigorously for 30 min at ambient temperature and pressure, before being transferred into an 18 mL Teflon reactor. The reactor was then placed in a 95(±5) °C water bath, covered with a polypropylene cover and located in a domestic microwave oven (Whirlpool XT-25ES/S, 900 W, 2.45 GHz). Although the microwave power can be adjusted to a full range of 100%, reactions were conducted under autogenous pressure using a constant power of 70% (630 W) for varying duration between 1- and 3-h. After the microwave power was switched off, the reaction was cooled down to room temperature in a conventional oven using a cooling rate of 0.5°C/min. Due to the static model of the reactor, the temperature inside the reactor was not measured, and it should be referred to solely by the employed microwave power. The solid products were separated from the supernatant solution by filtration, washed with deionized water and dried in air. Yields of the synthesized solid products were typically *ca.* 60% based on the V_2O_5. Size and habit of the crystals were examined using a field-emission scanning electron microscope (FESEM: JEOL JSM-6335F). In order to study the influence of DABCO on the formation of **1**, the V_2O_5:DABCO molar ratio was varied from 1:0.5 to 1:1.5. The pH of each mixture was measured before and after each reaction using a pH meter (Metrohm Siam Model 744). No attempt to adjust the pH of reaction mixtures prior to synthesis was carried out.

The crystals of **1** were separated under optical microscope from the solid product of the reaction using an equimolar V_2O_5:DABCO ratio and 2 h of microwave heating, and ground for further experiments. Elemental analysis was performed using a Perkin Elmer Series II 2400 CHN/S analyzer. Infrared spectra were collected on a Bruker Tensor 27 FT - IR instrument (4000–400 cm^{-1}, resolution 0.5 cm^{-1}) using a KBr (BDH 98.5%) pellet. The UV spectrum of **1** was collected on a Perkin Elmer UV LAMDA 25 spectrophotometer. The X-ray powder diffraction (XRD) pattern was collected using a Bruker D8 Advance diffractometer, operating with a Ni filtered Cu K_α radiation ($\lambda = 1.540558$ Å, 48 kV and 30 mA).

2.2 X-Ray Crystal Structure Determination

A number of batches of products were examined and apparently crystalline material was present in all of them. Crystals of two morphologies were identified from the reaction using a V_2O_5:DABCO ratio of 1:1; namely hexagonal plates and rhombic bars. A large number of crystals were of examined. The plates were frequently found to be twinned with diffraction images showing the presence of multiple crystallites. Full data sets were collected from two such crystals and afforded moderate quality solutions on account of unresolved twinning. The rhombic bars were not subject to the same accidental twinning and diffraction images did not suggest the presence of multiple crystallites. Data were collected from an orange bar of size 0.1 × 0.05 × 0.05 mm^3 at 150(2) K using a Stöe IPDS2 image plate diffractometer operating with Mo Kα radiation using a single ω—scan. Crystals were cooled using an Oxford Instruments nitrogen gas cryostream. The faces of the crystal were indexed and an analytical absorption correction applied to the data.

Systematic absences in the data suggested one of two orthorhombic space groups, either *Pna2₁* (no. 33, non–centrosymmetric) or *Pnam* (no. 62, centrosymmetric). It was not possible to solve the structure in *Pnam* but routine automatic Direct Methods implemented within SHELXS-93 [17] located all non-hydrogen atoms in the structure in *Pna2₁*. Following completion of the structure by using SHELXL-97 [18], there was no evidence for additional symmetry found by PLATON [19]. The crystal examined was found to be racemically twinned with two roughly equal components, but there was no evidence that the true symmetry of the structure was centrosymmetric. Data were weak but the final refinement converged with excellent R-factors ($R_1 = 0.0431$) with a structure very similar to that obtained from the hexagonal plates. Hydrogen atoms in the organic components were located in final difference Fourier maps. These were placed at geometrically calculated positions. Hydrogen atoms on water and the amine

A3

functionality of the DABCO were placed so as to generate chemically sensible hydrogen bonds where necessary. The balancing of charge suggested the decavanadate unit bears a single proton. The protonation site was determined from Bond Valence Sum (BVS) calculations [20, 21].

3 Results and Discussion

3.1 Microwave—Assisted Crystal Growth and Spectroscopic Characterization

In the synthesis and crystal growth of **1**, microwave heating has been proved to afford crystals suitable for single crystal diffraction experiments, although twinning seems to be common. Non-merohedral twinning may be an inherent drawback. This may be due to the fast mass transport near surface and/or at structural interface associated with the growth of the crystals, which is known to induce disorder to the growth [16]. Variation of the V_2O_5:DABCO molar ratio from 1:0.5 to 1:1.5, which results in slightly different pH—6.44, 6.52 and 6.58 for 1:0.5, 1:1 and 1:1.5, respectively,—evidently led to different phase formation using the same microwave heating time of 3 h. Figure 1 shows the XRD patterns of the solid products synthesized using different V_2O_5:DABCO molar ratio (Fig. 1d–f) in comparison to the simulated pattern of **1** (Fig. 1a). It can be clearly seen that the usage of equimolar V_2O_5:DABCO ratio (Fig. 1d) provides the nearly phase-pure product of **1**. The SEM micrographs of the crystals obtained from this reaction show two crystal habits—hexagonal plates and rhombic bars (Fig. 2a, b), the single crystal experiments, however, reveal the common crystal structure. The deviation of the V_2O_5:DABCO ratio from the equimolar

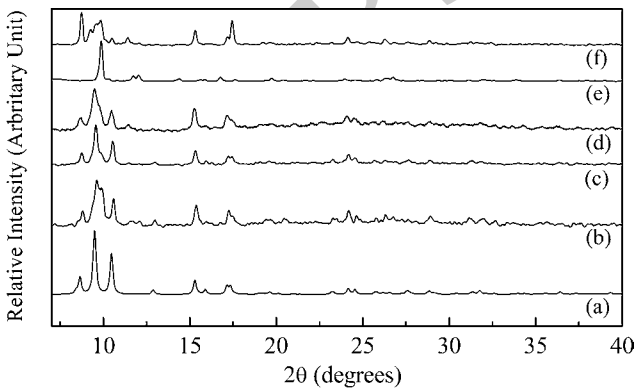

Fig. 1 The powder XRD patterns of the products obtained from the reactions using 1:1 V_2O_5:DABCO but different reaction time—(b) 1 h, (c) 2 h and (d) 3 h—and a constant 3 h of microwave heating but different V_2O_5:DABCO molar ratio—(d) 1:1, (e) 1:0.5 and (f) 1:1.5—in comparison to (a) the simulated pattern of **1**

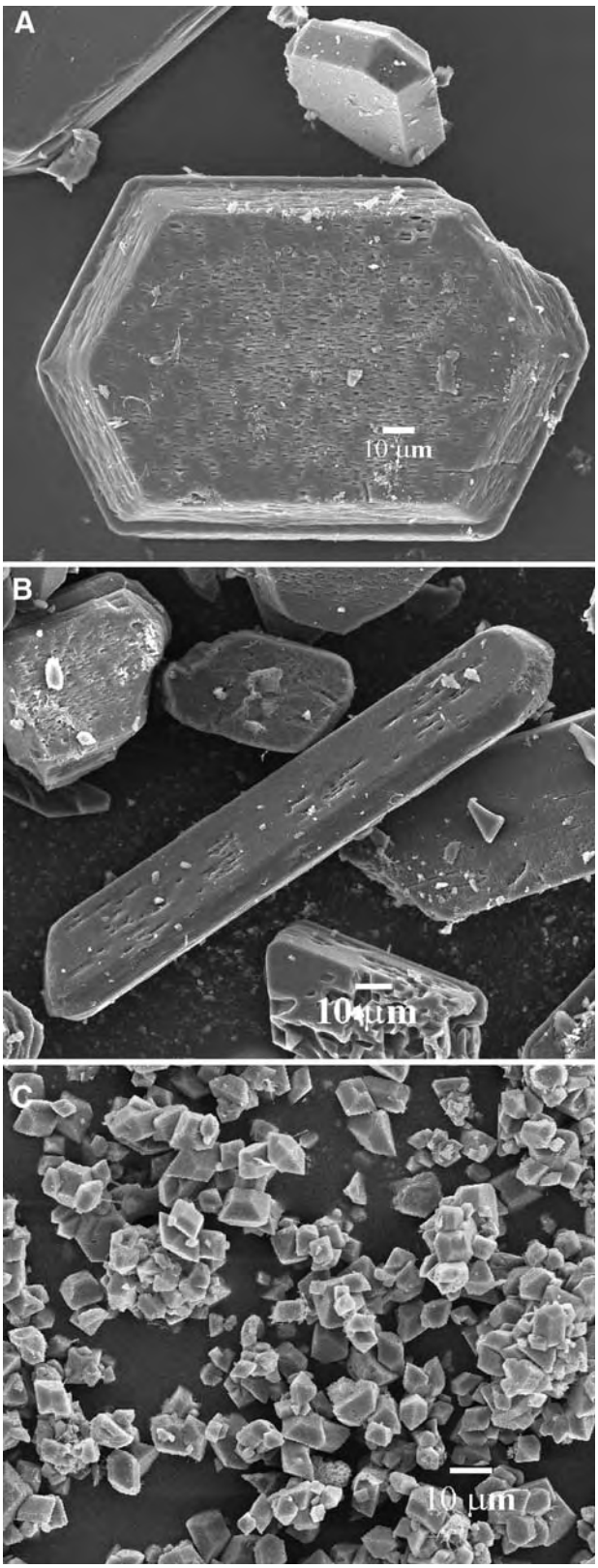

Fig. 2 SEM micrographs showing different crystals habits in the products obtained from the reactions using different V_2O_5:DABCO molar ratios—**a** and **b** 1:1, and **c** 1:1.5

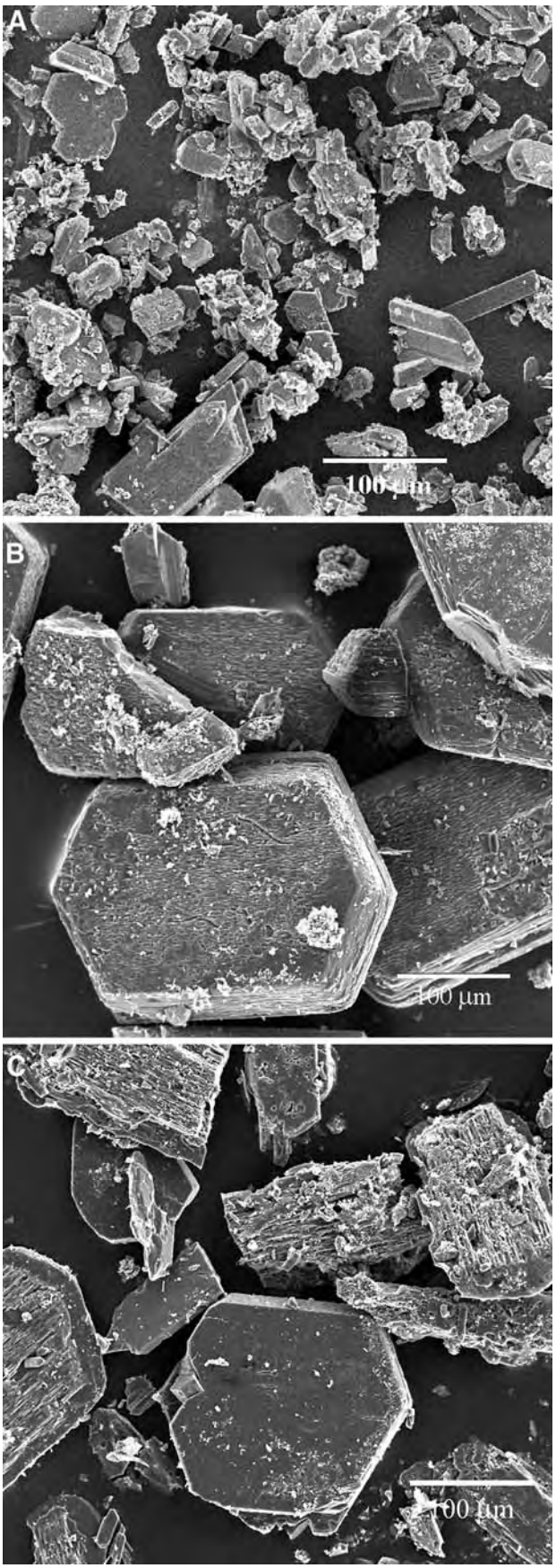

◀ **Fig. 3** SEM micrographs showing different crystals habits and size in the products obtained from the reactions using an equimolar V_2O_5:DABCO molar ratio but different microwave heating time—**a** 1 h, **b** 2 h and **c** 3 h

stoichiometry results in the formation of the totally different phases (Fig. 1e, f) of possibly layer structures. These phases could not be identified due to the insufficient number of the diffraction peaks. The SEM micrographs of the crystals obtained from the reaction using 1:0.5 and 1:1.5 of V_2O_5:DABCO accordingly reveal different crystal habit of truncated octahedra of relatively smaller sizes as illustrated in Fig. 2c.

Based on the XRD result (Fig. 1b–c), a reduction of microwave heating time to 2 h gave similar result of a nearly phase-pure **1.** This indicates the formation of **1** to commence as a dominant phase since the first 2 h of microwave heating. SEM photographs (Fig. 3) reveal the crystals obtained from the reaction employing 2 h of microwave heating to be larger and better quality than those from the 3 h duration synthesis. A reduction of the microwave reaction time to 1 h however resulted in a mixed product of **1** and the other unidentified phase. Sizes

Table 1 Crystallographic data for structural solution and refinement of **1**

CCDC no.	688180
Formula	$[V_{10}O_{27}(OH)] \cdot 2(C_6N_2H_{14}) \cdot (C_6N_2H_{13}) \cdot (C_6N_2H_{12}) \cdot 2H_2O$
Formula weight	1448.18
Crystal size/mm^3	0.1 × 0.05 × 0.05
Crystal system	Orthorhombic
Space group	*Pna2$_1$*
a/Å	20.972(4)
b/Å	10.3380(14)
c/Å	20.432(3)
V_{cell}/Å^3	4429.83(12)
Z	4
ρ_{calc}/gcm^{-3}	2.171
T/K	150(2)
Radiation (λ/Å)	Mo (0.71073)
μ/mm^{-1}	2.117
θ_{min}, θ_{max}	1.94, 26
Total data	8693
Unique data	3451
Parameters no.	665
Restraints no.	272
Goodness of fit	0.643
R(F^2), R_w (all data)	0.1395, 0.0878
R(F^2), R_w($I > 2\sigma(I)$)	0.0431, 0.0674

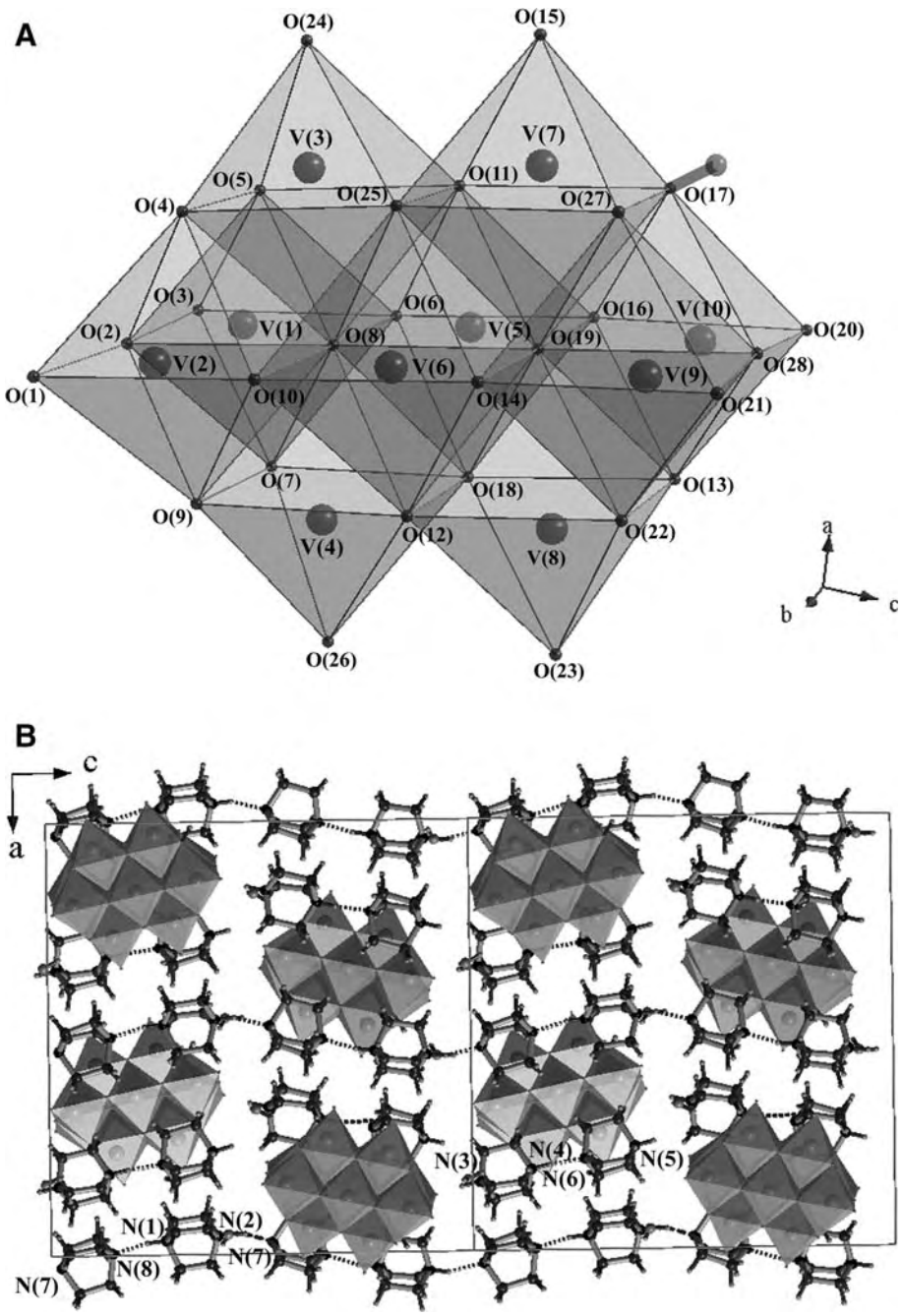

Fig. 4 **a** Polyhedral representation of the decavanadate complex anion and **b** the spatial arrangement of the decavanadate and the DABCO molecules/ions viewed along the *b*-axis

of the obtained crystals were also smaller than the other cases and the morphology was irregular. The single crystal experiments were then conducted on the crystals chosen from the reaction using equimolar stoichiometry of V_2O_5:DABCO and 2 h of microwave heating. A reduction in the synthesis time required for the growth of single crystals of appropriate quality for full structure determination from days or weeks to only a few hours demonstrates the possible advantage of microwave synthesis. The current study indicates the induced kinetic enhancement in the growth of single crystals of new compounds in an inorganic—organic hybrid system. The phase purity, crystal quality and crystal size depend, however, on both the reagent stoichiometry and microwave heating time.

The UV spectrum of **1** exhibited an intense and broad peak at 204-227 nm, which can be ascribed to the O → V charge transfer band, and in accordance with the existence of the decavanadate monomer. The elemental analysis shows an acceptable agreement between the experimental and the calculated figures: element, %calc. (%found): C, 19.89(20.19(5)); N, 7.73 (6.97(7)). The FT-IR spectrum also affirms the presence of the functionalities in **1** (frequency assignment, cm^{-1}): ν(N–H), 3436 s; ν(C–H), 3015 m; δ_{as}(N–H), 1616 m; δ(C–H), 1466 m; δ_s(N–H),

1338 m; ν(C–N), 1056 m; ν_s(V–O_T), 956vs; ν_{as}(V–O_T), 835vs; ν_s(V–O_b–V), 750 s; ν_{as}(V–O_b–V), 619 s.

3.2 Crystal Structure Determination of **1**

The structure of **1** determined by single crystal diffraction has the empirical formula, $[V_{10}O_{27}(OH)] \cdot 2(C_6N_2H_{14}) \cdot (C_6N_2H_{13}) \cdot (C_6N_2H_{12}) \cdot 2H_2O$, and is built up from the following building units: a monoprotonated decavanadate cation $[V_{10}O_{27}(OH)]^{5-}$, two water molecules, and three different types of the organic moieties, including two diprotonated H_2DABCO^{2+}, a monoprotonated $HDABCO^{+}$ and a neutral DABCO molecule. Crystal data for **1** are summarized in Table 1. The decavanadate anion comprises ten crystallographically distinct vanadium atoms. These all adopt a distorted coordination octahedral geometry (Fig. 4a), which are connected *via* edge-sharing. Four distinct types of oxygen coordination are present; these can be classified as the bridging μ6-O (O8, O19), μ3-O (O11, O12, O18, O25), μ2-O (O2, O4, O5, O6, O7, O9, O10, O13, O14, O16, O17, O22, O27, O28) and the terminal oxygen O_T (O1, O3, O15, O20, O21, O23, O24, O26) [8]. The bond lengths and angles found in the decavanadate anion are in good accordance with those found in previously reported decavanadate structures [10–12]. The BVS calculations based on the refined bond lengths listed in Table 2 suggest the pentavalence of vanadium, V^V, and the under-bonded character of O17 (BVS = 1.35) is indicative of the protonation site. Table 3 summarizes the calculated BVS results. The location of a single proton determined by BVS calculations corresponds well with the slight acidity of the reaction mixture promoting the protonation and a known tendency of the decavanadate-to-oxygen atom basicity where μ2-O and μ3-O are the most probable atoms to be protonated [8]. The existence of the protonation is also supported by the formation of the hydrogen bonding network in **1**, which is discussed later in detail. The monoprotonated decavanadate, $\left[V^V_{10}O_{27}(OH)\right]^{5-}$, is accordingly composed of two $[V(\mu2\text{-O})_2(\mu3\text{-O})_2(\mu6\text{-O})_2]$ (V5, V6), four $[VO_T(\mu2\text{-O})_2(\mu3\text{-O})_2(\mu6\text{-O})]$ (V3, V4, V7, V8) and four $[VO_T(\mu2\text{-O})_4(\mu6\text{-O})]$ (V1, V2, V9, V10). The existence of only the fully oxidized V^V suggests that under the conditions employed DABCO is stable. This is intriguing because the reactions between V_2O_5 and organodiamines, including

Table 2 Selected bond lengths (Å) with their standard deviations in brackets for **1**

O1–V2	1.589(10)	O15–V7	1.582(9)	C3–C4	1.561(15)
O2–V1	1.829(10)	O16–V5	1.704(9)	C4–N1	1.469(16)
O2–V2	1.838(10)	O16–V10	1.986(9)	C5–N1	1.488(16)
O3–V1	1.605(9)	O21–V9	1.595(8)	C5–C6	1.512(15)
O4–V3	1.828(9)	O22–V8	1.812(9)	C6–N2	1.477(15)
O4–V2	1.880(9)	O22–V9	1.819(9)	C31–N3	1.509(17)
O5–V3	1.802(9)	O23–V8	1.586(9)	C31–C32	1.547(14)
O5–V1	1.846(8)	O24–V3	1.575(9)	C32–N4	1.483(15)
O6–V5	1.670(8)	O25–V7	1.931(9)	C33–N4	1.488(16)
O6–V1	2.082(8)	O25–V6	1.926(10)	C33–C34	1.548(14)
O7–V4	1.805(9)	O25–V3	2.029(9)	C34–N3	1.467(15)
O7–V1	1.902(9)	O26–V4	1.576(9)	C35–N3	1.469(16)
O8–V5	2.086(10)	O27–V7	1.851(9)	C35–C36	1.540(15)
O8–V6	2.093(10)	O27–V9	1.933(9)	C36–N4	1.469(16)
O8–V3	2.237(9)	O28–V9	1.844(9)	C55—N6	1.472(15)
O8–V4	2.251(9)	O28–V10	1.854(9)	C55–C56	1.527(15)
O8—V1	2.351(9)	O17–V7	1.916(9)	C51–N5	1.473(15)
O8–V2	2.344(9)	O17–V10	1.984(9)	C51–C52	1.544(15)
O9–V4	1.812(8)	O18–V5	1.930(1)	C52–N6	1.478(16)
O9–V2	1.840(9)	O18–V8	1.960(9)	C53–N6	1.487(16)
O10–V6	1.688(9)	O18–V4	2.017(8)	C53–C54	1.544(15)
O10–V2	2.038(9)	O19–V6	2.115(11)	C54–N5	1.501(17)
O11–V5	1.915(9)	O19–V5	2.135(10)	C56–N5	1.510(16)
O11–V7	1.988(8)	O19–V7	2.263(10)	C71–N7	1.482(15)
O11–V3	2.015(8)	O19–V8	2.241(10)	C71–C72	1.540(16)
O12–V6	1.929(9)	O19–V9	2.281(10)	C72–N8	1.484(16)
O12–V8	1.940(9)	O19–V10	2.307(10)	C73–N8	1.447(18)
O12–V4	2.023(9)	O20–V10	1.601(10)	C73–C74	1.577(17)
O13–V10	1.783(10)	C1–N1	1.495(17)	C74–N7	1.457(16)
O13–V8	1.885(9)	C1–C2	1.532(15)	C75–C76	1.549(15)
O14–V6	1.696(8)	C2–N2	1.495(15)	C75–N7	1.493(16)
O14–V9	2.034(9)	C3–N2	1.445(15)	C76–N8	1.483(16)

Table 3 Calculated BVS for vanadium and oxygen atoms involving decavanadate anion

Atom	BVS	Atom	BVS
V1	4.99	V6	5.02
V2	5.17	V7	5.03
V3	5.21	V8	5.23
V4	5.23	V9	5.12
V5	5.06	V10	5.13
μ2-O2	1.84	μ6-O8	1.99
μ2-O4	1.75	μ6-O19	1.96
μ2-O5	1.89	μ3-O11	1.91
μ2-O6	1.90	μ3-O12	1.95
μ2-O7	1.76	μ3-O18	1.92
μ2-O9	1.88	μ3-O25	1.97
μ2-O10	1.89	$O1_T$	1.78
μ2-O13	1.86	$O3_T$	1.71
μ2-O14	1.87	$O15_T$	1.82
μ2-O16	1.92	$O20_T$	1.73
μ2-O17	1.35	$O21_T$	1.75
μ2-O22	1.93	$O23_T$	1.78
μ2-O27	1.58	$O24_T$	1.85
μ2-O28	1.77	$O26_T$	1.85

Table 4 Distances (Å) and angles (°) involving hydrogen bonds for **1**

D	A	H···A	D···A	∠D–H··A
N1	N8	1.76	2.682(12)	170
O1w	O20	2.24(8)	2.963(14)	152(8)
N2	N7#2	1.84	2.729(13)	160
O1w	O7#7	2.09(9)	2.855(12)	147(9)
O1w	O9#7	2.53(9)	3.263(12)	142(8)
N3	O28#5	1.76	2.657(12)	161
O2w	O4	2.14(5)	2.910(13)	146(8)
N4	N6	1.72	2.649(12)	176
O2w	O27#8	2.21(9)	2.960(14)	139(7)
N5	O1w	2.19	2.938(13)	137
N5	O2#7	2.13	2.818(12)	129
O17	O2w#1	2.11(9)	2.926(13)	177(11)
C1	O27#3	2.50	3.328(16)	140
C1	O23#4	2.42	3.102(17)	125
C2	O23#4	2.46	3.108(15)	123
C2	O21#3	2.36	3.223(15)	145
C3	O21#3	2.38	3.219(16)	142
C3	O20	2.49	3.268(16)	135
C4	O17	2.44	3.207(17)	134
C4	O14#3	2.41	3.358(17)	159
C5	O23#4	2.59	3.199(15)	119
C5	O15	2.57	3.544(15)	169
C6	O23#4	2.42	3.121(15)	127
C31	O1#3	2.50	3.174(16)	125
C31	O3	2.49	3.222(17)	131
C32	O6	2.43	3.363(15)	157
C32	O9#3	2.49	3.274(15)	136
C33	O24#6	2.50	3.156(17)	123
C33	O7	2.44	3.296(16)	144
C34	O3	2.38	3.222(15)	143
C34	O24#6	2.43	3.079(15)	123
C35	O24#6	2.30	3.056(16)	132
C35	O20#5	2.56	3.278(15)	129
C36	O26#3	2.56	3.516(15)	163
C55	O23#3	2.56	3.299(16)	131
C51	O16	2.57	3.277(16)	128
C51	O20	2.49	3.422(16)	156
C51	O22#3	2.47	3.287(16)	139
C52	O12#3	2.45	3.412(16)	163
C52	O16	2.47	3.199(17)	130
C53	O16	2.53	3.352(17)	140
C53	O15#6	2.56	3.414(17)	144
C54	O2w#7	2.57	3.521(18)	160
C56	O22#3	2.51	3.380(15)	146
C56	O23#3	2.54	3.261(15)	129
C71	O5	2.55	3.435(16)	148
C72	O24	2.59	3.366(16)	135
C73	O10#3	2.51	3.239(18)	130
C73	O11	2.47	3.443(17)	168
C74	O5	2.52	3.317(16)	138
C74	O1#3	2.43	3.374(16)	158
C74	O10#3	2.59	3.307(16)	129
C75	O4#3	2.55	3.436(16)	149
C76	O26#4	2.55	3.411(15)	146

Symmetry codes: *#1* −x, 2−y, 1/2 + z ; *#2* −x, 1−y, 1/2 + z; *#3* x, −1 + y, z; *#4* −1/2 + x, 3/2-y, z; *#5* 1/2−x, −1/2 + y, −1/2 + z; *#6* 1/2 + x, 3/2−y, z; *#7* 1/2−x, −1/2 + y, 1/2 + z; *#8* −x, 2−y, −1/2 + z

DABCO, under solvothermal conditions generally result in a partial reduction of V^{V}–V^{IV} and, therefore, a degree of mixed valence states in the final structures. Each decavanadate anion is surrounded by organic moieties and water molecules and shows no direct contact with the same species (Fig. 4b). It can therefore be flagged as a monomer according to the classification of the decavanadate network structures proposed by J.L. Ferreira da Silva [8]. This agrees well with the assumption that approximately spherical organic molecules, DABCO in this case, promote the monomer function of the decavanadate in the formation of organic–inorganic supramolecular assemblies [8, 10].

Regarding the organic building units in **1**, there are two distinct pairs of H_2DABCO^{2+}-$HDABCO^{+}$ and H_2DABCO^{2+}-DABCO units in the asymmetric unit (Fig. 4b). The significantly short intermolecular N···N distances—N1···N8 2.65(2) Å, N2···N7 2.67(2) Å and N4···N6 2.64(2) Å—are an indication of the presence of hydrogen atoms and hence hydrogen bonds between each pair of these DABCO molecules [22]. Each H_2DABCO^{2+}-$HDABCO^{+}$ hydrogen—bonded pair forms an isolated unit, whereas the H_2DABCO^{2+}-DABCO pairs are arranged in a fashion that leads to an infinite H-DABCO-H···DABCO···H-DABCO-H···DABCO··· hydrogen—bonded sinusoidal chain, each of which is aligned along the *c*-axis. According to the hydrogen bonding analysis results conducted using PLATON, there are both conventional and weak hydrogen bonds established between these building units as summarized in Table 4 and illustrated in Fig. 5. The large number of the otherwise weak hydrogen bonds is not common and should be noted. These weak interactions help enforce the spatial arrangement of the organic building units in the network and, therefore, impart a distinct influence on the supramolecular organization in addition to the stronger hydrogen—bonding and electrostatic interactions. The single proton attached to the decavanadate forms a classical hydrogen bond with the water oxygen atom, which acts as the hydrogen—bond acceptor (O17···O2w 2.926(13) Å, ∠O17–H···O2w 177(11)°). The

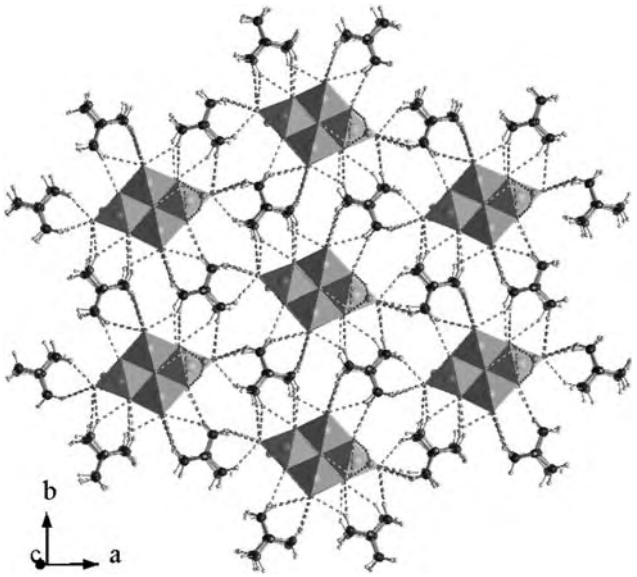

Fig. 5 The abundance of the hydrogen bonding interactions (*dotted lines*) between the supramolecular assemblies building units, viewed along the *c*-axis

formation of this hydrogen bond supports the choice of protonation site suggested by BVS calculations. The impact of the electrostatic interactions undoubtedly results in the dense network of **1**, which is characteristic of an ionic structure. Therefore, the electrostatic and hydrogen bonding interactions are synergistically responsible for the observed dense supramolecular assemblies in **1**.

4 Conclusion

Microwave heating has been successfully applied to the synthesis and growth of single crystals in a very short reaction time of a new three-dimensional hydrogen bond-assisted organic–inorganic supramolecular assembly based on decavanadate and DABCO. Single crystals suitable for complete structural characterization can be produced although twinning seems to be an inherent problem due to the fast mass transport induced by microwave heating. The nature of the crystalline product in the V_2O_5—DABCO—water system depends on the initial V_2O_5:DABCO ratio and microwave heating time; to generate single crystals of **1**, an equimolar mixture of reactants and a few hours of microwave heating is required. The single crystal experiment reveals the importance of both the abundant hydrogen bonds and the stronger electrostatic interactions in regulating the architecture of the assembly. The hydrogen bonding on the other hand is governed by the number and spatial orientation of protonation on the structural building units.

5 Supplementary Material

Crystallographic data (excluding structure factors) for structure **1** has been deposited with the Cambridge Crystallographic Data Centre (deposition numbers: CCDC 688180). Copies of this information may be obtained free of charge from The Director, CCDC, 12 Union Road, Cambridge CB2 1EZ, UK (fax: +44 1223 336033; e-mail: deposit@ccdc.cam.ac.uk).

Acknowledgments The Thailand Research Fund, the Thailand Toray Science Foundation and the Center of Excellence for Innovation in Chemistry are acknowledged for financial support. B. Yotnoi thanks to the Royal Golden Jubilee Ph.D Program and the Graduate School of Chiang Mai University for Graduate Scholarship.

References

1. D.E. Katsoulis, Chem. Rev. **98**, 359 (1998)
2. N. Mizuno, M. Misono, Chem. Rev. **98**, 199 (1998)
3. M. Aureliano, J. Inorg. Bio. **80**, 141 (2000)
4. M. Aureliano, R.M.C. Gandara, J. Inorg. Bio. **99**, 979 (2005)
5. L.J. Csányi, K. Jákya, G. Dombi, F. Evanics, G. Dezso, Z. Kóta, J. Mol. Catal. A: Chem. **195**, 101 (2003)
6. S.S. Soares, H. Martins, R.O. Duarte, J.J.G. Moura, J. Coucelo, C. Gutiérrez-Merino, M. Aureliano, J. Inorg. Bio. **101**, 80 (2007)
7. D.C. Crans, B. Baruah, N.E. Levinger, Biomed. Pharmacother. **60**, 174 (2006)
8. J.L. Ferreira da Silva, M.F. Minas da Piedade, M.T. Duarte, Inorg. Chim. Acta **356**, 222 (2003)
9. H. Kumagai, M. Arishima, S. Kitagawa, K. Ymada, S. Kawata, S. Kaizaki, Inorg. Chem. **41**, 1989 (2002)
10. I. Correia, F. Avecilla, S. Marcao, J.C. Pessoa, Inorg. Chim. Acta **357**, 4476 (2004)
11. K. Pavani, S. Upreti, A. Ramanan, J. Chem. Sci. **118**, 159 (2006)
12. D. Wang, W. Zhang, K. Gruning, D. Rehder, J. Mol. Struct. **656**, 79 (2003)
13. C.O. Kappe, Angew. Chem. Int. Ed. **43**, 6284 (2004)
14. S. Shi, J.-Y. Hwang, J. Mineral Mater. Charac. Eng. **2**, 101 (2003)
15. D.E. Clark, W.H. Sutton, Annu. Rev. Mater. Sci. **26**, 299 (1996)
16. J.H. Boosk, R.F. Cooper, S.A. Freeman, Mat. Res. Innovat. **1**, 77 (1997)
17. G.M. Sheldrick, *SHELEXS-93: A Program for Sloving Crystal Structure* (University of Goettingen, Germany, 1993)
18. G.M. Sheldrick, in *SHELEXL-97: a program for crystal structure refinement* (University of Goettingen, Germany, 1997) Release 97–2
19. A.L. Spek, *A preliminary Introduction to the PLATON Program* (Utrecht, Netherlands, 1997)
20. V.S. Urusov, I.P. Orlov, Cryst. Rep. **44**, 686 (1999)
21. I.D. Brown, *The Chemical Bond in Inorganic Chemistry: The Bond Valence Model* (Oxford University Press, Oxford, 2002)
22. T. Akutagawa, S. Takeda, T. Hasegawa, T. Nakamura, J. Am. Chem. Soc. **126**, 291 (2004)

J Chem Crystallogr (2009) 39:525–529
DOI 10.1007/s10870-009-9529-9

A9

ORIGINAL PAPER

Preparation and Characterization of Bis(μ-1,2-diaminoethane)cobalt(II) Hexavanadate: A Layered Polyoxovanadate Pillared by a Cobalt Coordination Complex

Bunlawee Yotnoi · Jumras Limtrakul · Timothy Prior · Apinpus Rujiwatra

Received: 7 October 2008 / Accepted: 17 February 2009 / Published online: 26 February 2009

Abstract The first example of polyoxovanadate layered framework with a cobalt coordination complex as a pillaring unit, $Co^{II}(\mu\text{-}C_2N_2H_8)_2[V^{IV}_4V^{V}_2O_{14}]$, was readily synthesized under hydrothermal conditions. The structure can be solved and refined in monoclinic $P2_1/n$ with $a = 9.143(3)$ Å, $b = 6.5034(11)$ Å, $c = 15.874(4)$ Å, $\beta = 101.90(2)$, $V = 923.6(4)$ Å^3 and $Z = 2$. The crystal structure comprises two-dimensional $\{V^{IV}_4V^{V}_2O_{14}\}^{2-}$ layers extending parallel to [101], constructed from tetrahedral $\{V^{V}O_4\}$ and square pyramidal $\{V^{IV}O_5\}$ building units. Adjacent layers are linked through the octahedral $\{Co^{II}O_2(\mu\text{-}C_2N_2H_8)_2\}$ pillars, within which the Co^{II} resides on an inversion center. The structure displays N–H···O and C–H···O hydrogen bonding between the ethylenediamine and vanadium oxide layers.

Keywords Polyoxovanadate · Cobalt · Pillaring · Ethylenediamine · Crystal structure · Hydrothermal synthesis

Introduction

Polyoxovanadate frameworks (POVs) have been capturing broad interest from materials chemists primarily because of their technological potential, e.g., as oxidative catalysts and secondary cathode materials for advanced lithium batteries [1, 2]. The inherent ability of vanadium atom to adopt various coordination geometries and oxidation states while being a good electron-acceptor and electron relay-station is also a driving force for the research in the field [3, 4]. Current interest regarding the preparation of POVs focuses on the introduction of a secondary metal, particularly a transition metal to the coordinate covalent POV frameworks. Cobalt is unique in its coordination chemistry, redox activity and potential magnetic functionality, and therefore has been one of the most studied secondary metals. Although there are earlier reports on the successful introduction of cobalt into POV frameworks (Co-POV) e.g. $[Co(2,2'\text{-bpy})_2]_2[As_8VO_{42}(H_2O)].H_2O$ [5], $[Co(en)_2(H_2O)]\{[Co(en)_2]_2As_8V_{14}O_{42}(SO_4)\}.3H_2O$ [6], $[Co(Hdpa)_2V_4O_{12}]$ [7], $Co_2(4,4'\text{-bipy})_2(V_4O_{12})$ [8] and $\{[H_2(en)]Co(ox)(V_4O_{12})\}_n$ [9], none of these are the Co-POV structures in which the cobalt present as a pillaring unit. Examples of POV frameworks where the secondary metal present acts as a pillar motif between POV sheets are rare, and limited to $(C_2N_2H_8)_2Zn[V_6O_{14}]$, $(C_2N_2H_8)_2Cu[V_6O_{14}]$, $[Ni(C_2N_2H_8)_2]_{0.5}[V_3O_7]$ and $[Ni(en\text{-}Me)_2]_{0.5}[H_2enMe]_{0.5}[V_6O_{14}]$ [10, 11]. Here, we report the preparation and crystal structure of $Co^{II}(\mu\text{-}C_2N_2H_8)_2[V^{IV}_4V^{V}_2O_{14}]$, which is the first example of a layered POV pillared by cobalt.

Experimental

Crystals of $Co^{II}(\mu\text{-}C_2N_2H_8)_2[V^{IV}_4V^{V}_2O_{14}]$ (**I**) were readily prepared from a reaction between $Co(NO_3)_2 \cdot 6H_2O$ (98% Aldrich, 0.1006 g), V_2O_5 (99% Fluka, 0.2519 g) and ethylenediamine (99% Fluka, 0.0719 g) in deionized water (2.80 cm^3) using a 17 cm^3 Teflon container. The reaction

B. Yotnoi · A. Rujiwatra (✉)
Inorganic Materials Research Unit, Department of Chemistry, Faculty of Science, Chiang Mai University, Chiang Mai 50200, Thailand
e-mail: apinpus@chiangmai.ac.th

J. Limtrakul
Department of Chemistry, Faculty of Science, Kasetsart University, Bangkok 10900, Thailand

T. Prior
Department of Chemistry, University of Hull, Kingston upon Hull HU6 7RX, UK

was conducted under autogenous pressure at 473 K for 60 h before being cooled down to room temperature using a rather rapid rate of 30 K h^{-1}. Black crystals of **I** were then separated from the supernatant solution by filtration, washed with deionized water and dried in air. The elemental composition in **I** was determined using the energy dispersive X-ray spectroscopic (EDS) microanalyzer present on the scanning electron microscope (FESEM, JEOL JSM-6335F) and a Perkin Elmer Series II 2400 CHN/S analyzer. Infrared spectra of also the ground crystals were collected on a Bruker Tensor 27 FT-IR instrument (4,000–400 cm^{-1}, resolution 0.5 cm^{-1}) using a KBr (BDH 98.5%) pellet. The X-ray powder diffraction (XRD) pattern was collected using a Bruker D8 Advance diffractometer, operating with a Ni filtered Cu K_α radiation (λ = 1.5405 Å, 48 kV and 30 mA).

In order to determine the crystal structure of **I**, a full set of intensity data was collected on a single crystal of size 0.20 × 0.04 × 0.04 mm^3 at 150(2) K using a Stoe IPDS2 image plate diffractometer operating with Mo Kα radiation, employing a single ω-scan. The crystal was cooled using an Oxford Instruments nitrogen gas cryostream. The collected data were analytically corrected for absorption using the Tompa method [12]. The structure was then solved by direct methods implemented within SHELXS-97 [13] and full-matrix least squares refinement carried out within SHELXL-97 [14] via the WinGX [15] program interface. All non-hydrogen atoms were located from direct and difference Fourier maps and refined anisotropically. The hydrogen atoms in the ethylenediamine were apparent from final difference Fourier maps, and were then placed and refined using a riding model with the following bond lengths: C–H 0.99(3) Å; N–H 0.92(3) Å. Details of the data collection and structure refinements are summarized in Table 1.

Table 1 Crystallographic data for structural solution and refinement of **I**

CCDC no.	704646
Formula	$Co(C_2N_2H_8)_2[V_4^{IV}\ V_2^{V}O_{14}]$
Formula weight	708.78
Crystal size/mm	0.20 × 0.04 × 0.04
Crystal system	Monoclinic
Space group	$P2_1/n$
a (Å)	9.143(3)
b (Å)	6.5034(11)
c (Å)	15.874(4)
β (°)	101.90(2)
V_{cell} (Å^3)	923.6(4)
Z	2
ρ_{calc} (g cm^{-3})	2.549
T (K)	150(2)
Radiation (λ/Å)	Mo K_α(0.71069)
μ (mm^{-1})	3.854
θ_{min}, θ_{max}	2.85, 26.00
Unique data	1,799
Observed data	1,071
Parameters no.	134
Restrains no.	4
Goodness of fit	0.840
R, Rw (all data)	0.0853, 0.0730
R, Rw ($I > 2\sigma(I)$)	0.0399, 0.0652

CCDC 704646 contains the supplementary crystallographic data for this paper. These data can be obtained free of charge by e-mailing to data_request@ccdc.cam.ac.uk, or by contacting The Cambridge Crystallographic Data Centre 12 Union Road Cambridge CB2 1EZ, UK, fax: +44-1223-336033

Results and Discussion

The crystal structure of $Co^{II}(\mu\text{-}C_2N_2H_8)_2[V_4^{IV}V_2^{V}O_{14}]$ (**I**) was successfully solved and refined in the monoclinic space group $P2_1/n$ with the final refined cell parameters a = 9.143(3) Å, b = 6.5034(11) Å, c = 15.874(4) Å, β = 101.90(2)° and V = 923.6(4) Å^3. The ORTEP plot of the extended asymmetric unit showing the coordination environments of the structural building motifs and atomic numbering scheme is shown in Fig. 1. The atomic coordinates and equivalent isotropic displacement parameters are listed in Table 2. There are three crystallographically distinct sites of vanadium. The bond valence calculations based on a single point energy model [16], and refined bond distances listed in Table 3 suggest the presence of both pentavalent vanadium (V_1) and tetravalent vanadium (V_2, V_3). Although the starting vanadium source is V_2O_5, the mild reducing power of the organic component results in the mixed V^{IV}/V^{V} structure. The tetravalent V_2 and V_3 are characterized by square pyramidal geometry, $\{V^{IV}O_5\}_{sq}$, of 4 + 1 type, each of which shows four long equatorial bonds—V_2–O_2, V_2–O_3, V_2–O_6, V_3–O_2, V_3–O_3, V_3–O_5 and V_3–O_6 in range 1.894(4)–2.017(4) Å with an average of 1.958(4) Å and one short vanadyl bond—$V_2 = O_4$ (1.609(5) Å) and $V_3 = O_7$ (1.616(5) Å). The pentavalent V_1 on the other hand shows a 3 + 1 tetrahedral coordination, $\{V^{V}O_4\}_{tet}$, of which the bond lengths of the bridging V_1–O_2 (1.821(4) Å), V_1–O_5 (1.695(4) Å) and V_1–O_6 (1.792(4) Å) bonds are longer than the terminal V_1–O_1 (1.599(5) Å) bond. The distortion of the $\{V^{V}O_4\}_{tet}$ from the regular tetrahedron is apparent. The interatomic distances involving with the triply bridging oxygen, i.e. μ_3–O_2 and μ_3–O_6, are significantly longer than that of the doubly bridging oxygen, i.e. μ_2–O_5. The correlation between the refined bond distances and their corresponding polyhedral configurations agree well with the previously

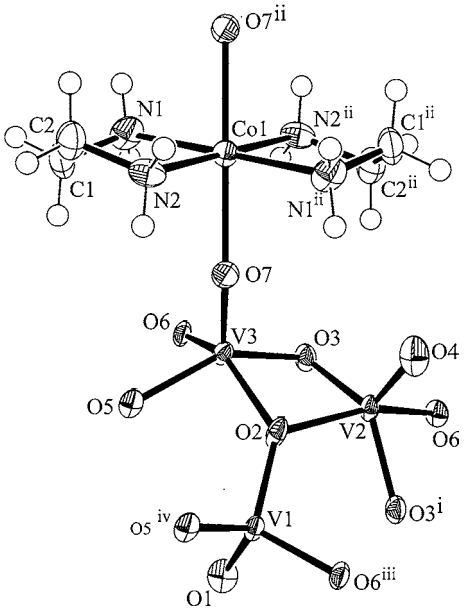

Fig 1 An ORTEP view of the extended asymmetric unit of I drawn at 80% probability level with hydrogen atoms omitted for clarity. [Symmetry codes: (i) $-x, -y + 2, -z$; (ii) $x, y + 1, z$; (iii) $-x + 1/2, y + 1/2, -z + 1/2$; (iv) $-x + 1, -y + 1, -z$]

Table 2 Atomic coordinates and equivalent isotropic displacement parameters of non-hydrogen atoms

	x	*y*	*z*	*Ueq*
V_1	0.04285(11)	1.21858(15)	0.09298(6)	0.0112(2)
V_2	0.32600(11)	1.00000(15)	0.23310(6)	0.0120(2)
V_3	0.19319(11)	0.71902(15)	0.10076(6)	0.0116(2)
O_1	−0.1016(5)	1.1633(6)	0.1306(3)	0.0195(10)
O_2	0.1848(5)	1.0192(6)	0.1188(2)	0.0147(9)
O_3	0.2778(4)	0.7166(6)	0.2232(3)	0.0149(9)
O_4	0.4825(5)	1.0572(6)	0.2077(3)	0.0236(11)
O_5	0.0077(5)	0.7489(5)	0.0151(2)	0.0144(9)
O_6	0.1161(4)	0.4589(6)	0.1384(2)	0.0133(9)
O_7	0.3237(5)	0.6607(6)	0.0501(3)	0.0184(10)
Co_1	0.50000	0.50000	0.00000	0.0140(3)
N_1	0.3691(6)	0.2363(8)	−0.0417(3)	0.0228(13)
N_2	0.3993(6)	0.6049(8)	−0.1210(4)	0.0189(12)
C_1	0.2589(7)	0.2940(11)	−0.1201(4)	0.0239(16)
C_2	0.3322(8)	0.4276(10)	−0.1741(4)	0.0242(17)

reported POV layer frameworks of the same composition and registry, e.g. $[V_6O_{14}](C_4H_{14}N_2)$, $[V_6O_{14}](C_5H_{16}N_2)$, $(C_2N_2H_8)_2Zn[V_6O_{14}]$ and $(C_2N_2H_8)_2Cu[V_6O_{14}]$ [10, 17].

Two adjacent $\{V^{IV}O_5\}_{sq}$ units share edges in a *trans* conformation to form a larger binuclear $\{V_2^{IV}O_8\}$ unit, which is then fused through *cis* edge sharing to the neighboring binuclear units to generate the {UuDd} or {Z} chain with a zigzag configuration as shown in Fig. 2. Each chain is connected to the adjacent chains by the $\{V^{V}O_4\}_{tet}$,

Table 3 Selected bond distances for **I**

V_1–O_1	1.599(5)	V_3–O_5	1.953(4)
V_1–O_5^{I}	1.695(4)	V_3–O_6	1.972(4)
V_1–O_6^{II}	1.792(4)	V_3–O_2	1.976(4)
V_1–O_2	1.821(4)	Co_1–O_7	2.202(5)
V_2–O_4	1.609(5)	Co_1–N_2^{IV}	2.067(5)
V_2–O_3	1.894(4)	Co_1–N_2	2.067(5)
V_2–O_3^{III}	1.908(4)	Co_1–N_1	2.118(5)
V_2–O_2	2.002(4)	Co_1–N_1^{IV}	2.118(5)
V_2–O_6^{III}	2.017(4)	N_1–C_1	1.479(8)
V_3–O_7	1.616(5)	N_2–C_2	1.484(8)
V_3–O_3	1.938(4)	C_1–C_2	1.475(10)

Symmetry codes: (i) $-x, -y + 2, -z$; (ii) $x, y + 1, z$; (iii) $-x + 1/2, y + 1/2, -z + 1/2$; (iv) $-x + 1, -y + 1, -z$

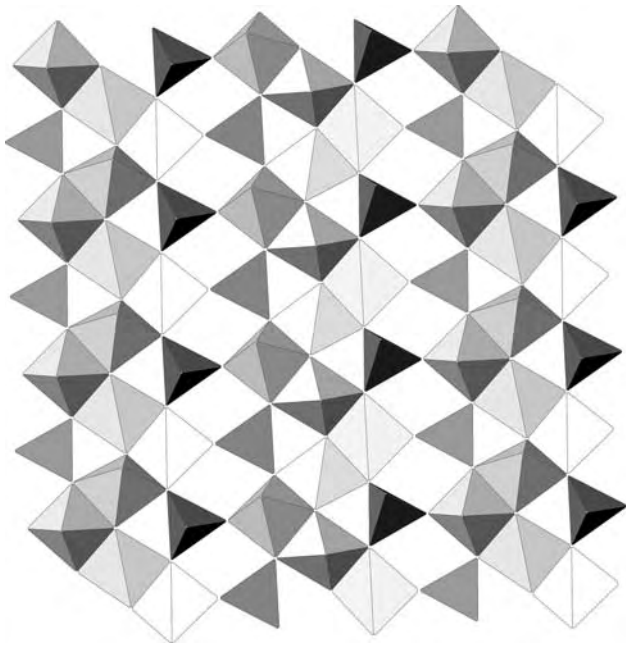

Fig 2 A polyhedral view of the ({UuDd}:T.) β-POV layer in **I**

each of which share two basal corners with one chain and the other basal corner with the other chain. This results in a mixed valence $[V_4^{IV}O_{10}V_2^{V}O_4]^{2-}$ anionic layer of ({UuDd}:T.)β type in SP + T class and Z-T subclass [18]. These anionic POV layers extend parallel to the [101], and are linked further by the octahedral $\{Co^{II}O_2\,(C_2N_2H_8)_2\}$ pillars via the two *trans* apical O_7 atoms of the $\{V^{IV}O_5\}_{sq}$ from two adjacent layers to generate a three-dimensional pillared Co-POV structure (Fig. 3), which is isostructural with the zinc, copper and nickel analogues, $(C_2N_2H_8)_2Zn[V_6O_{14}]$, $(C_2N_2H_8)_2Cu[V_6O_{14}]$ and $[Ni(C_3N_2H_{11})_2]_{0.5}[C_3N_2H_{13}]_{0.5}[V_6O_{14}]$ [10, 11]. This implies the template function of the ethylenediamine and therefore the feasibility in crystal engineering of other analogous pillared structures. The pseudo-octahedral coordination of the cobalt is completed

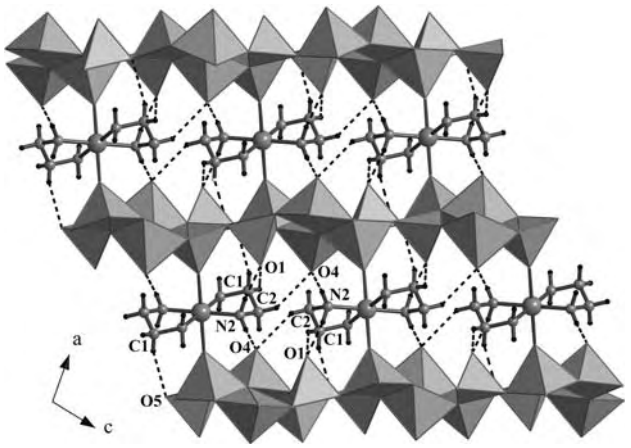

Fig 3 View of the three-dimensional structure of **I** with hydrogen bonds shown in *dotted lines*

by four nitrogen atoms from two *trans* ethylenediamine ligands, locating about the inversion center at the cobalt atom. The bond valence calculations suggested the divalent state of the cobalt and therefore a dipositively charged $\{Co^{II}O_2(C_2N_2H_8)_2\}$ pillar, which consequently balances the negatively charged POV layer. **I** is similar in some respects to the framework $[\{Co(pyz)\}(V_2O_5)_2]$, pyz = pyrazine [19], which has been reported recently. In **I** the layers are linked by discrete $Co(en)_2^{2+}$ units, but in $[\{Co(pyz)\}(V_2O_5)_2]$ layers are linked by a series of 1-D chains of formulation $Co(pyz)^2$. However, a different POV layer of type 2({UUDD}) is present within $[\{Co(pyz)\}(V_2O_5)_2]$.

The analysis of hydrogen bonding interactions as listed in Table 4 suggests the spatial arrangement of the ethylenediamine to be partially imparted by the hydrogen bonds established between both the polar nitrogen atoms and the methylene carbon atoms of the organic molecule, and the vanadyl oxygen atoms of the POV layer, i.e. N–H···O and C–H···O. Although the established C–H···O hydrogen bonds are very weak [20], they may play a part in synergistic with the octahedral coordination geometry of the Co^{II} ion, in regulating the spatial arrangement of the ethylenediamine in relative to the POV layer. It is apparent from Fig. 3 that the ethylenediamines acting as a bidentate ligand are arranged roughly in a plane parallel to the POV layers, which is also the case for the analogous $(C_2N_2H_8)_2Zn[V_6O_{14}]$ and $(C_2N_2H_8)_2Cu[V_6O_{14}]$ structures [17].

Table 4 Hydrogen bonding geometry for **I**

D–H···A	D–H	H···A	D···A	D–H···A
N_2–H_2C···O_1^{I}	0.92	2.21	3.088(7)	159
N_2–H_2D···O_4^{V}	0.92	2.12	2.916(7)	144
C_1–H_1A···O_1^{VI}	0.99	2.47	3.293(8)	140
C_1–H_1B···O_5^{VI}	0.99	2.51	3.237(9)	130
C_2–H_2A···O_4^{VII}	0.99	2.54	3.359(8)	140

Symmetry codes: (i) $-x, -y + 2, -z$; (v) $-x + 1, -y + 2, -z$; (vi) $-x, -y + 1, -z$; (vii) $x - 1/2, -y + 3/2, z - 1/2$

Elemental analysis of ground crystal using an energy dispersive X-ray spectroscopic (EDS) microanalyzer confirms the crystallographically observed ratio of 1:6 for Co:V. CHNS analysis data of bulk samples fit rather poorly to the crystallographically observed formulation. [found—C 46.61%, N 39.97%, H 13.42%; calculated—C 50.04%, N 39.45%, H 10.50%]. The data suggest impurities are present, possibly with coordinated water. However, the X-ray powder diffraction data show that the pillared phase is the dominant crystalline component present in the bulk. The FT-IR spectrum collected on the ground crystals reveals the existence of the major functional groups of the ethylenediamine and the ligated atoms to the cobalt; 3452vs, 3015vs (ν(N–H; NH_2)); 1630s (δ(N–H)); 1463m (δ(C–H; CH_2)); 1055m (ν(C–N)); 973s (ν(V–O_t)); 740s (ν(V–O_b)); 673m (ν(Co–N)); 465m (ν(Co–O)). The broadening effect is also observed in the spectrum which is consistent with the presence of the hydrogen bonds.

In conclusion, a new pillared POV layer structure of the Co-POV system has been prepared and fully characterized. This expands a series of the pillared POV layer structures to include Zn-POV, Cu-POV, Ni-POV and Co-POV, which in turn suggest the template function of the ethylenediamine and therefore the feasibility in extending this structural series to other secondary metals with possibly better potential functions. Work to prepare a pure sample of **I** is underway with a view to examining the magnetic behavior of the pillared framework.

Acknowledgments The Thailand Research Fund, the Commission for Higher Education, the Center of Excellence for Innovation in Chemistry, and the Thailand Toray Science Foundation are acknowledged for financial support. B. Yotnoi thanks the Royal Golden Jubilee Ph.D. Program and the Graduate School of Chiang Mai University for Graduate Scholarship.

References

1. Hagrman PJ, Finn RC, Zubieta J (2001) Solid State Sci 3:745
2. Davi RN, Zubieta J (2003) Inorg Chim Acta 343:313
3. Li GH, Shi Z, Xu YH, Feng SH (2003) Inorg Chem 42:1170
4. Coronado E, Gomez-Garcya CL (1999) Chem Soc 121:11459
5. Wang CM, Zeng QX, Zhang J, Yang GY (2005) J Clust Sci 16:65
6. Zhou G, Xu Y, Guo C, Zheng X (2007) Inorg Chem Commun 10:849
7. LaDuca RL, Rarig RS, Zubieta J (2001) Inorg Chem 40:607
8. Zheng LM, Wang X, Wang Y, Jacobson AJ (2001) J Mater Chem 11:1100
9. Pan CL, Xu JQ, Wang KX, Cui XB, Ye L, Lu ZL, Chu DQ, Wang TG (2003) Inorg Chem Commun 6:370
10. Zhang Y, DeBord JRD, O'Connor CJ, Haushalter RC, Clearfield A, Zubieta J (1996) Angew Chem Int Ed Engl 35:989
11. Shi Z, Zhang L, Zhu G, Yang G, Hua J, Ding H, Feng S (1999) Chem Mater 11:3565

12. de Meulener J, Tompa H (1965) Acta Crystallogr 19:1014
13. Sheldrick GM (1997) SHELXS-97, program for solving crystal structure. University of Gottingen, Germany
14. Sheldrick GM (1997) SHELXL-97, program for crystal structure refinement. University of Gottingen, Germany
15. Farrugia LJ (1999) J Appl Crystallogr 32:837
16. Urusov VS, Orlov IP (1999) Crystallogr Rep 44:686
17. Settheeworrarit T, Prior TJ, Meansiri S, Limtrakul J, Rujiwatra A (2008) J Inorg Organomet Polym 18:253
18. Zavalij PY, Whittingham MS (1999) Acta Crystallogr B55:627
19. Khan MI, Yohannes E, Golub VO, O'Connor CJ, Doedens RJ (2007) Chem Mater 19:1890
20. Desiraju G (2003) J Mol Struct 656:5

Acta Crystallographica Section E
Structure Reports Online
ISSN 1600-5368

(1-Butyl-1,4-diazabicyclo[2.2.2]octon-1-ium-κN^4)trichloridocobalt(II)

Sanchai Luachan,[a] Bunlawee Yotnoi,[a] Timothy J. Prior[b] and Apinpus Rujiwatra[a]*

[a]Department of Chemistry, Faculty of Science, Chiang Mai University, Chiang Mai 50200, Thailand, and [b]Department of Chemistry, University of Hull, Kingston upon Hull HU6 7RX, England
Correspondence e-mail: apinpus@chiangmai.ac.th

Received 11 February 2009; accepted 19 February 2009

Key indicators: single-crystal synchrotron study; T = 120 K; mean σ(C–C) = 0.007 Å; R factor = 0.045; wR factor = 0.098; data-to-parameter ratio = 30.2.

The title compound, $[Co(C_{10}H_{21}N_2)Cl_3]$, was obtained as the by-product of the attempted synthesis of a cobalt sulfate framework using 1,4-diazabicyclo[2.2.2]octane as an organic template. The asymmetric unit comprises two distinct molecules, and in each, the cobalt(II) ions are tetrahedrally coordinated by three chloride anions and one 1-butyldiazabicyclo[2.2.2]octan-1-ium cation. The organic ligands are generated *in situ*, and exhibit two forms differentiated by the eclipsed and staggered conformations of the butyl groups. These molecules interact by way of C—H···Cl hydrogen bonds, forming a three-dimensional hydrogen-bonding array.

Related literature

Examples of closely related structures are *N*-methyl-1,4-diazabicyclo(2.2.2) octonium trichloro-aqua-nickel(II) (Ross & Stucky, 1969) and *N*,*N*′-dimethyl-1,4-diazaniabicyclo[2.2.2]-octane tetrachlorocobaltate $(C_8H_{18}N_2)[CoCl_4]$ (Qu & Sun, 2005). The organic cation in both structures do not coordinate to the cobalt ion but, in each case, the C—H···Cl hydrogen-bonding interactions are similar to those in the title compound. For hydrogen bonding in related structures, see: Bremner & Harrison (2003).

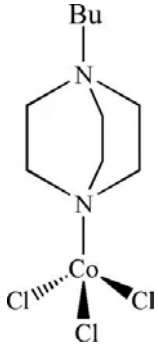

Experimental

Crystal data

$[Co(C_{10}H_{21}N_2)Cl_3]$
M_r = 334.57
Monoclinic, $P2_1$
a = 8.379 (2) Å
b = 12.1090 (13) Å
c = 14.711 (4) Å
β = 91.683 (4)°
V = 1492.0 (6) Å^3
Z = 4
Synchrotron radiation
λ = 0.69430 Å
μ = 1.67 mm^{-1}
T = 120 K
0.12 × 0.02 × 0.02 mm

Data collection

Bruker D8 with APEXII detector diffractometer
Absorption correction: multi-scan (TWINABS; Bruker, 2004)
T_{min} = 0.597, T_{max} = 0.746
(expected range = 0.774–0.967)
12848 measured reflections
8831 independent reflections
7018 reflections with $I > 2\sigma(I)$
R_{int} = 0.054

Refinement

$R[F^2 > 2\sigma(F^2)]$ = 0.045
$wR(F^2)$ = 0.098
S = 1.04
8831 reflections
292 parameters
1 restraint
H-atom parameters constrained
$\Delta\rho_{max}$ = 0.65 e Å^{-3}
$\Delta\rho_{min}$ = −0.44 e Å^{-3}
Absolute structure: Flack (1983), 3980 Friedel pairs
Flack parameter: 0.064 (17)

Table 1
Hydrogen-bond geometry (Å, °).

D—H···A	D—H	H···A	D···A	D—H···A
C2—H2B···Cl6^{i}	0.99	2.66	3.567 (5)	153
C4—H4A···Cl1^{ii}	0.99	2.66	3.511 (5)	145
C6—H6B···Cl3^{ii}	0.99	2.69	3.606 (5)	154
C7—H7B···Cl3^{iii}	0.99	2.80	3.729 (5)	157
C12—H12B···Cl5^{iv}	0.99	2.62	3.485 (4)	146
C14—H14A···Cl6^{iv}	0.99	2.75	3.567 (5)	140
C16—H16A···Cl1^{v}	0.99	2.60	3.548 (4)	161
C16—H16B···Cl5^{v}	0.99	2.81	3.739 (4)	156

Symmetry codes: (i) $x-1, y, z-1$; (ii) $-x, y-\frac{1}{2}, -z+1$; (iii) $x-1, y, z$; (iv) $-x+2, y-\frac{1}{2}, -z+2$; (v) $x+1, y, z$.

Data collection: *APEX2* (Bruker, 2007); cell refinement: *APEX2*; data reduction: *TWINABS* (Bruker, 2004); program(s) used to solve structure: *SHELXS86* (Sheldrick, 2008); program(s) used to refine structure: *SHELXL97* (Sheldrick, 2008); molecular graphics: *DIAMOND* (Brandenburg & Putz, 2005); software used to prepare material for publication: *PLATON* (Spek, 2009).

The authors thank the Thailand Research Fund, Center for Innovation in Chemistry and Thailand Toray Science Foundation for financial support. BY thanks the Royal Golden Jubilee PhD program and the Graduate School of Chiang Mai University for a Graduate Scholarship.

Supplementary data and figures for this paper are available from the IUCr electronic archives (Reference: LH2775).

References

Brandenburg, K. & Putz, H. (2005). *DIAMOND*. Crystal Impact GbR, Bonn, Germany.
Bremner, C. A. & Harrison, W. T. A. (2003). *Acta Cryst.* E**59**, m425–m426.
Bruker (2004). *TWINABS*. Bruker AXS Inc., Madison, Wisconsin, USA.
Bruker (2007). *APEX2*. Bruker AXS Inc., Madison, Wisconsin, USA.
Flack, H. D. (1983). *Acta Cryst.* A**39**, 876–881.

Qu, Y. & Sun, X.-M. (2005). *Acta Cryst.* E**61**, m2121–m2123.
Ross, F. K. & Stucky, G. D. (1969). *Inorg. Chem.* **8**, 2734–2740.
Sheldrick, G. M. (2008). *Acta Cryst.* A**64**, 112–122.
Spek, A. L. (2009). *Acta Cryst.* D**65**, 148–155.

Acta Cryst. (2009). E**65**, m321-m322 [**doi:10.1107/S1600536809005893**]

(1-Butyl-1,4-diazabicyclo[2.2.2]octon-1-ium-κN^4)trichloridocobalt(II)

S. Luachan, B. Yotnoi, T. J. Prior and A. Rujiwatra

Comment

The crystals of $Co(C_{10}H_{21}N_2)Cl_3$ (**I**) were unintentionally obtained as a by-product from the hydrothermal reaction between cobalt(II) sulfate heptahydrate and 1,4-diazabicyclo[2.2.2]octane in a water/butan-1-ol mixture. The *N*-butyl-1,4-diazabicyclo[2.2.2]octanium ligand was presumably generated *in situ* under acidic conditions. The structure of I is built up from two distinct $[Co(C_{10}H_{21}N_2)Cl_3]$ molecules as shown in Fig. 1. They are different in the spatial orientation of the butyl group of the *N*-butyl-1,4-diazabicyclo[2.2.2]octanium ligand, one of which is in the eclipsed conformation (**A**) and the other is in the staggered conformation (**B**). The **A** molecules are connected by the C—H···Cl hydrogen bonding interactions to form a two-dimensional **A** sheet in the *ab* plane (Fig. 2), whereas the **B** molecules form the **B** sheet also in the*ab* plane using similar C—H···Cl hydrogen bonding interactions (Fig. 3). The **A** and **B** sheets are then regularly alternated in the **ABAB** fashion, and linked by way of also the C—H···Cl hydrogen bonding interactions along *c* to give the infinite three-dimensional hydrogen bonding array (Fig. 4).

The hydrogen bond geometries found in **I** (H···Cl, 2.62–2.81 Å; C···Cl, 3.485 (4)–3.739 (4) Å; C—H···Cl, 140.00–164.00°) are well comparable to those found in related structures, *e.g.* $(C_6H_{14}N_2)[CoCl_4]$ (Bremner & Harrison, 2003) and $(C_8H_{18}N_2)[CoCl_4]$ (Qu & Sun, 2005).

Experimental

Crystals of **I** were obtained as a by-product from the hydrothermal reaction of cobalt(II) sulfate heptahydrate, 1,4-diazabicyclo[2.2.2]octane and hydrochloric acid in a water/butan-1-ol mixture at 453 K for 120 h.

Refinement

H atoms were placed in calcluated positions with C-H = 0.99Å or 0.98Å for methyl H atoms and were included in the refinement in a riding-model approximation with $U_{iso}(H) = 1.2U_{eq}(C)$ or $1.5U_{eq}(C)$ for methyl H atoms.

The examined crystal was found to be twinned, composing of two crystal components which were miss-set by about two degrees. The crystal was therefore treated as a twin and the two components integrated separately using the same unit cell. Both components were used for the structure refinement and the twin fraction was found to be 0.698:0.302 (1).

Three alerts from checkCIF:

PLAT220_ALERT_2_C

PLAT222_ALERT_2_C

supplementary materials

The rather weak van der Waals interactions involving the *n*-butyl chains mean there is considerable freedom for these carbon and hydrogen atoms to vibrate. The slightly enlarged displacement parameters observed are entirely expected on chemical grounds.

PLAT341_ALERT_3_C

The calculated estimated standard uncertainties associated with the unit-cell parameters are faithfully reproduced from the Bruker APEXII suite (Bruker, 2004). All observed data were used in their calculation. These give rise to moderate precision in the C—C bonds. To some extent this is a consequence of the integration procedure which uses two twin components - deconvolution of the low angle components is problematic as the two componenets are miss-set by approximately 2°.

Figures

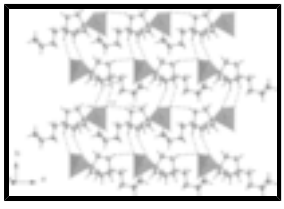

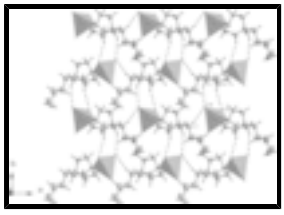

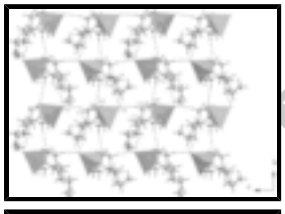

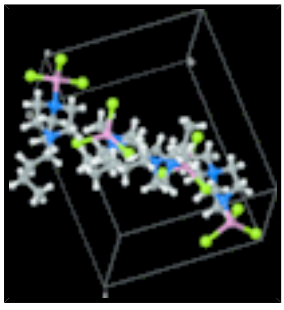

View of the title compound with the atom numbering scheme. Displacement ellipsoids for non-H atoms are drawn at the 70% probability level.
View of the **A** sheet along the *ab* plane with the hydrogen bonding atoms indicated.
View of the **B** sheet along the *ab* plane with the hydrogen bonding atoms indicated.
The packing of **A** and **B** sheets along *c* in **ABAB** fashion.

(1-Butyl-1,4-diazabicyclo[2.2.2]octon-1-ium-κN^4)trichloridocobalt(II)

Crystal data

$[Co(C_{10}H_{21}N_2)Cl_3]$
$M_r = 334.57$
Monoclinic, $P2_1$
Hall symbol: P 2yb
$a = 8.379\ (2)$ Å
$b = 12.1090\ (13)$ Å
$c = 14.711\ (4)$ Å
$\beta = 91.683\ (4)^o$
$V = 1492.0\ (6)$ Å^3
$Z = 4$
$F_{000} = 692$
$D_x = 1.490$ Mg m^{-3}
Synchrotron radiation
$\lambda = 0.69430$ Å
Cell parameters from 12848 reflections
$\theta = 1.4–30.7^o$
$\mu = 1.67$ mm^{-1}
$T = 120$ K
Needle, blue
0.12 × 0.02 × 0.02 mm

Data collection

Bruker D8 with APEXII detector diffractometer
Radiation source: Daresbury SRS, UK
Monochromator: silicon 111
$T = 120$ K
ω scans
Absorption correction: multi-scan (TWINABS; Bruker, 2004)
$T_{min} = 0.597$, $T_{max} = 0.746$
12848 measured reflections
8831 independent reflections
7018 reflections with $I > 2\sigma(I)$
$R_{int} = 0.054$
$\theta_{max} = 30.7^o$
$\theta_{min} = 1.4^o$
$h = -12\rightarrow12$
$k = -17\rightarrow17$
$l = -20\rightarrow20$

Refinement

Refinement on F^2
Least-squares matrix: full
$R[F^2 > 2\sigma(F^2)] = 0.045$
$wR(F^2) = 0.098$
$S = 1.04$
8831 reflections
292 parameters
1 restraint
Primary atom site location: structure-invariant direct methods
Secondary atom site location: difference Fourier map
Hydrogen site location: inferred from neighbouring sites
H-atom parameters constrained
$w = 1/[\sigma^2(F_o^2) + (0.0352P)^2 + 0.2945P]$ where $P = (F_o^2 + 2F_c^2)/3$
$(\Delta/\sigma)_{max} = 0.001$
$\Delta\rho_{max} = 0.65$ e Å^{-3}
$\Delta\rho_{min} = -0.43$ e Å^{-3}
Extinction correction: none
Absolute structure: Flack (1983), 3980 Friedel pairs
Flack parameter: 0.064 (17)

Special details

Geometry. All e.s.d.'s (except the e.s.d. in the dihedral angle between two l.s. planes) are estimated using the full covariance matrix. The cell e.s.d.'s are taken into account individually in the estimation of e.s.d.'s in distances, angles and torsion angles; correlations between e.s.d.'s in cell parameters are only used when they are defined by crystal symmetry. An approximate (isotropic) treatment of cell e.s.d.'s is used for estimating e.s.d.'s involving l.s. planes.

Refinement. Refinement of F^2 against ALL reflections. The weighted *R*-factor *wR* and goodness of fit *S* are based on F^2, conventional *R*-factors *R* are based on *F*, with *F* set to zero for negative F^2. The threshold expression of $F^2 > \sigma(F^2)$ is used only for calculating *R*-factors(gt) *etc*. and is not relevant to the choice of reflections for refinement. *R*-factors based on F^2 are statistically about twice as large as those based on *F*, and *R*- factors based on ALL data will be even larger.

Fractional atomic coordinates and isotropic or equivalent isotropic displacement parameters (Å^2)

	x	*y*	*z*	U_{iso}*/U_{eq}
Co1	0.17969 (6)	0.70552 (4)	0.56075 (3)	0.02973 (12)
Cl1	0.08844 (13)	0.78922 (10)	0.68543 (6)	0.0382 (2)
Cl2	0.28560 (14)	0.53800 (9)	0.58911 (8)	0.0416 (2)
Cl3	0.32696 (13)	0.81305 (9)	0.47062 (7)	0.0373 (2)
N1	−0.0308 (4)	0.6782 (3)	0.48346 (19)	0.0264 (7)
N2	−0.2901 (4)	0.6376 (3)	0.3900 (2)	0.0278 (7)
C1	−0.1094 (5)	0.7827 (4)	0.4539 (3)	0.0304 (8)
H1A	−0.0310	0.8306	0.4240	0.037*
H1B	−0.1485	0.8224	0.5077	0.037*
C2	−0.2502 (5)	0.7587 (3)	0.3875 (3)	0.0296 (9)
H2A	−0.3443	0.8026	0.4047	0.036*
H2B	−0.2216	0.7801	0.3251	0.036*
C3	0.0056 (5)	0.6132 (4)	0.4005 (3)	0.0327 (9)
H3A	0.0741	0.5495	0.4175	0.039*
H3B	0.0647	0.6601	0.3578	0.039*
C4	−0.1487 (5)	0.5719 (4)	0.3539 (3)	0.0319 (9)
H4A	−0.1630	0.4923	0.3665	0.038*
H4B	−0.1430	0.5818	0.2872	0.038*
C5	−0.1470 (5)	0.6141 (4)	0.5373 (3)	0.0318 (8)
H5A	−0.1588	0.6499	0.5972	0.038*
H5B	−0.1048	0.5386	0.5480	0.038*
C6	−0.3093 (5)	0.6065 (4)	0.4892 (2)	0.0315 (8)
H6A	−0.3853	0.6575	0.5179	0.038*
H6B	−0.3516	0.5305	0.4937	0.038*
C7	−0.4381 (6)	0.6160 (4)	0.3329 (3)	0.0351 (9)
H7A	−0.4196	0.6415	0.2701	0.042*
H7B	−0.5264	0.6607	0.3569	0.042*
C8	−0.4898 (7)	0.4966 (4)	0.3294 (3)	0.0477 (13)
H8A	−0.5210	0.4732	0.3909	0.057*
H8B	−0.3982	0.4504	0.3118	0.057*
C9	−0.6289 (7)	0.4765 (5)	0.2626 (3)	0.0541 (15)
H9A	−0.7187	0.5257	0.2779	0.065*
H9B	−0.5958	0.4951	0.2004	0.065*

C10	−0.6843 (9)	0.3581 (7)	0.2648 (4)	0.086 (3)
H10A	−0.5968	0.3094	0.2473	0.129*
H10B	−0.7752	0.3484	0.2221	0.129*
H10C	−0.7167	0.3393	0.3264	0.129*
Co2	0.86290 (6)	0.69012 (4)	1.06702 (3)	0.02719 (12)
Cl4	0.74916 (13)	0.52684 (9)	1.09830 (7)	0.0360 (2)
Cl5	0.70380 (13)	0.79352 (9)	0.97538 (7)	0.0361 (2)
Cl6	0.97391 (13)	0.78267 (9)	1.18605 (6)	0.0331 (2)
N3	1.0632 (4)	0.6586 (3)	0.98991 (19)	0.0256 (7)
N4	1.3114 (4)	0.6133 (3)	0.8981 (2)	0.0266 (7)
C11	1.1771 (5)	0.5881 (4)	1.0443 (2)	0.0335 (9)
H11A	1.1303	0.5138	1.0523	0.040*
H11B	1.1955	0.6211	1.1052	0.040*
C12	1.3367 (5)	0.5778 (3)	0.9963 (2)	0.0290 (8)
H12A	1.4181	0.6254	1.0268	0.035*
H12B	1.3748	0.5005	0.9990	0.035*
C13	1.0170 (5)	0.5989 (4)	0.9044 (3)	0.0323 (9)
H13A	0.9572	0.6493	0.8628	0.039*
H13B	0.9464	0.5360	0.9186	0.039*
C14	1.1659 (5)	0.5563 (4)	0.8579 (2)	0.0303 (9)
H14A	1.1755	0.4755	0.8667	0.036*
H14B	1.1569	0.5712	0.7918	0.036*
C15	1.1471 (5)	0.7610 (3)	0.9650 (3)	0.0314 (8)
H15A	1.1927	0.7963	1.0206	0.038*
H15B	1.0701	0.8131	0.9361	0.038*
C16	1.2827 (5)	0.7362 (3)	0.8985 (2)	0.0279 (8)
H16A	1.2516	0.7618	0.8366	0.033*
H16B	1.3814	0.7755	0.9183	0.033*
C17	1.4589 (5)	0.5863 (4)	0.8441 (3)	0.0345 (9)
H17A	1.5547	0.6134	0.8782	0.041*
H17B	1.4522	0.6265	0.7855	0.041*
C18	1.4796 (5)	0.4631 (4)	0.8249 (3)	0.0348 (9)
H18A	1.4422	0.4199	0.8773	0.042*
H18B	1.4131	0.4424	0.7708	0.042*
C19	1.6527 (5)	0.4346 (4)	0.8082 (3)	0.0385 (10)
H19A	1.6602	0.3550	0.7935	0.046*
H19B	1.7167	0.4477	0.8648	0.046*
C20	1.7244 (6)	0.5012 (4)	0.7312 (3)	0.0417 (11)
H20A	1.6572	0.4932	0.6760	0.062*
H20B	1.8321	0.4739	0.7197	0.062*
H20C	1.7300	0.5793	0.7485	0.062*

Atomic displacement parameters (Å^2)

	U^{11}	U^{22}	U^{33}	U^{12}	U^{13}	U^{23}
Co1	0.0326 (3)	0.0238 (3)	0.0327 (2)	−0.0009 (2)	−0.0002 (2)	0.0029 (2)
Cl1	0.0502 (6)	0.0355 (6)	0.0288 (4)	−0.0037 (5)	0.0015 (4)	−0.0005 (4)
Cl2	0.0429 (6)	0.0268 (5)	0.0546 (6)	0.0019 (5)	−0.0071 (5)	0.0055 (4)

Cl3	0.0385 (5)	0.0285 (5)	0.0454 (5)	−0.0021 (4)	0.0099 (4)	0.0031 (4)
N1	0.0319 (17)	0.0216 (17)	0.0260 (13)	0.0059 (13)	0.0046 (12)	0.0006 (12)
N2	0.0305 (18)	0.0259 (18)	0.0271 (15)	0.0015 (14)	0.0002 (13)	−0.0009 (12)
C1	0.034 (2)	0.023 (2)	0.0347 (18)	0.0029 (17)	0.0007 (15)	0.0025 (15)
C2	0.036 (2)	0.024 (2)	0.0297 (18)	0.0071 (16)	0.0058 (16)	−0.0001 (14)
C3	0.035 (2)	0.036 (2)	0.0273 (17)	0.0080 (18)	0.0036 (15)	−0.0027 (15)
C4	0.035 (2)	0.026 (2)	0.0349 (19)	0.0051 (17)	0.0052 (16)	−0.0050 (15)
C5	0.040 (2)	0.028 (2)	0.0277 (17)	−0.0031 (18)	0.0017 (15)	0.0001 (14)
C6	0.041 (2)	0.031 (2)	0.0230 (16)	−0.0036 (19)	0.0033 (15)	0.0048 (14)
C7	0.040 (2)	0.036 (2)	0.0294 (18)	0.0053 (19)	0.0000 (16)	−0.0029 (15)
C8	0.058 (3)	0.045 (3)	0.040 (2)	−0.015 (2)	−0.005 (2)	−0.0049 (19)
C9	0.045 (3)	0.077 (4)	0.040 (2)	−0.015 (3)	0.005 (2)	−0.018 (2)
C10	0.086 (5)	0.118 (7)	0.054 (3)	−0.066 (5)	0.020 (3)	−0.032 (4)
Co2	0.0293 (3)	0.0241 (3)	0.0285 (2)	−0.0002 (2)	0.00579 (18)	−0.0004 (2)
Cl4	0.0406 (6)	0.0265 (5)	0.0415 (5)	−0.0042 (4)	0.0101 (4)	0.0004 (4)
Cl5	0.0366 (5)	0.0301 (6)	0.0414 (5)	0.0042 (4)	−0.0033 (4)	−0.0018 (4)
Cl6	0.0415 (5)	0.0306 (5)	0.0276 (4)	−0.0026 (5)	0.0055 (4)	−0.0014 (4)
N3	0.0284 (17)	0.0228 (17)	0.0258 (14)	−0.0007 (13)	0.0045 (12)	−0.0004 (11)
N4	0.0296 (17)	0.0228 (17)	0.0276 (15)	−0.0018 (14)	0.0030 (12)	−0.0029 (12)
C11	0.033 (2)	0.041 (2)	0.0269 (17)	0.0037 (19)	0.0052 (15)	0.0063 (16)
C12	0.034 (2)	0.0229 (19)	0.0305 (17)	0.0007 (16)	0.0021 (15)	0.0017 (14)
C13	0.028 (2)	0.039 (2)	0.0296 (18)	−0.0032 (18)	0.0005 (15)	−0.0075 (16)
C14	0.028 (2)	0.032 (2)	0.0308 (18)	−0.0036 (17)	0.0071 (15)	−0.0063 (15)
C15	0.040 (2)	0.021 (2)	0.0335 (18)	−0.0005 (17)	0.0088 (17)	0.0034 (14)
C16	0.030 (2)	0.026 (2)	0.0269 (17)	−0.0035 (15)	0.0037 (15)	0.0036 (14)
C17	0.035 (2)	0.035 (2)	0.035 (2)	−0.0053 (19)	0.0128 (17)	−0.0069 (17)
C18	0.037 (2)	0.031 (2)	0.036 (2)	−0.0011 (18)	0.0072 (17)	−0.0030 (16)
C19	0.034 (2)	0.046 (3)	0.036 (2)	0.006 (2)	0.0090 (18)	0.0050 (19)
C20	0.045 (3)	0.046 (3)	0.035 (2)	−0.003 (2)	0.0141 (19)	−0.0008 (19)

Geometric parameters (Å, °)

Co1—N1	2.096 (3)	Co2—N3	2.088 (3)
Co1—Cl2	2.2483 (13)	Co2—Cl4	2.2482 (12)
Co1—Cl1	2.2491 (12)	Co2—Cl5	2.2487 (12)
Co1—Cl3	2.2521 (11)	Co2—Cl6	2.2564 (11)
N1—C1	1.486 (5)	N3—C15	1.477 (5)
N1—C3	1.491 (5)	N3—C13	1.493 (5)
N1—C5	1.491 (5)	N3—C11	1.495 (5)
N2—C7	1.500 (6)	N4—C14	1.507 (5)
N2—C2	1.505 (5)	N4—C16	1.508 (5)
N2—C6	1.520 (5)	N4—C12	1.516 (5)
N2—C4	1.536 (5)	N4—C17	1.524 (5)
C1—C2	1.537 (6)	C11—C12	1.536 (6)
C1—H1A	0.9900	C11—H11A	0.9900
C1—H1B	0.9900	C11—H11B	0.9900
C2—H2A	0.9900	C12—H12A	0.9900
C2—H2B	0.9900	C12—H12B	0.9900
C3—C4	1.530 (6)	C13—C14	1.530 (5)

C3—H3A	0.9900	C13—H13A	0.9900
C3—H3B	0.9900	C13—H13B	0.9900
C4—H4A	0.9900	C14—H14A	0.9900
C4—H4B	0.9900	C14—H14B	0.9900
C5—C6	1.517 (6)	C15—C16	1.550 (5)
C5—H5A	0.9900	C15—H15A	0.9900
C5—H5B	0.9900	C15—H15B	0.9900
C6—H6A	0.9900	C16—H16A	0.9900
C6—H6B	0.9900	C16—H16B	0.9900
C7—C8	1.510 (7)	C17—C18	1.530 (6)
C7—H7A	0.9900	C17—H17A	0.9900
C7—H7B	0.9900	C17—H17B	0.9900
C8—C9	1.522 (7)	C18—C19	1.518 (6)
C8—H8A	0.9900	C18—H18A	0.9900
C8—H8B	0.9900	C18—H18B	0.9900
C9—C10	1.508 (9)	C19—C20	1.528 (6)
C9—H9A	0.9900	C19—H19A	0.9900
C9—H9B	0.9900	C19—H19B	0.9900
C10—H10A	0.9800	C20—H20A	0.9800
C10—H10B	0.9800	C20—H20B	0.9800
C10—H10C	0.9800	C20—H20C	0.9800
N1—Co1—Cl2	106.21 (10)	N3—Co2—Cl4	107.62 (10)
N1—Co1—Cl1	102.29 (9)	N3—Co2—Cl5	104.35 (9)
Cl2—Co1—Cl1	113.39 (5)	Cl4—Co2—Cl5	111.41 (5)
N1—Co1—Cl3	103.81 (9)	N3—Co2—Cl6	101.11 (10)
Cl2—Co1—Cl3	114.25 (5)	Cl4—Co2—Cl6	116.46 (4)
Cl1—Co1—Cl3	115.14 (5)	Cl5—Co2—Cl6	114.35 (5)
C1—N1—C3	108.0 (3)	C15—N3—C13	108.1 (3)
C1—N1—C5	107.9 (3)	C15—N3—C11	108.1 (3)
C3—N1—C5	108.2 (3)	C13—N3—C11	108.7 (3)
C1—N1—Co1	112.5 (2)	C15—N3—Co2	112.2 (2)
C3—N1—Co1	109.8 (2)	C13—N3—Co2	110.7 (2)
C5—N1—Co1	110.3 (2)	C11—N3—Co2	108.9 (2)
C7—N2—C2	109.7 (3)	C14—N4—C16	109.0 (3)
C7—N2—C6	112.7 (3)	C14—N4—C12	109.5 (3)
C2—N2—C6	107.1 (3)	C16—N4—C12	107.1 (3)
C7—N2—C4	110.5 (3)	C14—N4—C17	110.9 (3)
C2—N2—C4	108.8 (3)	C16—N4—C17	110.2 (3)
C6—N2—C4	108.0 (3)	C12—N4—C17	110.1 (3)
N1—C1—C2	110.5 (3)	N3—C11—C12	110.6 (3)
N1—C1—H1A	109.5	N3—C11—H11A	109.5
C2—C1—H1A	109.5	C12—C11—H11A	109.5
N1—C1—H1B	109.5	N3—C11—H11B	109.5
C2—C1—H1B	109.5	C12—C11—H11B	109.5
H1A—C1—H1B	108.1	H11A—C11—H11B	108.1
N2—C2—C1	109.6 (3)	N4—C12—C11	108.4 (3)
N2—C2—H2A	109.8	N4—C12—H12A	110.0
C1—C2—H2A	109.8	C11—C12—H12A	110.0
N2—C2—H2B	109.8	N4—C12—H12B	110.0

C1—C2—H2B	109.8	C11—C12—H12B	110.0
H2A—C2—H2B	108.2	H12A—C12—H12B	108.4
N1—C3—C4	110.4 (3)	N3—C13—C14	110.2 (3)
N1—C3—H3A	109.6	N3—C13—H13A	109.6
C4—C3—H3A	109.6	C14—C13—H13A	109.6
N1—C3—H3B	109.6	N3—C13—H13B	109.6
C4—C3—H3B	109.6	C14—C13—H13B	109.6
H3A—C3—H3B	108.1	H13A—C13—H13B	108.1
C3—C4—N2	109.0 (3)	N4—C14—C13	109.4 (3)
C3—C4—H4A	109.9	N4—C14—H14A	109.8
N2—C4—H4A	109.9	C13—C14—H14A	109.8
C3—C4—H4B	109.9	N4—C14—H14B	109.8
N2—C4—H4B	109.9	C13—C14—H14B	109.8
H4A—C4—H4B	108.3	H14A—C14—H14B	108.3
N1—C5—C6	112.0 (3)	N3—C15—C16	111.0 (3)
N1—C5—H5A	109.2	N3—C15—H15A	109.4
C6—C5—H5A	109.2	C16—C15—H15A	109.4
N1—C5—H5B	109.2	N3—C15—H15B	109.4
C6—C5—H5B	109.2	C16—C15—H15B	109.4
H5A—C5—H5B	107.9	H15A—C15—H15B	108.0
C5—C6—N2	108.3 (3)	N4—C16—C15	108.3 (3)
C5—C6—H6A	110.0	N4—C16—H16A	110.0
N2—C6—H6A	110.0	C15—C16—H16A	110.0
C5—C6—H6B	110.0	N4—C16—H16B	110.0
N2—C6—H6B	110.0	C15—C16—H16B	110.0
H6A—C6—H6B	108.4	H16A—C16—H16B	108.4
N2—C7—C8	114.7 (4)	N4—C17—C18	113.8 (3)
N2—C7—H7A	108.6	N4—C17—H17A	108.8
C8—C7—H7A	108.6	C18—C17—H17A	108.8
N2—C7—H7B	108.6	N4—C17—H17B	108.8
C8—C7—H7B	108.6	C18—C17—H17B	108.8
H7A—C7—H7B	107.6	H17A—C17—H17B	107.7
C7—C8—C9	112.8 (5)	C19—C18—C17	111.5 (4)
C7—C8—H8A	109.0	C19—C18—H18A	109.3
C9—C8—H8A	109.0	C17—C18—H18A	109.3
C7—C8—H8B	109.0	C19—C18—H18B	109.3
C9—C8—H8B	109.0	C17—C18—H18B	109.3
H8A—C8—H8B	107.8	H18A—C18—H18B	108.0
C10—C9—C8	111.6 (6)	C18—C19—C20	113.4 (4)
C10—C9—H9A	109.3	C18—C19—H19A	108.9
C8—C9—H9A	109.3	C20—C19—H19A	108.9
C10—C9—H9B	109.3	C18—C19—H19B	108.9
C8—C9—H9B	109.3	C20—C19—H19B	108.9
H9A—C9—H9B	108.0	H19A—C19—H19B	107.7
C9—C10—H10A	109.5	C19—C20—H20A	109.5
C9—C10—H10B	109.5	C19—C20—H20B	109.5
H10A—C10—H10B	109.5	H20A—C20—H20B	109.5
C9—C10—H10C	109.5	C19—C20—H20C	109.5
H10A—C10—H10C	109.5	H20A—C20—H20C	109.5

H10B—C10—H10C	109.5	H20B—C20—H20C	109.5

Hydrogen-bond geometry (Å, °)

D—H···*A*	*D*—H	H···*A*	*D*···*A*	*D*—H···*A*
C2—H2B···Cl6^{i}	0.99	2.66	3.567 (5)	153
C4—H4A···Cl1^{ii}	0.99	2.66	3.511 (5)	145
C6—H6B···Cl3^{ii}	0.99	2.69	3.606 (5)	154
C7—H7B···Cl3^{iii}	0.99	2.80	3.729 (5)	157
C12—H12B···Cl5^{iv}	0.99	2.62	3.485 (4)	146
C14—H14A···Cl6^{iv}	0.99	2.75	3.567 (5)	140
C16—H16A···Cl1^{v}	0.99	2.60	3.548 (4)	161
C16—H16B···Cl5^{v}	0.99	2.81	3.739 (4)	156

Symmetry codes: (i) *x*−1, *y*, *z*−1; (ii) −*x*, *y*−1/2, −*z*+1; (iii) *x*−1, *y*, *z*; (iv) −*x*+2, *y*−1/2, −*z*+2; (v) *x*+1, *y*, *z*.

Acta Crystallographica Section E
Structure Reports Online
ISSN 1600-5368

Intercalated brucite-type layered cobalt(II) hydroxysulfate

Bunlawee Yotnoi,[a] Sanchai Luachan,[a] Timothy J. Prior[b] and Apinpus Rujiwatra[a]*

[a]Department of Chemistry, Faculty of Science, Chiang Mai University, Chiang Mai 50200, Thailand, and [b]Department of Chemistry, University of Hull, Kingston upon Hull HU6 7RX, England
Correspondence e-mail: apinpus@chiangmai.ac.th

Received 27 May 2009; accepted 12 June 2009

Key indicators: single-crystal X-ray study; T = 150 K; mean σ(S–O) = 0.006 Å; disorder in main residue; R factor = 0.048; wR factor = 0.132; data-to-parameter ratio = 12.4.

In an attempt to synthesize new cobalt(II) sulfate framework structures using 1,4-diazabicyclo[2.2.2]octane as a template, crystals of poly[0.35-[hexaaquacobalt(II)] [tri-μ-hydroxido-μ-sulfato-dicobalt(II)]], $\{[Co(H_2O)_6]_{0.35}[Co_2(OH)_3(SO_4)]\}_n$, were obtained as a mixture with $[Co(H_2O)_6]SO_4$ crystals. The crystal structure can be described as being constructed from discrete brucite-type $[Co_4(OH)_6(SO_4)_2]$ layers, each of which is built up from edge-shared $[Co(OH)_6]$ and $[Co(OH)_4(OSO_3)_2]$ octahedra, with partial intercalation by $[Co(H_2O)_6]^{2+}$ ions. The absence of *ca* 30% of the $[Co(H_2O)_6]^{2+}$ cations indicates partial oxidation of cobalt(II) to cobalt(III) within the layer.

Related literature

The crystal structure of the title compound is closely related to that of $Co_5(OH)_6(SO_4)_2(H_2O)_4$ (Ben Salah *et al.*, 2004, 2006), which is composed of brucite-type cobalt hydroxide layers. The fundamental difference lies in the way that adjacent layers are linked; being pillared by $\cdots O_3SO{-}Co(H_2O)_4{-}OSO_3\cdots$ groups in $Co_5(OH)_6(SO_4)_2(H_2O)_4$ but partially intercalated by $[Co(H_2O)_6]^{2+}$ ions in the title compound. For the crystal structures of layered materials of this type, see: Poudret *et al.* (2008). For a description of the Cambridge Structural Database, see: Allen (2002).

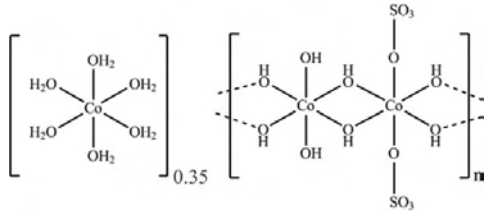

Experimental

Crystal data

$[Co(H_2O)_6]_{0.35}[Co_2(OH)_3(SO_4)]$
M_r = 323.41
Trigonal, $P\bar{3}m1$
a = 6.3627 (19) Å
c = 12.180 (4) Å
V = 427.0 (2) Å^3
Z = 2
Mo $K\alpha$ radiation
μ = 4.80 mm^{-1}
T = 150 K
0.21 × 0.13 × 0.03 mm

Data collection

Stoe IPDS2 diffractometer
Absorption correction: multi-scan (*X-RED*; Stoe & Cie, 2008)
T_{min} = 0.415, T_{max} = 0.862
1663 measured reflections
497 independent reflections
325 reflections with $I > 2\sigma(I)$
R_{int} = 0.097

Refinement

$R[F^2 > 2\sigma(F^2)]$ = 0.048
$wR(F^2)$ = 0.132
S = 0.90
497 reflections
40 parameters
3 restraints
Only H-atom coordinates refined
$\Delta\rho_{max}$ = 1.04 e Å^{-3}
$\Delta\rho_{min}$ = −1.05 e Å^{-3}

Data collection: *X-AREA* (Stoe & Cie, 2008); cell refinement: *X-AREA*; data reduction: *X-RED* (Stoe & Cie, 2008); program(s) used to solve structure: *SHELXS86* (Sheldrick, 2008); program(s) used to refine structure: *SHELXL97* (Sheldrick, 2008); molecular graphics: *DIAMOND* (Brandenburg & Putz, 1999); software used to prepare material for publication: *PLATON* (Spek, 2009).

The authors thank the Thailand Research Fund, the Center for Innovation in Chemistry and the Thailand Toray Science Foundation for financial support. BY thanks the Royal Golden Jubilee PhD program and the Graduate School of Chiang Mai University for a Graduate Scholarship.

Supplementary data and figures for this paper are available from the IUCr electronic archives (Reference: LH2832).

References

Allen, F. H. (2002). *Acta Cryst.* B**58**, 380–388.
Ben Salah, M., Vilminot, S., Andre, G., Richard-Plouet, M., Mhiri, T., Takagi, S. & Kurmoo, M. (2006). *J. Am. Chem. Soc.* **128**, 7972–7981.
Ben Salah, M., Vilminot, S., Richard-Plouet, M., Andre, G., Mhiri, T. & Kurmoo, M. (2004). *Chem. Commun.* pp. 2548–2549.
Brandenburg, K. & Putz, H. (1999). *DIAMOND*. Crystal Impact GbR, Bonn, Germany.
Poudret, L., Prior, T. J., McIntyre, L. J. & Fogg, A. M. (2008). *Chem. Mater.* **20**, 7447–7453.
Sheldrick, G. M. (2008). *Acta Cryst.* A**64**, 112–122.
Spek, A. L. (2009). *Acta Cryst.* D**65**, 148–155.
Stoe & Cie (2008). *X-AREA* and *X-RED*. Stoe & Cie, Darmstadt, Germany.

Acta Cryst. (2009). E**65**, i52 [**doi:10.1107/S160053680902251X**]

Intercalated brucite-type layered cobalt(II) hydroxysulfate

B. Yotnoi, S. Luachan, T. J. Prior and A. Rujiwatra

Comment

Layered transition-metal hydroxides, in particular those exhibiting the brucite structure, have gained serious interest in both chemical and physical aspects. While the intercalation chemistry and potential application as catalysts are of the prime interest for the chemists, the physical interest primarily stems from the long-rang magnetic ordering in two dimensions. Examples of two dimensional triangular networks exhibiting such ordering are very rare, and the information on the crystal structures of layered materials of this type is yet rarer (Poudret, 2008). Thusfar there has been only one structure, $Co_5(OH)_6(SO_4)_2(H_2O)_4$, having the truely brucite-type magnetic layer (Ben Salah et al., 2004). The nuclear and magnetic structures, and magnetic properties of the compound were extensively reported (Ben Salah et al., 2006). The crystal structure of $Co_5(OH)_6(SO_4)_2(H_2O)_4$ consists of brucite-type cobalt hydroxide layers of edge-sharing octahedra, which are pillared by ··· O_3SO—$Co(H_2O)_4$—OSO_3··· groups. The compound exhibits ferromagnetic coupling with purely two dimensional magnetic ordering in an easy-plane magnet, which is a rare example of a single-layer magnet.

The crystal structure of $[Co(H_2O)_6]_x[Co_4(SO_4)_2(OH)_6]$ (I) where x ≃ 0.70 is closely related to that of $Co_5(OH)_6(SO_4)_2(H_2O)_4$ (Fig. 1), also comprised of brucite-type $[Co_4(SO_4)_2(OH)_6]$ layers, each of which is built up from the edge-shared $[Co(OH)_6]$ and $[Co(OH)_4(OSO_3)_2]$ octahedra in the ab plane (Fig. 2). Two of three crystallographically distinct cobalt ions (Fig. 3), Co1 and Co2, are within the layers and located on the 1b and 3f Wyckoff sites, respectively. Unlike the $Co_5(OH)_6(SO_4)_2(H_2O)_4$ structure, the sulfate anion acts as a monodentate ligand and is coordinate covalently connected to the layered Co2 ion via the apical O atom, leaving the three basal O atoms pointing into the interlayered space (Fig. 3). The $[Co_4(SO_4)_2(OH)_6]$ layers are stacked in the ABAB fashion along c, with a repeat distance of 12.180 (4) Å. In the interlayered gallery, there are intercalated discrete $[Co(H_2O)_6]^{2+}$ ions in which the Co3 is located on the 1a site. These $[Co(H_2O)_6]^{2+}$ ions are aligned in a way to maximize the hydrogen bonding interactions of O—H···O type between the aquo ligands and the basal O atoms of the layered sulfate pendants (Fig. 1). The orientation of the sulfate is also regulated by the hydrogen bonds established between the sulfate basal O atoms and the layered hydroxy groups. The Co—O bond length (2.065 (8) Å) within the hexaaquo ion is in good agreement with similar cations in the Cambridge Structural Database (Allen, 2002). The mean of similar Co—O distances is 2.09 (3) Å, but is notable that the majority of these structures were collected at room temperature. 97% of the structures containing cobalt hexaaquo ions are explicitly recorded at Co^{2+}, none are recorded as Co^{3+}.

The refined site occupancy of the intercalated $[Co(H_2O)_6]^{2+}$ ions and the assumption of total charge neutrality imply the partial oxidation (15%) of the layer Co^{II} to Co^{III}. This yields an overall composition $[Co^{II}(H_2O)_6]_{0.7}[Co^{II}{}_{3.4}Co^{III}{}_{0.6}(SO_4)_2(OH)_6]$ for I .

Experimental

In the attempt to synthesize new cobalt(II) sulfate frameworks, crystals of **I** were unintentionally obtained from the hydrothermal reaction of cobalt(II) sulfate heptahydrate and 1,4-diazabicyclo[2.2.2]octane in acidic aqueous solution (pH 4.4) under autogenous pressure at 453 K for 72 h.

Refinement

Hydrogen atoms were located by difference Fourier methods. The positions of these were refined subject to weak bond length restraints. Displacement parameters for the hydrogen atoms were set at 1.5 times the isotropic diaplcement parameter of the oxygen atom.

Prior to the refinement of site ocupancy of $[Co(H_2O)_6]^{2+}$, all atoms were located using Fourier difference methods. The displacement parameters of the intercalating ion were anomalously large. There were large maxima and minima in the residual electron density: e-max = 2.59 e Å^{-3} (centered on Co2); e-min = -2.58 e Å^{-3}. At this stage $wR(F^2)$ = 0.1914.

Refinement of the occupancy of the $[Co(H_2O)_6]^{2+}$ cation resulted in a significant improvement in the quality of the fit to the data: e-max = 1.044 e Å^{-3}; e-min = -1.046 e Å^{-3} and $wR(F^2)$ = 0.132.

Careful inspection of the diffraction images did not reveal any weak reflections which might indicate ordering of the partially occupied cation.

Figures

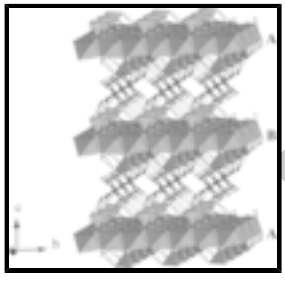

Fig. 1. View of the crystal structure of **I** along the *a* axis showing the brucite-type $[Co_4(SO_4)_2(OH)_6]$ layers which are intercalatated by the hydrogen bonded (dash lines) $[Co(H_2O)_6]^{2+}$ ions.

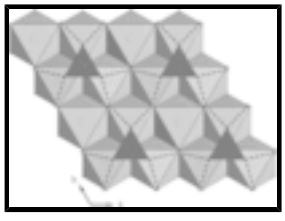

Fig. 2. Polyhedral representation of the cobalt hydroxysulate layer, built up of the edge-shared $[Co(OH)_6]$ and $[Co(OH)_4(OSO_3)_2]$ octahedra.

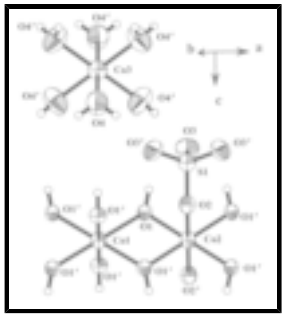

Fig. 3. View of the extended asymmetric unit of **I** with atom numbering scheme. Displacement ellipsoids are drawn at the 80% probability level.

poly[0.35-[hexaaquacobalt(II)] [tri-μ-hydroxido-μ-sulfato-dicobalt(II)]]

Crystal data

$[Co(H_2O)_6]_{0.35}[Co_2(OH)_3(SO_4)]$	$Z = 2$
$M_r = 323.41$	$F_{000} = 318.9$
Trigonal, $P\bar{3}m1$	$D_x = 2.515$ Mg m^{-3}
Hall symbol: -P 3 2"	Mo $K\alpha$ radiation, $\lambda = 0.71073$ Å
$a = 6.3627$ (19) Å	Cell parameters from 1764 reflections
$b = 6.3627$ (19) Å	$\theta = 1.7$–$29.3°$
$c = 12.180$ (4) Å	$\mu = 4.80$ mm^{-1}
$\alpha = 90°$	$T = 150$ K
$\beta = 90°$	Plate, pale pink
$\gamma = 120°$	0.21 × 0.13 × 0.03 mm
$V = 427.0$ (2) Å^3	

Data collection

Stoe IPDS2 diffractometer	497 independent reflections
Radiation source: fine-focus sealed tube	325 reflections with $I > 2\sigma(I)$
Monochromator: graphite	$R_{int} = 0.097$
Detector resolution: 6.67 pixels mm^{-1}	$\theta_{max} = 29.3°$
$T = 150$ K	$\theta_{min} = 1.7°$
ω scans	$h = -7 \rightarrow 8$
Absorption correction: multi-scan (X-RED; Stoe & Cie, 2008)	$k = -7 \rightarrow 8$
$T_{min} = 0.415$, $T_{max} = 0.862$	$l = -14 \rightarrow 16$
1663 measured reflections	

Refinement

Refinement on F^2	Secondary atom site location: difference Fourier map
Least-squares matrix: full	Hydrogen site location: difference Fourier map
$R[F^2 > 2\sigma(F^2)] = 0.048$	Only H-atom coordinates refined
$wR(F^2) = 0.132$	$w = 1/[\sigma^2(F_o^2) + (0.0839P)^2]$ where $P = (F_o^2 + 2F_c^2)/3$

S = 0.90	$(\Delta/\sigma)_{max} < 0.001$
497 reflections	$\Delta\rho_{max}$ = 1.04 e Å^{-3}
40 parameters	$\Delta\rho_{min}$ = −1.05 e Å^{-3}
3 restraints	Extinction correction: none
Primary atom site location: structure-invariant direct methods	

Special details

Geometry. All e.s.d.'s (except the e.s.d. in the dihedral angle between two l.s. planes) are estimated using the full covariance matrix. The cell e.s.d.'s are taken into account individually in the estimation of e.s.d.'s in distances, angles and torsion angles; correlations between e.s.d.'s in cell parameters are only used when they are defined by crystal symmetry. An approximate (isotropic) treatment of cell e.s.d.'s is used for estimating e.s.d.'s involving l.s. planes.

Refinement. Refinement of F^2 against ALL reflections. The weighted *R*-factor *wR* and goodness of fit *S* are based on F^2, conventional *R*-factors *R* are based on *F*, with *F* set to zero for negative F^2. The threshold expression of $F^2 > \sigma(F^2)$ is used only for calculating *R*-factors(gt) *etc*. and is not relevant to the choice of reflections for refinement. *R*-factors based on F^2 are statistically about twice as large as those based on *F*, and *R*- factors based on ALL data will be even larger.

Fractional atomic coordinates and isotropic or equivalent isotropic displacement parameters (Å^2)

	x	*y*	*z*	U_{iso}*/U_{eq}	Occ. (<1)
Co2	0.5000	0.0000	0.5000	0.0170 (3)	
Co1	0.0000	0.0000	0.5000	0.0163 (5)	
S1	0.6667	0.3333	0.2679 (2)	0.0214 (6)	
O1	0.1717 (3)	−0.1717 (3)	0.4215 (3)	0.0164 (9)	
O2	0.6667	0.3333	0.3913 (6)	0.0188 (15)	
O3	0.5403 (5)	0.0807 (9)	0.2298 (4)	0.0292 (11)	
Co3	0.0000	0.0000	0.0000	0.0250 (11)	0.700 (11)
O4	0.1574 (8)	0.3148 (16)	0.0920 (7)	0.039 (2)	0.700 (11)
H1	0.188 (9)	−0.188 (9)	0.355 (3)	0.059*	
H4	0.073 (9)	0.353 (18)	0.128 (5)	0.059*	0.700 (11)

Atomic displacement parameters (Å^2)

	U^{11}	U^{22}	U^{33}	U^{12}	U^{13}	U^{23}
Co2	0.0146 (5)	0.0156 (6)	0.0211 (6)	0.0078 (3)	0.0001 (2)	0.0002 (4)
Co1	0.0144 (6)	0.0144 (6)	0.0202 (9)	0.0072 (3)	0.000	0.000
S1	0.0220 (9)	0.0220 (9)	0.0203 (12)	0.0110 (4)	0.000	0.000
O1	0.0177 (16)	0.0177 (16)	0.0167 (18)	0.0111 (17)	−0.0002 (8)	0.0002 (8)
O2	0.017 (2)	0.017 (2)	0.023 (4)	0.0083 (11)	0.000	0.000
O3	0.034 (2)	0.023 (2)	0.027 (2)	0.0116 (12)	−0.0034 (10)	−0.0069 (19)
Co3	0.0256 (13)	0.0256 (13)	0.0238 (17)	0.0128 (7)	0.000	0.000
O4	0.034 (3)	0.043 (5)	0.044 (4)	0.022 (2)	−0.0080 (18)	−0.016 (4)

Geometric parameters (Å, °)

Co2—O1	2.047 (3)	S1—O3^{ix}	1.467 (5)

Co2—O1^{i}	2.047 (3)	S1—O2	1.502 (7)
Co2—O1^{ii}	2.047 (3)	O1—Co2^{x}	2.047 (3)
Co2—O1^{iii}	2.047 (3)	O1—H1	0.83 (3)
Co2—O2	2.264 (4)	O2—Co2^{viii}	2.264 (4)
Co2—O2^{i}	2.264 (4)	O2—Co2^{ix}	2.264 (4)
Co1—O1^{iv}	2.121 (4)	Co3—O4^{xi}	2.065 (8)
Co1—O1^{iii}	2.121 (4)	Co3—O4	2.065 (8)
Co1—O1^{v}	2.121 (4)	Co3—O4^{iv}	2.065 (8)
Co1—O1^{vi}	2.121 (4)	Co3—O4^{vi}	2.065 (8)
Co1—O1	2.121 (4)	Co3—O4^{xii}	2.065 (8)
Co1—O1^{vii}	2.121 (4)	Co3—O4^{xiii}	2.065 (8)
S1—O3	1.467 (5)	O4—H4	0.82 (3)
S1—O3^{viii}	1.467 (5)		
O1—Co2—O1^{i}	180.000 (1)	O3^{viii}—S1—O3^{ix}	110.49 (19)
O1—Co2—O1^{ii}	97.8 (2)	O3—S1—O2	108.4 (2)
O1^{i}—Co2—O1^{ii}	82.2 (2)	O3^{viii}—S1—O2	108.4 (2)
O1—Co2—O1^{iii}	82.2 (2)	O3^{ix}—S1—O2	108.4 (2)
O1^{i}—Co2—O1^{iii}	97.8 (2)	Co2—O1—Co2^{x}	102.00 (17)
O1^{ii}—Co2—O1^{iii}	180.0 (2)	Co2—O1—Co1	99.51 (14)
O1—Co2—O2	95.83 (13)	Co2^{x}—O1—Co1	99.51 (14)
O1^{i}—Co2—O2	84.17 (13)	Co2—O1—H1	112 (4)
O1^{ii}—Co2—O2	95.83 (13)	Co2^{x}—O1—H1	112 (4)
O1^{iii}—Co2—O2	84.17 (13)	Co1—O1—H1	129 (7)
O1—Co2—O2^{i}	84.17 (13)	S1—O2—Co2^{viii}	125.79 (14)
O1^{i}—Co2—O2^{i}	95.83 (13)	S1—O2—Co2	125.79 (14)
O1^{ii}—Co2—O2^{i}	84.17 (13)	Co2^{viii}—O2—Co2	89.3 (2)
O1^{iii}—Co2—O2^{i}	95.83 (13)	S1—O2—Co2^{ix}	125.79 (14)
O2—Co2—O2^{i}	180.0	Co2^{viii}—O2—Co2^{ix}	89.3 (2)
O1^{iv}—Co1—O1^{iii}	180.0 (2)	Co2—O2—Co2^{ix}	89.3 (2)
O1^{iv}—Co1—O1^{v}	78.77 (13)	O4^{xi}—Co3—O4	180.0 (4)
O1^{iii}—Co1—O1^{v}	101.23 (13)	O4^{xi}—Co3—O4^{iv}	86.7 (4)
O1^{iv}—Co1—O1^{vi}	101.23 (13)	O4—Co3—O4^{iv}	93.3 (4)
O1^{iii}—Co1—O1^{vi}	78.77 (13)	O4^{xi}—Co3—O4^{vi}	86.7 (4)
O1^{v}—Co1—O1^{vi}	180.00 (15)	O4—Co3—O4^{vi}	93.3 (4)
O1^{iv}—Co1—O1	101.23 (13)	O4^{iv}—Co3—O4^{vi}	93.3 (4)
O1^{iii}—Co1—O1	78.77 (13)	O4^{xi}—Co3—O4^{xii}	93.3 (4)
O1^{v}—Co1—O1	78.77 (13)	O4—Co3—O4^{xii}	86.7 (4)
O1^{vi}—Co1—O1	101.23 (13)	O4^{iv}—Co3—O4^{xii}	86.7 (4)
O1^{iv}—Co1—O1^{vii}	78.77 (13)	O4^{vi}—Co3—O4^{xii}	180.0 (4)
O1^{iii}—Co1—O1^{vii}	101.23 (13)	O4^{xi}—Co3—O4^{xiii}	93.3 (4)
O1^{v}—Co1—O1^{vii}	101.23 (13)	O4—Co3—O4^{xiii}	86.7 (4)

O1^{vi}—Co1—O1^{vii}	78.77 (13)	O4^{iv}—Co3—O4^{xiii}	180.0 (4)
O1—Co1—O1^{vii}	180.0 (2)	O4^{vi}—Co3—O4^{xiii}	86.7 (4)
O3—S1—O3^{viii}	110.49 (19)	O4^{xii}—Co3—O4^{xiii}	93.3 (4)
O3—S1—O3^{ix}	110.49 (19)	Co3—O4—H4	120 (5)

Symmetry codes: (i) −*x*+1, −*y*, −*z*+1; (ii) −*x*+*y*+1, −*x*, *z*; (iii) *x*−*y*, *x*, −*z*+1; (iv) −*x*+*y*, −*x*, *z*; (v) *y*, −*x*+*y*, −*z*+1; (vi) −*y*, *x*−*y*, *z*; (vii) −*x*, −*y*, −*z*+1; (viii) −*y*+1, *x*−*y*, *z*; (ix) −*x*+*y*+1, −*x*+1, *z*; (x) −*y*, *x*−*y*−1, *z*; (xi) −*x*, −*y*, −*z*; (xii) *y*, −*x*+*y*, −*z*; (xiii) *x*−*y*, *x*, −*z*.

Hydrogen-bond geometry (Å, °)

D—H···*A*	*D*—H	H···*A*	*D*···*A*	*D*—H···*A*
O1—H1···O3^{x}	0.83 (3)	2.54 (5)	3.125 (6)	129 (4)
O1—H1···O3	0.83 (3)	2.54 (5)	3.125 (6)	129 (4)
O4—H4···O3^{vi}	0.82 (3)	1.90 (9)	2.712 (1)	170 (7)

Symmetry codes: (x) −*y*, *x*−*y*−1, *z*; (vi) −*y*, *x*−*y*, *z*.

Journal of Alloys and Compounds 475 (2009) 473–478

Contents lists available at ScienceDirect

Journal of Alloys and Compounds

journal homepage: www.elsevier.com/locate/jallcom

Fabrication and dielectric properties of lead titanate nanocomposites

R. Wongmaneerung[a], A. Rujiwatra[b], R. Yimnirun[c], S. Ananta[c,*]

[a] Department of Physics, Faculty of Science, Maejo University, Chiang Mai 50290, Thailand
[b] Department of Chemistry, Faculty of Science, Chiang Mai University, Chiang Mai 50200, Thailand
[c] Department of Physics, Faculty of Science, Chiang Mai University, Chiang Mai 50200, Thailand

ARTICLE INFO

Article history:
Received 14 January 2008
Received in revised form 8 July 2008
Accepted 13 July 2008
Available online 6 September 2008

Keywords:
Lead titanate
Perovskite
Composites
Microstructure
Dielectric properties

ABSTRACT

A simple powder mixing and pressure-less sintering process for fabrication of $PbTiO_3$ (PT) nanocomposites (micron-sized PT matrix reinforced with either PT nanoparticles or nanofibers) has been developed to enhance both densification and dielectric properties. The potentiality of a ceramic-nanocomposite technique as a low-cost and simple ceramic fabrication to obtain highly dense and pure PT/PT composites was demonstrated. It has been found that both densification and dielectric properties of the composites fabricated in this work were significantly enhanced, as compared to the two-stage sintering and the conventional PT ceramics.

1. Introduction

Pure and dense lead titanate ($PbTiO_3$ or PT) ceramic, which is of interest as a component in commercial electroceramic materials, is regarded to be one of the most difficult lead-based perovskite ferroelectric ceramics to produce [1–3]. The most important properties of PT ceramics are high Curie temperature (~490 °C), large mechanical-quality factor and pyroelectric coefficient [4,5]. Moreover, PT when combined with other oxides can form a series of ferroelectric materials that exhibit many of the most desirable dielectric, piezoelectric and pyroelectric properties for use in electronic and electro-optic devices at high frequency and high temperature, such as infrared sensors, actuators and hydrophones [1–3]. However, PT ceramic is mechanically weak due to large distortion of the tetragonal phase at room temperature which is characterized by the ratio between the lattice parameters (c/a, hereafter called tetragonality, ~1.06 [6,7]). Apart from general problems of PbO volatilization and associated high porosity, the stress induced by cooling through the phase transition can create cracking in bulk ceramics.

To overcome these problems, several techniques have been introduced, such as utilizing nanopowders, using additives, employing spark-plasma sintering and carrying out appropriated milling and sintering conditions [8–13]. All these techniques are aimed at reducing the lattice tetragonality of bulk ceramics, even though they inevitably affect the phase formation, structure and electrical properties of materials in different ways. Amongst all the issues reported so far, most attention has been concentrated on the use of additives and chemically derived powder processing, whereas investigations on modified particle packing or composite techniques have not been widely carried out [14,15].

Recently, ceramic-nanocomposites in which nanosized phases were dispersed within the matrix grains and/or at the grain boundaries have emerged as a novel approach of improving materials properties [16]. The mechanical properties of ceramics are known to be improved significantly by dispersing ceramic-nanoparticles into the ceramic-matrix grains or grain boundaries. However, the degree of improvement in their properties is dependent on the type of composite system involved [16]. Few studies have reported on ferroelectric matrix/metal nanodispersoid [17] and ferroelectric matrix/non-ferroelectric nanodispersoid [18] composite systems, and it is not yet clear how these dispersoids affect the properties of nanocomposites. Moreover, the problem of property trade-off, i.e., a deterioration of electrical properties still remains unsolved. In other words, the improvement of mechanical property can only be realized only by sacrificing electrical properties. So far, a little has been reported on the fabrication of ferroelectric matrix/ferroelectric nanodispersoid composite systems [19]. However, no work on the perovskite PT ceramic-nanocomposites has been reported yet.

Therefore, in this work, ferroelectric matrix/ferroelectric nanodispersoid PT composite has been developed to resolve these problems. With this new scheme, instead of using only micron-

* Corresponding author. Tel.: +66 53 943367; fax: +66 53 943445.
E-mail address: suponananta@yahoo.com (S. Ananta).

0925-8388/$ – see front matter © 2008 Elsevier B.V. All rights reserved.
doi:10.1016/j.jallcom.2008.07.074

sized PT powders as reported in our previous works [13,20], two different types of PT nanodispersoid (nanoparticles and nanofibers) were adopted as starting materials. The influence of both PT nanodispersoids on densification, microstructure and dielectric properties of the composites will be discussed and compared with the conventional method.

2. Experimental procedure

The starting PT materials for the fabrication of self-reinforced PT matrix/PT nanodispersoid composites were micron-sized PT powders, nanopowders, and nanofibers (Fig. 1), which were synthesized via ball-milling, vibro-milling, and hydrothermal techniques, respectively. The characteristics of each starting PT materials and their processing details are described in our previous works [21–23]. The powder mixtures (matrix:dispersoid ratio of 1:1) were formed into pellets by adding 3 wt.% polyvinyl alcohol (PVA) binder, prior to pressing in a pseudo-uniaxial die press at 100 MPa. It should be noted here that preliminary study of other matrix:dispersoid ratios, e.g. 0.7:0.3 and 0.6:0.4 was carried out and the complete solid-solution microstructure type commonly observed in the conventional PT processing was observed in all cases, indicating the solubility effect of the perovskite PT/PT (although their morphologies are different) limiting the possibility of composite formation. Each pellet was placed in an alumina crucible together with an atmosphere powder of identical chemical composition [20]. Such a composite cannot be fabricated by hot-pressing in the reduced atmosphere because the Pb-based perovskite is easily decomposed in the atmosphere. In this work, the composites were prepared by using simple pressure-less sintering method. Sintering was carried out at various temperatures (1000–1225 °C), for 1 h with heating/cooling rates of 1 °C/min [13,20] applied. These firing conditions were advocated from our previous work on PT ceramics with experimental details presented in Refs. [13,20].

Densities of the sintered products were determined by using the Archimedes principle. X-ray diffraction (XRD; Siemens-D500 diffractometer) was carried out at room temperature using Cu Kα radiation to identify the phase formed. The lattice parameters and tetragonality factor (c/a) of the sintered ceramics were calculated from the XRD patterns [24]. The microstructural development was characterized using a scanning electron microscopy (SEM; JEOL JSM-840A), equipped with an energy dispersive X-ray (EDX) analyzer. Mean grain sizes of the sintered ceramics were subsequently estimated by employing the linear intercept method [25]. In order to evaluate the dielectric properties, densified ceramics were polished to form flat and parallel faces. The samples were coated with silver-paste electrodes which were fired on both sides of the samples at 700 °C for 1 h. The dielectric properties were measured using a HIOKI 3532-50 LCR meter, on cooling through the transition range (550–25 °C) with a rate of 5 °C/min at high frequencies ranging from 1 to 5 MHz. Values of the dielectric constant were corrected for porosity by using the relationship $\varepsilon_r = \varepsilon_{r(measured)} \times$ theoretical density/sintered density [26].

3. Results and discussion

X-ray diffraction patterns of the PT composites reinforced with various PT dispersoids and sintered at various temperatures are displayed in Fig. 2, indicating the formation of single phase perovskite in all cases. The strongest reflections in the majority of all XRD traces indicate the formation of the PT perovskite phase of lead titanate which could be matched with JCPDS file no. 6-452, in agreement with other works [10–13]. To a first approximation, this phase has a tetragonal perovskite-type structure in space group $P4/mmm$ with cell parameters $a = 389.93$ pm and $c = 415.32$ pm [27]. All the peaks were assigned to PT, and no reaction phase between different PT starting materials was detected. Moreover, there is no significant difference between the PT nanocomposites reinforced with either PT nanopowders or nanofibers, after sintered at temperatures ranging from 1150 to 1200 °C. This observation could be attributed mainly to the high purity of the employed starting materials together with the optimized firing conditions. The samples sintered with temperature below 1150 °C were broken into pieces after sintering process, whilst the samples sintered at 1225 °C exhibited severe melted areas. Thus, no further characterization can be performed on these samples.

It should be noted that a single phase of perovskite is found in all PT composites similar with the two-stage sintering samples [20], in contrast to the observations for the conventional case [13] (Table 1). No evidence of pyrochlore phase of $PbTi_3O_7$ composition

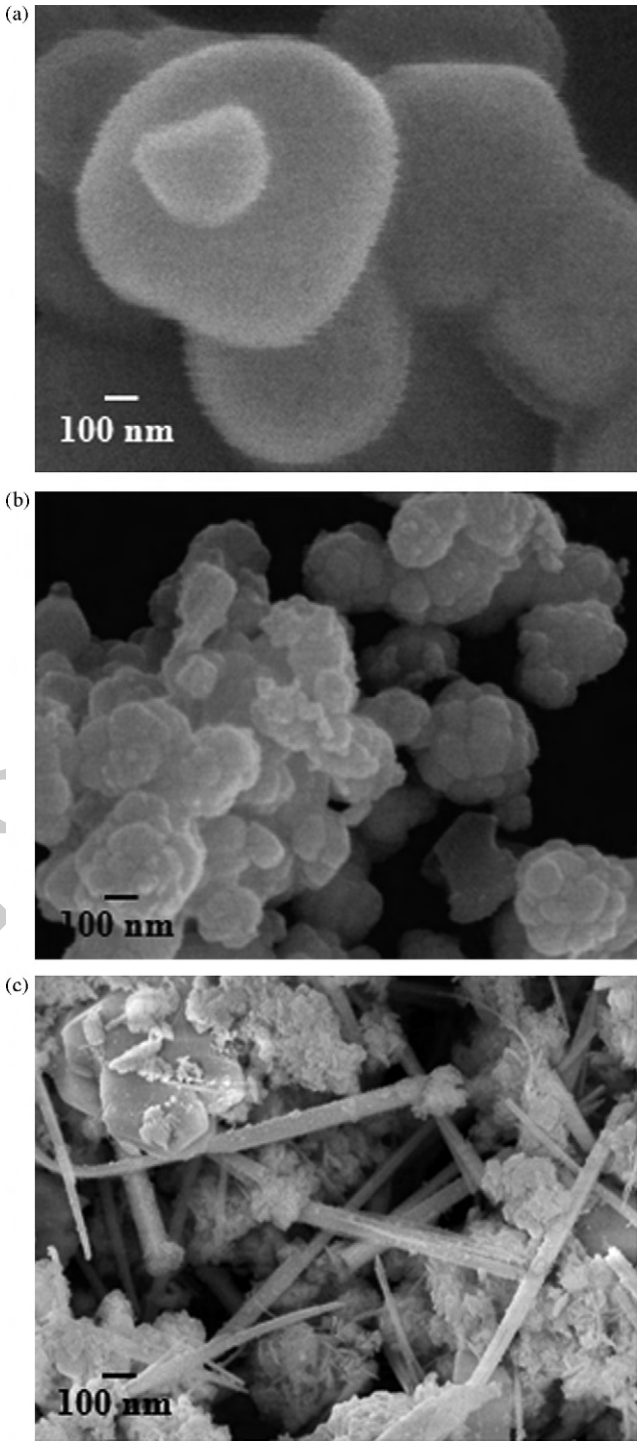

Fig. 1. SEM micrographs of the starting PT dispersoids: (a) micron-sized powders, (b) nanopowders, and (c) nanofibers.

reported earlier by other workers [21,28] was found, nor was any evidence of other second phases [29] being present. This could be due to the lower firing temperature of the nanocomposite samples as compared to the conventional PT ceramics, leading to a smaller degree of lead losses and consequently avoiding the pyrochlore formation, in consistent with other works [30,31], whilst a sufficient arrangement of grain-packing required for ceramic densification still be reached. However, many other factors come into play, e.g. homogeneity of materials, reactivity of starting powders, and pro-

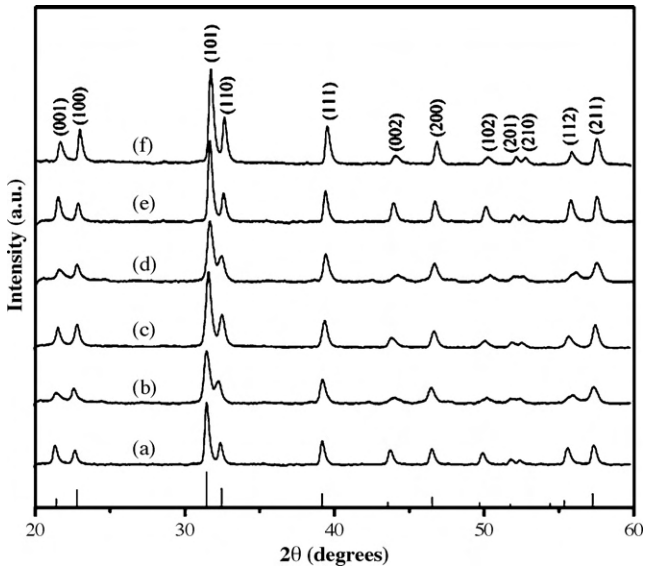

Fig. 2. XRD patterns of PT composites reinforced with PT nanopowders after sintered at (a) 1150 °C, (b) 1175 °C and (c) 1200 °C, and reinforced with PT nanofibers after sintered at (d) 1150 °C, (e) 1175 °C and (f) 1200 °C, for 2 h.

cessing variables. These XRD results clearly show that, in general, the different processing methods used for preparing PT ceramics gave rise to a different phase formation in the sintered materials. The absence of minor phase in composite samples was related to the more reactive process used.

Table 1 also shows tetragonality factor (c/a), relative density and average grain size of each nanocomposite sample, comparing with the conventional and the two-stage sintered samples, respectively. Generally, it is evident that as the sintering temperature increases, the density of almost all the samples increases. However, it can be seen that the sintering behavior of PT ceramics derived from different processing techniques were dissimilar. Two-stage sintering PT ceramics reached a maximum density of ~97% at 900/1200 °C [20]. Whilst conventional PT samples exhibit reduced densification, and a temperature of 1225 °C was required to reach a densification level of ~94% [13]. On the other hand, both types of PT nanocomposites sintered at 1200 °C exhibit the highest relative density of about 98% with a smallest average grain size of less than 1.0 μm. By comparison with conventional PT ceramics, lower values of tetragonality (c/a) are found in all nanocomposite cases, equivalent to those observed in the two-stage sintering case, indicating lower internal stress in these nanocomposites. More interestingly, all nanocomposite samples do not suffer from severe stresses as a result of the high c/a ratio so they have not broken into pieces after experienced the sintering process or once subjected to a cycle of high temperature measurement of dielectric properties, as reported previously for the conventional and two-stage sintering PT cases [13,20].

Microstructural features (free and fracture surfaces) of both PT nanocomposites sintered at different temperatures for 2 h are shown in Figs. 3 and 4. It was found that average grain sizes increase with the sintering temperature (Fig. 3). The PT nanodispersoids were found to locate both within the matrix and at the grain boundaries (see enlarged insertion in Fig. 3(d)). The microstructure of the composites is that of the nanocomposites classified as "nanomicro" and "nanofiber" types [16].

Representative fracture surfaces for both types of PT nanocomposites are given in Fig. 4. It is seen that a uniform grain shape of typical perovskite ceramics [9,30,31] is observed, with sizes in the range of 0.2–2.8 μm. It should be noted that the average grain size of both PT nanocomposites is <1.7 μm, which is less than the critical value of 3 μm [11,32,33] and gives rise to a volumetric percentage enough to buffer the anisotropic stress caused by the phase transition [32]. Here, it is believed that PT nanodispersoids with random orientations result in lower internal stress in composite samples because they compensate the anisotropy of thermal expansion coefficients.

By comparison with conventional PT ceramics [13], almost clean microstructures with highly uniform, denser angular grain-packing and more homogeneous are generally observed in both types of self-reinforced PT nanocomposites. These microstructures are typical of a solid-state sintering mechanism. In the present study (Figs. 3 and 4), the microstructural features of both types of PT nanocomposites with various sintering temperatures ranging from 1150 to 1200 °C are not significantly different. However, it should be noted that higher angularly grains were evidenced for higher sintering temperature. The observation that the sintering temperature effect may also play an important role in obtaining a high angularity grains of perovskite ceramics is also consistent with other similar systems [30,31]. Moreover, abnormal grain growth probably due to the inhibition of grain growth mechanism during doubly sintering process [20,34] was also found in some samples, as shown in Figs. 3(c and d) and 4(f). It is also of interest to point out that evidence of intergranular fracture has been found for the existence of microcracks (arrowed) along the grain boundaries of the composite samples self-reinforced with PT nanoparticles (Fig. 4(a–c)). The different microstructure evolution of PT nanocomposites confirms the importance of the processing method including the morphological characteristics of the dispersed phase, consistent with other works [32,35]. Whilst the grain size of both nanocomposites is approximately the same, the density and microstructure of PT samples sintered at higher temperatures indicated that the composite

Table 1
Sintering behavior of PT ceramics derived from different fabrication techniques

Processing [Ref.]	Sintering temperature (°C)	Perovskite phase[a] (%)	Relative density[b] (%)	Tetragonality factor (c/a)	Grain size[c] (μm)	Average grain size (μm)
Normal sintering [13]	1225	89.20	93.00	1.063	41.0–83.0	62.0
Two-stage sintering [20]	900/1200	100.00	97.02	1.061	1.0–2.2	1.6
Composite reinforced with nanopowders	1150	100.00	96.33	1.059	0.2–0.6	0.40
	1175	100.00	97.02	1.053	0.3–1.0	0.65
	1200	100.00	97.85	1.061	0.6–2.0	1.30
Composite reinforced with nanofibers	1150	100.00	95.68	1.053	0.3–1.3	0.80
	1175	100.00	96.76	1.058	0.4–1.3	0.85
	1200	100.00	97.45	1.061	0.5–2.8	1.65

[a] The estimated precision of the perovskite phase is ±0.1%.
[b] The estimated precision of the density is ±0.1%.
[c] The estimated precision of the grain size is ±10%.

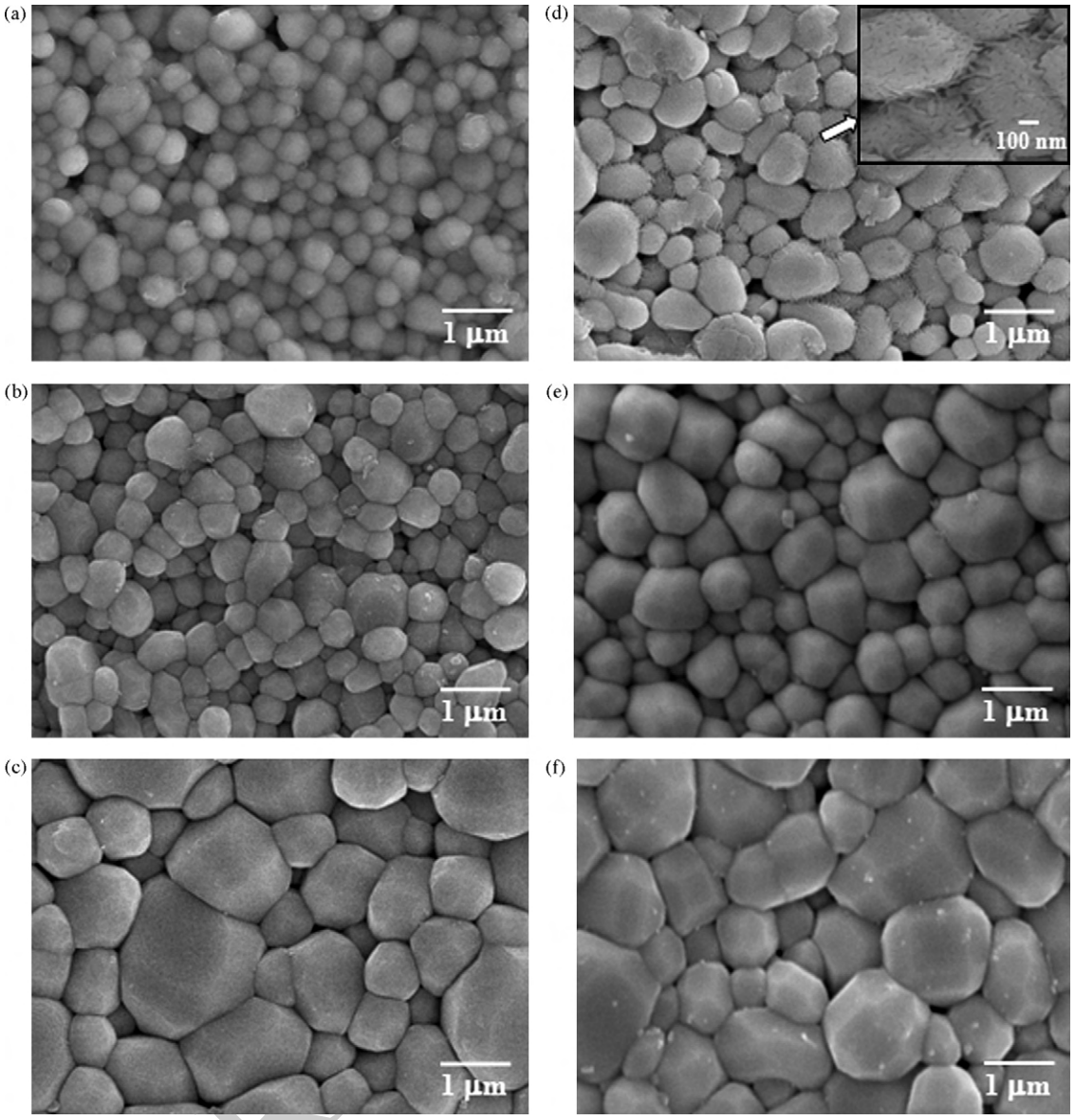

Fig. 3. Free surface of PT composites reinforced with PT nanopowders after sintered at (a) 1150 °C, (b) 1175 °C and (c) 1200 °C, and reinforced with PT nanofibers after sintered at (d) 1150 °C, (e) 1175 °C and (f) 1200 °C, for 2 h.

method of PT matrix reinforced with PT nanofibers was preferable for obtaining dense PT ceramics.

Interestingly, all the nanocomposite samples sintered at 1150–1200 °C remained unbroken. It may be assumed that the nanocomposites consisting of very fine dispersoids suffer less deformation, caused by the high value of c/a ratio, than the ceramics with significantly large grains (Table 1). Consequently, the experimental work carried out here suggests that the optimum conditions for forming the highly dense PT samples in this work are both types of PT/PT nanocomposites sintered at 1200 °C, 2 h dwell time, and 1 °C/min heating/cooling rates.

The dielectric properties of PT samples fabricated with different techniques are also compared in Table 2. In general, they all behave as typical normal ferroelectric materials [3]. The Curie temperatures are about the same for all samples measured whilst the variation of dielectric constant and dielectric loss of both types of PT nanocomposites seems to be somewhat related to the sintering temperatures. This observation indicates that densification and the presence of the second phases accompanied with porosities are the key factors responsible for the dielectric response of the products. Moreover, this study demonstrated that the dielectric properties of PT ceramics are also influenced by microstructural features and arrangement especially the microcracks and final density rather than by only grain size itself.

Table 2
Dielectric properties of PT ceramics derived from different fabrication techniques

Processing [Ref.]	Frequency (MHz)	T_C (°C)	$\varepsilon_{25°}$	$\varepsilon_{r,max}$	tan δ_{max}
Normal sintering [13]	1	482	243	7680	1.07
Two-stage sintering [20]	1	484	209	8198	0.95
Composite reinforced with nanopowders	1	486	244	8523	1.09
	3	486	245	7517	0.91
	5	487	247	7144	0.76
Composite reinforced with nanofibers	1	488	248	9104	0.81
	3	489	246	7110	0.57
	5	489	242	6801	0.45

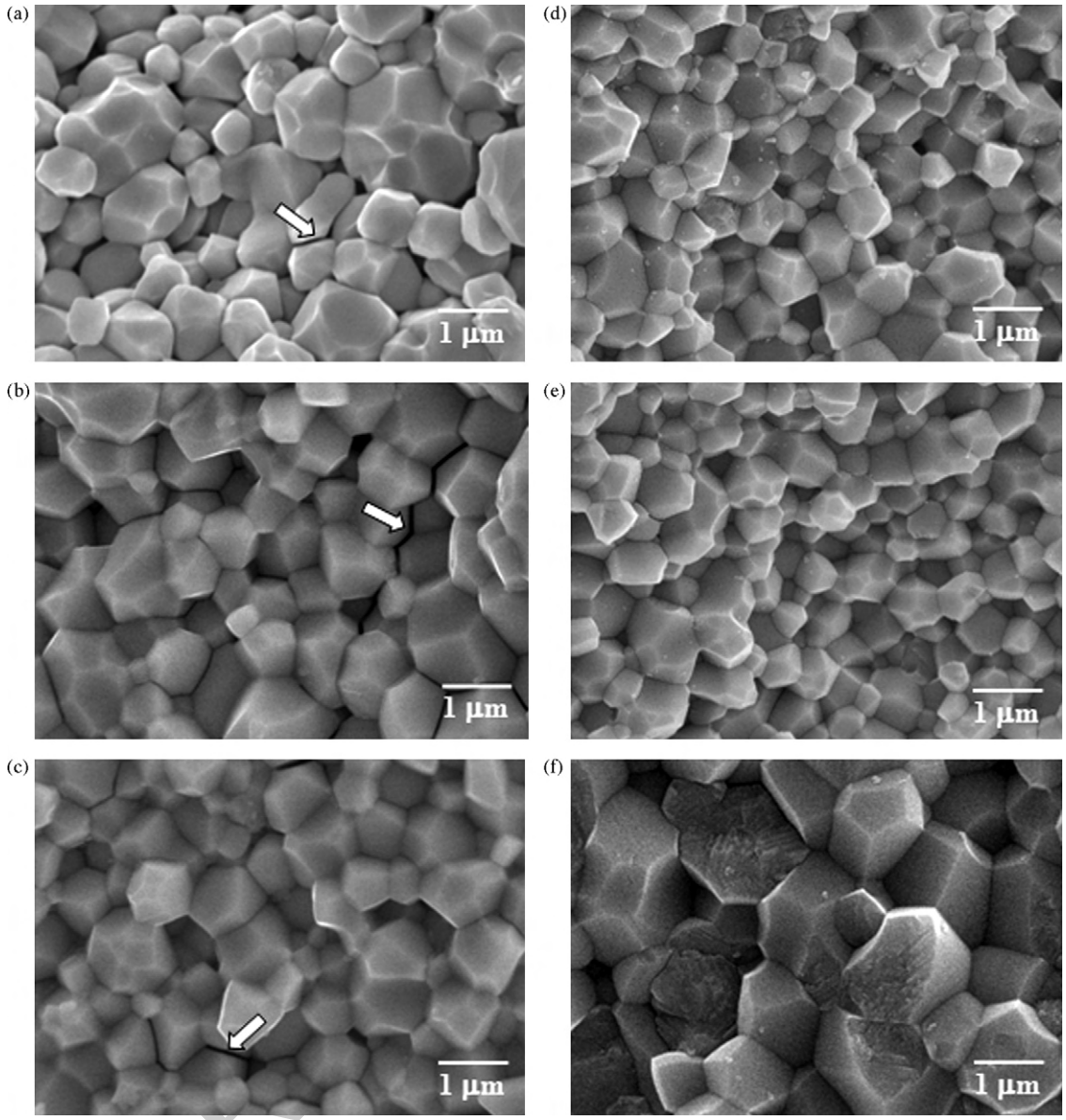

Fig. 4. Fracture surface of PT composites reinforced with PT nanopowders after sintered at (a) 1150 °C, (b) 1175 °C and (c) 1200 °C, and reinforced with PT nanofibers after sintered at (d) 1150 °C, (e) 1175 °C and (f) 1200 °C, for 2 h.

The different microstructure and the different amount of secondary phases present in the sintered PT ceramics strongly influence the dielectric properties of these materials, leading to relatively superior dielectric behavior in PT/PT nanocomposites. The secondary phases in conventional PT sample are interconnected at grain boundaries and, as suggested by Wang and Schulze [31], exert more influence on the dielectric properties than when they are isolated. The influence of densification and microcracks on dielectric properties of these PT composites can be clearly observed in Fig. 5, where the dielectric constant and dissipation factor as a function of temperature are shown, respectively.

The maximum dielectric constant values at 1 MHz in both PT nanocomposites were 2–5% higher than in two-stage sintering and conventional PT samples (Table 2). As mentioned earlier, the reason for this is the high amount of secondary phase present in conventional PT ceramics and the presence of a PbO-rich secondary phase, with low dielectric constant, which could form a continuous layer between grains, decreasing the dielectric constant of the two-stage sintering samples [13,36].

The results obtained in this work suggest that, in general, these PT/PT nanocomposites exhibit complex microstructures which are inherently heterogeneous. The heterogeneity is a result of variation in grain size and orientation; variation in chemical homogeneity; and the presence and distribution of additional minor phase, pores and (micro) cracks. These factors, which are strongly influenced by the sintering conditions, have an important effect on the dielectric properties of the materials and their reproducibility. However, these results suggest that better densification can be introduced into piezoceramics by fabricating ceramic-nanocomposites reinforced with piezoelectric nanodispersoids. Two aspects of this study are significant: (i) reductions in the maximum required sintering temperature (or the required prolong firing time) are possible as compared to the conventional (or the two-stage sintering) method and (ii) a framework has been established for developing self-reinforced piezoceramic-nanocomposite technique for better

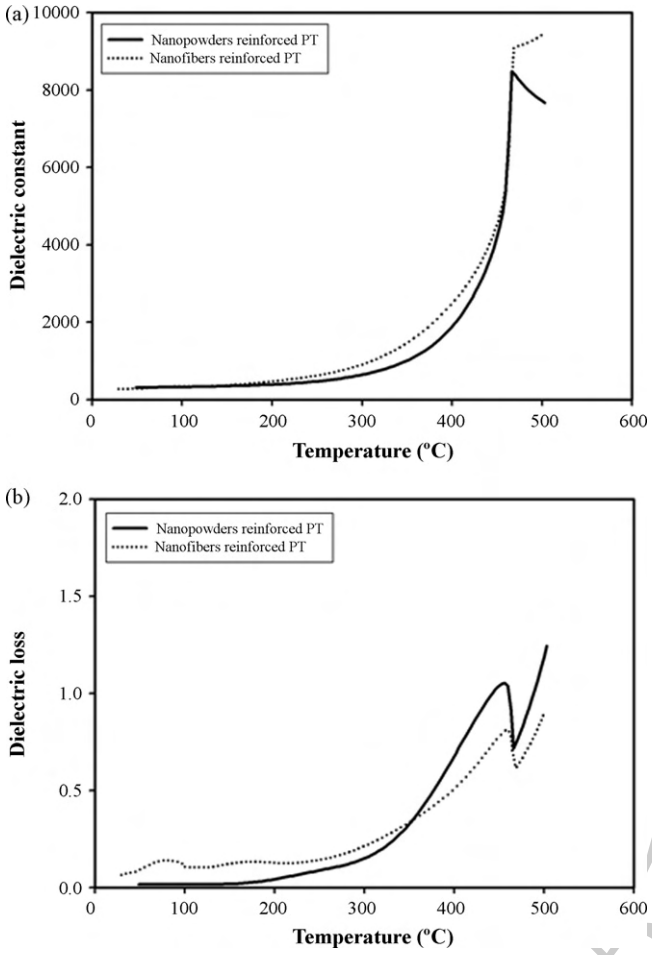

Fig. 5. Variation with temperature of (a) dielectric constant (ε_r) and (b) dielectric loss ($\tan\delta$) at 1 MHz for PT composites reinforced with PT nanopowders compared with those reinforced with PT nanofibers.

densification with retainable electrical properties of other piezoelectric materials, particularly those containing low melting point constituents.

For better understanding and verifying the attractiveness of the nanocomposite technique further, a systematic study on the effect of another piezoelectric nanodispersoids such as $BaTiO_3$ or PZT on the phase formation, densification, microstructure and electrical properties of the piezoelectric-based ceramic-nanocomposites is required.

4. Conclusions

The potentiality of a ceramic-nanocomposite technique as a low-cost and simple ceramic fabrication to obtain highly dense and pure PT/PT composites was demonstrated. It has been found that both densification and dielectric properties of the composites fabricated in this work were significantly enhanced, as compared to the two-stage sintering and the conventional PT ceramics, which is likely due to the fine-grain and reduced tetragonality as well as anisotropies of stress and domain motion in the composites.

Acknowledgements

We thank the Thailand Research Fund (TRF), the Commission on Higher Education (CHE) and the National Nanotechnology Center (NANOTEC), NSTDA, for all support.

References

[1] B. Jaffe, W.R. Cook, H. Jaffe, Piezoelectric Ceramics, Academic Press, New York, 1971.
[2] G.H. Haertling, J. Am. Ceram. Soc. 82 (1999) 797–818.
[3] A.J. Moulson, J.M. Herbert, Electroceramics, 2nd ed., Wiley, Chichester, 2003.
[4] T. Takahashi, Am. Ceram. Soc. Bull. 69 (1990) 691–695.
[5] L.E. Cross, Mater. Chem. Phys. 43 (1996) 108–115.
[6] G. Shirane, S. Hoshino, J. Phys. Soc. Jpn. 6 (1951) 265–270.
[7] G. Shirane, R. Pepinsky, B.C. Frazer, Acta Crystallogr. 9 (1956) 131–140.
[8] H. Takeuchi, S. Jyomura, E. Yamamoto, Y. Ito, J. Acoust. Soc. Am. 72 (1982) 1114–1120.
[9] L.B. Kong, W. Zhu, O.K. Tan, J. Mater. Sci. Lett. 19 (2000) 1963–1966.
[10] T. Suwannasiri, A. Safari, J. Am. Ceram. Soc. 76 (1993) 3155–3158.
[11] T. Takeuchi, M. Tabuchi, I. Kondoh, N. Tamari, H. Kageyama, J. Am. Ceram. Soc. 83 (2000) 541–544.
[12] J.S. Forrester, J.S. Zobec, D. Phelan, E.H. Kisi, J. Solid State Chem. 177 (2004) 3553–3559.
[13] A. Udomporn, K. Pengpat, S. Ananta, J. Eur. Ceram. Soc. 24 (2004) 185–188.
[14] F. Ye, L. Liu, J. Zhang, M. Iwasa, C.L. Su, Compos. Sci. Technol. 65 (2005) 2233–2239.
[15] R. Gadow, F. Kern, A. Killinger, Mater. Sci. Eng. B 148 (2008) 58–64.
[16] T. Ohji, Y.K. Jeong, Y.H. Choa, K. Niihara, J. Am. Ceram. Soc. 81 (1998) 1453–1460.
[17] H.T. Chung, D.S. Cheong, C.S. Kim, Mater. Lett. 59 (2005) 920–924.
[18] S. Jiansirisomboon, A. Watcharapasorn, Curr. Appl. Phys. 8 (2008) 48–52.
[19] H. Beltran, N. Maso, E. Cordoncillo, A.R. West, J. Electroceram. 18 (2007) 277–282.
[20] R. Wongmaneerung, R. Yimnirun, S. Ananta, Appl. Phys. A 86 (2007) 249–255.
[21] A. Udomporn, S. Ananta, Mater. Lett. 58 (2004) 1154–1159.
[22] R. Wongmaneerung, R. Yimnirun, S. Ananta, Mater. Lett. 60 (2006) 2666–2671.
[23] A. Rujiwatra, N. Thammajak, T. Sarakonsri, R. Wongmaneerung, S. Ananta, J. Crystal Growth 289 (2006) 224–230.
[24] H. Klug, L. Alexander, X-ray Diffraction Procedures for Polycrystalline and Amorphous Materials, 2nd ed., Wiley, New York, 1974.
[25] R.L. Fullman, Trans. AIME 197 (1953) 447–452.
[26] S.L. Swartz, T.R. Shrout, W.A. Schulze, L.E. Cross, J. Am. Ceram. Soc. 67 (1984) 311–315.
[27] JCPDS-ICDD Card no. 6-452, International Centre for Diffraction Data, Newtown Square, PA, 2000.
[28] J. Tartaj, C. Moure, L. Lascano, P. Durán, Mater. Res. Bull. 36 (2001) 2301–2310.
[29] M.L. Calzada, M. Alguero, L. Pardo, J. Sol–Gel Sci. Technol. 13 (1998) 837.
[30] S. Ananta, N.W. Thomas, J. Eur. Ceram. Soc. 19 (1999) 1873–1881.
[31] H.C. Wang, W.A. Schulze, J. Am. Ceram. Soc. 73 (1990) 825–832.
[32] Y. Matsuo, H. Sasaki, J. Am. Ceram. Soc. 49 (1966) 229–230.
[33] S.R. Dhage, Y.B. Khollam, H.S. Potdar, S.B. Deshpande, B.D. Sarwade, D.K. Date, Mater. Lett. 56 (2002) 564–570.
[34] S. Ananta, N.W. Thomas, J. Eur. Ceram. Soc. 19 (1999) 2917–2930.
[35] S. Chattopadhyay, P. Ayyub, V.R. Palkar, M. Multani, Phys. Rev. B 52 (1995) 13177–13179.
[36] M. Villegas, A.C. Caballero, M. Kosec, C. Moure, P. Duran, J.F. Fernandez, J. Mater. Res. 14 (1999) 891–897.

Acta Crystallographica Section E
Structure Reports Online
ISSN 1600-5368

Tris(ethylenediamine)cobalt(II) sulfate

Bunlawee Yotnoi, Athittaya Seeharaj, Yothin Chimupala and Apinpus Rujiwatra*

Department of Chemistry, Faculty of Science, Chiang Mai University, Chiang Mai 50200, Thailand
Correspondence e-mail: apinpus@gmail.com

Received 27 April 2010; accepted 3 May 2010

Key indicators: single-crystal X-ray study; T = 298 K; mean σ(C–C) = 0.003 Å; disorder in main residue; R factor = 0.028; wR factor = 0.069; data-to-parameter ratio = 14.6.

The structure of the title compound, $[Co^{II}(C_2H_8N_2)_3]SO_4$, the cobalt example of $[M(C_2H_8N_2)_3]SO_4$, is reported. The Co and S atoms are located at the 2*d* and 2*c* Wyckoff sites (point symmetry 32), respectively. The Co atom is coordinated by six N atoms of three chelating ethylenediamine molecules generated from half of the ethylenediamine molecule in the asymmetric unit. The O atoms of the sulfate anion are disordered mostly over two crystallographic sites. The third disorder site of O (site symmetry 3) has a site occupancy approaching zero. The H atoms of the ethylenediamine molecules interact with the sulfate anions *via* intermolecular N—H···O hydrogen-bonding interactions.

Related literature

For isostructural $[M(C_2H_8N_2)_3]SO_4$ complexes, see: Haque *et al.* (1970); Cullen & Lingafelter (1970); Daniels *et al.* (1995); Lu (2009) for the nickel, copper, vanadium and manganese analogues, respectively.

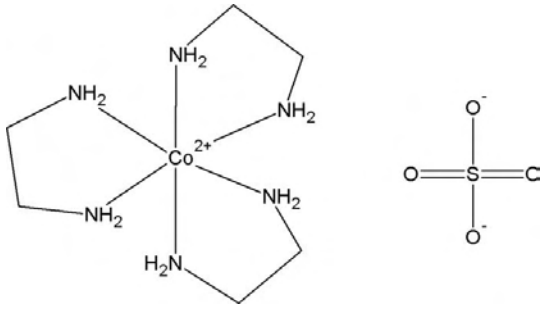

Experimental

Crystal data

$[Co(C_2H_8N_2)_3]SO_4$
M_r = 335.30
Trigonal, $P\bar{3}1c$
a = 8.9920 (2) Å
c = 9.5927 (3) Å
V = 671.71 (3) Å^3
Z = 2
Mo $K\alpha$ radiation
μ = 1.45 mm^{-1}
T = 298 K
0.48 × 0.22 × 0.20 mm

Data collection

Bruker SMART CCD area-detector diffractometer
Absorption correction: multi-scan (*SADABS*; Sheldrick, 1996)
T_{min} = 0.543, T_{max} = 0.760
3638 measured reflections
688 independent reflections
589 reflections with $I > 2\sigma(I)$
R_{int} = 0.027

Refinement

$R[F^2 > 2\sigma(F^2)]$ = 0.028
$wR(F^2)$ = 0.069
S = 1.06
688 reflections
47 parameters
16 restraints
H-atom parameters constrained
$\Delta\rho_{max}$ = 0.25 e Å^{-3}
$\Delta\rho_{min}$ = −0.29 e Å^{-3}

Table 1
Hydrogen-bond geometry (Å, °).

D—H···A	D—H	H···A	D···A	D—H···A
N1—H1A···O3^{i}	0.90	2.13	2.889 (12)	142
N1—H1A···O1^{i}	0.90	2.15	3.049 (7)	176
N1—H1A···O2^{ii}	0.90	2.22	3.054 (8)	155
N1—H1A···O2^{iii}	0.90	2.32	3.104 (11)	145
N1—H1B···O2^{iv}	0.90	1.98	2.843 (6)	161
N1—H1B···O1	0.90	2.48	3.353 (14)	165
N1—H1B···O1^{v}	0.90	2.52	3.256 (10)	139

Symmetry codes: (i) $-x+1, -y+1, -z$; (ii) $y, -x+y, -z$; (iii) $x-y+1, x, -z$; (iv) $-x+y, -x+1, z$; (v) $-y+1, -x+1, -z+\frac{1}{2}$.

Data collection: *SMART* (Bruker, 2003); cell refinement: *SAINT* (Bruker, 2003); data reduction: *SAINT*; program(s) used to solve structure: *SHELXS97* (Sheldrick, 2008) and *WinGX* (Farrugia, 1999); program(s) used to refine structure: *SHELXL97* (Sheldrick, 2008) and *WinGX* (Farrugia, 1999); molecular graphics: *DIAMOND* (Brandenburg, 2006); software used to prepare material for publication: *publCIF* (Westrip, 2010).

This work was supported financially by the Thailand Research Fund and the Center of Excellence for Innovation in Chemistry. BY thanks the Royal Golden Jubilee PhD program and the Graduate School of Chiang Mai University for a graduate scholarship.

Supplementary data and figures for this paper are available from the IUCr electronic archives (Reference: TK2667).

References

Brandenburg, K. (2006). *DIAMOND*. Crystal Impact GbR, Bonn, Germany.
Bruker (2003). *SMART* and *SAINT*. Bruker AXS Inc., Madison, Wisconsin, USA.
Cullen, D. L. & Lingafelter, E. C. (1970). *Inorg. Chem.* **9**, 1858–1864.
Daniels, L. M., Murillo, C. A. & Rodriguez, K. G. (1995). *Inorg. Chim. Acta*, **229**, 27–32.
Farrugia, L. J. (1999). *J. Appl. Cryst.* **32**, 837–838.
Haque, M.-U., Caughlan, C. N. & Emerson, K. (1970). *Inorg. Chem.* **9**, 2421–2424.
Lu, J. (2009). *Acta Cryst.* E**65**, m1187.
Sheldrick, G. M. (1996). *SADABS*. University of Göttingen, Germany.
Sheldrick, G. M. (2008). *Acta Cryst.* A**64**, 112–122.
Westrip, S. P. (2010). *J. Appl. Cryst.* **43**. Submitted.

Acta Cryst. (2010). E**66**, m628 [**doi:10.1107/S1600536810016168**]

Tris(ethylenediamine)cobalt(II) sulfate

B. Yotnoi, A. Seeharaj, Y. Chimupala and A. Rujiwatra

Comment

The title complex, $[Co^{II}(C_2H_8N_2)_3]SO_4$ (Fig. 1), is isostructural to the earlier reported $[Ni^{II}(C_2H_8N_2)_3]SO_4$ (Haque *et al.*,, 1970), $[V^{II}(C_2H_8N_2)_3]SO_4$ (Daniels *et al.*, 1995), $[Mn^{II}(C_2H_8N_2)_3]SO_4$ (Lu, 2009) and $[Cu^{II}(C_2H_8N_2)_3]SO_4$ (Cullen & Lingafelter, 1970) complexes, constituting the $[M^{II}(C_2H_2N_2)_3]SO_4$ series. The $[M^{II}(C_2H_2N_2)_3]SO_4$ structures crystallize in the same trigonal space group of $P\bar{3}1c$ with quite similar cell parameters. Likewise, the metal and sulfur atoms are positioned in the same crystallographic sites; M^{II} on the 2*d* and S on the 2*c* Wyckoff sites (each with point symmetry 32). The disorder about the six-fold rotation axis found in the sulfate anion is intriguingly common in each structure, although the number of unique O atoms varies from two to four. In the structure of $[Co^{II}(C_2H_8N_2)_3]SO_4$, the O atoms were refined as being disordered over three crystallographic sites, although the site occupancy of O3 located on the 4*f* Wyckoff site approaches zero. The bond length associated with this O3 atom (S1—O3; 1.382 (16) Å) is notably shorter than the other S—O bonds (1.431 (5)–1.445 (5) Å). The disordered sulfate anions are linked to the $[Co^{II}(C_2H_8N_2)_3]^{2+}$ cations by hydrogen bonding interactions of N—H···O type to form a hydrogen-bonding supramolecular network. The hydrogen bonding geometries are consistent with those of the previously reported $[M^{II}(C_2H_2N_2)_3]SO_4$ complexes.

Experimental

Orange blocks of the title complex were synthesized and grown from the sovolthermal reaction of $Co(NO_3)_2.6H_2O$ (1.34 mmol), NH_2SO_3H (1.34 mmol), $NH_2C_2H_4NH_2$ (3.89 mmol) in ethylene glycol (160 mmol), conducted at 453 K for 72 h.

Refinement

The O atoms were positioned from a difference Fourier map, and refined with restraints using commands SUMP, SADI and SIMU in *SHELXL* (Sheldrick, 2008). Although there was an indication for further splitting of the O2 atom, after the final cycles of refinement, such action did not give a better result. All H-atoms were treated as riding groups on the bonded atoms, with C—H = 0.97 Å and N—H 0.90 Å, and with $U_{iso}(H) = 1.2U_{equiv}(C, N)$.

Figures

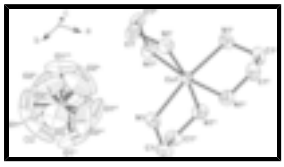

Fig. 1. View of the title complex showing atom numbering scheme. Displacement ellipsoids for non-H atoms are drawn at the 50% probability level. [Symmetry codes: (i) -y+1, x-y, z; (ii) -x+y+1, -x+1, z; (iii) -y+1, -x+1, -z+1/2; (iv) -x+y+1, y, -z+1/2; (v) x, x-y, -z+1/2; (vi) -y+1, x-y+1, z, (vii) -x+y, -x+1, z; (viii) -x+y, y, -z+1/2; (ix) x, x-y+1, -z+1/2]. Hydrogen atoms are omitted.

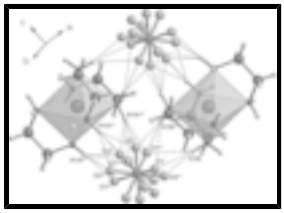

Fig. 2. View of the hydrogen bonding interactions (dotted lines) between the disordered sulfate O atoms and the amino-H atoms of the $[Co^{II}(C_2H_8N_2)]^{2+}$ cations. [Symmetry codes: (ii) -x+y+1, -x+1, z; (iii) -y+1, -x+1, -z+1/2; (viii) -x+y, y, -z+1/2; (ix) x, x-y+1, -z+1/2; (xiii) y, x, z+1/2; (xiv) -y+x, -y+1, -z+1/2; (xv) -x+1, -x+y+1, z+1/2].

Tris(ethylenediamine)cobalt(II) sulfate

Crystal data

$[Co(C_2H_8N_2)_3]SO_4$	$D_x = 1.658$ Mg m^{-3}
$M_r = 335.30$	Mo $K\alpha$ radiation, $\lambda = 0.71073$ Å
Trigonal, $P\bar{3}1c$	Cell parameters from 589 reflections
Hall symbol: -P 3 2c	$\theta = 2.6–31.0°$
$a = 8.9920$ (2) Å	$\mu = 1.45$ mm^{-1}
$c = 9.5927$ (3) Å	$T = 298$ K
$V = 671.71$ (3) Å^3	Block, orange
$Z = 2$	0.48 × 0.22 × 0.20 mm
$F(000) = 354$	

Data collection

Bruker SMART CCD area-detector diffractometer	688 independent reflections
Radiation source: fine-focus sealed tube	589 reflections with $I > 2\sigma(I)$
graphite	$R_{int} = 0.027$
? scan	$\theta_{max} = 31.0°$, $\theta_{min} = 2.6°$
Absorption correction: multi-scan (SADABS; Sheldrick, 1996)	$h = -8\rightarrow10$
$T_{min} = 0.543$, $T_{max} = 0.760$	$k = -11\rightarrow11$
3638 measured reflections	$l = -11\rightarrow13$

Refinement

Refinement on F^2	Primary atom site location: structure-invariant direct methods
Least-squares matrix: full	Secondary atom site location: difference Fourier map
$R[F^2 > 2\sigma(F^2)] = 0.028$	Hydrogen site location: inferred from neighbouring sites
$wR(F^2) = 0.069$	H-atom parameters constrained
$S = 1.06$	$w = 1/[\sigma^2(F_o^2) + (0.0354P)^2 + 0.1217P]$ where $P = (F_o^2 + 2F_c^2)/3$
688 reflections	$(\Delta/\sigma)_{max} < 0.001$
47 parameters	$\Delta\rho_{max} = 0.25$ e Å^{-3}
16 restraints	$\Delta\rho_{min} = -0.29$ e Å^{-3}

Special details

Geometry. All esds (except the esd in the dihedral angle between two l.s. planes) are estimated using the full covariance matrix. The cell esds are taken into account individually in the estimation of esds in distances, angles and torsion angles; correlations between esds in cell parameters are only used when they are defined by crystal symmetry. An approximate (isotropic) treatment of cell esds is used for estimating esds involving l.s. planes.

Refinement. Refinement of F^2 against ALL reflections. The weighted *R*-factor wR and goodness of fit *S* are based on F^2, conventional *R*-factors *R* are based on *F*, with *F* set to zero for negative F^2. The threshold expression of $F^2 > \sigma(F^2)$ is used only for calculating *R*-factors(gt) etc. and is not relevant to the choice of reflections for refinement. *R*-factors based on F^2 are statistically about twice as large as those based on *F*, and *R*- factors based on ALL data will be even larger.

Fractional atomic coordinates and isotropic or equivalent isotropic displacement parameters (Å^2)

	x	*y*	*z*	U_{iso}*/U_{eq}	Occ. (<1)
Co1	0.6667	0.3333	0.2500	0.02175 (16)	
N1	0.68784 (18)	0.54599 (18)	0.12760 (13)	0.0332 (3)	
H1A	0.6936	0.5265	0.0363	0.040*	
H1B	0.5954	0.5579	0.1418	0.040*	
S1	0.3333	0.6667	0.2500	0.0240 (2)	
C1	0.8446 (2)	0.7024 (2)	0.17145 (19)	0.0388 (4)	
H1C	0.8405	0.8031	0.1409	0.047*	
H1D	0.9444	0.7056	0.1297	0.047*	
O1	0.3029 (19)	0.5088 (9)	0.1852 (8)	0.096 (3)	0.319 (8)
O2	0.339 (2)	0.7851 (9)	0.1475 (6)	0.096 (4)	0.316 (9)
O3	0.3333	0.6667	0.1059 (16)	0.086 (8)	0.094 (10)

Atomic displacement parameters (Å^2)

	U^{11}	U^{22}	U^{33}	U^{12}	U^{13}	U^{23}
Co1	0.0226 (2)	0.0226 (2)	0.0201 (2)	0.01129 (10)	0.000	0.000
N1	0.0410 (8)	0.0330 (7)	0.0283 (7)	0.0204 (6)	−0.0033 (5)	0.0031 (5)
S1	0.0243 (3)	0.0243 (3)	0.0233 (4)	0.01215 (14)	0.000	0.000
C1	0.0445 (10)	0.0267 (8)	0.0413 (9)	0.0147 (7)	0.0058 (7)	0.0076 (6)
O1	0.185 (9)	0.051 (4)	0.063 (4)	0.069 (5)	−0.012 (5)	−0.016 (3)
O2	0.194 (12)	0.055 (4)	0.044 (3)	0.067 (5)	−0.012 (4)	0.012 (3)
O3	0.118 (11)	0.118 (11)	0.021 (11)	0.059 (5)	0.000	0.000

Geometric parameters (Å, °)

Co1—N1^{i}	2.1696 (13)	S1—O2^{vi}	1.431 (5)
Co1—N1^{ii}	2.1696 (13)	S1—O2^{v}	1.431 (5)
Co1—N1^{iii}	2.1696 (13)	S1—O2^{vii}	1.431 (5)
Co1—N1^{iv}	2.1696 (13)	S1—O2^{viii}	1.431 (5)
Co1—N1	2.1696 (13)	S1—O2^{ix}	1.431 (5)
Co1—N1^{v}	2.1696 (13)	S1—O1^{ix}	1.445 (5)

N1—C1	1.469 (2)	S1—O1^{viii}	1.445 (5)
N1—H1A	0.9000	S1—O1^{vi}	1.445 (5)
N1—H1B	0.9000	S1—O1^{vii}	1.445 (5)
S1—O3	1.382 (16)	C1—C1^{iv}	1.512 (4)
S1—O3^{v}	1.382 (16)	C1—H1C	0.9700
S1—O2	1.431 (5)	C1—H1D	0.9700
N1^{i}—Co1—N1^{ii}	80.49 (7)	O2^{viii}—S1—O1^{viii}	110.7 (4)
N1^{i}—Co1—N1^{iii}	93.48 (5)	O2^{ix}—S1—O1^{viii}	138.0 (11)
N1^{ii}—Co1—N1^{iii}	93.17 (8)	O1^{ix}—S1—O1^{viii}	63.4 (8)
N1^{i}—Co1—N1^{iv}	93.17 (8)	O3—S1—O1^{vi}	64.5 (3)
N1^{ii}—Co1—N1^{iv}	93.48 (5)	O3^{v}—S1—O1^{vi}	115.5 (3)
N1^{iii}—Co1—N1^{iv}	171.28 (7)	O2—S1—O1^{vi}	57.2 (5)
N1^{i}—Co1—N1	93.48 (5)	O2^{vi}—S1—O1^{vi}	110.7 (4)
N1^{ii}—Co1—N1	171.28 (8)	O2^{v}—S1—O1^{vi}	138.0 (11)
N1^{iii}—Co1—N1	93.48 (5)	O2^{vii}—S1—O1^{vi}	69.9 (6)
N1^{iv}—Co1—N1	80.49 (7)	O2^{viii}—S1—O1^{vi}	45.7 (4)
N1^{i}—Co1—N1^{v}	171.28 (8)	O2^{ix}—S1—O1^{vi}	119.2 (10)
N1^{ii}—Co1—N1^{v}	93.48 (5)	O1^{ix}—S1—O1^{vi}	93.3 (11)
N1^{iii}—Co1—N1^{v}	80.49 (7)	O1^{viii}—S1—O1^{vi}	102.9 (4)
N1^{iv}—Co1—N1^{v}	93.48 (5)	O3—S1—O1^{vii}	115.5 (3)
N1—Co1—N1^{v}	93.17 (8)	O3^{v}—S1—O1^{vii}	64.5 (3)
C1—N1—Co1	107.94 (10)	O2—S1—O1^{vii}	138.0 (11)
C1—N1—H1A	110.1	O2^{vi}—S1—O1^{vii}	69.9 (6)
Co1—N1—H1A	110.1	O2^{v}—S1—O1^{vii}	57.2 (5)
C1—N1—H1B	110.1	O2^{vii}—S1—O1^{vii}	110.7 (4)
Co1—N1—H1B	110.1	O2^{viii}—S1—O1^{vii}	119.2 (10)
H1A—N1—H1B	108.4	O2^{ix}—S1—O1^{vii}	45.7 (4)
O3—S1—O3^{v}	180.000 (3)	O1^{ix}—S1—O1^{vii}	102.9 (4)
O3—S1—O2	46.6 (3)	O1^{viii}—S1—O1^{vii}	93.3 (11)
O3^{v}—S1—O2	133.4 (3)	O1^{vi}—S1—O1^{vii}	161.1 (12)
O3—S1—O2^{vi}	46.6 (3)	N1—C1—C1^{iv}	108.84 (12)
O3^{v}—S1—O2^{vi}	133.4 (3)	N1—C1—H1C	109.9
O2—S1—O2^{vi}	78.0 (5)	C1^{iv}—C1—H1C	109.9
O3—S1—O2^{v}	133.4 (3)	N1—C1—H1D	109.9
O3^{v}—S1—O2^{v}	46.6 (3)	C1^{iv}—C1—H1D	109.9
O2—S1—O2^{v}	104.4 (11)	H1C—C1—H1D	108.3
O2^{vi}—S1—O2^{v}	99.7 (7)	O2^{vi}—O1—O2^{viii}	91.9 (8)
O3—S1—O2^{vii}	133.4 (3)	O2^{vi}—O1—S1	66.5 (5)
O3^{v}—S1—O2^{vii}	46.6 (3)	O2^{viii}—O1—S1	60.9 (3)
O2—S1—O2^{vii}	99.7 (7)	O2^{vi}—O1—O1^{vii}	75.7 (11)
O2^{vi}—S1—O2^{vii}	176.3 (13)	O2^{viii}—O1—O1^{vii}	117.8 (4)

O2^{v}—S1—O2^{vii}	78.0 (5)	S1—O1—O1^{vii}	58.3 (4)
O3—S1—O2^{viii}	46.6 (3)	O2^{vi}—O1—O2^{ix}	108.3 (7)
O3^{v}—S1—O2^{viii}	133.4 (3)	O2^{viii}—O1—O2^{ix}	92.2 (8)
O2—S1—O2^{viii}	78.0 (5)	S1—O1—O2^{ix}	54.6 (4)
O2^{vi}—S1—O2^{viii}	78.0 (5)	O1^{viii}—O2—O1^{vi}	129.8 (7)
O2^{v}—S1—O2^{viii}	176.3 (13)	O1^{viii}—O2—S1	67.8 (4)
O2^{vii}—S1—O2^{viii}	104.4 (11)	O1^{vi}—O2—S1	61.9 (4)
O3—S1—O2^{ix}	133.4 (3)	O1^{viii}—O2—O1^{ix}	63.3 (12)
O3^{v}—S1—O2^{ix}	46.6 (3)	O1^{vi}—O2—O1^{ix}	87.5 (9)
O2—S1—O2^{ix}	176.3 (13)	S1—O2—O1^{ix}	55.5 (3)
O2^{vi}—S1—O2^{ix}	104.4 (11)	O1^{viii}—O2—O2^{vi}	49.8 (6)
O2^{v}—S1—O2^{ix}	78.0 (5)	O1^{vi}—O2—O2^{vi}	95.3 (5)
O2^{vii}—S1—O2^{ix}	78.0 (5)	S1—O2—O2^{vi}	51.0 (2)
O2^{viii}—S1—O2^{ix}	99.7 (7)	O1^{ix}—O2—O2^{vi}	91.9 (8)
O3—S1—O1^{ix}	115.5 (3)	O1^{viii}—O2—O2^{viii}	106.1 (5)
O3^{v}—S1—O1^{ix}	64.5 (3)	S1—O2—O2^{viii}	51.0 (2)
O2—S1—O1^{ix}	69.9 (6)	O1^{ix}—O2—O2^{viii}	102.2 (4)
O2^{vi}—S1—O1^{ix}	119.2 (10)	O2^{vi}—O2—O2^{viii}	60.000 (1)
O2^{v}—S1—O1^{ix}	45.7 (4)	O2^{vi}—O3—O2^{viii}	107.9 (8)
O2^{vii}—S1—O1^{ix}	57.2 (5)	O2^{vi}—O3—S1	69.0 (8)
O2^{viii}—S1—O1^{ix}	138.0 (11)	O2^{viii}—O3—S1	69.0 (8)
O2^{ix}—S1—O1^{ix}	110.7 (4)	O2^{vi}—O3—O1^{viii}	61.1 (6)
O3—S1—O1^{viii}	64.5 (3)	O2^{viii}—O3—O1^{viii}	128.2 (13)
O3^{v}—S1—O1^{viii}	115.5 (3)	S1—O3—O1^{viii}	59.8 (5)
O2—S1—O1^{viii}	45.7 (4)	O2^{vi}—O3—O1^{vi}	128.2 (13)
O2^{vi}—S1—O1^{viii}	57.2 (5)	O2^{viii}—O3—O1^{vi}	47.4 (6)
O2^{v}—S1—O1^{viii}	69.9 (6)	S1—O3—O1^{vi}	59.8 (5)
O2^{vii}—S1—O1^{viii}	119.2 (10)	O1^{viii}—O3—O1^{vi}	96.9 (7)

Symmetry codes: (i) −*x*+*y*+1, −*x*+1, *z*; (ii) *x*, *x*−*y*, −*z*+1/2; (iii) −*y*+1, *x*−*y*, *z*; (iv) −*x*+*y*+1, *y*, −*z*+1/2; (v) −*y*+1, −*x*+1, −*z*+1/2; (vi) −*y*+1, *x*−*y*+1, *z*; (vii) −*x*+*y*, *y*, −*z*+1/2; (viii) −*x*+*y*, −*x*+1, *z*; (ix) *x*, *x*−*y*+1, −*z*+1/2.

Hydrogen-bond geometry (Å, °)

D—H···*A*	*D*—H	H···*A*	*D*···*A*	*D*—H···*A*
N1—H1A···O3^{x}	0.90	2.13	2.889 (12)	142
N1—H1A···O1^{x}	0.90	2.15	3.049 (7)	176
N1—H1A···O2^{xi}	0.90	2.22	3.054 (8)	155
N1—H1A···O2^{xii}	0.90	2.32	3.104 (11)	145
N1—H1B···O2^{viii}	0.90	1.98	2.843 (6)	161
N1—H1B···O1	0.90	2.48	3.353 (14)	165
N1—H1B···O1^{v}	0.90	2.52	3.256 (10)	139

Symmetry codes: (x) −*x*+1, −*y*+1, −*z*; (xi) *y*, −*x*+*y*, −*z*; (xii) *x*−*y*+1, *x*, −*z*; (viii) −*x*+*y*, −*x*+1, *z*; (v) −*y*+1, −*x*+1, −*z*+1/2.

Chiang Mai J. Sci. 2010; 37(1) : 92-98
www.science.cmu.ac.th/journal-science/josci.html
Contributed Paper

Hydrothermal Synthesis of Lead Titanate Fine Powders at Water Boiling Temperature

Chaiyos Chankaew [a,b], and Apinpus Rujiwatra*[a,b]

[a] Department of Chemistry, Faculty of Science, Chiang Mai University, Chiang Mai 50200, Thailand.

[b] Center of Excellence for Innovation in Chemistry (Chiang Mai University), Commission on Higher Education, Ministry of Education, Thailand.

*Author for correspondence; e-mail: apinpus@gmail.com

Received: 10 June 2009
Accepted: 22 July 2009

ABSTRACT

Lead titanate fine powders comprising of a single tetragonal phase and well characterized particles were successfully synthesized at an exceptionally low temperature of 100 °C. The important role of the ultrasonication in reducing the thermodynamic barrier of the hydrothermal reaction, and the slow rate of hydrothermal reaction at 100°C were underlined. The synthesized particles were revealed to be tetragonal in shape, mostly submicrometers in size, and generally present as large aggregates. The layer-by-layer model was also proposed as the particle growth mechanism.

Keywords: lead titanate, perovskite, ultrasonication, hydrothermal synthesis.

1. INTRODUCTION

Among several wet-chemical routes available for the synthesis of advanced materials, hydrothermal technique has been proved to be very promising due to its uniqueness in being facile, cost effective, environmentally benign and applicable for the tailored synthesis of various phases in different forms [1]. Along this line, the hydrothermal technique has been applied for the synthesis of lead titanate ($PbTiO_3$ or PT) [2,3] which is one of the most important ferroelectric materials. The high spontaneous polarization and piezoelectric coefficients, but low aging rate of dielectric constant as well as a remarkable anisotropy make the PT-based compounds suitable for a wide range of high temperature and frequency applications, *e.g.* infrared sensors, electro-optic devices and ultrasonic transducers [4-6]. Compared to the other techniques *e.g.* sol-gel [7], chemical precipitation [8] and emulsion [9], the hydrothermal technique is somewhat superior in providing controllability on phase formation, chemical stoichiometry, particle size and morphology by simply fine tuning the processing parameters [3]. The recent stage of development for this technique involves the usage of other heating sources, *e.g.* a sand bath, an ultrasonic wave and a microwave, instead of the conventional oven [10-11]. The application of an ultrasonic wave on the reaction mixture in precedence to the hydrothermal reaction in particular has added advantages to the technique by both reducing

the reaction temperature providing the phase-pure PT nanoparticles, and promoting better size homogeneity [10]. The observed phenomena were rationalized by the formation of hot spots and local acoustic microjets from a sudden collapse of cavitational bubbles induced by the ultrasonic wave.

In the present work, a further investigation on the developed technique which has led to a dramatic reduction in the reaction temperature affording the phase-pure PT to an extraordinary low temperature of 100°C is reported. The influences of the ultrasonication and hydrothermal processing conditions on phase formation, particle size and habits of the PT powders are discussed.

2. MATERIALS AND METHODS

Due to the recent report on the apparent possibility in the synthesis of phase-pure PT fine powders at the water boiling temperature, there were therefore the attempts to conduct the reactions at 100 °C following the previously reported experimental procedure [10]. Mixtures of lead (II) nitrate ($Pb(NO_3)_2$, Univar 99.0%) and titanium (IV) oxide (TiO_2, Riedel-de Haen 99.5-100%) in anatase form were prepared in aqueous media. The amount of Pb^{II} and Ti^{IV} was controlled to be equimolar, and the final concentrations for each precursor were fixed at 1.32 $mol.dm^{-3}$. The pellets of potassium hydroxide (KOH, Merck 85%) as mineralizer were gradually added to each reaction mixture to adjust the pH of the mixture to be 14, reported as the minimal pH required yielding well crystallized powder [2]. Such a high alkalinity is allegedly necessary for the dissolution of the oxide precursors under hydrothermal conditions. The mixtures were transferred into Teflon liners, which were then sealed and ultrasonicated at 70(±5)°C for varied durations ranging from 1 h to 6 h, using a laboratory ultrasonic bath (Bandelin Electronic RK255H, 160/320W, 35kHz). The liners were fitted in stainless steel cases for further hydrothermal reactions conducted under autogenous pressure at 100°C for 1.5-144 h. The particles were then recovered by filtration, washed with deionized water, and dried in air.

Powder X-ray diffractometer (PXRD, Siemen D500/D501, CuK_a, Ni filter, l=1.54 Å) was used to characterize the crystalline phases, and field emission scanning electron microscope (FESEM, JEOL JSM-6335F) equipped with an energy dispersive X-ray (EDX) analyzer was employed for the investigation of particle morphology, size and elemental composition. In order to study the aggregation of the synthesized PT particles, size distributions of the bulk samples were analyzed by laser diffraction technique (Malvern Instruments Limited, Mastersizer S).

3. RESULTS AND DISCUSSION

According to the PXRD results as shown in Figure 1 to Figure 3, the preceding ultrasonication was an important factor in reducing the hydrothermal reaction temperature affording the phase-pure PT powders although the bargaining between the ultrasonication duration and the hydrothermal reaction time was mandatory. It was evident that the tetragonal phase-pure PT powders could be synthesized from the hydrothermal reactions conducted at 100°C for reasonable reaction times, *i.e.* 24 and 48 h in this study (Figure 1 and Figure 2), when the reaction mixtures were ultrasonicated for at least 1.5 h. The achievement of the phase-pure PT at this extraordinary low temperature has thus far never been reported. The application of an ultrasonic wave for an hour nonetheless seemed to be feasibly in affording the phase-pure PT, according to the PXRD pattern of the powder obtained from the 48 h reaction as shown in Figure 2(a) where the desired PT

was present as the major phase. Further experiments revealed that the purity of the obtained powders in this case was however rather ambiguous even when the hydrothermal reaction was prolonged for over 120 h, as shown in Figure 3. This indicated the significance of the ultrasonication in rendering the success of the hydrothermal synthesis of the phase-pure PT at the water boiling temperature. The ultrasonication of 6 h nonetheless led to the formation of other oxide phases instead of the desired PT when the hydrothermal reaction was conducted for 24 h (Figure 1). This was not the case when the reaction was prolonged for 48 h (Figure 2), suggesting the influences of the reaction time to overpower that of the ultrasonication.

Two observations can be made on the basis of the PXRD results. In the view of the ultrasonication time, it was apparent that the lengthy ultrasonication could reduce the hydrothermal reaction time affording the phase-pure PT powders. This suggests the promotion of the reaction activities by the ultrasonic wave, which may be due to (1) the reduced particle sizes of the starting precursors and/or oxide intermediates caused by the local acoustic microjets, and (2) the better probability for nucleation induced by the formation of the confined hot spots. The important role of the ultrasonication in lessening the thermodynamic barrier and therefore increasing the reactivity of the hydrothermal reaction has therefore been underlined. In the aspect of the hydrothermal reaction time, a distinctly slow reaction rate can be presumed at 100°C. For the same ultrasonication duration of 1 and 3 h, the tetragonal phase-pure PT could be yielded hydrothermally in only 6 an 3.5 h at 130°C [10], but 72 and 24 h at 100°C. The hydrothermal reaction rate should therefore be governed mainly by the hydrothermal reaction temperature, which was well agreed with that reported previously [10].

The obtained PT powders could be well refined in tetragonal *P4/mmm* (JCPDS 6-0425) with a = 3.8940(41)-3.9000(43) Å, and c = 4.185(11)-4.218(55) Å. The variation in ultrasonication time showed no distinct influences on the refined cell parameters and therefore the corresponding c/a ratios,

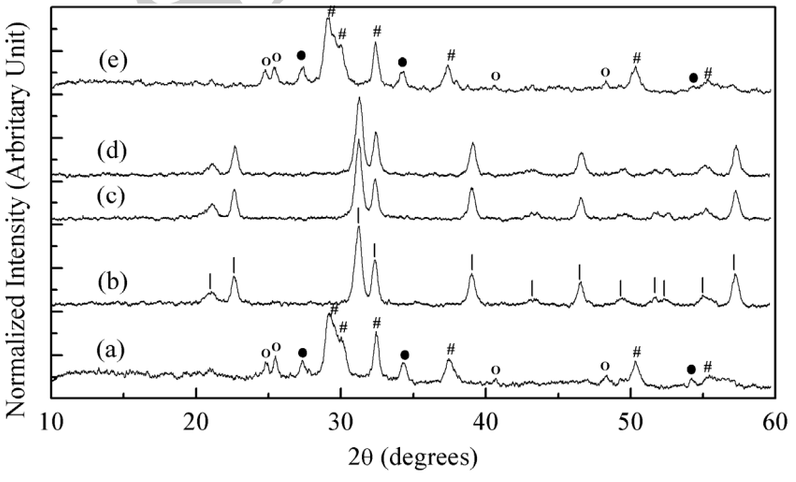

Figure 1. PXRD patterns of the particles obtained from the hydrothermal reactions conducted at 100°C for 24 h with prior ultrasonication for (a) 1 h (b) 1.5 h (c) 3 h (d) 4.5 h and (e) 6 h; | = tetragonal PT, # = non-stoichiometric PT, ● = TiO_2 rultile/anatase and ○ = Ti_xO_y.

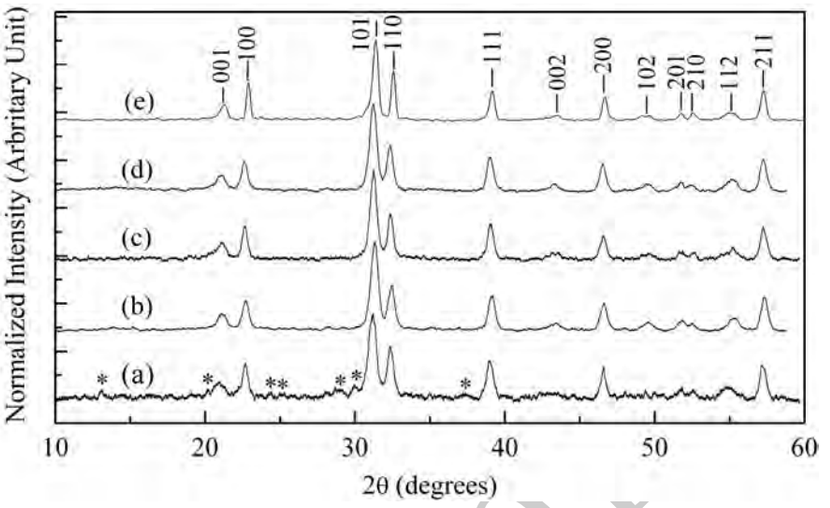

Figure 2. PXRD patterns of the particles obtained from the hydrothermal reactions conducted at 100°C for 48 h with prior ultrasonication for (a) 1 h (b) 1.5 h (c) 3 h (d) 4.5 h and (e) 6 h, where the asterisks indicate unidentified peaks.

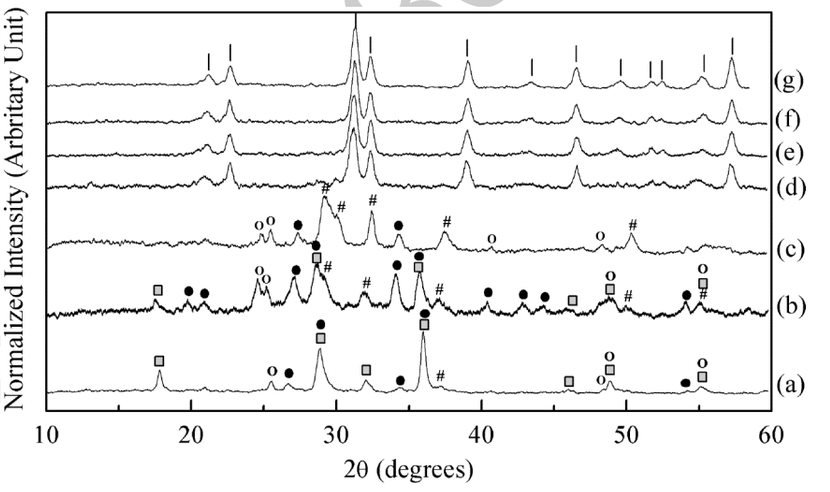

Figure 3. PXRD patterns of the particles obtained from the hydrothermal reactions conducted at 100°C for (a) 6 h (b) 12 h (c) 24 h (d) 48 h (e) 72 h (f) 120 h and (g) 124 h with the prior ultrasonication for an hour; | = tetragonal PT, # = non-stoichiometric PT, ● = TiO_2 rultile/anatase, ○ = Ti_xOy and ■ = PbO.

1.073(3)-1.083(2). These values were in good agreement with the values commonly yielded for the hydrothermally derived PT particles [2,3,10], but larger than those of the solid state reactions [12]. Regarding the interpretation of the PXRD results, although the presence of other phases beside the desired PT (JCPDS 6-0425) in some cases was plain, the index of these phases to certain JCPDS could be ambiguous. These phases were therefore shown as groups of feasible phases in Figure 1 and Figure 3; #, ●, ○ and ■ were therefore

employed to represent lead titanates of other stoichiometry than $PbTiO_3$, a mixture of rultile and anatase TiO_2, various oxides of titanium, and different PbO phases, respectively.

The SEM images as typically illustrated in Figure 4(a) showed the PT particles to be tetragonal in shape, which was well reflecting the crystallographic internal order, regardless of the synthetic conditions. Sizes of these particles were accordingly measured in two directions along the short and long axes from

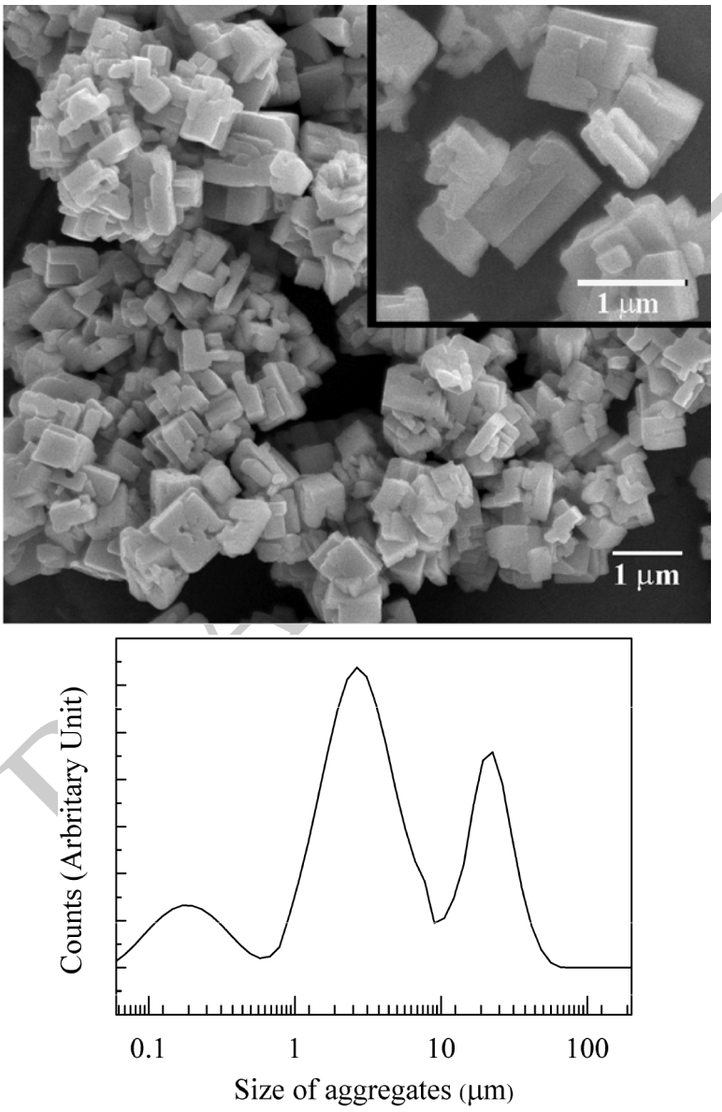

Figure 4. (a) Typical SEM image the PT aggregates obtained from the reaction conducted at 100°C for 48 h with 4.5 h ultrasonication with the magnified image to illustrate the layer-by-layer growth of the particle in the inset, and (b) the corresponding tri-nodal aggregate size distribution.

the SEM images, and summarized in Table 1. Being independent of also the synthetic conditions, sizes of these particles were distributed regularly from few hundred nanometers to just over one micron, with most of the population distributed in the submicrometer region. The average sizes were *ca.* 500-600 nm alike. According to the SEM images, the PT particles were mostly present as hard aggregates, with the growth of small particles on the surfaces of the larger ones as exemplified in the inset of Figure 4(a). This observation could lead to the assumption of the layer-by-layer crystal growth model where the nucleation and growth of the new crystals occur on the surfaces of the mature ones [13]. In spite of the variation in synthetic conditions, sizes of the PT aggregates disseminated in a similar tri-nodal fashion as typically illustrated in Figure 4(b), centering at *ca.* 0.20, 2.0 and 20 μm. The mean aggregate sizes were rather similar, falling into a narrow range of *ca.* 5-8 μm. There was no apparent correlation between the aggregate sizes and the ultrasonication time (Table 1). The prolongation of the hydrothermal reaction time nonetheless led to the enlargement of both the length of the particles and mean aggregate sizes. This should be due to the growth of the particle with the extended hydrothermal reaction time.

Table 1. Sizes of PT particles measured from the SEM images, and of the aggregates obtained from laser diffraction experiments.

Hydrothermal reaction time (h)	Ultrasonication time (h)	Particle sizes (μm)			Aggregate sizes (μm)	
		Short axis	Long axis	Average	D50	Mean
24	1.5	0.19-0.98	0.21-1.30	0.57	2.60(6)	6.14(1)
	3.0	0.16-1.00	0.35-1.62	0.65	1.99(4)	5.18(2)
	4.5	0.23-1.41	0.28-1.26	0.55	3.37(4)	7.59(3)
48	1.5	0.12-0.92	0.28-1.27	0.53	3.37(1)	9.23(7)
	3.0	0.15-1.28	0.17-1.69	0.48	2.72(6)	6.90(7)
	4.5	0.12-0.73	0.22-1.30	0.47	3.01(1)	7.65(2)
72	1	0.19-1.20	0.23-1.30	0.57	1.69(2)	6.05(6)
120		0.13-1.11	0.28-1.32	0.60	2.20(7)	6.54(2)
144		0.18-1.35	0.26-1.59	0.63	2.14(2)	6.73(6)

4. CONCLUSIONS

In summary, the ultrasonication of the reaction mixture has been proved to be able to reduce the thermodynamic barrier in the synthesis of fine PT powders under hydrothermal conditions, and the sonocatalyzed hydrothermal concept was underlined. The tetragonal phase-pure PT could be achieved at an exceptionally low temperature of 100 °C for the first time, irrespective to the slow kinetic at this temperature. The synthesized PT particles were tetragonal in shape and mostly submicrometers in sizes. These PT particles were in general comparable to those obtained at high reaction temperature either with or without the ultrasonication process. They were present mostly as hard aggregates of few micrometers. Under the studied conditions, the growth of the PT particles was manifestly occurred *via* the layer-by-layer mechanism.

ACKNOWLEDGEMENTS

The Synchrotron Light Research Institute (Public Organization), the Thailand Research Fund and the Thailand Toray Science Foundation (TTSF) are acknowledged for financial support. Chaiyos Chankaew thanks also to the Graduate School of Chiang Mai University for Graduate Scholarship.

REFERENCES

[1] Byrappa K. and Yoshimura M., *Handbook of Hydrothermal Technology: A Technology for Crystal Growth and Materials Processing*, Noyes Publication, New Jersey, 2001.

[2] Rujiwatra A., Jongphiphan J. and Ananta S., Stoichiometric synthesis of tetragonal phase pure lead titanate under mild chemical conditions employing NaOH and KOH, *Mater. Lett.*, 2005; **59**: 1871–1875.

[3] Rujiwatra A., Thammajak N., Sarakonsri T., Wongmaneerung R. and Ananta S., Influence of alkali reagents on phase formation and crystal morphology of hydrothermally derived lead titanate, *J. Cryst. Growth*, 2006; **289**: 224-230.

[4] Moulson A.J. and Herbert J.M., *Electroceramics: Materials, Properties, Applications*, 2nd Edn., Wiley, New York, 2003.

[5] Xu Y., *Ferroelectric Materials and Their Applications*, North-Holland, New York, 1991.

[6] Jona F. and Shirane G., *Ferroelectric Crystals*, Dover Publications, New York, 1993.

[7] Udomporn A., Pengpat K. and Ananta S., Highly dense lead titanate ceramics from refined processing, *J. Eur. Ceram. Soc.*, 2004; **24**: 185-188.

[8] Tartaj J., Fernandez J.F. and Villafuerte-Castrejon F.M.E., Preparation of $PbTiO_3$ by seeding-assisted chemical sol-gel, *Mater. Res. Bull.*, 2001; **36**: 479-486.

[9] Fang J., Wang J., Gan L.M. and Ng S.C., Comparative study on phase development of lead titanate powders, *Mater. Lett.*, 2002; **52**: 304-312.

[10] Rujiwatra A., Wongtaewan C., Pinyo W. and Ananta S., Sonocatalyzed hydrothermal preparation of lead titanate nanopowders, *Mater. Lett.*, 2007; **61**: 4522–4524.

[11] Tapala S., Thammajak N., Laorattanakul P. and Rujiwatra A., Effects of microwave heating on sonocatalyzed hydrothermal preparation of lead titanate nanopowders, *Mater. Lett*, 2008; **62**: 3685-3687.

[12] Wongmaneerung R., Yimnirun R. and Ananta S., Effect of vibro-milling time on phase formation and particle size of lead titanate nanopowders, *Mater. Lett.*, 2006; **60**: 1447-1452.

[13] Chen X., Fan H. and Liu L., Synthesis and crystallization behavior of lead titanate from oxide precursors by a hydrothermal route, *J. Cryst. Growth*, 2005; **284**: 434-439.

Polyhedron 30 (2011) 259–268

Contents lists available at ScienceDirect

Polyhedron

journal homepage: www.elsevier.com/locate/poly

Microwave synthesis and crystal structures of two cobalt-4,4′-bipyridine-sulfate frameworks constructed from 1-D coordination polymers linked by hydrogen bonding

Timothy J. Prior [a,*], Bunlawee Yotnoi [b], Apinpus Rujiwatra [b]

[a] Department of Chemistry, University of Hull, Kingston upon Hull, HU6 7RX, UK
[b] Department of Chemistry, Faculty of Science, Chiang Mai University, Chiang Mai 50200, Thailand

ARTICLE INFO

Article history:
Received 27 July 2010
Accepted 19 October 2010
Available online 26 October 2010

Keywords:
Cobalt
Bipyridine
Sulfate
Framework
Template
Microwave

ABSTRACT

Two extended solids displaying both one-dimensional coordination polymer and two-dimensional hydrogen-bonded structural features has been prepared under microwave-assisted hydrothermal conditions. $[Co(H_2O)_4(4,4'\text{-bipyridine})](4,4'\text{-bipyridine}H_2)\cdot 2(SO_4)\cdot 2H_2O$ (**1**) contains one-dimensional coordination polymer chains of composition $[Co(4,4'\text{-bipyridine})(H_2O)_4^{2+}]_n$ that are linked into a three dimensional framework by hydrogen bonding through uncoordinated sulfate and water. Within this framework is located a twice protonated 4,4′-bipyridine molecule ($C_{10}N_2H_{10}^{2+}$) which forms two short N–H···O hydrogen bonds and eight further non-classical C–H···O interactions. The close approach of guest and framework and the large number of interactions between them suggest the cation is important in templating this phase.

$[Co_2(4,4'\text{-bipyridine})_2(SO_4)_2(H_2O)_6]\cdot 4(H_2O)$ (**2**) displays one dimensional chains of cobalt-bipyridine which are sinusoidal in nature. Two sets of these chains run parallel to the crystallographic [2 1 2] and [$\bar{2}$ 1 $\bar{2}$] directions. Two-dimensional hydrogen-bonded sheets parallel to the *xz* plane link these; further hydrogen bonds to uncoordinated water help to form a three-dimensional honeycomb network with the centroids of the six-membered rings aligned parallel to the *a*-axis.

The use of microwave synthesis for framework solids of this type is described and the structures of the frameworks and the interactions responsible for their assembly are discussed. The thermal and spectroscopic behaviour of the two phases are described.

1. Introduction

Historically, the best known of the framework solids were the naturally-occurring aluminosilicate zeolites which have extended structures based on tetrehedra [1]. The synthesis of artificial zeolites led to a huge interest in the synthesis of other phases based on tetrahedra such as the aluminophosphates and gallophosphates [2]. The basic technique for directing the formation of these phases is to utilise suitable sources of metal and non-metal with a so-called structure directing agent (a template), typically a quaternary amine. The size, shape, and charge of this template are all important in determining the nature of the framework obtained [3,4]. In some examples the hydrogen-bonding propensity of the template was also shown to be important [5].

There has been considerable interest in simulating and expanding upon the structures displayed by the aluminosilicate zeolites and other oxide frameworks through the construction of metal–organic frameworks (MOFs) [6,7]. The different range of metal–ligand interactions and other parameters, such as metal co-ordination, ligand geometry and co-ordination preference, have produced chemistry in MOFs which is not known for classical framework solids [8]. In particular, structural design in MOFs is now well-established [9,10]. This chemistry has generated a huge range of novel structures with potentially useful properties, for example, porosity [11], chirality [12], selective sorption [13], gas storage [14–16], catalysis [17], non-linear optical properties [18], and guest-responsive magnetism [19]. Some examples exist where MOFs have been templated by a specific guest species [20–22]. For example, naphthalene has been shown to have a profound influence on the structures of frameworks constructed from Ni^{2+} with 1,3,5-benzenetricarboxylate and 4,4′-bipyridine [23].

In the construction of MOFs, assembly of the structural building units is by strong co-ordinative covalent bonds. In many MOF examples, weaker interactions such as classical (e.g. O–H···O) [24] and non-classical [25] (e.g. C–H···O) hydrogen bonding interactions are present as secondary structural components [26]. Examples are also emerging where there are genuinely two distinct

* Corresponding author. Tel.: +44 (0)1482466389; fax: +44 (0)1482466410.
E-mail address: t.prior@hull.ac.uk (T.J. Prior).

0277-5387/$ - see front matter © 2010 Elsevier Ltd. All rights reserved.
doi:10.1016/j.poly.2010.10.010

structural units including a coordination polymer and a hydrogen-bonded architecture [26–29].

One of the most widely studied linear bidentate ligands is 4,4′-bipyridine (4,4′-bipy) which is found in a very great number of MOFs, with examples extending from 1-D to 2-D and 3-D architectures [30]. The inflexibility of the ligand along its long axis and the predictable coordination chemistry make the ligand a very attractive framework-former, both on its own and with auxiliary ligands. For example, a hybrid framework, $[Co_2(4,4'\text{-bipy})_3(SO_4)_2(H_2O)_2](4,4'\text{-bipy})(CH_3OH)$, in which both 4,4′-bipy and sulfate act as framework-forming ligands has been reported [31]. This compound displays remarkable, reversible, behaviour upon dehydration; unbound encapsulated 4,4′-bipy becomes involved in the formation of a new framework when coordinated water is removed. Sulfate is found as a framework former in many examples with linear dipyridines. It has diverse coordination chemistry to transition metal ions, sometimes displaying more than one coordination mode in a single framework [32]. Sulfate is also a very suitable anion for the construction of hydrogen-bonded networks because it readily forms strong hydrogen bonds [33].

In our study, we sought to combine the ability of 4,4′-bipy to form coordination polymers with the strong (classical) hydrogen bonding properties of the sulfate anion to produce solids which featured both coordination polymer and hydrogen-bonding motifs in the extended structures. Our previous experience of this system suggested it would be important that the pH of the solution and the amount of water present were carefully controlled [34] to achieve this aim, so that other previously observed phases were not formed [31,35–37].

Hydrothermal synthesis is one widely exploited route for crystal growth of MOFs and this typically takes days or weeks to generate crystals of an appropriate size for diffraction experiments. Despite the great success of microwave heating in organic synthesis [38], the application of this technique to inorganic materials is poorly developed. Recently, microwave-assisted hydrothermal chemistry has been utilised in the crystal growth of MOFs [39,40]. The microwave heating helps to shorten the reaction time to minutes [41]. Here, microwave-assisted hydrothermal synthesis was employed in growing crystals of two new extended metal–organic frameworks. The two extended solids have both coordination polymer and hydrogen-bonding structural features. Intriguingly though, one of these solids is assembled around a twice-protonated 4,4′-bipy molecule which appears to act as a template. The other has a much more extensive 3-D hydrogen bonding arrangement.

2. Materials and methods

2.1. Microwave-assisted hydrothermal crystal growth

Each reaction was conducted using a tightly closed Teflon container under an autogenous pressure generated at 630 W for 5 min using a domestic microwave oven (Whirlpool XT – 25ES/S, 900 W, 2.45 GHz). The pH of each mixture was measured using universal pH strips (Merck, 1.09535.0001), and in each case there was no change in the pH of the mixture after the reaction. Crystalline products were separated from supernatant, washed with deionized water and dried in air. In each case the solid products had a uniform appearance under magnification and the chemical analysis described in Sections 3.2 and 3.3 show these are single phase products. The yield of each reaction was of the order of 30%.

Reaction A: Pale pink needles were grown from the mixture of 0.1395 g cobalt(II) nitrate hexahydrate ($Co(NO_3)_2{\cdot}6H_2O$, 98% Aldrich), 0.4475 g 4,4′-bipyridine ($C_{10}H_8N_2$, 99% Fluka) and sulphuric acid (H_2SO_4, 98% Merck) in 9.50 g of deionized water. (Co:bipy:sulfate:water molar ratio = 1:6:1:1128) The initial pH of the solution was 6.

Reaction B: Pale orange sagittate crystals of $[Co(H_2O)_4(4,4'\text{-bipy})](4,4'\text{-bipyH}_2){\cdot}2(SO_4){\cdot}2H_2O$ (**1**) were grown from the mixture of 0.1400 g cobalt(II) nitrate hexahydrate, 0.4502 g 4,4′-bipyridine and 0.0923 g sulphuric acid in 9.50 g of deionized water. (Co:bipy:sulfate:water molar ratio = 1:6:2:1100) The initial pH of the solution was 4.

Reaction C: Pink acicular crystals of $[Co_2(4,4'\text{-bipy})_2(SO_4)_2(H_2O)_6]{\cdot}4(H_2O)$ (**2**) were grown from the mixture of 0.3299 g cobalt(II) sulphate heptahydrate ($Co(SO_4)_2{\cdot}7H_2O$, 99% Fluka) and 0.1833 g 4,4′-bipyridine in 9.50 g of deionized water. (Co:bipy:sulfate:water molar ratio = 1:1:2:454) The pH of the mixture was 6. No further attempt was performed to vary the pH of the mixture.

2.2. X-ray diffraction structure determination

Routine data collection and structure solution procedures were adopted. Data were collected in series of ω-scans using a Stoe IPDS2 diffractometer. Full matrix least squares refinement against F^2 was employed for structure refinement. Crystals of each phase displayed a tendency to form aggregates. This may prove to be a general feature of microwave hydrothermal synthesis [42]. The crystal of **2** examined was found to be subject to non-merohedral twinning which was dealt with using the program ROTAX [43]. Use of this and omission of a few partially overlapped reflections yielded a vast improvement in the quality of the final structure. Final residual electron density maxima and minima were improved thus: initially 4.11 and −0.943 e Å^{-3}; after treatment these were 0.564 and −0.564 e Å^{-3} (*sic*).

For each structure the final data were of good quality and hydrogen atoms were located from difference Fourier maps. Hydrogen atoms attached to 4,4′-bipyridine were refined using a riding model. Those of water were located in difference Fourier maps and refined with sensible restraints. A small portion of disorder within the crystal structure of **2** was modelled using standard techniques. Full details of data collection, treatment of twinning, and the modelling of disorder are contained in the Supplementary Information.

2.3. Spectroscopic studies of *1* and *2*

The Fourier-transform IR spectra of the ground crystals of **1** and **2** were recorded using a Bruker Tensor 27 FT-IR instrument (4000–400 cm^{-1}, resolution 0.5 cm^{-1}) using KBr (BDH 98.5%) disks. Raman spectra were collected using a HORIBA JOBIN YVON T64000 spectrophotometer, employing the 514.5 nm line of an Ar laser excitation source with 0.5 mW at the sample for a total integration time of 120 s. The UV–Vis spectra of **1** and **2** were collected on both the aqueous solution and the suspension in hexane at room temperature from 200 nm to 800 nm using UV-1800 spectrophotometer (Shimudzu, Japan).

3. Results and discussion

3.1. Microwave synthesis

Although the microwave-assisted hydrothermal process is not new, examples of the application of the process in growing single crystals of MOFs are limited. Here the process was successfully applied for the rapid synthesis of single crystals of two new phases in the cobalt-4,4′-bipy-sulfate-water system. In each case the reaction duration was only 5 min, in contrast to traditional hydrothermal chemistry reactions lasting days. The reaction products are

Reaction A – initial pH = 6	**$CoSO_4(H_2O)_3(4,4'\text{-bipy}).2H_2O$** [35]
Co:bipy:sulfate:water molar ratio = 1:6:1:1128	
Reaction B – initial pH = 4	**$[Co(H_2O)_4(4,4'\text{-bipy})].(4,4'\text{-bipyH}_2).2(SO_4).2H_2O$**
Co:bipy:sulfate:water molar ratio = 1:6:2:1100	(compound **1**)
Reaction C – initial pH = 6	**$[Co_2(4,4'\text{-bipy})_2(SO_4)_2(H_2O)_6].4(H_2O)$**
Co:bipy:sulfate:water molar ratio = 1:1:2:454	(compound **2**)

Scheme 1. Reaction products.

summarised within Scheme 1 below. During the synthesis it was found that the nature of the product obtained was very sensitive to the initial pH; no crystalline products were obtained where the initial pH of the mixture was lower than 4. If the reaction is too acidic, the 4,4′-bipy present should all be protonated and thus not available for coordination. Reaction A (pH 6) yielded crystals of the phase $CoSO_4(H_2O)_3(4,4'\text{-bipy})\cdot 2H_2O$ which has been reported before [35]. Reaction B (pH 4) rapidly yielded pale orange sagittate crystals that were shown by X-ray diffraction to be an unknown phase, hereafter labelled **1**. A third synthesis (Reaction C) with subtly different initial conditions yielded compound **2**.

3.2. Bipyridinium-templated phase, *1*

This compound crystallises in the centrosymmetric space group $P2_1/n$ (number 14) with a single Co^{2+} ion within the asymmetric unit located on a 4e Wyckoff position. Crystal data and basic refinement information is contained within Table 1. The chemical formula for **1** is best expressed as $[Co(H_2O)_4(4,4'\text{-bipy})](4,4'\text{-bipyH}_2)\cdot(SO_4)_2\cdot 2H_2O$ and in this formulation the diprotonated 4,4′-bipy may be regarded as an occluded cation which is enclosed within an anionic framework composed of 1-D coordination polymer extended into 3-D by hydrogen bonding of sulfate and water. The asymmetric unit is depicted in Fig. 1. Full crystal structure data are included within the Supplementary Information. The composition of a bulk sample of **1** was determined by chemical analysis and this demonstrated a good fit between the calculated and observed compositions. Percentage C/H/N composition was as follows; *Anal.* Calc.: C, 35.78; H, 4.51; N, 8.35. Found: C, 35.63; H, 4.45; N, 8.31%.

Each Co^{2+} adopts pseudo-octahedral coordination and is surrounded by four water molecules in a square plane and furthermore by two trans 4,4′-bipy molecules, the first of which binds

Table 1
Summary of crystal and refinement data for **1** and **2**.

Identification code	**1**	**2**
Structural formula	$[Co(H_2O)_4(4,4'\text{-bipy})](4,4'\text{-bipyH}_2)\cdot 2(SO_4)\cdot 2H_2O$	$[Co(H_2O)_3(SO_4)(4,4'\text{-bipy})_2]_2\ Co(H_2O)_4Co(H_2O)_2(SO_4)_2\cdot 8H_2O$
Empirical formula	$C_{20}H_{30}CoN_4O_{14}S_2$	$C_{20}H_{36}Co_2N_4O_{18}S_2$
Formula weight	673.54	802.52
Temperature (K)	150(2)	150(2)
Wavelength (Å)	0.71073	0.71073
Crystal system	monoclinic	monoclinic
Space group	$P2_1/n$	$P2_1/c$
Unit cell dimensions		
a (Å)	9.4120(18)	7.4347(5)
b (Å)	13.0143(13)	40.573(4)
c (Å)	22.155(3)	11.4833(8)
α (°)	90	90
β (°)	97.943(13)	117.405(5)
γ (°)	90	90
Volume (Å^3)	2687.8(7)	3075.2(4)
Z	4	4
D_{calc} (mg/m^3)	1.664	1.733
Absorption coefficient (mm^{-1})	0.872	1.301
F(0 0 0)	1396	1656
Crystal size (mm^3)	0.35 × 0.14 × 0.12	0.4 × 0.1 × 0.1
θ Range for data collection (°)	3.09–26.14	2.01–27.13
Index ranges		
	$-11 \leqslant h \leqslant 11$	$0 \leqslant h \leqslant 9$
	$0 \leqslant k \leqslant 16$	$-51 \leqslant k \leqslant 51$
	$0 \leqslant l \leqslant 27$	$-14 \leqslant l \leqslant 13$
Reflections collected	5150	6320
Independent reflections	5150 [R_{int} = 0.068]	6320 [R_{int} = 0.048]
Completeness to θ = 26.00°	95.8%	94.0%
Absorption correction	analytical	analytical
Maximum and minimum transmission	0.8324 and 0.6966	0.9624 and 0.8381
Refinement method	full-matrix least-squares on F^2	full-matrix least-squares on F^2
Data/restraints/parameters	5150/22/408	6320/235/474
Goodness-of-fit on F^2	1.087	1.091
Largest difference in peak and hole (e Å^{-3}) (sic)	0.729 and −0.594	0.564 and −0.564
Final R indices [$I > 2\sigma(I)$]	R_1 = 0.0683, $wR(F^2)$ = 0.2381	R_1 = 0.0559, $wR(F^2)$ = 0.1514
R indices (all data)	R_1 = 0.1105, $wR(F^2)$ = 0.2469	R_1 = 0.0832, $wR(F^2)$ = 0.1566

Where $R_1 = \frac{\sum||F_o|-|F_c||}{\sum|F_o|}$, $wR(F^2) = \sqrt{\frac{\sum w(F_o^2-F_c^2)^2}{\sum wF_o^4}}$ and F_o and F_c are the observed and calculated structure factors for each reflection and w is the weight for each reflection.

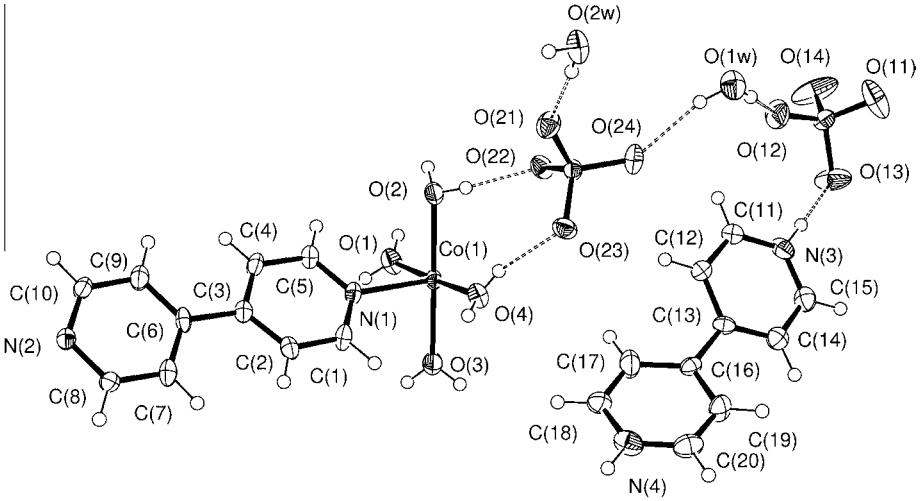

Fig. 1. ORTEP representation of the asymmetric unit of **1**. Atoms are drawn as 50% thermal ellipsoids. Only non-hydrogen atoms are labelled for clarity. Selected bonds lengths (in Å): Co1–O1 2.075(7); Co1–O2 2.109(6); Co1–O3 2.062(7); Co1–O4 2.112(6); Co1–N2^{i} 2.154(6); Co1–N1 2.155(6); S1–O11 1.426(9); S1–O12 1.438(7); S1–O14 1.460(8); S1–O13 1.490(7); S2–O21 1.465(7); S2–O22 1.491(6); S2–O23 1.477(6); S2–O24 1.453(6). Symmetry equivalent atom generated by the operator (i) $x - ½, -y + ½, z - ½$.

through N1, while the second binds through N2 and is generated from the first by the symmetry operator $x - ½, ½ - y, z - ½$. The Co^{2+} and 4,4′-bipy therefore form a one-dimensional chain which runs parallel to the crystallographic [1 0 1] direction. There is a little twisting of the 4,4′-bipy about the central C–C bond; the angle between the mean planes of the two six-membered rings is 10.36(10)°. This chain is illustrated in Fig. 2. The 1-D linear chain is an important motif in metal-bipyridine frameworks; there are a large number of MOFs based on this arrangement [30]. The arrangement of metal and 4,4′-bipy in **1** is typical of this type of chain. Co–N distances are in good agreement with those of similar frameworks [44]. The angle subtended by the bipyridine molecules at the Co^{2+} is 178.9(3)°. There are two unbound sulfate anions in the asymmetric unit and these are located such that four sulfates are arranged around the Co^{2+} ion forming hydrogen bonds to the four water molecules bound in a square plane with O···O hydrogen bond distances indicative of relatively strong hydrogen bonds (Table 2). The hydrogen bonds formed to each sulfate have the effect of linking together the 1-D coordination polymer chains; each sulfate is involved in bridging between the $Co(H_2O)_4$ square planes to form infinite 2-D hydrogen-bonded sheets in the *xy* plane. Each of the 1-D cobalt-bipyridine polymer chains cuts this plane at any angle of 61.37°. Fig. 3 illustrates the interaction between the cobalt centres and each sulfate. Two sulfate molecules (central atom S1) form an embrace with multiple hydrogen bonds while for the second sulfate (central atom S2) a centrosymmetric $R_4^2(8)$ embrace is observed and this is augmented by other hydrogen bonds.

Located between these sulfate anions are two further symmetry independent water molecules. These two unbound water molecules act as hydrogen bond donors to the sulfate anions. Short O-H···O interactions form infinite sulfate–water–sulfate chains which run parallel to the [1 0 1] direction (illustrated in the Supplementary Information). These chains runs parallel to the cobalt-bipyridine 1-D chain and reinforce the bonding in this direction. Finally, contained between the chains is located twice protonated 4,4′-bipy ($C_{10}H_{10}N_2^{2+}$). This cation forms a remarkable set of contacts to the framework and to sulfate, which are detailed in Table 2. Each protonated pyridine function forms one hydrogen

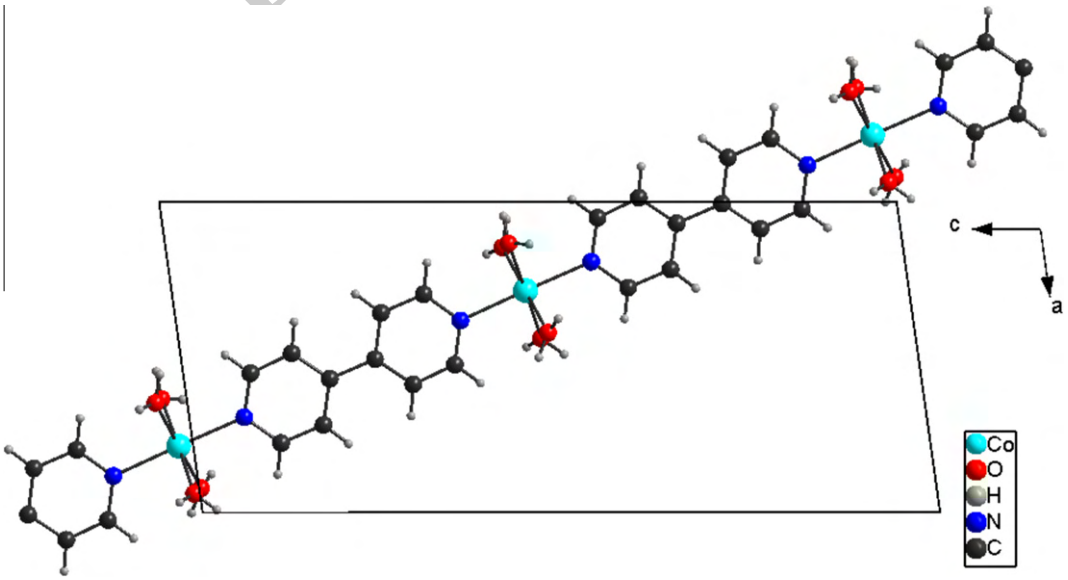

Fig. 2. Illustration of the one-dimensional coordination polymer chain within **1** that has composition $[Co(4,4'\text{-bipyridine})(H_2O)_4]^{2+}$.

Table 2
Details of the classical hydrogen bonds and C–H···O interactions in **1**. A hydrogen bond donor is signified as D–H, where D is the donor atom. The hydrogen bond acceptor atom is labelled A.

Hydrogen bond donor (D–H)	D–H bond length (Å)	H···A distance (Å)	D–H···A angle (°)	D···A distance (Å)	Acceptor atom (A) [symmetry operator]
O1–H1A	0.83(4)	1.82(8)	173(7)	2.645(12)	O14 [$x+1/2, -y+1/2, z+1/2$]
O1–H1B	0.86(4)	1.89(5)	165(8)	2.735(10)	O2W [$-x, -y+1, -z+1$]
O2–H2A	0.82(4)	1.88(7)	168(8)	2.674(9)	O22
O2–H2B	0.85(4)	1.93(6)	169(10)	2.773(10)	O21 [$-x, -y+1, -z+1$]
O3–H3A	0.80(4)	1.97(8)	157(8)	2.729(10)	O13 [$x+1/2, -y+1/2, z+1/2$]
O3–H3B	0.84(4)	2.08(8)	173(11)	2.919(12)	O11 [$-x+1/2, y-1/2, -z+1/2$]
O3–H3B	0.84(4)	2.47(8)	126(8)	3.048(10)	O13 [$-x+1/2, y-1/2, -z+1/2$]
O4–H4A	0.76(4)	2.05(8)	155(8)	2.755(9)	O23
O4–H4B	0.82(4)	2.02(8)	160(8)	2.807(9)	O23 [$-x+1, -y+1, -z+1$]
O1W–H1X	0.85(4)	2.01(9)	166(10)	2.845(9)	O24
O1W–H1Y	0.80(4)	2.00(8)	165(8)	2.782(10)	O12
O2W–H2X	0.86(5)	1.89(5)	173(11)	2.746(10)	O21
O2W–H2Y	0.81(5)	2.19(9)	151(10)	2.933(12)	O11 [$x+1/2, -y+3/2, z+1/2$]
O2W–H2Y	0.81(5)	2.49(8)	150(8)	3.222(13)	O14 [$x+1/2, -y+3/2, z+1/2$]
N3–H3C	0.88	1.712	177	2.592(11)	O13
N4–H4C	0.88	1.791	162	2.641(10)	O22 [$x+1, y, z$]
C7–H7	0.95	2.57	163	3.487(11)	O1W [$1+x, y, z$]
C11–H11	0.95	2.54	124	3.167(12)	O12 [$1/2-x, 1/2+y, 1/2-z$]
C12–H12	0.95	2.46	125	3.110(11)	O24 [$1/2-x, 1/2+y, 1/2-z$]
C14–H14	0.95	2.52	143	3.329(13)	O14 [$3/2-x, 1/2+y, 1/2-z$]
C15–H15	0.95	2.33	147	3.168(11)	O2W
C18–H18	0.95	2.49	153	3.367(11)	O21 [$1/2+x, 1/2-y, 1/2+z$]
C19–H19	0.95	2.42	137	3.181(12)	O12 [$3/2-x, 1/2+y, 1/2-z$]
C20–H20	0.95	2.44	134	3.176(12)	O24 [$3/2-x, 1/2+y, 1/2-z$]

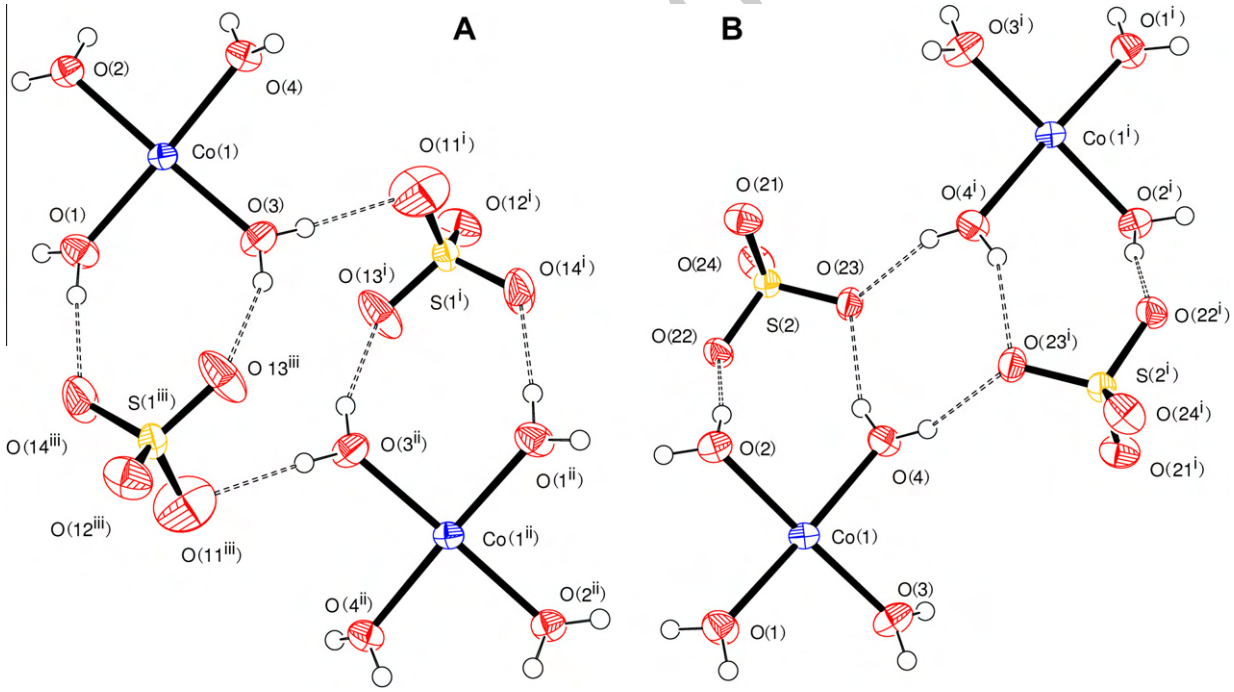

Fig. 3. (A) Hydrogen bonding of sulfate (S1) linking two $Co(H_2O)_4$ units. Symmetry equivalent atoms are generated by the symmetry operations: (i) $0.5-x, y-0.5, 0.5-z$; (ii) $1-x, -y, 1-z$; (iii) $0.5+x, 0.5-y, 0.5+z$. (B) Augmented $R_4^2(8)$ embrace between two $Co(H_2O)_4$ units mediated by sulfate (S2). Symmetry equivalent atoms are generated by the symmetry operation: (i) $1-x, 1-y, 1-z$.

bond (through N3 and N4) to sulfate and there are supplementary C–H···O interactions which hold the dication in place; for example there are six C–H···O contacts where the C···O distance is in the range 3.1–3.2 Å. These are in good agreement with other species containing this cation and somewhat shorter than many of those for uncharged 4,4′-bipy bound to a metal [44]. Alone, this is a relatively weak interaction, but the cumulative effect of six such interactions becomes important. The protonation of the 4,4′-bipy must play a role in strengthening these interactions through an additional coulombic interaction not present for uncharged species. Interestingly the two rings of the diprotonated 4,4′-bipy are not coplanar with the angle between the mean planes of the two six-membered rings being 29.9(2)°. This rotation facilitates the formation of these non-classical hydrogen bonds by rotating the 4,4′-bipy towards the sulfate ions. The relatively short C–H···O distances promoted by protonation of the 4,4′-bipy, suggest this dication has a key role in templating **1**. The protonated 4,4′-bipy is crucial in filling space within the other network, but the close interaction with surrounding species suggests this acts as a template around which the framework assembles. Fig. 4 shows the

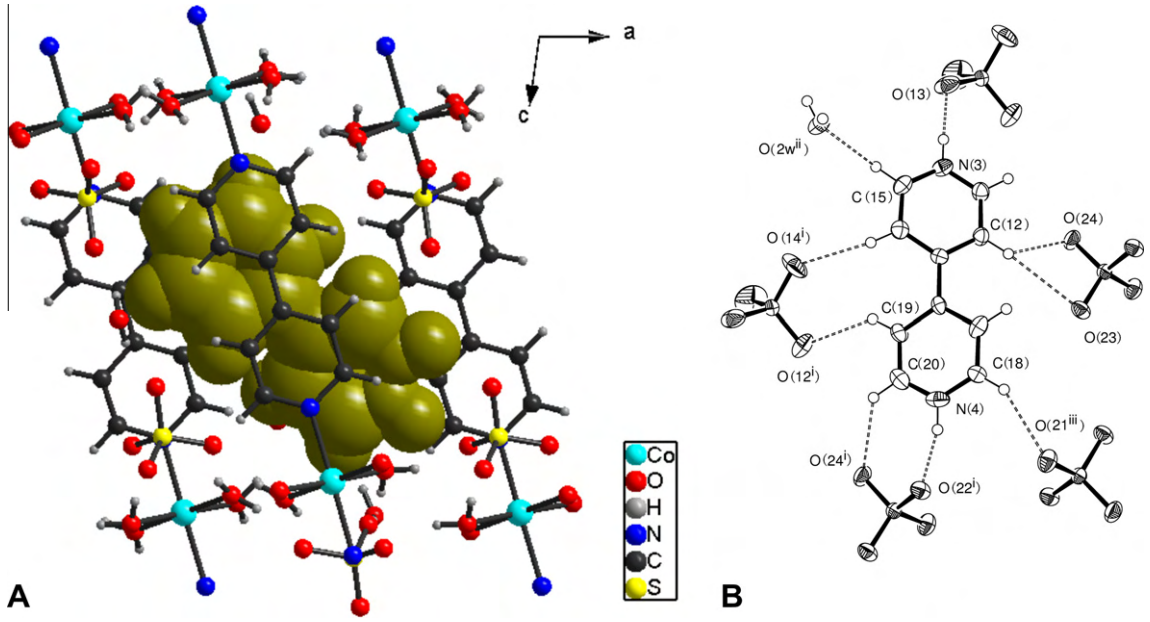

Fig. 4. (A) Space filling representation of the bipyridinium cation $(C_{10}N_2H_{10})^{2+}$ occluded within the coordination polymer and hydrogen bonding framework. (B) ORTEP representation of the bipyridinium cation and the interactions it makes to the surrounding species. Short contacts which are indicative of favourable interactions are shown as dashed lines. Symmetry equivalent atoms are generated by the symmetry operations: (i) $1 + x, y, z$; (ii) $0.5 - x, y - 0.5, 0.5 - z$; (iii) $1 - x, 1 - y, 1 - z$.

location of the $(4,4'\text{-bipyH}_2)^{2+}$ cation within the framework and the interactions between cation and framework. The role of the 4,4′-bipy may be considered directly analogous to its role in templating the gallium oxyfluorophosphate DIPYR-GaPO [45]. The interaction between framework and twice protonated 4,4′-bipy in the two phases is very similar when the hydrogen bonds between cation and framework are considered. The $(4,4'\text{-bipyH}_2)^{2+}$ cation has been observed in similar phases before [20,21] but to our knowledge a detailed description of the interaction of this cation with a framework has not appeared.

The 1-D coordination polymer chain with composition $M(H_2O)_4(4,4'\text{-bipy})$ is known in other examples [46,47], but this is the first example of any 1-D cobalt-bipyridine chain that is templated by $(4,4'\text{-bipyH}_2)^{2+}$. A similar compound containing manganese has recently been reported [48] but the description of the interaction of template and framework is rather scant. One similar example composed of chains of 4,4′-bipy with Co^{2+} that contains a guest molecule is $[Co(H_2O)_4(4,4'\text{-bipy})](SO_4)\cdot 3H_2O$ (PABA) (where PABA = para-aminobenzoic acid) [49]. This phase is less dense than **1** and has a greater cobalt to sulfate ratio but has similar structural features. However, the guest is uncharged and forms fewer short contacts with the framework than **1** suggesting a less important role in templating the framework. A similar example containing $(4,4'\text{-bipyH}_2)^{2+}$ but with a framework composed Co^{2+} coordinated by both 4,4′-bipy and 1,2,4,5-benzene-tetracarboxylate has been reported [50].

Data concerning the thermal behaviour of **1** are contained within the Supplementary Information. As **1** is heated under nitrogen, it decomposes in well-defined steps. First the coordinated and uncoordinated water is lost in the range 70–155 °C to form a species with approximate composition Co(4, 4′-bipy)(4, 4′-bipyH$_2$)(SO$_4$)$_2$. This loses the template above 155 °C to form Co(4, 4′-bipy)(SO$_4$H)$_2$ at 270 °C. This is stable until 320 °C above which it decomposes to $CoSO_4$. The sulphate is stable up to 700 °C when it decomposes to Co_3O_4.

3.3. Sulfate-decorated coordination polymer, *2*

A second reaction with similar initial conditions to those used to generate **1** but employing a different source of sulfate (Reaction C), and therefore the most basic reaction attempted, was found to yield pink needles of a compound with an unknown structure, hereafter **2**. Compound **2** crystallises in the centric space group $P2_1/c$ with three independent Co^{2+} ions within the asymmetric unit, located on **4e**, **2a**, and **2c** Wyckoff positions. The chemical formula may be written in a short form as $[Co_2(4,4'\text{-bipy})_2(SO_4)_2(H_2O)_6]\cdot 4(H_2O)$ although this formulation does not elucidate the structure very effectively. It is more enlightening to write the composition of **2** as $[Co(H_2O)_3(SO_4)(4,4'\text{-bipy})_2]_2Co(H_2O)_4Co(H_2O)_2(SO_4)_2\cdot 8H_2O$ where the coordination about each cobalt is more clearly defined. An ORTEP representation of the asymmetric unit is shown in Fig. 5 and basic crystal structure and refinement data are contained within Table 1. Full crystal structure data are included within the Supplementary Information. The composition of a bulk sample of **2** was determined by chemical analysis and this demonstrated a satisfactory fit between the calculated and observed compositions. Percentage C/H/N composition was as follows; *Anal.* Calc.: C, 30.67; H, 4.47; N, 7.01. Found: C, 29.91; H, 4.49; N, 6.98%.

The structure has many features in common with **1** but there are important differences. Compound **2** is a rather more dense phase than **1** and contains one-dimensional coordination polymer chains based on linear coordination of Co^{2+} by *trans* 4,4′-bipy which is further decorated with coordinated water and sulfate. Importantly in **2**, there is no uncoordinated sulfate, but further uncoordinated water is found within the structure. Hydrogen bonding between the ligands (sulfate and water) and uncoordinated water forms a three dimensional honeycomb net which is in addition to the 1-D polymer.

Each Co^{2+} adopts pseudo-octahedral geometry, linking *trans* 4,4′-bipy molecules to form a 1-D chain. The chain contains two symmetry independent 4,4′-bipy molecules which display very similar geometry. The planes of the six-membered rings of each of the two 4,4′-bipy molecules are twisted a little way from being parallel. The angles between the mean planes of the two sets of rings are 8.5(3)° and 9.3(3)°. The coordination environment about each of the three Co^{2+} ions is different and varies in the amount of bound sulfate. Coordination about Co1 is completed by three water molecules and one sulfate. The sulfate is disordered by

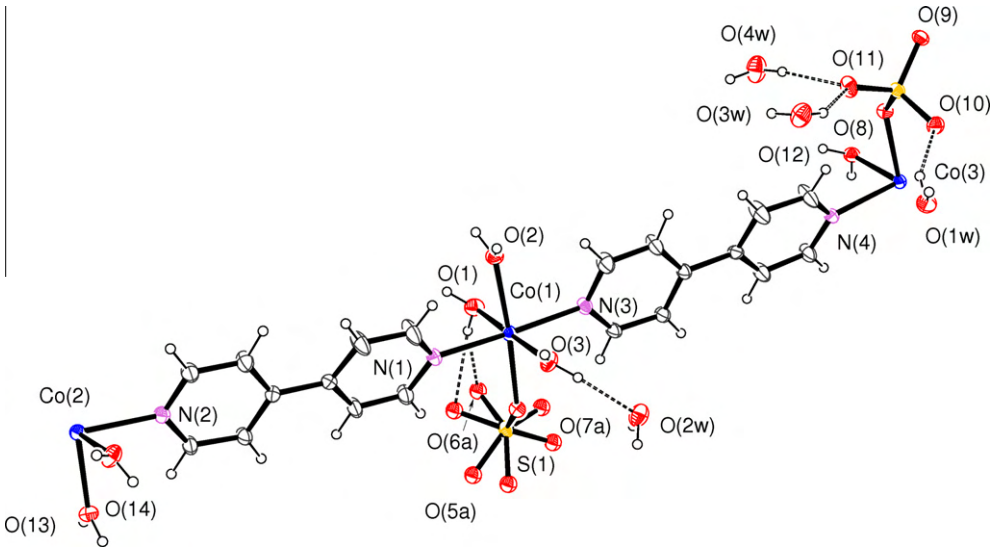

Fig. 5. ORTEP representation of the asymmetric unit of **2**. Atoms are drawn as 50% thermal ellipsoids. Carbon and hydrogen atoms have not been labelled to aid clarity. Similarly only the major orientation of the disordered sulfate is labelled. Selected bonds lengths (in Å): Co1–O1 2.030(6); Co1–O2 2.160(5); Co1–O3 2.032(6); Co1–N1 2.168(5); Co1–N3 2.180(5); Co1–O4 2.197(4); Co2–O13 2.127(5); Co2–O14 1.997(5); Co2–N2 2.168(5); Co3–O8 2.168(4); Co3–O12 2.068(5); Co3–N4 2.189(5); S1–O4 1.492(5); S1–O5A 1.488(5); S1–O6A 1.493(6); S1–O7A 1.475(5); S2–O8 1.491(5); S2–O9 1.479(5); S2–O10 1.484(5); S2–O11 1.462(5).

rotation about the S1–O4 bond. The two orientations which are approximately 39.3° apart are occupied in the ratio 82.1:17.9(5). Co2 resides on an inversion centre and coordination is completed by four bound water molecules. Similarly Co3 is located on an inversion centre, but is coordinated by two sulfate groups and two molecules of water in an 'all *trans*' arrangement. For Co2 and Co3 the N–Co–N angle is 180°, but for Co1, this angle is 174.0(2)°, possibly as a result of the greater steric demand of the sulfate group than the water molecule *trans* to it. The deviation from linearity that occurs at Co1 produces a sinusoidal form to the chain as shown in Fig. 6. This gentle curvature at Co1 is rather unusual in chains of this type. Examination of the Cambridge Structural Database [44] reveals a strong preference for a strictly linear coordination in transition metal compounds in which a metal cations links two 4,4′-bipy ligands in a *trans* arrangement. (See Supplementary Information) These infinite chains run parallel to the [2 1 2] direction and the sinusoidal variation has a wavelength of four 4,4′-bipy links which corresponds to a translation of $(x+2, y+1, z+2)$; a distance of 45.611(4) Å. Adjacent chains are related by a translation of $(x+1, y, z+1)$. A second set of identical chains related to the first by the symmetry operator $-x, \frac{1}{2}+y, \frac{1}{2}-z$ run parallel to the $[\bar{2}1\bar{2}]$ direction and are interdigitated with the first. The set of infinite chains are illustrated in Fig. 7.

The sulfate is not observed bridging between cations in contrast to other 4,4′-bipy frameworks [32]. It is monodentate and decorates the chain rather than being involved in framework formation. By careful choice of metal-sulfate ratio we sought to limit the coordination of sulfate and to promote the formation of hydrogen bonds involving sulfate. The water and sulfate ligands attached to each Co^{2+} ion have considerable hydrogen bonding capability. This is augmented by the presence of four molecules of uncoordinated water in the asymmetric unit. Compound **2** contains a three dimensional O–H···O hydrogen bond network in addition to the coordination polymers. If the structure is viewed along the [1 0 0] direction, a network which contains rings of six sulfate anions is visible (Fig. 7). The coordinated sulfate, and bound and unbound water assemble into network reminiscent of honeycomb with channels along *a*. Each six-ring has a sulfate at each vertex; one side is composed of two sulphates bound to Co^{2+}; another side is formed from sulfates bridged by a $Co(H_2O)_4$ square plane; two more are formed from two uncoordinated water molecules bridging between two sulphates to form an $R_4^2(8)$ embrace; a further two sides exist with two sulfates bridged by two bound water and one unbound water molecule to give an asymmetric motif with the graph set notation $R_5^3(10)$. The hydrogen bonding within **2** is very complicated and there are further interactions which sustain the formation of this honeycomb arrangement. The 3-D honeycomb array is easier to visualise in the Supplementary Fig. S1. Full details of the O–H···O hydrogen bonds in **2** are given in Table 3. There are a small number of C–H···O interactions present in the structure of **2**. The majority of these are short contacts between the 4,4′-bipy hydrogen atoms and sulfate or water bound to the

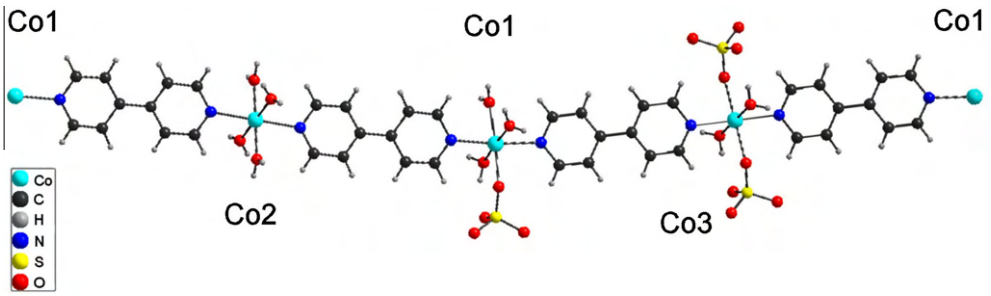

Fig. 6. Part of the infinite coordination polymer chain in **2**. The section drawn represents one period of the sinusoidal chain.

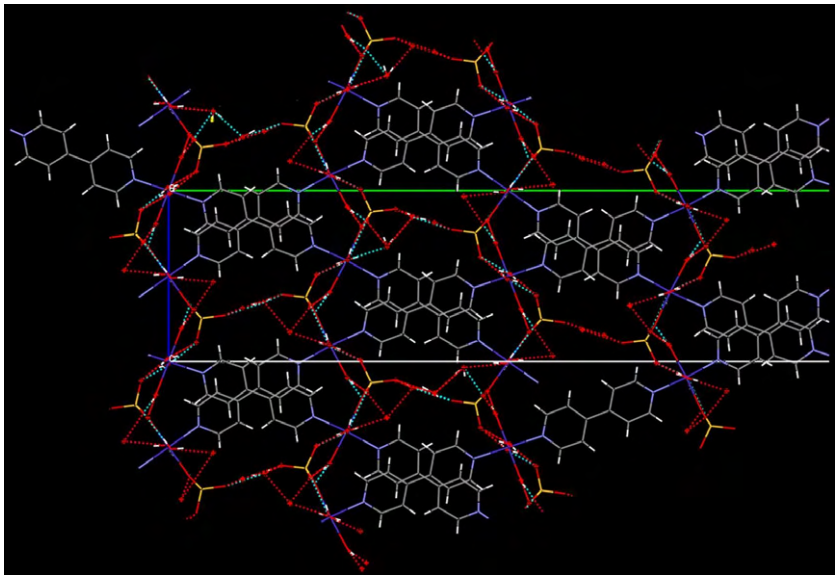

Fig. 7. The structure of **2** viewed down [1 0 0] showing the interdigitated Co^{2+}-4,4′-bipy chains. The six-membered rings of the 3-D hydrogen bonding network are also shown.

Table 3
Details of the classical hydrogen bonds and selected C–H···O interactions in **2**. A hydrogen bond donor is signified as D–H, where D is the donor atom. The hydrogen bond acceptor atom is labelled A.

Hydrogen bond donor (D–H)	D–H bond length (Å)	H···A distance (Å)	D–H···A angle (°)	D···A distance (Å)	Acceptor atom (A) [symmetry operator]
O1–H1B	0.83(6)	1.87(4)	157(8)	2.65(8)	O6A
O1–H1B	0.83(6)	2.16(6)	149(10)	2.90(2)	O6B
O1–H1A	0. 83(6)	1.79(4)	166(10)	2.602(8)	O5A [x, $-y+1/2$, $z+1/2$]
O1–H1A	0. 83(6)	2.19(4)	165(9)	3.00(2)	O5B [x, $-y+1/2$, $z+1/2$]
O2–H2A	0. 83(6)	2.03(4)	164(9)	2.845(8)	O6A [$x+1$, $-y+1/2$, $z+1/2$]
O2–H2A	0. 83(6)	2.20(6)	138(8)	2.87(2)	O6B [$x+1$, $-y+1/2$, $z+1/2$]
O2–H2B	0. 83(6)	2.13(3)	169(8)	2.949(7)	O4 [x, $-y+1/2$, $z+1/2$]
O3–H3B	0.82(6)	1.88(3)	176(10)	2.701(8)	O5A [$x+1$, $-y+1/2$, $z+1/2$]
O3–H3B	0.82(6)	2.14(8)	131(9)	2.75(2)	O6B [$x+1$, $-y+1/2$, $z+1/2$]
O3–H3A	0.82(6)	1.92(4)	162(8)	2.715(7)	O2W
O12–H12A	0.83(6)	1.90(4)	168(9)	2.713(7)	O1W [$x-1$, y, z]
O12–H12B	0.82(6)	1.94(4)	161(10)	2.731(7)	O10 [$-x+2$, $-y+1$, $-z+2$]
O13–H13B	0.84(6)	2.01(4)	164(10)	2.827(7)	O10 [$x-2$, $-y+1/2$, $z-3/2$]
O13–H13A	0.83(6)	2.09(3)	171(10)	2.916(7)	O8 [$x-1$, $-y+1/2$, $z-3/2$]
O14–H14B	0.83(6)	1.86(4)	162(10)	2.656(7)	O9 [$-x+2$, $y-1/2$, $-z+3/2$]
O14–H14A	0.83(6)	1.86(4)	163(10)	2.665(7)	O9 [$x-1$, $-y+1/2$, $z-3/2$]
O1W–H1D	0.83(6)	2.05(5)	152(9)	2.800(8)	O10
O1W–H1C	0.82(6)	1.94(4)	166(9)	2.744(9)	O4W [$x+1$, y, z]
O2W–H2D	0.84(6)	1.96(4)	159(9)	2.757(9)	O6A [$x+1$, y, z]
O2W–H2D	0.84(6)	2.45(7)	146(9)	3.18(2)	O7B [$x+1$, y, z]
O2W–H2C	0.84(6)	1.94(5)	160(10)	2.740(8)	O3W [$x-1$, y, $z-1$]
O3W–H3C	0.83(6)	2.04(5)	155(9)	2.808(9)	O11
O3W–H3D	0.83(6)	1.98(3)	172(11)	2.808(9)	O7A [$x+1$, y, $z+1$]
O4W–H4C	0.84(6)	2.02(3)	171(11)	2.851(9)	O11
O4W–H4D	0.83(6)	2.01(8)	136(9)	2.666(16)	O7B [$x+1$, y, $z+1$]
O4W–H4D	0.83(6)	2.20(8)	137(10)	2.860(9)	O7A [$x+1$, y, $z+1$]
C2–H2	0.95	2.48	170	3.420(9)	O2W [$x-1$, $1/2-y$, $z-1/2$]
C7–H7	0.95	2.68	173	3.625(9)	O2W [$x-1$, $1/2-y$, $z-1/2$]
C9–H9	0.95	2.49	148	3.333(9)	O1W [$x-1$, $1/2-y$, $z-1/2$]
C19–H19	0.95	2.41	147	3.254(8)	O9 [$x-1$, y, $z-1$]

same infinite chain. However, it is noteworthy that H2 and H7 form contacts to the uncoordinated water, O2W. Although these contacts are rather long, they are close to linear, which has been identified as signifying a hydrogen bond rather than van der Waals contact [51]. Notably, H19 forms a contact to one of the sulfate anions attached to a neighbouring parallel chain, enhancing the interaction between adjacent chains. Details of selected C–H···O interactions are given in Table 3.

Thermogravimetric data for **2** are presented within the Supplementary Information. As **2** is heated in flowing nitrogen, it decomposes in well-defined steps. Similarly to **1**, when **2** is heated it loses all of the coordinated and uncoordinated water first in the range 60–160 °C to produce a phase with approximate composition $Co(bipy)(OH)(SO_4)$ which is stable until 285 °C. Above this temperature it decomposes slowly until at 420 °C a phase with composition $Co(OH)(SO_4)$ is formed. This is stable until 570 °C at which point $CoSO_4$ forms rapidly and is stable until 680 °C. Above this point cobalt oxide is obtained. Phase 1 contains much more sulfate than **2** and this appears to have a profound influence on the nature of the intermediate phases upon thermal decomposition. In phase 2,

it appears that some water is retained as hydroxide (perhaps bridging) to satisfy the coordination requirement of the cobalt.

The control of synthesis for frameworks of this type is clearly dependent upon a number of factors. The reactions presented here are examples of different regions of a complex composition space. For example, in reactions A and B, a small change in the initial pH of the mixture coupled with variation of the cobalt to sulfate ratio leads to different products. It is notable that variation of cobalt to 4,4′-bipy ratio leads to different products (Reactions B and C). Experiments are currently underway to alter the initial pH of the mixture while preserving the cobalt to sulfate ratio, along with an investigation of the effect of metal source on the nature of the products.

3.4. Spectroscopic characterisation of *1* and *2*

3.4.1. Vibrational spectra of *1* and *2*

The differences in coordination modes of sulfate and 4,4-bipy with the additional influence of hydrogen bonding interactions and local structural disorder in structures **1** and **2** are clearly manifested in the IR and Raman spectra of the ground crystals of **1** and **2**. Four normal modes of vibration including the stretching $\nu_1(A_1)$ and $\nu_3(T_2)$, and the bending $\nu_2(E)$ and $\nu_4(T_2)$ are expected for uncoordinated sulfate anions with a regular tetrahedral geometry of T_d point symmetry. While all of these vibrations are expected to be Raman-active, only the stretching $\nu_3(T_2)$ and the bending $\nu_4(T_2)$ are IR-active. Upon coordination, the symmetry of the coordinated sulfate will be lowered; C_{3v} and C_{2v} for monodentate and bidentate sulfate ligands, respectively. A reduction in point symmetry should result in the appearance of $\nu_1(A_1)$ and $\nu_2(E)$, and the splitting of $\nu_3(T_2)$ and $\nu_4(T_2)$ in the IR. The presence of one, three and four ν(S–O) bands can therefore be expected in the IR for the uncoordinated, monodentate and bidentate sulfate. However, in the spectrum of uncoordinated sulfate the appearance of a weak $\nu_1(A_1)$ band and a broadening of the $\nu_3(T_2)$ band is commonly reported, due to the other non-bonding interactions of the sulfate with the neighbouring species in the crystal structures [52,53].

Fig. 8 shows portions of the IR spectra of **1** and **2**. Full spectra and detailed assignment of peaks are contained within the Supplementary Information. Despite a different coordination mode of the sulfate anions, the IR spectra of the two compounds are rather similar at the first glance, notably the presence of the very intense ν_3 and ν_4 and the very weak ν_1 and ν_2, with the broadening of ν_3 band. The broadening of these ν_3 bands is similar in each case and clearly visible. The clear splitting of the ν_4 band in **2** compared with that of **1** is notable. The observed features in the IR spectra indicate the lowering of point symmetry of both the uncoordinated sulfate in **1** and the monodentate sulfate in **2**, which is consistent with the crystallographic information. In the structure of **2**, although the two distinct sulfate ligands adopt the same coordination mode, crystallographic disorder and the dissimilarity of the hydrogen bonding interactions (Tables 2 and 3) differentiate the two sulfate ligands, which accounts for the apparent features in the IR spectrum. Regarding the uncoordinated sulfate anions in structure **1**, a distortion of the sulfate local environment is due to O–H···O hydrogen bonding (Fig. 3) reducing the symmetry from the expected T_d. The influence of hydrogen bonding interactions in lowering local symmetry is demonstrated by the observed spectra.

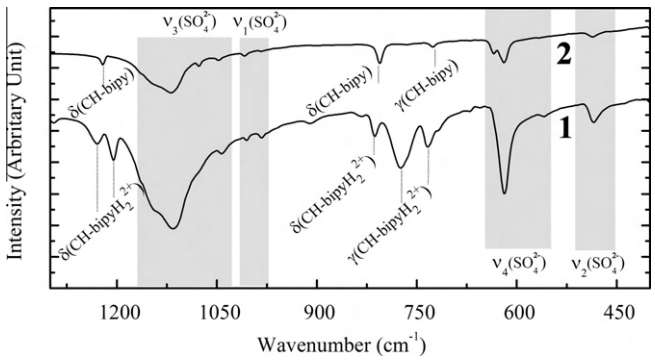

Fig. 8. Portions of the FT-IR spectra of **1** and **2** in the range 400–1300 cm^{-1}. Selected band assignments are overlaid to illustrate the difference between the spectra.

The vibrational bands of the sulfate anions are not clearly visible in the Raman spectra, (contained within the Supplementary Information) which are dominated by bands due to the 4,4-bipy species. The di-protonation of the 4,4-bipy (4,4-bipyH$_2^{2+}$) and range of local environments for 4,4-bipy introduce a huge degree of splitting in the characteristic vibrational bands in the IR. However, the presence of characteristic bands for the ν(NH$^+$) and the δ(NH$^+$) of the protonated species is obvious in the IR spectra of **1**. The splitting of the breathing modes in the Raman can also be used to distinguish the protonated 4,4-bipyH$_2^{2+}$ in **1** from the neutral 4,4-bipy molecule in **2**.

3.5. UV–Vis spectra of *1* and *2*

The electronic spectra of **1** and **2** in hexane are noticeably similar, both dominated by a broad band centred around 42 500 cm^{-1} with a shoulder centred on 37 200 cm^{-1}, which are characteristic of the phenyl ring of 4,4′-bipy and can be assigned as the ligand π–π^* transitions. In addition to these intense bands, there are also weak absorptions at frequencies lower than 30 000 cm^{-1}, particularly in the case of **1**. A weak broad band centred on 16 000 cm^{-1} is consistent with two overlapped transitions, $^4T_{1g}(P) \leftarrow {}^4T_{1g}(F)$ and $^4A_{2g}(F) \leftarrow {}^4T_{1g}(F)$ of the high spin Co^{II} in a distorted octahedral field demonstrated by the crystal structure.

4. Conclusion

Microwave-assisted hydrothermal synthesis is an extremely promising technique for the growth of MOFs. It cuts typical reaction times from a few days to a few minutes. In this study and others though, we have noticed the tendency for the products to grow as aggregates of crystals which can complicate structure determination. However, it is emerging as a very useful synthetic protocol in this field.

In a previous study, changes to the cobalt source and reaction conditions were found to influence the nature of the products in a similar system [54]. The frameworks described here suggest that even in the seemingly simple system cobalt-4,4′-bipy-sulfate-water, there is considerable scope for the synthesis of new frameworks by small changes in the initial conditions. We are currently exploring this system with a view to mapping how the nature of the product varies with initial composition. Furthermore, alteration of the amount of water present will prove another variable to control the nature and likely density of framework obtained.

Fortified by the success of our approach, we are also investigating similar syntheses using other positively charged species such as quaternary amines that may act as templates for cavities of this sort of 3-D network composed of 1-D coordination polymer and 2-D hydrogen-bonded sheets in attempts to mimic 1.

Acknowledgements

AR thanks the Thailand Research Fund, the Royal Golden Jubilee, and the Centre for Innovation in Chemistry, PERCH-CIC, for

support with this work. We thank Mr. I. Dobson for the collection of thermogravimetric data.

Appendix A. Supplementary data

CCDC 780738 and 780739 contain the supplementary crystallographic data for this paper. These data can be obtained free of charge via http://www.ccdc.cam.ac.uk/conts/retrieving.html, or from the Cambridge Crystallographic Data Centre, 12 Union Road, Cambridge CB2 1EZ, UK; fax: (+44) 1223-336-033; or e-mail: deposit@ccdc.cam.ac.uk. Supplementary data associated with this article can be found, in the online version, at doi:10.1016/j.poly.2010.10.010.

References

[1] A. Dyer, Introduction to Zeolite Molecular Sieves, John Wiley & Sons, 1988.
[2] A.K. Cheetham, G. Ferey, T. Loiseau, Angew. Chem., Int. Ed. Engl. 38 (1999) 3268.
[3] C.R.A. Catlow, D.S. Coombes, J.C.G. Pereira, Chem. Mater. 10 (1998) 3249.
[4] M.E. Davis, R.F. Lobo, Chem. Mater. 4 (1992) 756.
[5] S. Natarajan, M.P. Attfield, A.K. Cheetham, J. Solid State Chem. 132 (1997) 229.
[6] C.N.R. Rao, S. Natarajan, R. Vaidhyanathan, Angew. Chem., Int. Ed. 43 (2004) 1466.
[7] S. Natarajan, P. Mahata, Chem. Soc. Rev. 38 (2009) 2304.
[8] O.M. Yaghi, M. O'Keeffe, N.W. Ockwig, H.K. Chae, M. Eddaoudi, J. Kim, Nature 423 (2003) 705.
[9] H.K. Chae, J. Kim, O.D. Friedrichs, M. O'Keefe, O.M. Yaghi, Angew. Chem., Int. Ed. Engl. 42 (2003) 3907.
[10] H. Li, M. Eddaoudi, M. O'Keeffe, O.M. Yaghi, Nature 402 (1999) 276.
[11] G. Ferey, Mol. Networks 132 (2009) 87.
[12] R.E. Morris, X.H. Bu, Nat. Chem. 2 (2010) 353.
[13] R.J. Kuppler, D.J. Timmons, Q.R. Fang, J.R. Li, T.A. Makal, M.D. Young, D.Q. Yuan, D. Zhao, W.J. Zhuang, H.C. Zhou, Coord. Chem. Rev. 253 (2009) 3042.
[14] R.Q. Zou, A.I. Abdel-Fattah, H.W. Xu, Y.S. Zhao, D.D. Hickmott, Cryst. Eng. Commun. 12 (2010) 1337.
[15] H.J. Park, M.P. Suh, Chem. Commun. 46 (2010) 610.
[16] L.J. Murray, M. Dinca, J.R. Long, Chem. Soc. Rev. 38 (2009) 1294.
[17] D. Farrusseng, S. Aguado, C. Pinel, Angew. Chem., Int. Ed. Engl. 48 (2009) 7502.
[18] J.D. Lin, X.F. Long, P. Lin, S.W. Du, Cryst. Growth Des. 10 (2010) 146.
[19] K.S. Murray, C.J. Kepert, Cooperativity in Spin Crossover Systems: Memory, Magnetism and Microporosity, Springer-Verlag, 2004.
[20] M.L. Tong, X.M. Chen, Cryst. Eng. Commun. 2 (2000) 1.
[21] M.L. Tong, B.H. Ye, J.W. Cai, X.M. Chen, S.W. Ng, Inorg. Chem. 37 (1998) 2645.
[22] D.T. De Lill, N.S. Gunning, C.L. Cahill, Inorg. Chem. 44 (2005) 258.
[23] E.Y. Choi, Y.U. Kwon, Inorg. Chem. 44 (2005) 538.
[24] T. Steiner, Angew. Chem., Int. Ed. Engl. 41 (2002) 48.
[25] T. Steiner, Chem. Commun. (1997) 727.
[26] M.D. Stephenson, T.J. Prior, M.J. Hardie, Cryst. Growth Des. 8 (2008) 643.
[27] T.J. Prior, M.J. Rosseinsky, Chem. Commun. (2001) 1222.
[28] A.D. Burrows, D.M.P. Mingos, A.J.P. White, D.J. Williams, Chem. Commun. (1996) 97.
[29] S.R. Breeze, S.N. Wang, Inorg. Chem. 32 (1993) 5981.
[30] K. Biradha, M. Sarkar, L. Rajput, Chem. Commun. (2006) 4169.
[31] D. Bradshaw, J.E. Warren, M.J. Rosseinsky, Science 315 (2007) 977.
[32] S.D. Huang, R.G. Xiong, P.H. Sotero, J. Solid State Chem. 138 (1998) 361.
[33] G.A. Jeffrey, An Introduction to Hydrogen Bonding, OUP, 1997.
[34] L.S. Long, Cryst. Eng. Commun. 12 (2010) 1354.
[35] S. Luachan, C. Pakawatchai, A. Rujiwatra, J. Inorg. Organomet. Polym. Mater. 17 (2007) 561.
[36] X.H. Li, Q. Miao, H.P. Xiao, M.L. Hu, Acta Crystallogr., Sect. E 60 (2004) m1784.
[37] W.J. Lu, Y.M. Zhu, K.L. Zhong, Acta Crystallogr., Sect. C 62 (2006) m448.
[38] C.O. Kappe, Angew. Chem., Int. Ed. Engl. 43 (2004) 6250.
[39] H. Phetmung, S. Wongsawat, C. Pakawatchai, D.J. Harding, Inorg. Chim. Acta 362 (2009) 2435.
[40] P. Amo-Ochoa, G. Givaja, P.J.S. Miguel, O. Castillo, F. Zamora, Inorg. Chem. Commun. 10 (2007) 921.
[41] Z. Ni, R.I. Masel, J. Am. Chem. Soc. 128 (2006) 12394.
[42] B. Yotnoi, S. Yimklan, T.J. Prior, A. Rujiwatra, J. Inorg. Organomet. Polym. Mater. 19 (2009) 306.
[43] R.I. Cooper, R.O. Gould, S. Parsons, D.J. Watkin, J. Appl. Cryst. 35 (2002) 168.
[44] F.H. Allen, Acta Crystallogr., Sect. B 58 (2002) 380; (see <www.ccdc.cam.ac.uk>.)
[45] S.J. Weigel, R.E. Morris, G.D. Stucky, A.K. Cheetham, J. Mater. Chem. 8 (1998) 1607.
[46] L.P. Zhang, L.G. Zhu, Acta Crystallogr., Sect. E 61 (2005) m1264.
[47] Z.-X. Lian, J. Cai, C.-H. Chen, Polyhedrom 26 (2007) 2647.
[48] S.R. Fan, L.G. Zhu, Acta Crystallogr., Sect. E 61 (2005) m1689.
[49] H. Chen, (Jiegou Huaxue) Chin. J. Struct. Chem. 24 (2005) 236.
[50] C. Ruiz-Pérez, P. Lorenzo-Luis, M. Hernández-Molina, M.M. Laz, F.S. Delgado, P. Gili, M. Julve, Eur. J. Inorg. Chem. (2004) 3873.
[51] T. Steiner, G.R. Desiraju, Chem. Commun. (1998) 891.
[52] C. Papatriantafyllopoulou, E. Manessi-Zoupa, A. Escuer, S.P. Perlepes, Inorg. Chim. Acta 362 (2009) 634.
[53] V.P. Mahadevan Pillai, V.U. Nayar, V.B. Jordanovska, J. Solid State Chem. 133 (1997) 407.
[54] J. Lu, C. Yu, T. Nui, T. Paliwala, G. Crisci, F. Somosa, A.J. Jacobsen, Inorg. Chem. 37 (1998) 4637.

CRYSTAL GROWTH & DESIGN

A62

ARTICLE

pubs.acs.org/crystal

Lanthanide Sulfate Frameworks: Synthesis, Structure, and Optical Properties

Published as part of a virtual special issue on Structural Chemistry in India: Emerging Themes

Bunlawee Yotnoi,[†] Apinpus Rujiwatra,[†] M. L. P. Reddy,[‡] Debajit Sarma,[§] and Srinivasan Natarajan*[,§]

[†]Department of Chemistry, Faculty of Science, Chiang Mai University, Chiang Mai, Thailand, 50200

[‡]Chemical Sciences and Technology Division, National Institute for Interdisciplinary Science & Technology (NIIST), Thiruvananthapuram 695019, India

[§]Framework Solids Laboratory, Solid State and Structural Chemistry Unit, Indian Institute of Science, Bangalore-560012, India

Supporting Information

ABSTRACT: Layered lanthanide sulfate compounds with three different structures have been prepared and characterized. The compounds $[C_{10}H_{10}N_2][La(SO_4)_2]\cdot 2H_2O$ (**I**), $[C_{10}H_{10}N_2][La(SO_4)_2(H_2O)_2]_2$ (**IIa**), $[C_{10}H_{10}N_2][Pr(SO_4)_2(H_2O)_2]_2$ (**IIb**), $[C_{10}H_{10}N_2][Nd_2(SO_4)_4(H_2O)_2]_2$ (**IIIa**), $[C_{10}H_{10}N_2][Sm_2(SO_4)_4(H_2O)_2]_2$ (**IIIb**), and $[C_{10}H_{10}N_2][Eu_2(SO_4)_4(H_2O)_2]_2$ (**IIIc**) have anionic lanthanide sulfate layers separated by protonated bipyridine molecules. The layers are formed by the connectivity between the lanthanide polyhedra and sulfate tetrahedra. The formation of a two-dimensional La−O−La layer (**Ia**), Pr−O−Pr chains (**IIb**), and a tetramer cluster (**IIIa**) is noteworthy. The compounds exhibit honeycomb (**I**), square (**IIa**, **IIb**), and honeycomb (**IIIa**−**IIIc**) net arrangements, when the connectivity between the lanthanide ions is considered. Optical studies indicate the observation of characteristic metal-centered emission at room temperature. The Nd compound (**IIIa**) exhibits a two-photon upconversion behavior.

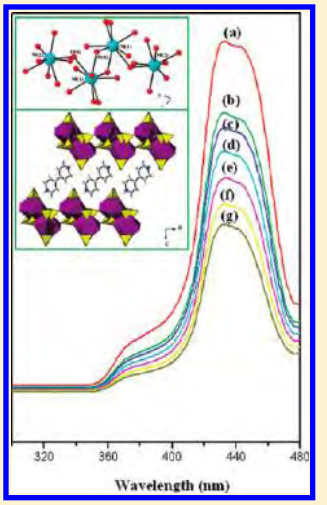

INTRODUCTION

Traditional open-framework compounds are based on tetrahedral anions such as silicates and phosphates.[1] Persistent research over the years has established that other tetrahedral anions such as the arsenates,[2] sulfates,[3] selenates,[4] and borates[5] can, in fact, become part of the extended structures. The wide structural and compositional diversity exhibited by this class of compounds is a testimony for the flexible nature of the structures. Of the many open-framework compounds that have been synthesized and characterized, those of the sulfates are an important family. The synthesis, structure, and properties of a number of transition metal sulfates have been reported in recent years.[6] Many transition metal sulfates have one- or two-dimensional structures, and it has been observed that the formation of three-dimensionally extended sulfate networks is difficult.[7] It is likely that the sulfate, $[SO_4]^{2-}$, is much less reactive compared to the phosphate, $[PO_4^{3-}]$, and the arsenate, $[AsO_4^{3-}]$, anions. It has been shown that the elements that prefer a higher coordination environment could be employed for the synthesis of the sulfate networks with three-dimensional structures. One such family of elements is the lanthanides.[8]

Lanthanide-based compounds are being studied for their varied structural, physical, and chemical properties. It is known that the lanthanide-based compounds exhibit interesting luminescence behavior.[9] Lanthanides exhibit intense photoluminescence behavior and find applications as fluorescent probes in biochemistry and other emission-related properties.[10] It has been known that the lanthanide ions exhibit narrow f−f transitions, which could be exploited for light emitting device applications. Unfortunately, the f−f transitions are spin and parity forbidden, and exploiting such sharp transitions requires the use of sensitizers. Recently, aromatic carboxylates have been employed as a sensitizer for observing the metal-centered emission of the rare earth ions.[11] Among the rare earth ions, Eu^{3+}, Tb^{3+}, and Nd^{3+} ions are important for use as optical centers. Eu^{3+} and Tb^{3+} ions

Received: November 30, 2010
Revised: January 25, 2011
Published: February 16, 2011

Table 1. Synthesis Conditions Employed for the Compounds

synthesis condition				composition
mole ratio	temp (°C)	time (h)	yield (%)	product
0.70 La_2O_3 + 2.10 4,4′-bipyridine + 0.3 mL of H_2SO_4 (conc) + 556 H_2O	200	24	68	$[C_{10}H_{10}N_2][La(SO_4)_2]\cdot 2H_2O$, (**I**)
0.70 La_2O_3 + 2.10 4,4′-bipyridine +0.5 mL of H_2SO_4 (conc) + 556 H_2O	125	24	65	$[C_{10}H_{10}N_2][La(SO_4)_2(H_2O)_2]_2$, (**IIa**)
0.23 Pr_6O_{11} + 2.10 4,4′-bipyridine +0.5 mL of H_2SO_4 (conc) + 556 H_2O	125	24	63	$[C_{10}H_{10}N_2][Pr(SO_4)_2(H_2O)_2]_2$, (**IIb**)
0.23 Nd_2O_3 + 2.10 4,4′-bipyridine +0.5 mL of H_2SO_4 (conc) + 556 H_2O	125	24	72	$[C_{10}H_{10}N_2][Nd_2(SO_4)_4(H_2O)_2]_2$, (**IIIa**)
0.23 Sm_2O_3 + 2.10 4,4′-bipyridine +0.5 mL of H_2SO_4 (conc) + 556 H_2O	125	24	68	$[C_{10}H_{10}N_2][Sm_2(SO_4)_4(H_2O)_2]_2$, (**IIIb**)
0.23 Eu_2O_3 + 2.10 4,4′-bipyridine +0.5 mL of H_2SO_4 (conc) + 556 H_2O	125	24	70	$[C_{10}H_{10}N_2][Eu_2(SO_4)_4(H_2O)_2]_2$, (**IIIc**)

are useful in the visible region (λ = ~400−800 nm), whereas Nd^{3+} ions are useful in the near infrared (IR) region (λ = 800−1700 nm). It has been shown that the Nd^{3+} ions also exhibit upconversion behavior of converting the IR radiation to the visible region through a two-photon absorption process.[12]

In spite of the considerable progress achieved toward the understanding of the photophysical behavior of the lanthanides, the subtle relationship that exists between the photophysical properties and the structure suggests the need for further studies. It occurred to us that the lack of higher dimensional structures in sulfates and the need for larger coordination numbers for the lanthanide ions can be gainfully employed in preparing new three dimensionally extended lanthanide sulfate compounds. It has been shown that the use of 4,4′-bipyridine enhances the dimensionality of the structures by acting as a rigid linker between the metal centers.[13] In addition, the use of 4,4′-bipyridine might assist in the luminescence behavior of the lanthanides through initial absorption and energy transfer. We used a combination of these during the preparation of a new family of lanthanide sulfate compounds. Our efforts were successful and we have isolated three new lanthanide sulfate compounds. The compounds $[C_{10}H_{10}N_2][La(SO_4)_2]\cdot 2H_2O$ (**I**), $[C_{10}H_{10}N_2][La(SO_4)_2(H_2O)_2]_2$ (**IIa**), $[C_{10}H_{10}N_2][Pr(SO_4)_2(H_2O)_2]_2$ (**IIb**), $[C_{10}H_{10}N_2][Nd_2(SO_4)_4(H_2O)_2]_2$ (**IIIa**), $[C_{10}H_{10}N_2][Sm_2(SO_4)_4(H_2O)_2]_2$ (**IIIb**), and $[C_{10}H_{10}N_2][Eu_2(SO_4)_4(H_2O)_2]_2$ (**IIIc**) all have a two-dimensional layer structure formed by the connectivity between the rare earth ions and the sulfate units. The 4,4′-bipyridine ligand occupies the interlamellar spaces. In this paper, we present the synthesis, structure, and photophysical properties of all the compounds.

EXPERIMENTAL SECTION

Synthesis and Initial Characterization. The compounds were prepared by employing the hydrothermal method. In a typical synthesis, for **I**, La_2O_3 (0.2283 g, 0.70 mmol) was added to 10 mL of deionized water. To this, 4,4′-bipyridine (0.3283 g, 2.10 mmol) and concentrated sulfuric acid (0.3 mL) were added under continuous stirring. The mixture was homogenized for 30 min at room temperature. The final mixture was transferred, sealed in a 23 mL PTFE lined autoclave, and heated at 200 °C for 24 h under autogenous pressure. The final product contained large quantities of colorless rod-shaped single crystals, which were filtered under a vacuum, washed with deionized water, and dried at ambient conditions (yield ~68% based on La). The other compounds were obtained employing similar conditions (Table 1). In the case of Pr (**IIb**), Nd (**IIIa**), Sm (**IIIb**), and Eu (**III**), the final product contains large quantities of light green (Pr), light purple (Nd), light purple (Sm), and colorless (Eu) rod-type single crystals. In the case of compound **IIa**, the product was found to be a polycrystalline white powder. The product was later characterized by powder X-ray diffraction (PXRD) studies by comparing with the PXRD pattern of the related Pr compound (**IIb**). The PXRD pattern of **IIa** matched well with the simulated XRD pattern generated from the single crystal structure of Pr (**IIa**) compound. The microcrystalline phase **IIa** was indexed and the unit cell parameters were obtained from the PXRD patterns by the Le Bail method (Supporting Information Figure S1).[14] The Eu doped (4 mol % and 8 mol %) and Tb doped (4 mol % and 8 mol %) in place of La in **I** and Eu doped (4 mol % and 8 mol %) and Tb doped (4 and 8 mol) in place of La in **IIa** were prepared using the same experimental procedure as that employed for **I** and **IIa**. Initial characterizations were carried out by elemental analysis, PXRD, thermogravimetric analysis (TGA), and IR studies.

PXRD patterns were recorded in the 2θ range 5−50° using Cu Kα radiation (Philips X'pert) (Supporting Information, Figures S2−S8). The IR spectra for the compounds were recorded as KBr pellets (Perkin-Elmer, SPECTRUM 1000). The IR spectroscopic studies exhibit typical peaks corresponding to the hydroxyl group, the amino groups, etc. (Supporting Information, Figure S9). The main IR bands are (KBr): ν (H_2O) = 3230−3450 cm^{-1}, ν (N−H) = 3070−3110 cm^{-1}, ν (C−H) = 2670−2780 cm^{-1}, ν (C−H) = 1300−1500 cm^{-1}, $\nu_1(SO_4)$ = 950−1000 cm^{-1}, $\nu_3(SO_4)$ = 1100−1150 cm^{-1}, δ(SO4) = 500−700 cm^{-1}. The IR spectrum can be useful for investigating the sulfate species. In general, the free sulfate ions exhibit two bands at 1105 and 615 cm^{-1}, which are assigned to the ν_3(F2) stretching [ν_d(SO)] and ν_4(F2) stretching [δ_d(OSO)] modes, respectively. The coordination of the free sulfate group to the metal centers would lower the overall symmetry of the sulfate group and lead to the splitting of the ν_3 and ν_4 modes. The IR spectrum of the present compounds exhibits characteristic IR bands for the sulfate ions, SO_4^{-2}, with the IR-active region for the SO_4 tetrahedron located between 500 and 1150 cm^{-1}. In addition, we observed that the sulfate site symmetry is also lowered due to the many bridging coordination modes of the sulfate ions. The observed shoulders in the IR bands, thus, in the region 1025−1185 cm^{-1} may be attributed to the ν_3 modes and the shoulders in the region 554−670 cm^{-1} can be assigned to the ν_4 modes.

Single Crystal Structure Determination. A suitable single crystal of each compound was carefully selected under a polarizing microscope and glued to a thin glass fiber. The single crystal data were collected on a Bruker AXS smart Apex CCD diffractometer at 293(2) K. The X-ray generator was operated at 50 kV and 35 mA using Mo Kα (λ = 0.71073 Å) radiation. Data were collected with ω scan width of 0.3°. A total of 606 frames were collected in three different settings of φ (0, 90, 180°) keeping the sample-to-detector distance fixed at 6.03 cm and the detector position (2θ) fixed at −25°. The data were reduced using SAINTPLUS,[15] and an empirical absorption correction was applied using the SADABS program.[16] The structure was solved and refined using SHELXL97[17] present in the WinGx suite of programs (Version 1.63.04a).[18] All the hydrogen positions were initially located in the difference Fourier maps, and for the final refinement, the hydrogen atoms were placed in geometrically ideal positions and refined in the riding mode. Final refinement included atomic positions for all the atoms, anisotropic thermal parameters for all the non-hydrogen atoms, and isotropic thermal parameters for all the hydrogen atoms. Full-matrix

Table 2. Crystal Data and Structure Refinement Parameters for the Compounds $[C_{10}H_{10}N_2][La(SO_4)_2]\cdot 2H_2O$, (I) $[C_{10}H_{10}N_2][Pr(SO_4)_2(H_2O)_2]_2$, (IIb), $[C_{10}H_{10}N_2][M_2(SO_4)_4(H_2O)_2]_2$[a]

empirical formula	$C_5H_7NLaS_2O_9$	$C_5H_9NPrS_2O_{10}$	$C_{10}H_{14}N_2Nd_2S_4O_{18}$	$C_{10}H_{14}N_2Sm_2S_4O_{18}$	$C_{10}H_{14}N_2Eu_2S_4O_{18}$
formula weight	426.13	448.16	866.95	875.14	878.36
crystal system	triclinic	triclinic	triclinic	triclinic	triclinic
space group	$P\bar{1}$	$P\bar{1}$	$P\bar{1}$	$P\bar{1}$	$P\bar{1}$
a/Å	5.6238(2)	5.0354(1)	8.0119(5)	7.9585(2)	7.9370(6)
b/Å	7.3489(3)	7.0079(1)	9.4075(6)	9.3752(3)	9.3612(7)
c/Å	12.9709(5)	16.6321(3)	14.9538(9)	14.9270(4)	14.9214(10)
α/°	90.821(2)	88.50	79.439(1)	79.327(2)	79.348(1)
β/°	96.912(2)	87.94	83.749(1)	83.927(2)	83.996(1)
γ/°	100.159(2)	75.47	73.988(1)	73.830(2)	73.777(1)
vol/Å^3	523.48(3)	567.67(2)	1062.99(11)	1049.44(5)	1044.52(13)
Z	2	2	2	2	2
T/K	293(2)	293(2)	293(2)	293(2)	293(2)
ρ_{calc} (g cm^{-3})	2.703	2.622	2.696	2.769	2.793
μ (mm^{-1})	4.522	4.711	5.320	6.036	6.448
θ range (deg)	1.58−26.00	2.45−26.00	2.28−26.00	2.48−26.00	1.39−26.00
λ (Mo Kα) (Å)	0.71073	0.71073	0.71073	0.71073	0.71073
R_{int}	0.0262	0.0244	0.0252	0.0568	0.0416
reflection collected	7955	8568	11057	25572	10666
unique reflections	2007	2217	4159	4119	4082
no. of parameters	163	188	325	325	325
R indices $[I > 2\sigma(I)]$	$R_1 = 0.0161$, $wR_2 = 0.0438$	$R_1 = 0.0160$, $wR_2 = 0.0428$	$R_1 = 0.0215$, $wR_2 = 0.0538$	$R_1 = 0.0420$, $wR_2 = 0.1141$	$R_1 = 0.0534$, $wR_2 = 0.1400$
R indices (all data)	$R_1 = 0.0163$, $wR_2 = 0.0439$	$R_1 = 0.0166$, $wR_2 = 0.0431$	$R_1 = 0.0249$, $wR_2 = 0.0551$	$R_1 = 0.0438$, $wR_2 = 0.1154$	$R_1 = 0.0542$, $wR_2 = 0.1412$

[a] M = Nd^{3+} (**IIIa**), Sm^{3+} (**IIIb**), and Eu^{3+} (**IIIc**). $R_1 = \Sigma||F_o| - |F_c||/\Sigma|F_o|$; $wR_2 = \{\Sigma[w(F_o^2 - F_c^2)]/\Sigma[w(F_o^2)^2]\}^{1/2}$. $w = 1/[\rho^2(F_o)^2 + (aP)^2 + bP]$. $P = [\max(F_o, 0) + 2(F_c)^2]/3$, where $a = 0.0188$ and $b = 0.7083$ for **I**, where $a = 0.0190$ and $b = 0.7399$ for **IIb**, where $a = 0.0257$ and $b = 1.0297$ for **IIIa**, where $a = 0.0879$ and $b = 4.0864$ for **IIIb**, where $a = 0.1103$ and $b = 2.2382$ for **IIIc**.

Table 3. Selected Observed Bond Distances in the Lanthanide Sulfate Compounds[a]

bond	distance (Å)	bond	distances (Å)	bond	distances (Å)
		I			
La(1)−O(1)#1	2.473(2)	La(1)−O(4)	2.555(1)	La(1)−O(6)#5	2.610(2)
La(1)−O(2)#2	2.474(2)	La(1)−O(5)#4	2.575(2)	La(1)−O(3)	2.613(2)
La(1)−O(3)#3	2.555(2)	La(1)−O(5)	2.589(2)	La(1)−O(6)	2.623(2)
		IIb			
Pr(1)−O(1)#1	2.402(2)	Pr(1)−O(4)#3	2.480(2)	Pr(1)−O(7)	2.602(2)
Pr(1)−O(2)#2	2.434(2)	Pr(1)−O(5)	2.504(2)	Pr(1)−O(8)	2.615(2)
Pr(1)−O(3)	2.469(2)	Pr(1)−O(6)	2.527(2)	Pr(1)−O(7)#3	2.820(2)
		IIIa			
Nd(1)−O(1)	2.378(3)	Nd(1)−O(4)	2.471(2)	Nd(1)−O(7)	2.526(2)
Nd(1)−O(2)	2.429(3)	Nd(1)−O(5)#2	2.482(2)	Nd(1)−O(4)#3	2.603(2)
Nd(1)−O(3)#1	2.460(3)	Nd(1)−O(6)	2.490(3)	Nd(1)−O(8)	2.731(2)
Nd(2)−O(9)#2	2.340(2)	Nd(2)−O(12)	2.473(3)	Nd(2)−O(8)	2.517(2)
Nd(2)−O(10)	2.423(3)	Nd(2)−O(13)#4	2.489(2)	Nd(2)−O(15)	2.548(3)
Nd(2)−O(11)	2.470(3)	Nd(2)−O(14)#5	2.509(2)		

[a] Symmetry transformations used to generate equivalent atoms: For **I**: #1 $x+1, y, z$. #2 $x-1, y, z$. #3 $-x+1, -y+1, -z+2$. #4 $-x, -y+1, -z+2$. #5 $-x, -y, -z+2$. For **II**: #1 $-x+1, -y, -z$ #2 $x, y+1, z$ #3 $x+1, y, z$. For **IIIa**: #1 $x, y+1, z$. #2 $-x+1, -y, -z+1$ #3 $-x+1, -y+1, -z+1$. #4 $x, y-1, z$ #5 $-x, -y, -z+1$.

least-squares refinement against $|F^2|$ was carried out using the WinGx package of programs.[18] Details of the structure solution and final refinements for the compounds are given in Table 2. CCDC: 802347−802351 contains the crystallographic data for this paper. These data can be obtained free of charge from The Cambridge Crystallographic Data Center (CCDC) via www.ccdc.cam.ac.uk/data_request/cif.

RESULTS AND DISCUSSION

Structure of $[C_{10}H_{10}N_2][La(SO_4)_2]\cdot 2H_2O$, (I). The asymmetric unit of **I** consists of 18 non-hydrogen atoms. It has one crystallographically independent La^{3+} ion, two sulfate groups, half a molecule of protonated bipyridine molecule, and a lattice

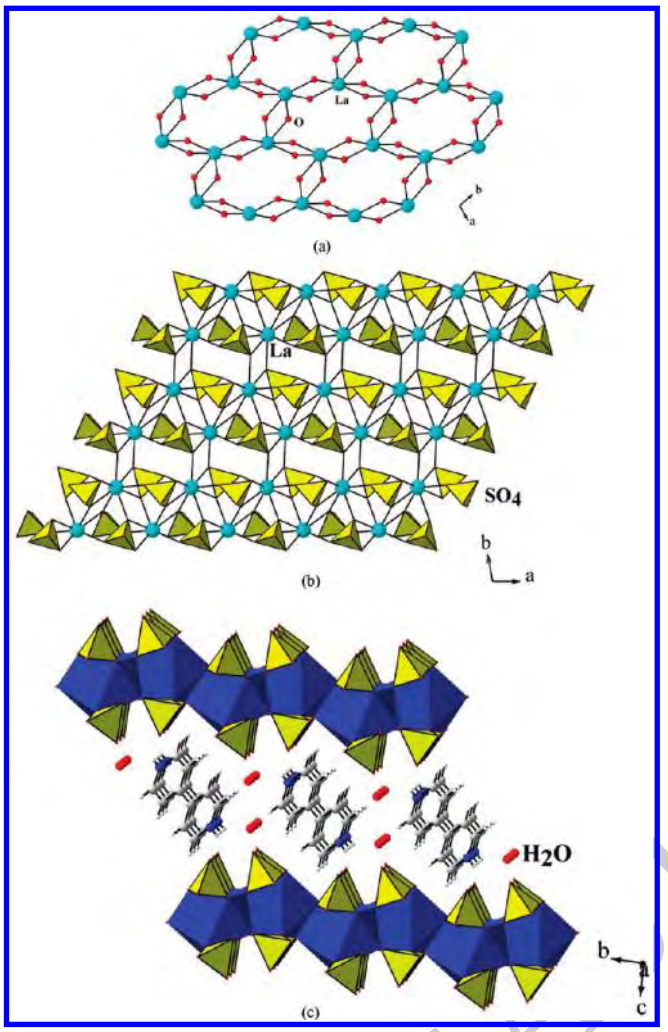

Figure 1. (a) View of the two-dimensional infinite La−O−La layer in $[C_{10}H_{10}N_2][La(SO_4)_2]\cdot 2H_2O$, **I**. Only the lanthanide ion connectivity is shown (see text). (b) View of the two-dimensional lanthanide sulfate layer in the *ab* plane. (c) The arrangement of layers in the *bc* plane. Note that the bipyridine molecules occupy interlamellar spaces along with the water molecules.

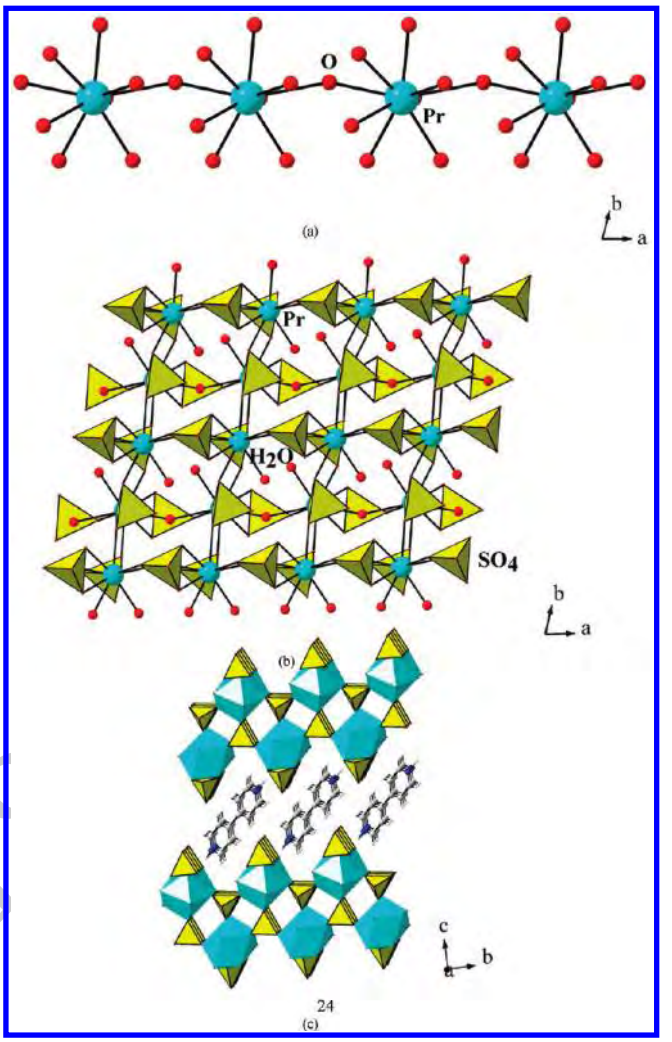

Figure 2. (a) The one-dimensional infinite Pr−O−Pr chains observed in $[C_{10}H_{10}N_2][Pr(SO_4)_2(H_2O)_2]_2$, **IIb**. (b) View of the two-dimensional praseodymium sulfate layer in the *ab* plane. Note that the bound water molecules project out of the plane of the layers. (c) Arrangement of the layers in the *bc* plane.

water molecule (Supporting Information, Figure S10). The half bipyridine unit is related to the other half through the C−C bond, which lies on the center of symmetry. The La^{3+} ions are surrounded by nine sulfate oxygens forming a LaO_9 polyhedra, with a distorted tricapped trigonal prismatic coordination environment (Supporting Information, Figure S11). The oxygen atoms O(3), O(5), and O(6) were found to be three coordinated, binding two La atoms and one S atom. The La−O bond distances are in the range of 2.474(2)−2.624(2) Å (av. 2.563 Å). The O−La−O bond angles are in the range 53.59(6)−160.11(6)°. The selected bond distances are given in Table 3.

The structure of **I** consists of linkages between LaO_9 tricapped trigonal prisms and SO_4 tetrahedral units. The LaO_9 units are connected through three coordinated oxygen atoms [O(3), O(5), and O(6)] forming an infinite two-dimensional La−O−La network (Figure 1a). The two sulfate tetrahedral units, $S(1)O_4$ and $S(2)O_4$, are connected to the La−O−La two-dimensional layers in such a way that they connects with 4 and 3 La atoms respectively, and each possess one terminal S═O bond [S(1)−O(7) and S(2)−S(8)] (Figure 1b). The layers are arranged in a *ABABAB*··· fashion and are stabilized by the N−H···O interaction between the protonated bipyridinium cation and the framework oxygen [N(1)−H(1)···O(7), N−O = 2.72 Å, angle = 143°] (Figure 1c).

Structure of $[C_{10}H_{10}N_2][Pr(SO_4)_2(H_2O)_2]_2$, (IIb). The asymmetric unit of **IIb** consists of 19 non-hydrogen atoms. It has one crystallographically independent Pr^{3+} atoms, two sulfate units, half a molecule of protonated bipyridine molecule, and two coordinated water molecules (Figure S12, Supporting Information). The Pr^{3+} ions are coordinated by seven sulfate oxygen and two aqua oxygen forming a PrO_9 polyhedra with a distorted tricapped trigonal prism arrangement (Figure S13, Supporting Information). The half bipyridine molecule is related to the other half via the C−C bond, which lies on the center of symmetry. The Pr−O bond distances are in the range of 2.402(2)−2.820(2) Å (av. 2.539 Å). The O−Pr−O bond angles are in the range 54.65(6)−149.31(6)°. The selected bond distances are given in Table 3.

dx.doi.org/10.1021/cg101589d |*Cryst. Growth Des.* 2011, 11, 1347–1356

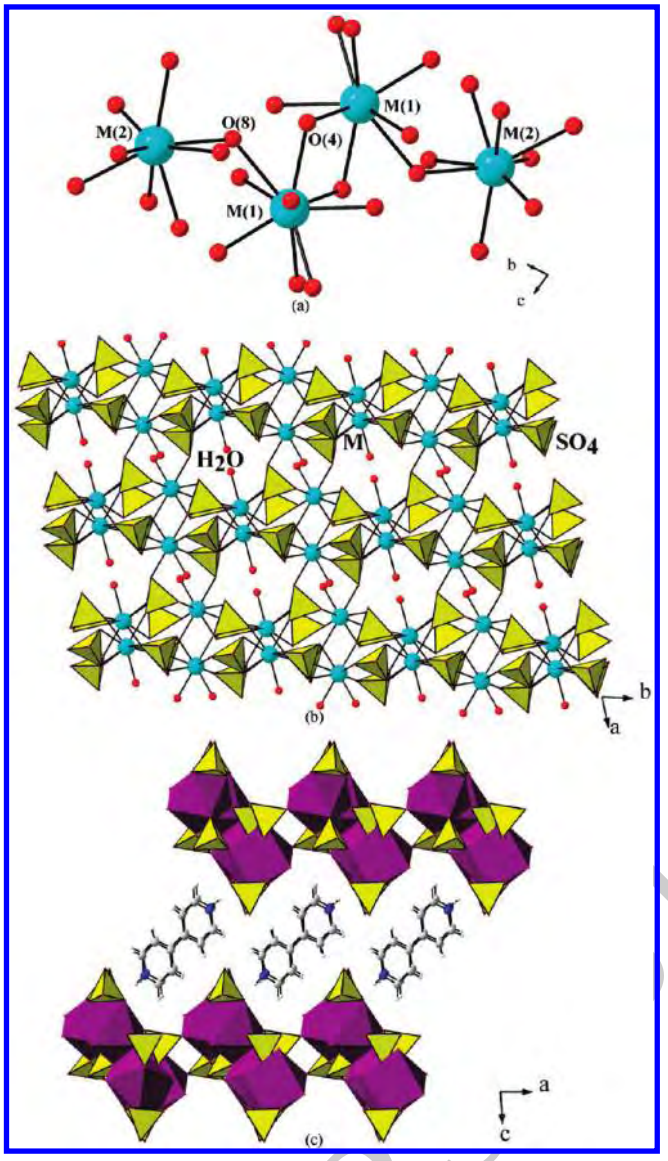

Figure 3. (a) View of the tetrameric unit found in $[C_{10}H_{10}N_2][Nd_2(SO_4)_4(H_2O)_2]_2$, **IIIa**. (b) The two-dimensional layer in the *ab* plane. (c) The arrangement of the layers in **IIIa**.

The structure of **IIb** consists of a linkage between PrO_9 and SO_4 units forming a two-dimensional structure. The Pr atoms are connected through a μ_2 oxygen atom forming one-dimensional Pr−O−Pr infinite chains (Figure 2a). The sulfate tetrahedra $S(1)O_4$ connects the Pr−O−Pr chains forming the two-dimensional structure, which is anionic. The other sulfate tetrahedral $S(2)O_4$ connects only to the Pr centers and is not employed in extending the dimensionality of the structure. This arrangement appears to satisfy the coordination requirement of the central Pr atoms only (Figure 2b). Another view to understand the structure is to consider the connectivity between PrO_9 and $S(1)O_4$ polyhedral units, which forms a one-dimensional edge-shared ladder-like structure (Figure S14, Supporting Information). The ladder units are connected with the Pr−O−Pr linkages giving rise to the two-dimensional layers. The layers are arranged in a *ABABAB*··· fashion and the interlamellar space is occupied by the protonated bipyridinium cataions (Figure 2c). Only one hydrogen bond interaction is observed [N(1)−H(1)−O(8); N−O = 2.77 Å, angle = 155°] between the bipyridinium cation and the framework oxygen, which is not very strong.[19]

Structure of $[C_{10}H_{10}N_2][M_2(SO_4)_4(H_2O)_2]_2$, M = Nd^{3+} (IIIa), Sm^{3+} (IIIb), and Eu^{3+} (IIIc). The asymmetric unit of $[M_2(SO_4)_4(H_2O)_2](C_{10}H_{10}N_2)$, M = Nd^{3+} (**IIIa**), Sm^{3+} (**IIIb**) and Eu^{3+} (**IIIc**) consists of 36 non-hydrogen atoms. It has two crystallographically independent M^{3+} ion, four sulfate groups, one protonated bipyridine molecule, and two coordinated water molecules (Figure S15, Supporting Information). The $M(1)^{3+}$ ions are surrounded by eight sulfate oxygen and one aqua oxygen to form a $M(1)O_9$ polyhedra, which has a distorted tricapped trigonal prismatic coordination environment. In the case of $M(2)^{3+}$ ions, seven sulfate oxygen and one aqua oxygen surround the central metal atom forming a $M(2)O_8$ polyhedra, with a distorted square antiprism coordination geometry (Figure S16, Supporting Information). The oxygen atoms, O(4) and O(8), are three coordinated connecting two metal centers and a sulfate unit. The M−O bond distances are in the range for Nd: 2.340(2)−2.731(2) Å (av. 2.490 Å); for Sm: 2.306(4)−2.734(4) Å (av. 2.462 Å) and for Eu: 2.292(4)−2.733(4) Å (av. 2.450 Å). The O−M−O bond angles are in the range for Nd: 53.76(7)−151.02(9)°; for Sm: 54.14(12)−150.76(14)° and for Eu: 54.04(13)−151.09(15)°. The selected bond distances are given in Table 3.

In the structure of **IIIa**, the MO_9 and MO_8 polyhedral units are linked with the sulfate tetrahedra giving rise to a two-dimensional anionic layer structure. The $M(1)O_9$ units are linked through the three-connected oxygen atom, [O(8)], with $M(2)O_8$ units forming a four-membered cluster (Figure 3a). The sulfate tetrahedral units bridge the four-membered clusters giving rise to the two-dimensional layer arrangement with an overall anionic layer of the formula, $[M_2(SO_4)_4(H_2O)_2]^-$ (Figure 3b). The charge is balanced by the presence of the protonated bipyridinium cations, which occupies the interlamellar spaces. N−H···O hydrogen bond interactions [N(1)−H(1)···O(1); N−O = 2.757 Å, angle = 170°, N(2)−H(2)···O(6); N−O = 2.830 Å, angle = 171°] have been observed, which appears to be strong.[18]

Structural Comparison. The three structures (**I**, **IIb**, and **IIIa**) identified in the present study have some common features: (i) The lanthanide ions have predominantly a tricapped trigonal prismatic coordination, (ESI, X); (ii) the lanthanide ions are connected through the three-coordinated oxygen atoms forming two-dimensional La−O−La layers in **Ia**, a one-dimensional chain in **IIb** and a four-member cluster in **IIIa**.

In addition, the sulfate connectivity in these structures also exhibit subtle differences. The sulfate groups participate in bonding between two lanthanide centers in **I**, while half the sulfate units in **IIa** and **IIIa** appear to satisfy the coordination requirement of the lanthanide centers only. The larger coordination (8 and 9) requirement of the lanthanide ions could be responsible for this, which also resulted in having coordinated aqua ligands in the structures of **IIa** and **IIIa**. Exclusive use of ligands for coordination requirements is not new, and examples of such roles for the participating ligands have been observed earlier in framework compounds.[20] The presence of bipyridine as a cation in the structure is also important and noteworthy. In many framework compounds, the bipyridine generally binds with the metal centers extending dimensionality,[21] but here it performs the role of a template molecule.

When the lanthanide connectivity alone is considered in these structures, we observed a honeycomb arrangement in the case of **I** and **IIIa**, whereas a square-grid results for **IIb** (Figure 4).

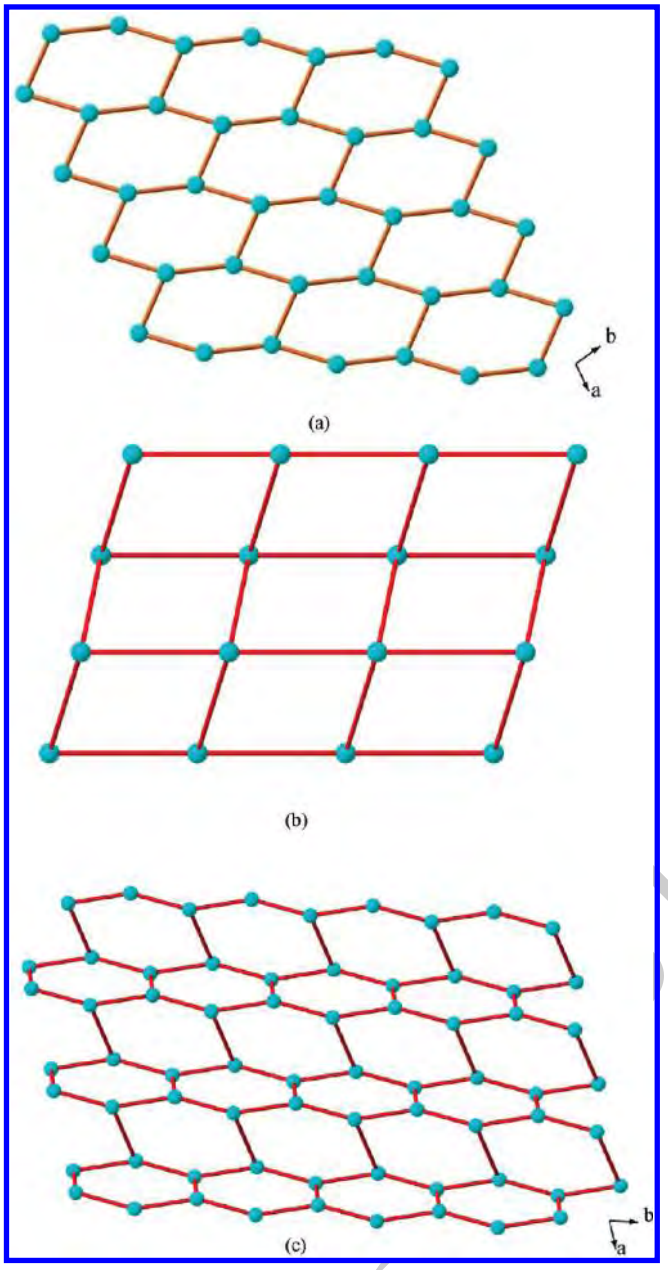

Figure 4. The lanthanide ion connectivity in the present structures: (a) the honeycomb layer in **I**; (b) the square-grid layer in **IIb**; (c) the honeycomb layer in **IIIa**.

The formations of such networks in lanthanide containing compounds are rare.

Thermogravimetric Studies. TGA on all the compounds has been carried out in flowing air (flow rate = 20 mL min^{-1}) in the temperature range 30−850 °C (heating rate = 5 °C min^{-1}) (Supporting Information, Figures S17−19). All the compounds exhibit comparable thermal behavior. For compound **I**, two step weight loss was observed (Supporting Information, Figure S17). The first weight loss of 3.7% observed in the range 150−250 °C corresponds to the loss of water molecules (4.2%). The second sharper weight loss of 44.9% in the range 480−520 °C corresponds to the loss of the bipyridine and some sulfate (calc. 46.5%). In the case of **IIa** and **IIb** we observed a near identical behavior in terms of the weight losses though the total weight loss

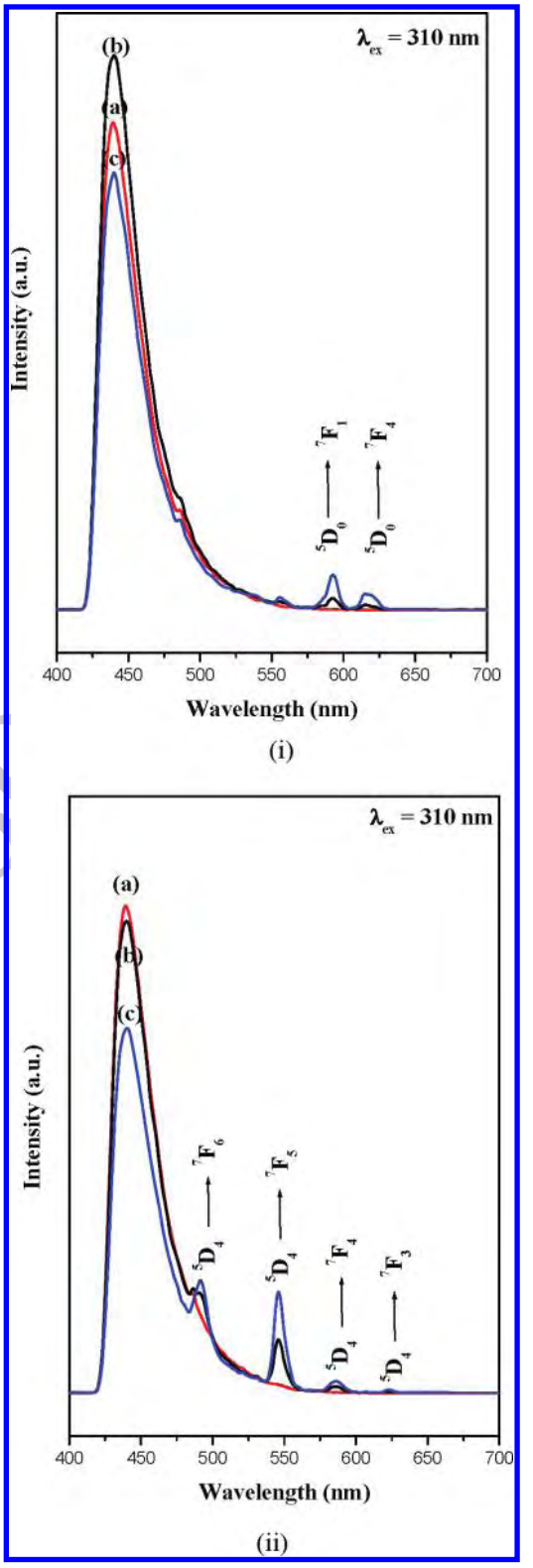

Figure 5. Room temperature photoluminescence spectra of compound **I** and the corresponding Eu^{3+} and Tb^{3+} doped samples. (i) (a) Compound **I**, (b) 4 mol % and (c) 8 mol % Eu^{3+} doped samples. (ii) (a) Compound **I**, (b) 4 mol % and (c) 8 mol % Tb^{3+} doped samples.

was different (Supporting Information, Figure S18). The first weight loss of 7.8% in the range 140−190 °C corresponds to the loss of water molecules (calc. 8% for **IIa** and **IIb**). The second

dx.doi.org/10.1021/cg101589d |*Cryst. Growth Des.* 2011, 11, 1347–1356

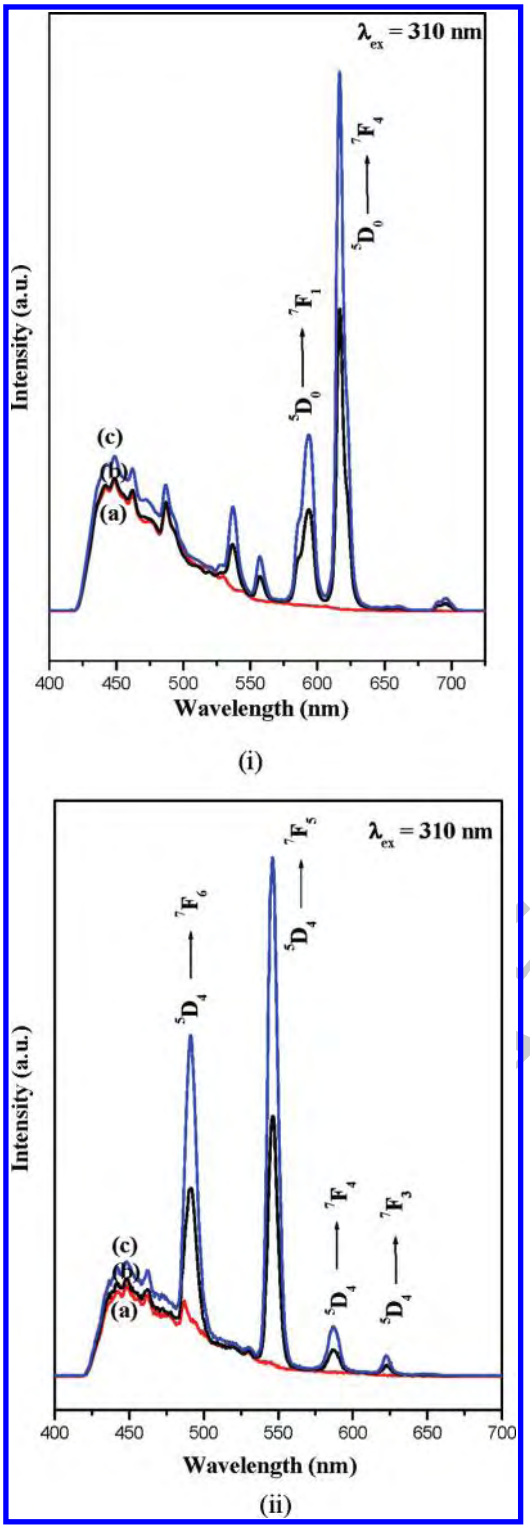

Figure 6. Room temperature photoluminisence spectra of compound **IIa** and the corresponding Eu^{3+} and Tb^{3+} doped samples.(i) (a) Compound **IIa**, (b) 4 mol % and (c) 8 mol % Eu^{3+} doped samples. (ii) (a) Compound **IIa**, (b) 4 mol % and (c) 8 mol % Tb^{3+} doped samples.

weight loss 31.2% for **IIa** and 44.2% for **IIb** in the range 410−500 °C corresponds to the loss of the bipyridine and sulfate (calc 44.4% for **IIa**: 45.6% for **IIb**). In the case of compounds **I** and **IIa**, the calcined product was found to be crystalline and corresponds to the compound $La_2O_2SO_4$ (JCPDS: 85-1535). In the case of

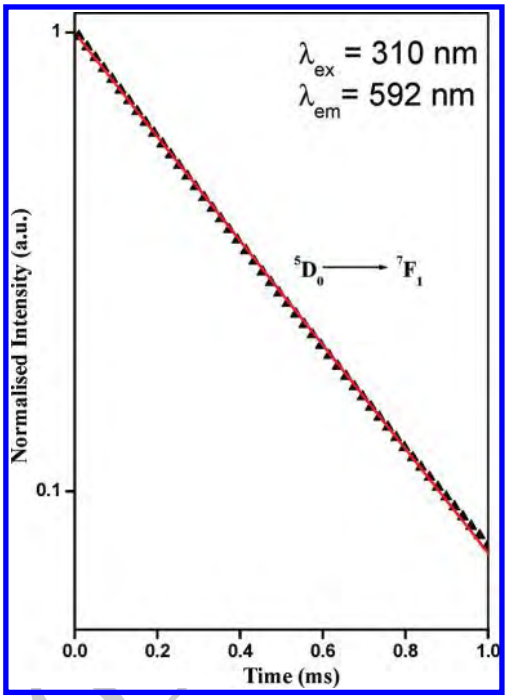

Figure 7. Room temperature luminescence decay of the $^5D_0 \rightarrow {}^7F_1$ emission band for the 4 mol % Eu^{3+} doped compound **I**.

IIb, the final calcined product was found to be $Pr_2O_2SO_4$ (JCPDS: 29-1073). The TGA behavior of compounds **IIIa**, **IIIb**, and **IIIc** are also similar, exhibiting a two-step weight loss. For **IIIa**, the first weight loss of 3.7% in the range 180−250 °C, corresponds to the loss of the coordinated water molecules (calc. 4.4%). The second weight loss of 25.3% in the range 470−500 °C is followed by another loss. The total weight loss of 55% corresponds to the loss of the bipyridine along with some sulfate. The calcined product was found to be crystalline and corresponds to the phase $Nd_2O_2SO_4$ (JCPDS: 48-1829). Similarly for **IIIb** and **IIIc**, we observed the formation of $Sm_2O_2SO_4$ (JCPDS: 41-0681) and $Eu_2O_2SO_4$ (JCPDS: 48-1211) phases after the TGA studies.

Luminescence Studies. All the compounds exhibited one strong absorption band centered around 450 nm, which corresponds to the ligand to metal charge transfer (LMCT) band, when excited using a wavelength of λ = 310 nm. To probe and to appreciate the LMCT effect further, we have prepared two sets of compounds by doping a small concentration of Eu^{3+} and Tb^{3+} (4% and 8%) in place of La^{3+} (compounds **I** and **IIa**). The results of the photoluminescence studies were shown in Figures 5 and 6. The doped samples exhibited sharp characteristics peaks, in addition to the LMCT peak at 450 nm. We also observed a pink color for Eu^{3+} doped samples and a green color for the Tb^{3+} doped samples when observed under the UV illumination (Supporting Information, Figure S20−S21). When excited using a wavelength of λ = 310 nm, we observed the characteristic $^5D_0 \rightarrow {}^7F_J$ (J = 1, 2) emission lines for Eu^{3+} and $^5D_4 \rightarrow {}^7F_J$ (J = 3, 4, 5, 6) emission lines for Tb^{3+}, respectively (Figures 5 and 6). It may be noted the intensity of the characteristic lanthanide emission due to Eu^{3+} and Tb^{3+} is not strong, suggesting that the energy transfer process in the present compounds are quite poor. This situation is in contrast to the behavior observed in many of the lanthanide benzene carboxylate frameworks, where intense lanthanide emissions have been observed.[22] Even though the

dx.doi.org/10.1021/cg101589d |Cryst. Growth Des. 2011, 11, 1347–1356

Table 4. Lifetime Values for the Compounds I (4% Eu), IIa (4% Eu), I (4% Tb), and IIa (4% Tb)

S. no.	compound	lifetime (in ms)
		$^5D_0 \rightarrow {}^7F_1$
1.	**I** (4 mol % Eu)	0.3833
2.	**IIa** (4 mol % Eu)	0.2726
		$^5D_4 \rightarrow {}^7F_6$
4.	**I** (4 mol % Tb)	1.1801
5.	**IIa** (4 mol % Tb)	1.3420

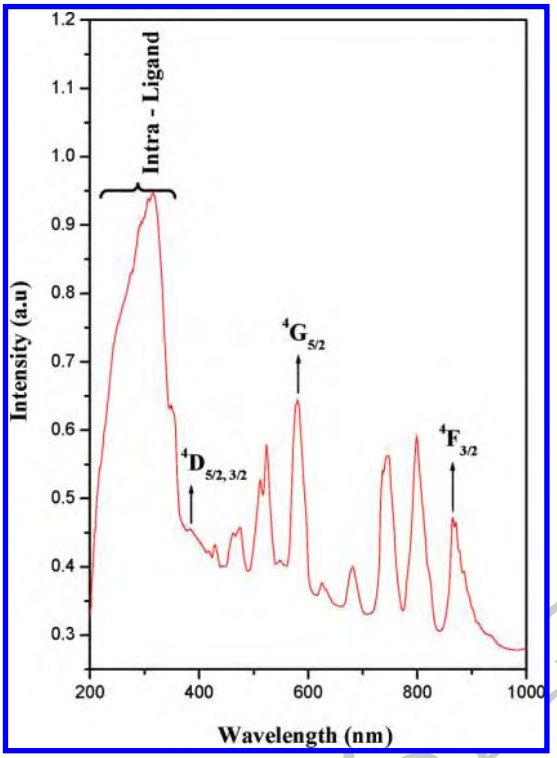

Figure 8. Room temperature UV−vis spectra of compound $[Nd_2(SO_4)_4(H_2O)_2](C_{10}H_{10}N_2)$, **IIIa**.

intensity of the emission in the present compounds is not strong, we sought to investigate the lifetime of the excited states in the doped compounds.

Lifetime Studies. The luminescence lifetimes of the excited states of the 4 mol % doped samples of **I** and **IIa** were investigated. The $^5D_0 \rightarrow {}^7F_1$ band for the Eu^{3+} samples **I** (4% Eu) and **IIa** (4% Eu) and the $^5D_4 \rightarrow {}^7F_6$ emission band for the Tb^{3+} samples **I** (4% Tb) and **IIa** (4% Tb) were monitored for the lifetime studies employing 310 nm excitation at room temperature. The experimental luminescent decay curve was fitted to a single exponential decay function as,

$$I = I_0 \exp(-t/\tau)$$

where I and I_0 stands for the luminescent intensities at time $t = t$ and $t = 0$ and τ is defined as the luminescent lifetime. The fit of the curve for a single exponential decay suggests a lifetime value of 0.38 ms for **I** (4% Eu) (Figure 7). The lifetime values for the other samples are given in Table 4 (Supporting Information, Figure S22−S24). The values of the lifetime observed in the present compounds are comparable to the values generally

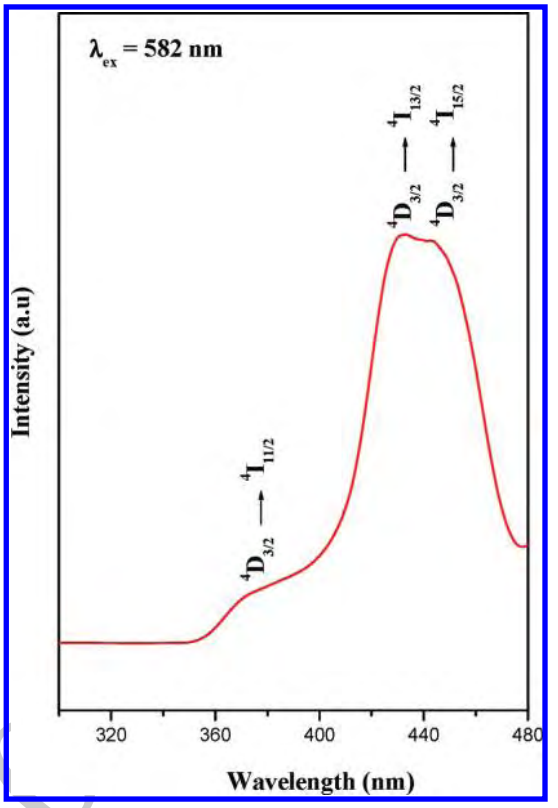

Figure 9. Room temperature upconversion spectra of compound **IIIa**, using 582 nm radiation.

known for the pure Eu^{3+} and Tb^{3+} compounds reported in the literature.[23]

Upconversion Studies. There has been some recent interest in the study of a possible two-photon upconversion processes in compounds containing Nd^{3+} ions.[24] The upconversion in these compounds are actually anti-Stokes emissions. Among the present compounds, $[C_{10}H_{10}N_2][Nd_2(SO_4)_4(H_2O)_2]_2$, **IIIa**, could exhibit this upconversion emission. The room temperature UV−vis spectrum of **IIIa** indicated that the absorption increases rapidly with decreasing wavelength due to the intraligand absorption (Figure 8). From the UV studies, the absorption bands of the Nd^{3+} ions appear to exhibit primary ground state Stark splitting of the eigenstates due to the possible crystal field effects.[25]

A schematic of the energy transfer process in the upconversion using Nd^{3+} ions suggests the possible pathway for the two-photon upconversion processes (Supporting Information, Figure S25). The Nd^{3+} compound (**IIIa**) has an intense absorption at ~582 nm, which corresponds to the $^4I_{9/2} \rightarrow {}^4G_{5/2}$ transition. This is a hypersensitive band and also satisfies the selection rules of $\Delta J = \pm 2$, $\Delta L = \pm 2$, and $\Delta S = 0$. The luminescence of **IIIa** at short wavelength results from the $^4D_{3/2}$ levels. In order to observe the possible two-photon absorption in **IIIa**, one needs to excite the photon to either the $^4D_{3/2}$ or $^4D_{5/2}$ levels. The direct excitation to this level may be limited due to the intraligand absorption by the short wavelength radiation. In addition, the excitation wavelength (λ = 582 nm) is far from the wavelength that may be required for the intraligand absorption. Thus, during our studies, the first excited $^4G_{5/2}$, level can relax nonradiatively to the $^4F_{3/2}$ level where some population can occur. This photon may further undergo excited state absorption (ESA), while the

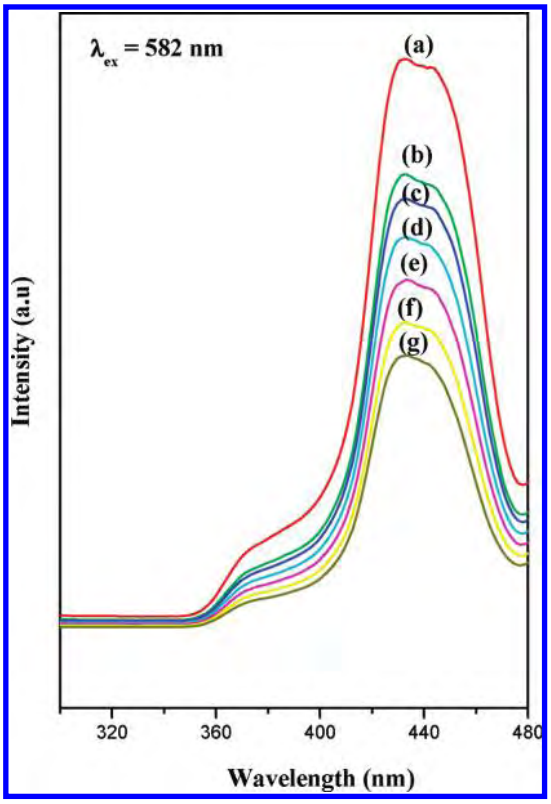

Figure 10. The observed emission dependence on the excitation intensity of $[Nd_2(SO_4)_4(H_2O)_2](C_{10}H_{10}N_2)$, **IIIa**. (a) 100%, (b) 90.32% (c) 85.19%, (d) 81.34%, (e) 74.86%, (f) 69.38% and (g) 63.56%.

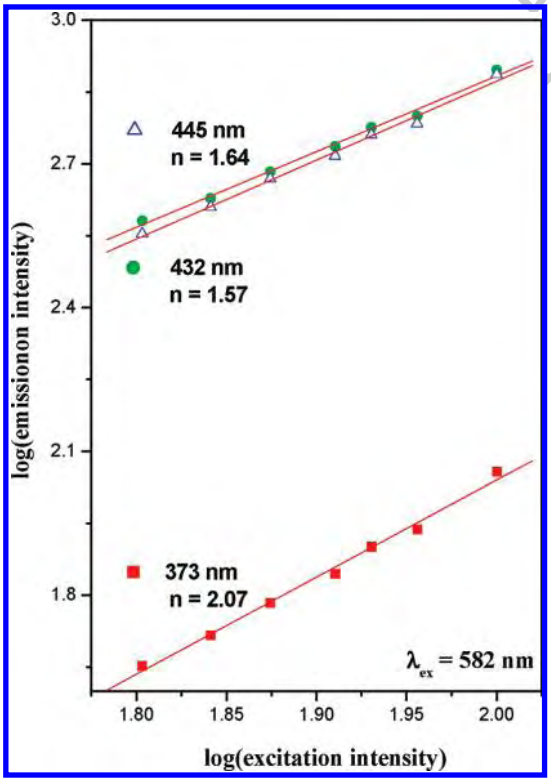

Figure 11. The log−log plot of the excitation intensity dependence of the luminescence intensity for λ = 373, 432, and 445 nm.

others relax to lower energy levels. The excitation wavelength (~582 nm) was used to populate the $^4F_{3/2}$ levels and efficient re-excitation from the $^4F_{3/2}$ to the $^4D_{5/2}$ levels. It is likely that the excited $^4D_{5/2}$ levels from the ESA also relax nonradiatively to the $^4D_{3/2}$ levels from which the upconverted luminescence may be observed. The upconverted luminescence spectra for this yellow pumping (582 nm excitation) from $^4D_{3/2}$ levels are shown in Figure 9.

To study the dependence of the excitation intensity on the upconverted luminescence intensity, we have also performed a simple power dependence study. Here a series of sterile glass plates are placed sequentially in the pathway between the excitation source and the sample. The decrease in excitation intensity per glass plate was precalibrated using the UV−vis spectrometer in the transmission mode and also normalized with respect to the transmission obtained in the absence of any glass slides. The decrease in the luminescence intensity for six successive glass plates is shown in Figure 10. We have plotted the log−log plot of the luminescence intensity versus the excitation intensity, and a fit could provide a clue to the number of photons involved in the upconversion process (Figure 11). The plot for the three emission peaks at 373, 432, and 445 nm was found to be linear with a slope of 2.07, 1.57, and 1.64, respectively. These values suggest that the excitation may be due to two photons that are employed successfully. The ideal value for the two photon absorption should be closer to 2, and the decreased value may be due to the loss of some of the excitation energy at the one-photon absorption level, which could result from the $^4F_{3/2} \rightarrow {}^4I_{11/2}$, $^4F_{3/2} \rightarrow {}^4I_{9/2}$ level in the near-IR region.

CONCLUSIONS

The synthesis, structure, and characterization of a family of layered lanthanide sulfate phases have been accomplished. The formation of related compounds by subtle variations of the synthesis conditions suggests the importance of the reaction parameters in the formation of framework compounds. The observation of bipyridine molecules being protonted and occupying the interlamellar spaces is important and not common. The formation of two-dimensional La−O−La network in **I** is noteworthy as such networks are not commonly observed. The observation of two-photon upconversion behavior in the Nd-containing compound (**IIIa**) and metal centered emission in Eu^{3+} (red) and Tb^{3+} (green) doped samples of lanthanum (**I** and **II**) indicates the possibility of using these compounds as optical probes. Further study is required to evaluate the structure−property relationship in these compounds.

ASSOCIATED CONTENT

Supporting Information. Simulated and experimental powder XRD patterns of the compounds **I**−**III** and the doped samples, TGA curves of **I**−**III**, IR spectra and bond angles of **I**−**III** are presented. The decay curves of the excited state of the doped samples and the Le Bail fit for the compounds **IIa** are also presented. This material is available free of charge via the Internet at http://pubs.acs.org.

AUTHOR INFORMATION

Corresponding Author

*E-mail: snatarajan@sscu.iisc.ernet.in.

■ ACKNOWLEDGMENT

S.N. thanks the Department of Science and Technology (DST), Government of India, for the award of a research grant and the authors thanks the Council of Scientific and Industrial Research (CSIR), Government of India, for the award of a fellowship (DS) and a research grant. S.N. also thanks the Department of Science and Technology, Government of India, for the award of the RAMANNA fellowship. B.Y. and A.R. thank the Royal Golden Jubilee program (RGJ), Thailand, and Thailand Research Fund (TRF), Thailand, for a fellowship (B.Y.) and a research grant (A.R.).

■ REFERENCES

(1) (a) Natarajan, S.; Mandal, S. *Angew. Chem., Int. Ed.* **2008**, *47*, 4798. (b) Murugavel, R.; Choudhury, A.; Walawalkar, M. G.; Pothiraja, R.; Rao, C. N. R. *Chem. Rev.* **2009**, *109*, 4283. (c) Cheetham, A. K.; Ferey, G.; Loiseau, T. *Angew. Chem., Int. Ed.* **1999**, *38*, 3268. (d) Wilson, S. T.; Lok, B. M.; Messina, C. A.; Cannan, T. R.; Flanigen, E. M. *J. Am. Chem. Soc.* **1982**, *104*, 1146.(e) Meier, W. M.; Oslen, D. H.; Baerlocher, C. *Atlas of Zeolite Structure Types*; Elsevier: London, 1996; (f) Chen, L.; Bu, X. *Inorg. Chem.* **2006**, *45*, 4654. (g) Rao, C. N. R.; Natarajan, S.; Choudhury, A.; Neeraj, S.; Ayi, A. A. *Acc. Chem. Res.* **2001**, *34*, 80. (h) Murugavel, R.; Walawalkar, M. G.; Dan, M.; Roesky, H. W.; Rao, C. N. R. *Acc. Chem. Res.* **2004**, *37*, 763.

(2) (a) Rao, V. K.; Chakrabarti, S.; Natarajan, S. *Inorg. Chem.* **2007**, *46*, 10781. (b) Rao, V. K.; Green, M. A.; Pati, S. K.; Natarajan, S. *J. Phys. Chem. B* **2007**, *111*, 12700. (c) Chakrabarti, S.; Natarajan, S. *Angew. Chem., Int. Ed.* **2002**, *41*, 1224. (d) Chakrabarti, S.; Pati, S. K.; Green, M. A.; Natarajan, S. *Eur. J. Inorg. Chem.* **2003**, 4395. (e) Ekambaram, S.; Sevov, S. C. *Inorg. Chem.* **2000**, *39*, 2405. (f) Bu, X.; Gier, T. E.; Ferey, G. *Chem. Commun.* **1997**, 2271.

(3) (a) Lin, J.; Dong-Wei Guo, D.-W.; Tian, Y.-Q. *Cryst. Growth Des.* **2008**, *8*, 4571. (b) Rao, C. N. R.; Behera, J. N.; Dan, M. *Chem. Soc. Rev.* **2006**, *35*, 375. (c) Paul, G.; Choudhury, A.; Rao, C. N. R. *Chem. Mater.* **2003**, *15*, 1174.

(4) Krivovichev, S. V.; Kahlenberg, V.; Tananaev, I. G.; Myasoedov, B. F. *Z. Anorg. Allg. Chem.* **2005**, *631*, 2358.

(5) (a) Paul, A. K.; Natarajan, S. *Cryst. Growth Des.* **2010**, *10*, 765. (b) Paul, A. K.; Sachidananda, K.; Natarajan, S. *Cryst. Growth Des.* **2010**, *10*, 456.

(6) (a) Fu, Y.; Xu, Z.; Ren, J.; Wu, H.; Yuan, R. *Inorg. Chem.* **2006**, *45*, 8452. (b) Behera, J. N.; Rao, C. N. R. *Chem. Asian J.* **2006**, *1*, 742. (c) Behera, J. N.; Gopalkrishnan, K. V.; Rao, C. N. R. *Inorg. Chem.* **2004**, *43*, 2636. (d) Paul, G.; Choudhury, A.; Sampathkumaran, E. V.; Rao, C. N. R. *Angew. Chem., Int. Ed.* **2002**, *41*, 4297.

(7) (a) Rujiwatra, A.; Kepert, C. J.; Rosseinsky, M. J. *Chem. Commun.* **1999**, 2307. (b) Rujiwatra, A.; Kepert, C. J.; Claridge, J. B.; Rosseinsky, M. J.; Kumagai, H.; Kurmoo, M. *J. Am. Chem. Soc.* **2001**, *123*, 10584. (c) Behera, J. N.; Rao, C. N. R. *Can. J. Chem.* **2005**, *83*, 668.

(8) (a) Akkari, H.; Benard-Rocherulle, P.; Merazig, H.; Roisnel, T.; Rocherulle *J. Solid State Sci.* **2006**, *8*, 704. (b) Ding, S.; Xu, Y.; Nie, L.; Feng, W. *J. Cluster Sci.* **2006**, *17*, 627. (c) Bataille, T.; Louer, D. *J. Mater. Chem.* **2002**, *12*, 3487.

(9) (a) Binnemans, K. *Chem. Rev.* **2009**, *109*, 4283. (b) Yan, L.; Yue, Q.; Jia, Q. −X.; Lemercier, G.; Gao, E.-Q. *Crys. Growth Des.* **2009**, *9*, 2984. (c) Pope, S. J. A.; Coe, B. J.; Faulkner, S.; Bichenkova, E. V.; Yu, X.; Douglas, K. *J. Am. Chem. Soc.* **2004**, *126*, 9490. (d) Zhao, B.; Chen, X. Y.; Cheng, P.; Liao, D. Z.; Yan, S. P.; Jiang, Z. H. *J. Am. Chem. Soc.* **2004**, *126*, 15394. (e) Rudzinski, C. M.; Young, A. M.; Nocera, D. G. *J. Am. Chem. Soc.* **2002**, *124*, 1723. (f) Justel, T.; Nikol, H.; Ronda, C. *Angew. Chem., Int. Ed.* **1998**, *37*, 3084.(g) Blasse, G.; Grabmaier, B. C. *Luminescent Materials*; Springer: Berlin, 1994; (h) Bunzli, J. C. G.; Choppin, G. R. *Lanthanide Probes in Life, Chemical and Earth Science, Theory and Practice*; Elsevier: Amsterdam, 1989.

(10) (a) Sendor, D.; Hilder, M.; Juestel, T.; Junk, P. C.; Kynast, U. H. *New J. Chem.* **2003**, *27*, 1070. (b) de Lill, D. T.; de Bettencourt-Dias, A.; Cahill, C. L. *Inorg. Chem.* **2007**, *46*, 3960. (c) Crosby, G. A. *Mol. Cryst.* **1966**, *1*, 37. (d) Eisinger, J.; Lamola, A. A. *Biochem. Biophys. Acta* **1971**, *240*, 299. (e) Filipescu, N.; Mushrush, G. W. *J. Phys. Chem.* **1968**, *72*, 3516. (f) Heller, A.; Wasserman, E. *J. Chem. Phys.* **1956**, *42*, 949.

(11) (a) Sarma, D.; Prabu, M.; Biju, S.; Reddy, M. L. P.; Natarajan, S. *Eur. J. Inorg. Chem.* **2010**, 3813. (b) Mahata, P.; Natarajan, S. *Inorg. Chem.* **2007**, *46*, 1250.

(12) (a) Kiritsis, V.; Michaelides, A.; Skoulika, S.; Golhen, S.; Ouahab, L. *Inorg. Chem.* **1998**, *37*, 3407. (b) Reineke, T. M.; Eddaoudi, M.; Moler, D.; O'Keeffe, M.; Yaghi, O. M. *J. Am. Chem. Soc.* **2000**, *122*, 4843. (c) Pan, L.; Adams, K. M.; Hernandez, H. E.; Wang, X. T.; Zheng, C.; Hattori, Y.; Kaneko, K. *J. Am. Chem. Soc.* **2003**, *125*, 3062. (d) Zhao, B.; Cheng, P.; Chen, X. Y.; Cheng, C.; Shi, W.; Liao, D. Z.; Yan, S. P.; Jiang, Z. H. *J. Am. Chem. Soc.* **2004**, *126*, 3012. (e) Long, D. L.; Hill, R. J.; Blake, A. L.; Champness, N. R.; Hubberstey, P.; Proserpio, D. M.; Wilson, C.; Schroder, M. *Angew. Chem., Int. Ed.* **2004**, *43*, 1851. (f) Zhang, M. B.; Zhang, J.; Zheng, S. T.; Yang, G. Y. *Angew. Chem., Int. Ed.* **2005**, *44*, 1385. (g) Chen, B.; Wang, L.; Zapata, F.; Qian, G.; Lobkovsky, B. *J. Am. Chem. Soc.* **2008**, *130*, 6718. (h) Shi, F. N.; Cunha-Silva, L.; Sa Ferreira, R. A.; Mafra, L.; Trindade, T.; Carlos, L. D.; Almeida Paz, F. A.; Rocha, J. *J. Am. Chem. Soc.* **2008**, *130*, 150.

(13) (a) Jiang, Y.; Huang, J.; Kasumaj, B.; Jeschke, G.; Hunger, M.; Mallat, T.; Baiker, A. *J. Am. Chem. Soc.* **2009**, *131*, 2058. (b) Li, Y.; Xie, L.; Liu, Y.; Yang, R.; Li, X. *Inorg. Chem.* **2008**, *47*, 10372. (c) Pichon, A.; Fierro, C. M.; Nieuwenhuyzen, M.; James, S. L. *CrystEngComm* **2007**, *9*, 449. (d) Maji, T. K.; Ohba, M.; Kitagawa, S. *Inorg. Chem.* **2005**, *44*, 9225. (e) Biradha, K.; Fujita, M. *Chem. Commun.* **2001**, 15. (f) Noro, S.; Kitagawa, S.; Kondo, M.; Seki, K. *Angew. Chem., Int. Ed.* **2000**, *39*, 2082. (g) Kondo., M.; Yoshitomi., T.; Seki., K.; Matsuzaka., H.; Kitagawa., S. *Angew. Chem., Int. Ed.* **1997**, *36*, 1725.

(14) Le Bail, A.; Duroy, H.; Fourquet, J. L. *Mater. Res. Bull.* **1988**, *23*, 447–452.

(15) *SMART (V 5.628), SAINT (V 6.45a), XPREP, SHELXTL*; Bruker AXS Inc.: Madison, Wisconsin, USA, 2004.

(16) Sheldrick, G. M. *Siemens Area Correction Absorption Correction Program*; University of Göttingen: Göttingen, Germany, 1994.

(17) Sheldrick, G. M. *SHELXL-97 Program for Crystal Structure Solution and Refinement*; University of Göttingen: Göttingen, Germany, 1997.

(18) Farrugia, J. L. WinGx suite for small-molecule single crystal crystallography. *J. Appl. Crystallogr.* **1999**, *32*, 837.

(19) (a) Desiraju, G. R. *Angew. Chem., Int. Ed. Engl.* **1995**, *34*, 2311. (b) Desiraju, G. R. *Perspective in Supramolecular Chemistry: The Crystal as a Supramolecular Entity*; Wiley: Chichester, 1996, 2.

(20) (a) Ramaswamy, P.; Hegde, N. N.; Prabhu, R.; Vidya, V. M.; Datta, A.; Natarajan, S. *Inorg. Chem.* **2009**, *48*, 11697. (b) Mandal, S.; Natarajan, S. *Chem.—Eur. J.* **2007**, *13*, 968.

(21) (a) Paul, A. K.; Madras, G.; Natarajan, S. *Dalton Trans.* **2010**, *39*, 2263. (b) Paul, A. K.; Madras, G.; Natarajan, S. *CrystEngComm* **2009**, *11*, 55. (c) Paul, A. K.; Madras, G.; Natarajan, S. *Phys. Chem. Chem. Phys.* **2009**, *11*, 11285.

(22) (a) Mahata, P.; Ramya, K. V.; Natarajan, S. *Chem.—Eur. J.* **2008**, *14*, 5839. (b) Mahata, P.; Ramya, K. V.; Natarajan, S. *Dalton Trans.* **2007**, *36*, 4017.

(23) Zhang, Z. H.; Okamura, T.; Hasuchika, Y.; Kawaguchi, H.; Kong, L. Y.; Sun, W. Y.; Ueyam, N. *Inorg. Chem.* **2005**, *44*, 6219.

(24) Auzel, F. *Chem. Rev.* **2004**, *104*, 139.

(25) Ju, J. J.; Kwon, T. Y.; Kim, H. K.; Kim, J. H.; Kim, S. C.; Cha, M.; Yun, S. I. *Mater. Lett.* **1996**, *29*, 13.

Maejo Int. J. Sci. Technol. **2011**, *5*(01), 24-31

Maejo International Journal of Science and Technology

ISSN 1905-7873
Available online at www.mijst.mju.ac.th

Communication

Microwave-assisted hydrothermal synthesis of lead zirconate fine powders

Saowalak Tapala and Apinpus Rujiwatra*

Centre for Innovation in Chemistry, Department of Chemistry, Faculty of Science, Chiang Mai University, Chiang Mai 50200, Thailand

* Corresponding author, e-mail: apinpus@gmail.com

Received: 3 August 2010 / Accepted: 18 January 2011 / Published: 19 January 2011

Abstract: A rapid synthesis of lead zirconate fine powders by microwave-assisted hydrothermal technique is reported. The influences of type of lead precursor, concentration of potassium hydroxide mineraliser, applied microwave power and irradiation time are described. The synthesised powders were characterised by powder X-ray diffraction, field emission scanning electron microscopy, energy-dispersive X-ray spectroscopic microanalysis and light scattering technique. The merits of the microwave application in reducing reaction time and improving particle mono-dispersion and size uniformity as well as the drawbacks, viz. low purity of the desired phase and increasing demand of mineraliser, are discussed in relation to conventional heating method.

Keywords: lead zirconate, hydrothermal synthesis, microwave-assisted synthesis

INTRODUCTION

Lead zirconate ($PbZrO_3$ or PZ) is an important precursor in the preparation of a number of technologically important solid solutions, particularly those of the $PbZr_{1-x}Ti_xO_3$ series [1-2]. Recently, new studies have revealed novel applications of PZ as a phase-transformation-induced electro-mechanical actuator and a pyroelectric sensor [3-4]. The findings resulted in the reviving of interest in the synthesis of nano-sized PZ powders. Along this line, various synthetic techniques are available, e.g. hydrothermal, vibro-milling, sol-gel and precipitation, each of which exhibits characteristic drawbacks. The formation of aggregates, for instance, is an inherent problem for the hydrothermal technique [5-8]. The synthesis of fine PZ powders composing of mono-dispersed particles of uniform shape and size by this technique is therefore a challenge. According to our previous study, the fine powders of

Maejo Int. J. Sci. Technol. **2011**, *5*(01), 24-31

orthorhombic PZ could be synthesised as a single phase under hydrothermal conditions at a temperature of at least 180°C for 24 hours [8]. The space group of the resulting PZ was the unusual *Pbma* with refined cell parameters *a*=5.88(6) Å and *c*=4.27(3) Å. The formation of aggregates was the major drawback. Nonetheless, the highly dispersed and well-defined cubic particles could be afforded when the reaction temperature and time were increased to 200°C and 72 hours respectively [8]. The attempt to use organic additives, e.g. polyvinyl alcohol, polyvinylpyrrolidone and cetyltrimethylammonium bromide, which are commonly employed in the synthesis of other oxide powders [9-11], may be an answer to this problem, although they need to be removed in the post-synthesis step.

Herein, the application of the microwave heating in the synthesis of PZ fine powders under hydrothermal conditions is reported. The primary objective of the synthesis is to promote the mono-dispersion of particles of the synthesised PZ powders without the assistance of organic additives. The influences of various synthetic parameters on the obtained powders and the advantages and shortcomings of the microwave heating are described and discussed.

MATERIALS AND METHODS

Equimolar mixtures of zirconyl nitrate hexahydrate [$ZrO(NO_3)_2.6H_2O$, 27% Zr (gravimetric), Fluka, 0.0115 mole] and one of the following lead precursors, i.e. lead(II) nitrate (99.0%, Univar), lead(II) acetate (99.5%, Ajax Chemicals), lead(II) fluoride (99.0%, Univar), lead(II) chloride (99.0%, Riedel de Haën) and lead(II) iodide (99.0%, Aldrich), were prepared in 10.0 cm^3 of deionised water. Pellets of potassium hydroxide (85%, Merck) was gradually added to each mixture with stirring to a concentration ranging from 6 to 14 moles dm^{-3}. Each mixture was then transferred to an 18-cm^3 Teflon reactor, which was sealed and placed in a 95(±5)°C water bath placed in a domestic microwave oven (Whirlpool XT-25ES/S, 900W, 2.45 GHz). The reaction was performed under autogenous pressure developed by the microwave heating (720W and 810W) for 3-5 hours. The resulting powder was recovered by filtration and washed with deionised water until the pH of the filtrate was approximately 7, followed a final washing with dilute acetic acid.

The synthesised powders were characterised for crystalline phases by powder X-ray diffraction (XRD) (using D8 Advance, Bruker, Cu *K*α, Ni filter, λ=1.540598 Å, 40 kV, 30 mA). A field-emission scanning electron microscope equipped with energy-dispersive X-ray spectrometer (JSM-6335F, Jeol) was used in the examination of particle shape and size and elemental composition. In order to evaluate the aggregation, size distributions of the bulk powder samples were measured by light scattering technique (using Zetasizer Nano S, Malvern Instruments, 4mW He-Ne laser operated at 633 nm, particle size range 0.3nm-10μm).

RESULTS AND DISCUSSION

Although different lead precursors were used in the study, every reaction apparently provided the same off-white powders mixed with some red-block crystals, which were identified as lead oxide by XRD study. Although the contamination of lead oxide in the prepared powders seemed to be inevitable, they could be simply removed by washing with dilute acetic acid solution [12]. After the acid washing, it was found that only $Pb(NO_3)_2$ gave the well crystallised PZ while poorly crystallised powders were

Maejo Int. J. Sci. Technol. **2011**, *5*(01), 24-31

obtained from the other lead precursors as depicted in Figure 1. This could be attributed to the low solubility of these lead precursors in aqueous solution compared to the readily dissolved $Pb(NO_3)_2$ [13]. The hardly dissolved lead precursors might bring about an insufficient nutrient in the solution and consequently the nucleation and crystal growth could not occur properly.

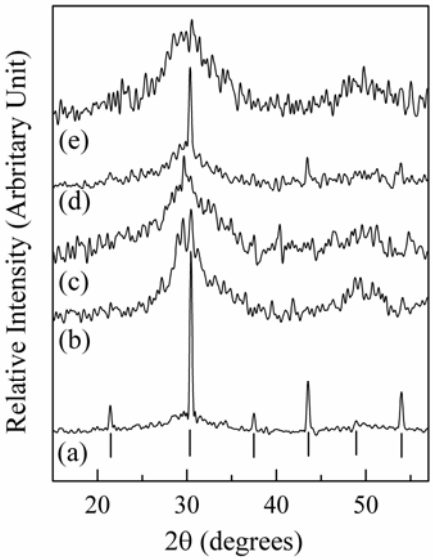

Figure 1. XRD patterns of the powders obtained from reactions between $ZrO(NO_3)_2.H_2O$ and different lead precursors in 14 moles dm^{-3} KOH solution for 3 hours: (a) $Pb(NO_3)_2$, (b) $Pb(CH_3COO)_2$, (c) PbF_2, (d) $PbCl_2$ and (e) PbI_2. The vertical bars indicate diffraction characteristics of PZ (ICSD 077-0856).

For the $Pb(NO_3)_2$ case, according to the XRD patterns of the acid-treated powders as shown in Figure 2, a very high KOH concentration of 14 moles dm^{-3} was required for the success of the synthesis. Lower concentrations resulted in poorly crystallised powders. However, a development in intensity of the *(200)* diffraction peak with increasing KOH concentration was apparent, suggesting the evolvement of the desired PZ. Another observation was a substantial reduction of the effective reaction time from days to hours when compared with the conventional hydrothermal synthesis [8].

According to former studies on similar issues, the observed phenomena could be explained as follows. Under commonly used hydrothermal conditions, the formation of nanocrystalline ZrO_2 as the hydrolysis product of aqueous $ZrO(NO_3)_2$ [14] could also be accelerated by microwave heating. This caused the breaking of large water clusters in the hydration sphere and the formation of the smaller ones [15]. Such mechanism increased the mobility of the dissolved lead species as well as the number of reaction sites on the occurring ZrO_2 surfaces for the hydrated lead ion-water clusters to react. A rapid synthesis should therefore be expected. According to the same studies, the hydrolysis of the aqueous $ZrO(NO_3)_2$ also resulted in the generation of nitric acid, which could neutralise the hydroxide species in solution [14]. In addition, there was evidence for the reduced electrolytic reaction of the KOH solution by the microwave radiation [16]. These phenomena were probably responsible for the increase in the high KOH concentration required in this study. This assumption was supported by the

Maejo Int. J. Sci. Technol. **2011**, *5*(01), 24-31

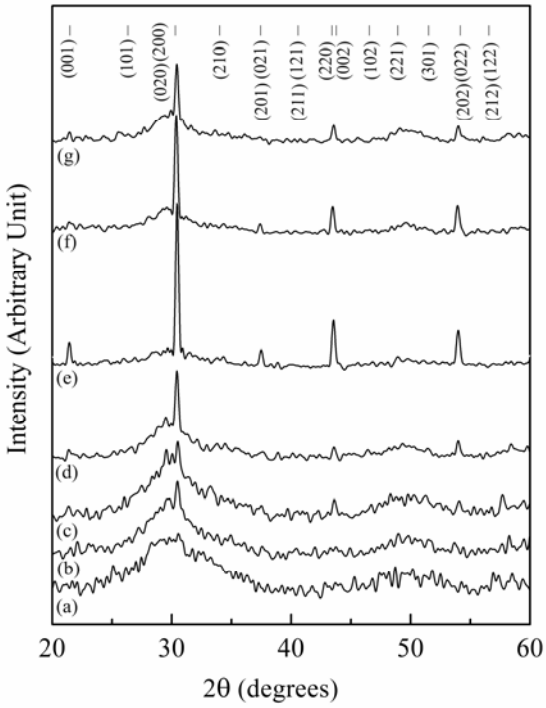

Figure 2. XRD patterns of the powders obtained from the reaction between $ZrO(NO_3)_2.H_2O$ and $Pb(NO_3)_2$ at 720 W for 3 hours in different concentrations of KOH solution: (a) 6 (b) 8 (c) 10 (d) 12 and (e) 14 moles dm^{-3}, compared to those obtained in 14 moles dm^{-3} KOH solution with different reaction times: (f) 4 hours and (g) 5 hours. The reference pattern is shown with vertical bars (ICSD 077-0856).

experiment in which a higher microwave power of 810 W was used. Rather than the desired PZ, mixtures of different oxides of lead and zirconium were obtained, which are the expected products of the hydrolysis reactions of the metal salts.

Based on the XRD patterns of the acid-treated powders, the synthesised PZ could be readily indexed as the orthorhombic *Pbma* phase with refined cell parameters a=5.87(1) Å, b=5.88(2) Å and c=4.15(2) Å (ICSD 077-0856). These results were well consistent with the conventional hydrothermal case, although the refined c parameter was shorter than the conventional heating case, c=4.27(3) Å [8], but closer to the standard, c=4.134 Å (ICSD 077-0856).

The field-emmision scanning electron microscopic (FESEM) images, as typically illustrated in Figure 3(a), showed that the powders largely consisted of discrete cubic particles although some particles with irregular shape were also present. The energy-dispersive X-ray spectroscopic measurements on the surface of several cubic particles indicated stoichiometric Pb:Zr, whereas the irregular-shape particles were found to be Zr-rich. This could account for the noisy background observed for the XRD patterns [Figure 2(e)]. The sizes of the cubic particles measured from the FESEM images were distributed in a significantly narrow range of 0.4-1.2 μm with approximately 60% of the population having a size of about 1 μm [Figure 4(a)]. Light scattering experiment on the bulk powder samples showed slightly larger particle sizes distributed mostly between 1-2 μm [Figure 4(b)]. The difference in particle sizes obtained from the two techniques should be due to a potentially biased

Maejo Int. J. Sci. Technol. **2011**, *5*(01), 24-31

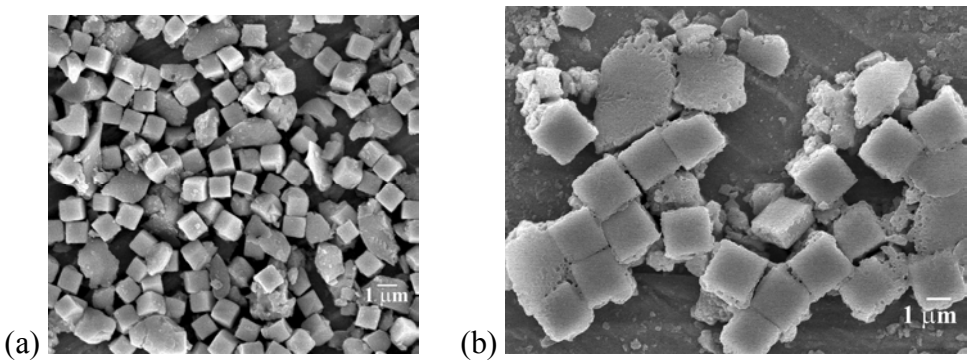

Figure 3. Typical FESEM photographs of PZ particles with corresponding XRD patterns shown in Figures 2(e) and 2(g) for crystals (a) and (b) respectively.

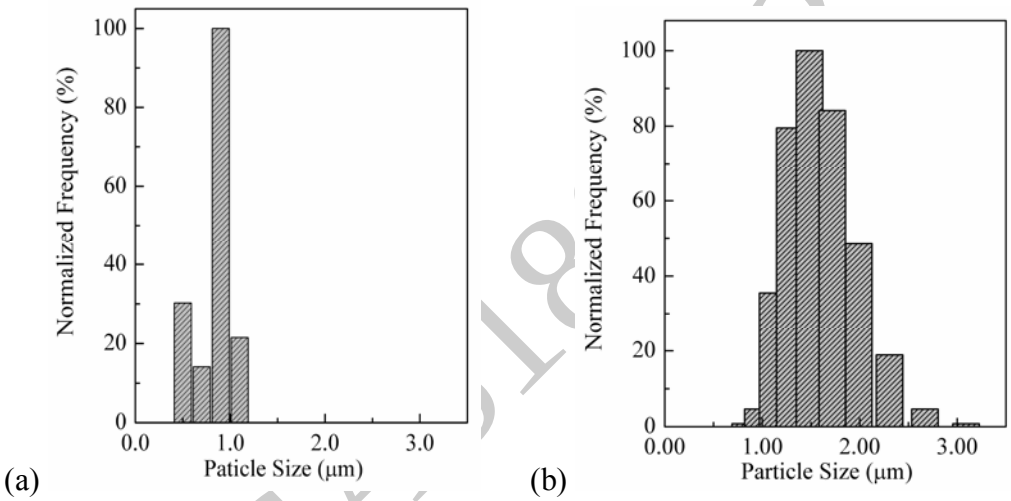

Figure 4. Particle size distribution of the cubic PZ particles measured from (a) FESEM images and (b) light scattering experiment (measured on the same powder sample)

analysis of the data. The non-spherical morphology of the particles normally introduces statistical errors to the laser light scattering data while a tendency of the particles to rest with preferred orientation on stub can induce bias in the data representation of the FESEM [17].

Thus, in comparison to the PZ powders derived from a conventional hydrothermal reaction where the particles were reportedly distributed in a 5-15 μm range with an average diameter of 7.5 μm [8], the pronouncedly narrower size distribution and the substantially smaller PZ particles have been achieved, although the negative effect on phase purity of the synthesised PZ and the contamination of some irregular Zr-rich particles were observed. A large number of nucleation induced by the localised microwave heating and the mechanism as described above, coupled with a poor crystal growth due to instantaneous and rapid ramping of such heating, could be the reasons for the approximate uniformity in the particle size [18-19]. Considering the PZ powders obtained from other chemical routes such as precipitation [20] and microemulsion [21], the apparent uniformity in particle shape and size may not be new. Both of these techniques can also give PZ powders composing of mono-dispersed spherical

Maejo Int. J. Sci. Technol. **2011**, *5*(01), 24-31

particles typically 20 nm in diameter. However, calcination is required by both techniques, resulting in an unavoidable high temperature treatment and disadvantages incurred therein. As for the modified solid-state preparation of PZ powders, the problems with aggregation and particles with irregular shapes cannot be surmounted even though the vibro-milling is applied for over 25 hours [22].

The extension of the microwave heating time from 3 to 5 hours resulted in a reduction in intensity of the most intense *(200)* diffraction peak of the orthorhombic PZ and the appearing of a broad lump at the base of this peak as shown in Figure 2 (e-g). The FESEM images [Figure 3(b)] showed that the particles remained in the same cubic shape, although the bubbled surfaces and the necking between the adjacent particles could be observed. This indicated the boiling on the surfaces of these cubic PZ particles, which could be the result of a heat accumulation. The enlargement of the particles, which is a reflection of the particle growth process, and the disappearing of irregular particles with extended reaction time were also apparent.

CONCLUSIONS

In order to promote the mono-dispersion and the uniformity in shape and size of the hydrothermally derived PZ particles without the assistance of organic additives, microwave heating was attempted. The occurrence of lead oxide seemed to be inevitable and washing with dilute acetic acid was necessary. Among different variables studied, the type of lead precursor and the KOH concentration were most critical in the success of the synthesis. It was shown that the critical KOH concentration and the optimal microwave heating time were 14 moles dm^{-3} and 3 hours respectively. The highly dispersed cubic lead zirconate particles of approximately 1 μm in size could be synthesised in only 3 hour at 720 W of microwave heating. In comparison to conventional hydrothermal synthesis, the merits of the microwave method were clearly reflected by a shortening in hydrothermal reaction time, a reduction in particle size, an improved particle mono-dispersion, and a uniform particle size. However, the negative effects on the purity of synthesised powders, viz. the contamination of irregular particles, and the requirement for a very high concentration of potassium hydroxide mineraliser should be noted.

ACKNOWLEDGEMENTS

This work is financially supported by Thailand Research Fund (TRF) and the Synchrotron Light Research Institute (Public Organisation). S. T. thanks the Royal Golden Jubilee Program of the TRF and the Graduate School of Chiang Mai University for their graduate scholarships.

REFERENCES

1. T. Asada and Y. Koyama, "Ferroelectric domain structures around the morphotropic phase boundary of the piezoelectric material $PbZr_{1-x}Ti_xO_3$", *Phys. Rev. B*, **2007**, *75*, 214111-214121.
2. C. Z. Rosen, B. V. Hiremath and R. E. Newnham, "Key Papers in Physics; Piezoelectricity", American Institute of Physics, New York, **1992**, pp.159-181.
3. K. Yamakawa, S. Trolier-McKinstry and J. P. Dougherty, "Reactive magnetron co-sputtered antiferroelectric lead zirconate thin films", *Appl. Phys. Lett.*, **1995**, *67*, 2014-2016.

4. P. Ayyub, S. Chattopadhyay, K. Sheshadri and R. Lahiri, "The nature of ferroelectric order in finite systems", *Nano Mater.*, **1999**, *12*, 713-718.
5. O. Khamman, W. Chaisan, R. Yimnirun and S. Ananta, "Effect of vibro-milling time on phase formation and particle size of lead zirconate nanopowders", *Mater. Lett.*, **2007**, *61*, 2822-2826.
6. E. D. Ion, B. Malic and M. Kosec, "Characterization of $PbZrO_3$ prepared using an alkoxide-based sol–gel synthesis route with different hydrolysis conditions", *J. Eur. Ceram. Soc.*, **2007**, *27*, 4349-4352.
7. E. E. Oren, E. Taspinar and A. C. Tas, "Preparation of lead zirconate by homogeneous precipitation and calcination", *J. Am. Ceram. Soc.*, **1997**, *80*, 2714-2716.
8. A. Rujiwatra, S. Tapala, S. Luachan, O. Khamman and S. Ananta, "One-pot hydrothermal synthesis of highly dispersed, phase-pure and stoichiometric lead zirconate", *Mater. Lett.*, **2006**, *60*, 2893-2895.
9. G. Xu, G. Zhao, Z. Ren, G. Shen and G. Han, "PVA assisted synthesis of nanosized perovskite PZT powder by a two-stage precipitation route", *Mater. Lett.*, **2006**, *60*, 685-688.
10. Z. Lu, J. Liu, Y. Tang and W. Li, "Hydrothermal synthesis of $CaSnO_3$ cubes", *Inorg. Chem. Commun.*, **2004**, *7*, 731-733.
11. W. L. Sin, K. H. Wong and P. Li, "Surfactant effect on synthesis of nanocrystalline $La_xSr_{1-x}MnO_3$ by hydrothermal method", *Acta Physica. Polonica. A*, **2007**, *111*, 165-171.
12. S. Tapala, N. Thammajak, P. Laorattanakul and A. Rujiwatra, "Effects of microwave heating on sonocatalyzed hydrothermal preparation of lead titanate nanopowders", *Mater. Lett.*, **2008**, *62*, 3685-3687.
13. J. G. Speight, "Lange's Handbook of Chemistry", 16th Edn., McGraw-Hill, New York, **2005**, Ch. 1.
14. Y. V. Kolen'ko, V. D. Maximov, A. A. Burukhin, V. A. Muhanov and B. R. Churagulov, "Synthesis of ZrO_2 and TiO_2 nanocrystalline powders by hydrothermal process", *Mater. Sci. Eng. C*, **2003**, *23*, 1033-1038.
15. R. Walczak and J. A. Dziuban, "Microwave enhanced wet anisotropic etching of silicon utilizing a memory effect of KOH activation-A remote E2msi process", *Sens. Actuators A*, **2004,** *116*, 161-170.
16. D. R. Stanisavljev, T. D. Grozdić, M. P. Marĉeta Kaninski, A. R. Djordjević and D. Lj. Stojić, "The microwave influence on the electrolytic decomposition of KOH water solution", *Electrochem. Commun.*, **2007**, *9*, 901-904.
17. A. Jillavenkatesa, S. J. Dapkunas and L.-S. H. Lum, "Particle Size Characterization; Practice Guide", U.S. Government Printing Office, Washington, D.C., **2001**, Ch. 5-6.
18. D. E. Clark and W. H. Sutton, "Microwave processing of materials", *Annu. Rev. Mater. Sci.*, **1996**, *26*, 299-331.
19. P. Lidström, J. Tierney, B. Wathey and J. Westman, "Microwave assisted organic synthesis - A review", *Tetrahedron*, **2001**, *51*, 9225-9283.
20. T. Ko and D. -K. Hwang, "Preparation of nanocrystalline lead zirconate powder by homogeneous precipitation using hydrogen peroxide and urea", *Mater. Lett.*, **2003**, *57*, 2472-2479.

21. J. Fang, J. Wang, S. -C. Ng, L. -M. Gan, C. H. Quek and C. -H. Chew, "Synthesis of lead zirconate powders via a polyaniline-mediated microemulsion processing route", *Mater. Lett.*, **1998**, *36*, 179-185.
22. O. Khamman, W. Chaisan, R. Yimnirun and S. Ananta, "Effect of vibro-milling time on phase formation and particle size of lead zirconate nanopowders", *Mater. Lett.*, **2007**, *61*, 2822-2826.

Maejo Int. J. Sci. Technol. **2011**, *5*(01), 83-95

Maejo International Journal of Science and Technology

ISSN 1905-7873
Available online at www.mijst.mju.ac.th

Full Paper

Crystal growth and characterisation of a unique trinuclear V^{IV}/V^{V} complex

Yothin Chimupala [1], Wasinee Phonsri [1], Timothy J. Prior [2] and Apinpus Rujiwatra [1,*]

[1] Department of Chemistry and Centre for Innovation in Chemistry, Faculty of Science, Chiang Mai University, Chiang Mai 50200 Thailand
[2] Department of Chemistry, University of Hull, Kingston upon Hull, UK, HU6 7RX
* Corresponding author, e-mail: apinpus@chiangmai.ac.th

Received: 10 August 2010 / Accepted: 15 February 2011 / Published: 28 February 2011

Abstract: Single crystals of a mixed-valence trinuclear cluster of formula $[V_2^{V}V^{IV}O_5(C_{12}H_8N_2)_3(SO_4)_2(H_2O)_3]\cdot 6H_2O$ were grown by layer diffusion technique and characterised by single-crystal X-ray diffraction; $P2_1/c$, a = 20.5448(11) Å, b = 11.7647(9) Å, c = 18.1871(9) Å, β = 92.64(0)°, V = 4391.22 (93) Å^3, R = 0.0941 and Rw = 0.1345. A distinct characteristic of the structure is the existence of the rare linear mono-μ-oxo $[V_2^{V}V^{IV}O_5]^{4+}$ building units and the presence of a large number of hydrogen bonds and π-π interactions. The study on the mixed valence state of vanadium by valence bond sum calculations, manganometric titration and cyclic voltammetry, and the presence of π-π interactions by calculation of the harmonic oscillator model of aromaticity indices are presented. The thermogravimetric and differential scanning calorimetric analysis is also reported. The results of UV-Vis spectroscopic study and band gap energy calculation are included.

Keywords: vanadium complex, trinuclear complex, crystal structure, single-crystal X-ray diffraction

INTRODUCTION

Prompted by a variety of valences and coordination chemistry that can be adopted by vanadium and a wide range of potential applications of its complexes [1-3], the interest in vanadium complexes has been unceasing, particularly in those of high nuclearity and mixed valence state. The bi-nuclear complexes containing a mono-μ-oxo $[V_2O_3]^{2+}$ core are thus far the largest class in which the mixed valence state of vanadium is common. Examples of polynuclear V^{IV}/V^{V} complexes with mono-μ-oxo-

Maejo Int. J. Sci. Technol. **2011**, *5*(01), 83-95

vanadium cores are still limited: the tetra-nuclear $[V_40_6(C_2H_5O)_6(C_{12}H_8N_2)_2]$, penta-nuclear $\{[V_2O_4(C_{12}H_8N_2)_2(PO_4)]2VO(OH)\}_{3/4}\{[V_2O_4(C_{12}H_8N_2)_2(HPO_4)]_2\}_{1/4}\cdot 4.5H_2O$ and nona-nuclear $K_7[V_9O_{16}(bdta)_4]\cdot 27H_2O$ (bdta = butanediaminetetraacetate) are known [4-6]. To the best of our knowledge, the first example of the tri-nuclear vanadium complex of this kind with a chemical formula of $[VO_2(\textit{phen})(SO_4)(H_2O)]_2(VO(\textit{phen})(H_2O)]\cdot 4H_2O$ (*phen* = phenanthroline ligand) was reported by Huang et al. in 2008 [7]. Its hydrothermal synthesis and the novel characteristic of its structure in exhibiting a practically linear $[V_3O_5]^{4+}$ core were reported with a brief description on the EPR and UV-Vis study of the complex.

As a continuation of our interest in the synthesis of new polyoxovanadates using organodiamines of different molecular flexibility and aromaticity, we embark on the synthesis and growing of single crystals of compound $[V_2^{V}V^{IV}O_5(C_{12}H_8N_2)_3(SO_4)_2(H_2O)_3]\cdot 6H_2O$ **(1)**. Although reported earlier [7], the synthesis and crystal growth of **1** by a different route carried out in this study and a detailed description of its crystal structure should be worth reporting. Different ways of determining the mixed valence state of vanadium are presented. The UV-Vis spectroscopic study, cyclic voltammetric analysis and thermorgravimetric-differential scanning calorimetric analysis of **1** were also performed.

MATERIALS AND METHODS

Chemicals

All chemicals were used as-received: 1,10-phenanthroline ($C_{12}H_8N_2$; Fluka, 99%), ethyl alcohol (Merck, 99.9%), ammonium metavanadate (Ajax, 99.5%), sodium hydroxide (Merck, 99%), sulfuric acid (Merck, 95-97%), potassium permanganate (BDS, 99%), sodium sulphite (Ajax, 98%) and potassium bromide (BDH 98.5%).

Crystal Growth and Characterisation

An ethanolic solution of organic ligand (solution A) was prepared by dissolving 0.495 g of 1,10-phenanthroline (*phen*) in 15.0 cm^3 of ethyl alcohol. An aqueous solution of VO_2^+ (solution B) was prepared by dissolving 2.00 g of ammonium metavanadate in 50.0 cm^3 of warm 1.00 mol dm^{-3} sodium hydroxide solution, followed by addition of 80.0 cm^3 of 1.00 mol dm^{-3} sulfuric acid . A portion of solution B (1.50 cm^3) was gently loaded into a glass test tube of 5 mm in diameter and 10 cm in length, followed by 1.50 cm^3 of solution A. Dark green crystals of **1** appeared at the boundary between solutions A and B after leaving for 5 days at atmospheric condition.

The elemental composition of the crystals was semi-quantified using an energy-dispersive X-ray microanalyser equipped with a field-emission scanning electron microscope (JEOL JSM-6335F), whereupon a consistent V:S:O:C:N atomic ratio of 2.8:1.0:3.2:6.7:1.5 (exp.) compared to 2.4:1.0:5.5:6.7:1.3 (calc.) was obtained. A Fourier transform infrared (FTIR) spectrum of the ground crystals as a KBr pellet was collected on a Bruker Tensor 27 FT-IR instrument (4000-400 cm^{-1}, resolution 0.5 cm^{-1}): 3450 cm^{-1}, ν(O–H); 3065 cm^{-1}, ν(aromatic C–H); 1626, 1583, 1519 and 1427 cm^{-1}, ν(aromatic C=C); 1187, 1125 and 1032 cm^{-1}, ν(SO_4); 970 and 937 cm^{-1}, ν(V=O); 870, 848, 778, 736 and 723 cm^{-1}, δ_{oop}(aromatic C-H); 647 and 593 cm^{-1}, δ(V–O–V).

Maejo Int. J. Sci. Technol. **2011**, *5*(01), 83-95

The purity of **1** was assured by X-ray powder diffraction pattern collected on a Bruker D8 Advance diffractometer (Ni filter, Cu *K*α, λ=1.540558 Å, 48 kV, 30 mA). In order to determine the amount of V^{IV} and total $V^{IV,V}$, the aqueous solutions of **1** and its reduced form were titrated against standardised potassium permanganate solution. The solution of the reduced form of **1** was obtained by a reaction with sulphur dioxide generated from sodium sulphite. Cyclic voltammetry (CV) was also conducted using a BAS CV-50W voltammetric analyser (Bioanalytical System, Inc., USA) with Pt (MF-2013, 1.6 mm in diameter), Ag/AgCl (MF-2063) and Pt wire (MW-1032) as working, reference and auxiliary electrodes respectively.

Themogravimetric-differential scanning calorimetric (TG-DSC) analysis was performed using ETZSCH STA 409 PC/PG thermal analyser (Netzsch-Gerätebau GmbH, Germany) (20-1200°C, rate 10°C/min, N_2 gas) to evaluate the thermal stability of **1**. A UV-Vis spectrum of an aqueous solution of **1** from 200 nm to 800 nm was measured with a Perkin Elmer UV LAMDA 25 spectrophotometer. The loss of crystal colour after complete dissolution was noted.

Crystal Structure Determination

Data of 8699 independent reflections were collected in a range of 2.5≤θ/°≤26.1 on a 0.45×0.25×0.15 mm^3 greenish lozenge crystal of **1** using a Stoe IPDS2 diffractometer (Stoe & Cie GmbH, Germany) and Stoe *X*-Area software [8]. A face indexed absorption correction was applied within the Stoe *X*-RED software using Tompa method [9-10]. The data were then reduced and refined resulting in 5365 reflections with $I > 2\sigma(I)$ and internal R of 0.070. The structure was determined by direct method and refined by full-matrix least-square methods using SHELXS97 and SHELXL97 programs via the WinGx program interface [11-13]. The structure was solved and refined in $P2_1/c$, a = 20.5448(11) Å, b=11.7647(9) Å, c = 18.1871(9) Å, β = 92.64(0)°, V = 4391.22 (93) $Å^3$, Z = 4, R =0.0941 and Rw = 0.1345. The data were of reasonable quality. However, it was not possible to locate hydrogen atoms of the included water molecules. Some disorder in the positions of the water molecules was also detected. Details on data collection and structural deduction and refinement are summarised in Table 1. A rather large deviation of the goodness of fit from unity due to local disorder in the structure of **1** may be noted.

The structure of **1** was first reported by Huang et al. in 2008 [7]. The synthesis by hydrothermal route and the uniqueness of the complex as the first mixed-valence polynuclear vanadium with linear mono-μ-oxo $[V_3O_5]^{4+}$ core were briefly reported. The study of the EPR and electronic spectrum was included. Crystallographic data of the formerly reported structure were compared with the presently reported structure as shown in Table 1, which suggests an approximate equivalence.

Maejo Int. J. Sci. Technol. **2011**, *5*(01), 83-95

Table 1. Crystal data and structure refinement for **1**

	1	Data abstracted from Huang et al. [7]
Formula	$[V_2^{V}V^{IV}O_5(phen)_3(SO_4)_2(H_2O)_3]\cdot 6H_2O$	$[VO_2(phen)(SO_4)(H_2O)]_2[VO(phen)(H_2O)]\cdot 4H_2O$
Formula weight	1117	1091.66
Crystal description	Dark green	*N/A*
Crystal system	Monoclinic	Monoclinic
Space group	$P2_{1/c}$	$P2_{1/c}$
a/ Å	20.5448(11)	20.747(4)
b/ Å	11.7647(9)	11.828(2)
c/ Å	18.1871(9)	18.316(4)
β / °	92.639(4)	93.07(3)
Unit cell volume/ Å^3	4391.2(5)	4488.2(16)
Z	4	4
ρ_{calc}/g.cm^{-3}	1.691	1.616
T/K	150(4)	293(2)
Radiation (λ/Å)	Mo K_α(0.71073)	Mo K_α(0.71073)
Total data collected	24523	37068
R_{int}	0.070	0.0384
Data (I>2σ(I))	8699	10059
Goodness of fit (S)	0.797	1.049
R, R_w (all data)	0.0941, 0.1345	*N/A*
R, R_w(I>2σ(I))	0.055, 0.135	0.0558, 0.1488

RESULTS AND DISCUSSION

Crystal Structure of 1

Compound **1,** $[V_2^{V}V^{IV}O_5(C_{12}H_8N_2)_3(SO_4)_2(H_2O)_3]\cdot 6H_2O$, crystallises in monoclinic space group $P2_1/c$ with cell parameters a = 20.5448(11) Å, b = 11.7647(9) Å, c = 18.1871(9) Å, β = 92.64(0)°, V = 4391.22 (93) Å^3 and Z = 4, which are similar to those of the previously reported structure [7]. Figure 1 shows an asymmetric unit of **1**, depicting three distinct vanadium atoms linked by two μ_2-O11 and μ_2-O12 to form an approximately linear trinulcear vanadium oxide backbone with bond angles being close to linearity: V1-O11-V2 = 163.1° and V(2)-O(12)-V(3) = 159.2°. Selected bond lengths and bond angles in **1** are listed in Table 2 and Table 3 respectively. The terminal V1 and V3 share the common distorted octahedral geometry, coordinated to two N atoms of the chelating *phen* and four O atoms from a monodentate sulphate, a terminal aqua ligand, the vanadyl bond and the oxo-bridge. Similar distorted octahedral geometry is adopted by the mediating V2, coordinated to two N atoms of the chelating *phen*, two *trans* μ_2-O atoms of oxo-bridges, and the vanadyl and sulfate O atoms. The chemical formula of $[V_3O_5(phen)_3(SO_4)_2(H_2O)_3]$ can thus be derived. A common question for polynuclear vanadium complexes is, however, the valence states of the vanadium atoms.

Maejo Int. J. Sci. Technol. **2011**, *5*(01), 83-95

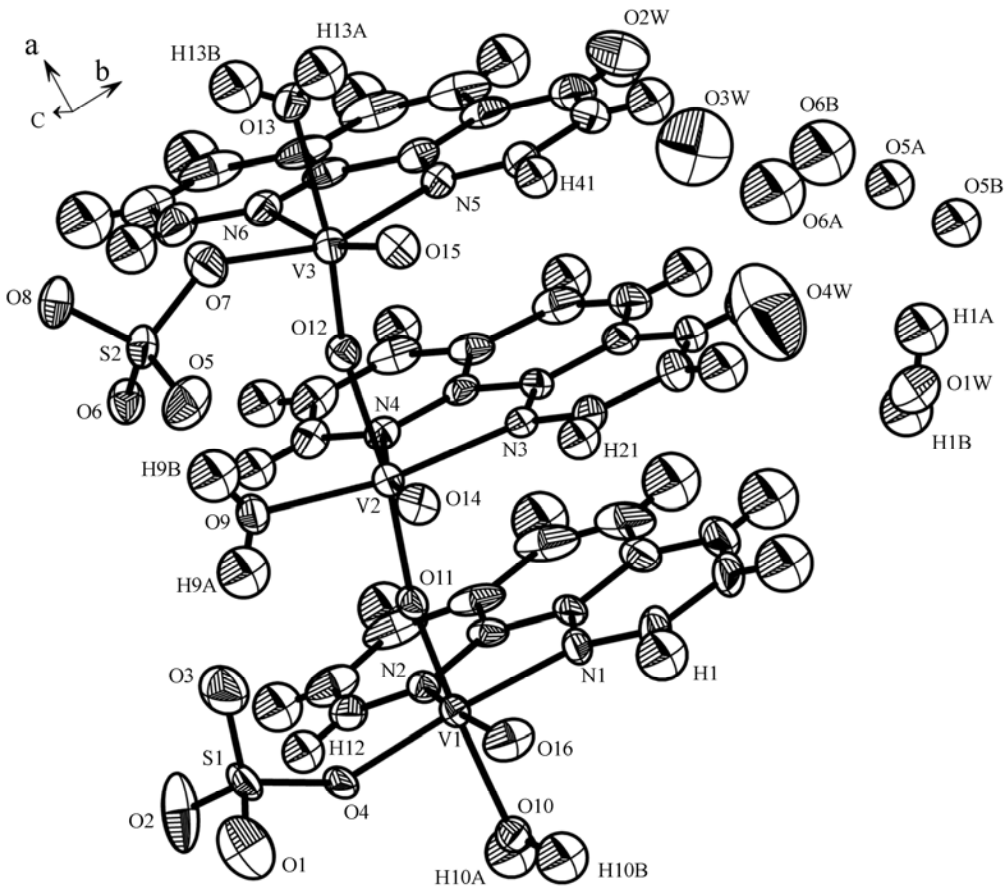

Figure 1. Asymmetric unit of **1** with atomic numbering scheme and drawn with 50% thermal elliptical possibility

Table 2. Selected bond distances (Å) in **1** with standard deviations in brackets

V1—O16	1.600(3)	V3—O12	1.677(3)
V1—O11	1.675(3)	V3—O7	1.930(3)
V1—O4	1.917(3)	V3—O13	2.123(4)
V1—N1	2.132(4)	V3—N5	2.136(4)
V1—O10	2.149(4)	V3—N6	2.296(4)
V1—N2	2.249(3)	S2—O5	1.430(4)
V2—O14	1.592(3)	S2—O8	1.455(3)
V2—O12	1.932(3)	S2—O6	1.468(3)
V2—O11	1.947(3)	S2—O7	1.521(4)
V2—O9	1.998(3)	S1—O2	1.421(4)
V2—N3	2.124(4)	S1—O1	1.457(4)
V2—N4	2.307(3)	S1—O3	1.462(5)
V3—O15	1.596(3)	S1—O4	1.510(3)

Maejo Int. J. Sci. Technol. **2011**, *5*(01), 83-95

Table 3. Selected bond angles (°) in **1** with standard deviations in brackets

O16—V1—O11	104.73(16)	O12-V2-N3	87.57(13)	N5-V3-N6	73.96(13)
O16—V1—O4	104.79(18)	O11-V2-N3	96.01(13)	O5-S2-O8	113.5(2)
O11—V1—O4	99.86(14)	O9-V2-N3	159.64(14)	O5-S2-O6	111.2(2)
O16—V1—N1	92.14(18)	O14-V2-N4	166.12(15)	O8-S2-O6	110.40(19)
O11—V1—N1	88.54(15)	O12-V2-N4	80.55(12)	O5-S2-O7	109.1(2)
O4 —V1—N1	158.32(14)	O11-V2-N4	82.81(12)	O8-S2-O7	103.9(2)
O16—V1—O10	87.57(16)	O9-V2-N4	86.43(14)	O6-S2-O7	108.3(2)
O11—V1—O10	165.39(13)	N3-V2-N4	73.57(13)	O2-S1-O1	109.3(3)
O4 —V1—O10	84.22(13)	O15-V3-O12	104.37(16)	O2-S1-O3	116.4(3)
N1 —V1—O10	83.05(14)	O15-V3-O7	104.52(17)	O1-S1-O3	105.5(3)
O16—V1—N2	161.26(17)	O12-V3-O7	97.97(15)	O2-S1-O4	106.8(2)
O11—V1—N2	88.14(14)	O15-V3-O13	93.89(15)	O1-S1-O4	107.2(2)
O4 —V1—N2	85.91(13)	O12-V3-O13	161.30(13)	O3-S1-O4	111.2(2)
N1 —V1—N2	74.35(14)	O7-V3-O13	81.01(15)	S1-O4-V1	140.7(2)
O10-V1-N2	78.10(13)	O15-V3-N5	89.66(15)	S2-O7-V3	137.3(2)
O14-V2-O12	99.86(15)	O12-V3-N5	95.24(14)	V1-O11-V2	163.10(18)
O14-V2-O11	98.38(15)	O7-V3-N5	157.48(16)	V3-O12-V2	159.23(18)
O12-V2-O11	161.23(12)	O13-V3-N5	80.64(14)		
O14-V2-O9	107.45(16)	O15-V3-N6	162.33(16)		
O12-V2-O9	85.36(14)	O12-V3-N6	84.12(14)		
O11-V2-O9	85.00(13)	O7-V3-N6	89.31(16)		
O14-V2-N3	92.56(15)	O13-V3-N6	77.20(13)		

The bond valence sum (BVS) calculation was attempted using the refined bond lengths listed in Table 2 with the following assumed parameters: $R_0(V^{V,IV}–O^{-II}) = 1.735$, $R_0(V^{V}–O^{-II}) = 1.803$, $R_0(V^{IV}–O^{-II}) = 1.780$, $R_0(V^{V,IV}–N^{-III}) = 1.875$, and $b = 0.370$ [14]. The BVS of 4.81, 4.15 and 4.85 were obtained for V1, V2 and V3 respectively, indicating the presence of the expected V^{IV} and V^{V} with twice the amount of the latter. The result of manganometric titration confirms the calculation: 0.915 mol of V^{IV} per formula unit. The CV analysis confirms this by the presence of an irreducible reduction peak of V^{V} to V^{IV} at +0.242 V vs Ag/AgCl with a maximum current of 4.48 A. Based on the BVS calculation, manganometric titration and the CV experiment, a mixed $2V^{V}:V^{IV}$ valence state for vanadium and the precise formula of $[V_2{}^{V}V^{IV}O_5(C_{12}H_8N_2)_3(SO_4)_2(H_2O)_3]$ can thus be deduced. This leads to the conclusion on charge neutrality for the cluster, which confirms the presence of only water molecules as the extra-cluster species and justifies the assignment of the extra-cluster O atoms as water during the crystal structure deduction and refinements. The chemical formula with six extra-cluster water molecules, viz. $[V_2{}^{V}V^{IV}O_5(C_{12}H_8N_2)_3(SO_4)_2(H_2O)_3]\cdot 6H_2O$, is then established.

Maejo Int. J. Sci. Technol. **2011**, *5*(01), 83-95

The phenanthroline (*phen*) ligands are located on the same side of the vanadium oxide backbone with the distances of 3.689 Å and 3.670 Å between the centroids of two adjacent molecular planes as shown in Figure 2. These distances are in a range possible for the π-π interactions to occur [15-17], which can be regarded as an important parameter regulating the spatial arrangement of these chelating ligands. It is apparent that these phenanthroline ligands are not exactly parallel to each other but slightly converge towards the free end of the molecule. Figure 3 depicts the centroids of the central benzene rings of the *phen* ligands, showing the panning angles of 9.48° and 21.80° for the superjacent and subjacent ligands from the middle one. The relative arrangement of these organic ligands indicates that other interactions are present that subjugate the weak π-π interactions, which favour the superimposed position of the ligands.

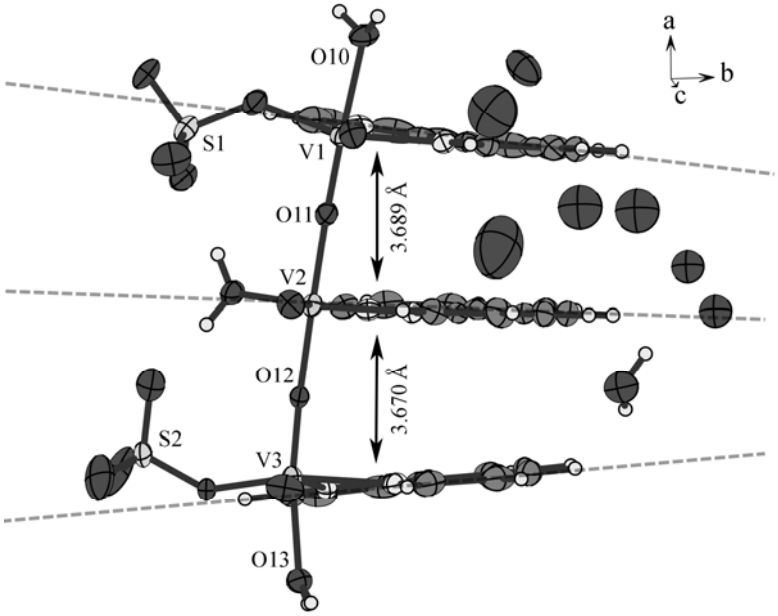

Figure 2. Illustration showing the relative spatial arrangement of *phen* and the corresponding inter-molecular planar distances

The interaction between π electrons commonly encountered in the stacking of aromatic molecules should impart an influence on their aromaticity. Here, the harmonic oscillator model of aromaticity (HOMA) index was used to evaluate the presence of this interaction [18-20]. According to a survey of structures consisting of *phen* in the molecules both in coordination and non-coordination modes found in the Cambridge structural databases [21], it is evident that the values of HOMA indices are distributed in different ranges depending on both the coordination and the π-π interaction. For non-coordinated *phen*, the average indices of three fused benzene rings are distributed in a range of 0.25-0.50 for those without π-π interactions and 0.66-0.83 for those with the interactions. On the other hand, the presence of π-π interactions seems to be common with coordination with average indices distributed in a higher range of 0.70-0.94, suggesting the preference of these aromatic ligands to arrange themselves in such a way as to maximise the interactions. In the structure of **1**, the HOMA indices were calculated at similar values of ca. 0.80 for each *phen* ligand. This is in very good

Maejo Int. J. Sci. Technol. **2011**, *5*(01), 83-95

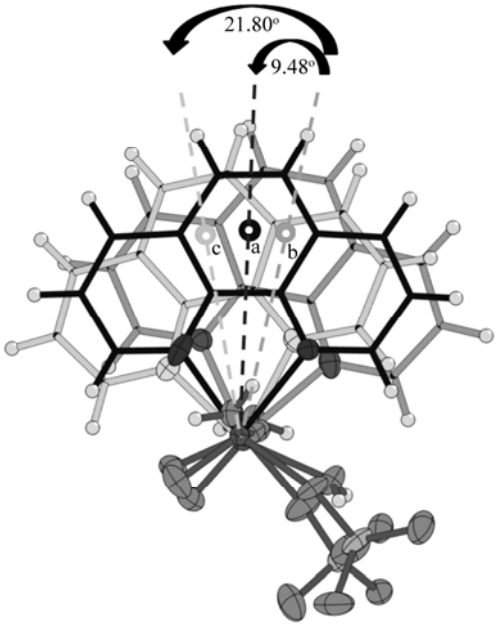

Figure 3. Illustration showing relative locations of the centroids (*a*, *b* and *c*) of the central benzene rings of the superjacent, middle and subjacent *phen* ligands respectively, with relative panning angles of a and c from b

agreement with the surveyed HOMA indices for those complexes with π-π interacting *phen* ligands, hence the suggested presence of such weak interaction in **1**.

The analysis for hydrogen bonding according to the definition proposed by Jeffrey [22] was performed on the crystal structure and revealed a large number of hydrogen bonding interactions as depicted in Figure 4 and listed in Table 4. The weak C-H···O hydrogen bonds formed between *phen* and the neighbouring O atoms of both ligated and free water molecules as well as the nearby sulphate group may account for the subjugation of the π-π interactions and the consequent orientation of these organic ligands. The strong hydrogen bonds of O-H···O type between the ligated water of the mediated V2 and the nearby sulphates also provide explanation for the orientation of the pending SO_3 motifs of V1 and V3 that incline towards each other with the bending angles of 140.71° and 137.32° for V1-O3-S1 and V3-O7-S2 respectively.

Compared to the complex, $[VO_2(phen)(SO_4)(H_2O)]_2(VO(phen)(H_2O)]\cdot 4H_2O$, reported by Huang et al. [7], structure **1** contains two more molecules of water of crystallisation and therefore a larger number of hydrogen bonding interactions. This may stem from the difference in crystal growth technique and condition. Crystals of **1** were grown at ambient temperature and pressure, whereas those of the former were obtained hydrothermally. The larger number of water outside the coordination sphere, however, does not significantly affect the solid state registry of the compound.

Maejo Int. J. Sci. Technol. **2011**, *5*(01), 83-95

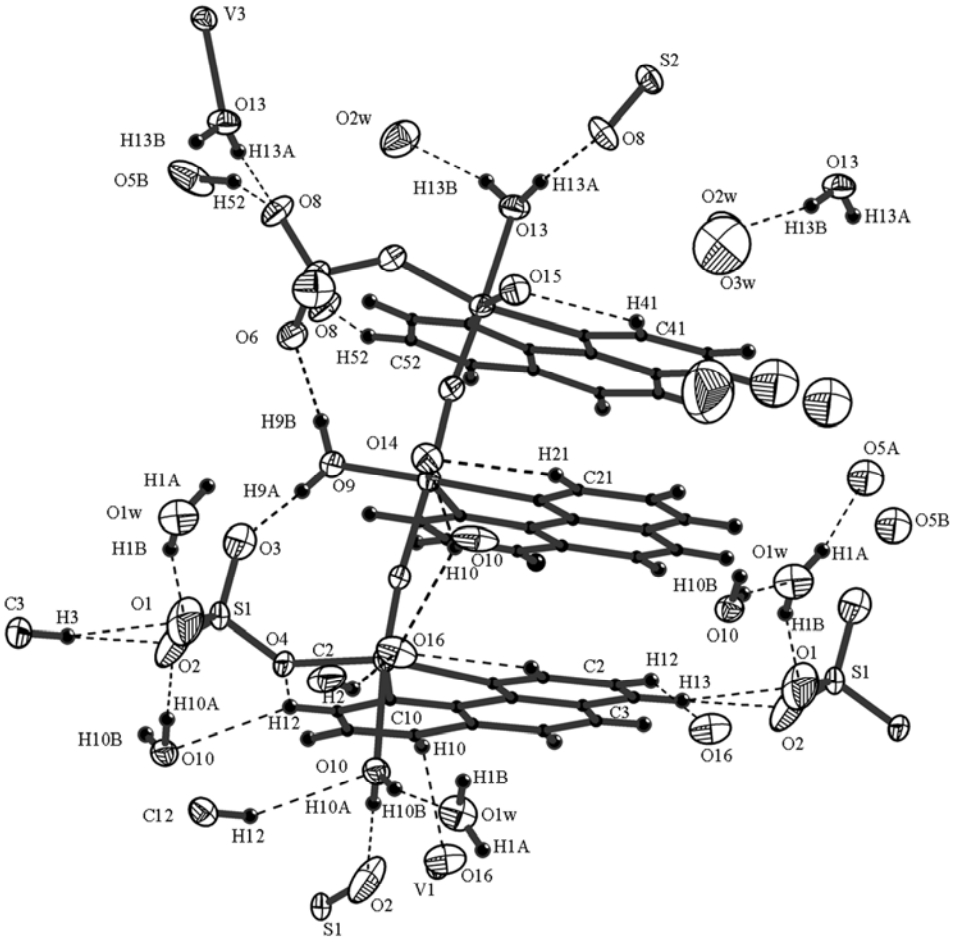

Figure 4. Hydrogen bonding interactions (dotted lines) of different types as listed in Table 4

UV-Vis Spectroscopic Study

The UV-Vis spectrum measured on the aqueous solution of **1** at a concentration of 5×10^{-4} mol dm^{-3} (Figure 5) exhibits absorption only in the UV region. The absorption bands characteristic of *phen* are clearly present with the maxima at 230 nm (3,205 $dm^3mol^{-1}cm^{-1}$) and 264 nm (2,150 dm^3mol^{-1} cm^{-1}), both of which are attributable to the intraligand π-π* transitions. The most intense band at 206 nm (10,584 $dm^3mol^{-1}cm^{-1}$) can be assigned to the LMCT process of the terminal oxygen while a broad band appearing as shoulder at 270 nm is the characteristic band associated to the LMCT of the bridging oxygen [23-25]. The absorption coefficients (α) can be calculated from the maximum (λ_{max}) of each band, and the plot between $(\alpha h\nu)^2$ and $h\nu$ can be made (inset of Figure 5) if only the direct electronic transition is assumed [26]. The band gap energy for each transition can be obtained by extrapolation of the positive tangent line for each $h\nu$ to α=0: 4.3017, 5.2317 and 5.8182 eV for the transitions with λ_{max} at 264, 230 and 206 nm respectively.

Maejo Int. J. Sci. Technol. **2011**, *5*(01), 83-95

Table 4. Summary of hydrogen bonding geometry for **1** (Standard deviations are in brackets)

D	A	H···A (Å)	D···A (Å)	∠ D-H···A (°)
$O1_W$	$O5_A$	2.17(5)	2.981(7)	158(5)
$O1_W$	O1	1.99(4)	2.807(5)	161(6)
O9	O3	1.72(4)	2.560(5)	175(7)
O9	O6	1.76(4)	2.604(5)	176(5)
O10	O2	1.91(4)	2.750(5)	179(7)
O10	$O1_W$	1.87(5)	2.690(5)	164(5)
O13	O8	1.82(5)	2.656(5)	174(5)
O13	$O2_W$	1.93(5)	2.728(5)	163(4)
C1	O16	2.57	2.994(7)	108
C2	O16	2.46	3.308(7)	149
C3	O1	2.50	3.270(7)	138
C3	O2	2.35	3.272(8)	163
C10	O14	2.56	3.243(7)	129
C10	O16	2.49	3.212(7)	133
C12	O4	2.56	3.058(5)	113
C12	O10	2.57	3.365(6)	142
C21	O14	2.49	2.957(6)	110
C41	O15	2.43	2.894(6)	110
C52	O8	2.45	3.246(7)	142

It is intriguing that there was no absorption in the visible light region (325-800 nm) for the solution of **1**, which was also colourless. This might be due to the loss of long-range order of the solid state structure when it was made into solution. It has been reported, however, that a broad absorption band which should be evidence for the inter-valence charge transfer between V^{IV} and V^{V} was observed in this region for the spectrum collected on a solid sample [7].

Thermogravimetric and Differential Scanning Calorimetric Analysis

On heating **1** under the flow of N_2 gas, four stages of endothermic weight loss were observed (Figure 6). The first weight loss of 9.86% occurring between 80-150°C agrees well with the weight of six non-coordinating water molecules (9.58%), while the second loss of 5.14% observed at 150-340°C is approximately equivalent to the weight of three coordinating water molecules (4.79%). The corresponding endothermic features found in the DSC curve reflect the influence of the hydrogen bonding interactions involved with these water molecules. The next two subsequent weight losses found from 340°C to 700°C totalled 45.00%, which corresponds well with the release of three coordinated *phen* ligands. It should be noted that the argument is made based only on the agreement of weight percentages; further experiments on identification of the liberated species have to be performed if a definite conclusion is to be obtained.

Maejo Int. J. Sci. Technol. **2011**, *5*(01), 83-95

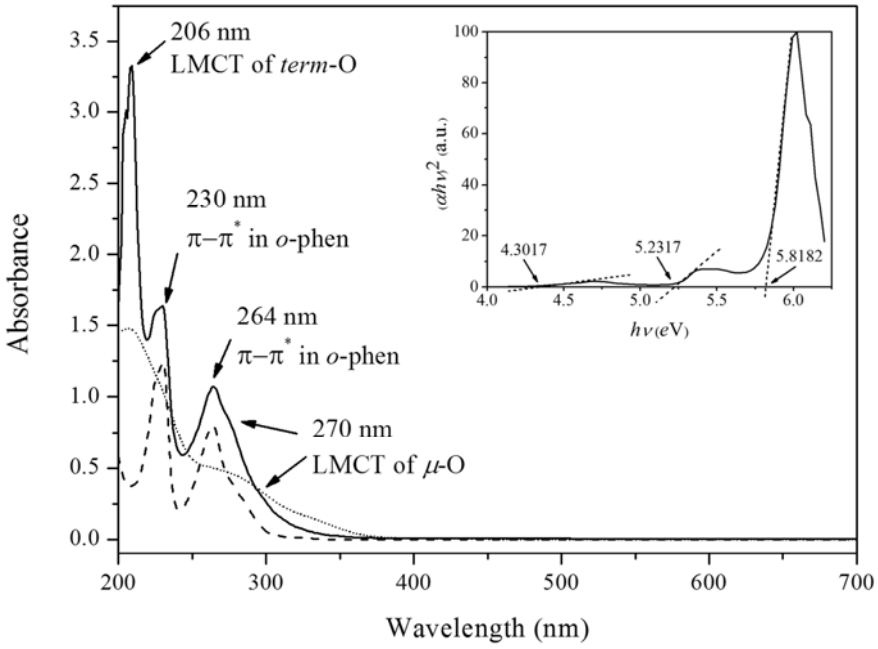

Figure 5. The UV-Vis spectrum of aqueous solution of **1** ($5x10^{-4}$ $moldm^{-3}$, solid line) compared with those of the ligand (dash line) and vanadium precursor (dotted line). The plot between $(\alpha hv)^2$ and hv is provided in the inset

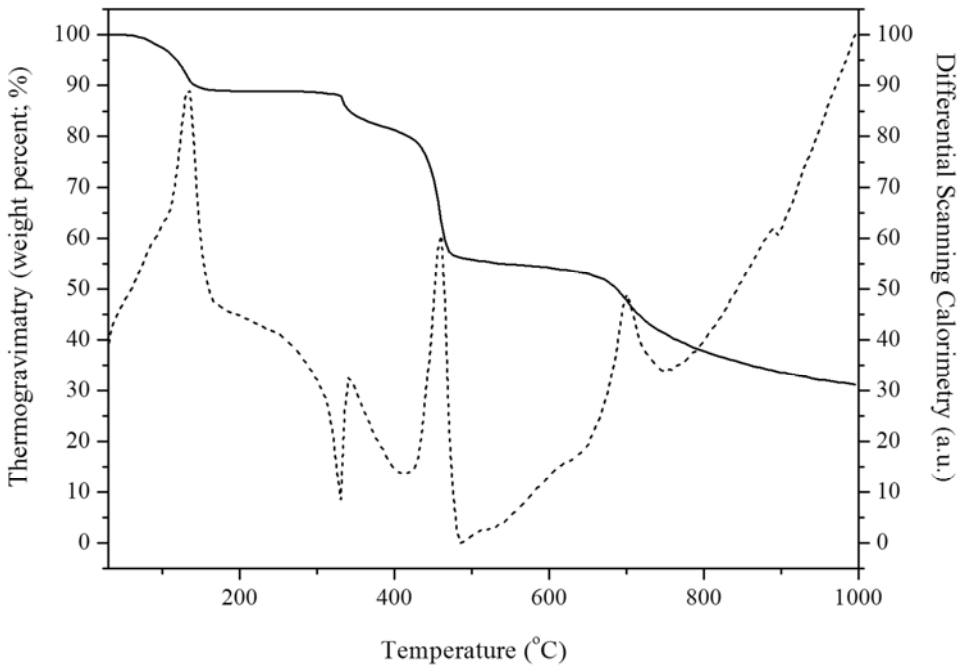

Figure 6. Thermogravimetric (solid line) and differential scanning calorimetric (dash line) graphs collected on **1**

Maejo Int. J. Sci. Technol. **2011**, *5*(01), 83-95

CONCLUSIONS

A rare example of mixed-valence trinuclear cluster, $[V_2^{V}V^{IV}O_5(C_{12}H_8N_2)_3(SO_4)_2(H_2O)_3]\cdot 6H_2O$, has been synthesised at ambient atmosphere. Its crystal structure has been determined and refined with excellent agreement with the previously reported structure which had fewer water of crystallisation. Detailed analysis of the structure indicates the presence of both π-π interactions and a large number of intra- and inter-cluster hydrogen bonds, which impart influence on spatial orientation of the cluster-building motifs. According to the bond valence sum calculations, the manganometric titration and cyclic voltammetry, the mixed valence of V^{IV} and V^{V} in the ratio of 1:2 can be deduced. The presence of six molecules of water of crystallisation is consistent with the results of the thermogravimetric/differential scanning calorimetric analysis, which suggest sequential loss of water of crystallisation, ligated water and the phenanthroline ligands.

ACKNOWLEDGEMENTS

This work is financially supported by the Thailand Research Fund (TRF). Y. C. and W. P. thank the Graduate School of Chiang Mai University and the Development and Promotion of Science and Technology Talent Project, Institute for Promotion of Teaching Science and Technology for graduate scholarships.

SUPPLEMENTARY MATERIAL

Crystallographic data for compound **1** is available as supplementary material of this article in cif format [download].

REFERENCES

1. M. R. Maurya and A. Kumar, "Oxovanadium (IV) based coordination polymers and their catalytic potentials for the oxidation of styrene, cyclohexene and *trans*-stilbene", *J. Mol. Catal. A: Chem.*, **2006**, *250*, 190-198.
2. C. Hiort, J. Goodisman and J. C. Dabrowiak, "Cleavage of DNA by the insulin-mimetic compound $NH_4[VO(O_2)_2(phen)]$", *Biochem.*, **1996**, *35*, 12354-12362.
3. J. H. Hwang, R. K. Larson and M. M. Abu-Omar, "Kinetics and mechanistic studies of anti-carcinogenic bisperoxovanadium(V) compounds: Ligand substitution reactions at physiological pH and relevance to DNA interactions", *Inorg. Chem.*, **2003**, *42*, 7967-7977.
4. L. Mafra, F .A. Almeida Paz, F. Shi, C. Fernandez, T. Trindade, J. Klinowski and J. Roch, "A pentanuclear oxovanadium(V) phosphate complex with phenanthroline", *Inorg. Chem. Commun.*, **2006**, *9*, 34-38.
5. H. Kumagai, M. Endo, S. Kawata and S. Kitagawa, "A mixed-valence tetranuclear vanadium(IV,V) complex $[V_4O_4(\mu\text{-}OEt)_2\text{-}(\mu\text{-}O)2(OEt)_4(phen)_2]$", *Acta Crystallogr. C*, **1996**, *52*, 1943-1945.
6. J. P. Launay, Y. Jeannin and M. Daoudi, "Mixed-valence complexes containing the $V_2O_3^{3+}$ core. Structure and properties of $H[V_2O_3(pmida)_2]\cdot 4H_2O$ and $K_7[V_9O_{16}(bdta)_4]\cdot 27H_2O$", *Inorg. Chem.*, **1985**, *24*, 1052-1059.

Maejo Int. J. Sci. Technol. **2011**, *5*(01), 83-95

7. X. H. Huang, C. C. Huang, X. H. Qin, L. S. Zhai and D. S. Liu, "A novel mixed-valence vanadium(IV/V) complex containing linear mono-μ-oxo $[V_3O_5]^{4+}$ core", *Inorg. Chem. Commun.*, **2008**, *11*, 1236-1238.
8. Stoe & Cie X-AREA (Version 1.18), Stoe & Cie , Darmstadt, Germany (**2002**).
9. Stoe & Cie X-RED (Version 1.04), Stoe & Cie, Darmstadt, Germany (**2002**).
10. J. D. Meulener and H. Tompa, "The absorption correction in crystal structure analysis", *Acta Crystallogr.*, **1965**, *19*, 1014-1018.
11. G. M. Sheldrick, "SHELXS-97: Program for solving crystal structure", University of Gottingen, Germany (**1997**).
12. G. M. Sheldrick, "SHELXL-97: Program for crystal structure refinement", University of Gottingen, Germany (**1997**).
13. L. J. Farrugia, "*WinGX* Suite for small-molecule single-crystal crystallography", *J. Appl. Crystallogr.*, **1999**, *32*, 837-838.
14. V. S. Urusov and I. P. Orlov, **"**State-of-art and perspectives of the bond-valence model in inorganic crystal chemistry", *Crystallogr. Rep.*, **1999**, *44*, 686-709.
15. F. J. Carver, C. A. Hunter and E. M. Seward, "Structure-activity relationship for quantifying aromatic interactions", *Chem. Commun.*, **1998**, 775-776.
16. S. B. Ferguson, E. M. Sanford, E. M. Seward and F. Diederich, "Cyclophane-arene inclusion complexation in protic solvents: Solvent effects versus electron donor-acceptor interactions", *J. Am. Chem. Soc.*, **1991**, *113*, 5410-5419.
17. C. A. Hunter and J. K. M. Sanders, "The nature of π-π interactions", *J. Am. Chem. Soc.*, **1990**, *112*, 5525-5534.
18. T. M. Krygowski, M. K. Cyranski, Z. Czarnocki, G. Hafelinger and A. R. Katritzky, "Aromaticity: A theoretical concept of immense practical importance", *Tetrahedron*, **2000**, *56*, 1783-1796.
19. T. M. Krygowski, "Crystallographic studies of inter- and intramolecular interactions reflected in aromatic character of π-electron systems", *J. Chem. Inf.: Comput. Sci.*, **1993**, *33*, 70-78.
20. T. M. Krygowski and M. K Cyranski, "Two faces of the structural aspects of aromaticity", *Phys. Chem. Chem. Phys.*, **2004**, *6*, 249-255.
21. F. H. Allen and W. D. S. Motherwell, "Applications of the Cambridge structural database in organic chemistry and crystal chemistry", *Acta Cryst.*, **2002**, *B58*, 380-388.
22. G. A. Jeffrey, "An introduction to hydrogen bonding", Oxford University Press, New York, **1997**.
23. L. Chen, F. Jiang, Z. Lin, Y. Zhou, C. Yue and M. Hong, "A basket tetradecavanadate cluster with blue luminescence", *J. Am. Chem. Soc.*, **2005**, *127*, 8588-8589.
24. Y. C. Liu, Z. F. Chen, S. M. Shi, H. S. Luo, D. C. Zhong, H. L. Zou and H. Liang, "Synthesis, crystal structure of polyoxovanadate complex of ciprofloxacin: $V_4O_{10}(\mu_2\text{-}O)_2[VO(H\text{-}Ciprof)_2]_2\cdot 13H_2O$ by hydrothermal reaction**",** *Inorg. Chem. Commun.*, **2007**, *10*, 1269-1272.
25. Y. Gong, C. Hu and H. Li, "Synthesis and crystal structure of a novel organic-inorganic hybrid hexavanadate $[(phen)_4V_6O_{12}(CH_3OH)_4]\cdot 2CH_3OH\cdot 4H_2O$", *J. Mol. Struct.*, **2005**, *749*, 31-35.
26. J. I. Pankove, "Optical processes in semiconductors", Prentice-Hall, Englewood Cliffs, **1971**, 34-42.

Chiang Mai J. Sci. 2011; 38(2) : 252-262
www.science.cmu.ac.th/journal-science/josci.html
Contributed Paper

Solvothermal Synthesis, Sintering Behavior and Dielectric Properties of Potassium Niobate Fine Powders

Kittichai Jinachai [a], Athipong Ngamjarurojana [b] and Apinpus Rujiwatra*[a]
[a] Department of Chemistry and Center for Innovation in Chemistry (PERCH-CIC), Faculty of Science, Chiang Mai University, Chiang Mai 50200, Thailand.
[b] Department of Physics and Materials Science, Chiang Mai University, Chiang Mai 50200, Thailand.
*Author for correspondence; e-mail: apinpus@gmail.com

Received: 22 July 2010
Accepted: 30 December 2010

ABSTRACT

Fine potassium niobate powders composing of sub-micrometer sized lumber particles were synthesized under solvothermal conditions, with the use of mixed water-ethyl alcohol as the reaction medium and the application of the prior ultrasonication as the activation step. The influences of ethyl alcohol on particle shape and size, and the prior ultrasonication on the sintering behavior of the synthesized powders are present and discussed in relative to the conventional hydrothermal cases. The temperature dependent dielectric constants (ε_r) and dielectric losses (tan δ) of the sintered ceramics are also included, showing the origin of the losses to stem from the loss of potassium oxide in the sintering process.

Keywords: potassium niobate, solvothermal synthesis, sonocatalyzation, sintering, dielectric property.

1. INTRODUCTION

The emergence of the "*green attitude*" has resulted in the attempts to develop the green alternatives for various technologically important materials and processes including lead, despise of its important role technologically. Along this line, potassium niobate ($KNbO_3$, KN) has appeared as one of potential candidates for the lead-free piezoelectric materials. This is due to its excellent inherent properties and potential applications, for example, as an optical wave guide and devices for frequency doubling, holographic storage and surface acoustic wave [1-5]. The material is conventionally prepared by solid state reactions, which demand high temperatures and multiple cycles of heating-and-grinding to assure the completeness of the reactions [6]. Besides being the energy-consumable process, the other drawbacks of the solid-state processes such as the formation of undesired impurities and aggregations are inherent [7]. During the last decade, the hydrothermal technique has been proved to be efficient for the preparation of KN in various forms, including fine powder, one-dimensional structure and thin film [8-11]. Despise of the promising future of the material and the technique, the practical application and commercialization of KN yet faces a major problem with sintering. At effective sintering temperature and duration,

the rapid vaporization of potassium oxide (K_2O) and the large difference in properties of the cation involved result in the chemical control and densification problems [1]. The additions of other aiding compounds, such as magnesium oxide (MgO) and lead oxide (PbO), were reported to relieve the problems [12, 13].

Here, the adaptation of hydrothermal process by the use of mixed water-ethyl alcohol as reaction medium for the preparation of KN fine powders is described. The application of the ultrasonic wave on the reaction mixtures in prior to the synthesis is discussed. The sintering behavior and the preliminary investigation of the dielectric properties of the sintered ceramics are reported.

2. MATERIALS AND METHODS

The mixtures of niobium oxide (Nb_2O_5, Sigma-Aldrich 99.99%, 0.0056 mol) and potassium hydroxide (KOH, Merck 85%, 0.0028 mol) were first prepared in mixed water-ethyl alcohol liquid medium (0.278 mol of water, 0.086 mol of ethyl alcohol; C_2H_5OH, Merck 99.9%). The employed amount of KOH functioning as both reagent and mineralizer in the synthesis is the amount reported as the critical limit providing the successful synthesis [14]. Each mixture was then stirred and transferred into Teflon liners up to *ca.* 80% filling volume capacity. The mixtures were subsequently subjected to an autogenous pressure developed at 200°C for 1-24 hours. In order to study the effect of ultrasonication, some samples are ultrasonicated at 40(±5)°C for 1 h using a laboratory ultrasonic bath (Bandelin Electronic RK255H, 160/320W, 35kHz) before the reactions. The synthesized powders were finally recovered by filtration and washed with water until the pH of the filtrate was *ca.* 7 to assure the complete removal of the alkali.

Powder X-ray diffraction (XRD; Bruker D8 Advance diffractometer, Ni-filtered, CuK_a, λ=1.54098 Å, 40 kV, 30 mA) was used in characterizing the synthesized crystalline phases. Lattice parameters of these phases were refined from the collected XRD patterns. Selected area electron diffraction (SAED) equipped by a transmission electron microscope (TEM; JEOL JEM-2010) was also used in characterizing growth direction of the elongated particles, whereas a field emission scanning electron microscope (SEM; JEOL JSM-6335F) was used in examining morphologies and sizes of the composing particles.

The synthesized powders composing of a single orthorhombic KN according to the XRD results were chosen for the sintering experiments. The powders were ground and pressed uniaxially at 100 bars and room temperatures to make the pellets of 10.15 mm in diameter and 2.45-2.75 mm in thickness. The obtained pellets were then sintered at 1,025°C for 1 hour (Carbolite, 2416CG) using a heating-cooling rate of 3°C min^{-1}. After the sintering, densities of the sintered ceramics were evaluated uisng Archimedes technique [15]. Phase and microstructure of the sintered pellets were investigated by XRD and FESEM, respectively.

The dielectric properties of the sintered ceramics were studied as functions of both temperature and frequency using an automated dielectric measurement system and a silver electrode (Dupont, QS 171), which was prepared by printing on the lapped surfaces followed by firing at 600°C for 1 h. The computer-controlled dielectric measurement system consists of a precision LCR meter (Thonghui, TH2819A) and a temperature chamber. The temperature dependent measurements were performed using a Keithley Model 2,000-digit multimeter which was equipped by a temperature chamber, when the capacitance and the dielectric loss

tangent were determined over the temperature range of 50-500°C with the frequency ranging from 0.1 to 100 kHz.

3. RESULTS AND DISCUSSION

Figure 1 and 2 shows the XRD patterns of the powders obtained from the reactions conducted at 200°C for varied reaction times, with and without prior ultrasonication for an hour, respectively. The application of the ultrasonication as described did not showed any significant difference in the XRD patterns of the synthesized powders. When the reactions were conducted for an hour, the presence of the other diffraction peaks which were not of the desired KN was plain. The identification of these phases could not be precisely done due to a deficiency in number and intensity of these peaks. It can be nonetheless ascertained that the formation of KN, which could be indexed as the orthorhombic phase with space group *Cm2m* (JCPDS 32-822), already occurred as the major phase. According to the XRD results, the pure phase of KN could be obtained after 3 h, irrespective to the application of the prior ultrasonication on the reaction mixtures. The obtained KN powders could be readily indexed and refined in orthorhombic *Cm2m* (JCPDS 32-822), giving a = 5.689(8)-5.695(8) Å, b = 5.721(11)-5.737(10) Å and c = 3.982(11)-3.984(12) Å). There was not therefore any apparent effect of the ultrasonication on the formation and phase of the synthesized KN powders, within a limit of the XRD technique.

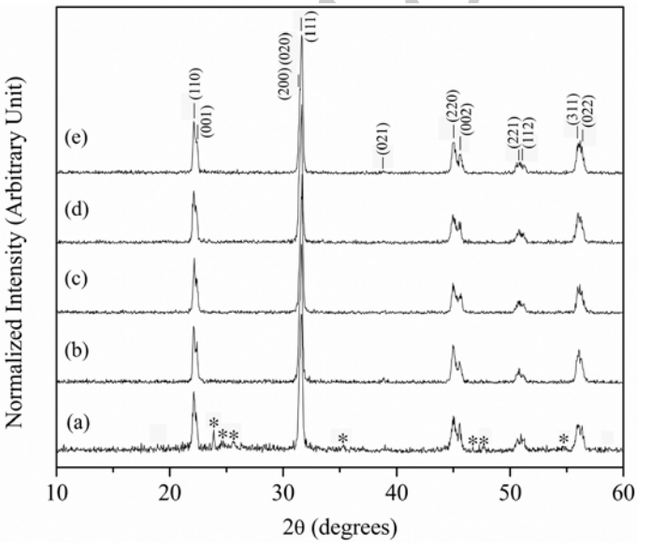

Figure 1. The XRD patterns of the powders obtained from the reactions conducted at 200°C for (a) 1 h, (b) 3 h, (c) 6 h, (d) 12 h and (e) 24 h on the ultrasonicated mixtures; * indicates unidentified diffraction.

The SEM images show the synthesized KN powders to compose mostly of lumber particles with a few fraction of pseudo-cubic particles, independent also on the preparative conditions. Figure 3 shows the representative images of the particles obtained from the reactions with and without the prior ultrasonication, illustrating well-defined shape

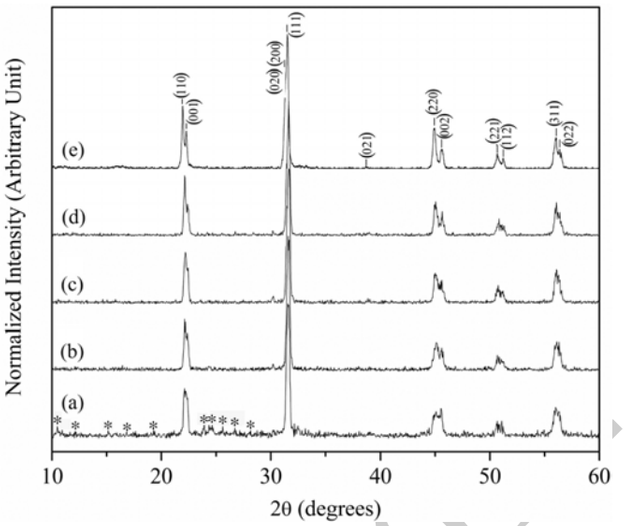

Figure 2. The XRD patterns of the powders obtained from the reactions conducted at 200°C for (a) 1 h, (b) 3 h, (c) 6 h, (d) 12 h and (e) 24 h on the mixtures without the prior ultrasonication; * indicates unidentified diffraction.

of the KN particles for the powders obtained from the reactions with the prior ultrasonication. Sizes of these KN particles measured directly from the SEM were distributed in a range of approximately 0.1-1 mm and 0.15-2.5 μm, for the short and long axes, respectively. In contrast, the particles with a serious melting and poor-defined particle boundary were obtained from the reactions conducted without the prior application of the ultrasonic wave. This may be rationalized by the ability of the ultrasonic wave in inducing the nucleation and in creation of the highly reactive and clean surface on the created nuclei which should promote the clean crystal growth in the afterward reactions [16]. The pressure generated under the solvothermal conditions generally causes the nucleation to occur as simultaneously as the crystal growth, which commonly results in hard aggregates [17].

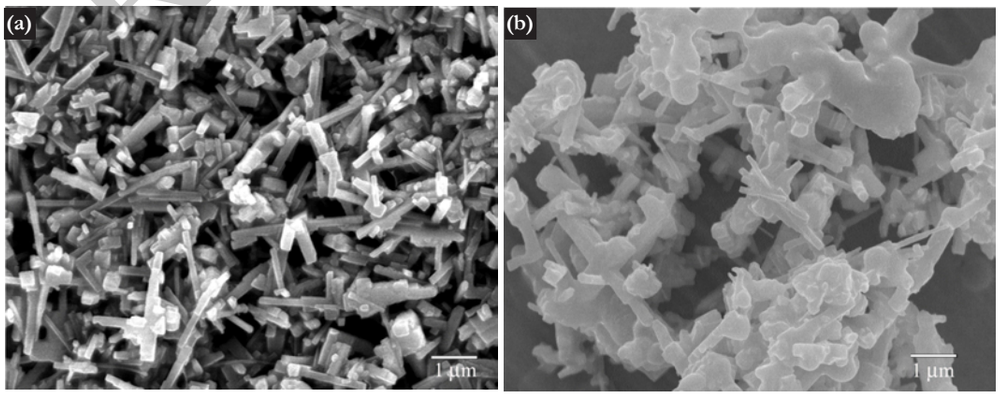

Figure 3. The SEM images exemplifying the lumber particles of potassium niobate derived from the reactions on (a) the ultrasonicated reaction mixture and (b) the mixture without prior ultrasonication, conducted under the same synthesis conditions.

In comparison to the former reports on the synthesis of KN fine powders using the hydrothermal reactions at the same temperature and KOH concentration of 200°C and 8 moldm^{-3}, several differences could be pointed out, although phase of the obtained KN is the same, which is the orthorhombic phase [14]. First, shape of the hydrothermally derived KN particles was largely psuedocubic, when the lumber particles could be obtained in this study. Second, sizes of the pseudocubic particles were also distributed in a larger size region of 1-4 mm, compared to the sub-micrometer sizes reported here. The use of mixed water-ethyl alcohol as a liquid medium apparently provided smaller sized and more elongated particles. Regarding the effective reaction, the employment of ethyl alchohol and the application of ultrasonic wave on the reaction mixtures did not result in any significant change.

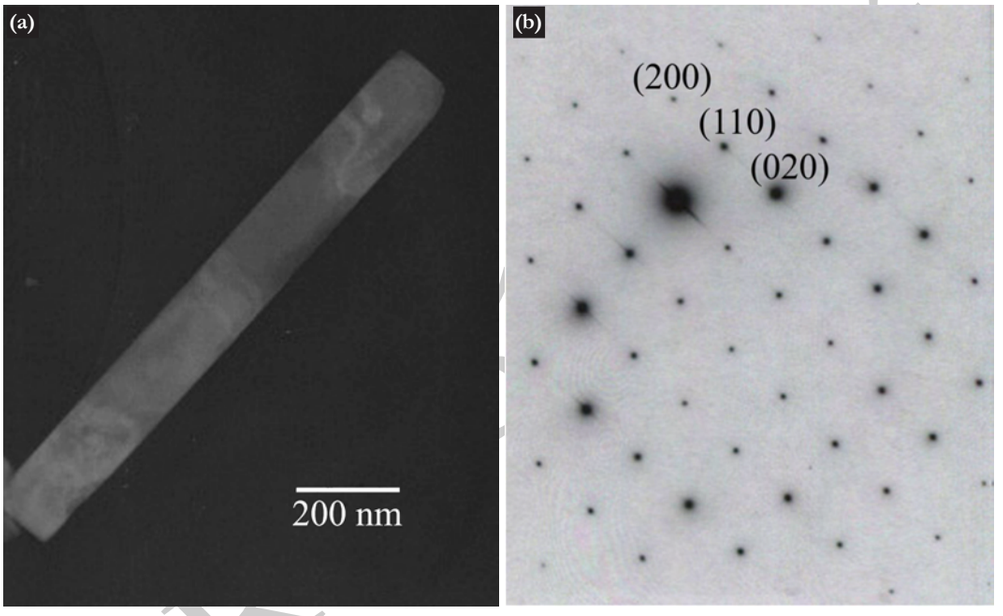

Figure 4. (a) The TEM image of the typical lumber potassium niobate particle with (b) the corresponding indexed SAED pattern based on the orthorhombic *Cm2m* (JCPDS 32-822).

The structure of the lumber particles was also evaluated through selected area electron diffraction (SAED) in the transmission electron microscope. Figure 4 shows the TEM images of the typical particle and the corresponding SAED pattern, which could be well indexed in the assigned orthorhombic *Cm2m* phase. The growth direction apparently lied along the crystallographic [*110*] direction.

The KN powders characterized by the XRD to be of the single orthorhombic phase were chosen for the sintering experiments, including those obtained from the reactions conducted for 3-24 h, both with and without the prior ultrasonication. After the sintering, the diameters and thickness of the sintered bodies were substantially reduced; 8.35-8.60 mm and 2.10-2.30 mm for the sintered pellets compared to 10.15 mm and 2.45-2.75 mm for the green bodies. The contraction in diameter of *ca.* 18% was slightly better than the contraction in thickness, *ca.* 14-16%. This

corresponded to the volume shrinkage of *ca.* 36-42%. The densities of the sintered ceramics were measured, giving the results of *ca.* 95-98% in relative to the crystallographic density, 4.62 gcm^{-3}. No correlation between the obtained values and the variation in synthesis reaction time could be observed, although the powders obtained from the reactions with the prior ultrasonication showed slightly better volume shrinkage and densification. The shrinkage and relative densities of *ca.* 40-42% and 96-98%, respectively, could be calculated for the ultrasonication cases, when the shrinkage of 36-39% with the corresponding relative densities of *ca.* 95% were obtained for the other cases. This could be due to the better defined particle shape and less melting between the particles in the former case as revealed by the SEM images.

The SEM images taken on the sintered KN pellets gave supportive evidence, as exemplified in Figure 5. The grain sizes of the sintered ceramic were measured and a slight growth of the sintered grain was revealed; 0.15-3.95 μm and 0.25-4.45 μm for the short and long axes. These results agree well with the calculated volume shrinkages and the calculated relative densities. It is apparent that the growth process occurred better along the short axis than the long axis, and resulted in an evolution of a pseudo-cubic grain from the pressurized lumber particles. It is also evident that the melting between grains was serious for the pellets which were prepared from the powders derived from prolonged solvothermal reaction, particularly those with the prior ultrasonication treatment. Regarding the hygroscopic problem commonly encountered with the sintering of KN [18], it was not the case in this study if the washing of the remaining alkali was performed carefully. The sensitivity to the atmospheric water may therefore attribute to the remaining of KOH which is hygroscopic.

The XRD was used to follow the change in phase, if any, after the sintering and the results are shown in Figure 6(a) and Figure 7(a). The remaining of the orthorhombic KN was significant, although the formation of the niobium-rich phase, KNb_3O_8, suggesting the loss of K_2O during the sintering were evident. A develop of a big lump at low 2θ region was additionally plain, implying the corruption of the long range order in the structure although the distinction between the three most intense peaks, including (*020*), (*200*) and (*111*), were clearer after the sintering. The exception was apparent for the sintered pellets which were prepared from the powders obtained from 24 h reaction with the prior ultrasonication, where there was no signature of the KNb_3O_8 phase in the XRD pattern. This again reflects the merit of the application of the prior ultrasonication.

Figure 6(b) and Figure 7(b) show the temperature dependence of dielectric constants (ε_r) and dielectric loss tangents (tan δ) at 100 kHz for the sintered KN ceramics, revealing a difference in the measured values depending on the purity of KN according to the XRD patterns shown in the corresponding Figure 6(a) and Figure 7(a), respectively. Phase transition from the ideal cubic phase to the tetragonal phase was found around 425°C, while the tetragonal to the orthorhombic occurred around 225°C. The results are well consistent with the formerly reported values for the KN ceramics [18-21]. In the case of the ceramic composing of KN as nearly a single phase which was the one derived from the powders prepared from 3 h - 24 h reaction with the prior ultrasonication, the dielectric constants has increased with also a sharp peak transition, especially for the KN ceramics of high densities and good crystallinity. The KN ceramics which were fabricated from the powders prepared from the same conditions but without the prior ultrasonication, showed

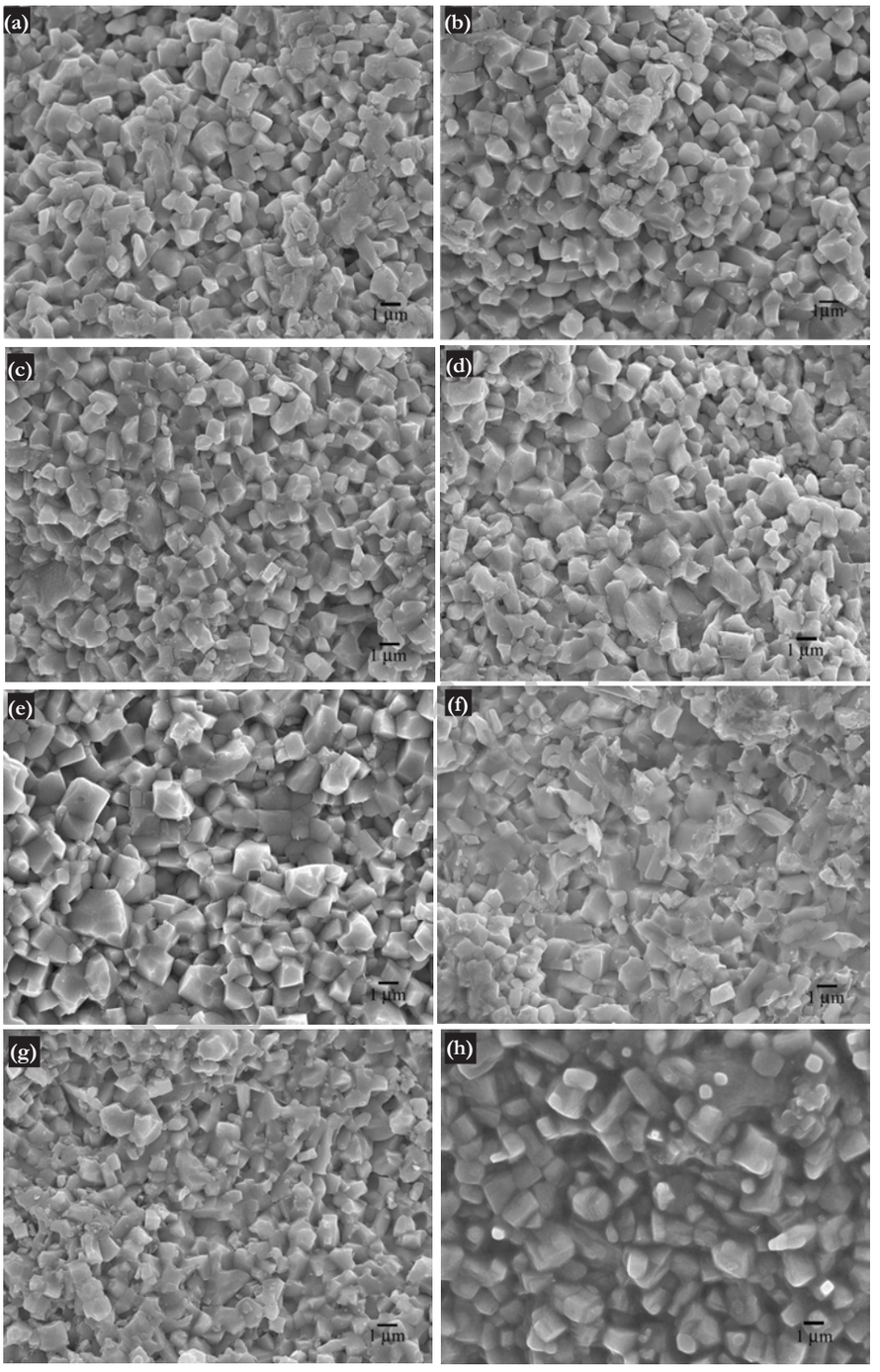

Figure 5. The SEM images of the sintered KN ceramics prepared from the powders obtained from the reactions conducted at 200°C for (a) 3 h, (b) 6 h, (c) 12 h and (d) 24 h on the mixtures without the prior ultrasonication, compared with those of the sonicated mixtures; (e) 3 h, (f) 6 h, (g) 12 h and (h) 24 h.

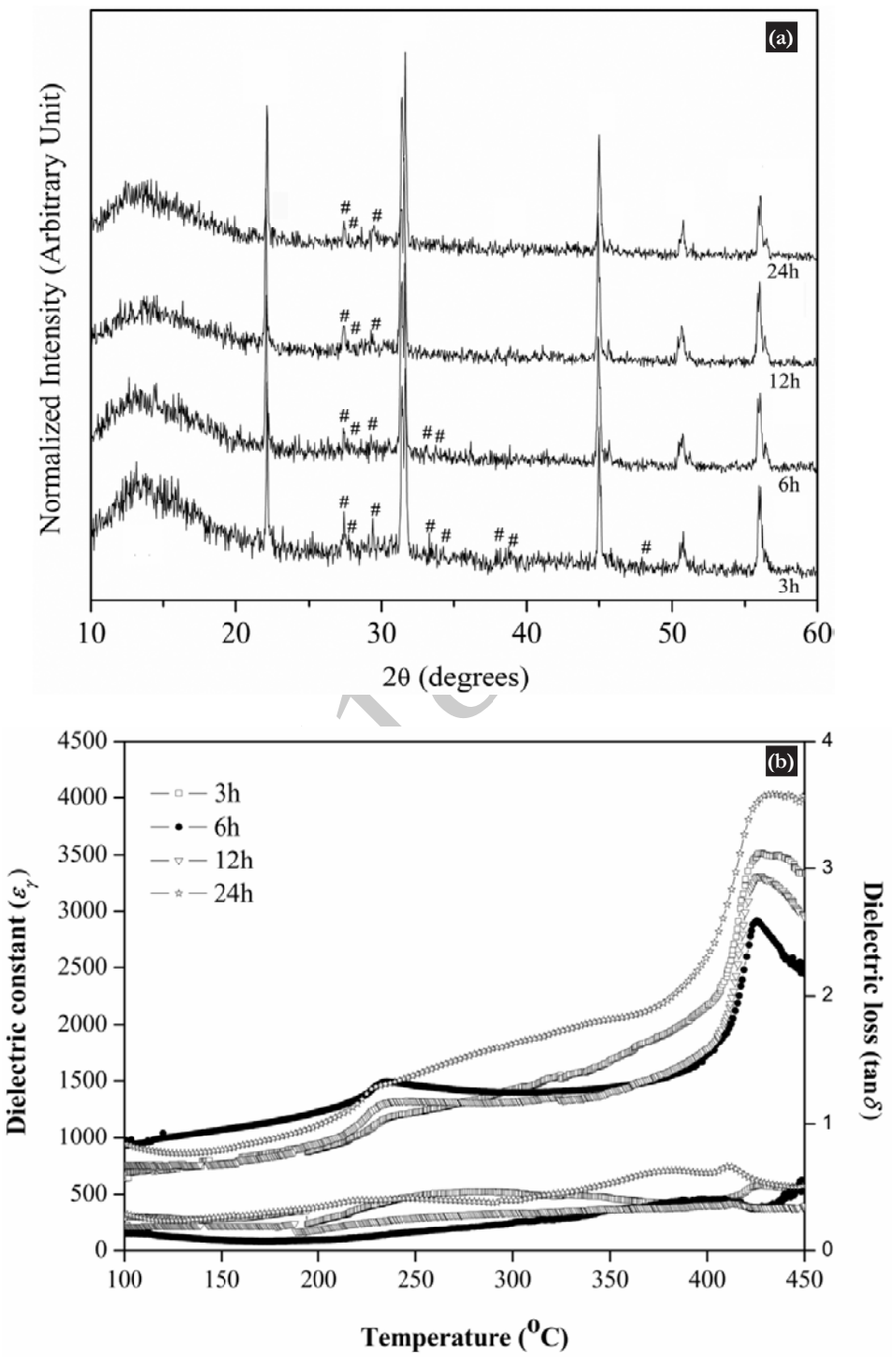

Figure 6. (a) The XRD patterns (# = KNb_3O_8) and (b) temperature dependence of dielectric properties measured on the KN ceramics prepared from the powders obtained from the reactions conducted at 200°C for (a) 3 h, (b) 6 h, (c) 12 h and (d) 24 h on the mixtures without the prior ultrasonication.

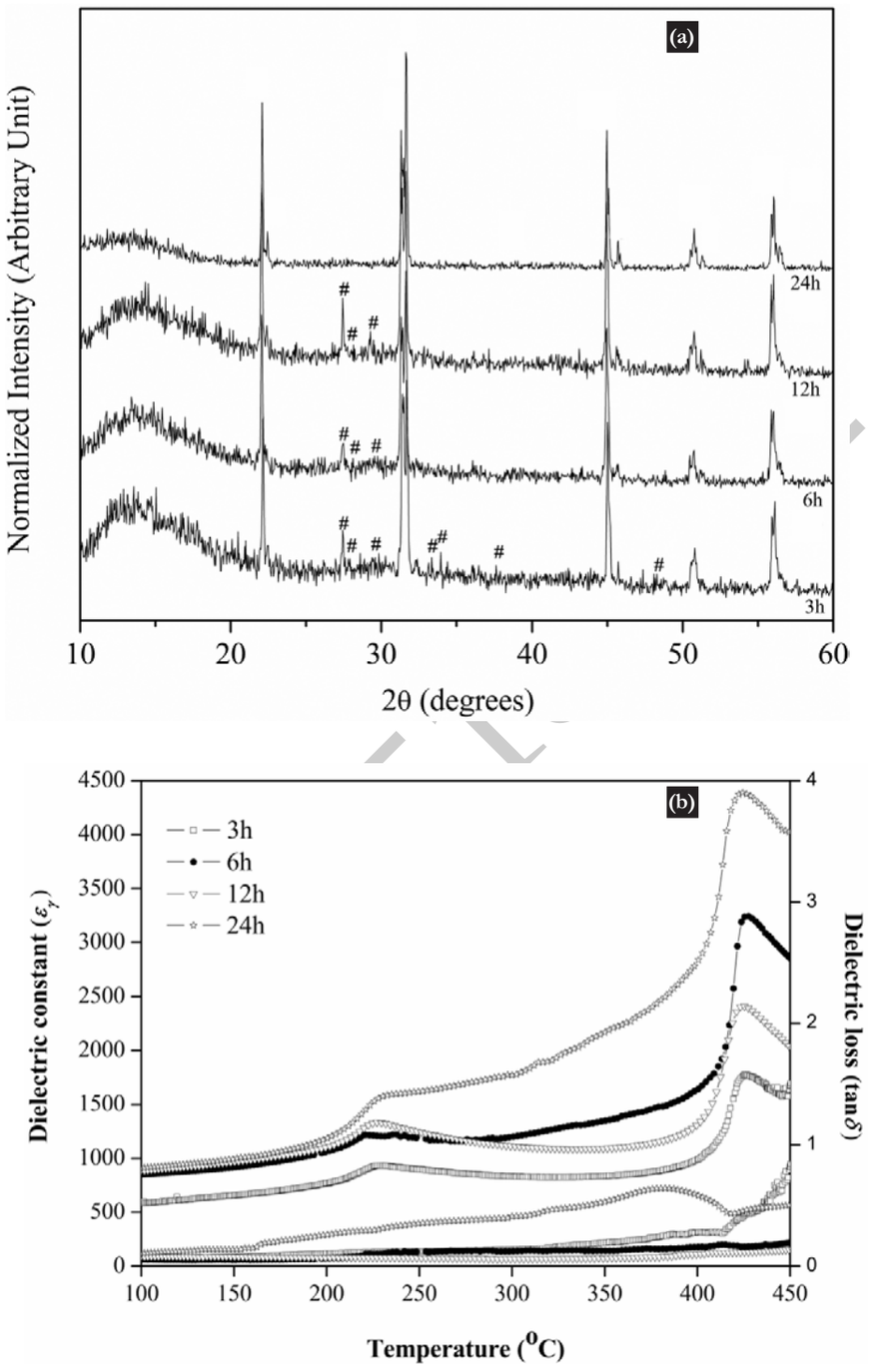

Figure 7. (a) The XRD patterns (# = KNb_3O_8) and (b) temperature dependence of dielectric properties of the KN ceramics prepared from the powders obtained from the reactions conducted at 200°C for (a) 3 h, (b) 6 h, (c) 12 h and (d) 24 h on the mixtures with the prior ultrasonication.

a broad peak transition, which should probably be due to the presence of the liquid phase in microstructure. This results were consistent with the XRD and SEM results that showed the formation of the second phase KNb_3O_8 and the liquid phase in the microstructure due to the evaporation of K_2O. In general, it was evident that the ceramics prepared from the powders which were derived from the reactions with the prior ultrasonication showed higher dielectric constants and lower dielectric loss than those without the prior ultrasonication. This may attribute to the increase in oxygen vacancies which on the other hand contribute to the increase in conductivity [22].

4. Conclusions

In summary, the sonocatalyzed ethanothermal process has been attempted with the synthesis of potassium niobate fine powders, and proved to be able to provide the orthorhombic phase-pure KN powders under mild condition and rapid reaction times of at least 3 h. The use of mixed water-ethyl alcohol liquid medium apparently favored the formation of elongated lumber KN particles of sub-micrometer sizes, when the application of the prior ultrasonication on the reaction mixtures led to significant differences in sintering behavior, loss of K_2O and the tolerance of the orthorhombic KN to the sintering, as well as the corresponding dielectric properties. Dense KN ceramics of over 95% relative densities could be fabricated by conventional sintering without the hygroscopic problem. The significance of the prior ultrasonication on the reaction mixtures during the synthesis in enhancing both physical and electrical properties of the sintered ceramics was clearly illustrated.

Acknowledgements

The Thailand Research Fund is acknowledged for financial support. K. Jinachai thanks to Department of Chemistry, Faculty of Science and the Graduate School, Chiang Mai University for a teaching assistant scholarship.

References

[1] Kakimoto K., Masuda I. and Ohsato H., Lead-free $KNbO_3$ piezoceramics synthesized by pressure-less sintering, *J. Euro. Ceram. Soc.*, 2005; **25**: 2719-2722.

[2] Tanaka K., Kakimoto K.I. and Ohsato H., Morphology and crystallinity of $KNbO_3$- Based nano powder fabricated by sol–gel process, *J. Euro. Ceram. Soc.*, 2007; **27**: 3591-3595.

[3] Pribosic I., Makovec D. and Drofenik M., Chemical synthesis of $KNbO_3$ and $KNbO_3$– $BaTiO_3$ ceramics, *J. Euro. Ceram. Soc.*, 2005; **25**: 2713-2717.

[4] Yang R., Shen S.Y., Wang C.B., Shen Q. and Zhang L.M., Pulsed laser deposition of stoichiometric $KNbO_3$ films on Si (100), *Thin Solid Films*, 2008; **516**: 8559-8563.

[5] Muthurajan H., Kumar H.H., Samuel V., Gupta U.N. and Ravi V., Novel hydroxide precursor to prepare $NaNbO_3$ & $KNbO_3$, *Ceram. Int.*, 2008; **34**: 671-673.

[6] Su T., Jiang H., Gong H., Zhai Y., An alternative approach of solid-state reaction to prepare nanocrystalline $KNbO_3$, *J. Mater. Sci.*, 2010; **45**: 3778–3783.

[7] Fluckiger U., Arend H., Oswald H.R., Synthesis of potassium niobate (V) powder, *Am. Ceram. Soc. Bull.*, 1977; **56**: 575-577.

[8] Kumada N., Kyoda T., Yonesaki Y., Takei T. and Kinomura N., Preparation of $KNbO_3$ by hydrothermal reaction, *Mater. Res. Bull.*, 2007; **42**: 1856-1862.

[9] Liu J.W., Chen G., Li Z.H. and Zhang

Z.G., Hydrothermal synthesis and photocatalytic properties of $ATaO_3$ and $ANbO_3$ (A=Na and K), *Int. J. Hydrogen Energy*, 2007; **32**: 2269-2272.

[10] Suchanek W.L., Synthesis of potassium niobiate ($KNbO_3$) thin films by low-temperature hydrothermal epitaxy, *Chem. Mater.*, 2004; **16**: 1083-1090.

[11] Kajiyoshi K., Yanagisawa K., Feng Q. and Yoshimura M., Preparation of complex oxide thin film under hydrothermal and hydrothermal electro-chemical conditions, *J. Mater. Sci.,* 2006; **41**: 1535-1540.

[12] Kosec M., Kolar D., On activated sintering and electrical properties of $NaKNbO_3$, *Mater. Res. Bull.*, 1975; **10**: 335-340.

[13] Pribošič I., Makovec D., Drofenik M., PTCR effect in Pb-doped $KNbO_3$, *J.Mater. Res.*, 2002; **17** (12): 2989-2992.

[14] Lu C.H., Lo S.Y., Lin H.C., Hydrothermal synthesis of non linear optical potassium niobate ceramic powder, *Mater. Lett.*, 1998; **34**: 172-176.

[15] Morrel R., Handbook of properties of technical & engineering ceramics, *HMSO Publications*, London, 1989.

[16] Suslick K.S., Sonochemistry, *Science*, New Series, 1990; **247**(4949): 1439-1445.

[17] Riman R.E., Suchanek W.L. and Lencka M.M., Hydrothermal crystallization of ceramics, *Ann. Chim. Sci. Mat.*, 2002; **27** (6): 15-21.

[18] Matsumoto K., Hiruma Y., Nagata H. and Takenaka T., Piezoelectric properties of $KNbO_3$ ceramics prepared by ordinary sintering, *Ferroelectrics*, 2007; **358**: 169-174.

[19] Ishikawa M., Takiguchi N., Hosaka H. and Morita T., Nondoped potassium niobate ceramics synthesized by hydrothermal method with optimum temperature condition, *Jpn. J. Appl. Phys.*, 2008; **47** (5): 3824-3828.

[20] Tan C.K., Goh G.K.L. and Cheah W.L., Dielectric properties of hydrothermally epitaxied I-V perovskite thin films, *Thin Solid Films*, 2007; **515**: 6577-6581.

[21] Ishikawa M., Kadota Y., Takiguchi N., Hosaka H. and Morita T., Synthesis of Nondoped Potassium Niobate Ceramics by Ultrasonic Assisted Hydrothermal Method , *Jpn. J. Appl. Phys.*, 2008; **47**(9): 7673-7677.

[22] Singh G., Tiwari V.S. and Gupta P.K., Role of oxygen vacancies on relaxation and conduction behavior of $KNbO_3$ ceramic, *J. Appl. Phys.,* 2010; **107**: 064103.